Mechanoresponsive Supramolecular Systems for Drug Release

Inaugural-Dissertation

zur Erlangung des Doktorgrades der

Mathematisch-Naturwissenschaftlichen Fakultät

der Heinrich-Heine-Universität Düsseldorf

vorgelegt von

Robin Marius Küng

aus Düsseldorf

Düsseldorf, März 2023

Aus dem Institut für Organische Chemie und Makromolekulare Chemie
der Heinrich-Heine-Universität Düsseldorf

Gedruckt mit Genehmigung der

Mathematisch-Naturwissenschaftlichen Fakultät der

Heinrich-Heine-Universität Düsseldorf

Berichterstatter:

1. Dr. Bernd M. Schmidt
2. Prof. Dr. Thomas J. J. Müller

Tag der mündlichen Prüfung: 22.06.23

Die hier vorliegende Arbeit wurde im Zeitraum von Dezember 2018 bis Februar 2023 unter Anleitung von Dr. Bernd M. Schmidt am Institut für Organische Chemie und Makromolekulare Chemie an der Heinrich-Heine-Universität Düsseldorf angefertigt.

Publications of the author during the work on this thesis

1) R. Küng, A. Germann, M. Krüsmann, L. P. Niggemann, J. Meisner, M. Karg, R. Göstl, B. M. Schmidt, *Chem. Eur. J.*, **2023**, doi: 10.1002/chem.202300079.

   Highlighted in ChemistryViews

   R. Küng, R. Göstl, J. Meisner, M. Karg and B. M. Schmidt wrote the manuscript. R. Küng performed the majority of the experiments in cooperation with A. Germann. M. Krüsmann performed the SAXS measurements and L. P. Niggemann performed the GPC measurements.

2) R. Küng, R. Göstl, B. M. Schmidt, *Chem. Eur. J.*, **2022**, *28*, e202103860.

   Awarded as outstanding review

   R. Küng, R. Göstl and B. M. Schmidt wrote the manuscript. R. Küng designed the cover graphic.

3) R. Küng, T. Pausch, D. Rasch, R. Göstl, B. M. Schmidt, *Angew. Chem. Int. Ed.*, **2021**, *60*, 13626-13630.

   Highlighted on the Cover

   R. Küng, R. Göstl and B. M. Schmidt designed the project; R. Küng performed the majority of the experiments, analyzed the data and wrote the manuscript with R. Göstl and B. M. Schmidt. T. Pausch performed the guest encapsulation studies. D. Rasch performed the GPC measurements. T. Kunde designed the cover graphic.

Poster presentation of national and international conferences of the author during the work on this thesis

1) R. Küng, T. Pausch, D. Rasch, R. Göstl and B. M. Schmidt: “Polymer mechanochemical release of non-covalently bound guests”, SupraChem, Mainz, 2022.
2) R. Küng, T. Pausch, D. Rasch, R. Göstl and B. M. Schmidt: “Polymer mechanochemical release of non-covalently bound guests”, International Symposium on Macrocyclic and Supramolecular Chemistry (ISMSC 2021), online, 2021.
3) R. Küng, T. Pausch, D. Rasch, R. Göstl and B. M. Schmidt: “Polymer mechanochemical release of non-covalently bound guests”, Multiscale Mechanochemistry and Mechanobiology (MechanoChemBio 2021), online, 2021.

Bachelor thesis and research internship

1) “Supramolecular Hydro- and Organogels Synthesis and characterisation”, Anne Germann, bachelor thesis, 2020.
2) Research report about the encapsulation of different guests, Tobias Pausch, research internship, 2020.

Danksagung

An dieser Stelle möchte ich mich direkt bei allen bedanken, die mich während meiner Promotion unterstützt haben.

Ein besonderer Dank gilt an erster Stelle Dr. Bernd M. Schmidt für sein Vertrauen, die finanzielle Unterstützung sowie seine unzähligen Ratschläge und Ideen. Nicht nur hast du es mir ermöglicht während meiner Promotion an einem so interessanten Thema zu arbeiten, sondern ich hatte auch die Möglichkeit, den AK BMSchmidt von Anfang an zu begleiten und mit aufzubauen. Es ist einfach unglaublich, wie schnell die Arbeitsgruppe in dieser kurzen Zeit gewachsen ist und wie viel wir in dieser Zeit erreicht haben. Danke, dass ich ein Teil davon sein durfte!

Prof. Dr. Constantin Czekelius möchte ich nicht nur für die bereitgestellten Chemikalien danken, sondern auch für die zahlreichen, sowie hilfreichen wissenschaftlichen Gespräche.

Außerdem möchte ich Dr. Robert Göstl und seiner Arbeitsgruppe für die hervorragende Kooperation danken. Deine zahlreichen Ratschläge, sowie die technische Unterstützung waren essenziell für das Gelingen der Projekte.

Prof. Dr. Matthias Karg und Marcel Krüsmann danke ich für die SAXS-Messungen der Hydrogele und Jun.-Prof. Dr. Jan Meisner für die CoGEF-Rechnungen.

Herzlich bedanken möchte ich mich bei Mohanad Aian, Tanja Muth, Ralf Bürgel und Dr. Peter Tommes für die Anfertigung der NMR-, sowie Massenspektren.

Ich möchte mich bei den besten Laborkolleg*innen bedanken, die sowohl durch Feedback als auch durch direkte Zusammenarbeit maßgeblich zu dieser Arbeit beigetragen haben. Es war mir eine Freude, Tom, mit dir die Arbeitsgruppe aufzubauen und in all den Jahren zusammenzuarbeiten. Und auch wenn du in deiner Danksagung geschrieben hast, dass du meinen Musikgeschmack oft nicht teilst, hätte ich mir niemanden besseren vorstellen können, um abends nach der Uni mal eben in die Niederlande zu düsen, Rammstein zu hören und morgens um sechs Uhr wieder zurückzufahren, um pünktlich in der Uni zu sein.

Auch Esther möchte ich für eine unvergessliche Zeit im Labor danken. Zwar mochte Tom auch deinen Musikgeschmack nicht, ich dafür umso mehr. Außerdem möchte ich mich auch bei dir für deine Ideen und dein Feedback bedanken.

Besonders bedanken möchte ich mich bei Tobi, welcher während seines Forschungspraktikums einen wichtigen Beitrag zu dieser Dissertation geliefert hat. Es war mir immer eine Freude mit dir über wissenschaftliche oder nicht-wissenschaftliche Themen zu diskutieren und durch deine zahlreichen guten Ideen schätze ich dich sehr als Arbeitskollegen. Viel mehr möchte ich mich jedoch für die mittlerweile sehr gute Freundschaft bedanken, die sich über die Jahre entwickelt hat! Und auch wenn es für dich im Moment schwierig aussieht, sage ich dir als guter Freund: „Du schaffst das schon!“

Anne möchte ich für die großartige Zusammenarbeit an den Hydrogelen danken. Auch wenn Bernd und ich noch immer etwas enttäuscht sind, dass du in die TC gegangen bist.
Der kompletten TI-Gruppe danke ich für die vielen lustigen Momente mit euch.
Vielen Dank an Olli, dass du mich während des Studiums immer zum Weitermachen motiviert hast und auch für den gesunden Konkurrenzkampf, den wir hatten. Ich glaube, ohne dich hätte ich das Studium des Öfteren gerne abgebrochen.
Auch dir, Maki Mark, danke ich für eine super Studienzeit!
Stephan, Ich danke dir für die tolle Freundschaft und auch wenn wir beide im Moment zeitlich sehr eingespannt sind, freue ich mich jetzt schon drauf, dich und deine Familie wiederzusehen!

Meinen Eltern möchte ich ganz besonders dafür danken, dass sie mich bei all meinen Entscheidungen immer unterstützt haben. Ohne euch wäre das alles nicht möglich gewesen und ich bin euch unendlich dankbar dafür.
Zu guter Letzt möchte ich dir danken, Valeria. Ohne deinen Rückhalt, deine Liebe und deine Kraft wäre ich niemals so weit gekommen.

Abstract

Self-assembled metal organic cages are known for their distinct internal cavity, which can be utilized to encapsulate molecules for a variety of purposes. The encapsulation of pharmaceutically active compounds facilitates the transport of those incorporated molecules to release them at a targeted destination. They are therefore particularly intriguing for biomedical applications, since they may both stabilize the incorporated drug and improve its selectivity. However, these cages are often limited by their solubility under physiological conditions or are unable to precisely release their cargo load. Thus, the use of polymer-substituted metal organic cages would make them susceptible to ultrasound irradiation, allowing for a selective drug release by host disassembly.

In this work, a series of polymer-embedded metal organic cages are synthesized. These cages are investigated with respect to their encapsulation properties and, subsequently, for targeted cargo release induced by ultrasound irradiation. The resulting cages are capable of incorporating a variety of hydrophobic guests, including testosterone, progesterone, and ibuprofen. Two of these star-shaped metal organic cages respond to ultrasound irradiation and completely release their cargo load. These cages are the first reported self-assembled metal organic cages that decompose and release their guests upon sonification.

Based on these results, three metal coordination complexes are synthesized to investigate the bond dissociation mechanism. Through the investigation of these mechanoresponsive systems, a reversible bond dissociation process was identified.

Furthermore, the cross-linking of metal organic cages results in the formation of hydrogels, which are investigated in terms of their host-guest behavior as well as their mechanical properties and demonstrate an unusually high thermal stability. Finally, ultrasound irradiation experiments with these hydrogels show their disassembly with subsequent guest release.

Zusammenfassung

Metallorganische supramolekulare Käfigverbindungen sind bekannt für Ihre Eigenschaften einen inneren Hohlraum auszubilden, welcher in der Lage ist, Moleküle aufzunehmen. Die Verkapselung von pharmazeutisch aktiven Substanzen durch jene Käfige ermöglicht es, Medikamente gezielt zu transportieren und bei Bedarf wieder frei zu setzen. Aus diesem Grund finden metallorganische Käfigverbindungen immer häufiger Anwendung für biomedizinische Verfahren. Zum einen können diese Käfige ihren Gast stabilisieren, zum anderen erhöhen sie aber auch die Selektivität des eingeschlossenen Medikaments. Jedoch sind diese oft durch ihre schlechte Löslichkeit unter physiologischen Bedingungen limitiert oder sie sind nicht in der Lage Ihren Gast gezielt freizusetzen. Aus diesem Grund kann in Erwägung gezogen werden, die Käfige mit Polymerketten zu funktionalisieren, um zum einen ihre Löslichkeit unter den gewünschten Bedingungen zu erhöhen als auch eine mechanochemische Aktivierung mit Ultraschall zu ermöglichen. Somit könnte der Wirt gezielt zersetzt werden, um daraufhin den Gast am Wirkort freizusetzen.

In der vorliegenden Arbeit werden mehrere polymersubstituierte Käfigverbindungen synthetisiert. Diese werden auf ihre Wirt/Gast-Eigenschaften untersucht, sowie gezielt auf ihre Fähigkeit, diese Gäste wieder freizugeben. Die hier vorgestellten Käfige sind in der Lage eine Vielzahl von Gästen zu verkapseln, darunter Testosteron, Progesteron und Ibuprofen. Zwei der synthetisierten Käfige können mechanochemisch aktiviert werden, um ihre komplette Fracht freizusetzen und sind die ersten publizierten Käfige ihrer Art.

Aufbauend auf diesen Ergebnissen werden drei kleinere „Mechanophore“ synthetisiert, um Einblicke in den Zersetzungsmechanismus zu erhalten. Durch die so erhaltenen Erkenntnisse konnte erkannt werden, dass es sich bei diesem Zersetzungsmechanismus mit großer Wahrscheinlichkeit um einen reversiblen Prozess handelt.

Schließlich wurden die metallorganischen Käfige durch Polymere quervernetzt und auf ihre Wirt/Gast-Eigenschaften untersucht, als auch ihr Verhalten gegenüber Ultraschall. In diesen Experimenten konnte gezeigt werden, dass die Hydrogele in der Lage sind ihre Fracht gezielt freizusetzen.

Table of content

1 Introduction

1.1 General introduction

At the end of 2019, COVID-19 was identified for the first time and rapidly developed to one of the deadliest pandemics in human history. After three years, COVID-19 has created several social and economic issues, including a global recession and worldwide supply shortages. This pandemic was responsible for approximately 6.6 million deaths, and studies imply that this figure might be even three times higher, culminating in 18.2 million deaths.[1] The first vaccines were distributed only one year after the first appearance of COVID-19, and by December 2021, an anticipated 56 % of the world's population had already been vaccinated. Not only was the development and distribution of these vaccines extraordinarily fast, but they potentially saved the lives of an estimated 14.4 to 19.8 million people.[2] While it is fascinating to see what advances modern medicine has accomplished, other diseases still pose significant challenges. For instance, cancer is one of the top causes of mortality worldwide, despite the fact that Percivall Pott identified the first environmental trigger for this illness 250 years ago.[3] Globally, there are 10 million cancer-related deaths per year and an increase of 23.6 million new cases. This is a 26 % and 21 % increase over the previous decade, respectively.[4] Due to the severe effects, Richard Nixon even declared a "war on cancer" in 1971, and hundreds of billions of dollars have since been spent on research to better understand this disease and develop more efficient treatments. Unfortunately, the concept of a "silver bullet" treatment for several cancer types at once was flawed, and it is doubtful that there will ever be a single cure for cancer.[5] This is due to the fact that when cancer spreads, tumors become incredibly diverse, resulting in a mixed population of cells with a range of biological properties and treatment responses. Even though, tumors are still frequently treated as a whole cell population and as a single, homogeneous disease.[6] And for many decades, only a few options of treatment were available, including surgery, radiation therapy, and chemotherapy.[7, 8] Unfortunately, almost all chemotherapeutic drugs have serious side effects that harm healthy cells as well. However, various pathways involved in the course of cancer therapy have significantly improved, shifting the focus from a generic treatment to a patient-specific therapy.[9] These novel methods include not only combinatorial strategies, but also targeted therapy and nanomedicine. In order to reduce administration dosages, avoid unwanted cytotoxicity and drug resistance, and target cancer cells exclusively, researchers have recently focused a lot of their efforts on developing highly bioavailable nanomedicines.[10] These nanoparticles can subsequently be loaded with drugs and directed to certain areas of the body, where the guest would be released on demand to interact only with the diseased tissue. By using this medicine, it could be feasible to target particular cells with precision, reducing overall drug consumption and associated side effects. In comparison to

conventional methods, substantially higher local drug concentrations can be reached when the medication is delivered to the tissue it is intended to treat (Figure 1).[11]

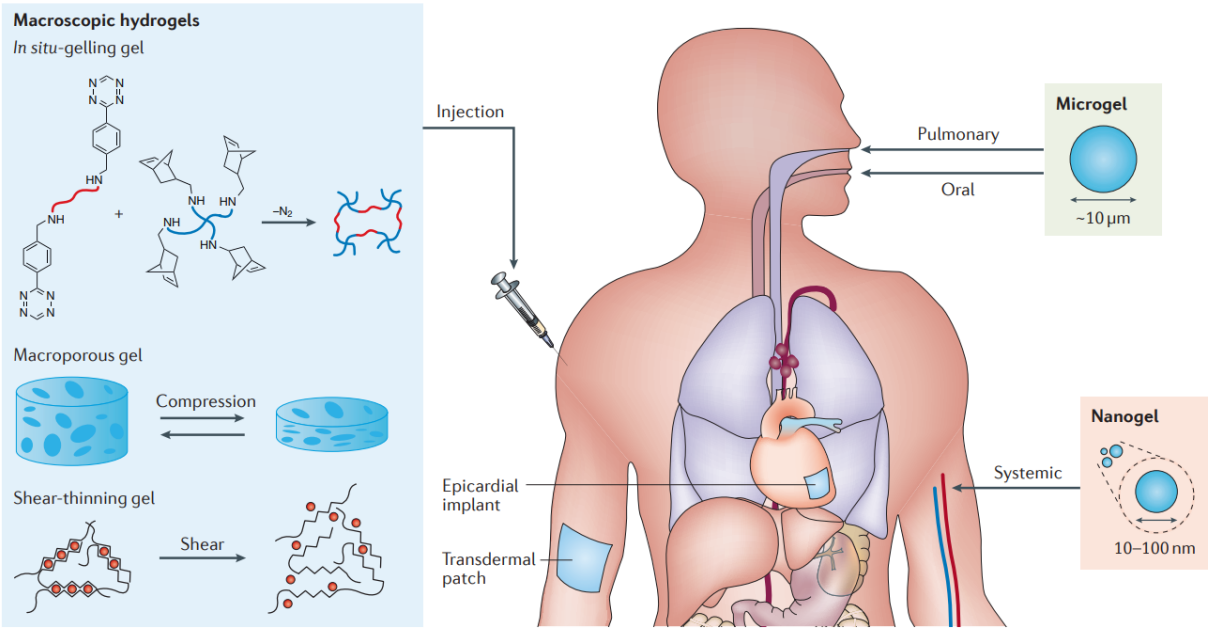

Figure 1: The macroscopic design of a hydrogel determines its delivery route. Substantially higher local drug concentrations can be achieved by utilizing this approach. This graphic was reproduced with permission from Springer Nature.[11]

Nanomaterials, which are defined as materials with diameters between 1 and 100 nm, have a significant impact on the frontiers of nanomedicine, including tissue engineering, drug delivery, microfluidics, and biosensors.[12] A growing interest in these materials resulted in the rapid development of different hosts for drug delivery. Liposomes and micelles, which have received FDA approval, were part of the first generation of nanoparticle-based treatments.[13] These self-assembled systems were capable to incorporate nanoparticles, emphasizing their use for drug delivery or even imaging. Further development was conducted and resulted in a number of successfully employed delivery systems,[12] including supramolecular metal organic cage systems.[14]

It is important to note that each drug delivery system has distinct morphological, physical, and chemical characteristics. Thus, every system exhibits different covalent or noncovalent interactions (hydrogen bonds, π-π-interactions, covalent bonds, Van der Waals interactions) to incorporate the desired drug. The strength of the host-guest properties is determined by these factors, which also affect how fast a guest can be subsequently released.[12] Since drugs often have a very low water solubility, they exhibit simultaneously poor bioavailability and a restricted capacity to diffuse through the outer membrane. As a result, a larger dosage of the medicine is frequently required for the desired outcome. Micelles, liposomes, or supramolecular systems could overcome these issues by incorporating the guest into their cavity and delivering it to the desired place.[15]

The guest encapsulation process can be divided into two methods: passive- and self-delivery. Passive delivery is the most commonly employed strategy for guest uptake and either covalently or non-covalently binds the molecule in its cavity. Drugs that are non-covalently incorporated into their hosts are stabilized by different forces and effects, especially the hydrophobic effect. These systems are designed to disassemble at their target site and subsequently release their incorporated guests. One downside of this strategy is that the drug load of these systems frequently falls below 5 % by weight. A covalent conjugation for guest uptake can be conducted in order to obtain more control over the targeted release. Therefore, the guest will be directly attached to its carrier. This raises the issue that if the medication cannot be cleaved from its carrier, its bioactivity and effectiveness will be decreased, but if the guest dissociates too soon, it will not reach its target location. Thus, the design of the nanocarrier and its purpose must be considered to achieve the desired delivery system.[16, 17]

Self-delivery systems have been of growing interest in recent years. In contrast to the previous approach, these systems use drugs as the building blocks for the delivery system. These nanostructures obtain various morphologies, ranging from nanospheres and rods to nanotubes.[17, 18]

After the successful guest encapsulation, the drug release can be conducted in several ways, whereby the release mechanisms are differentiated into four categories (diffusion, solvent, chemical reactions, and stimuli-responsive release).[19] While solvent-induced and diffusion-related releases can occur at any time, the release caused by chemical reactions or stimuli are precisely triggered by internal or external factors. Internal forces such as pH,[20] ionic strength,[21] or external forces such as light,[22] heat,[23] and ultrasound will trigger the stimuli-responsive release.[12, 24] Each of these triggers has unique advantages and disadvantages that must be taken into account while developing the drug carrier. For example, light illumination is used to provide spatiotemporal control over drug release but can simultaneously result in photothermal damage to healthy tissue and suffer from low tissue penetration depths.[25] Ultrasound, on the other hand, is used in clinical applications for the targeted drug release from nanocarriers like liposomes and micelles (Figure 1 and Scheme 1).[26] Although ultrasound has its drawbacks, including cavitation, acoustic heating, pressure, and torque, it is nevertheless a helpful technique since variables like tissue penetration depth may be controlled by adjusting frequency and energy through exposure time.[27]

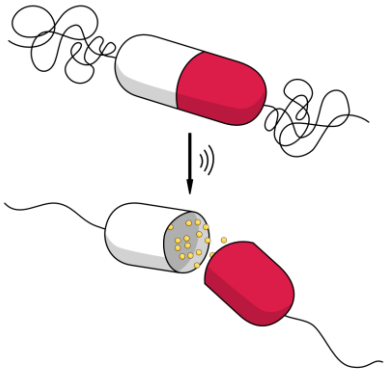

Scheme 1: Schematic representation of the cargo release, induced by ultrasound irradiation.

The primary target of this work is to investigate drug release systems using supramolecular metal organic cages (**MOCs**) as frameworks. Initially, the synthesis of model compound **MOC$_1$**, which bears no polymer chains, will be carried out, and subsequently, its host-guest characteristics will be examined (Section 3.1). Based on these results, two polymer decorated metal organic cages (**polyMOCs**) will be synthesized, and the influence of their increasing molecular weight will be investigated. Encapsulation studies are then carried out to improve understanding of the cavity properties of the M_6L_4-based cages used in this work (Section 3.1.3). Initial sonication experiments reveal the potential of the utilized **polyMOCs** and indicate a necessity of the attached polymer chains. With these results, it was aimed to achieve a targeted guest release by exposing all **MOCs** to ultrasound irradiation (Section 3.1.4). To have a better understanding of the mechanism of bond dissociation, two mechanophores (**MP**) and one control mechanophore (**CMP**) will be synthesized. All **MPs** will then be analyzed with regard to their sonochemical behavior and subsequently compared to the previously synthesized **polyMOCs** (Section 3.2). Computational calculations were performed to provide more details about the actual mechanism during bond scissioning. Ultimately, three hydrogels (**HG$_{1\text{-}6}$**) were synthesized to increase guest uptake while preserving sonochemical susceptibility. These three-dimensional networks were examined with regard to their host-guest properties as well as their guest encapsulation potential. Final release experiments confirm the mechanochemical origin of the cage disassembly and unambiguously prove the successful targeted cargo release (Section 3.3).

1.2 Synthesis of supramolecular coordination cages

The synthesis of three-dimensional **MOCs** starts by assembling different preorganized building blocks. These building blocks consist of metal ions on the one hand and organic ligands on the other. Upon reaction, they form a two- or three-dimensional coordination system, which is often the thermodynamically favored product. The structural outcome of the supramolecular system is therefore highly influenced by the geometry of the utilized ligands and the coordination sphere of the metal ions. Due to the significance of the reversible metal→ligand bond, this approach was coined as "coordination-driven self-assembly".[28] These metal→ligand bonds possess energies between 15 and 25 kcal mol^{-1}, which is substantially lower than the energies of covalent bonds (60-120 kcal mol^{-1}) but still stronger than dispersive interactions (0.5-10 kcal mol^{-1}). This intermediate strength of the metal-ligand bond enables self-repair and self-healing to achieve thermodynamic control over the supramolecular structure. Thus, it allows “incorrectly” formed bonds between different building blocks, intermediates, or supramolecular systems to dissociate and subsequently reassociate to form the "correct" and thermodynamically stable product.[29] In addition, since these metal ions obtain a well-defined coordination geometry, it is even possible to predict the supramolecular structure by deploying rigid donor ligands.

These principles were used to develop a variety of different two-dimensional and three-dimensional metal organic systems. Over time, four methods of synthesizing and predicting high symmetry three-dimensional structures or metalla-macrocycles were established: the directional-bonding approach,[30] symmetry-interaction approach,[31] weak-link approach,[32] and the molecular paneling approach.[33] What all these strategies have in common is that they are mostly used for the formation of platonic geometries. Furthermore, the metal-ligand bond serves as the foundation for all four concepts, and the desired product is the thermodynamically preferred in most cases.

1.2.1 Directional-bonding

This method was first applied by Stang[34] and Fujita[35] in the early 1990s and has since been successfully applied for a variety of metalla-macrocycles as well as supramolecular cages. By combining various building blocks in a combinatorial way, it makes it fairly simple to construct the geometry of a desired assembly. Two requirements must be met by the building blocks in this strategy. Working with stoichiometric ratios is essential to ensure that the required supramolecular structure is formed. And second, in order to create a successful architecture, the building blocks that are used must be largely rigid.

The angular orientation of the two building blocks (organic ligand and metal subunit) ranges from 0 to 180°. In this instance, the metal subunits serve as acceptors, while the organic building blocks serve as

donor ligands. The acceptor must be chosen carefully due to its coordination sites that are fixedly angled with respect to one another. In order to form monocyclic supramolecular systems, both ligands must have symmetry axes that are no higher than 2-fold. When one of the used ligands has a symmetry axis larger than twofold, a polycyclic architecture is produced, whereas three-dimensional supramolecular structures can be produced by combining linear and angular subunits with more than two binding sites (Figure 2).[30, 36]

Different linkers may now be connected in various ways, much like a modular approach, to produce the desired supramolecular architecture. For instance, a rectangle is created when two 0° donors and two 180° acceptors are combined. Due to its modular design, this rectangle may also be created by pairing two 180° donors with two 0° acceptors. The creation of a square can be done in a variety of ways. One method may involve pairing up two 90° donors with two 90° acceptors. Another strategy makes use of four angulated ligands in addition to four linear ligands (Figure 2a). The same modularity is still present in the three-dimensional supramolecular systems, allowing them to be combined much like the two-dimensional systems. A tetrahedron can therefore be designed by combining four 60° tritopic subunits with six linear ditopic subunits (Figure 2b).

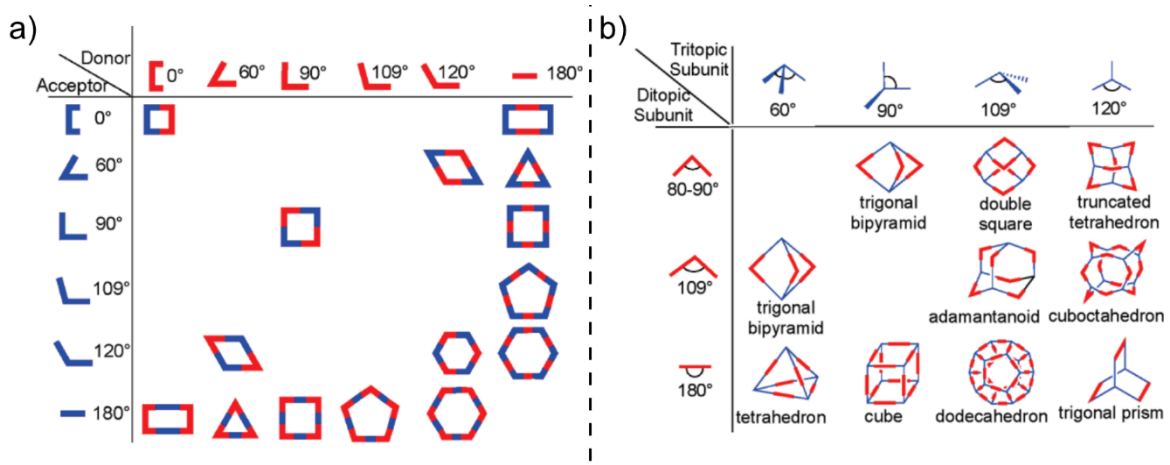

Figure 2: Different combinations to achieve a variety of supramolecular structures. a) Two-dimensional architectures, b) three-dimensional systems. This graphic was reproduced with permission from the American Chemical Society.[30]

1.2.2 Paneling approach

The paneling approach was significantly influenced by the work of Saalfrank[37] 1988 and Fujita 1995.[38] This strategy reduces the polyhedral structure to molecular components and, unlike the directional-bonding approach, concentrates on the faces of a three-dimensional structure rather than its edges. In other words, an octahedral molecule may be constructed by combining eight triangular panels, whereas a tetrahedron consists only of four panels (Scheme 2a). In order to prevent the formation of

oligomers, these supramolecular structures frequently have *cis*-blocked metal ions occupying their corners. Additionally, to enable the efficient formation of distinctive supramolecular architectures, these metal ions are frequently square planar Pd(II) or Pt(II) metal centers. Furthermore, the cage's stability can be significantly affected by the metal ions that were used to construct it.[39] Triangular molecular panels, first presented by Fujita, are the basis for a wide range of supramolecular assemblies, from the M_6L_4 octahedron[38] and M_8L_4 cone[40] up to the $M_{18}L_6$ trigonal bipyramidal structure.[41]

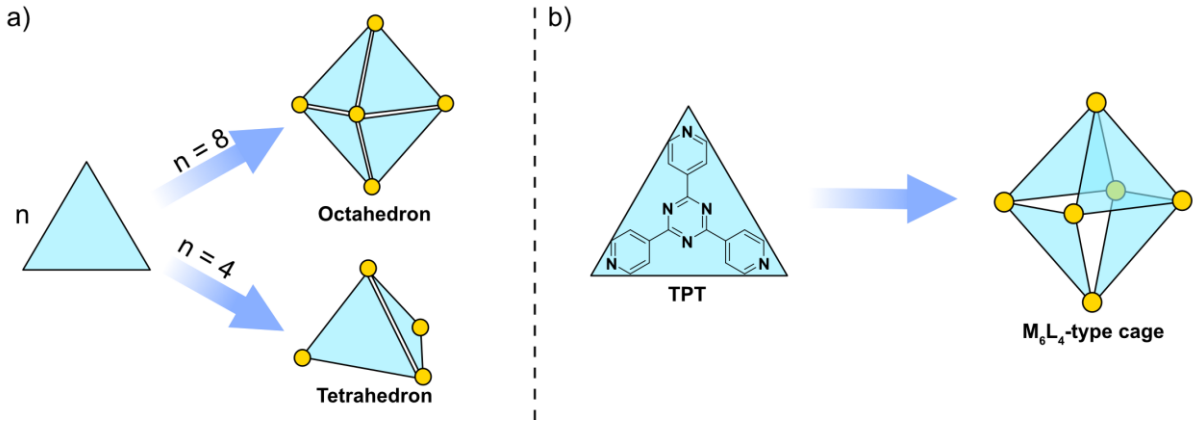

Scheme 2: Representation of the paneling approach. a) The formation of an octahedron can be achieved by using eight triangular panels, while a tetrahedron can be prepared by using four panels. b) Considering the ligand binding sites an octahedron can be achieved by combining four triangular panels (three binding sites) with six cis-blocked metal ligands (two binding sites each).

Similar to the previous technique, diverse supramolecular structures may now be imagined and, due to the modular strategy, assembled in a variety of ways. An octahedron will be created by combining four triangular panels, which have three binding sites on each vertex, with six *cis*-blocked metal ligands (two binding sites each, Scheme 2b). Prisms,[42] cubes,[43] and other structures are obtained by swapping the triangular panels with rectangular or square ones.

The paneling approach has the advantage that the supramolecular structures produced by this strategy frequently exhibit large, easily accessible cavities that may be used for a variety of tasks. These tasks include, for example, the separation of different molecules, cavity-driven catalysis, drug delivery, molecular recognition, and more.[44]

The directional-bonding and panel approaches are satisfactory to characterize the majority of self-assembled cages, despite the fact that there are additional methods for the development of such supramolecular structures.

1.2.3 Formation of water-soluble metal organic cages

The prior methods may be used to design and synthesize a variety of self-assembling supramolecular structures. However, often organic solvents were used in the preparation of these systems. This is because the design of water-soluble cages is often more complicated due to three reasons. First, water can also function as a coordinating ligand and thus interfere during cage assembly.[45] Another reason is that the hydrophobic effect may change how aromatic ligands arrange themselves around metal ions, leading to catenation rather than the formation of a supramolecular cage with a cavity. The third and potentially most practical reason is that many of the ligands used to form cages are extremely hydrophobic and, as a result, have poor water solubility. In order to synthesize the desired cage, solvent mixtures are also commonly utilized.[46]

Due to these reasons, it is not surprising that the first discovered metal organic cage, by Saalfrank,[37] was in fact not water soluble. This tetrahedral self-assembled cage was discovered by coincidence while attempting to prepare allene compounds (Scheme 3). The group of Saalfrank obtained magnesium malonate structure **1** by a condensation reaction of diethyl malonate with oxalyl chloride and methyl magnesium iodide as a base. This cage is composed of four magnesium ions that are organized tetrahedrally and are surrounded by six *bis*-bidentate malonate ligands as edges.[47] Despite its lack of water solubility, the discovery of this cage may have been the prerequisite for the development of numerous complex metal organic systems.

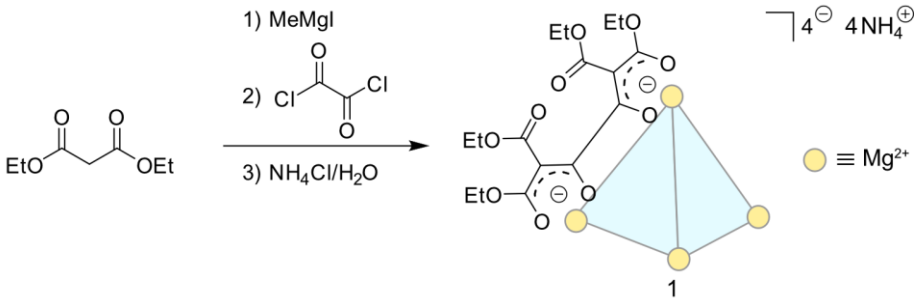

Scheme 3: Synthesis of the Mg^{2+}-based tetrahedral cage discovered by Saalfrank. This graphic was reproduced and modified with permission from the American Chemical Society.[37]

Seven years later, the first water soluble metalorganic coordination cage was synthesized by Fujita *et al*.[39] The group was able to design an octahedral supramolecular M_6L_4 structure with alternate open and closed faces by using the paneling method. Six *cis*-blocked palladium(II) centers are located in each of the octahedra's corners, while its faces are composed of four triazine panels (**TPT**) (Figure 3). A cavity void volume for this cage of 462 $Å^3$ was observed and is large enough to encapsulate up to four

adamantane moieties. The use of [Pd(ethylenediamine)$(NO_3)_2$] as a ligand was crucial for the water solubility of cage **2a**. Hydrophilic nitrate counterions on the one hand and the hydrogen-bond-donating capacity of the utilized *cis*-blocking $[Pd(en)]^{2+}$ ligand on the other hand contributed to the increase in its water solubility. It was later observed that similar *cis*-blocking ligands and different metal ions (e. g. Pt(II)) can be used for the self-assembly of isostructural cages (Figure 3, 2b-d). Interestingly, the cavity properties of the self-assembled cages are often unaffected by the exchange of the peripherical *cis*-capped ligands or metal ions, thus they maintain the same size, shape, and binding capacities. But ligands that either block the cavity windows or reduce the N-Pd-N bite angle can significantly influence the properties of a cavity. For example, the exchange of $[Pd(en)]^{2+}$ to $[Pd(bipyridine)]^{2+}$ increases the void volume from 462 $Å^3$ to 482 $Å^3$. However, ligands that have the ability to minimize the N-Pd-N bite angle, such as $[Pd(Mes\text{-}phen)]^{2+}$ (Figure 3, 2d) reduce the void volume significantly (V = 380 $Å^3$).[48]

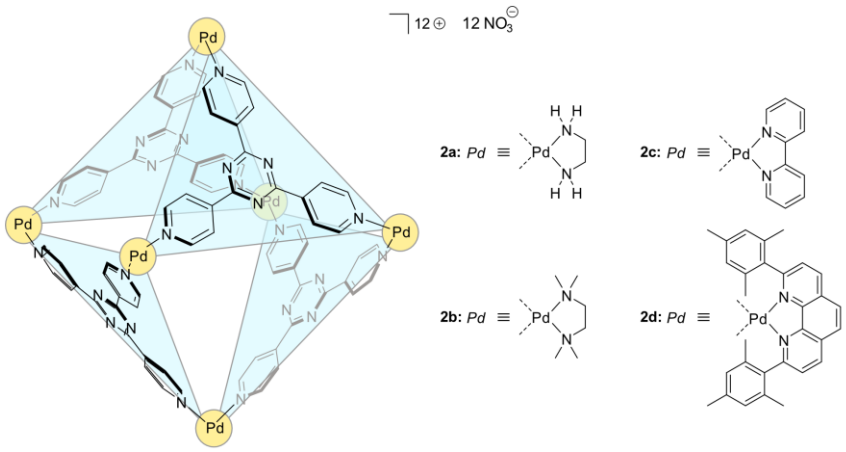

Figure 3: Different self-assembled coordination cages based on the M_6L_4. This graphic was reproduced and modified with permission from the American Chemical Society.[48]

In order to achieve different cavity properties in self-assembled supramolecular cages, an exchange of the cavity-forming ligand is necessary. By using the previously described strategies as well as the principles for constructing water soluble cages, the Fujita group presented a variety of distinct $[Pd(en)(NO_3)_2]$-based supramolecular structures (Scheme 4).

The construction of a M_6L_4 square pyramidal cone **3** was successfully conducted by exchanging the **TPT** through a similarly constructed triangular tridentate panel. In aqueous environments, this supramolecular structure further assembled into a dimeric capsule and was capable of encapsulating up to six organic molecules.[49]

Deploying an *exo*-hexadentate triangular ligand instead of **TPT** led to the assembly of trigonal-bipyramidal $M_{18}L_6$ supramolecular cage **4**, which in fact gives a cavity of 900 $Å^3$ but once assembled does not allow organic guest molecules to enter or depart.[41, 50] These simple adjustments already demonstrate the ability to precisely tailor the cavity parameters for the intended task.

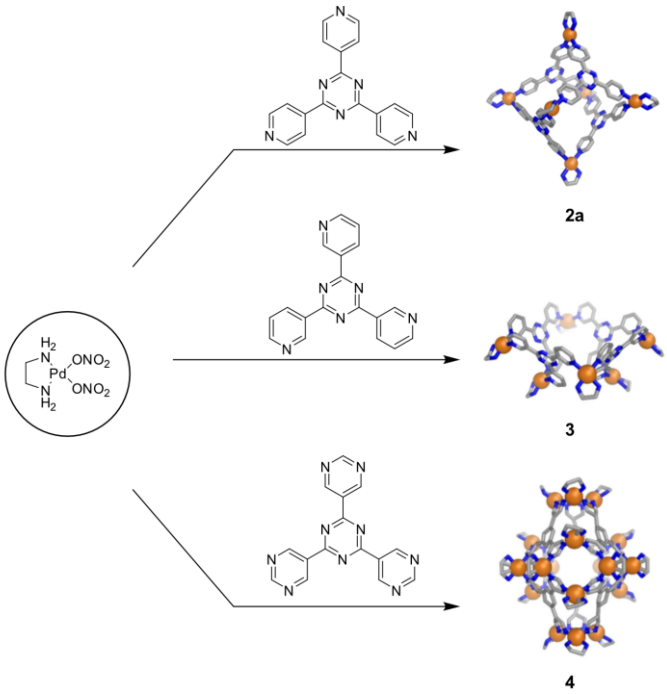

Scheme 4: Reactions of [Pd(en)(NO$_3$)$_2$] with different triazine-based ligands. This graphic was reproduced and modified with permission from the American Chemical Society.[47]

To enable successful self-assembly, all of these systems employ $[Pd(en)]^{2+}$-corner units as well as nitrate counterions. As mentioned before, these units are crucial to provide geometrical stability during the assembly and further function as solubilizing groups. Examples from the Klajn[51] and Mukherjee[52] group, who also proved that imidazole-containing ligands may be deployed instead of the previously used pyridine ligands, further illustrate the universality of this strategy.[47]

All depicted cages in Scheme 4 were highly positively charged and due to their counter nitrate ions extremely water soluble. However, a solely overall charge of the supramolecular structure is often insufficient for a cage to be water soluble. Due to this reason, the Nitschke group developed a method of "subcomponent self-assembly" in which dynamic coordinative (N→Metal) and covalent (C=N) bonds are formed simultaneously. This reaction leads *in situ* to a chelating ligand, which is subsequently used for the self-assembly of a tetrahedral metal coordination cage **5**. By utilizing this strategy, the group of Nitschke was able to generate cage **5** in extraordinarily high yields. Four Fe(II) metal ions, coordinated by a total of six bis-bidentate ligands, are positioned on each vertex of the tetrahedral cage (Scheme 5).

The use of 4,4'-diaminobiphenyl-2,2'-disulfonic acid moieties, which include two highly water-soluble sulfonate groups arranged toward the outside, finally yields an iron-based cage that is highly stable, water-soluble, and contains a hydrophobic cavity (141 Å^3), making it a useful tool for a variety of guest encapsulation experiments. To improve their water solubility even further, the 4,4'-diaminobiphenyl-2,2'-disulfonic acid linker can be modified without significantly changing the properties of the cage cavity.[53]

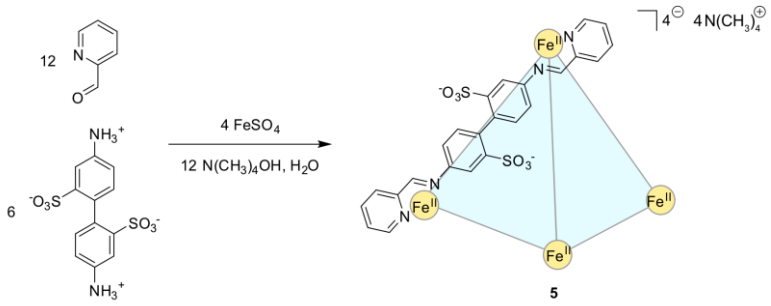

*Scheme 5: Synthesis of the tetrahedra **5** by in situ formation of the chelating ligand.*[53]

In order to increase the water solubility, Yoshizawa *et al.* also effectively used this strategy of adding solubilizing groups to the outward-facing ligands. Their supramolecular cage's original design had two anthracene panels and two methoxyethoxy groups on the main *m*-phenylene ring, but this cage was only soluble in DMSO or a solution of MeOH and water. A greatly improved water solubility was attained after the addition of a total of four hydrophilic methoxyethoxy groups to the *m*-phenylene ring.[54]

This idea of *'exo*-functionalization' can be used for a variety of cage modifications. This strategy may be used to increase its solubility in a desired solvent by including hydrophobic or hydrophilic chains, as described in detail by Casini *et al.* (Section 1.3.2). By adding polymer chains to the outward-facing ligands, a cage can also be made susceptible to ultrasound irradiation. This modification of the cage can be used for targeted disassembly and will be covered in Section 3.1.[24] By cross-linking different metal organic cages through polymers, a three-dimensional network can be formed, resulting in the formation of hydrogels (Section 3.3).[55]

1.2.4 From metal organic cages to hydrogels

Hydrogels are three-dimensional, cross-linked networks with the capacity to incorporate water due to their hydrophilic functional groups. These gels can be easily synthesized by the aggregation of a gelating substance with water. Small molecules or short polymer chains are frequently used to create this self-aggregation, which results in the formation of fibers, micelles, vesicles, and other structures.[56] To achieve a successful hydrogel formation, different approaches can be conducted. To achieve the formation of strong and permanent hydrogels, covalent bonds are necessary, whereas the formation of weaker and reversible hydrogels can be achieved by utilizing non-covalent interactions (such as hydrogen bonding, chain entanglement, π-π-stacking).[57] Both types of hydrogels provide unique benefits and may be specifically tailored for the required application.

The obtained hydrogel can then be categorized into three structural levels: primary, secondary, and tertiary. The primary structure covers the molecular level as well as the intermolecular forces that occur. The secondary structure of a hydrogel explains the morphology of the aggregated molecules (Fiber, vesicle, lamellae, etc.), whereas the tertiary structure describes the interaction between individual aggregates and therefore the macroscopic structure.[58]

Hydrogels are used for a range of applications, including drug delivery, agriculture, pharmaceuticals, tissue engineering, and many more.[59] Due to their network structure and their high water content, they are excellent hosts for drug delivery. These cross-linked structures can easily be tuned by increasing or decreasing the matrix density and thus regulating the affinity towards the aqueous environment. Even further, the so created porous network permits the encapsulation of a variety of hydrophilic drugs. The subsequent release is primarily regulated by diffusion and is hence reliant on the mesh size/structure of the utilized hydrogel.[11]

These cross-linked networks are widely used but often lack the ability to encapsulate their guests for a longer period of time or to release them precisely. To overcome this issue different approaches can be facilitated. One method is the use of cross-linking metal organic cages to create distinct cavities. The synthesis of supramolecular self-assembled hydrogels has gained increased popularity in recent years, and their modular design distinguishes them from traditional covalently linked hydrogels. By utilizing reversible noncovalent bonds these hydrogels exhibit unique features, like self-healing, stimuli responsiveness or degradability.[60] Hydrogels based on metal organic cages can be synthesized by two methods. The "MOC first" approach starts with the formation of the metal organic cage, which is followed by an inter-MOC cross-linking. In contrast to this procedure, the "polymer first" approach employs telechelic ligands, which form a robust cross-linked network *via* cage formation.[61]

The group of Nitschke successfully synthesized the supramolecular metal organic hydrogel **6** based on their previously mentioned tetrahedral cage **5**. This hydrogel is formed by six end-functionalized

polyethylene glycol-chains, six diamine linker and four Fe(II) metal-ions (Scheme 6). The subcomponent self-assembly approach allows for the simultaneous synthesis of the reversible imine bonds and coordinative bonds of the cage. This imine formation generates *in situ* the chelating ligand that is then utilized to self-assemble a tetrahedral metal coordination cage (**6**), eventually resulting in cross-linking and subsequent gel formation. Due to the reversible nature of the utilized imine and coordination bonds these gels exhibit self-healing behavior, which was demonstrated by rheological measurements. The tetrahedral cage's hydrophobic cavity can be used for guest encapsulation studies with small compounds such as furan, anisole, or benzene. Interestingly, these hydrophobic guests were also loosely encapsulated in the gel pores of the hydrogel. A triggered release could be achieved by guest competition, chemical stimuli (acid), or competing amine subcomponents.[62]

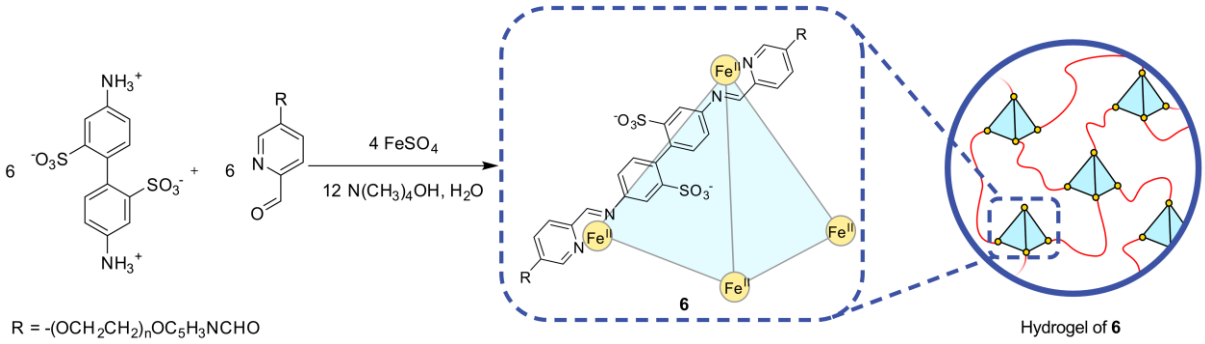

*Scheme 6: A metal-organic cage which was cross-linked to form hydrogel **6**. This graphic was reproduced and modified with permission from the American Chemical Society.[62]*

During the synthesis of cross-linked metal organic hydrogels, a phenomenon that occurs is the appearance of loop defects. These flaws arise when two terminal ligands of a distinct polymer chain *intra*-coordinate with a single metal organic cage rather than *inter*-connecting two separate cages. The group of Johnson *et al.* was the first group to address this issue by utilizing Pd(II) coordinated hydrogels. They discovered that by deploying *meta*-bispyridyl ligand **7**, they could construct the M_2L_4 paddelwheel-based hydrogel **8** with minimal loop flaws (Scheme 7). The *para*-bispyridyl ligand **9**, on the other hand, resulted in the formation of the $M_{12}L_{24}$ hydrogel **10**, accompanied by a large fraction of loop defects (Scheme 7b, red polymer chains are intra-connected). These flaws significantly affect the characteristics of hydrogels and may even prevent gel formation. Johnson *et al*. observed that these defects can be selectively exchanged by "free" ligands (**11** and **12**). These "free ligands" exhibit only one *para*-bispyridyl moiety, while the other end was modified with a fluorescent pyrene-based ligand. As a result, the loop defect could be significantly reduced while still maintaining the hydrogel's

properties (Scheme 7b, right side).[63] In contrast, for hydrogel **8**, the introduction of free ligands results in a significant decrease of network connectivity (decrease of f and G') (Scheme 7a, right side).

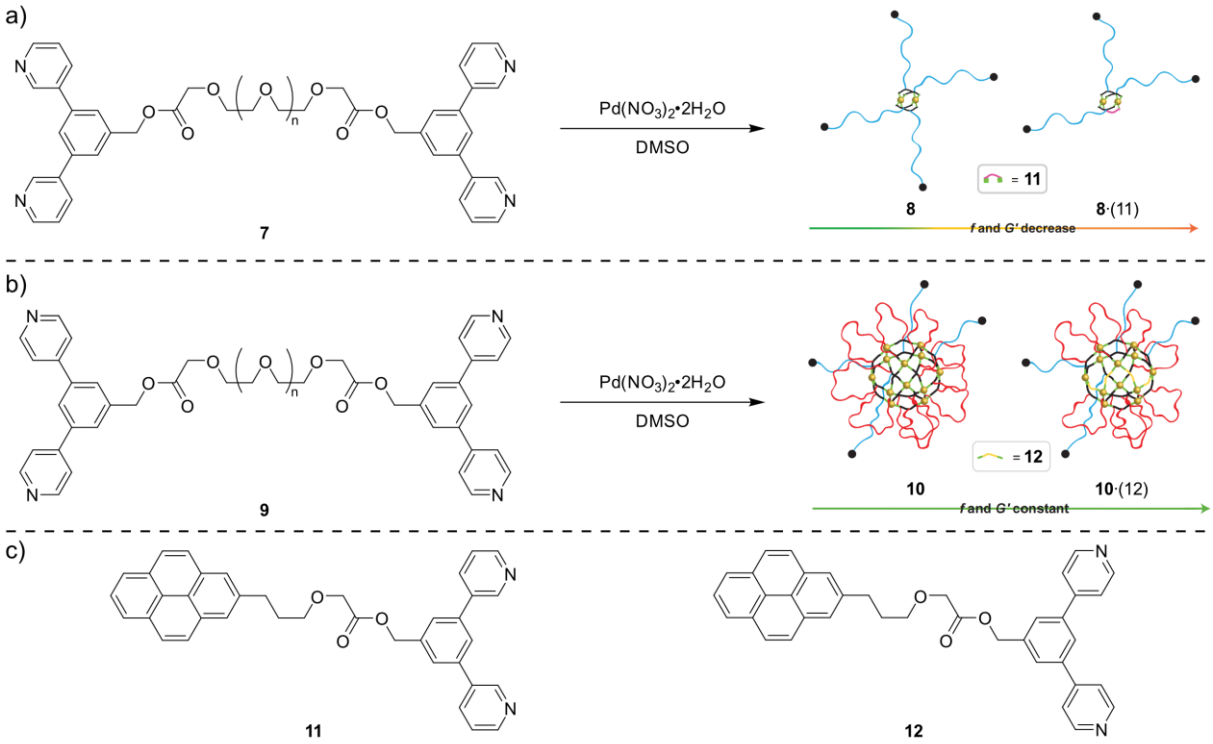

*Scheme 7: Synthetic approach for hydrogel **8** and **10**. Loop defects are indicated in red and active chains in blue. a) Synthesis of hydrogel **8**. The introduction of free ligand **11** results in decrease of network connectivity and therefore in a decrease of f and G'. b) Synthesis of hydrogel **10**. The introduction of free ligand **12** results in no decrease of network connectivity and therefore G' and f remain constant. c) "Free ligands". This graphic was reproduced and modified with permission from Springer Nature.[63]*

In order to receive a stimuli-responsive hydrogel, the group of Johnson deployed PEG-based polymer ligands, which feature two photoswitchable *bis*-pyridyl dithienylethene groups. In the presence of Pd(II), these ligands form small M_3L_6 metal organic cages that act as cross-linkers to synthesize the hydrogel depicted in Scheme 8. Upon irradiation, the bite angle of the ligands increases, resulting in a new $M_{24}L_{48}$ topology of the cage. This $M_{24}L_{48}$ cage can be reversibly switched between both topologies and thus change its properties.[64]

A different approach to receive stimuli responsive hydrogels was demonstrated by Severin *et al*. They designed several tetratopic N-donor ligands with polyethylene glycol spacers that, when combined with Pd(II), generate acid-sensitive Pd_nL_{2n}. By deploying a photoacid, they achieved a light-induced gel-sol transition by protonating the acid-sensitive Pd-N junctions. Due to the reversibility of this protonation, the hydrogel could cycle between both states.[65]

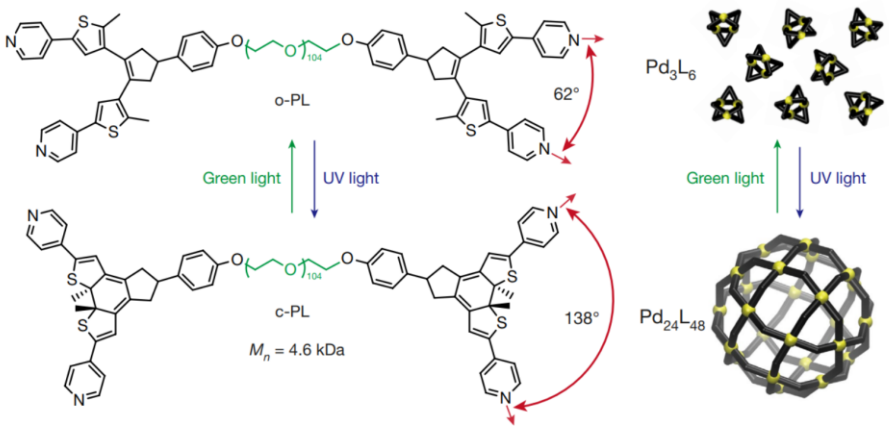

Scheme 8: A schematic illustration of photo-regulated conversion between a M_3L_6 and a $M_{24}L_{48}$ cage. This reversible conversion leads to an alteration of the network topology. This graphic was reproduced and modified with permission from Springer Nature.[64]

1.3 Host-guest chemistry of coordination cages

One of the most notable features of supramolecular metal organic cages is their internal cavity. A targeted guest uptake into this cage cavity is often facilitated by noncovalent forces and can influence the properties of its guest significantly.[66] This potential has led to an increased emphasis on the creation of novel cavity structures to precisely bind particular guests.

The previously described self-assembled cages of Fujita *et al.* proved that small adjustments to the outer cage immediately influence the internal cavity and therefore its guest uptake potential. Since guest encapsulation is dictated by similar shape and size properties of the host and guest, it is desirable for the chemist to have a direct influence over the cavity properties of the cage. This control can be achieved by modifying the "cage-forming" ligands of a cage to increase or decrease the cavity size. To determine if guest uptake might be feasible, Rebek has noted that the cavity should be occupied to 55 % by an encapsulated guest.[67]

1.3.1 Guest binding

The hydrophobic effect is what primarily facilitates guest encapsulation in the aqueous phase. For this reason, it is crucial to create a hydrophobic interior by enclosing the molecular cavity of a cage with extended aromatic ligands. Upon self-assembly of a supramolecular cage, its hydrophobic cavity is initially occupied by "high-energy" water. This water will be liberated during guest uptake and contribute enthalpically and entropically to the guest binding.[46, 68]

The group of Fujita *et al*. used these effects to facilitate guest uptake for a variety of neutral molecules in the M_6L_4. They observed that the addition of 1-adamantol results in enclathration of four guest

molecules inside the host cavity. An initial X-ray analysis revealed that the hydrophobic group of encapsulated 1-adamantol was positioned inside the cavity, whereas the hydrophilic group was outside the host cavity. ^{1}H NMR spectroscopy of encapsulated 1-adamantol confirmed this guest geometry. A significant upfield shift was observed for protons that are further away from the hydroxy group (inside the cavity), whereas those close to the hydroxy group (outside the cavity) are just marginally upfield shifted. Further guest encapsulations showed that small molecules like 1-adamantol are enclathrated in a 1:4 fashion, whereas medium sized guests, such as diphenylmethane or *cis*-stilbene, yield 1:2 host-guest formations. Larger guests form 1:1 systems, for example, tetrabenzylsilane.[69]

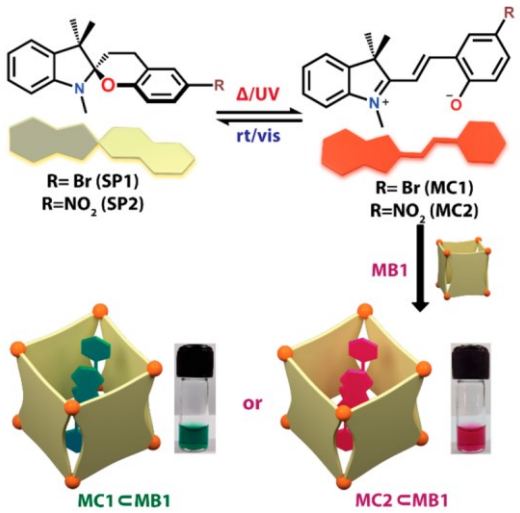

*Scheme 9: Encapsulation of **MC1** and **MC2** by deploying the Nanobarrel **MB1**. This graphic was reproduced and modified with permission from the American Chemical Society.*[70]

Mukherjee *et al.* demonstrated that the host cavity of nanobarrel **MB1** can be used for the stabilization of transient merocyanine isomers (Scheme 9). By subjecting the stable spiropyran (**SP1** or **SP2**) to UV light, a transformation into its unstable, color-emitting merocyanine form (**MC1** or **MC2**) was observed. When exposed to visible light or heat, this merocyanine form readily changes back to the stable spiro form. By employing container **MB1**, Mukherjee *et* al. have shown that stabilization of the planar merocyanine isomer can be achieved for several days (Scheme 9 bottom).[70]

1.3.2 Biomedical applications of metal organic cages.

In recent years, the development of supramolecular coordination cages for biomedical applications has increased significantly, due to their characteristic advantages of a large size and a defined cavity. These features can be used to bind specific drugs and improve their therapeutic profiles. This is especially intriguing when it comes to cancer treatment, whose success rate is constrained by the medication's low selectivity and high toxicity. Encapsulating a drug molecule in the cavity of a supramolecular cage increases its solubility significantly and also protects the drug from harsh physiological conditions.[71] Therrien *et al.* were the first to report in 2008 the use of a self-assembled cage for drug delivery of lipophilic molecules. In their study they used a water soluble hexanuclear ruthenium metallaprism **13** to encapsulate [Pt(acac)$_2$] (Scheme 10). They noticed that the metallaprism **13** on its own was moderately cytotoxic to human ovarian A2780 cancer cells, whereas [Pt(acac)$_2$] was completely ineffective. Only upon the encapsulation of **13**·([Pt(acac)$_2$]) a 20-fold increase in cytotoxicity was observed and was explained by a release of [Pt(acac)$_2$] inside the targeted biological cell. This method of hiding a hydrophobic complex inside a metal-containing host for drug delivery was defined as "the Trojan horse strategy".[72]

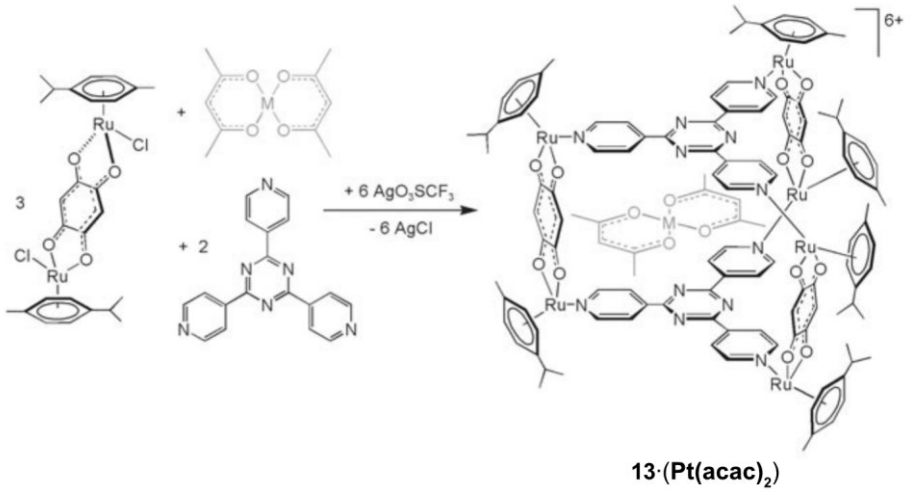

*Scheme 10: Synthesis of the water soluble metallaprism **13**. This graphic was reproduced and modified with permission from Wiley.[72]*

The group of Crowley was the first to incorporate cisplatin inside a Pd_2L_4 cage **14**, which is based on the work of Fujita. Cisplatin is a medication for chemotherapy and is used in a variety of different cancer treatments. Due to its low selectivity and numerous side effects, decreasing its toxicity would be beneficial. X-ray crystallography unambiguously confirmed the guest uptake of two cisplatin moieties inside the cage cavity, and ^{1}H NMR studies showed a distinctive downfield shift of the encapsulated guests. However, simply encapsulating the medication is often insufficient to realize its

full potential, and a targeted release is needed to deliver the drug to the desired cell. One straight forward approach for guest release is partial or total cage disintegration accompanied by drug release.[46] Therefore, Crowley *et al.* used competitive pyridine ligands (**L**) as chemical stimulus, which are capable to disassemble Cage **14**·(Cisplatin)$_2$ (Scheme 11).[71, 73]

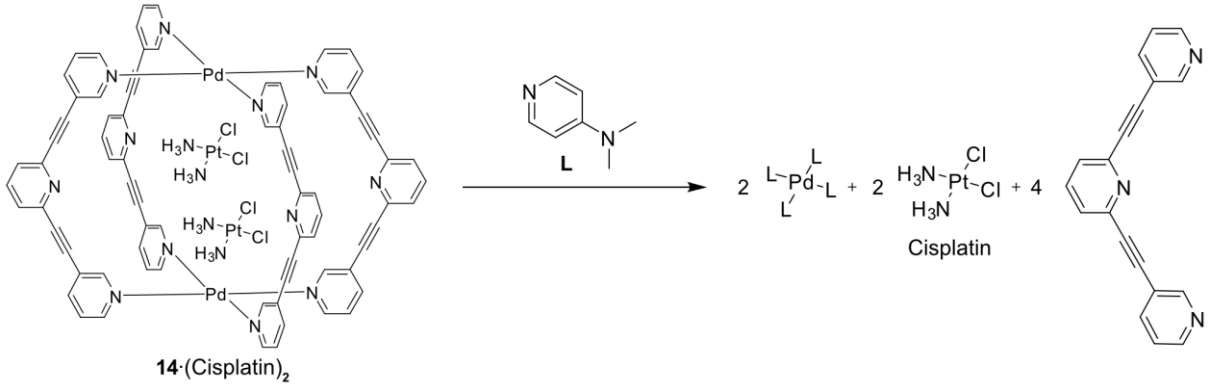

*Scheme 11: Depicted is the guest release of two cisplatin moieties by disassembling cage **14**. This graphic was reproduced and modified with permission from the Royal Society of Chemistry.[73]*

Unfortunately, its low water solubility renders cage **14** ineffective for biological applications under physiological conditions. To overcome this issue, two different approaches can be conducted. The first method includes an *exo*-functionalization of the cage/ligands and was performed by the group of Casini. Thus, they used several hydroxy and amino moieties that were introduced in *exo*-position to increase the hydrophilic properties of cage **14**. However, while the cages were still capable of encapsulating cisplatin, none of them were water soluble.[74] The group of Crowley utilized large glucose-functionalized ligands and successfully designed a cisplatin carrier system which is soluble in water.[75]

A second strategy, rather than altering the hydrophobic cage, functionalizes cisplatin in order to enclose this guest in a known water-soluble cage. Lippard *et al*. introduced an adamantylplatinum(IV) prodrug that can be encapsulated in a platinum(II) M_6L_4-type cage. The prodrug on its own has a low solubility in water but becomes soluble upon incorporation. Four equivalents of adamantylplatinum(IV) can be simultaneously encapsulated and subsequently delivered to their targeted destinations. This host-guest system demonstrated micromolar potency against several cancer cell lines (A549, A2780, A2780CP70) and obtained a higher cytotoxicity than the prodrug, as well as the platinum cage. It was proposed that ascorbic acid reduces the host-guest complex to subsequently release 1-adamantylamine, succinic acid, and most significantly, cisplatin.[76]

All of the previously mentioned systems have one thing in common: they require specific chemical triggers to initiate guest release, which complicates their universal application. Therefore, a variety of specific stimuli were developed to realize a controlled release. Internal stimuli often comprise endogenous or physiological factors, such as pH change[77] or redox activities,[76] and were already mentioned. External stimuli, on the other hand, are directly controlled by the operator. For instance, photopharmacology makes use of photoswitchable molecules that, when exposed to light, can be influenced in their biological activity.[78] However, this method is often limited by a low tissue penetration depth, biocompatibility, and long-term toxicity.[79]

Another method that allows a spatiotemporally controlled release of the guest is ultrasound (US). This external stimulus is already used for clinical applications and uses carriers such as liposomes, microbubbles, and micelles. An advantage of this method is the regulation of its tissue penetration depth, which can be controlled by varying energy and frequency through different exposure times.[26a, 80]

1.4 Ultrasound induced drug delivery

Ultrasound has been extensively studied in the last few decades for polymer mechanochemistry in solution.[81] This type of mechanochemistry uses US to generate cavitation, a process of nucleation, growth, and collapse of microbubbles (Figure 4a).[82] Polymer segments in close proximity to the collapsing microbubbles experience a stronger "pull" force than those farther away. Thus, an elongation of the polymer occurs, eventually leading to the development of tension along the polymer backbone. This stress is unevenly distributed throughout the polymer and accumulates in the middle of the chain, which explains why bond scissioning occurs more frequently close to the polymer's center (specific bond scissioning).[83] Nonetheless, random bond cleavage (nonspecific bond scissioning) can still appear during sonification and is an undesired side reaction (Figure 4b).[84] By deploying predetermined breaking points (mechanophores) inside a molecule a direct control over the bond scissioning position can be obtained. Thus, US induced bond scissioning can be utilized for a variety of applications, such as metal-ion release,[81d, 83a, 85] catalysis,[86] mechanogeneration of acids,[87] self-healing,[88] and drug release.[72-76]

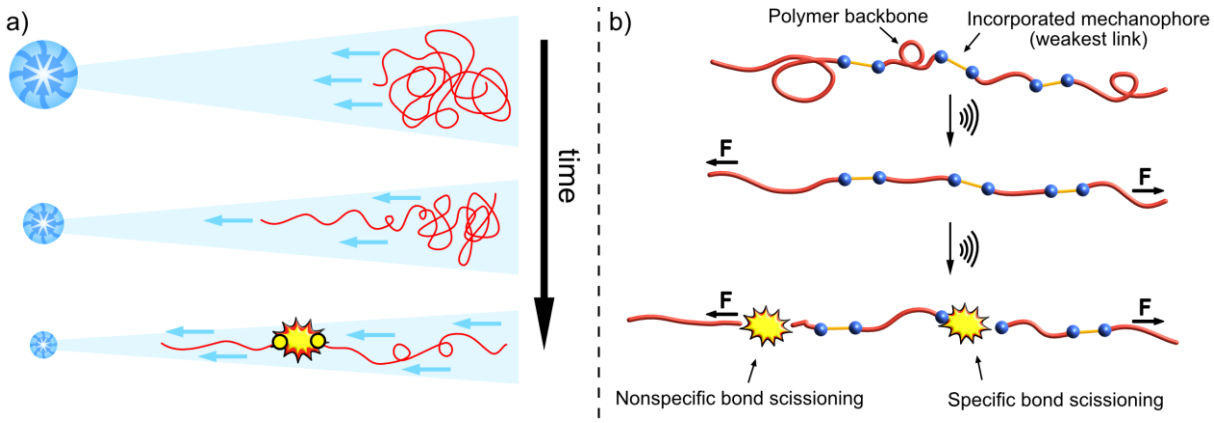

Figure 4: a) Schematic presentation of the ultrasound induced process of cavitation. The collapse of a microbubble results in the elongation of the polymer chain, eventually generating enough tension for bond scissioning. b) Depicted is the process of mechanochemical activation and the difference between nonspecific and specific bond scissioning.[82a]

The groups of Göstl and Herrmann examined the influence of US on the difunctionalized disulfide-based polymer **15**, in order to release a fluorophore alongside a drug. As a result, they used a theranostic agent (CPT) and a fluorescent probe (NAP), which were incorporated into a disulfide-centered oligo(ethylene glycol) methyl ether acrylate **15** (Scheme 12). They found that when **15** is exposed to ultrasound irradiation, the system is capable of simultaneously releasing a pharmacologically active compound and a fluorescent reporter molecule. The use of a fluorescent probe in conjunction with the medicine allows for precise determination of when, where, and how much of the pharmacologically active compound was delivered.[89]

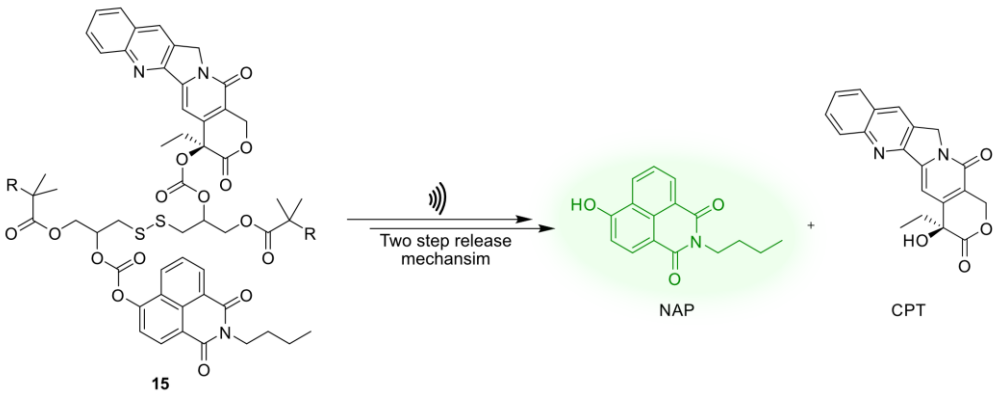

*Scheme 12: Reaction sequence of the mechanochemical bond scissioning of disulfide-centered polymers. After the disulfide bond breakage a 5-exo-trig cyclization leads to the release of **NAP** and **CPT**.*[89]

Moore investigated if this mechanochemical approach can also be utilized for cancer therapy and therefore exposed a polyethylene glycol-based hydrogel to high-intensity focused ultrasound (HIFU). Upon irradiation, bond scissioning occurred at the azo mechanophore moiety, resulting in a targeted release of reactive oxygen species. These species achieved a therapeutic efficacy of ~100 % after three days in *in vitro* tumor studies.[90]

All of the preceding studies illustrate that a variety of new approaches for targeted drug delivery have arisen, each with unique properties and advantages.

2 Motivation

The previous chapter illustrated the accessibility of a variety of different metal organic cages, their potential to bind hydrophobic guests in their nanoconfined cavities, as well as their use for targeted drug delivery. Unfortunately, these systems often lack water solubility, require drug modifications for a successful encapsulation, or need specific stimuli for a targeted release. The aim of this work is to overcome these issues by combining the benefits of water-soluble metal organic cages with the advantages of polymer mechanochemistry. Thus, a metal organic cage should be designed with a distinct cavity to encapsulate different hydrophobic guests, which can eventually be released upon ultrasound irradiation (Scheme 13).

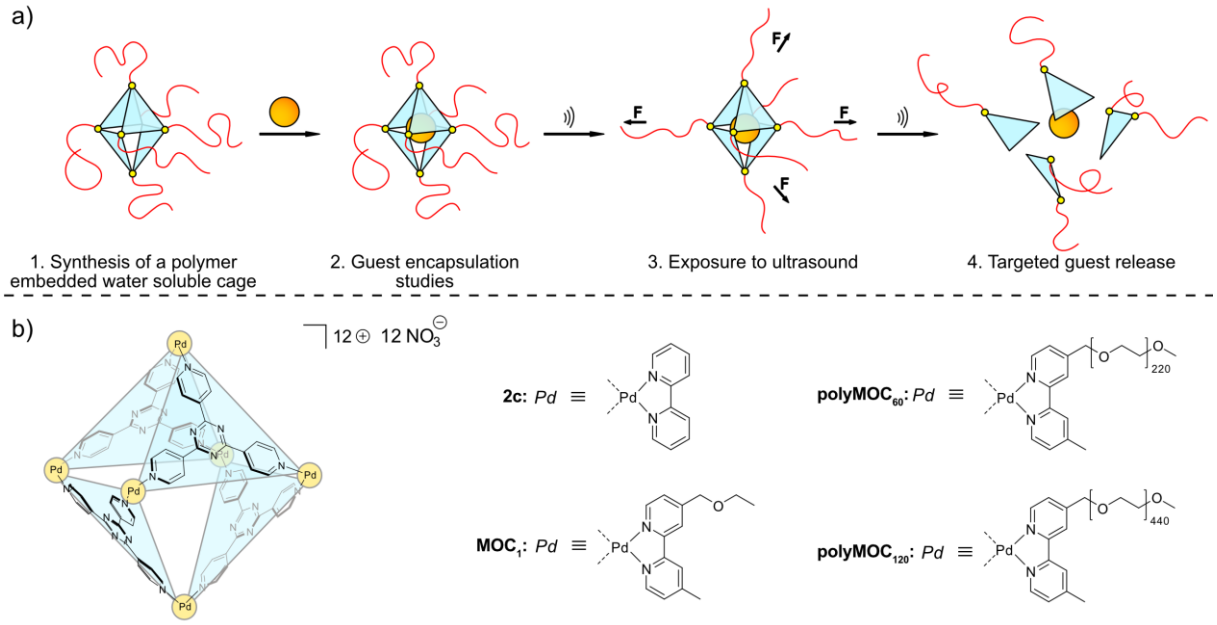

Scheme 13: a) Summary of all necessary steps to achieve a mechanoresponsive MOC. b) Depicted are all M_6L_4-based cages, which are synthesized for this work. ***2c*** *was synthesized by Fujita et al. and is depicted for comparison.*[46]

Due to its versatility, the M_6L_4 **2c** was chosen as the framework. This cage offers a variety of advantages, including high water solubility, excellent host-guest properties, and easy *exo*-functionalization. The functionalization of the peripheral bipyridine moieties is initially required to render the M_6L_4 cage **2c** susceptible to ultrasound irradiation. As a result, *exo*-modified bipyridine moieties were synthesized, which have the advantage of not influencing the shape and size of their host cavity, thus maintaining identical host/guest properties for all different synthesized cages throughout this work. Due to the similar properties the metal organic cage **MOC_1** will be utilized to

provide fundamental analytical data, which can subsequently be used to verify and compare guest encapsulation in the larger polymer metal organic cages (**polyMOC$_{60\text{-}120}$**).

As a result, various guest encapsulation studies will be performed in this work to prove the accessibility and versatility of *exo*-functionalized M_6L_4 cages. In addition to the guest uptake investigations, all loaded and unloaded cages will be exposed to ultrasound irradiation to illustrate their mechanoresponsive potential and demonstrate drug release. Despite the fact that ultrasound has been employed in a variety of drug release experiments, nothing has been published on the effect of ultrasonic induced bond scissioning of polymer embedded metal organic cages.

The nature of the mechanochemical disassembly will be studied in depth by using simplified **polyMOC** systems and subjecting them to ultrasonic irradiation. These prepared mechanophores (**MP$_{15\text{-}20}$**) will be compared before and after sonication to all **polyMOCs** in order to observe similarities or differences. Computational calculations are carried out in order to gain a better understanding of the sequence of mechanochemical bond scissioning in palladium coordination complexes.

A significant structural adaptation of the initially used bipyridine ligands will be conducted in order to obtain difunctionalized PEG-linkers. These difunctionalized polymers are used to form cross-linked metal organic M_6L_4 hydrogels (**HG$_{1\text{-}6}$**), which have similar host/guest features comparable to the **polyMOCs** but different mechanical properties (Scheme 14). This approach should guarantee an increasing guest-to-polymer ratio, in contrast to the **polyMOCs**, while maintaining its sonochemical responsiveness. These properties will be investigated in detail to further support the use of metal organic cages for drug delivery.

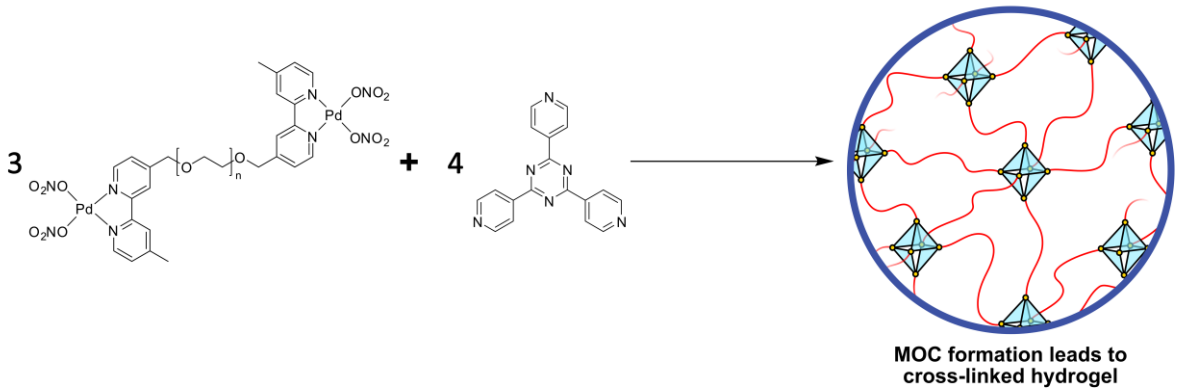

*Scheme 14: A structural adaption of linker **24** enables the formation of cross-linked metal organic cages and therefore the synthesis of hydrogels.*

In this work, it is aimed to highlight the advantages of water-soluble polymer embedded cages for guest uptake and release. It further investigates the responsive behavior of different *exo*-functionalized **MOCs** to ultrasound induced bond scissioning and will provide several reasons why the here synthesized **polyMOCs** and **HGs** are superior to other systems in terms of drug release.

3 Discussion

3.1 Mechanochemical activation of a supramolecular cage

3.1.1 Introduction

Because pharmaceuticals are inherently non-selective, systemic administration of medications results in a trade-off between desired therapy and side effects. In addition to this comes, that a systemic use and overuse of antibiotics leads to an increase in drug-resistant infections.[80a] One method is to deploy auxiliaries that are capable of delivering the drugs to a specific target and therefore increase the selectivity.[91] Another way to circumvent this issue is by controlling the targeted drug release through internal or external stimuli. The selection of stimuli for a controlled cargo release is versatile and depends mainly on the chosen host system. Internal stimuli include, for example, the pH-value[77] or redox reaction[92] and they enable precise control for targeted drug release. The focus of this work is the application of ultrasound as an external stimulus. This external stimulus can be precisely controlled for a targeted release and, in addition, can be easily used for clinical applications.[26b]

Several systems were already investigated in this regard, including the work of Kiessling *et al*.[93] who achieved successful drug release by utilizing microbubbles, whereas Husseini *et al.* employed liposomes and micelles for this task.[26] Göstl and Herrmann established polymer-embedded force-responsive mechanophores for a successful and precise cargo release.[89] An occurring compromise of the above mentioned systems is that they often rely on strong host-guest interactions or on a chemical alteration of the guest molecule to facilitate its uptake.

Employing self-assembled cages for this task might circumvent the need to chemically modify these drugs because these cages offer the opportunity to strongly and non-covalently bind a wide variety of guests in their cavity by taking advantage of the hydrophobic effect. The notoriously versatile cage **2c** was synthesized by the group of Makoto Fujita and, due to its high water solubility and hydrophobic cavity, is capable of encapsulating a variety of hydrophobic guests. This guest uptake was successfully confirmed for iodoperfluorocarbons,[94a] pH-indicators,[94b] secondary aryl amides[94c] and more, making this cage an ideal foundation for further guest encapsulation studies of pharmaceutical active compounds.

A modification of the M_6L_4 cage **2c** has to be conducted in order to make it susceptible to ultrasound irradiation, which can be performed in two ways. The first approach takes advantage of the cavity forming ligands. However, replacing or modifying these ligands frequently causes significant changes in the cage's characteristics, either as a result of steric obstruction of the cavity's "windows" or increasing/decreasing ligand size (Figure 5).[49, 95] To maintain the cavity properties, another method can be approached by functionalizing the peripherical ligands of the cage, facing outwards from the

cavity. These ligands can be modified or exchanged in a number of ways without actually affecting the cavity's characteristics or even blocking the portals.[69, 96]

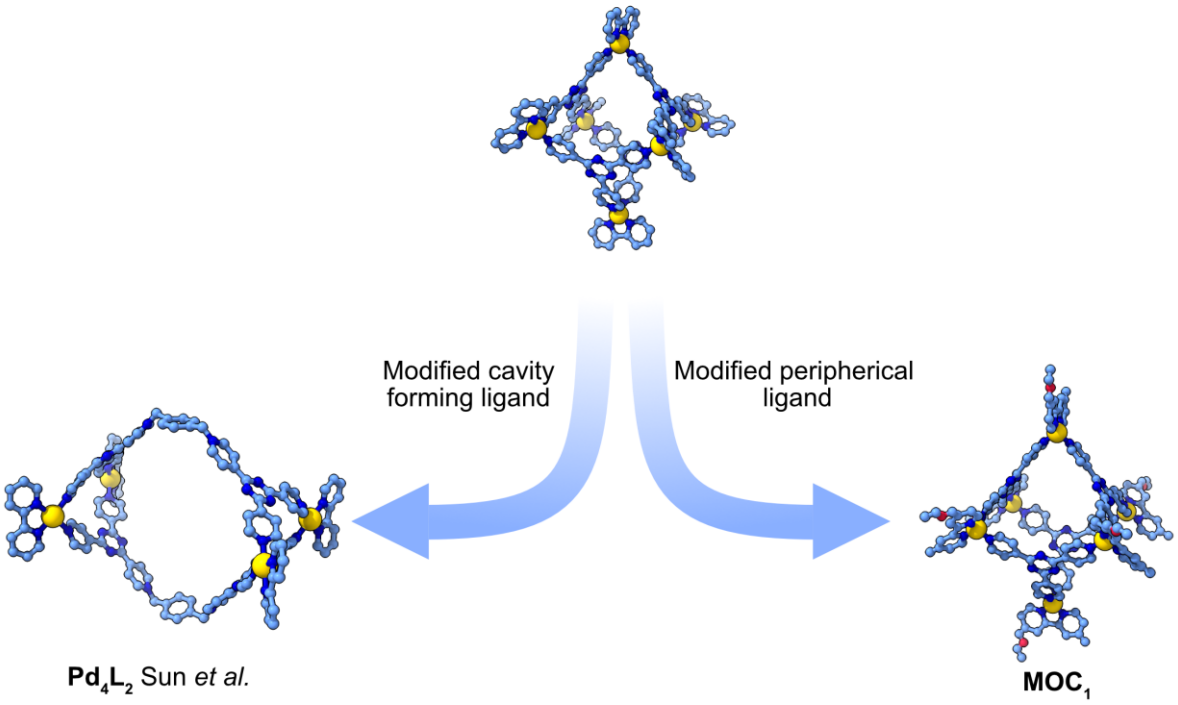

Figure 5: Depicted are possible methods for cage modifications. Modifying the cavity ligand results often in an in- or decrease of the cavity size and thus, directly influences the host-guest properties. A modification of the peripherical ligands can be used to alter the cage properties without influencing the cavity.

Another factor to consider when developing mechanoresponsive self-assembled cages with the goal of precise drug release is the polymer selection. Since the hydrophobic effect is what primarily drives guest encapsulation, this guest uptake can only be carried out in aqueous phases, which restricts the polymer choice. In addition to that, the selected polymer must not contain functional groups that are capable of interacting with the supramolecular cage or even decomposing it. It was demonstrated that poly(ethylene glycol) is not only a good choice for sonochemical activation,[90] but also that cage formation in the presence of this polymer is achievable,[62] making it a promising candidate for an initial investigation.

Inspired by these results, a novel supramolecular cage based on the M_6L_4 motif was synthesized with *exo*-modified 4,4'-dimethyl-2,2'-dipyridyl ligands, differing in their polymeric length, to investigate the mechanoresponsive behavior under sonochemical irradiation conditions.

3.1.2 Synthesis

Synthetic approach for the building blocks

For the formation of M_6L_4-type cages, three bidentate chelating ligands were synthesized (Figure 6). These isostructural linkers were chosen based on their sonochemical behavior upon ultrasound irradiation. It was anticipated that when the molecular weight of the polymer increases (**24** to **27**), bond cleavage of the designed supramolecular cages **polyMOC$_{60}$** and **polyMOC$_{120}$** would also increase.[97] To test this hypothesis, an additional linker **21** bearing no polymeric chains was synthesized for subsequent control experiments.

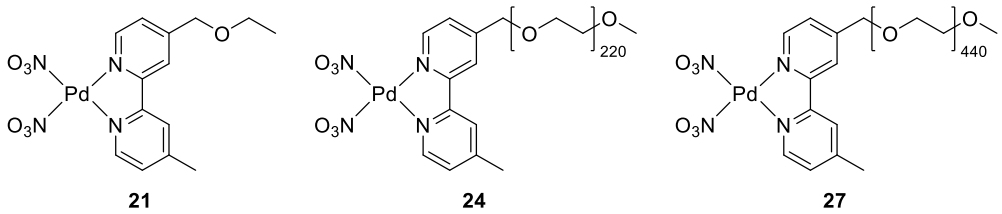

Figure 6: All linker used for the formation of M_6L_4-type cages.

Starting with a Riley-type oxidation of 4,4'-dimethyl-2,2'-bipyridine (**16**) using selenium(IV)-oxide, followed by a reduction with sodium borohydride yielded the corresponding alcohol **17**.[98] An exchange of the functional alcohol group was achieved through a nucleophilic substitution reaction with a mixture of aqueous hydrobromic acid and catalytic amounts of sulfuric acid to obtain bromide **18**.[98] In a subsequent Williamson ether synthesis, the organohalide **18** was reacted with an excess of ethanol under basic conditions to yield 4-(ethoxymethyl)-4'-methyl-2,2'-bipyridine (**19**) with a high conversion. Even though high yields for **19** could be achieved, it must be mentioned that under elevated temperatures the utilized bromide **18** acts as nucleophile and electrophile simultaneously, leading to homocoupling as a side reaction. Performing this reaction at 0 °C prevents the formation of the by-product almost entirely, and the remaining *N*-alkylbipyridinium **HC** was removed by column chromatography. The chelation of palladium(II) chloride with the bidentate bipyridine ligand **19** resulted in the formation of complex **20**. The corresponding Pd-complex **20** could be obtained in 83 % yield. In a halide abstraction reaction with $AgNO_3$, the chloride ligands were exchanged for the weaker coordinating nitrate ligands, yielding complex **21** in high conversion (Scheme 15).

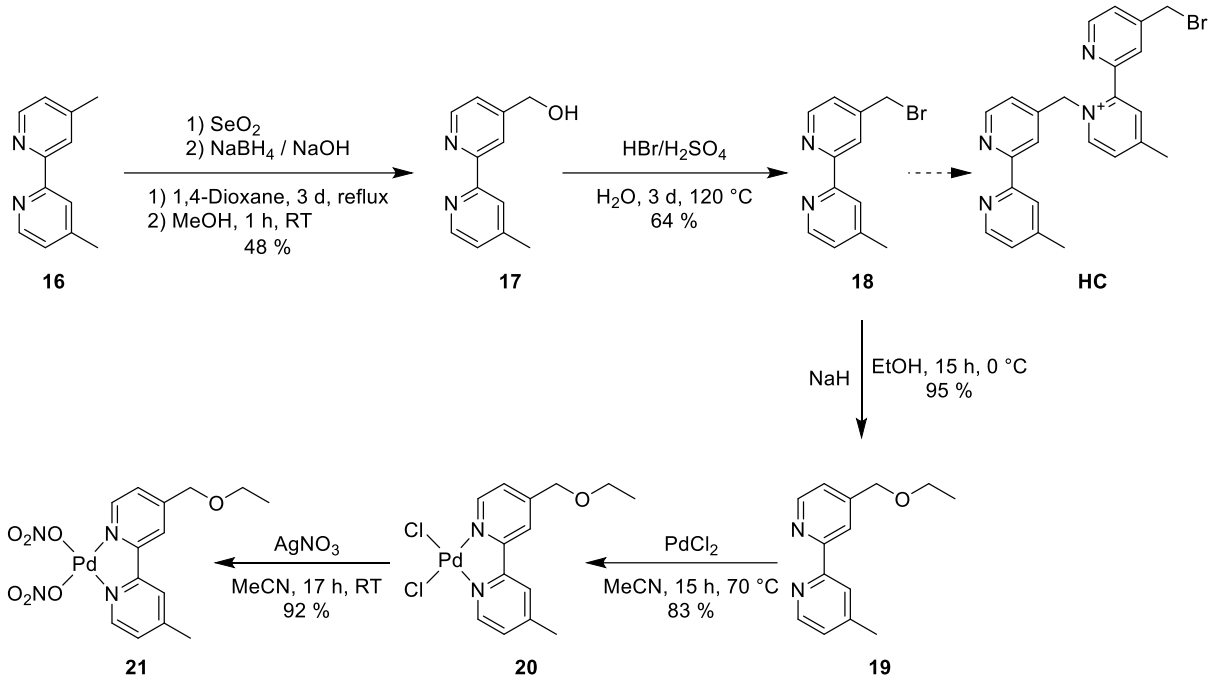

*Scheme 15: Synthesis of ethyl-substituted bipyridine **21** starting from bipyridine **16**.*

Based on the previously established synthesis route the poly(ethylene glycol) methyl ether (mPEG) substituted ligand **24** could be obtained, starting from bromide **18**. The here established poly(ethylene glycol) methyl ether had a number average molecular weight of 10 kDa (M_n = 10 kDa, $mPEG_{10}$), which represents approximately 220 repeat units. This length was specifically chosen because, on the one hand, it should guarantee sonochemical activation[83b] while on the other hand, it simplifies the analytical characterization of the later-formed supramolecular cage **polyMOC$_{60}$**.

The synthesis of polymer chain bearing nitrate **24** started with a Williamson ether synthesis where bromide **18** is used in a slight excess to yield $mPEG_{10}$ substituted ether **22** in high conversion. Although bromide **18** tends to react in a homocoupling reaction, it was nonetheless preferred to employ a small excess throughout the reaction. Due to identical physical properties between the substituted $mPEG_{10}$ ligand **22** and pristine $mPEG_{10}$, no separation could be achieved during the workup, wherefore the reaction conditions had to be optimized until complete conversion was observed. Therefore, the reaction was conducted at 0 °C for three days to suppress the homocoupling side reaction and to obtain quantitative conversion. Since $mPEG_{10}$ is highly water soluble, the aqueous work up led to diminished yields.

Followed by a complexation reaction of palladium(II) chloride with the chelating ligand **22**, compound **23** could be obtained in quantitative yields. Comparable to the previous halide abstraction reaction, $AgNO_3$ was employed to exchange the strong chloride ligand for nitrate. The resulting nitrate complex **24** could be obtained in 93 % yield (Scheme 16).

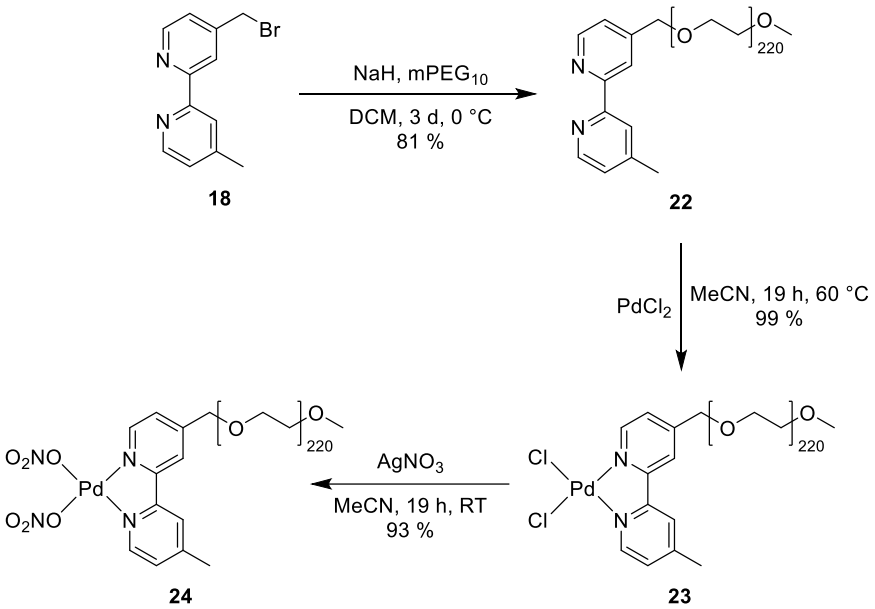

*Scheme 16: Synthesis of $mPEG_{10}$-substituted bipyridine **24** starting from bromide **18**.*

The last linker that was synthesized uses $mPEG_{20}$ with a M_n of 20 kDa (440 repeat units) and results in the later discussed formation of **polyMOC$_{120}$** (M_n = 120 kDa). While spectroscopic measurements reach their limits with a self-assembled cage of this size (3.1.2, cage assembly), it is interesting to observe the influence of the structural difference between those linkers on the later investigated sonochemical behavior. To synthesize ligand **27**, the same procedure as before was followed, starting with the Williamson-ether synthesis to give the $mPEG_{20}$ substituted bipyridine **25** in 76 % yield, followed by complexation of palladium(II) chloride. Palladium complex **26** could be obtained in 95 % before a slight excess of $AgNO_3$ was added, yielding the nitrate-bearing complex **27** in 91 % (Scheme 17). A problem that occurred in this reaction was that the precipitation of AgCl was hindered by the use of $mPEG_{20}$. In most cases, separation of AgCl and $AgNO_3$ was impossible, resulting in the light-induced decomposition to elemental silver.[99] This photo-decomposition was observed in both the solid and solution states by a significant color change from yellow to black. In many cases, centrifuging the reaction in acetonitrile several times for one hour at 10 °C removed enough silver for the following reactions, but was not sufficient for a complete removal. As a result, it was frequently observed that the subsequent cage self-assembly was unsuccessful. A way to circumvent this photo-decomposition from occurring could be by reacting $Pd(NO_3)_2$ directly with bipyridine **25** and therefore "skipping" the synthesis of the palladium chloride ligand **26**, and thus the usage of silver derivatives (See section 3.3.3).

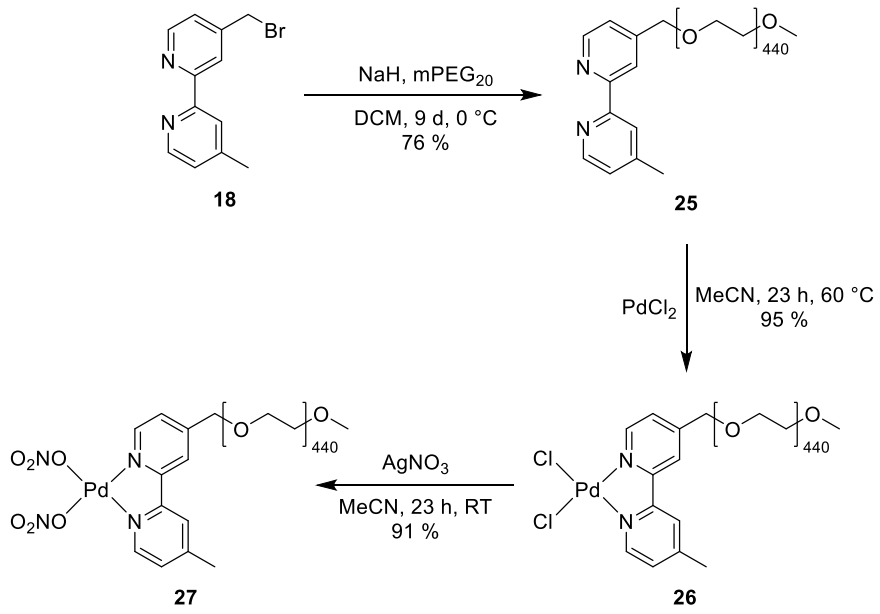

*Scheme 17: Synthesis of mPEG$_{20}$-substituted bipyridine **27** starting from bromide **18**.*

Following a literature procedure,[100] the tridentate, triangular ligand 2,4,6-tris(4-pyridyl)-1,3,5-triazine (**TPT**) could be synthesized in a trimerization reaction with neat 4-cyanopyridine (**28**) and NaOH at 160 °C (Scheme 18).

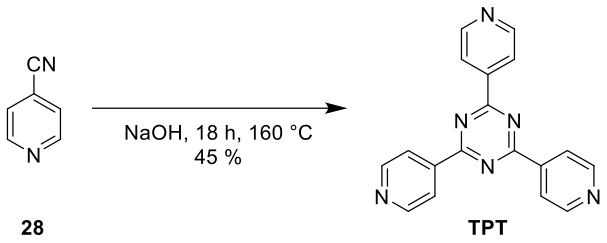

*Scheme 18: Trimerization of 4-cyanopyridine (**28**).*

Cage assembly

Following the successful synthesis of the three *cis*-blocked palladium nitrate complexes (**21**, **24** and **27**), the supramolecular self-assembly of different **MOCs** was investigated. Thus, the three isostructural cages shown in Scheme 19 were intended to be synthesized. These octahedral cages consist of four cavity forming **TPT** and six *cis*-blocked ligands (**21**, **24** and **27**) for the palladium corners. Utilizing non-polymer-bearing complex **21** gives access to the metal organic cage **MOC$_1$** which will be used for an analytical foundation as well as control experiments during the sonication experiments

(Scheme 19, left). Deploying the ligands **24** and **27** results in the formation of star-shaped mechanoresponsive cages, **polyMOC$_{60}$** and **polyMOC$_{120}$**, respectively (Scheme 19, right).

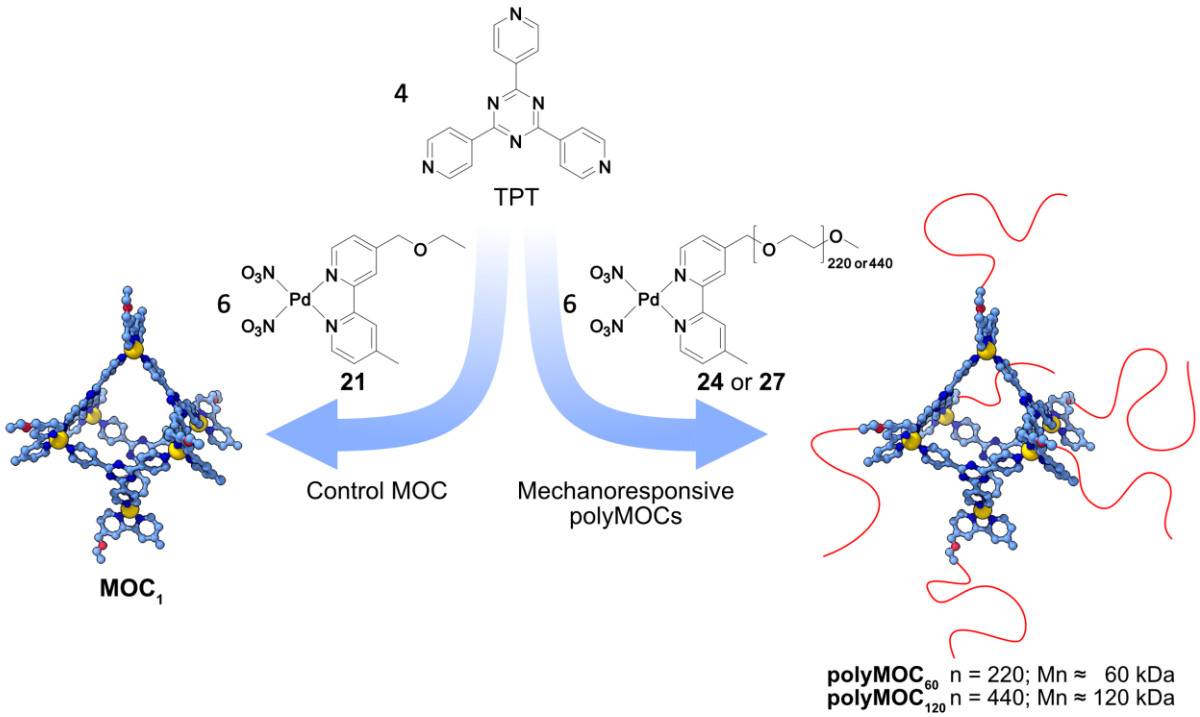

*Scheme 19: Depicted are the universal force field-optimized (UFF) geometries of the synthesized **MOCs** utilizing the previously introduced nitrate-bearing ligands and **TPT**.*

Cage formation was at first investigated with the small ether complex **21** which is a modified version of the work published by Makoto Fujita *et al*.[46] The building blocks (4.0 eq. of **TPT** and 6.0 eq. of palladium-nitrate complex **21**) were therefore stoichiometrically combined in water (5 mmol L^{-1}, related to the cage) and heated for three hours at 80 °C. After filtration and removal of the solvent, a pale-yellow powder was obtained in high yields of 92 %. The ^{1}H NMR spectra of the starting materials and self-assembled cage **MOC$_1$** demonstrate a distinct downfield shift for the **TPT** signals (9.46 ppm and 8.92 ppm, A and B, Figure 7c) after cage formation, indicating a decrease in electron density. At the same time, an upfield shift for the proton atoms of the palladium complex **21** can be observed, whereby the protons in close proximity to the nitrogen (7.66 – 7.44 ppm, b and b') experience the highest increase in electron density. These findings suggest that the electron density was transferred from the triazine to the metal complex **21**, therefore confirming self-assembly of the supramolecular cage **MOC$_1$**. The remaining signals can be assigned to the methyl group (2.64 ppm, f'), the methylene protons adjacent to the ether group (4.87 ppm, f), and the corresponding ethyl group (3.75 ppm and

1.30 ppm, g, h). Formation of the cage was further confirmed by ^{1}H DOSY experiments (Figure 127), ^{13}C NMR, and heteronuclear 2D measurements (Figure 123-126).

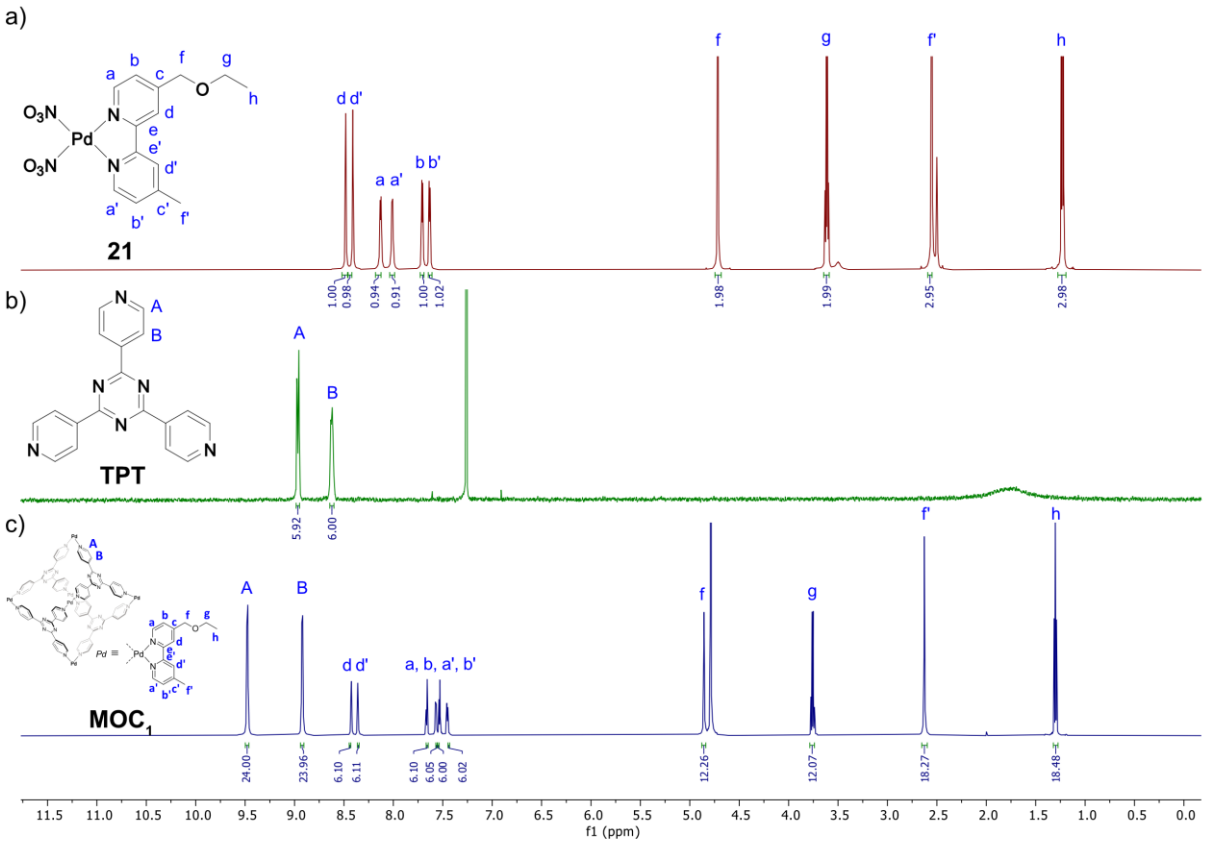

*Figure 7: a) ^{1}H NMR of the pristine palladium complex. b) ^{1}H NMR of **TPT**. c) The self-assembled supramolecular cage **MOC$_1$**.*

After the successful formation of the model compound **MOC$_1$**, the corner forming ligand **21** was exchanged in order to synthesize the larger poly(ethylene glycol) bearing cage **polyMOC$_{60}$**. The conditions were slightly adjusted by increasing the concentration of the cage to 6 mmol L^{-1} in D_2O as well as the reaction time to 16 hours. The building blocks were suspended in water stoichiometrically (6.0 eq. of ligand **21** and 4.0 eq. of **TPT**) and heated to 80 °C to yield a yellow solution. After filtration and solvent removal, the star-shaped **polyMOC$_{60}$**, with a M_n of approximately 60 kDa, could be obtained as a pale-yellow solid with an 86 % yield.

It has to be mentioned that in many cases, only a brown/black suspension was obtained for **polyMOC$_{60}$**, and formation of the desired cage could often not be observed by ^{1}H NMR. While the assembly of the small cage **MOC$_1$** occurred nearly quantitatively it seemed that the exchange to complex **24** either hinders the formation or completely prevents it. Different solvents (MeOH, DMSO, or H_2O) were tested, as well as different temperatures (50 – 90 °C) and basic or acidic conditions (NaOH, HNO_3), but

none were suitable for a reliable synthesis. It was observed that small amounts of AgCl/$AgNO_3$ were still present in the starting material, and the elevated temperatures during cage formation resulted in a possible reduction to elemental silver, explaining the color change to a brown/black suspension.

Under the utilized conditions it was assumed that a competition reaction between residual silver ($AgNO_3$) and palladium ($Pd(NO_3)_2$) metal ions might have occurred. According to ^{1}H NMR, a combination of various Pd and Ag cage compositions was formed, which was accompanied by the distinctive color shift during the reaction from yellow to brown. A method to successfully remove the AgCl and $AgNO_3$ was discussed at the start of section 3.1.2.

The successful synthesis of **polyMOC$_{60}$** was confirmed by ^{1}H NMR (Figure 8b) and shows a similar chemical shift as the previously discussed model compound **MOC$_1$** (Figure 8a). The characteristic 24 **TPT** (9.50 ppm and 8.95 ppm) and 36 bipyridine signals (8.46 and 7.57 ppm) of cage **polyMOC$_{60}$** were in accordance with the model compound **MOC$_1$**. The broad PEG polymer backbone, however, dominates the ^{1}H NMR at = 3.72 ppm. This poly(ethylene glycol) signal corresponds to approximately 5,000 protons per supramolecular cage **polyMOC$_{60}$**, preventing all heteronuclear NMR measurements while also increasing the measurement time for a single ^{1}H NMR to one hour at a concentration of 140 mg mL^{-1}. Furthermore, a considerable broadening of the resonances can already be observed. This coalescence of the resonance signals happens due to a low molecular rotation of the molecule. Additionally, the repeating units are situated in chemical environments that are marginally different from each other, resulting in a broad peak pattern.

The synthesis of **polyMOC$_{120}$** was carried out in a similar manner, and the cage was obtained in high yields of 78 %. Noticeable is a small decrease in the yield in contrast to **polyMOC$_{60}$**, which was attributed to the increasing difficulty of the removal of AgCl/$AgNO_3$ during the workup. The ^{1}H NMR analysis of **polyMOC$_{120}$** is in accordance with the previous cages, differing only in further resonance broadening induced by the increasing length of the polymer, as can be observed in Figure 8c.

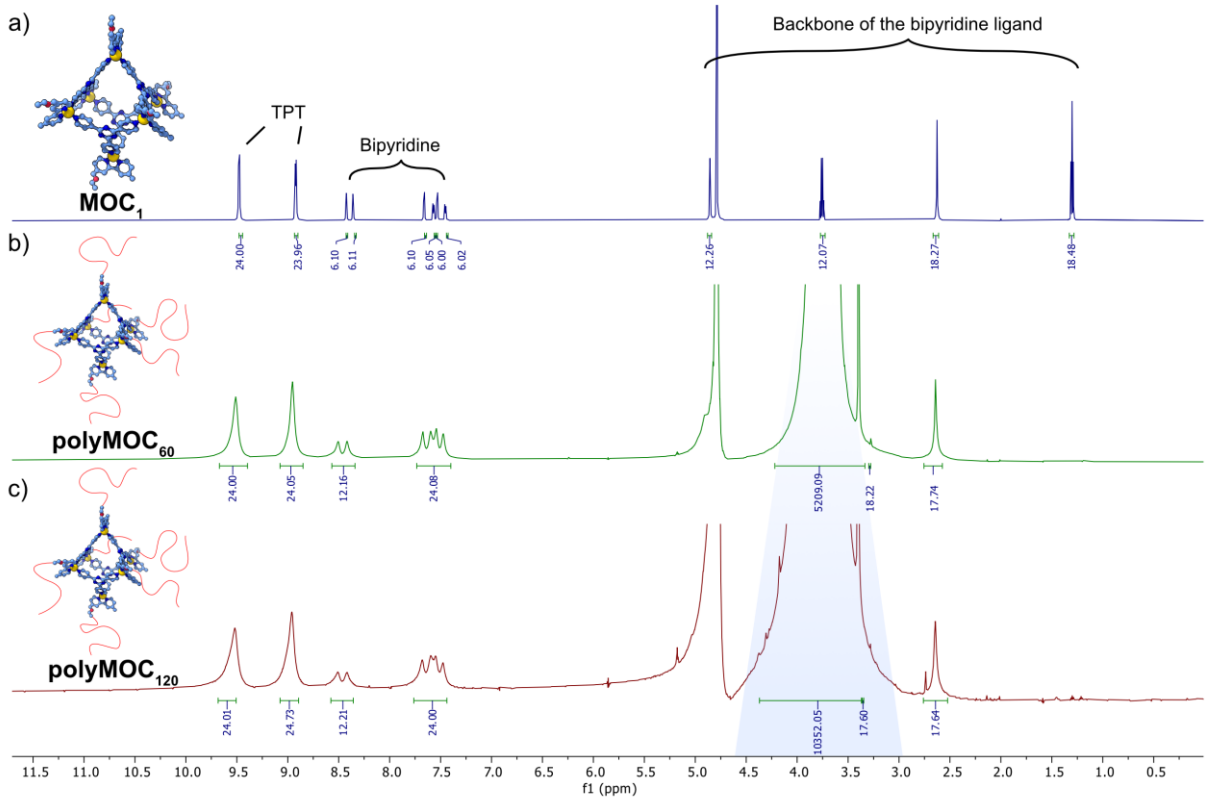

*Figure 8: Stacked ^{1}H NMR spectra for the comparisson of all synthesized MOCs, illustrating the smiliar structural properties of a) control cage **MOC$_1$**, b) **polyMOC$_{60}$** and c) **polyMOC$_{120}$**. The increasing polymer length is highlighted in blue.*

After obtaining all three supramolecular self-assembled cages in high conversion, the investigation of their host-guest properties was approached.

3.1.3 Guest encapsulation

Introduction

The following chapter covers the guest encapsulation for all synthesized **MOCs**. An initial occurring complication was the weak signal-to-noise ratio and resonance broadening during ^{1}H NMR analysis of the utilized cages **polyMOC$_{60}$** and **polyMOC$_{120}$**. Another issue that arose was a signal interference between the polymeric backbone of the cages **polyMOC$_{60\text{-}120}$** and those of their guests, as seen in Figure 9 (4.5 – 2.0 ppm, marked blue). For reasons of analytical simplicity, the area from approximately δ = 1.0 to -2.0 ppm will often be called "guest" region, even though some guest signals are not in this region. As a result of the previously mentioned complications, all guest encapsulations were initiated with the model compound **MOC$_1$** as an analytical foundation and are covered in the first section of this chapter. The second part contains detailed information on the host-guest properties of the larger star-shaped supramolecular cages, **polyMOC$_{60}$** and **polyMOC$_{120}$**, and compares them with their predecessor, **MOC$_1$**.

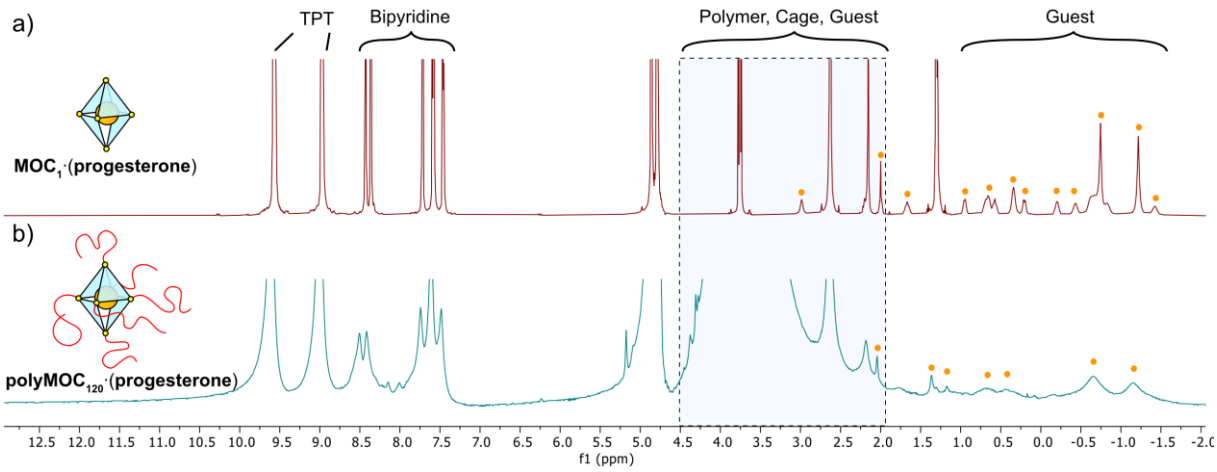

*Figure 9: ^{1}H NMR comparison of **MOC$_1$** and **polyMOC$_{120}$**. Highlighted in blue is the interference of the polymer backbone with the encapsulated guests.*

*Encapsulations studies of model compound **MOC$_1$***

The triazine based T_d-symmetric M_6L_4 cages are ideal hosts because they are both extremely water-soluble due to their cationic nature and have a hydrophobic cavity formed by the **TPT** panels (Figure 10). This combination of properties makes it a versatile tool for the encapsulation of hydrophobic guests (see section 1.3.1). The cage itself has a diameter of approximately 2 nm[101] and a portal size of *circa* 8 Å,[69] rendering it suitable to enclathrate up to four guests depending on their shape and size. The Fujita group has already demonstrated the host-guest properties of M_6L_4-type cages for a variety of interesting molecules, so this work will shift the focus to pharmaceutically more significant medications.

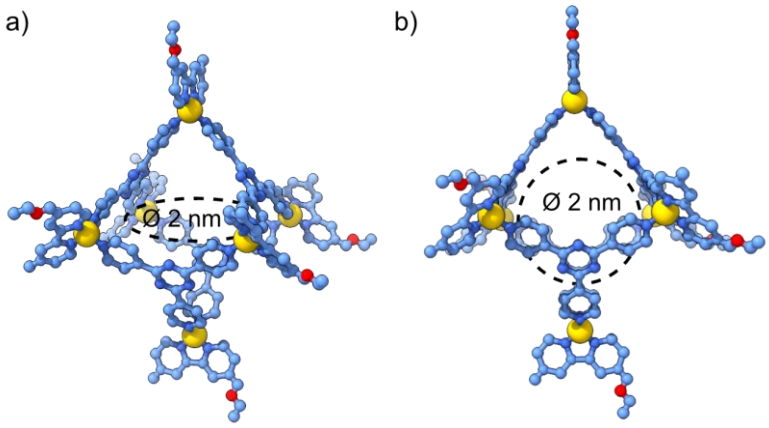

*Figure 10: Depicted are the universal force field-optimized (UFF) structures of **MOC$_1$**. Side view (left), front view (right).*

Every encapsulation was carried out in the same manner, whereby an excess of the desired guest (5.0 eq.) was suspended in a 5 mM aqueous solution of cage **MOC$_1$** and stirred for two hours at 80 °C. As described in Section 1.3.1, the guests used here are hydrophobic and thus mostly insoluble under the used aqueous conditions. Thus, only the exact number of guests that can be encapsulated by the host will be enclathrated, whereby the excess will remain insoluble and will subsequently be filtered off during the purification step.

Steroids

Steroids are organic molecules that have a core framework of four aliphatic rings organized in a certain chemical configuration that is physiologically active. Due to their therapeutic importance, which ranges from anti-inflammatory and immune-modulating properties to the control of salt and water levels, they are attractive compounds for guest encapsulation.[102]

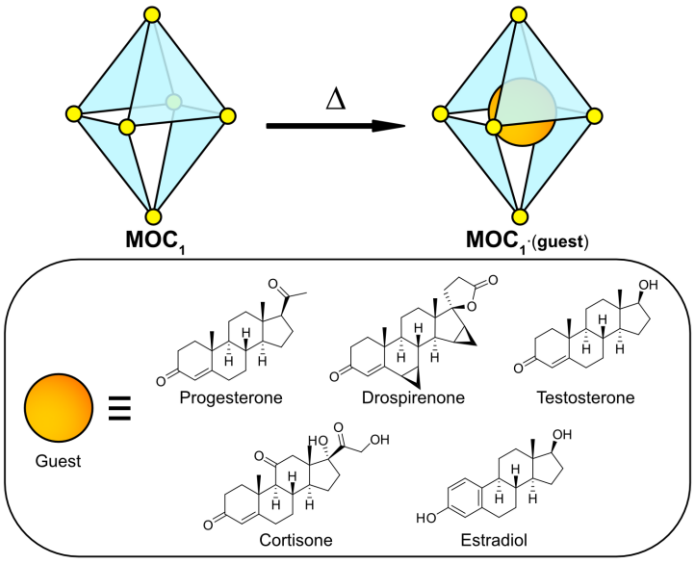

Scheme 20: Schematic overview of the encapsulation process and the here encapsulated steroids.

Progesterone, which is the major progestogen in the body, is involved in the menstrual cycle, embryogenesis,[103] and pregnancy. In addition to serving a number of vital bodily functions, it is also used as a contraceptive pill and as a drug to lower the chance of uterine[104] or cervical cancer.[105] The absence of functional groups capable of decomposing cage **MOC$_1$** on the one hand, its non-polar characteristics, and the existence of multiple unique methyl groups for future analytical characterization make progesterone an ideal choice for guest encapsulation studies (Scheme 20). This guest uptake can be observed by a large upfield shift of the guest protons in the ^{1}H NMR spectrum,

which is a consequence of the utilized **TPT**-panels and its pronounced shielding effect (Figure 11). The characteristic methyl groups of progesterone can be observed as two sharp singlets and therefore act as an excellent probe to follow a successful guest encapsulation. As shown in the ^{1}H NMR of cage **MOC$_1$·(progesterone)**, this self-assembled host is capable to encapsulate exactly one progesterone molecule per cage cavity (orange dots), which is indicated by the cage to guest integral proportion (Signals in ^{1}H NMR; cage: 144 H, guest: 30 H, Figure 11b). The characteristic **TPT** (9.50 ppm and 8.95 ppm) and bipyridine (8.43 – 7.45 ppm) protons experience a small downfield shift during guest uptake, which implies a decrease in the electron density of cage **MOC$_1$**. Whereas the encapsulated progesterone signals experience an unusually large upfield shift and occur between 3.00 and -1.42 ppm, induced by the shielding effect of **TPT**. As seen in Figure 11b the sharp signals of the progesterone methyl groups (-0.74, -1.21 ppm) act as a good probe to follow the analysis.

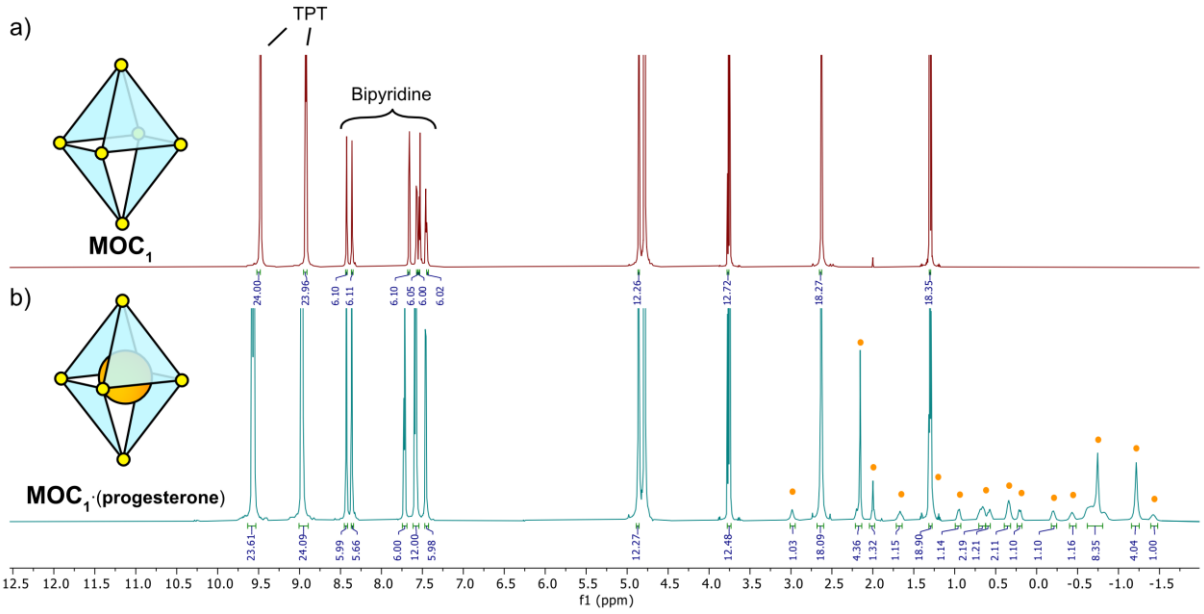

*Figure 11: ^{1}H NMR spectrum of a) **MOC$_1$** and b) the successful encapsulation of progesterone (bottom). The guest signals are marked with an orange dot.*

Also observable in the ^{1}H NMR spectrum of the model compound **MOC$_1$** is a split and downfield shift of the **TPT** signals (Figure 12), which can be caused by either an incomplete encapsulation of the guest or by a symmetry change of the self-assembled cage **MOC$_1$**. Additionally, a similar downfield shift for the outwards facing bipyridine group can be observed (Figure 12b). Incomplete enclathration would result in two sets of cage signals: one for the progesterone-encapsulating cage (**MOC$_1$·(progesterone)**) and one for an empty cage (**MOC$_1$**). Given that the remaining signals, such as the ethyl substituent, are absent from the ^{1}H NMR and only a split for the **TPT** signals was observed, this claim of an incomplete encapsulation, doesn't appear feasible. A full encapsulation was also demonstrated by DOSY NMR

(Figure 12c), which suggests that a symmetry change does in fact take place after the guest uptake.[94a] Noticeable in the ^{1}H DOSY spectrum is the diffusion coefficient of **MOC$_1$·(progesterone)** D = 2.01 x 10^{-10} m^2 s^{-1}, which results in a hydrodynamic radius of roughly 10 Å (Calculated by using the Stokes-Einstein-equation). As previously stated, the diameter of the cage **MOC$_1$** is approximately 2 nm (or a radius of 10 Å), which is consistent with the DOSY results shown in Figure 12c. These findings of a successful encapsulation were further supported by heteronuclear 2D measurements (Figure 143-145).

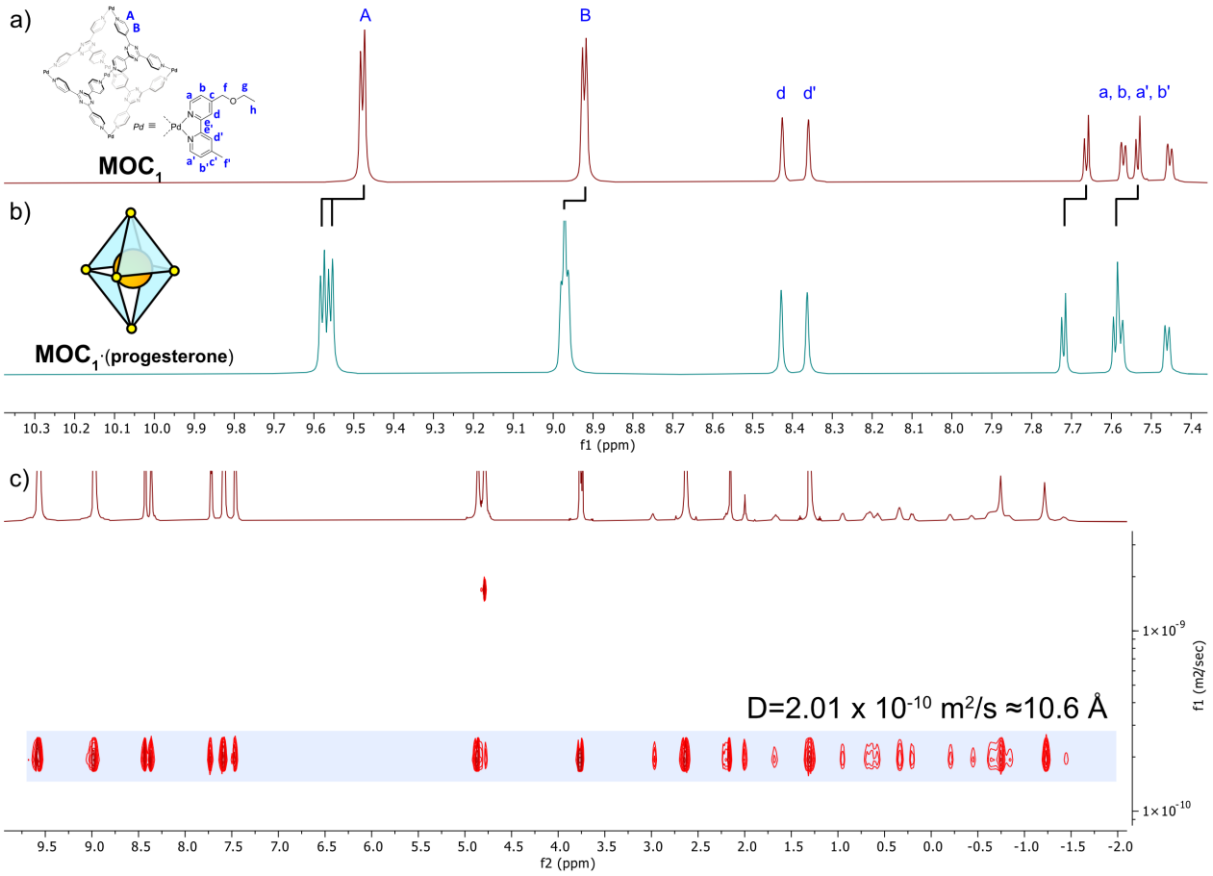

*Figure 12: a) ^{1}H NMR spectrum of the aromatic region of **MOC$_1$**. b) ^{1}H NMR spectrum of the guest encapsulation influencing the electronic properties of cage **MOC$_1$·(progesterone)**. Distinctive downfield shift for **TPT** can be observed. c) ^{1}H DOSY NMR confirming the successful guest uptake of progesterone. Using the stokes-Einstein-equation results in a solvodynamic radius of 10.6 Å.*

With the successful enclathration of progesterone, a subsequent guest screening of different steroids was performed. These steroids were either chosen because of their medical applications or because of their molecular structure. The investigation of these compounds gave similar results to those of the previously presented progesterone. Additionally, it was found that, due to the bulky nature of steroid molecules, it was never possible to encapsulate more than one guest molecule per host moiety. All

guest encapsulations were confirmed by ^{1}H NMR and DOSY measurements (except for estradiol) and are depicted in Table 1. In addition to the hydrodynamic radii, all relative shifts of the aliphatic protons from the free steroids in comparison to the encapsulated guest are added in Table 1 and are ranging from δ = -0.90 to -2.08 ppm, thus indicating a strong interaction between host and guest.

*Table 1: All encapsulated steroids for cage **MOC$_1$**. The most pronounced signals for the methyl groups are listed and show a clear upfield shift. Additionally, the relative shifts in contrast to the pristine steroids show the influence of encapsulation. The hydrodynamic radius was determined by ^{1}H DOSY NMR (D_2O, 298 K, 600 MHz) measurements and is in accordance with the literature.*

Steroid	Structure	Methyl proton [ppm]	Relative shift [ppm]	Hydrodynamic radius [Å]
Progesterone	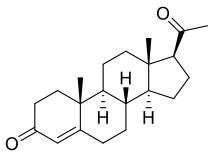	-0.74 and -1.22	-2.01 and -1.93	10.6
Drospirenone	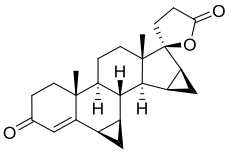	-0.98 and -1.12	-2.08 and -2.12	10.0
Testosterone	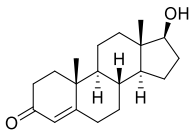	-0.87 and -0.97	-2.08 and -1.77	10.4
Cortisone	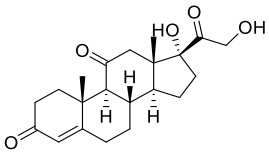	0.04 and -0.65	-1.28 and 1.12	8.55
Estradiol	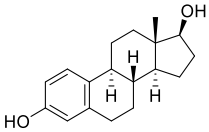	-0.27	-0.90	N/A

Pharmaceutical drugs

Another important goal for the following targeted guest release was the encapsulation of pharmaceutically active drugs. Therefore, six relevant substrates were investigated for potential guest encapsulation. The screening was initiated with Ibuprofen, which is the most commonly used and prescribed nonsteroidal anti-inflammatory drug. Ibuprofen is also used as an analgesic and an antipyretic agent.[102b] The same procedure as for progesterone was used for guest encapsulation. A successful uptake was confirmed by ^{1}H NMR and DOSY. Unlike the enclathrated steroids, it was discovered that two ibuprofen molecules could be incorporated into the cavity of each **MOC$_1$**. The ratio

of proton signals from cage to guests provided evidence of this occurrence and is depicted in Figure 13 (signals in ^{1}H NMR; cage:144 H, guest:36 H). Heteronuclear 2D measurements further supported the successful guest uptake (Figure 163-165). The two sharp signals for the methyl groups (highlighted blue in Figure 13), which experience a high upfield shift of δ = 1.5 ppm, make ibuprofen an excellent choice for subsequent ultrasound irradiation experiments and a concomitant targeted drug release.

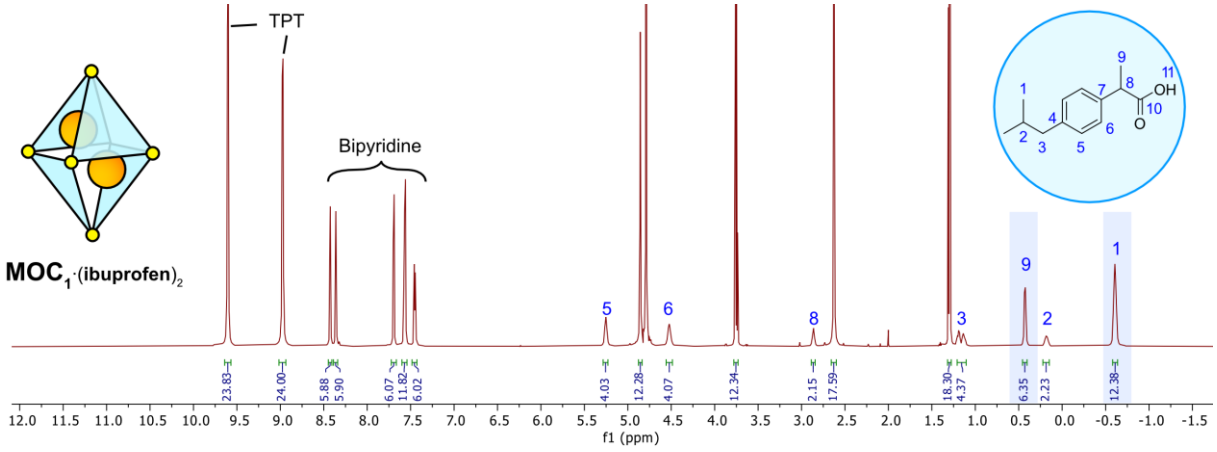

*Figure 13: Depicted is the ^{1}H NMR of encapsulated ibuprofen in **MOC$_1$·(ibuprofen)$_2$**.*

After successful guest uptake of ibuprofen, further pharmaceutically active compounds were probed for enclathration. Starting with the encapsulation of paracetamol, it could not unambiguously be proven that this guest was incorporated into the host cavity. The appearance of three new signals in the ^{1}H NMR (Figure 168) led to the assumption that four moieties of paracetamol were incorporated into the cavity, but the chemical shift of less than δ = 0.2 ppm suggested that the encapsulation was unsuccessful. In the instance of melatonin, it was possible to observe a color shift throughout the reaction from bright yellow to red, which indicates the formation of a charge transfer complex between the host and guest.[100] ^{1}H NMR revealed that, in fact, the broad signals of melatonin experienced an upfield shift (Figure 170). Nonetheless, the ^{1}H DOSY NMR for this encapsulation appeared to be solely the cage (Figure 171). Aspirin, lidocaine, and fluconazole were all unsuitable guests. They were either not encapsulated or, in the case of fluconazole, even decomposed the cage. This was explained by the heterocyclic triazole group, which functions as a competitive ligand, resulting in a slow decomposition of cage **MOC$_1$**.

It has to be noted that in almost all cases, decomposition of the self-assembled cages occurred at some point due to the here utilized drugs and their functional groups. This decomposition was often observed in dissolved samples and indicated by precipitation over time. Nonetheless, **MOC$_1$** was stable

for several weeks under these conditions, whereas decomposition of fluconazole was observed immediately after filtration. All results are summarized in Table 2.

*Table 2: All attempted encapsulated drugs of this section for cage **MOC$_1$**. The hydrodynamic radius was determined by ^{1}H DOSY NMR (D_2O, 298 K, 600 MHz) measurements. A checkmark indicates a successful encapsulation, whereas a cross indicates no encapsulation. Both signs indicate that encapsulation was not proven unambiguously.*

Medicament	Structure	Hydrodynamic radius [Å]	Encapsulated equivalents	Encapsulated
Ibuprofen	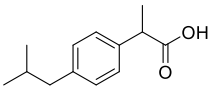	10.2	2	✓
Paracetamol	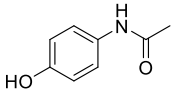	6.14	4	✓/×
Melatonin	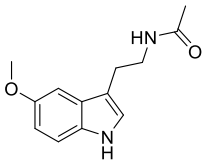	10.4	Can't be determined	✓/×
Aspirin	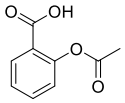	N/A	N/A	×
Lidocaine	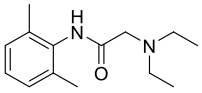	N/A	N/A	×
Fluconazole	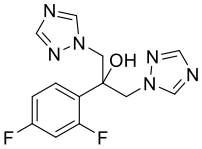	N/A	N/A	×

Intensely colored chromophores

The last group of potential guests that was investigated consists of compounds with chromophoric properties. Interestingly, these properties in the unbound state can change drastically upon encapsulation, making them a versatile tool for the visualization of host-guest interactions. The pH indicator phenolphthalein, for example, is a colored quinone dianion at high pH values but undergoes a ring-closing reaction to the colorless lactone at low pH. This pH-dependent reaction is well documented, but it can also be enforced through encapsulation, known as cavity-directed chromism.[94b] The spatial constraint of the confined cavity pushes the equilibrium towards the encapsulated ring-closed lactone form, resulting in the loss of its color even under basic conditions.

*Figure 14: a) Basic solution of phenolphthalein. b) After the rapid addition of cage **MOC$_1$**.*

The encapsulation of phenolphthalein was initially performed under neutral conditions to receive a confirmation by ^{1}H NMR and DOSY (Figure 172, 173). In contrast to the previous results, only around 75 % of the inclusion complex could be formed. The subsequent addition of model compound **MOC$_1$** to a basic carbonate buffer solution of phenolphthalein resulted in the mentioned enforced conformation change, leading to a color change from purple to a colorless solution (Figure 14). UV/Vis spectroscopy was conducted to measure the absorbance for phenolphthalein at 552 nm. Therefore, a 10 mM buffer solution of potassium carbonate with phenolphthalein (0.12 µmol) was prepared. Subsequently, 0.05 equivalents of the self-assembled cage **MOC$_1$** (6 pmol) were added, resulting in a decrease in the absorbance for phenolphthalein at 552 nm, clearly indicating the encapsulation. After the addition of 2.6 eq. of model compound **MOC$_1$** no complete guest uptake was noticed, which was attributed to the previously observed cage decomposition under basic conditions (Figure 15a). Thus, the experiment was repeated with a 1 mM buffer solution, and a rapid addition of 0.5 equivalents of the host **MOC$_1$** (0.06 µmol) was conducted. In contrast to the previous measurement, a complete disappearance of the absorbance for phenolphthalein was achieved (Figure 15b) but this was accompanied by the loss of the isosbestic point. Therefore, this indicates that the analytical concentrations of the substances did not gradually increased (**MOC$_1$**) and decreased (Phenolphthalein) during encapsulation throughout the measurement but instead a side reaction occurred (possible decomposition).

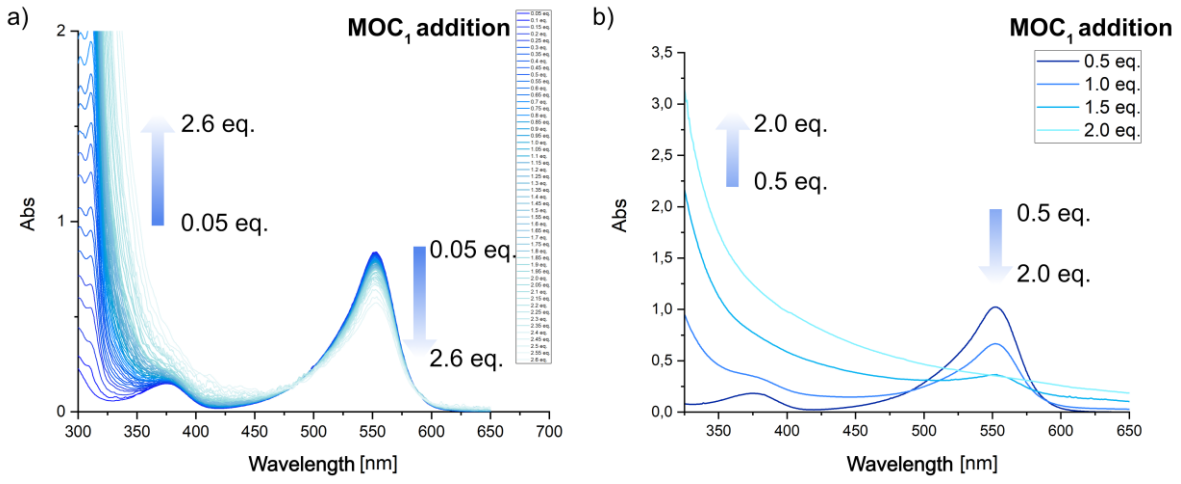

*Figure 15: a) UV/Vis spectrum of the encapsulation of phenolphthalein (4.0·10^{-5} M) by **MOC$_1$** in a carbonate buffer solution. b) UV/Vis spectrum of phenolphthalein (4.0·10^{-5} M) in a carbonate buffer solution after a fast addition of **MOC$_1$**. A complete disappearance of the phenolphthalein can be observed.*

A metal ion exchange from palladium to platinum might be used to prevent this decomposition, resulting in increased M_6L_4 stability.[46] However, this method is not suitable for the polymeric star-

shaped cages **polyMOC$_{60\text{-}120}$** since it would cause the polymeric backbone most likely to decompose due to the elevated temperatures (**PEG$_{60}$** can decompose at elevated temperatures above 80-90 °C) and time required for cage formation, and was therefore not investigated in this work.

The last encapsulation that will be discussed is the co-encapsulation of caffeine and pyrene in cage **MOC$_1$**. Interestingly, no individual encapsulation of caffeine nor pyrene could be achieved. Only in the combination of both guests (1:1) a complexation was detected, indicated by an orange suspension. By enforcing both guests into close proximity, a charge-transfer complex was formed, which explains the color change during the reaction.[100] ^{1}H NMR reveals a large upfield shift for both incorporated guests (Figure 178). In addition, ^{1}H DOSY NMR analysis shows that, in fact, a guest uptake can be confirmed, but the hydrodynamic radius is not in accordance with previous results (Figure 179).

*Table 3: All attempted encapsulations of this section for cage **MOC$_1$**. The hydrodynamic radius was determined by ^{1}H DOSY NMR (D_2O, 298 K, 600 MHz) measurements. A checkmark indicates a successful encapsulation, whereas a cross indicates no encapsulation. Both signs indicate that encapsulation was not proven unambiguously.*

Medicament	Structure	Hydrodynamic radius [Å]	Encapsulated equivalents	Encapsulated
Phenolphthalein	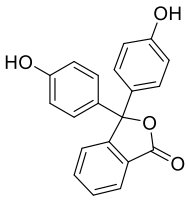	11.4	Less than 1	✓
Umbelliferon	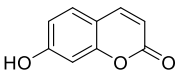	11.5	2	✓
Flavone	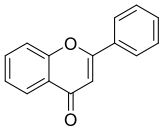	6.78	2	✓/×
Caffeine and pyrene	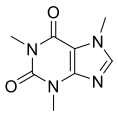 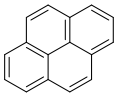	4.67	1 each	✓/×
Ferrocene	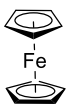	N/A	N/A	×
1,3,5-Trifluorobenzene		N/A	N/A	×

The analysis of umbelliferon was successfully conducted, whereas the uptake of flavone was only confirmed by ^{1}H NMR. The encapsulation of ferrocene and 1,3,5-trifluorobenzene proved to be unsuccessful. All results are summarized in Table 3.

In summary, **MOC$_1$** provides a versatile framework for targeted enclathration. Various guest molecules, ranging from biologically active steroids to spectroscopically relevant compounds, were incorporated by host **MOC$_1$** and confirmed by different analytical methods. With this insight, the host-guest properties of two larger polymeric supramolecular cages (**polyMOC$_{60\text{-}120}$**) were investigated.

*Encapsulations studies of star shaped self-assembled cages **polyMOC$_{60}$** and **polyMOC$_{120}$***

A main goal of this work was the targeted release of pharmaceutically relevant compounds by utilizing ultrasound. While the previously synthesized smaller cage **MOC$_1$** proved to be an excellent host, it is by nature not capable of being activated through sonochemical forces, thus cages with an increased M_n had to be employed for this task. It was assumed that all three cages (**MOC$_1$**, **polyMOC$_{60}$** and **polyMOC$_{120}$**) exhibit the same cavity properties regardless of its outwards facing substituents, meaning that the encapsulation should be mostly unaffected by the sterically demanding poly(ethylene glycol) groups of **polyMOC$_{60}$** and **polyMOC$_{120}$**. As a result, only two criteria for a targeted uptake must be fulfilled by the potential guest:

a) ^{1}H NMR signals of incorporated molecules must be mostly unaffected by the interfering polymer backbone of their host.

b) A suitable signal-to-noise ratio has to be given to investigate guest encapsulation and subsequent release.

Both of these requirements are completely met by ibuprofen and progesterone. A third candidate for guest binding is phenolphthalein. Even though this compound falls short of meeting all requirements, it is nevertheless a compelling candidate since encapsulation and release can be observed with the naked eye. Guest encapsulation studies were conducted by adding an excess of the desired guest (10 eq.) to a 3 mM aqueous solution of **polyMOC$_{60}$** or a 1 mM solution of **polyMOC$_{120}$**. These reactions were then heated for one hour at 50 °C before the residual guest was filtered out and the obtained solution was freeze-dried for a subsequent ^{1}H NMR analysis.

Progesterone

The unique shielding effect exhibited by the **TPT** panels on progesterone, which caused a considerable upfield shift of the distinct methyl group signals to approximately -1.15 ppm (Figure 16, guests marked

as orange dots), once more validated guest uptake by ^{1}H NMR, thus proving encapsulation within the cavity of cage **polyMOC$_{60}$·(progesterone)** and **polyMOC$_{120}$·(progesterone)** (Figure 16). Furthermore, it can also be observed that an increasing polymer length results in a smaller upfield shift for the guest signals (marked blue in Figure 16b and c). Although it has been demonstrated that cage **MOC$_1$** can incorporate one progesterone molecule per cavity, it was difficult to precisely determine the quantity of guest uptake for cage **polyMOC$_{60}$·(progesterone)** due to signals broadening (Figure 16b). Encapsulation in cage **polyMOC$_{120}$·(progesterone)** was challenging since integration of ^{1}H NMR signals proved to be unreliable as a result of the inherent low signal-to-noise ratio (Figure 16c). Although no integration was possible, it was assumed that the uptake of only one progesterone per cavity was achievable based on prior encapsulation results with **MOC$_1$·(progesterone)**. As a result of the disproportionate distribution of protons between polymer and guest (5500 to 30 protons), neither DOSY spectra nor heteronuclear measurements could be obtained.

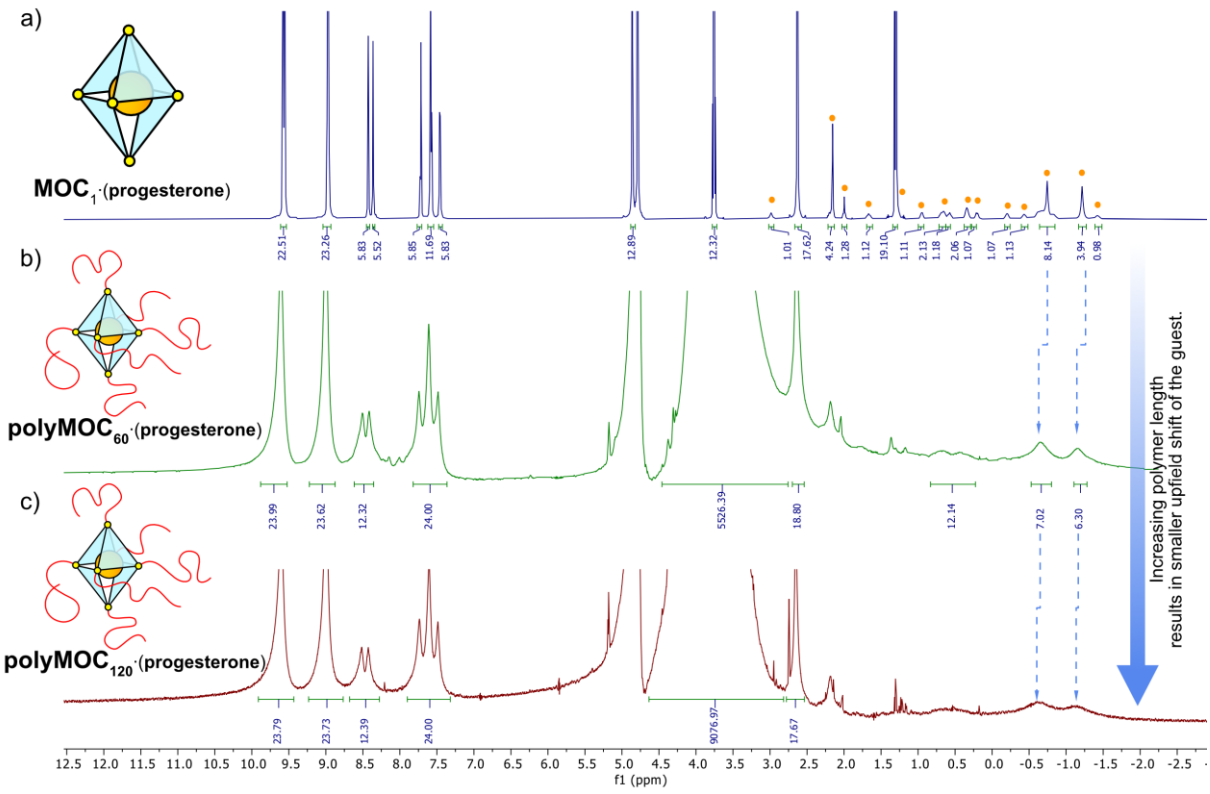

*Figure 16: Stacked ^{1}H NMR spectra of encapsulated progesterone by the respective **MOCs**. Progesterone was marked as orange dots. a) Encapsulated progesterone in **MOC$_1$·(progesterone)** for comparison. b) Encapsulated progesterone in **polyMOC$_{60}$·(progesterone)**. c) Encapsulated progesterone in **polyMOC$_{120}$·(progesterone)**.*

Ibuprofen

The successful encapsulation of ibuprofen for cage **polyMOC$_{60}$·(ibuprofen)$_2$** and **polyMOC$_{120}$·(ibuprofen)$_2$** was confirmed by ^{1}H NMR and is depicted in Figure 17. According to the preceding result, it can be shown that the upfield shift diminishes as polymer length increases, further strengthening the hypothesis that the electron density decreases in the polymer-embedded cavity. Despite the presence of resonance widening, an accurate estimation of guest uptake was attainable, resulting in the encapsulation of two ibuprofen moieties per cage cavity, which is in accordance with the results of cage **MOC$_1$·(ibuprofen)$_2$**.

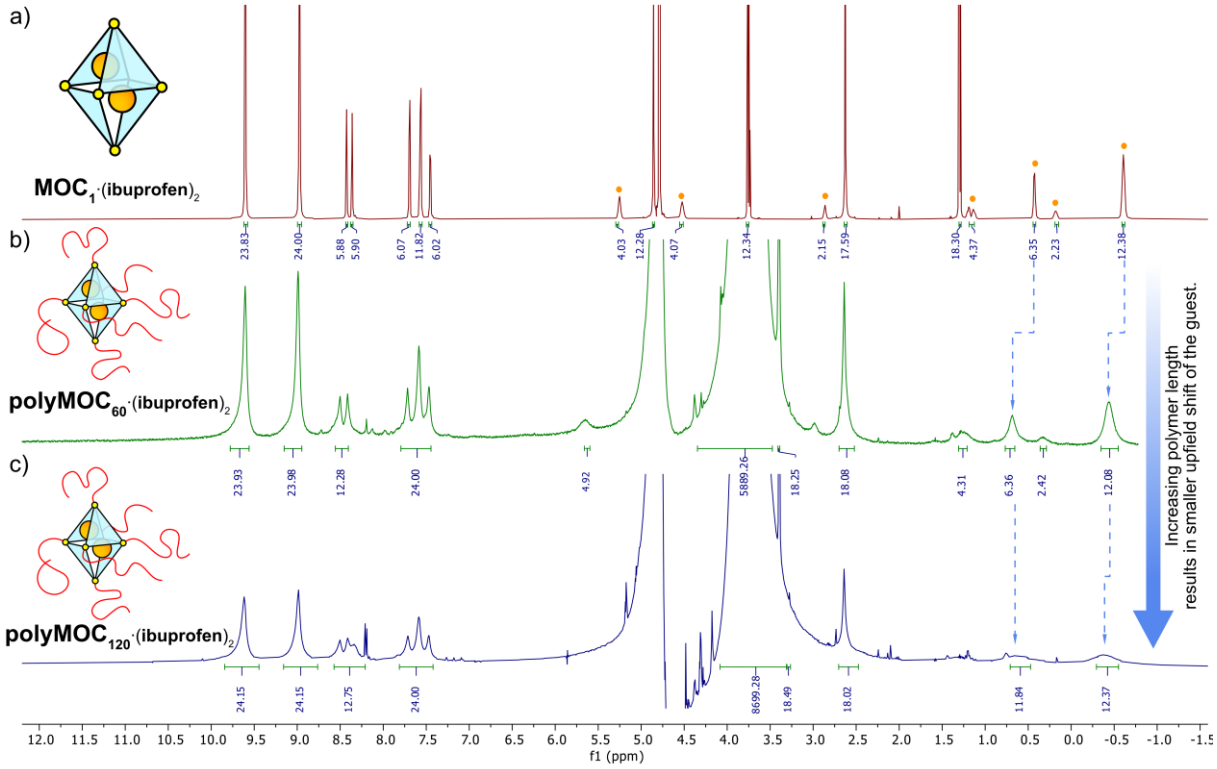

*Figure 17: Stacked ^{1}H NMR spectra of encapsulated ibuprofen by the respective **MOCs**. Ibuprofen was marked as orange dots. a) Encapsulated ibuprofen in **MOC$_1$·(ibuprofen)$_2$** for comparison. b) Encapsulated ibuprofen in **polyMOC$_{60}$·(ibuprofen)$_2$**. c) Encapsulated ibuprofen in **polyMOC$_{120}$·(ibuprofen)$_2$**. Due to the very low signal-to-noise ratio for the protons assigned to the cage signals in contrast to the corresponding PEG-backbone, the phase correction could not be further improved.*

Phenolphthalein

The last guest uptake that is going to be investigated for cage **polyMOC$_{60}$** is phenolphthalein.

*Figure 18: Basic solution of phenolphthalein after addition of cage **MOC$_1$**.*

Therefore, 0.5 equivalents of phenolphthalein were added to an aqueous 3.3 mM solution of cage **polyMOC$_{60}$** and heated to 50 °C for one hour. After the solvent was removed, a yellow solid was obtained. A confirmation that phenolphthalein was incorporated could not be determined by ^{1}H nor DOSY NMR due to the weak signal-to-noise ratio as depicted in Figure 19b. The addition of a 1.0 mM carbonate buffer solution to a 0.4 mM sample of cage **polyMOC$_{60}$·(phenolphthalein)** was performed to test the potential guest uptake. A color change from pale yellow to purple would indicate that phenolphthalein

was not incorporated. After several hours, no color change was observed, suggesting that guest uptake was successful. To further confirm the encapsulation, a phenolphthalein solution (c = 1.4 µg mL^{-1}) was adjusted to pH = 10 with potassium carbonate, and an excess (c = 1.4 mg mL^{-1}) of star-shaped polymeric cage **polyMOC$_{60}$** was added. The disappearance of the purple color was observed after the addition of cage **polyMOC$_{60}$** (Figure 18).

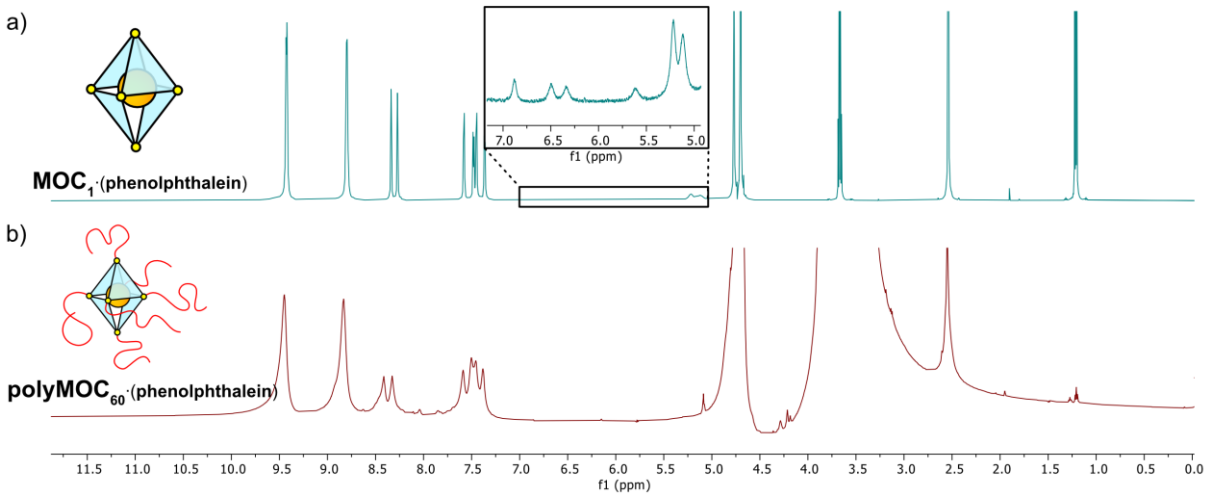

*Figure 19: a) ^{1}H NMR spectrum of the encapsulated phenolphthalein and the magnified area of the guest. b) Formation of **polyMOC$_{60}$·(phenolphthalein)** could not be confirmed by ^{1}H NMR due to resonance broadening and low signal-to-noise ratio.*

Interim conclusion

The successful encapsulation of 12 unique non-covalently bound and unmodified guests for the small model compound **MOC$_1$** was confirmed in this section by different spectroscopical analytical methods. While cage **MOC$_1$** exhibited great host-guest properties, it also offered a solid foundation for further encapsulation studies with the structurally bulkier polymeric hosts **polyMOC$_{60}$** and **polyMOC$_{120}$**. Ibuprofen, progesterone, and phenolphthalein were exemplary compounds chosen for guest uptake to prove that the host-guest properties of the star-shaped polymeric cages **polyMOC$_{60}$** and **polyMOC$_{120}$** are similar to the model compound **MOC$_1$**. These experiments were supported by ^{1}H NMR analysis. Subsequent ultrasound irradiation experiments will be conducted to probe the behavior of all synthesized cages under induced force.

3.1.4 Sonochemical experiments

Disassembly

Once all necessary guest encapsulations had been accomplished, the examination of a targeted guest release was conducted. To analyze the mechano-responsive potential of the previously synthesized cages, **polyMOC$_{60\text{-}120}$**, samples were exposed to an acoustic field using a sonicator with a frequency of 20 kHz. All samples were sonicated in water, ice cooled during the whole duration, and the concentrations are stated individually for each experiment. Here, three factors were analyzed in detail:

a) Is there any effect on selective bond scissioning during sonication by extending the polymer length?

b) Is the ultrasound-induced cage fragmentation time dependent?

c) Can a guest release be achieved, and if so, is it driven by the disassembly of its host, or can a guest slippage occur during sonication?

To answer the first question, all highly water-soluble cages (**MOC$_1$** and **polyMOC$_{60\text{-}120}$**) were sonicated without a cargo load. Starting with the self-assembled model compound **MOC$_1$** it was expected that no host decomposition would take place during ultra-sonification exposure due to absence of polymer chains needed to experience the required cleavage force. The supramolecular cage **MOC$_1$** was subjected to ultrasound for longer than necessary to ensure that cage defragmentation does not occur due to temperature- or pressure-induced processes. Therefore, a 1 mg mL^{-1} aqueous solution of the control cage **MOC$_1$** was filled into a suslick vessel and sonicated with a sequence of 1 s on and 1 s off, for three hours (on time) (Figure 20). For all subsequent sonication experiments, only the "on time" of the sonicator will be stated. Cage **MOC$_1$** exhibited a barely noticeable color change after exposure to ultrasound, resulting in a pale-yellow solution. After the solvent was removed by freeze-drying, **MOC$_1$** was subjected to ^{1}H NMR analysis. As anticipated, no defragmentation occurred even after extensive ultrasound irradiation, which is indicated by the unchanged ^{1}H NMR depicted in Figure 21.

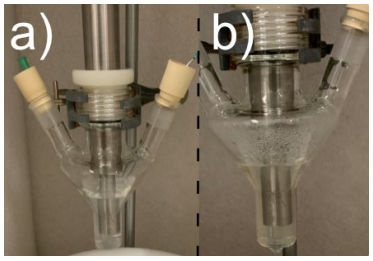

*Figure 20: Sonochemical apparatus. a) **MOC$_1$** before sonication. b) **MOC$_1$** after sonication.*

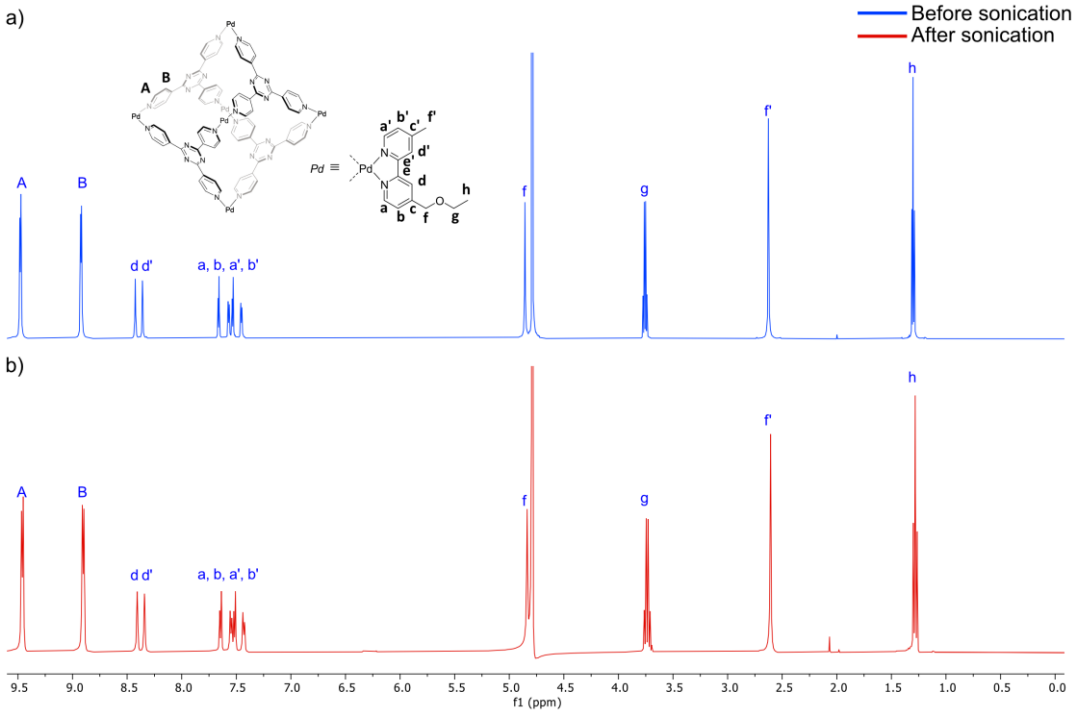

*Figure 21: Stacked ^{1}H NMR spectra before (top) and after (bottom) three hours of sonicating **MOC$_1$**. No cage fragmentation could be observed during this experiment.*

The investigation of the polymer-embedded star-shaped cage **polyMOC$_{60}$** was conducted in a similar manner as **MOC$_1$**, by exposing a 5 mg mL^{-1} aqueous solution to ultrasound for one hour (on time).

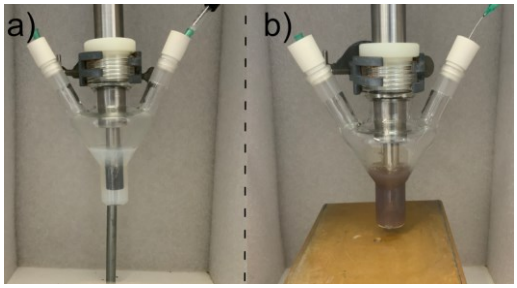

*Figure 22: Ultrasound irradiation was conducted for one hour. a) **polyMOC$_{60}$** before sonication. b) **polyMOC$_{60}$** after sonication.*

Interestingly, after several minutes, a color change of the reaction occurred, which ultimately resulted in a dark brown solution after one hour of irradiation and is depicted in Figure 22b. The origin of the color change was not unambiguously confirmed, but the hypothesis arose that this phenomenon might be attributed to the decomposition of the cage. After the solvent was removed, the compound was analyzed by ^{1}H NMR and GPC. Contrary to model compound **MOC$_1$**, it was observed that ultrasound exposure actually led to the mechanophore's disassembly. Figure 23 shows the appearance of three new sets of signals (8.65 - 8.55, 8.15 and 7.85 - 7.75 ppm, marked with an asterisk), which initially could not be assigned to a specific molecule or cage fragment. Comparing these signals to those from the pristine cage **polyMOC$_{60}$** (Figure 23b, top and bottom), a distinct downfield shift was observed.

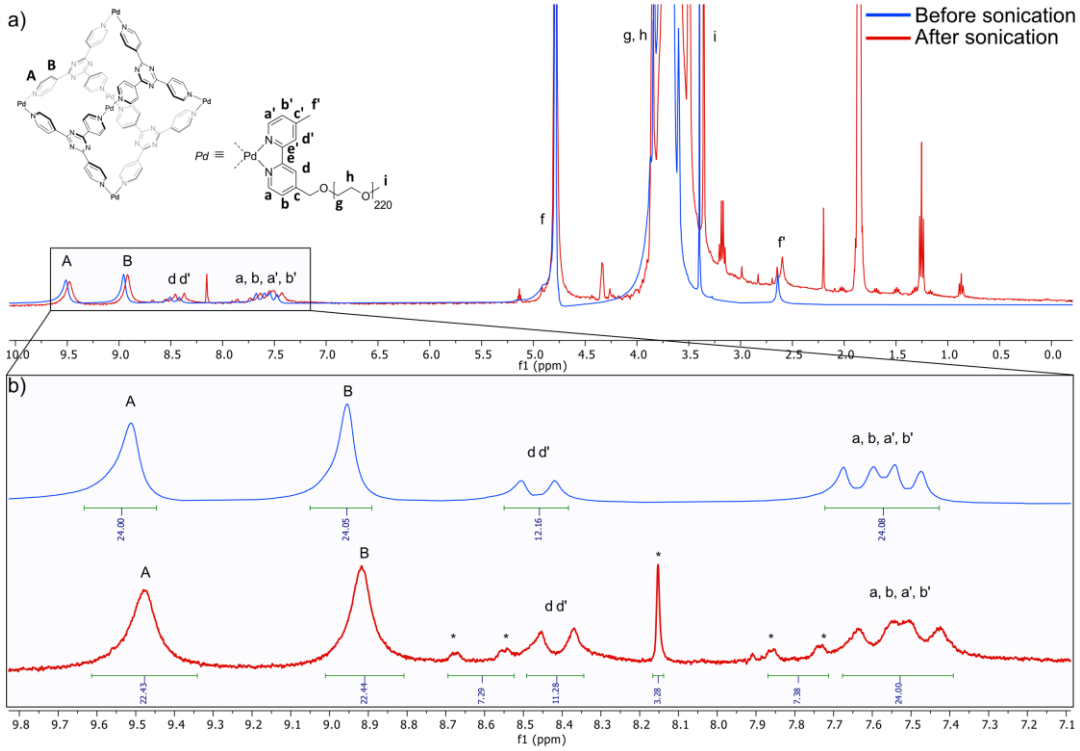

*Figure 23: ^{1}H NMR of **polyMOC$_{60}$** after one hour of sonication. a) Complete NMR spectrum. b) Magnified spectra of the aromatic region. Before (top) and after (bottom) sonication.*

There are three explanations for this phenomenon. In section 1.2 it was mentioned that upon cage formation, the protons of the bipyridine ligand experience a large upfield shift as a result of an increased electron density. Therefore, it is logical that during the cage disassembly, or more precisely during the bond scissioning between bipyridine complex **24** and **TPT**, a downfield shift for the bipyridine signals occurs (8.65-8.55, 8.15 and 7.85-7.75 ppm, marked with an asterisk). **TPT**, on the other hand, is insoluble in water and precipitates after cage rupture, resulting in no detectable signals in ^{1}H NMR (Scheme 21, top). As a result, only a derivative of the bipyridine ligand can be observed in the NMR spectra and is resembled by the asterisk marked signals (Figure 23b). The second explanation is, that the arising signals (asterisk) in Figure 23b represent a fragment of cage **polyMOC$_{60}$** which is lacking certain "parts" of the cage (Scheme 21, middle). A third hypothesis is that once bipyridine dissociates from the cage, it subsequently reacts with other fractured bipyridine ligands to form a new metal complex (Scheme 21, bottom). Further investigations of this hypothesis have to be performed to confirm the occurrence of these signals. However, evidence suggests that recombination to a bipyridine coordinated palladium complex is the most likely outcome, which will be discussed in greater detail later (see Section 3.2).

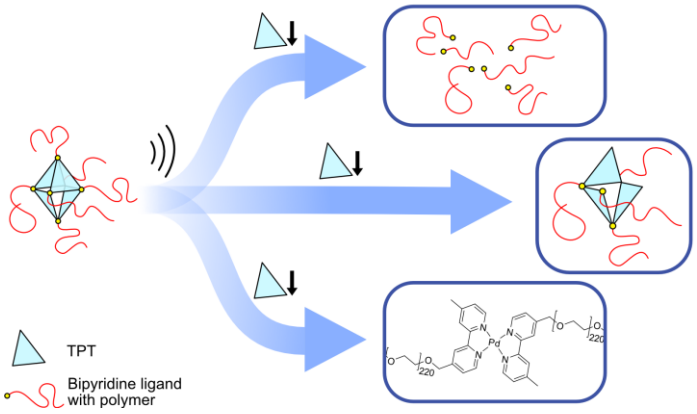

Scheme 21: Illustration of the different hypothetical processes of cage rupture. Top illustrates the reformation of pristine bipyridine derivatives. The middle depictures the disassembly in undefined fragmented cages. Bottom shows the recombination into a smaller metal complex. Counterions were omitted.

On the assumption that the appearing signals correspond to a bipyridine moiety, the integration of the fragment signals (7.4 protons, 7.85-7.75 ppm) and pristine cage signals of **polyMOC$_{60}$** (24 protons, 7.68-7.37 ppm) result in a distribution of 7.4:24 (Figure 23b). The proportion of activation can now be calculated by dividing the integral of the activated cage (7.4 protons) by the total integral for the bipyridine signals (31.4 protons, δ = 7.85-7.35 ppm).

$$\frac{7.4}{(24+7.4)} = 0.24 = 24\,\%$$

By this means, an activation of approximately 24 % was achieved. While this method was initially based on an assumption, it will be used throughout this chapter to calculate the corresponding activation. It was later observed that this method was in fact quite accurate for estimating the fragmentation (section 3.3.6).

To further probe the ultrasound induced defragmentation of the star shaped cage **polyMOC$_{60}$** with a M_n = 60 kDa, samples before and after one hour of sonification were analyzed *via* GPC. Under all employed GPC measurement conditions, a cage disassembly was observed either to the interference from organic solvents or due to the high salt concentrations in aqueous solvents. Therefore, the molar mass distribution of **polyMOC$_{60}$** and the sonicated **polyMOC$_{60}$** after one hour US (see Figure 24 and 72) matches those of the starting material **24** with a Mn = 10 kDa. The appearing shoulder at lower masses (8-9 kDa) can be attributed to non-specific bond scissioning of the utilized PEG units. It was reasoned that the cage structure, rather than the polymer chains, was the mechanochemically weakest link since the amount of non-specific scission that was detected was only negligible compared to the activation observed in ^{1}H NMR.

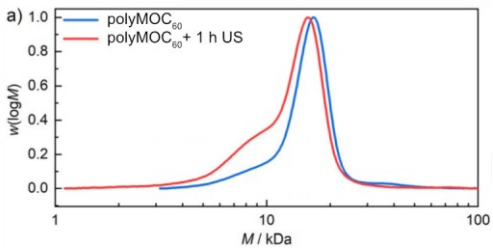

*Figure 24: GPC chromatogram of **polyMOC$_{60}$** obtained in $CHCl_3$. Before (blue) and after (red) one hour of sonication.*

Following the successful disassembly of star-shaped cage **polyMOC$_{60}$**, sonication experiments on the larger isostructural polymeric cage **polyMOC$_{120}$** were conducted. This self-assembled cage was dissolved in a 5 mg mL^{-1} aqueous solution and exposed to ultrasound for one hour, resulting in a similar color change as **polyMOC$_{60}$**, already indicating a successful disassembly. After removal of the solvent, the decomposition was investigated by ^{1}H NMR. Signals at 8.70 - 8.55 ppm, 8.15 ppm and 7.85 - 7.75 ppm were observed and assigned to fragments of **polyMOC$_{120}$** (Figure 25). By comparing these signals with the pristine cage, an estimated activation rate of approximately 44 % was achieved. Which corresponds to an increase of 83 % in contrast to the smaller utilized star-shaped cage **polyMOC$_{60}$**. These results already suggest that the mechanochemical activation of the supramolecular cages **polyMOC$_{60}$** and **polyMOC$_{120}$** can be influenced through the modification of the utilized polymer. Thus, proving the mechanochemical nature of the cleavage process for the synthesized **MOCs**.

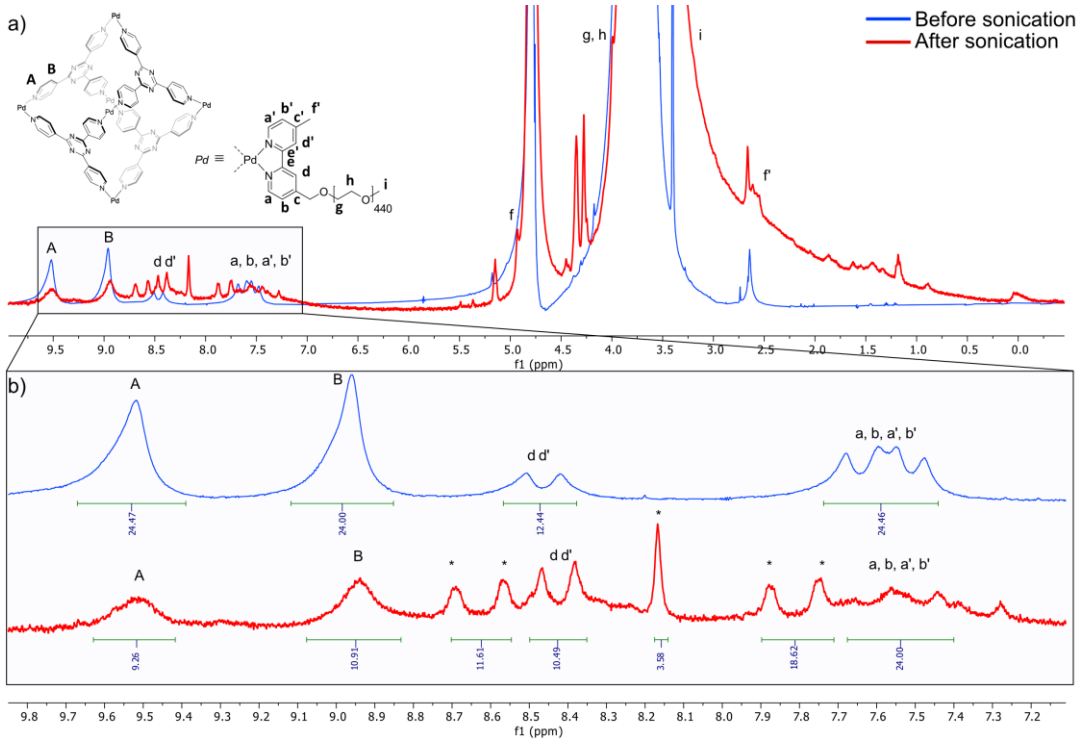

*Figure 25: ^{1}H NMR of **polyMOC$_{120}$** after one hour of sonication. a) Complete NMR spectrum. b) Magnified spectra of the aromatic region. Before (top) and after (bottom) sonication.*

Insight into the degradation mechanism was provided by an investigation of the influence of the initial molecular weight on ultrasonic-induced chain scissioning events. Both cages, **polyMOC$_{60}$** and **polyMOC$_{120}$**, were responsive to ultrasound induced bond scissioning. It was also observed that an increasing molecular weight of the attached polymer chains resulted in a more rapid bond rupture rate. An exchange of the 10 kDa (**24**) to the 20 kDa (**27**) mPEG led to a remarkable increase in activation rate of roughly 83 % (Figure 26b and c). The group of Taghizadeh *et al.*[106] reported a nonlinear dependence between the molecular weight and the rate coefficient *k* for bond rupture of poly(vinyl pyrrole), whereas Madras *et al*. suggests a linearly dependency for the bond scission rate coefficient *k*.[107] The presented data is insufficient to determine if the dependency between molecular weight and the rate coefficient is linear or not and must be investigated in further studies. In contrast to the analyzed linear polymers by Taghizadeh and Madras the here investigated polymer is star shaped, which also influences the bond scission rate. But there is strong evidence that the bond cleavage process for the polymeric cages (**polyMOC$_{60\text{-}120}$**) is mechanochemical in origin rather than the result of pressure and temperature variations caused by ultrasound. This molecular-weight dependency on the bond cleavage rate was unambiguously proven by the sonication of cage **MOC$_1$** bearing no polymer chains (Figure 26a). Figure 26 compares all of the sonication experiments that were conducted to investigate weight dependence and cage disassembly. The increasing bond rupture was highlighted in blue.

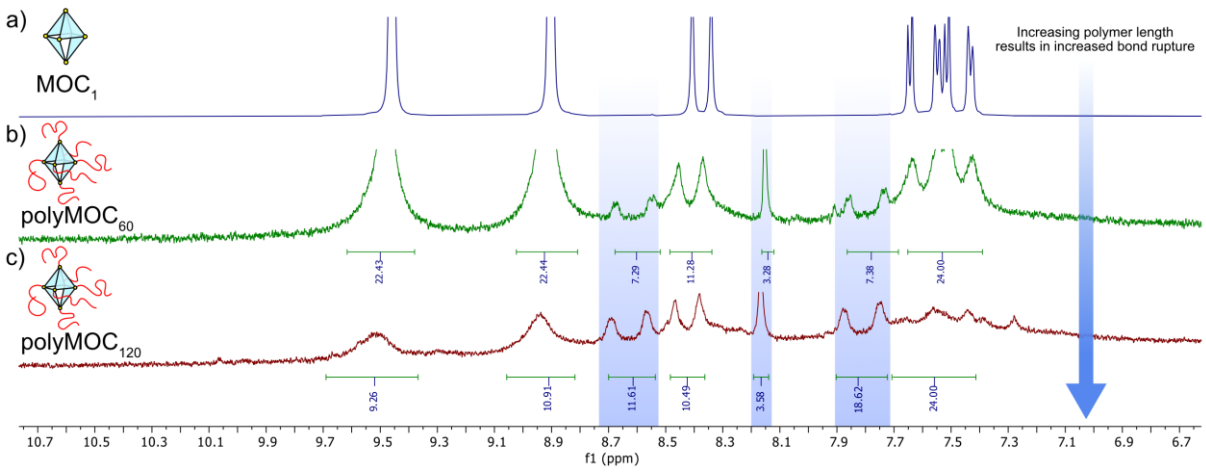

Figure 26: Stacked NMR spectra of all sonicated supramolecular cages. a) ***MOC$_1$*** *after three hours of ultrasound exposure. b)* ***polyMOC$_{60}$*** *after one hour of ultrasound exposure. c)* ***polyMOC$_{120}$*** *after one hour of ultrasound exposure. Highlighted in blue are the increasing fragmentation signals.*

After investigating the influence of the initial molecular weight on the cage disassembly, an analysis of the time dependency during sonication was conducted. Therefore, cage **polyMOC$_{60}$** was sonicated for one hour (Figure 27b) and for three hours (Figure 27c), respectively. In the ^{1}H NMR spectrum, the characteristic fragmented cage signals were observed in both cases (highlighted in blue). It was previously discovered that, after one hour of ultrasound irradiation, the star-shaped cage **polyMOC$_{60}$** had an activation of approximately 24 %. The activation was increased to 37 % by increasing the exposure time of the self-assembled cage **polyMOC$_{60}$** to three hours. This result is approximately of the same magnitude as that for the longer cage **polyMOC$_{120}$**, which after one hour of irradiation achieved an activation of 44 %.

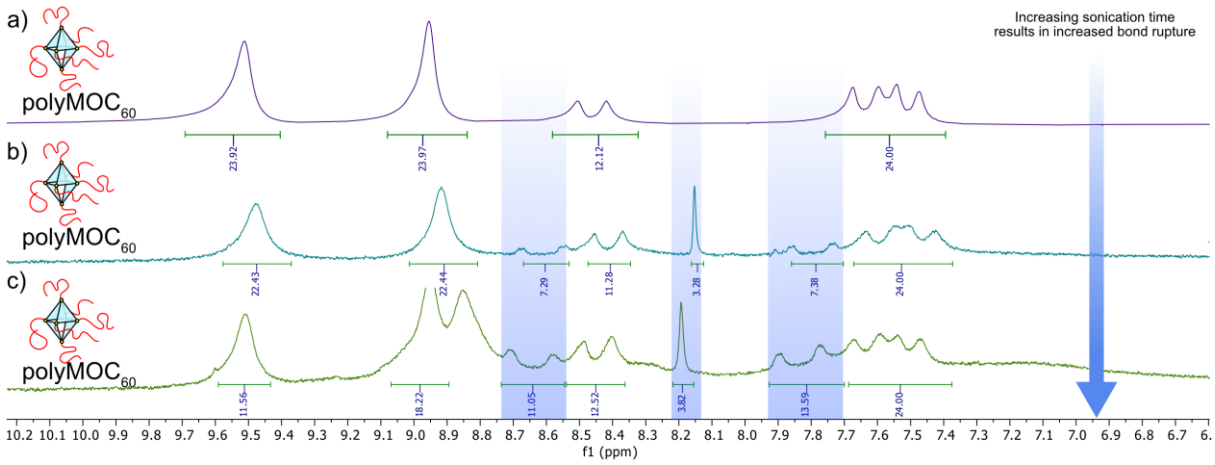

*Figure 27: Stacked NMR spectra of **polyMOC$_{60}$**. a) **polyMOC$_{60}$** before ultrasound exposure. b) **polyMOC$_{60}$** after one hour of ultrasound exposure. c) **polyMOC$_{60}$** after three hours of ultrasound exposure. Highlighted in blue are the increasing fragmentation signals.*

In conclusion, both polymeric cages, **polyMOC$_{60}$** and **polyMOC$_{120}$** were susceptible to ultrasound irradiation, and their dissociation was confirmed by ^{1}H NMR. The process of bond scissioning was proven to be dependent on the initial molecular weight that was used to form the cage. Additional experiments demonstrated the exposure time dependency and illustrated the fragmentation potential of cage **polyMOC$_{60}$**. Control studies were conducted using model compound **MOC$_{1}$** to ensure that cage defragmentation does not occur as a result of temperature- or pressure-induced processes, thereby proving unambiguously the mechanochemical character of the cleavage process. After the supramolecular cages **polyMOC$_{60}$** and **polyMOC$_{120}$** were successfully disassembled, a thorough investigation of the targeted guest release was conducted.

Guest release

After the ultrasound induced cage rupture was accomplished, it was investigated if a targeted guest release was feasible. Progesterone, ibuprofen, and phenolphthalein were successfully encapsulated, and the influence of ultrasound irradiation on the enclathration complexes will be the subject of this chapter.

Release of progesterone

To probe a targeted drug release from cage **polyMOC$_{60}$·(progesterone)** a 5 mg mL^{-1} aqueous solution was sonicated for three hours (on time). This period was chosen to maximize guest release throughout the subsequent experiments. As previously noticed, the characteristic color change occurred already after several minutes, indicating cage defragmentation. After the solvent was removed by freeze-drying, ^{1}H NMR analyses were conducted and revealed the distinctive signals for the cage fragments in the aromatic region (8.7-7.4 ppm). These results are in accordance with the previously investigated empty cages. Interestingly, a complete absence of the progesterone guest signals (0.0 ppm to -1.4 ppm) was noticed. Progesterone as a hydrophobic steroid is only detected in ^{1}H NMR when it is encapsulated in the hydrophobic cavity (Figure 28, blue). After disassembly of supramolecular cage **polyMOC$_{60}$·(progesterone)** and the concomitant release, progesterone precipitates from the aqueous solution and can no longer be detected by ^{1}H NMR (Figure 28, red). These results suggest that a quantitative on-demand release was achieved by utilizing ultrasound irradiation.

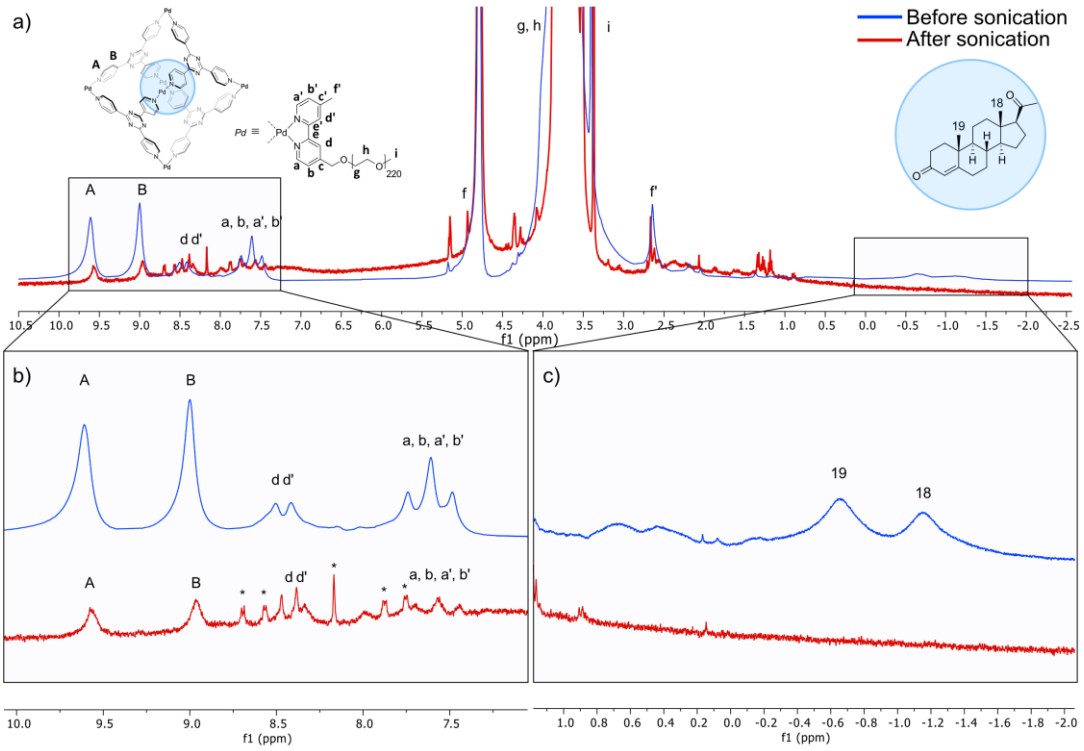

*Figure 28: ^{1}H NMR of **polyMOC$_{60}$·(progesterone)** after three hours of sonication. a) Complete NMR spectrum. b) Magnified spectra of the aromatic region. Before (top) and after (bottom) sonication. c) Magnified spectra of the guest region. Before (top) and after (bottom) sonication.*

Release of ibuprofen

Following that, ^{1}H NMR was used to monitor the release of the ibuprofen-loaded star-shaped cage **polyMOC$_{60}$·(ibuprofen)$_2$** (c = 5 mg mL^{-1}). The results were consistent with the previous disassembly and release experiments. A quantitative release was observed after three hours of sonication (on time) and is indicated by the disappearance of the distinctive upfield shifted guest signals (0.7 ppm to -0.5 ppm, Figure 29c). As observed for progesterone, ibuprofen precipitates due to its hydrophobic properties, resulting in the absence of proton signals in ^{1}H NMR. The broad singlet at 0.0 ppm is thought to correspond to ibuprofen (Figure 29c, bottom). However, a precise integration could not be achieved due to its wide resonance and low signal-to-noise ratio. Furthermore, its characteristic downfield shift indicates that it is not encapsulated in the cage cavity after ultrasonic exposure.

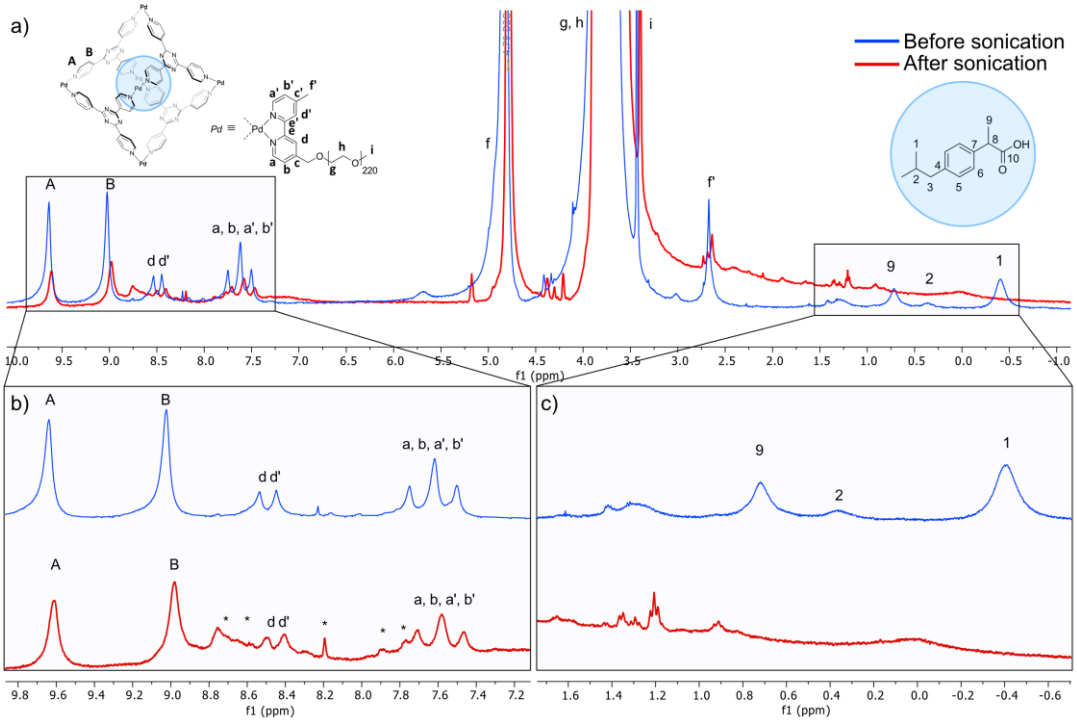

*Figure 29: ^{1}H NMR of **polyMOC$_{60}$·(ibuprofen)$_2$** after three hours of sonication. a) Complete NMR spectrum. b) Magnified spectra of the aromatic region. Before (top) and after (bottom) sonication. c) Magnified spectra of the guest region. Before (top) and after (bottom) sonication.*

To unambiguously confirm that the origin of guest release is the mechanochemical activation and disassembly of the polymeric cage **polyMOC$_{60}$** a control experiment with the smaller cage **MOC$_1$·(ibuprofen)$_2$** bearing no polymer chains was conducted. Therefore, ibuprofen was initially loaded into the hydrophobic cavity of cage **MOC$_1$** and was afterwards sonicated for three hours under similar conditions as the star shaped cage **polyMOC$_{60}$·(ibuprofen)$_2$**. A 1 mg mL^{-1} aqueous solution of **MOC$_1$·(ibuprofen)$_2$** was sonicated for three hours (on time). No color change during the experiment was observed, which is in accordance with previous sonication experiments of the unloaded host **MOC$_1$**

and indicates that no cage rupture occurred. Additionally, neither guest release nor cage fragmentation was detected (Figure 30b), which was confirmed after solvent removal by a subsequent NMR analysis. This result supports the theory that an ultrasound-induced cage disassembly is required for a controlled drug release.

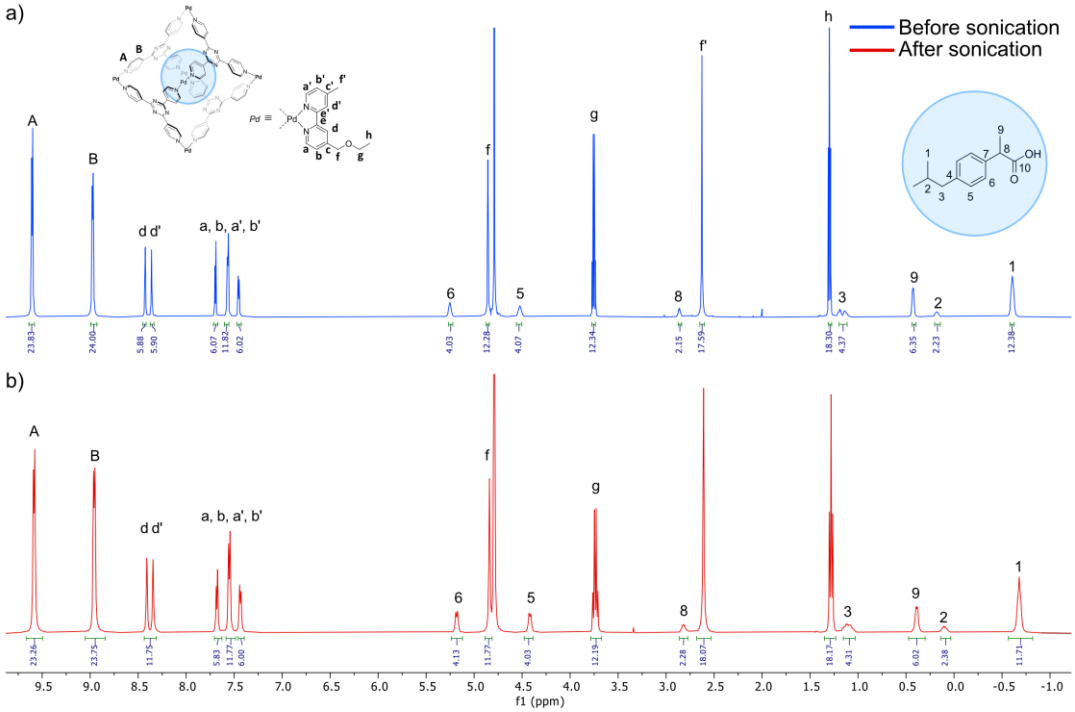

*Figure 30: ^{1}H NMR of **MOC$_1$**·(**ibuprofen**)$_2$ before (top) and after (bottom) three hours of sonication.*

A final hypothesis that emerged was the possibility of guest slippage during ultrasonic irradiation. The "windows" of a cavity can widen under certain conditions, allowing guest uptake of molecules that are slightly larger than the initial cavity opening. It was assumed that a widening of these windows might cause guest slippage under sonochemical circumstances and therefore release the incorporated guest without cage disassembly. To test the release hypothesis, ibuprofen was encapsulated into cage **polyMOC$_{60}$** and sonicated for only 15 minutes. ^{1}H NMR analyses of **polyMOC$_{60}$**·(**ibuprofen**)$_2$ revealed that, in this short period of time, only minute amounts of cage fragmentation occurred. Interestingly, no cage release was detected, supporting the hypothesis that mechanochemical activation by ultrasonic irradiation, followed by host disassembly, is required for a targeted drug release (Figure 31).[69, 108]

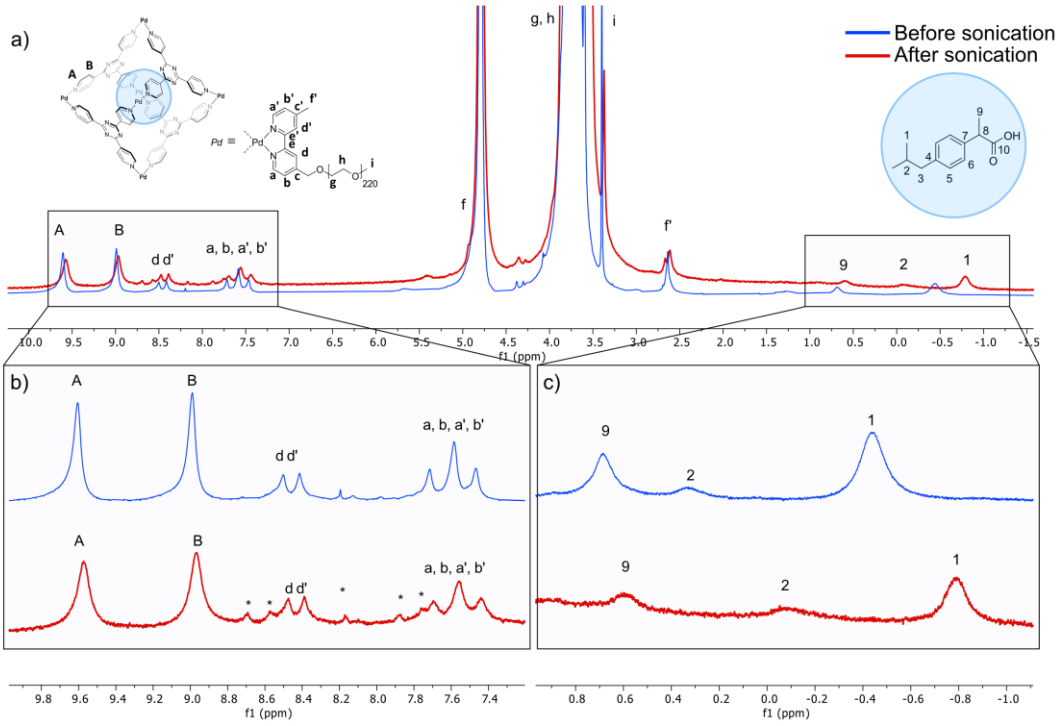

*Figure 31: ^{1}H NMR of **polyMOC$_{60}$·(ibuprofen)$_2$** after 15 minutes of sonication. a) Complete NMR spectrum. b) Magnified spectra of the aromatic region. Before (top) and after (bottom) sonication. c) Magnified spectra of the guest region. Before (top) and after (bottom) sonication.*

Release of phenolphthalein

The group of Fujita investigated the incorporation of phenolphthalein in a similarly structured cage and observed that upon addition of the host, a significant decrease in the absorption maximum at 552 nm occurred (Figure 32a).[94b] This can be explained by the phenomenon that, upon guest uptake of phenolphthalein, the equilibrium shifts to the ring-closed colorless lactone form. Similar results were observed by deploying **MOC$_1$** for the encapsulation of phenolphthalein (Section 3.3.5).

Vice versa, a targeted disassembly of the constraining cage would result in a release of phenolphthalein and the subsequent formation of its colored quinone dianion form at high pH values. To investigate this hypothesis **polyMOC$_{60}$·(phenolphthalein)** was exposed to ultrasound irradiation with subsequent analysis by UV/Vis. **PolyMOC$_{60}$·(phenolphthalein)** (0.3 mM) was dissolved in a 1 mM carbonate buffer solution and exposed to ultrasound irradiation for three hours (on time). Unfortunately, rather than the formation of the colored quinone dianion of phenolphthalein, an apparent color shift that resembled the disassembly of cage **polyMOC$_{60}$** was observed. During this reaction, 10 samples were taken and filtered. An UV/Vis investigation revealed that, in fact, a slight increase could be observed at 550 nm (Figure 32b), suggesting that a release of phenolphthalein was achieved. However, this increase was observed over the whole UV/Vis spectrum and might also be attributed to the previously observed color shift during cage disassembly. As stated, the group of Makoto Fujita has demonstrated

the encapsulation of phenolphthalein, which is depicted for comparison in Figure 32a.[94b] It has to be noted that they used a Pt_6L_4 cage instead of the palladium assembled **MOCs** utilized in this work. This might be due to the increased stability of the Pt-cages, which could prevent a premature or basic induced cage disassembly as previously mentioned and could be an interesting starting point for further investigations of mechanoresponsive **polyMOCs**.

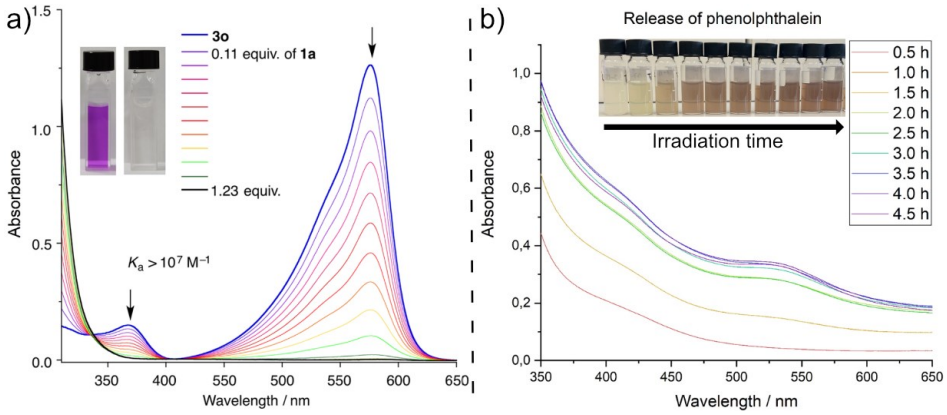

Figure 32: a) UV/Vis spectrum of the encapsulation of phenolphthalein successfully conducted by the group of Makoto Fujita et al. This figure was reproduced of ref 94b with the permission of the American Chemical Society. b) UV/Vis spectrum of the attempted targeted release from ***polyMOC$_{60}$·(phenolphthalein)****.*

3.1.5 Summary

In conclusion, the successful synthesis of one smaller supramolecular model compound, **MOC_1**, and two polymer-functionalized and mechanoresponsive cages, **$polyMOC_{60}$** and **$polyMOC_{120}$**, was presented. The model compound was employed for a complete characterization, including ^{1}H-, ^{13}C-, DOSY NMR, and other heteronuclear 2D measurements, and resembles in many features the similar M_6L_4 cage of the group of Fujita. Based on this work, two isostructural polymeric cages (**$polyMOC_{60\text{-}120}$**), were synthesized and confirmed by ^{1}H NMR measurements.

An investigation of guest uptake was conducted and revealed the excellent host/guest properties of cage **MOC_1**. A subsequent screening of various compounds showed that steroids are suitable guests due to their structural and electronic properties. It was further observed that in all cases, only one steroid moiety could be encapsulated in the self-assembled cavity. The encapsulation of two ibuprofen molecules was unambiguously proven by numerous methods, whereas the encapsulation of melatonin and paracetamol was only confirmed by ^{1}H NMR. Several UV/Vis or fluorescence active compounds were encapsulated in an attempt to "visualize" the guest release, with phenolphthalein proving to be the most reliable. Under this premise, progesterone, ibuprofen, and phenolphthalein were selected as the most promising guests for a targeted uptake with the larger supramolecular cages **$polyMOC_{60\text{-}120}$**.

By subjecting all cages to ultrasonic irradiation, their disassembly was investigated. It was successfully demonstrated by ^{1}H NMR studies that the mechanochemical activation correlates with the utilized molecular weight of the supramolecular cages, as well as the exposed irradiation time. This was unambiguously proven by control experiments with the smaller model compound, **MOC_1**. The GPC analysis was ineffective, only revealing that cage rupture occurs during sonication rather than non-specific bond scissioning of the polymer chains. Subsequent experiments for a targeted drug release demonstrated the full potential of the synthesized host cages (**$polyMOC_{60\text{-}120}$**). Progesterone was completely released from the host after three hours of sonication, whereas ibuprofen was most likely completely released. The absence of guest slippage during sonication was further confirmed, and as a result, the disassembly of the cage serves as the main driving force for guest release. Due to cage decomposition under basic conditions, the visualization of guest release using phenolphthalein was unsuccessful.

3.2 Mechanistic insight

3.2.1 Introduction

In the previous chapter, it was demonstrated that the synthesized novel polymeric cages, **polyMOC$_{60\text{-}120}$**, as well as the model compound **MOC$_1$**, exhibited excellent host-guest properties. In addition, the successful disassembly of **polyMOC$_{60}$** and **polyMOC$_{120}$** was confirmed by ^{1}H NMR with a concomitant guest release. Control experiments using model compound **MOC$_1$** confirmed the sonochemical origin of this decomposition. What remains unknown is the process and mechanism of the sonochemical induced cage rupture. Furthermore, it was uncertain if the method used to determine the sonochemical cage activation was precise. To gain further insight into this mechanism, simplified systems had to be designed for this investigation (Figure 33).

Sijbesma *et al*. synthesized palladium(II) based mechanophores that are susceptible to ultrasound irradiation, which served as inspiration for the molecules proposed here. They observed an interesting phenomenon: that after sonochemical induced ligand dissociation, a subsequent complete reversibility of the mechanochemical process occurs. Thus, forming the pristine metal coordinated complex upon re-equilibration.[81b]

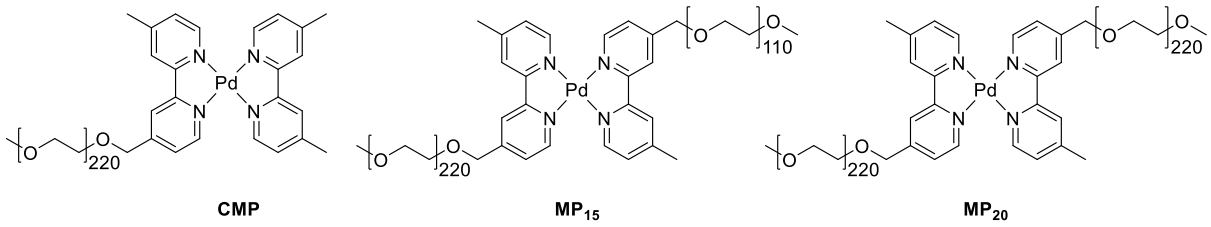

Figure 33: Three poly(ethylene glycol) complexes for the investigation of the sonochemical mechanism during bond scissioning.

Taking the previous results and the work of Sijbesma *et al.* into account, three isostructural Pd-based mechanophores (**MPs**) were envisioned based on the structural motif of the star-shaped cages **MOC$_1$** and **polyMOC$_{60\text{-}120}$**. Two mechanophores were designed bearing different polymer lengths (**MP$_{15}$** and **MP$_{20}$**) for sonochemical activation, whereas the Pd-complex of the control linker **CMP** was established in a terminal position, rendering it unsusceptible to ultrasound induced bond scissioning (Figure 33, left).

3.2.2 Synthesis

Three isostructural mechanophores were chosen to start the analysis of the ultrasound-induced bond rupture mechanism. To understand the behavior during bond scissioning, a rather simple system was targeted and is depicted in Scheme 22.

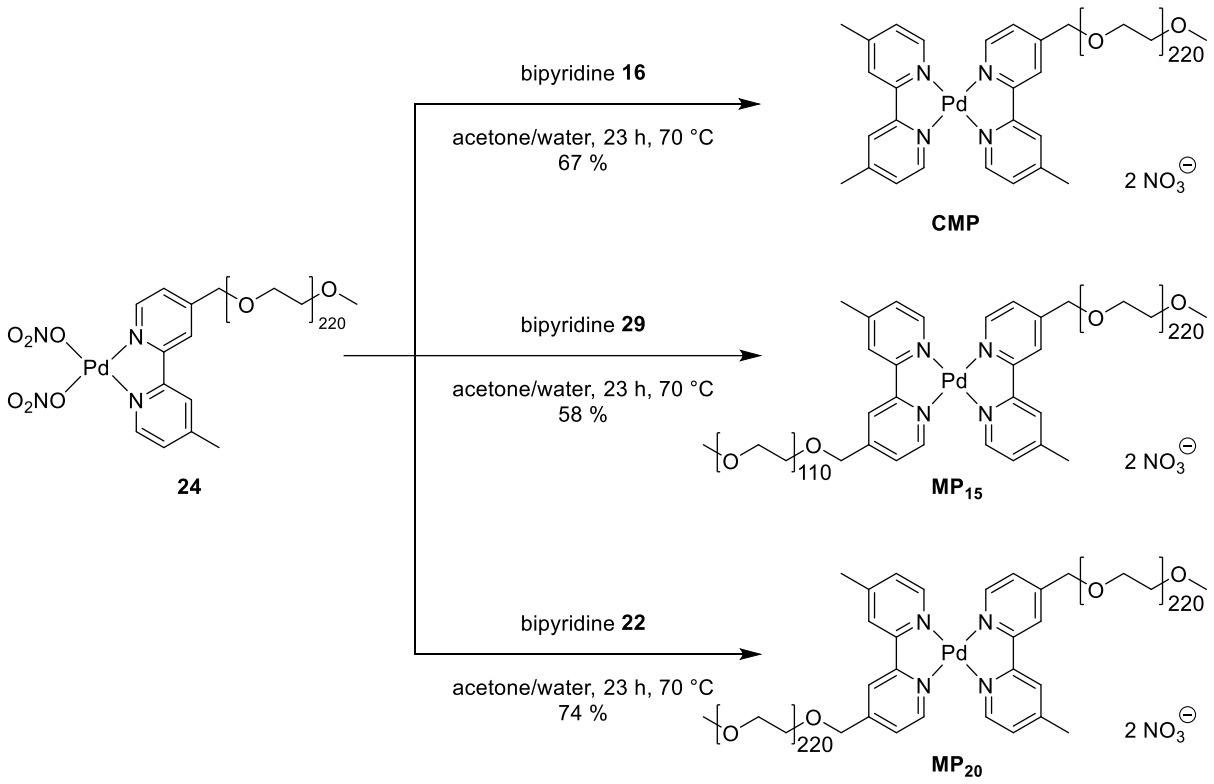

Scheme 22: Synthesis of all three investigated mechanophores.

The synthesis of nitrate-bearing complex **24** consists of a chelation reaction of $PdCl_2$ with bipyridine ligand **22** and a subsequent halide abstraction with $AgNO_3$ (section 3.1.2). The received dinitratopalladium(II) complex **24** functioned as a precursor for the following synthesis of three isostructural polymeric complexes: **CMP**, **MP_{15},** and **MP_{20}**. To obtain the control mechanophore **CMP**, dimethyl bipyridine **16** was initially added equimolar to a water/acetone solution of dinitratopalladium(II) complex **24** and heated. No evaluation of the obtained crude product was feasible, and it was considered that either complex fragmentation occurred during the workup or no full conversion was achieved. To test this hypothesis, an excess of dimethyl bipyridine **16** was added to a solution of nitrate complex **24** and again heated. After filtering off the insoluble dimethyl bipyridine, ^{1}H NMR revealed a clean formation of the desired control mechanophore **CMP** (Figure 34a). In the case of mechanophores **MP_{15}** (Mn = 15 kDa) and **MP_{20}** (Mn = 20 kDa), no excess of the bipyridine bidentate ligands **22** or **29** could be employed since separation of the unreacted starting material is

impossible due to the similar physical properties of the product. Therefore, an equimolar amount of the chelating ligands **22** or **29** were added to dinitratopalladium(II) complex **24** and heated before it was purified by precipitation. A successful conversion was accomplished in both instances, according to NMR data, and an increasing integral supports the trend of the attached polymer chain's rising molecular weight. Addition of 110 repeat units corresponds to approximately 400 protons (Figure 34, highlighted blue). The low yields can be attributed to the purification step and were often observed during test reactions involving PEG.

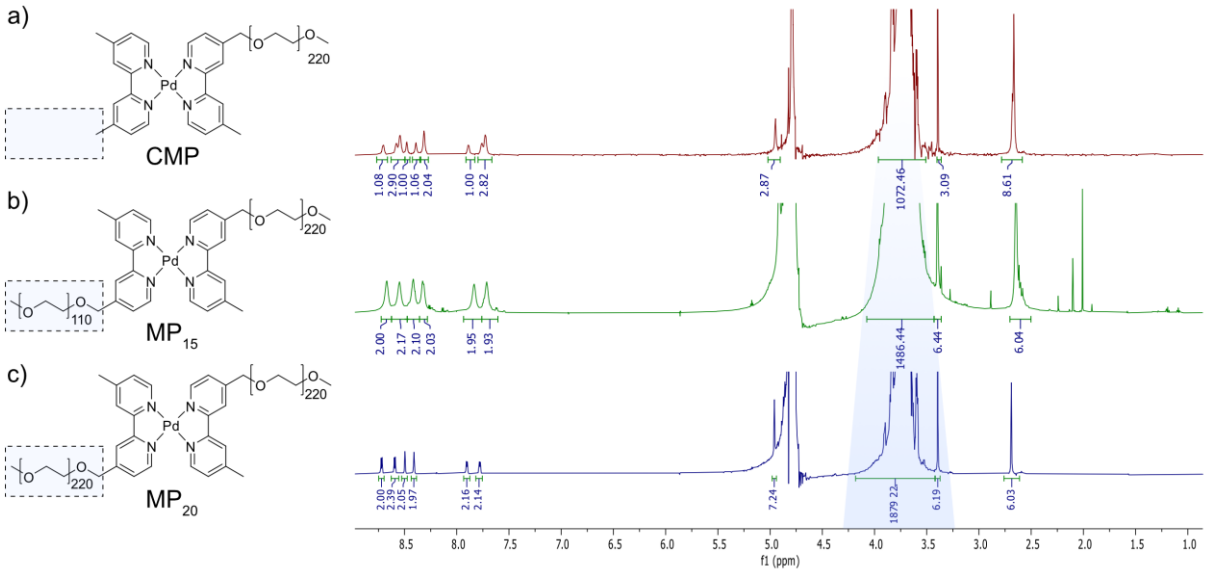

*Figure 34: Stacked ^{1}H NMR spectra of all synthesized mechanophores. a) ^{1}H NMR spectrum of the asymmetrical control linker **CMP**, which bears the shortest poly(ethylene glycol) chain. b) ^{1}H NMR spectrum of mechanophore **MP$_{15}$**. c) ^{1}H NMR spectrum of mechanophore **MP$_{20}$**.*

GPC analysis was performed for the mechanophores **MP$_{15}$** and **MP$_{20}$** to further investigate the formation of those complexes. In both cases, the GPC revealed that either the product was impure and contained still large amounts of the utilized starting materials (**22** or **29**) or a decomposition occurred during the GPC analysis. This behavior of complex decomposition was already observed for the self-assembled supramolecular cages from section 3.1. The reason for this is that GPC measurements are often run with additives, which are either required for an interaction-free separation or to prevent microbial growth.[109] In some cases, these additives can cause the decomposition of the investigated compound.

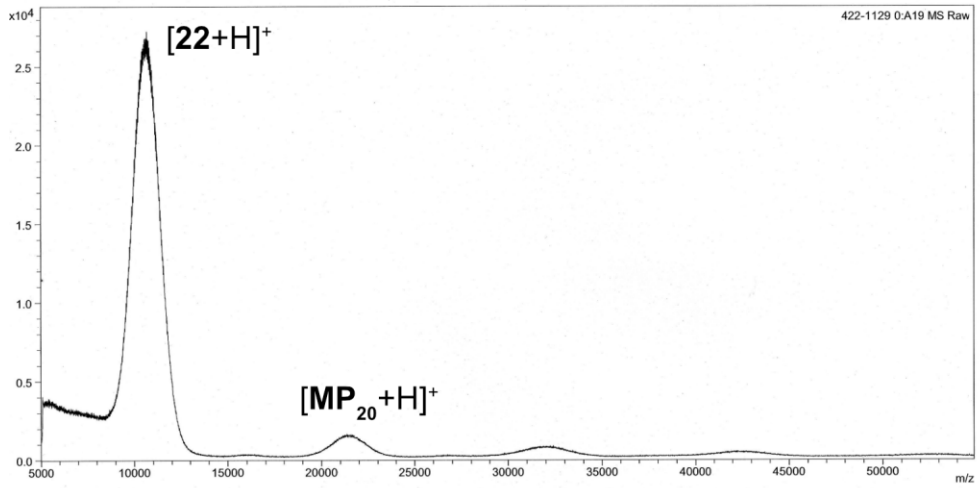

*Figure 35: MALDI MS spectrum for the mechanophore **MP$_{20}$**.*

To get further insight into the complex formation of **MP$_{15}$** and **MP$_{20}$**, matrix-assisted laser desorption/ionization time of flight (MALDI/TOF) mass spectrometry experiments were conducted (Figure 35). It was discovered that small amounts of the desired complex were formed for the longest mechanophore, **MP$_{20}$** ([**MP$_{20}$** + H]$^+$, calculated: 20.594 g/mol, found: 21.500). Additionally, it was also observed that either a threefold coordinated complex was obtained or that oligomeric structures were formed, as indicated by the increased molecular mass found during the MALDI/TOF MS experiments (Figure 35). The MADLI/TOF MS of the smaller complex **MP$_{15}$**, on the other hand, indicated no conversion at all. While these experiments contradict a potential formation of the palladium(II) complexes **MP$_{15}$** and **MP$_{20}$**, they were not unexpected. MALDI/TOF MS is a soft (low fragmentation) technique to analyze large molecules in the gas phase, but decomposition of molecules can still be observed.[110] This fragmentation depends for example on the chosen "hard" or "soft" matrix[111] but also on the bond strength of the analyzed molecule. Mechanophores are by nature rather unstable and therefore fragment upon force transmission, which not only explains the observed results but also the absence of MS spectra for mechanophores in the literature.[81b, 86]

Thus, NMR analyses of all starting materials and long-term stability measurements for complex **MP$_{20}$** were conducted. For comparative purposes, spectra of all building blocks were obtained in D_2O and are depicted in Figure 36. As shown in Figure 36c, a symmetrical compound was formed since only one pair of signals for the bipyridine-based complex **MP$_{20}$** was observed. The downfield shift is visible for both bipyridine moieties (Figure 36a and b) and is caused by decreasing electron density in the π-electronic structure. It was speculated that this shift was caused by the formation of a Pd-N bond and, therefore, the complexation. A subsequent ^{1}H DOSY NMR analysis revealed for **MP$_{20}$** a diffusion coefficient of D = 9.04 x 10^{-11} m s^{-2} which corresponds to a M_n of 18 kDa (Figure 36d). This is in

agreement with the estimated weight for the synthesized mechanophore **MP$_{20}$**.[112] Additionally, ^{1}H-^{1}H COSY NMR suggested the formation of a symmetrical palladium(II) complex (Figure 204).

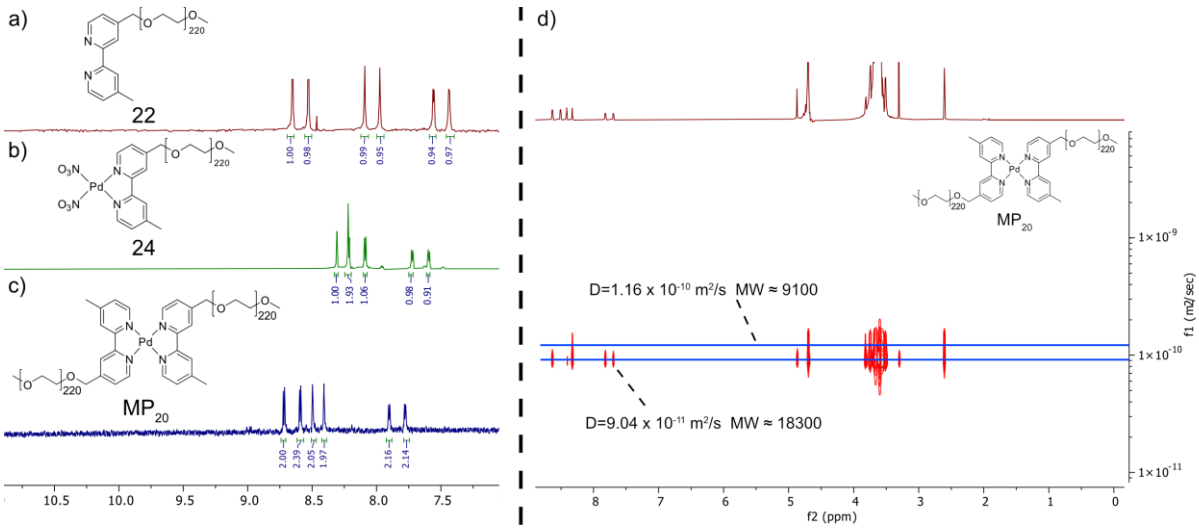

*Figure 36: Stacked ^{1}H NMR spectra: a) mPEG substituted bipyridine ligand **22**. b) Nitrate complex **24**. c) Successful formation of **MP$_{20}$** and d) DOSY NMR indicating a successful formation of the mechanophore **MP$_{20}$**.*

3.2.3 Sonication experiments

Although GPC and MALDI MS analyses of the synthesized mechanophores were unsuccessful, ^{1}H NMR, COSY, and DOSY NMR validated their formation. As a result, the mechanophores were exposed to ultrasound irradiation for two hours at a concentration of 2 mg mL^{-1}. Starting with the control linker **CMP**, it was envisioned that due to the terminal position of the Pd-complex, this linker should not be susceptible to ultrasound. During the experiment, only a minor color change was noticed, suggesting that no bond rupture occurred during the irradiation. Subsequent ^{1}H NMR analysis revealed that in fact no bond dissociation was achieved, which was confirmed by the unchanged integrals of the bipyridine signals (Figure 37a and b). Only a broadening of the resonance was noticed, which was attributed to nonspecific bond scissioning.

Deploying the mechanophore **MP$_{20}$** under similar conditions led to the distinctive color change that was already observed for the self-assembled star-shaped cages from section 3.1. The sample was freeze-dried and analyzed by ^{1}H NMR. A full investigation was complicated due to the resonance broadening that was frequently seen after sonication experiments. Integration reveals that the bipyridine structure remained mostly unchanged (Figure 37c and d).

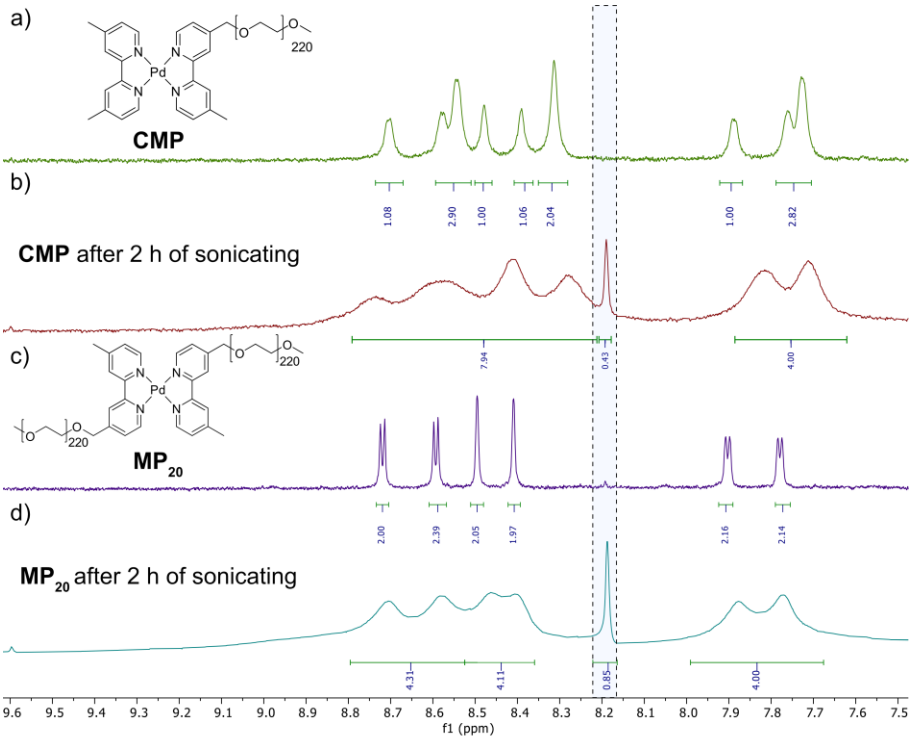

*Figure 37: Stacked ^{1}H NMRs. a) **CMP** before sonication. b) **CMP** after two hours of sonication. c) **MP$_{20}$** before sonication. d) **MP$_{20}$** after two hours of sonication.*

Three assumptions arise from these results:

1. Because there is a lack of thorough analytical data on complex formation, it is plausible that no sonochemical activation could be observed because the complex was not formed in the first place.
2. The complex was formed, but it is not susceptible to ultrasound irradiation.
3. The complex was formed, but the sonication process is completely reversible.

While ^{1}H NMR, DOSY, and COSY NMR studies are not sufficient for a complete characterization, they clearly indicate that the complex formation was successful, disproving the first hypothesis. The second assumption, that the complex might not be responsive to ultrasound irradiation due to its "low" molecular weight, can be excluded since this length of repeat units was successfully employed in previous works for palladium complexes,[86a] and also successfully employed for the star shaped polymers from section 3.1. The strongest hypothesis at the time of writing is that reversible sonochemical bond scissioning occurs, which is supported by ^{1}H NMR, DOSY, and COSY NMR. This phenomenon was also observed by the group of Sjibesma *et al.* who demonstrated that palladium(II) coordinated polymers can undergo reversible ligand dissociation upon ultrasound irradiation.[81b]

These experiments were initially conducted to get further insight into the bond dissociation process of the self-assembled star-shaped cages **polyMOC$_{60\text{-}120}$** of section 3.1. In this section, it was assumed that upon cage fragmentation, the bipyridine ligands dissociate from the self-assembled host, ultimately resulting in cage disassembly. Interestingly, after conducting the **MP$_{20}$** sonication experiments, it was discovered that the chemical shift for the **MP$_{20}$** mechanophore signals and the "fragmented cage" of **polyMOC$_{60}$** are identical (Figure 38b, c and d, highlighted in blue). This result might indicate that during a sonochemical disassembly of the **polyMOC$_{60\text{-}120}$** cages, a subsequent formation of mechanophore **MP$_{20}$** occurs. Thus, preventing a reversible formation to the star-shaped host **polyMOC$_{60\text{-}120}$** since **TPT** precipitates from the reaction after cage disassembly.

It was also argued in section 3.1 that the bipyridine signals at δ = 7.86-7.73 ppm can be used to determine the potential cage activation after exposure to ultrasound. According to Figure 38b, a sonochemical activation of approximately 24 % was calculated for **polyMOC$_{60}$** by dividing the integral of the fragment (7.38 protons, 7.86-7.73 ppm) by the total integral (31.38 protons, 7.86-7.35 ppm). This calculation was initially conducted under the assumption that the asterisk-marked signals in Figure 38b are a fragment of the cage and can therefore be used to determine the effect of activation. With the insight from the sonochemical experiments of this section, it can be confirmed that the arising asterisk marked signals are in fact corresponding to a bipyridine moiety and most likely to the mechanophore **MP$_{20}$**. And thereby validating the utilized technique for the determination of ultrasound activation.

Furthermore, Figure 38 (b and c) illustrates that the area of δ = 8.50-8.35 ppm is unsuitable to use for the calculations due to signal merging of **MP$_{20}$** (Signals 3 and 4) and **polyMOC$_{60}$** (Signals d and d'). Thus, these integrals give a falsified representation of the mechanochemical activation and eventually result in a false outcome.

The appearing singled δ = 8.19 ppm (Figure 38) was observed in all sonochemical activated samples throughout this work, independently from the deployed molecule. An assignment of this singlet is complicated due to the inability to employ heteronuclear measurements and occurring resonance broadening. Additionally, it was often observed that the integral of this signal has no correlation to any other observed signal. Therefore, further investigations are needed as the origin of this signal remains unclear.

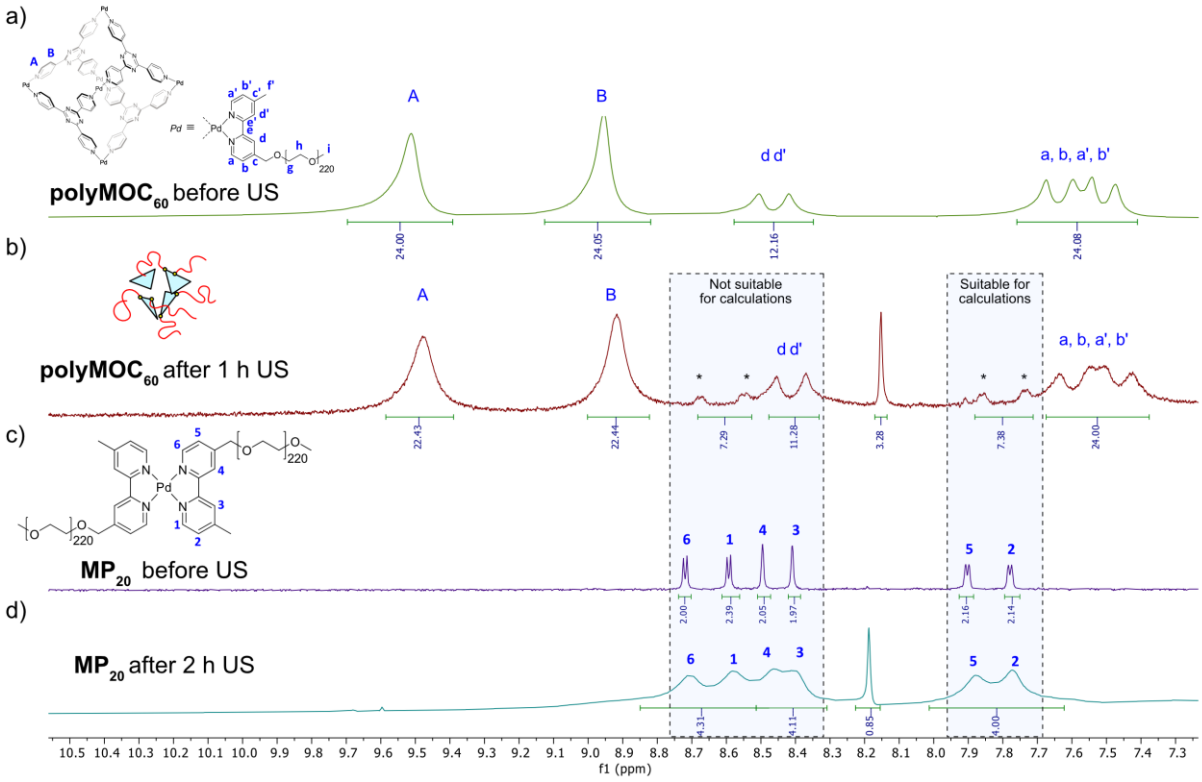

*Figure 38: Stacked ^{1}H NMR spectra. a) Previously synthesized supramolecular cage **polyMOC$_{60}$** before sonication. b) **polyMOC$_{60}$** after one hour of sonication. c) Mechanophore **MP$_{20}$** before sonication. d) Mechanophore **MP$_{20}$** after two hours of sonication. Highlighted in blue are the arising signals of **polyMOC$_{60}$** and the similar shifted signals of **MP$_{20}$**.*

The here conducted evaluation of the sonochemical activation of **MP$_{20}$** and **polyMOC$_{60}$** further nourishes the earlier established hypothesis of a recombination reaction after the initial Pd-N bond rupture. This recombination phenomenon was observed for the mechanophore **MP$_{20}$**, as well as the supramolecular star-shaped cages **polyMOC$_{60}$** and **polyMOC$_{120}$** (Section 3.1). Interestingly, in the case of the cage **polyMOC$_{60}$** the recombination does not yield the original supramolecular cage but apparently results in the formation of **MP$_{20}$** (Figure 38). Since **TPT** is insoluble in water, it precipitates upon cage rupture and was therefore removed from the reaction equilibrium. Thus, explaining the formation of **MP$_{20}$**. ^{1}H NMR DOSY experiments after sonication of **polyMOC$_{60}$** for example, would give further insight into the formed cage fragment, but this remains a target for further studies.

3.2.4 CoGEF calculations

To gain a better insight into the process of bond scissioning, a model system (**30**) based on the M_6L_4 moiety was investigated with CoGEF calculations using density functional theory at the B3LYP+D3/6-31G* level (Figure 39). These simulations were conducted by pulling on both ends and gradually increasing (0.01 Å) the distance. Eight H_2O molecules were added during these calculations and were

necessary to fill the arising palladium coordination sphere after bond scissioning (Figure 39c, water replaces pyridine). These calculations were conducted and evaluated by Dr. Jan Meisner.

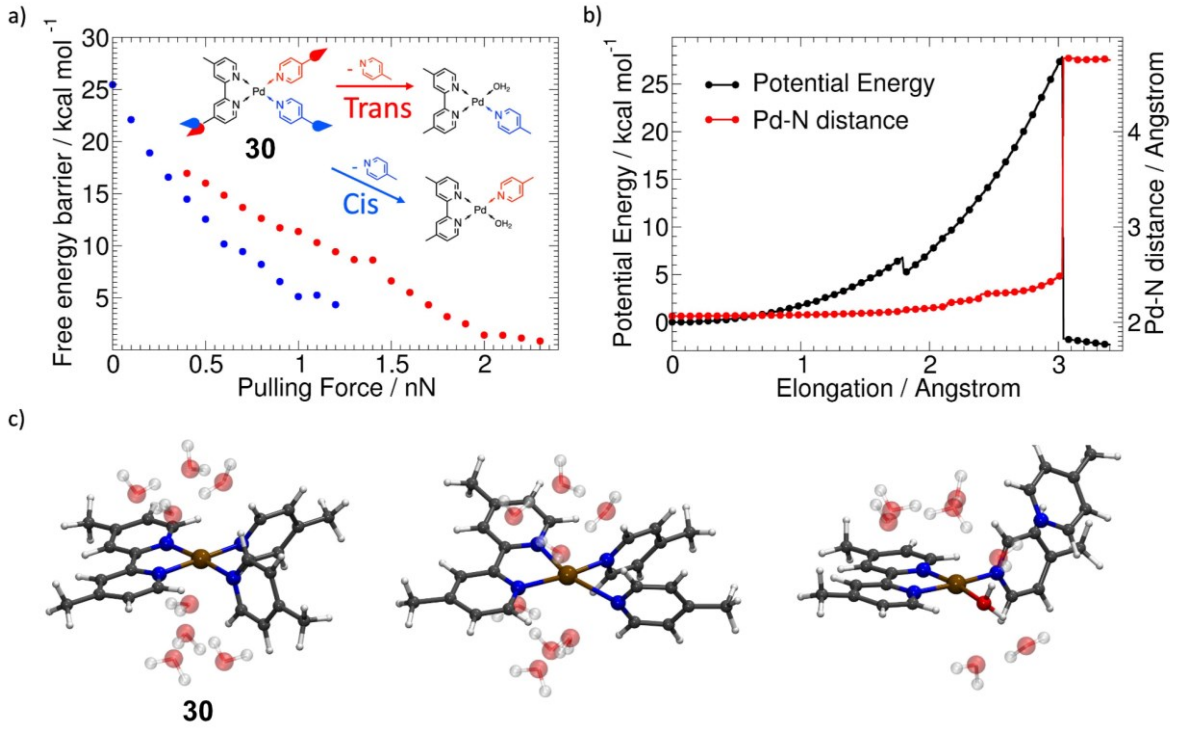

Figure 39: a) The free activation energies as a function of force for the two possible dissociation routes for Pd–N dissociation (red: trans, blue: cis). b) Depicted is the potential energy (black) and the Pd-N distance (red) for cis-pulling. (Trans-pulling is depicted in the experimental section: Figure 75). c) Three snapshots along the CoGEF path (cis-pulling) of [Pd(4-methylpyridine)$_2$(4,4'-dimethyl-2,2'-bipyridine)]$^{2+}$ complex. After a strong distortion of the pyridine-ligand and a subsequent dissociation, a coordination of a H_2O molecule can be observed. This image was kindly provided by Jan Meisner.

Since the used cage **polyMOC$_{60}$**, from section 3.1 was asymmetrical, both "pulling" paths, *cis*- as well as *trans*-pulling, were investigated. After applying force on complex **30** in *cis*- and *trans*- direction it was revealed that in both cases the preferred bond scissioning is taking place between the Pd^{2+} atom and the respective pyridine moiety (Figure 39a). This dissociation results in a re-coordination of a surrounding water molecule to regain the square planar coordination sphere. For both CoGEF paths of mechanochemical activation, similar values were obtained for the highest potential energy E_{max} resulting in 27.8 kcal mol^{-1} for *cis*-pulling (Figure 39b, 74) and 26.5 kcal mol^{-1} for *trans*-pulling (Figure 75). An easier dissociation was implied by the F_{max} value of 1.87 nN for *cis*-pulling instead of 2.57 nN (*trans*). Since the CoGEF method tends to yield values above the actual forces a more complex method had to be utilized, to evaluate the real barrier heights of the competing *cis*- and *trans*-pulling. Therefore, the approach of free-modified potential energy surface (FMPES) was used for a detailed investigation of the pulling force (Figure 39 a). To obtain the values for the free energy barrier, an optimization had to be conducted for every force step of 0.1 nN. The transition state structures for the *trans*-pulling could not be located for force values below 0.4 nN, and above 2.3 nN, the complex is not

stable, resulting in a dissociation of pyridine. In the case of *cis*-pulling, this phenomenon was observed at a value above 1.2 nN. Comparing the free energy barrier heights of the *cis*- and *trans*-path reveals that at 0.5 nN a barrier height of 12.6 kcal mol^{-1} (*cis*) and 16.0 kcal mol^{-1} (*trans*) can be obtained. Both barrier values decrease at 1.0 nN to 5.1 kcal mol^{-1} (*cis*) and 11.4 kcal mol^{-1} (*trans*). For *cis*-pulling these energy heights are low enough that it can be assumed that between 0.5 nN and 1.0 nN a dissociation of the pyridine-ligand and Pd^{2+} atom can take place. The higher values for the *trans*-pulling force in contrast to *cis*-pulling can be explained by the N-Pd-N angles. During *trans-pulling,* the Pd-N bond was directly stretched. In contrast, the *cis*-pulling results in a strong distortion, which leads to a smaller orbital overlap of Pd-N and therefore a weaker Pd-N bond. As a result of the *cis*-pulling, the mechanical induced force is coupled to the targeted dissociation, subsequently leading to an easier bond breaking of the Pd-N bond.

3.2.5 Summary

In conclusion, the synthesis of three isostructural metal complexes (**CMP**, **MP_{15}**, and **MP_{20}**) was described. Initial analytical investigations of these complexes did not unambiguously confirm their formation. Although the ^{1}H NMR, DOSY, and COSY experiments revealed that complex formation was indeed achieved, GPC and MS were inconsistent, wherefore this topic still needs to be investigated in more detail. Subsequent sonication experiments suggested that no ultrasound induced ligand dissociation was achieved, but the assumption arose that instead a reversible process took place. Thus, explaining the unchanged ^{1}H NMR of metal complex **MP_{20}** after two hours of sonication. A comparison with the star-shaped supramolecular cage **$polyMOC_{60}$** was conducted, and it was observed that the fragmentation signals of **$polyMOC_{60}$** resemble those of linker **MP_{20}**. This could be explained by a recombination taking place between different disassembled bipyridine moieties, originating upon cage rupture, ultimately resulting in the formation of metal complex **MP_{20}**. Thus, further nourishing the hypothesis of a recombination reaction.

Computational methods were included to simulate the effect of sonochemical force on the here utilized metal complexes and to predict the mechanochemical process during ligand rupture. Therefore, CoGEF calculations were used with free energy barrier heights based on the force-modified potential energy surface approach. These calculations suggested that decomposition of the metal complex started with the dissociation of one pyridine ligand at approximately 0.5 nN. Further, it was noticed that a dissociation occurs preferably during *cis*-pulling due to a distortion of the N-Pd-N angle.[113]

3.3 Hydrogels

3.3.1 Introduction

Hydrogels are three-dimensional, water-insoluble networks with the capability to incorporate fluids into their framework. These gels are frequently generated by covalent cross-linking,[114] but they can also be created through weak secondary forces like hydrogen bonds.[115] In this chapter, two different concepts of hydrogel formation will be investigated. The first method focuses on the synthesis of a novel class of hydrogels, which at the time of writing had not been reported. This class of hydrogels should be formed by polymer-connected guest molecules that, when encapsulated, act as a cross-linker between their hosts (Figure 40). The cross-linking density can then be tailored by either modifying the cavity for increased guest uptake or by altering the polymer. A variety of potential polymer linker modifications might be envisioned in order to increase cross linking, however this work focused on linear end functionalized poly(ethylene glycol) linker.[116] To achieve a sufficient cross-linking ratio for subsequent hydrogel formation, the utilized cage has to be capable of encapsulating at least three guest moieties to form a three-dimensional network (Figure 40b). Whereas a cage with a maximum of two guests would most likely result in either an extended linear polymer or some sort of macrocycle (Figure 40a).

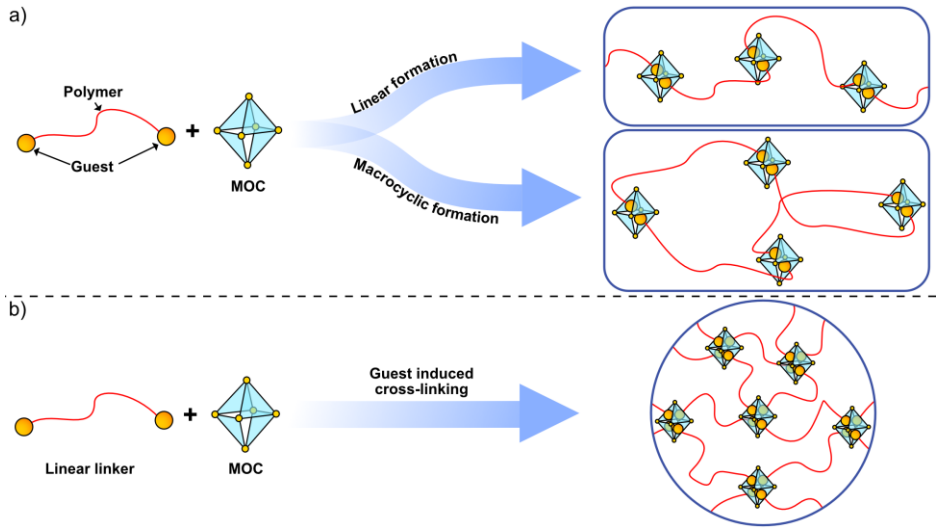

*Figure 40: The guest uptake of the **MOC** decides about the targeted compound properties. a) Low encapsulation of a linear linker results in an extended polymer or macrocyclic formation. b) High guest uptake leads to the formation of a three-dimensional network.*

The second approach, which will be covered in the second half of this chapter, focuses on hydrogels generated by self-assembled, cross-linked metal-organic cages (Figure 41). Nitschke *et al.* found that this type of hydrogel forms a mesoscopic pore between the three-dimensional network in addition to the well-defined cavity of metal-organic cages.[62] This network topology allowed for the selective

encapsulation of various guest molecules as well as their eventual release at different rates depending on their host-guest properties. However, due to the fact that this guest release was only triggered by the displacement of a stronger binding guest, its potential is quite limited. In section 3.1.3 it was observed that the larger mechanoresponsive self-assembled cages, **polyMOC$_{60}$** and **polyMOC$_{120}$**, exhibited extraordinary host-guest properties and, in addition, were also susceptible to ultrasound irradiation. By slightly modifying these ligands it was envisioned to receive metal-organic cage-cross-linked hydrogels with similar host-guest properties to **polyMOC$_{60}$** and **polyMOC$_{120}$**. Because of the poly(ethylene glycol) used, these hydrogels should be susceptible to ultrasound irradiation and thus capable of releasing their cargo load on demand. Therefore, four cross-linkers differing in polymer length were synthesized to investigate the molecular-weight dependency on the formation of hydrogels as well as their targeted bond scissioning (Section 3.3.3). In addition, profound material investigations were conducted by utilizing SAXS, rheology, and SEM measurements to get further insight into the properties.

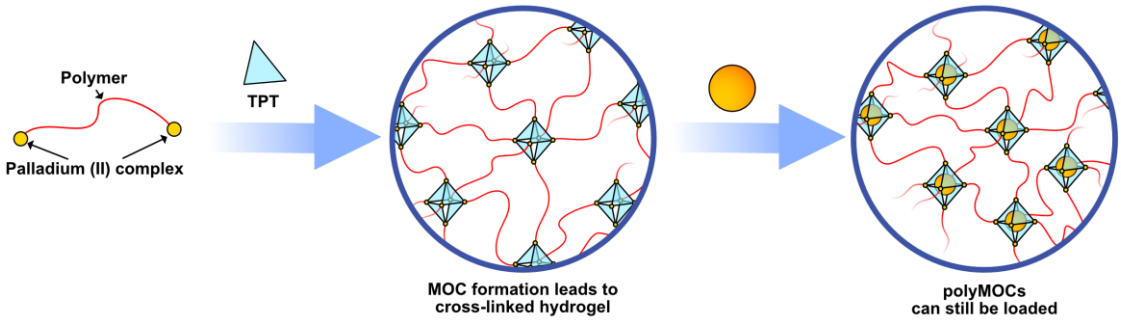

Figure 41: Formation of polyMOC gels crosslinked upon cage self-assembly. In contrast to the first proposed method, these gels are still suitable for guest uptake.

3.3.2 Synthesis and self-assembly

In order to obtain a potential end-group functionalized polymer that is capable of acting as a cross-linker, the investigation started with ibuprofen derivates. This guest was the starting point for research on guest-linked cages, even though it has previously been shown that it can only be encapsulated twice by a M_6L_4-type cage and would thus most likely not form a hydrogel. The group of Fujita has shown that guests with a hydrophilic (carboxyl acid) and a hydrophobic group (aryl) perfectly align in the self-assembled cavity. The hydrophobic group is located inside the cage, whereas the hydrophilic group is located outside the cavity.[69] This phenomenon was exploited to precisely functionalize the outward-facing hydrophobic group of the guest without significantly altering its hydrophobic properties. Therefore, the guest would still maintain its properties and still be suitable for encapsulation.

The preparation of alcohol **32** was initiated with the reduction of ibuprofen (**31**) by employing an excess of $LiAlH_4$ (Scheme 23). A subsequent Appel-reaction was conducted to yield bromide **33** in 19 %. The low yields during this reaction were attributed to rearrangement side reactions and were not further investigated. To circumvent these side reactions it was reasoned that instead of directly converting the primary alcohol of the ibuprofen derivative **34** into the corresponding bromide it might be more suitable to use *α*,*α*'-dibrom-*p*-xylol as a "spacer". This would prevent the primary bromide from being in close proximity to the tertiary alkyl group for rearrangement reactions, but also increase the reactivity due to its benzylic position. Although complete conversion of the starting material was observed and tried to be purified by conventional column chromatography, due to the similar R_f-values of the side products, it was not possible to successfully purify the product. A direct functionalization of PEG_{400} and PEG_{1000} was achieved by utilizing standard Steglich esterification conditions, yielding ibuprofen derivatives **35** and **36** in quantitative yields.

Encapsulation of the PEG-linked guest **35** was tested by employing one equivalent of cage **2c** or $\mathbf{MOC_1}$ to an aqueous solution of two equivalents of linker **35** with a total weight percentage of 20 % (20 wt%). After 12 hours of heating, no encapsulation of the guest was observed, rendering the usage of the even longer ibuprofen linker **36** obsolete. It was also noticed during the reaction that precipitation occurred after 12 hours of heating. Since both starting compounds **35** and $\mathbf{MOC_1}$ (or **2c**) are extremely water soluble, it was hypothesized that the hydrolysis of linker **35** led to the formation of ibuprofen, which precipitated due to its hydrophobic properties.

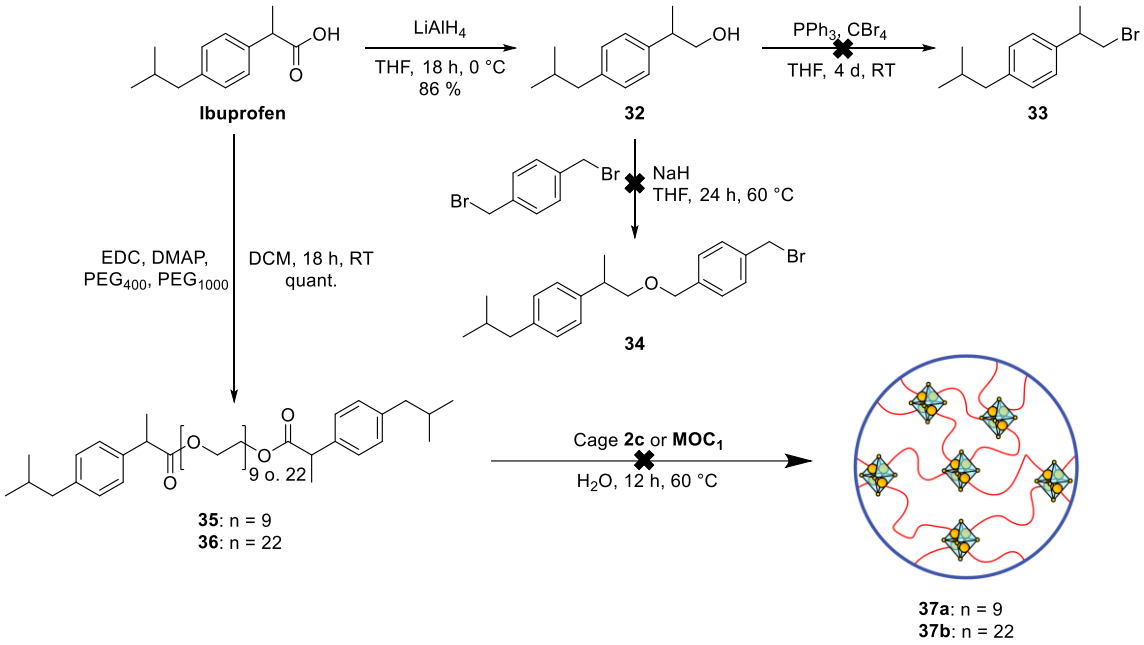

*Scheme 23: Depicted is the attempted synthesis of **33** and **34**. The synthesis of linker **35** and **36** was successful but resulted in no guest encapsulation.*

Based on the previous results, two problems occurred. The first was the hydrolysis of linker **35** and can easily be overcome by utilizing different functional groups, for example, an ether or amide group. A second problem that was noticed is the low cross-linking tendency of ibuprofen linker **35**. The cavity capacity only allows for two ibuprofen moieties to be encapsulated at once, which reduces the potential for cross-linking during self-assembly. Increasing guest uptake would simultaneously lead to stronger cross-linking and, therefore, a denser network. Exchanging ibuprofen with 1-adamantane derivatives addresses both previously mentioned problems at the same time. This guest exhibits similar properties to ibuprofen, its hydrophobic adamantyl core faces into the cavity during encapsulation, whereas its hydrophilic carboxylic acid group is located outside the cage.[69] In addition, four adamantly molecules can be encapsulated per cavity, instead of the previously two ibuprofen moieties and therefore tremendously increasing its cross-linking capabilities.

The investigation was started by transforming 1-adamantanecarboxylic acid (**38**) into adamantyl ester **39** followed by a reduction with $LiAlH_4$ to yield the corresponding alcohol **40** (Scheme 24). The resulting 1-adamantanemethanol (**40**) was converted into the mesylate **41** with a subsequent nucleophilic substitution to give azide **42** in adequate yields. Concomitantly, tetraethylenglycol (**43**) was reacted with an excess of propargyl bromide resulting in the formation of alkyne **44** in high conversion. A final 1,3-dipolar cycloaddition between alkyne **44** and azide **42** was employed to obtain the 1,4-regioisomer of linker **45** in 90 % yield. The formation of the 1,4-regioisomer was confirmed by HMBC NMR measurements.

Cage **MOC$_1$** was formed *in situ* before cross-linker **45** was added to yield a 20 wt% suspension. After heating over night, no gelation was observed, and the suspension was analyzed by ^{1}H NMR, indicating that, in fact, a disassembly of cage **MOC$_1$** occurred. This can be explained by the triazole group, which under the employed conditions can act as a competing coordinating ligand and therefore most probably resulted in a ligand exchange reaction replacing **TPT**.

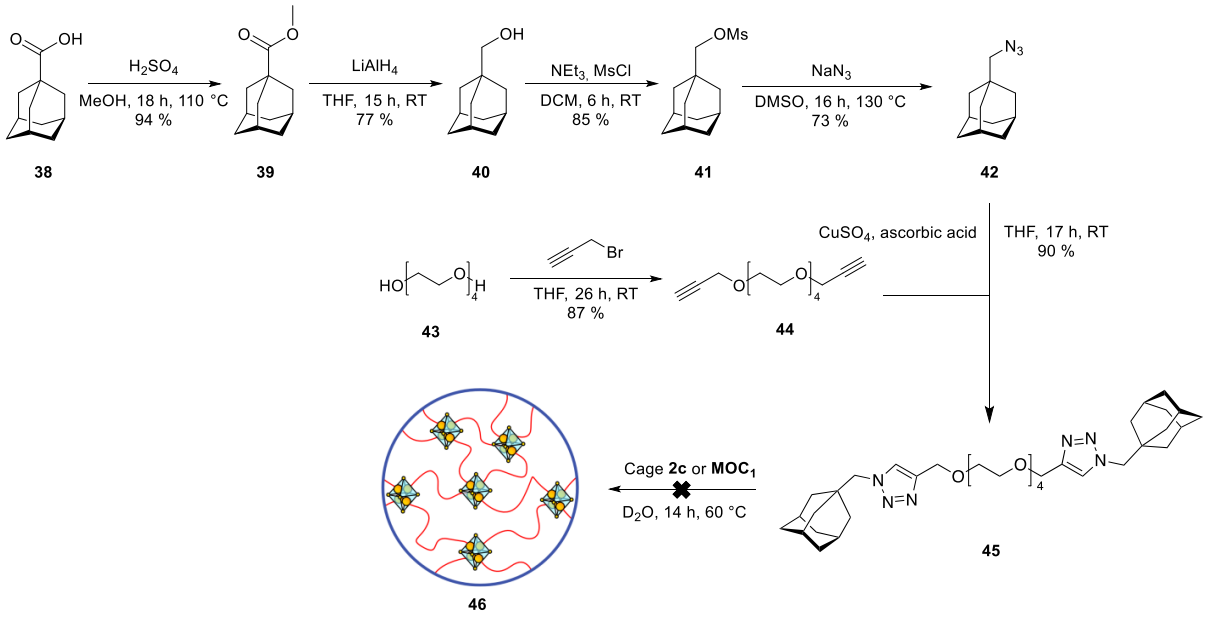

*Scheme 24: Synthesis of the triazole linker **45** and subsequent attempted conversion to gel **46**.*

To circumvent all previously mentioned challenges and minimize possible side reactions with the employed supramolecular cage **2c**, two linkers were envisioned. The first is based on a PEG backbone, whereas the second utilizes an octane backbone. Bromination of alcohol **40** to 1-(bromomethyl)adamantane (**47**), followed by a nucleophilic substitution of PEG_{400} or PEG_{1000}, yielded a PEG-based linker **48** (or **49**) in 30 % (Scheme 25). The unsatisfactory yields were attributed to a low conversion during the reaction and can be explained by steric hindrance of the utilized electrophile bromo-adamantane **47**. As a second approach, alcohol **40** was employed as the nucleophile, and under basic conditions, a successful conversion to ether linker **51** was achieved in approximately 63 % yield. Elimination was observed as a side reaction, whereby 1,7-octadiene was formed in a 2:1 ratio (linker:diene) and could not be separated by column chromatography due to similar R_f values in a variety of solvents, wherefore the crude product was used without further purification.

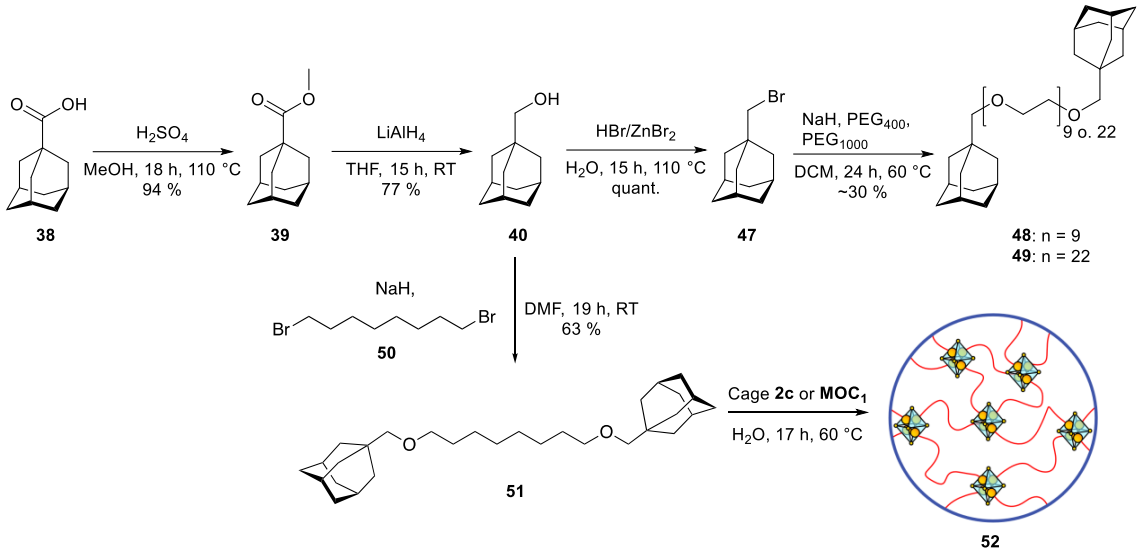

*Scheme 25: Synthesis of three adamantly based cross-linker (**48**, **49** and **51**) for subsequent gel formation.*

The hydrophobic adamantane-based linker **51** was dissolved in a small amount of *n*-hexane as a cosolvent and added to an aqueous solution of cage **2c** to yield a 5 wt% suspension, which was heated for 17 hours. Unfortunately, no hydrogel formation was observed, wherefore the reaction was analyzed by ^{1}H NMR. Surprisingly, even though the majority of the signals can be attributed to the free adamantane linker **51** (Figure 42a and b, highlighted in blue), a few upfield shifted signals in the region of 0.5 ppm to -0.1 ppm can be observed (Figure 42b, orange dots). This upfield shift only occurs for encapsulated guests and is induced through the shielding effect of the **TPT** moieties in cage **2c**. The reaction was repeated in a water/methanol mixture to investigate if guest encapsulation still occurs without *n*-hexane as a cosolvent. ^{1}H NMR revealed that a similar set of upfield shifted signals can be observed without the presence of "free" adamantyl linker **51** (Figure 42c). Unfortunately, no hydrogel was formed.

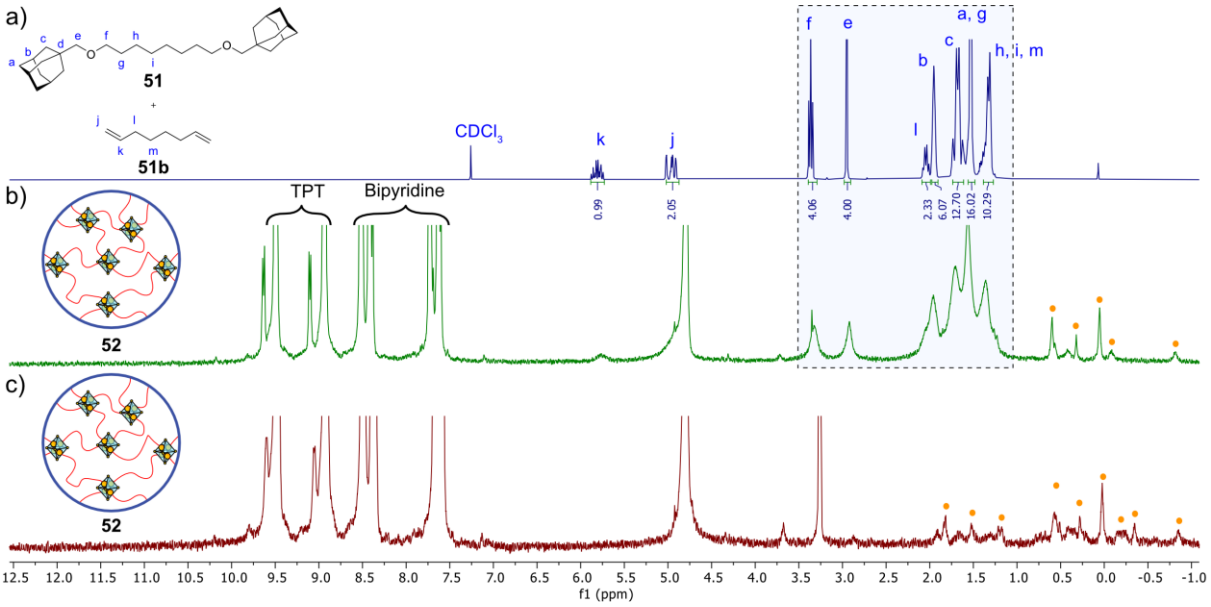

*Figure 42: Stacked NMR spectra of a) the free adamantyl cross-linker **51**. b) Gel formation in H_2O and n-hexane as cosolvent. c) Gel formation in H_2O/MeOH.*

So far, no successful gel formation has been achieved by this approach of cross-linking supramolecular entities. The attempted gel formation of **35** and **45** resulted either in linker decomposition or cage fragmentation but ultimately led to the design of the adamantly based polymer **51**. Although this linker was not capable of exhibiting the potential for hydrogel formation, it resembles an entry point for future investigations.

In the introduction (Section 3.3.1), a second method was mentioned that focuses on hydrogels, which are formed by cross-linking self-assembled metal-organic cages. These hydrogels will be investigated in the following section.

3.3.3 Synthesis of cross-linkers

Buildingblocks

To begin the investigation of supramolecular self-assembled hydrogels, four linkers (**61**-**64**) were synthesized. These linkers varied in length to receive hydrogels of various sizes and properties (Scheme 26).

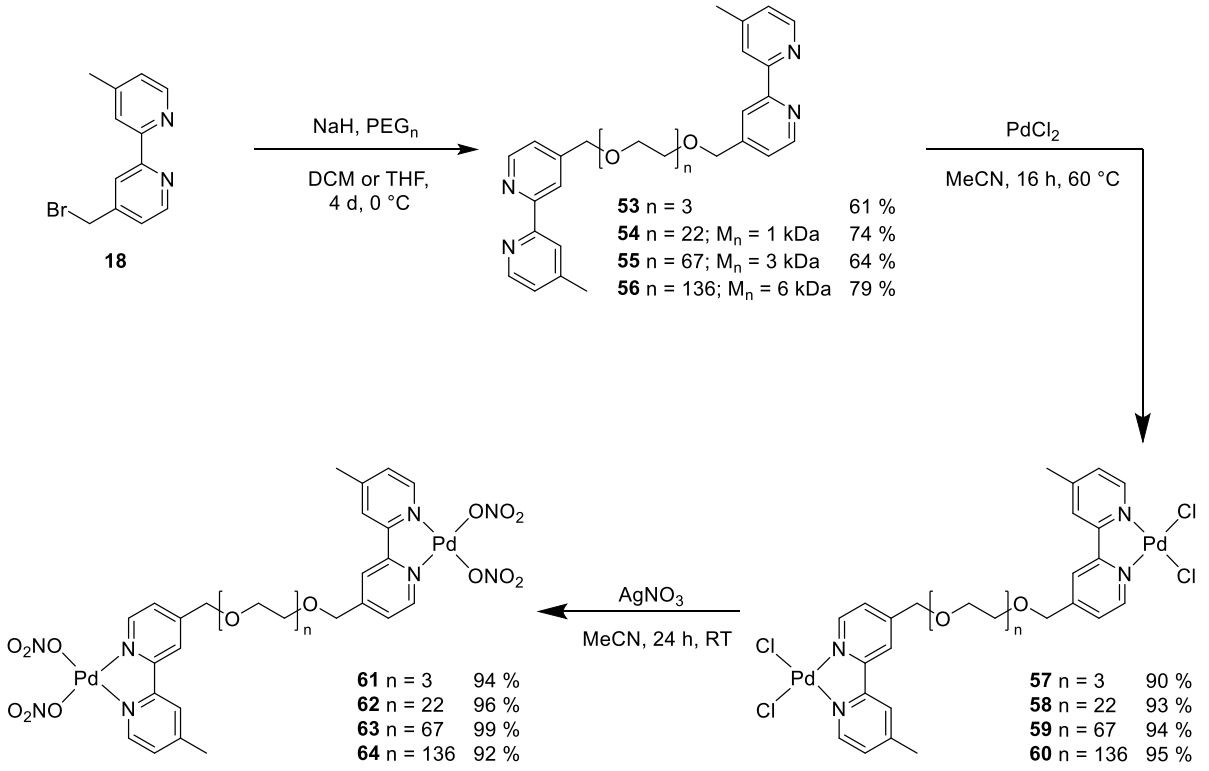

Scheme 26: Synthetic approach for different end-functionalized polymers.

Organohalide **18** was substituted in a twofold Williamson-ether synthesis under basic conditions with triethylene glycol to yield chelate ligand **53** in 61 %. These low yields were attributed to side reactions and purification issues, as on the one hand, **18** underwent a homocoupling reaction, and on the other hand, several column chromatographic separations were needed and significantly diminished the isolated yield. A following chelation of $PdCl_2$ was performed by utilizing chelate ligand **53** to receive the palladium coordinated complex **57** in 90 % yield. By employing a slight excess of $AgNO_3$ in the subsequent halide abstraction reaction, the nitrate complex **61** was obtained in 94 % yield. Following the same strategy, ligands **62**-**64** were obtained in high yields.

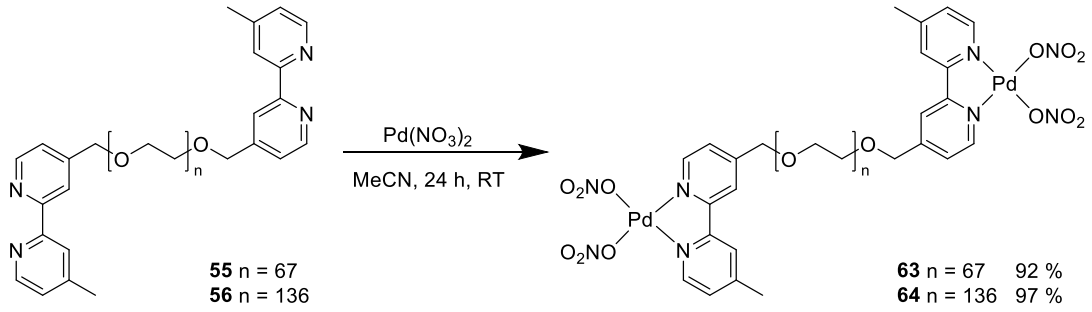

*Scheme 27: To circumvent the photo-decomposition of silver-adducts a direct synthesis of **63** and **64** was employed.*

Section 3.1.2 highlighted how the separation of $AgNO_3$ and AgCl from the reaction was frequently problematic and resulted in a considerable decrease in yield. The use of $Pd(NO_3)_2$ provided a solution to this issue since it reduced the synthesis by one step and produced no side products, eliminating the necessity for workup. In addition, it prevented the use of $AgNO_3$ and therefore circumvented the concomitant photodecomposition of $AgNO_3$ or AgCl (Scheme 27).

Self-Assembly of the hydrogels

The hydrogel self-assembly was investigated by reacting all four nitrate ligands **61**-**64** with **TPT** in a 3:4 ratio. Employing **61** as the shortest linker would result in a very stiff gel. This hydrogel would provide the highest host-to-polymer ration of all analyzed hydrogels but simultaneously features no polymer chains which are susceptible to ultrasonic irradiation. While switching to ligand **62** reduces the number of potential encapsulating sites, it also results in an increased susceptibility to ultrasound irradiation. This trend is expected to continue, with ligand **64** providing a more flexible gel and a greater likelihood of cage rupture during sonication (Scheme 28).

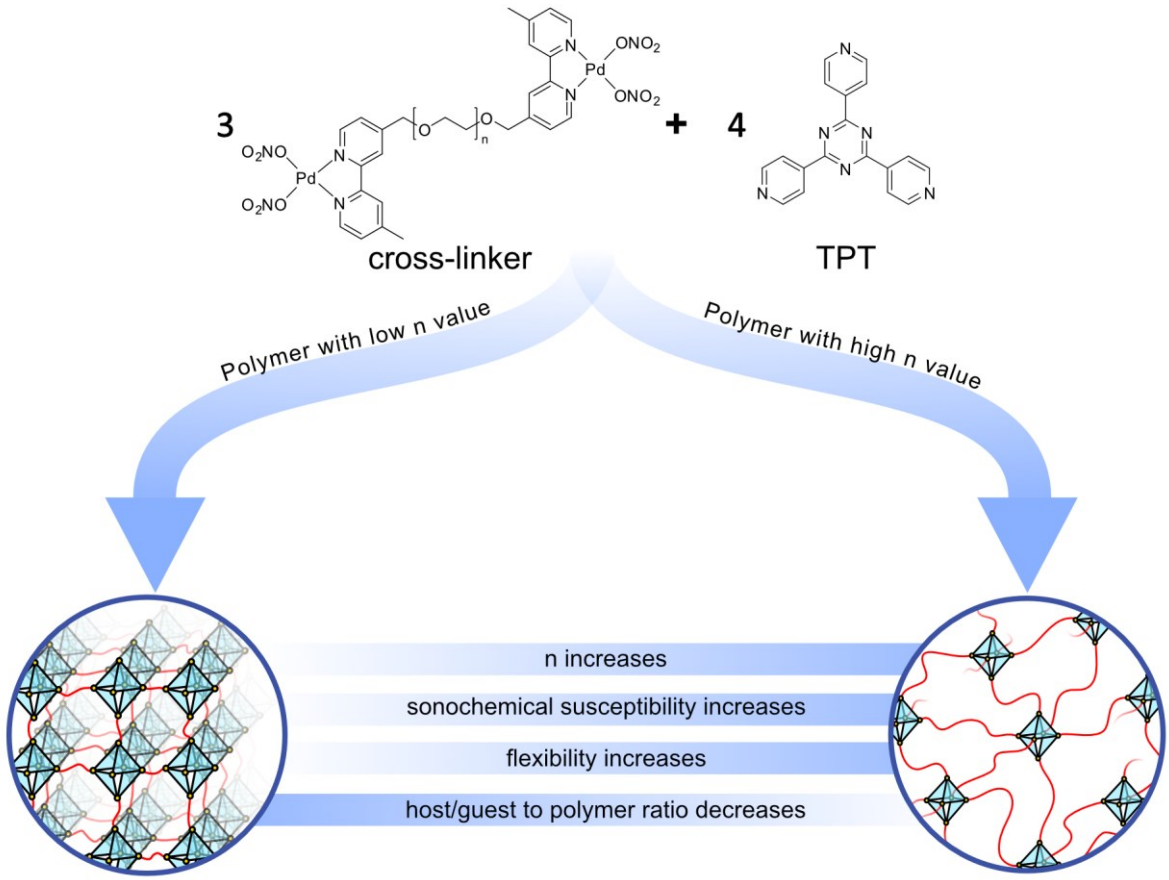

*Scheme 28: Synthetic scheme of the reaction of **TPT** and different cross-linker varying in length.*

Hydrogels exhibit the capability to absorb a large amount of water due to their three-dimensional structure.[117] To investigate this property, every hydrogel synthesis was conducted with 5 wt%, 10 wt% and 20 wt% of the building blocks, respectively. All hydrogels were synthesized in D_2O to facilitate ^{1}H NMR analysis directly after the synthesis. Starting with the shortest nitrate linker, a 20 wt% suspension of **61** and **TPT** was heated at 70 °C over night. A brown precipitate was observed, but no gel formation occurred under these conditions. **TPT** is not soluble in water but dissolves after being incorporated into the cage structure. During this synthesis, it was observed that, in addition to **TPT**, the nitrate ligand **61** is not hydrophilic enough to be completely dissolved. It was assumed that either no reaction occurred under these conditions or that the gel precipitated due to its potential hydrophobic properties. To test this hypothesis, an ^{1}H NMR analysis was attempted, but no solvent was suitable to dissolve the compound. The concentration was decreased in order to dissolve cross-linker **61**. As a result, a 5 wt% solution was heated for several hours but again resulted in the formation of a dark brown precipitate. Therefore, no further investigations for this building block were conducted.

The formation of the self-assembled gel **HG$_1$** was then probed by utilizing the bipyridine ligand **62** M_n = 1 kDa under similar conditions. A 20 wt% suspension of 4.0 equivalents of **TPT** and 3.0 equivalents of bipyridine linker **62** was heated at 50 °C. After two hours, a yellow gel was obtained that was stable to inversion (exemplary Figure 43a). Under similar conditions, gel formation for the 10 wt% self-assembled gel **HG$_1$** was achieved. A color shift was observed during the analysis of the 5 wt% reaction, but no gel could be obtained (Figure 43b). The exchange of water for DMSO resulted in the formation of visually more homogenous appearing gels, although ^{1}H NMR often indicated that no complete conversion was achieved under these conditions. (Figure 43c). It was also observed that DMSO organogels decomposed after several weeks and subsequently liquefied. This behavior, on the other hand, was not observed for the hydrogels.

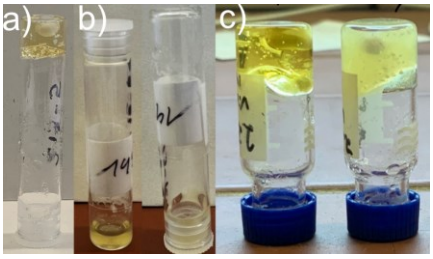

*Figure 43: a) A 20 wt% hydrogel of **HG$_6$** during the "inversion test", this picture was chosen as an example. As seen in the picture a small stir bar is incorporated into the gel. b) Reaction of 5 wt% **HG$_1$** before (left) and after (right) heating. No gel formation was observed, and the reaction is not stable to inversion. c) Organogel (left) and hydrogel (right).*

During the ^{1}H NMR investigation of hydrogel **HG$_1$**, similar **TPT** signals (δ = 9.7-8.8 ppm) and comparable bipyridine signals (**62**) (δ = 8.6-7.4 ppm) to the cages **MOC$_1$** (Figure 44a) and **polyMOC$_{60\text{-}120}$** were observed. The multiplet with an integral of 250 (δ = 4.0-3.5 ppm) was attributed to the polymer backbone and is in accordance with a PEG-chain of this length. The last two singlets can be attributed to the methylene (δ = 4.9 ppm) and the methyl group (δ = 2.6 ppm). The ^{1}H NMR analysis and the inversion test (Figure 43) prove a successful formation of a supramolecular self-assembled cage that is capable of functioning as a cross-linker. During ^{1}H NMR, a considerable broadening of the resonance was observed, resulting in a coalescence of the resonance signals caused by the molecule's hindered molecular rotation.

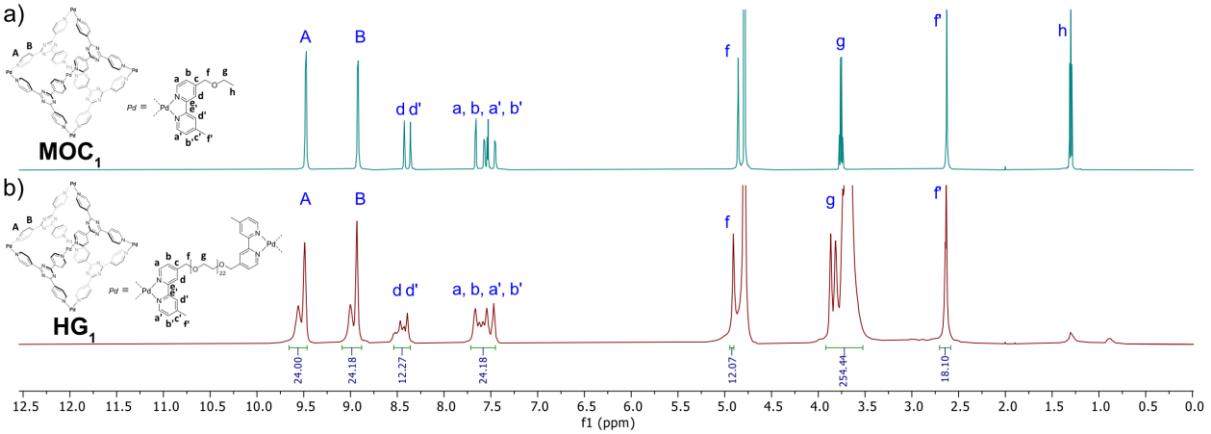

*Figure 44: Stacked NMR spectra. a) ^{1}H NMR of previously synthesized cage **MOC$_1$** for comparison. b) ^{1}H NMR of successfully synthesized hydrogel **HG$_1$**.*

Deploying PEG-based linker **63** led in both cases (10 wt% and 20 wt%) after one hour to the self-assembled hydrogel **HG$_3$** and after two weeks in the case of the 5 wt% gel. All samples of **HG$_6$** formed inversion-stable hydrogels.

Surprisingly, gel formation for the shortest gel **HG$_1$** was not achieved if only 5 wt% were used but was successful with rising polymer length (5 wt% of **HG$_3$** and **HG$_6$**). This occurrence is contradictory since the shorter polymer **HG$_1$** should form a denser network than the isostructural longer gels **HG$_3$** and **HG$_6$** at the same molecular weight percentage. All experiments were conducted at least twice but had the same outcome. It might be explained by the fact that the synthesis route, which employed $AgNO_3$, was used for the shorter linker **62** (See Section 3.1.2, photo-decomposition). But the exact reason for this occurrence remains unclear and is therefore a target for further investigations.

To demonstrate the modularity of the introduced supramolecular hydrogels, different compositions of Pd-linkers were reacted to produce mixed hydrogels. The investigation started with a 1/1 mixture of

the short **HG$_1$** and medium linker **HG$_3$**. After heating the 20 wt% reaction for 1.5 hours, it resulted in the formation of a stiff hydrogel. The exchange of **63** to 2,2'-bipyridinepalladium(II) dinitrate, which can't function as a cross-linker, results in a "network defect". 1.5 equivalents of the cross-linker **63** and 3.0 equivalents of 2,2'-bipyridinepalladium(II) dinitrate were added to a suspension of 4.0 equivalents of **TPT** and heated to 60 °C. After four hours in both cases, gel formation was observed (10 and 20 wt%).

3.3.4 Properties

Dynamic behavior

To investigate the dynamic behavior of the obtained hydrogels, swelling experiments were conducted, wherefore all hydrogels (**HG$_1$**-**HG$_6$**) were initially freeze-dried. A fixed amount of water was added to these aerogels (Figure 45) and allowed to equilibrate for one day. Subsequent addition of further water was continued until the hydrogel was incapable of more water uptake. This eventually caused the gel structure to collapse, resulting in a viscous solution that was not stable to inversion (Figure 45, last picture).

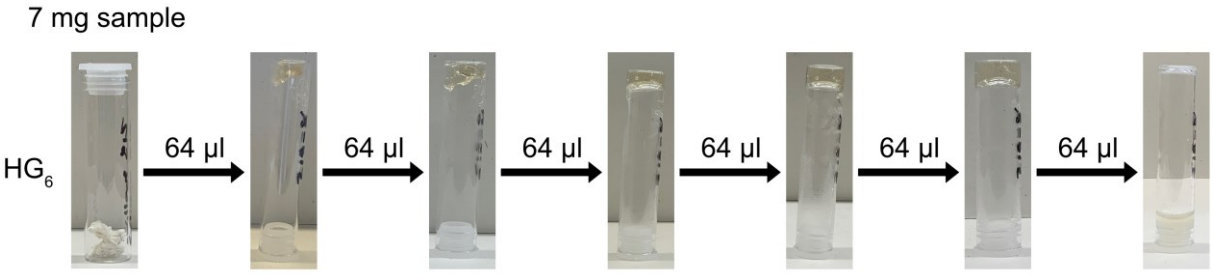

Figure 45: Subsequent addition of water to an aerogel (picture 1) results in the formation of a hydrogel (picture 2-6) and ultimately in the collapse of the structure (picture 7).

Interestingly, the smallest gel **HG$_1$** was capable of incorporating 18x of its own mass in H_2O before further addition resulted in a collapse of its network structure (Figure 91a). An increasing swelling ratio was observed for **HG$_3$**, which absorbed approximately 27x of its own weight (Figure 91b), and **HG$_6$**, which absorbed 45x of its own weight (Figure 91c). These results confirm that the uncoiled mesh size of **HG$_6$** is significantly greater than that of **HG$_1$**.

The self-healing behavior of all hydrogels **HG$_1$**-**HG$_6$** was investigated under similar conditions. A 10 wt% hydrogel of **HG$_1$** (Figure 46) was cut into two pieces and subsequently pressed together. After heating for 30 minutes at 70 °C the hydrogel was obtained in its original form, indicating self-healing behavior. Similar results were observed for the other hydrogels, **HG$_3$** and **HG$_6$**.

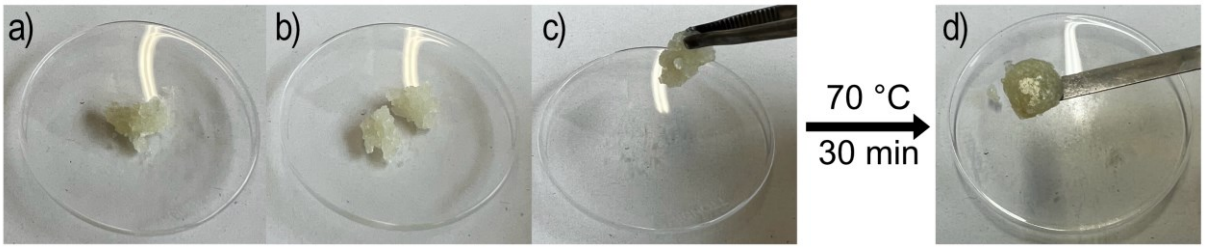

*Figure 46: a) 10 wt% hydrogel of **HG$_1$**. b) The hydrogel was cut into two pieces. c) The hydrogel was pressed together. d) **HG$_1$** after 30 minutes of heating.*

Rheology

To further probe the structure and mechanical properties of the hydrogels, shear rheology measurements were carried out for **HG$_3$** and **HG$_6$**. These measurements were conducted and evaluated by Luisa Niggemann and Dr. Robert Göstl. Therefore, the storage (G') and loss (G'') moduli during polymerization at 60 °C were measured and are depicted in Figure 47a. Noticeable is that gelation started immediately, thus, the typical crossover point of G' and G'' could not be measured. In accordance with the synthesis, full polymerization was achieved after approximately 60 minutes, which is demonstrated by the asymptotic development of G''. Interestingly, in comparison to the self-assembled hydrogel **HG$_6$**, the shorter **HG$_3$** was roughly one order of magnitude stiffer. This confirms that the obtained mesh size of **HG$_6$** is significantly greater than **HG$_3$**, which is in agreement with the trends from the swelling experiments. Both hydrogels were cooled to 25 °C (Figure 47b) and heated to 85 °C (Figure 47c) to probe if the mechanical properties were temperature dependent, which was expressed by the complex viscosity η^*. As seen in Figure 47c, the mechanical properties of both gels are largely unchanged when cooled. Heating to 80 °C resulted in a slight increase of η^* which is also considered mostly invariant to temperature. The occurring stiffening phenomenon upon heating might be explained by the lower critical solution temperature behavior of PEG in salt solution. These results demonstrated that **HG$_3$** and **HG$_6$** had an unexpectedly high thermal stability for hydrogels. Analyzing the frequency dependency revealed that both gels exhibit frequency-invariant G' moduli (Figure 47d). In contrast to previous self-healing experiments, no crossover point between G' and G'' was observed in the covered frequency range, which is characteristic for dynamic bond rearranging. However, the steeply increasing G'' moduli in Figure 47d indicates that this crossing point might be reached at frequencies above 100 Hz. Unfortunately, measurements above this frequency were not possible.

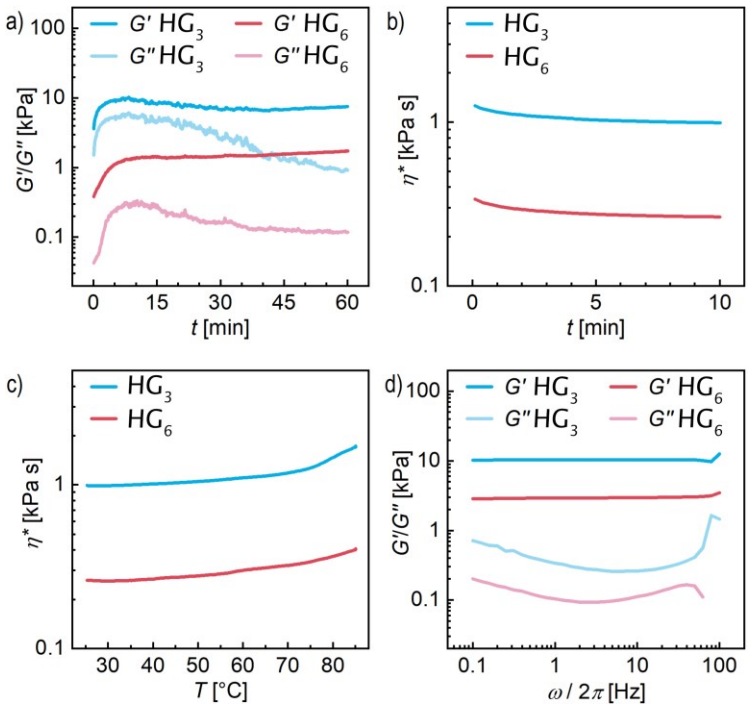

*Figure 47: Shear rheology of 10 wt% of hydrogel **HG₃** and **HG₆**. a) G′ and G′′ at strain amplitude γ_0 = 1%, frequency $\omega/2\pi$ = 1 Hz, and temperature T = 60 °C upon polymerization time sweep. b) η* at γ_0 = 1% and $\omega/2\pi$ = 1 Hz upon cooling to T = 25 °C. c) η* at γ_0 = 1% and $\omega/2\pi$ = 1 Hz upon temperature sweep. d) G′ and G′′ at γ_0 = 1% and T = 25 °C upon frequency sweep.*

SAXS

Complementary to the rheology analysis, small angle x-ray scattering (SAXS) measurements were performed and evaluated by Marcel Krüsmann and Prof. Dr. Matthias Karg to further investigate the hydrogel structure. Therefore, 10 wt% samples of all three hydrogels **HG₁**-**HG₆** were synthesized and analyzed in detail. Due to the containment of palladium ions and the predominant PEG in the hydrogels **HG₁**-**HG₆**, strong scattering signals were observed during SAXS measurements. Every sample was measured two times, once at minimum detector range (270 nm) and once at maximum range (2.50 m). At minimum range, the scattering of larger angles can be observed, which are attributed to small particles, whereas at maximum range, only small angles are detected and are associated with large particles. To minimize occurring scattering contributions of dynamic fluctuations, all hydrogels were freeze-dried before the analysis. Figure 48 illustrates the SAXS profile of **HG₁** with its related fits. This profile is characterized by three distinct features: At lower *q*, by a steeply linear increase of the scattering intensity, at mid *q*, by a correlation peak and at high *q*, by an additional separated correlation peak. A simple power law was used to describe the low *q* region (– – –), whereas mid (• • •) to high *q* (– • –) were described by broad peak functions (Figure 48). The power law resembles a Porod scattering and describes in detail the scattering from sharp interfaces. Inhomogeneities occurring on different length scales are described by the broad peak contributions. The sum of all three contributions is represented by the corresponding fit depicted as a solid black line (Figure 48).

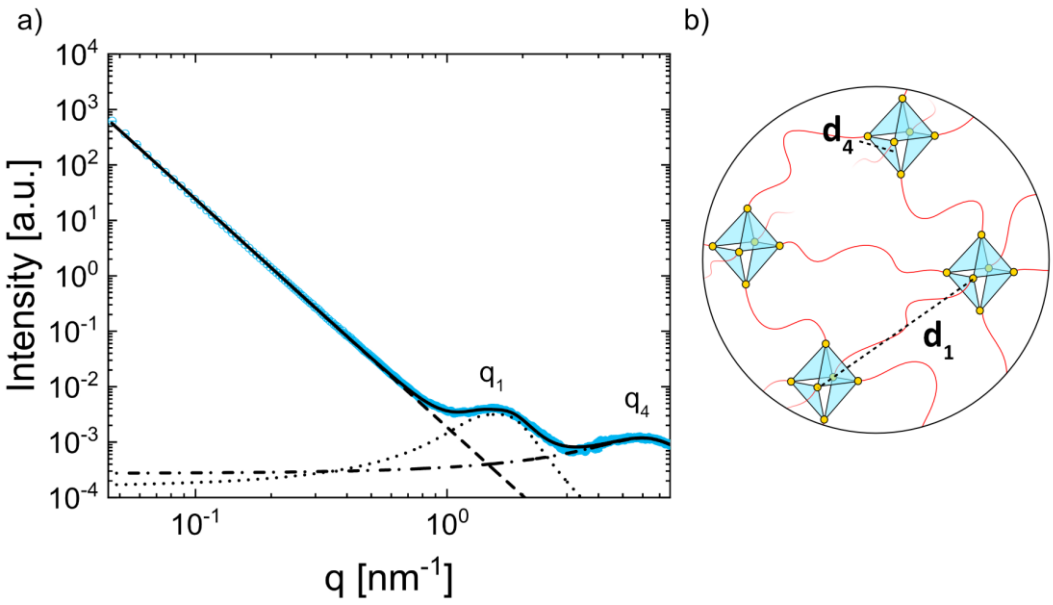

*Figure 48: SAXS profile o **HG$_1$** (freeze-dried) with the three fit contributions shown separately. The power law (– – –), the first broad peak (• • •) and the second broad peak (– • –). The black solid line is the full fit (sum of the three contributions) according to equation S1 (Section 5.5 SAXS). This image was kindly provided by Marcel Krüsmann. b) d_1 represents the network distance and is marked as a dotted line. d_4 represents the real space of a host complex and therefore potentially the distance between Pd–Pd.*

In Figure 48, the lowest *q* structure peak was attributed to the mesh size (q_1) of **HG$_1$**. It describes the average distance between two crosslinker points of the network and therefore the cage-to-cage distance. This value corresponds to a real-space distance of approximately d_1 = 4.03 nm and is in accordance with the utilized PEG under the assumption that these chains form coiled structures. The highest *q* peak for **HG$_1$** describes an approximately real space distance of d_4 = 1 nm and can either be attributed to the dimension of a host complex (q_4) or it originates from inhomogeneities of the utilized PEG chains.

Comparing all hydrogels **HG$_1$**-**HG$_6$** indicates, at first glance, that these hydrogels exhibit similar structural behavior. For all three hydrogels, the scattering intensity in the low *q* region increases linearly and can be described in the same manner as before, by a Porod power law (Figure 49). This scaling describes the scattering from sharp interfaces between the included air and the matrix. For all hydrogels, distinct peaks with a large peak width can be observed at mid-to-high *q* values. All these peaks were described by broad peak functions, which provide information about the structure (q_1). For the lowest *q* value, which describes the cage-to-cage distance (q_1), a shift can be observed that decreases to lower *q* values from **HG$_1$** to **HG$_6$**. This indicates that as the length of the utilized poly(ethylene glycol) increases, so does the average distance between the crosslinking locations. For **HG$_1$**, a real space distance of d_1 = 4.03 nm was observed. This distance increased to d_1 = 9.79 nm for **HG$_3$** and d_1 = 10.5 nm for **HG$_6$**. These results are in agreement with the previous conducted rheology

and swelling experiments. Interestingly, the highest *q* values are nearly identical ($q_4 \approx 6$ nm^{-1}) and all correspond to a space distance of approximately $d_4 = 1$ nm. As mentioned, this region agrees well with the dimension of cross-linked metal complexes but can also be attributed to local inhomogeneities of the PEG chain.

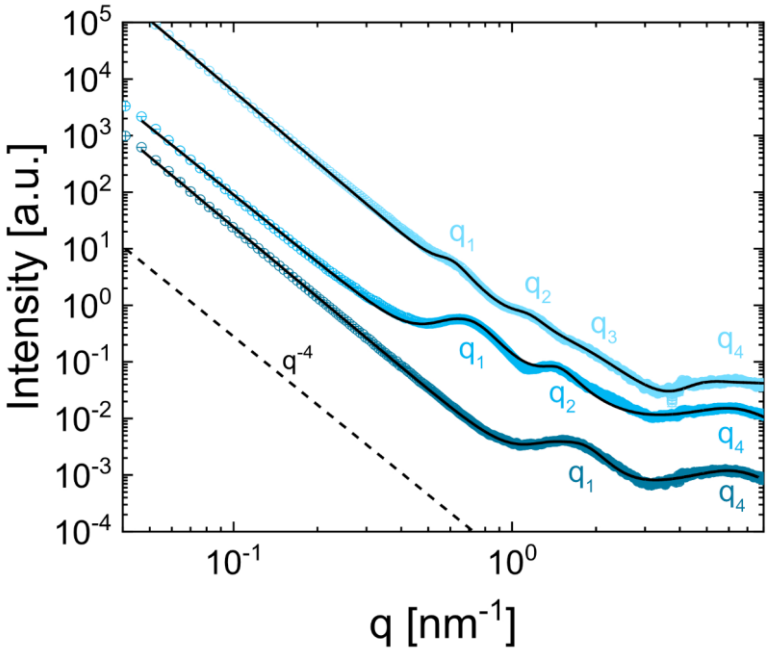

*Figure 49: SAXS profiles of the hydrogels **HG$_1$** (dark blue), **HG$_3$** (blue) and **HG$_6$** (light blue) after freeze-drying with corresponding fits according to equation S1 (black solid lines). The scattering profiles are shifted by fixed multipliers for better visibility. This image was kindly provided by Marcel Krüsmann.*

Scanning electron microscopy (SEM)

A final structure analysis was conducted by scanning electron microscopy to visualize the obtained hydrogel network. A 20 wt% sample of **HG$_3$** was freeze-dried and subsequently analyzed by SEM. As seen in Figure 50a sponge-like network was observed with a pore width of approximately 5 µm. At higher magnifications, a smooth structure of the material can be seen, resembling a small bowl. This surface enlargement, caused by the network structure, is required for solvent immobilization and is typical for hydrogels.

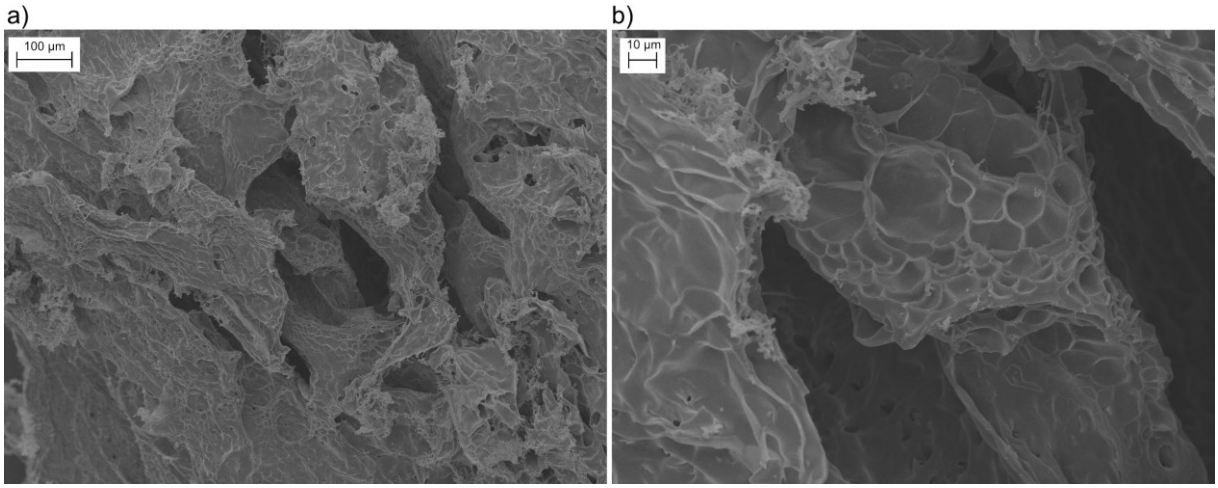

*Figure 50: SEM image of a 20 wt% **HG₃**, freeze-dried prior to the measurement (scale bar 100 µm); b) SEM image of a 20 wt% **HG₃**, freeze-dried prior to the measurement (scale bar 10 µm). These images were obtained during the bachelor thesis of Anne Germann.*

3.3.5 Guest encapsulation

After discovering the outstanding host-guest properties of **polyMOC$_{60\text{-}120}$** and its potential for targeted drug release, an investigation of the hydrogels for similar characteristics was conducted. The utilized M_6L_4 cage, which is incorporated in the hydrogels **HG$_{1\text{-}6}$**, exhibits the same hydrophobic cavity as **MOC$_1$**, therefore also enabling encapsulation of various relevant guests. During the guest screening (See section 3.1.3) several molecules were identified as suitable for encapsulation. To probe this behavior, two methods were initially investigated. In the first method, the guest was added once the hydrogel had been formed, preventing those guest molecules from interfering during cage self-assembly. Unfortunately, in some cases, no guest uptake could be achieved, which was explained by the stiff gel structure hampering diffusion processes. A way to improve the uptake was to add an excess of water, resulting in gel swelling and therefore "softening up" the structure, as well as an excess of the desired guest. In the second method, guest addition was performed simultaneously with the utilized building blocks. It was later observed that the investigated guests were not impeding host assembly, rendering this method superior.

The best approach to confirm guest uptake would be by visualizing enclathration. Melatonin and phenolphthalein were already employed semi-successfully for this task and seemed suitable for targeted uptake by hydrogels. Phenolphthalein (0.4 equivalents) was added to a basic suspension of the pristine building blocks of **HG$_3$** and resulted in a red suspension. Due to the cavity-directed chromism of phenolphthalein, it was expected that after two hours of heating, a yellow hydrogel would be formed.[94b] Instead, a brown suspension was obtained, and the ^{1}H NMR analysis revealed that under basic conditions no cage formation takes place but rather leads to the decomposition of the polymeric nitrate **63**. Melatonin, on the other hand, benefits from neutral conditions during the uptake

and was employed as a consequence. It was expected that upon encapsulation, a red gel would be formed as a result of the formation of a charge transfer complex between melatonin and the M_6L_4 moiety. A formation of a brown supramolecular network was observed and confirmed by ^{1}H NMR, but no guest signals were present, indicating no successful uptake.

Even though the encapsulation of melatonin was unsuccessful, the experiment proved that the presence of guest molecules does not interfere with gel formation. Therefore, employing an excess of progesterone (6 eq.) successfully yielded a yellow hydrogel **HG$_3$·(progesterone)**, which was analyzed by ^{1}H NMR. Integration revealed that exactly one progesterone moiety could be encapsulated into the hydrogel (Figure 51a, middle and 274). While the chemical upfield shift is identical for the three cages (**MOC$_1$**, **HG$_3$**, and **polyMOC$_{60}$**) (Figure 51a, from top to bottom), a noticeable growing resonance broadening can be observed and attributed to the decreasing host guest ratio.

Interestingly, upon encapsulation, a symmetry change of the T_d M_6L_4 moiety was observed, as indicated by the collapse of the **TPT** signals (Figure 51b). This phenomenon was observed for all guest molecules and in all hydrogels.

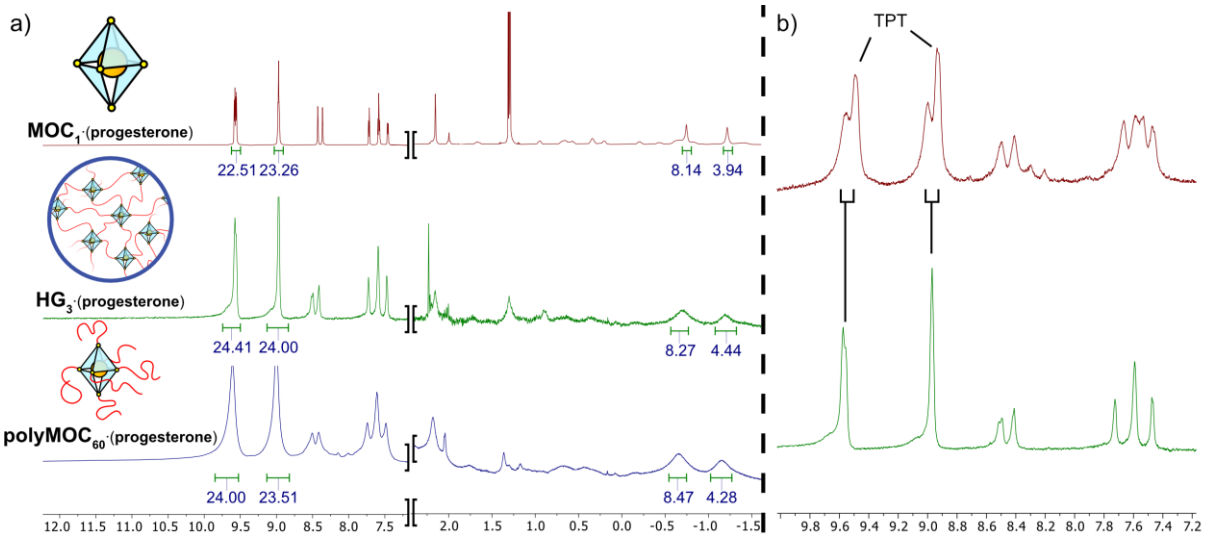

*Figure 51: a) Stacked ^{1}H NMR of encapsulated progesterone for different supramolecular cages. Only one progesterone moiety can be encapsulated in the cage. b) Stacked ^{1}H NMR of the empty cage **HG$_3$** (top) and the progesterone encapsulated **HG$_3$·(progesterone)** (bottom). A collapse of the **TPT** signals can be observed.*

Following the successful incorporation of progesterone, additional guests were incorporated into the hydrogels to demonstrate their versatility. Drospirenone and ibuprofen were encapsulated in the same manner as progesterone and confirmed by ^{1}H NMR. In the instance of ibuprofen, guest uptake was performed with all hydrogels (**HG$_1$-HG$_6$**) to examine the effect of polymer backbone length on the subsequent sonochemical studies. According to prior observations, a distinctive resonance broadening

occurs with increasing linker length (Figure 52). In addition, with increasing polymer length a downfield shift of the encapsulated guest was noticed, which was attributed to the guest's decreasing electron density. One important factor of the utilized hydrogels was the increasing capability of guest uptake. The previously investigated supramolecular cages **polyMOC$_{60\text{-}120}$** were adequate to precisely release its guest load but they fell short in terms of its guest encapsulation ratio. For example, cage **polyMOC$_{60}$** has a molecular weight of approximately 60.000 g mol^{-1} and is capable of incorporating two ibuprofen moieties with a combined molecular weight of 412 g mol^{-1}. This corresponds to a cargo load ratio of just 0.7 % and in the case of **polyMOC$_{120}$** to 0.3 %. By utilizing hydrogels, this guest uptake was improved to 1.9 % for the longest synthesized hydrogel **HG$_6$** and further increased to an outstanding 6.2 % for **HG$_1$**.

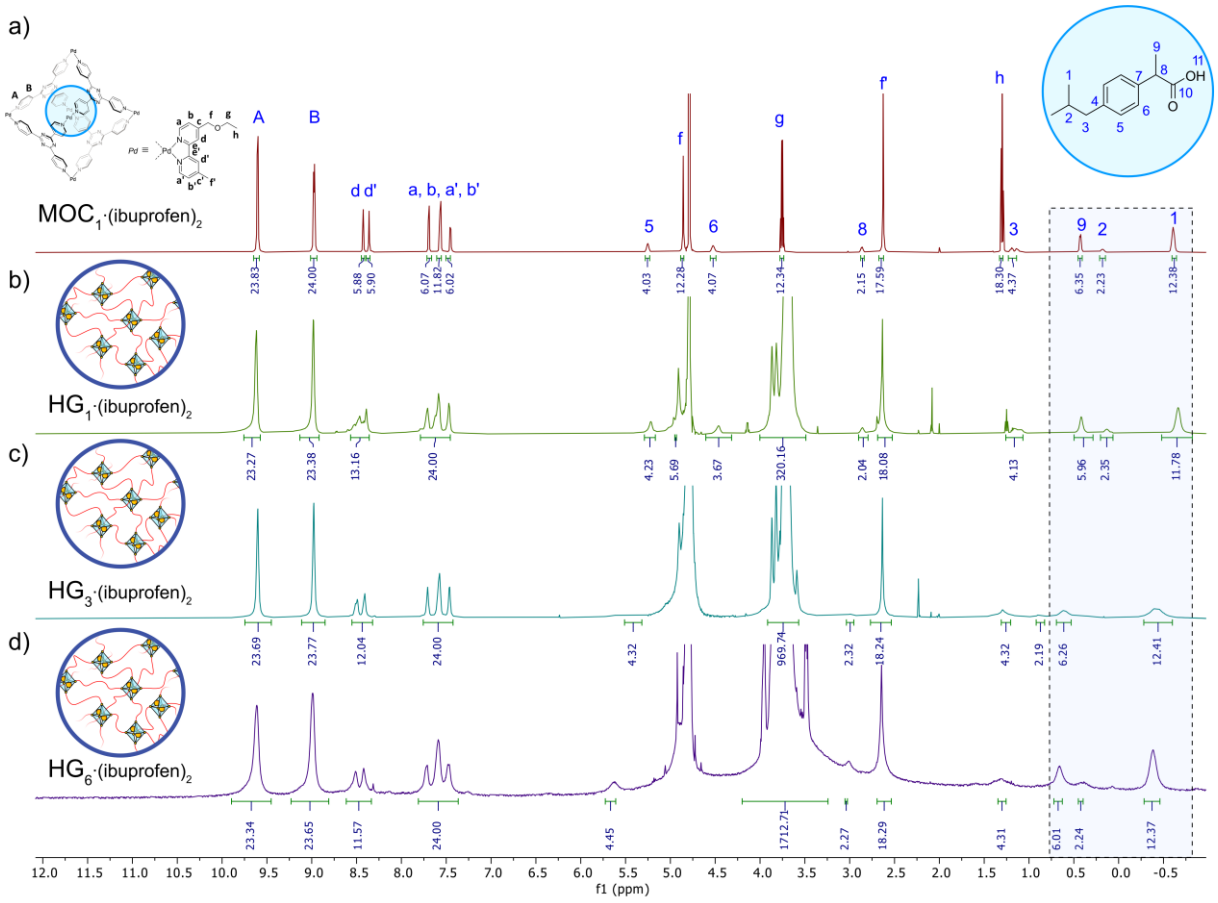

*Figure 52: Stacked ^{1}H NMR of encapsulated ibuprofen. a) ^{1}H NMR of **MOC$_1$·(ibuprofen)$_2$** for comparison. b-d) ^{1}H NMR of the corresponding hydrogels **HG$_{1\text{-}6}$·(ibuprofen)$_2$**.*

3.3.6 Activation and release studies

It is well known that a minimum chain length is required for mechanochemical activation in traditional mechanophores,[54, 81d, 118] but it was anticipated that the hydrogels' nearly infinite molar mass would significantly increase their susceptibility to shear forces, similar to microgels.[119] Thus, making the hydrogels susceptible to force-induced bond rupture.

Boydston's group demonstrated mechanochemical activation by employing pressure, induced by a carver press, using a similar approach by utilizing hydrogels for molecular release. A unique aspect of this system is a net strengthening of the polymer backbone, which was achieved by "flex-activation". Under compression (1200 MPa), an oxanorbornadien mechanophore was activated in a cycloreversion process that eventually released furfuryl, culminating in the conversion of an alkene into an alkyne moiety.[120] It was envisioned that this approach to mechanochemical activation might be suitable for **$HG_{1\text{-}6}$** and a subsequent guest release. For this experiment, **HG_1** was freeze-dried and subjected to continuous pressure for one hour. NMR analysis revealed that no activation was achieved with this method after one hour (Figure 53a). It was assumed that a consecutive subjection of force would result in an increasing activation. Therefore, the same hydrogel was exposed to pressure for five seconds and subsequently folded. This process was repeated ten times before the gel was analyzed by ^{1}H NMR. A marginal activation could be achieved with this method. The signals appearing at δ = 8.78 ppm, 8.13 ppm, and 7.87 ppm were assigned to cage fragmentation, resulting in an activation of roughly 3 % (Figure 53b). This method was not further examined since it appeared unsuitable for a targeted guest release.

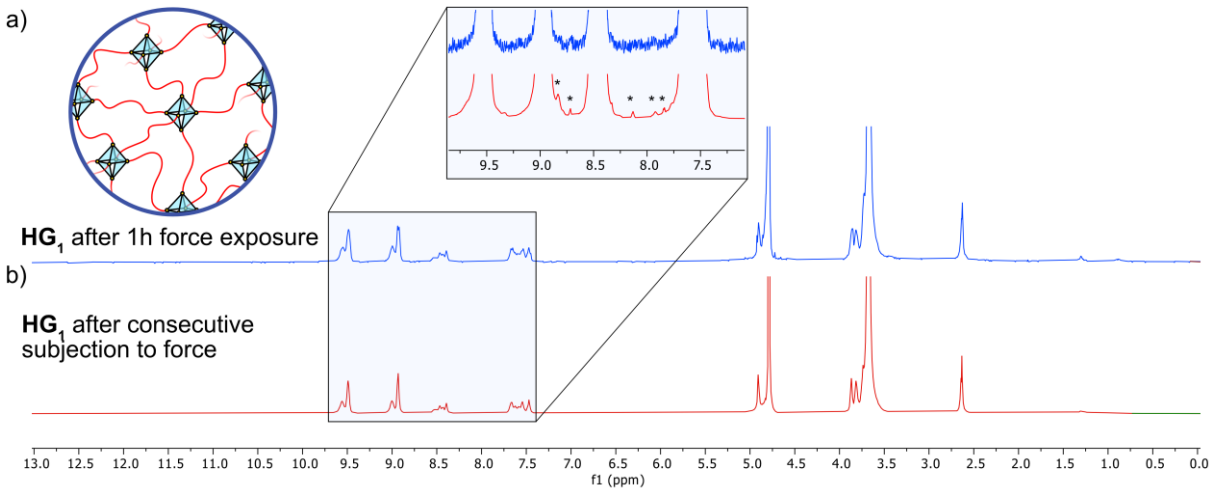

*Figure 53: Targeted disassembly of **HG_1** by utilizing a carver press. a) After one hour no activation was observed. b) Consecutive activation of **HG_1** resulted in a marginal activation.*

It was assumed that ultrasound irradiation would have the same impact on **HG$_{1-6}$** as it had on the cages **polyMOC$_{60-120}$** discussed in section 3.1.4. Therefore, their behavior was probed by employing a 20 kHz sonicator with subsequent analysis by ^{1}H NMR. To prove that this process is chain-length-dependent, all three hydrogels were successively sonicated and compared. Starting with the shortest hydrogel **HG$_1$**, the sample was freeze-dried in advance to yield a pale-yellow aerogel (Figure 54, left), which was then submitted into a suslick vessel. Water was added, and the received 2.5 mg mL^{-1} suspension was exposed to irradiation for three hours (on time of sonicator) (Figure 55). After one hour, a solution was obtained, accompanied by a color change to a light brown. This color change was more pronounced after increasing the sonication time, which suggested that **HG$_1$** might be activated by ultrasound. After the sample was freeze-dried to yield a brown aerogel, a ^{1}H NMR analysis was performed to investigate the sonochemical influences on **HG$_1$**. Surprisingly, after three hours of sonication, only minor activation of approximately 3% was achieved, as indicated by a small integral increase from 1.27 to 2.05 (δ = 7.78 ppm, Figure 56b). It has to be noted, that the signals at δ = 8.73 ppm, 8.60 ppm, 7.92 ppm and 7.78 ppm (Figure 56a, asterisk) were already present before sonication but are not originating from the starting material. Comparing them to a disassembled cage from section 3.1.4 shows that these signals exhibit an identical chemical shift as the fragmentation signals from cage **polyMOC$_{60}$** (Figure 56c, highlighted blue), but are missing the sharp singlet at δ = 8.17 ppm.

Figure 54: Aero gel before (left) and after (right) being exposed to ultrasound. Due to decomposition the brown colour can be observed.

Figure 55: Sonochemical apparatus. The hydrogel was submitted into the suslick vessle and dissolved during the sonication process.

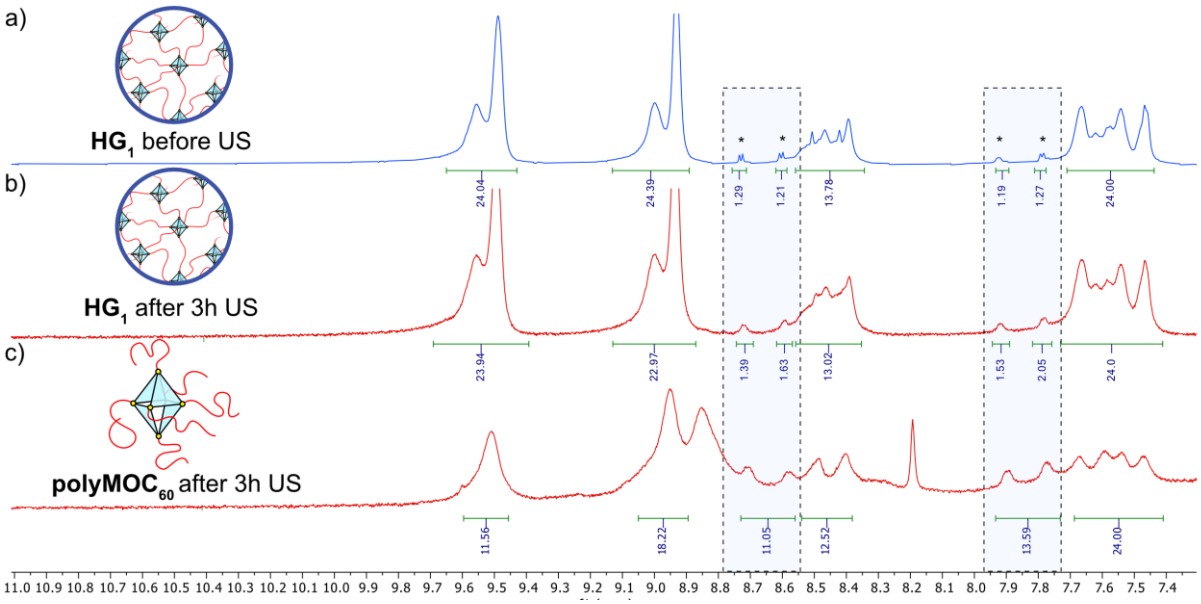

*Figure 56: a) ^{1}H NMR of **HG$_1$** before sonication. b) ^{1}H NMR of **HG$_1$** after one hour of ultrasound exposure. c) ^{1}H NMR of **polyMOC$_{60}$** after three hours of sonication, for comparison. Highlighted blue is the area of the fragment signals.*

Subsequently, the isostructural hydrogel **HG$_3$** was exposed to ultrasonic irradiation for three hours, with similar optical results as **HG$_1$**. In contrast, sonochemical activation was indeed observed in the ^{1}H NMR and an integration of fragmentation signals (δ = 7.88-7.77 ppm) suggested that approximately 29 % of **HG$_3$** were disassembled (See Figure 58a). A similar result was noticed for **HG$_6$**, where an activation of 36 % was successfully achieved. These results demonstrate the chain-length dependence of ultrasound-induced bond scissioning. With increasing polymer length, a more rapid occurrence of chain scission can be observed but ceases at a lower limiting value. This series of experiments further supports the results from section 3.1 that the length dependence of ultrasonic activation is evidence for a mechanochemical process and is not induced by pressure or temperature fluctuations.[82a]

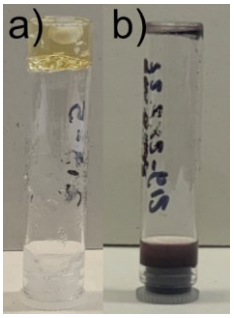

*Figure 57: a) **HG$_6$** before sonication. b) **HG$_6$** after sonication.*

Section 3.3.4 demonstrated the swelling behavior of all hydrogels and illustrated that the addition of water to a freeze-dried sample yields a hydrogel in its original form. Interestingly, several sonicated samples of **HG$_6$** were freeze-dried with a subsequent addition of water. No gelation could be seen in this manner, providing additional evidence that the cross-linked network was successfully decomposed after ultrasonic irradiation (Figure 57b).

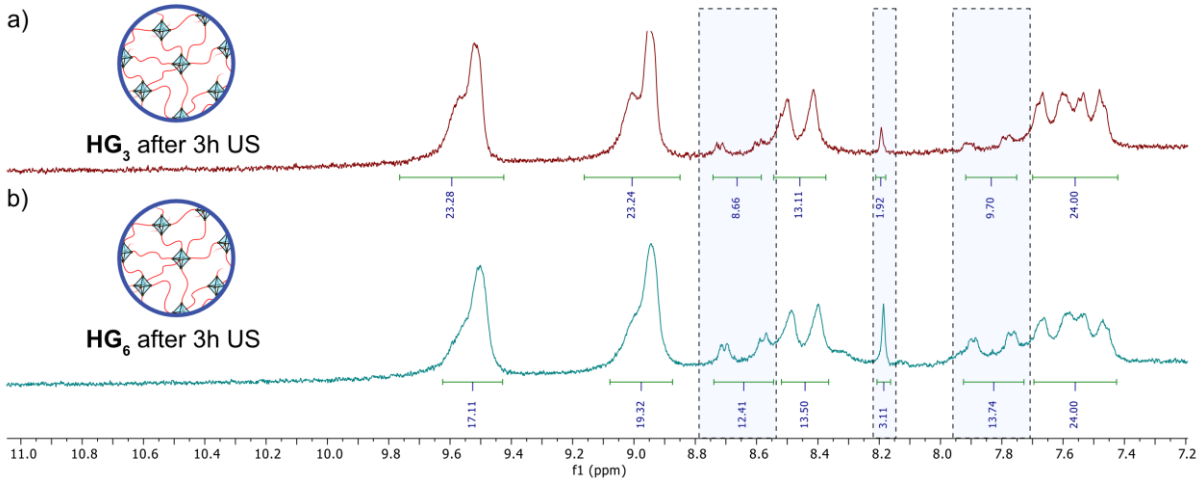

*Figure 58: a) ^{1}H NMR of **HG$_3$** after three hours of ultrasound exposure. b) ^{1}H NMR of **HG$_6$** after three hours of ultrasound exposure.*

SAXS

SAXS measurements were performed before (blue) and after (red) three hours of sonicating **HG$_3$** (Figure 59). These measurements were performed and evaluated by Marcel Krüsmann and Prof. Dr. Matthias Karg. Figure 59 illustrates that, upon disassembly, the overall SAXS regions are quite similar

in both profiles. While the peaks in the low *q* region stay in the same position, they lose significantly in intensity, which can be explained by non-specific bond scissioning. This phenomenon occurs in polymers and happens due to numerous reasons. It is dependent on the functional groups, the utilized polymer or for example the lack of extension of polymer chains.[82a] GPC measurements (section 3.3.4) indicated that this phenomenon can occur and is a good explanation for the decrease in intensity during the SAXS measurement. The complete disappearance of the high *q* peak ($q_4 \approx 6$ nm^{-1}, highlighted blue) in Figure 59 is predominant. This peak was initially attributed to the cross-linked metal complexes of the hydrogel or to inhomogeneities in the PEG chain. However, its complete disappearance supports the theory that this region corresponds to the cross-linked network since a mechanophore experiences the majority of the sonochemical force, resulting in its decomposition.

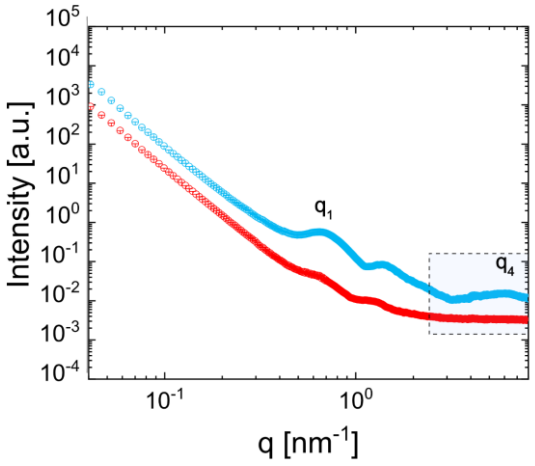

*Figure 59: SAXS profiles of **HG$_3$** before exposure to ultrasound (blue) and after exposure for 3 h of ultrasound with a sequence of 1 s on and 1 s off (only the "on" time is reported) (red). The scattering profiles are shifted by fixed multipliers for better visibility. This Figure was kindly provided by Marcel Krüsmann.*

After evidently demonstrating the successful decomposition of **HG$_3$** and **HG$_6$**, guest release studies were conducted in a similar manner as described before. The corresponding **HG** was submitted into a suslick-vessel and, after the addition of water (2.5 mg mL^{-1}), was sonicated for three hours (on time). For all gels, an optical change in the color of the solution was noticed, although it was more pronounced for hydrogels with larger molecular weights. Control studies with **HG$_1$**·(**ibuprofen**)$_2$ were carried out to initially show that the gel is not able to release its guest since it lacks the necessary polymer length for bond scissioning. As depicted in Figure 60a and b, no release was observed, as indicated by the cage signals at δ = 7.62 ppm (integral of 24) and the unchanged guest signals at δ = 0.42 and -0.67 ppm (integral of 6 and 12, respectively, highlighted blue). It was surprising to see that neither **HG$_3$**·(**ibuprofen**)$_2$ nor **HG$_6$**·(**ibuprofen**)$_2$ were capable of releasing their incorporated guest

after being exposed to ultrasound for several hours (Figures 60d and f), despite the fact that it had been shown that **HG$_3$** and **HG$_6$** are responsive to ultrasound.

Additionally, it was discovered that, in contrast to earlier sonication tests, the disassembly rate was considerably decreased after guest encapsulation. After three hours of sonicating, no activation could be observed for **HG$_3$**·(**ibuprofen**)$_2$, which is in contrast to the initial observed fragmentation of **HG$_3$** (29 %). The characteristic signals for cage disassembly were not observed in the ^{1}H NMR of **HG$_3$**·(**ibuprofen**)$_2$, and only the singlet at 8.19 ppm was detected. Integration suggests an activation of about 10-13%, although a decline in guest signals did not further support this claim. (δ = 1.4 to -0.4 ppm) (Figure 60d). A similar decrease in activation was noted for **HG$_6$**·(**ibuprofen**)$_2$. After three hours of exposure to ultrasound irradiation, the hydrogel **HG$_6$**·(**ibuprofen**)$_2$ experienced approximately 30 % cage rupture (Initially **HG$_6$** = 36 %). But no guest release of ibuprofen could be observed (Figure 60f).

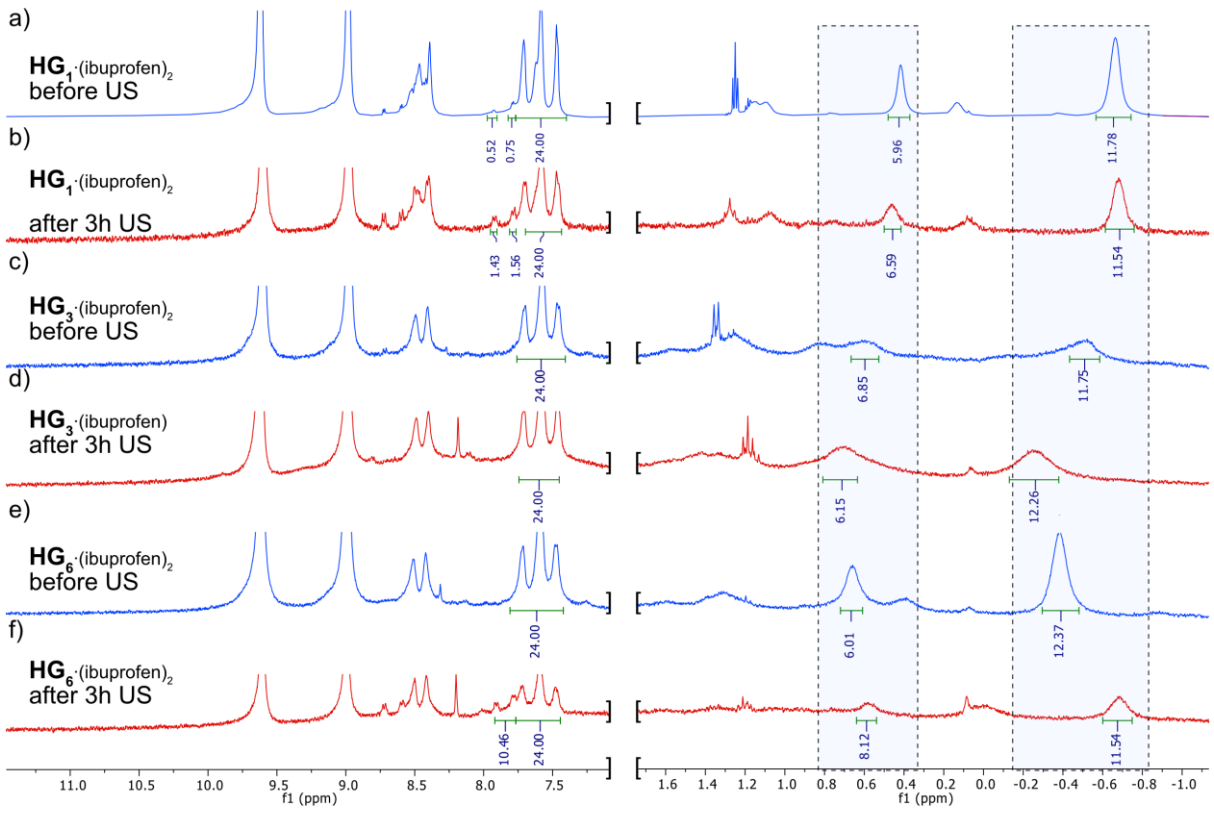

Figure 60: ^{1}H NMR spectra for all ibuprofen release experiments. Highlighted blue are the characteristic ibuprofen signals of the methyl group.

Treating the area from δ = 8.0-7.5 ppm as one cage (Figure 61b, total integral of 24 protons) instead of a "fragmented cage" and an "intact one" as before can lead to the assumption that in fact a release of 32 % was achieved for **HG$_6$**·(**ibuprofen**)$_2$, indicated by the decrease of the ibuprofen signal at δ = 0.67

ppm (from 12 to 8, Figure 61, highlighted in blue). While this might be in accordance with the previous results, it is no direct proof of a successful guest release. Furthermore, most of these results contradicted not just the mechanochemical activation of the used hydrogels, but also all earlier ultrasonic experiments from section 3.1.4, necessitating further investigation.

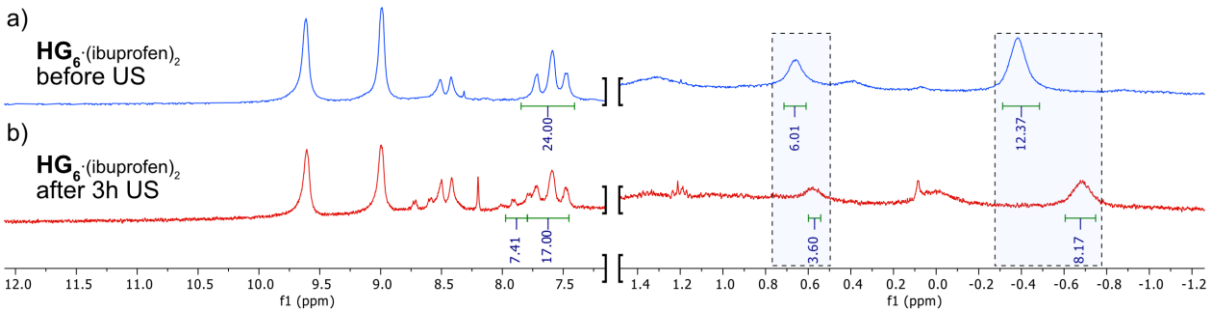

*Figure 61: a) **HG$_6$·(ibuprofen)$_2$** before exposure to ultrasound. b) **HG$_6$·(ibuprofen)$_2$** after three hours of ultrasound exposure. The area δ = 8.0-7.5 was treated as one cage, with a total integral of 24 protons.*

By employing 20 mM maleic acid as an external reference, the release could be quantitatively analyzed by ^{1}H NMR spectroscopy. Initially, the ultrasound-induced decomposition experiment with **HG$_6$** was repeated to observe the actual cage rupture. As shown in Figure 62a, **HG$_6$** (10 mg in 0.7 mL D_2O for both NMR spectra) was normalized to the distinctive aromatic bipyridine signals at δ = 7.6 ppm (a, a', b, b'), which resulted in an integral for maleic acid of 3.43 at δ = 6.4 ppm. A transfer of this integral to the NMR after ultrasonication provides detailed information about the process and the fragmentation. A decrease of all cage signals (7.6, 8.5, 9.0 and 9.5 ppm, Figure 62b) was observed. Since maleic acid was employed, the actual activation could be calculated by the initial integral of the pristine bipyridine signals (24, δ = 7.6 ppm, Figure 62a) and the bipyridine signals after exposure (13.65, δ = 7.6 ppm, Figure 62b). This resembles a decrease for the integral of 10.35 (δ = 7.6 ppm, Figure 62b). Thus, the activation can be calculated:

$$\frac{10.35}{24.00} = 0.43 = 43\ \%$$

This is in accordance with all measurements, wherefore this method was also utilized for the analysis of a subsequent targeted drug release. **HG$_6$·(ibuprofen)$_2$** was sonicated for three hours and analyzed by ^{1}H NMR (11 mg in 0.7 mL D_2O for both NMR spectra) in the presence of maleic acid as an external reference. The aromatic bipyridine signals were used once again as a reference to gain information about the maleic acid integral (2.35 at δ = 6.4 ppm). This information was transferred after the sonication to unambiguously prove guest release. Once again, an activation of approximately 47 % was achieved, and by comparing the ibuprofen signals at δ = 1.2, 0.6, 0.3 and -0.6 ppm a significant decrease

and therefore release of the guest was observed (decrease of approximately 65 %). These results successfully confirm that ultrasound is suitable to mechanochemically activate supramolecular hydrogels and subsequently release their molecular cargo load.

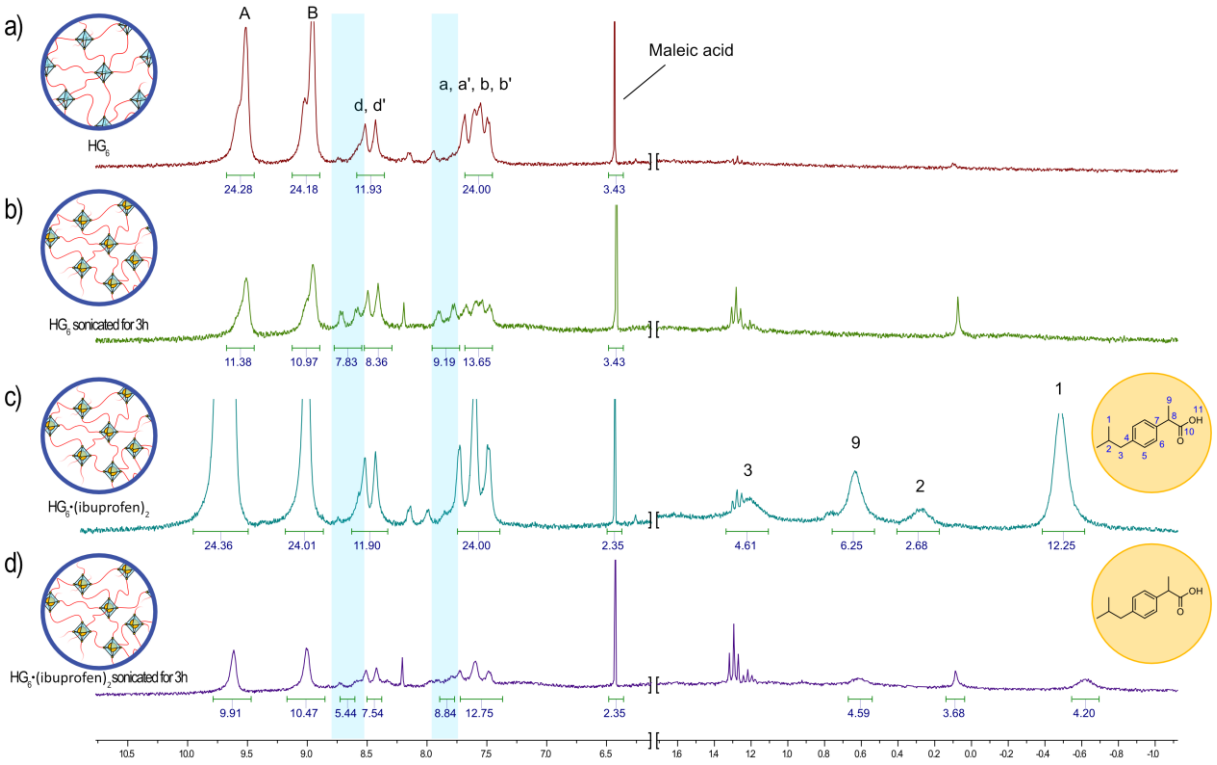

*Figure 62: ^{1}H NMR with maleic acid as a reference. a) **HG$_6$** prior to sonication. b) **HG$_6$** after three hours of sonication. c) **HG$_6$·(ibuprofen)$_2$** prior to sonication. d) **HG$_6$·(ibuprofen)$_2$** after three hours of sonication. Highlighted blue are the appearing signals originating from cage fragmentation products in solution.*

3.3.7 Summary

This chapter was initiated with the investigation of a novel class of guest-linked hydrogels. Three ibuprofen- and adamantly-based linkers were successfully synthesized and used to form hydrogels. Unfortunately, no effective gel formation was seen in these investigations; however, it should be mentioned that in the instance of adamantyl cross-linker **51**, indications of host-guest interaction were observed. Although unsuccessful, these results are the foundation for a new class of supramolecular hydrogels. The chapter continued with the successful synthesis of three isostructural polymeric linkers **62**-**64**, followed by the self-assembly of different hydrogels (**HG_{1-6}**) and organogels. These hydrogels vary not only in size but also in weight percentage and, hence, in structural characteristics. Those properties were thoroughly investigated using rheology, SAXS, and SEM measurements. Swelling experiments revealed the dynamic behavior of the utilized hydrogels and that the network structure was still maintained after freeze-drying. Further, self-healing experiments confirmed this dynamic behavior. The swelling studies also revealed an increasing mesh size, which was anticipated by the growing water uptake from **HG_1** to **HG_6**. Subsequent rheology measurements of **HG_3** and **HG_6** were conducted to gain insight into the storage (G') and loss (G'') moduli. These measurements confirmed the increasing mesh size trend that was observed during the swelling experiments. Rheology also indicated that the investigated hydrogels (**HG_3** and **HG_6**) exhibit an unusually high thermal stability. While this method could not validate self-healing behavior, the measurements suggested that it might be achievable; nonetheless, more studies are required to definitively verify this property. Small angle X-ray scattering analysis of the hydrogels revealed that these gels have comparable structural behavior. Furthermore, it was shown that the mesh size increases from **HG_1** to **HG_6**, which is consistent with both the rheological measurements and the swelling studies.

Subsequent guest encapsulation studies were performed for all supramolecular self-assembled hydrogels, showing similar behavior as the supramolecular cages (**MOC_1** and **$polyMOC_{60-120}$**) from section 3.1.4. Progesterone, drospirenone, and ibuprofen were effectively encapsulated in **HG_3**, and ibuprofen was successfully incorporated into all hydrogels (**HG_{1-6}**) to demonstrate its applicability. The guest uptake of the used hydrogels was significantly improved in contrast to the previously synthesized mechanoresponsive cages, **$polyMOC_{60-120}$**. It was observed that the cargo-load-ratio in relation to the polymer backbone was increased from 0.7 % (**$polyMOC_{120}$**) to 6.2 % (**HG_1**).

Initial mechanochemical studies by utilizing a carving press were unsuccessful. Instead, exposing the hydrogels to ultrasound resulted in cage rupture, which was confirmed by ^{1}H NMR. Analyzing the hydrogels revealed that the process of bond scissioning is of mechanochemical nature and not a result of temperature fluctuations. This was proven by the increased tendency for cage rupture in polymers with a larger molecular weight. It was also demonstrated that no chain scissioning occurred below a specific chain length value (**HG_1**). Swelling experiments before and after sonication revealed that the

network structure decomposes throughout the experiment, preventing hydrogel formation after being subjected to ultrasonic irradiation. The whole potential of the supramolecular self-assembled hydrogel **HG$_6$** was demonstrated by encapsulating different guests and releasing them on demand.

.

4 Conclusion

This doctoral thesis described the synthesis and exploration of novel mechanoresponsive systems for drug delivery and targeted guest release. The here presented supramolecular star-shaped coordination cages were the first reported examples of their kind, which were responsive to ultrasound induced bond rupture in solution. In this work, three Pd-based linkers, three supramolecular star-shaped cages, and three novel metal organic cage-based hydrogels were successfully synthesized and characterized. Four of these systems proofed to be susceptible to ultrasound irradiation and were utilized for a guest release.

An initial modification of the octahedral self-assembled M_6L_4 cage, published by Makoto Fujita, was carried out in order to examine the effects of such alterations on the host/guest characteristics. The received supramolecular cage **MOC$_1$** contained modified peripherical ligands but retained similar properties in terms of its encapsulation potential to the M_6L_4. Based on these results, the two polymer star-shaped metal organic cages, **polyMOC$_{60}$** and **polyMOC$_{120}$**, were successfully synthesized.

Subsequent encapsulation experiments offered an insight into the host/guest properties and revealed the potential of **MOC$_1$**. Of the twelve compounds that were effectively incorporated into the host, ibuprofen and different steroids turned out to be the ones that were most suited for guest encapsulation. In an attempt to "visualize" the encapsulation and release process, phenolphthalein was employed. The encapsulation of this guest was confirmed by NMR spectroscopy and UV/Vis experiments, but ultimately resulted in the decomposition of **MOC$_1$** due to the basic conditions. These results were utilized in order to successfully conduct guest uptake experiments for the larger star-shaped metal organic cages, **polyMOC$_{60}$** and **polyMOC$_{120}$**.

The next step was to initiate the cage disassembly by subjecting the **polyMOCs** to ultrasonic irradiation, which resulted in effective mechanochemical activation, as proven by ^{1}H NMR spectroscopy. Control experiments with **MOC$_1$** provided unambiguous confirmation that ultrasound-induced bond scissioning is of mechanochemical nature and also correlates with the molecular weight of the supramolecular cage. The targeted guest release showed the full potential of the cages once it was proven that the **polyMOCs** are responsive to ultrasonic irradiation. During the sonication experiments with progesterone and ibuprofen, a complete release from their host moiety was observed. During the analysis, it was observed that the release of progesterone is unambiguous, whereas the release of ibuprofen is not. However, due to the significant downfield shift in the NMR, a release was highly likely.

An investigation of three isostructural metal complexes (**CMP**, **MP$_{15}$,** and **MP$_{20}$**) offered further insight into the mechanism of the sonochemical fragmentation. Although initial GPC and MALDI MS

experiments were inconclusive, complex formation was eventually confirmed by ^{1}H NMR and heteronuclear 2D measurements. The received data from the sonication experiments suggested that for the simplified mechanophore systems, a reversible dissociation process occurred, which might be similar to the proposed mechanism published by Sijbesma *et al.* First results suggested that the fragmentation of **polyMOC$_{60}$** results in the formation of mechanophore **MP$_{20}$**. Hence, explaining why no reassembly of the star-shaped cages (**polyMOC$_{60}$** and **polyMOC$_{120}$**) was observed after the sonication experiments.

CoGEF computational simulations based on the FMPES approach showed that during bond scissioning *cis*-pulling was preferred, which was explained by an increasing distortion angle of the N-Pd-N moiety. To achieve the dissociation of a pyridine ligand, a force of approximately 0.5 nN was needed.

Lastly, three new cross-linkers based on the bipyridine motif of chapter 3.1 were introduced and employed for hydrogel self-assembly of **HG$_{1}$**, **HG$_{3}$**, and **HG$_{6}$**. These hydrogels varied in size and weight percentage, which affected their structural characteristics significantly. Initial swelling experiments indicated a dynamic behavior for the hydrogels as well as an increasing mesh size trend from **HG$_{1}$** to **HG$_{6}$**. To get further insight into the properties of the hydrogel's rheology measurements were performed and confirmed these results. Furthermore, the used metal organic cage-based gels demonstrated unusually high thermal stability in comparison to other hydrogels. Unfortunately, the rheology data did not confirm self-healing behavior and therefore remains a target for further research.

Subsequent guest encapsulation studies were performed based on the results from section 3.1.3. The supramolecular hydrogels obtained identical cavity properties as the cages **polyMOC$_{60\text{-}120}$**. Therefore, ibuprofen, progesterone, and drospirenone were successfully encapsulated in the self-assembled hydrogels. In contrast to the star-shaped supramolecular cages **polyMOC$_{60}$** and **polyMOC$_{120}$**, a significant increase in potential guest uptake was demonstrated.

Both **HG$_{3}$** and **HG$_{6}$** were susceptible to ultrasonic irradiation, which eventually led to bond scissioning and a disintegration of the gel network. In contrast to these results, activation of **HG$_{1}$** was not achieved, which was explained by the fact that chain scissioning stops once the polymer chain length reaches a lower limiting value. Furthermore, after the hydrogel was exposed to ultrasound irradiation, degradation of the gel network occurred and no reassembly could be achieved.

Finally, through the addition of an external reference the guest release of ibuprofen was unequivocally proven.

Drug uptake and subsequent release are still challenging tasks. Often, a chemical modification of the desired molecule is needed for the encapsulation, or the used systems rely on strong host-guest

interactions. As a result, several mechanoresponsive supramolecular structures were synthesized throughout this work, resulting in a novel strategy for drug delivery. By enabling unmodified guest uptake on demand, these systems proved their efficacy and provided a solid foundation for further studies.

5 Experimental part

5.1 General methods

Chemicals and solvents were purchased from Sigma-Aldrich, VWR/Merck, Tokyo Chemical Industry and were used without further purification. HPLC grade acetonitrile was used as received. Dichloromethane, tetrahydrofuran and dioxane were obtained from a solvent purification system from MBraun (SPS-800). Reactions were monitored by thin layer chromatography (TLC), using silica gel plates from Macherey Nagel (ALUGRAM® Xtra SIL G/UV254). Column chromatography was done with silica gel from Macherey Nagel (Silica 60 M, 0.04-0.063 mm). The eluents are stated individually for each reaction. If stated that the silica gel was deactivated, 1-2 % of NEt_3 was added to the eluent and the column was flushed three times. If not stated otherwise, solvents were removed under reduced pressure by using a rotary evaporator at 50 °C.

Reactions which had to be done under complete exclusion of water were prepared by drying the laboratory glassware and the stirring bar at 80 °C for several hours. Reactions were run using Schlenk techniques for working under an inert atmosphere of nitrogen or argon.

5.2 Instrumentation and procedures

NMR measurements

The measurements of ^{1}H NMR-, ^{13}C{^{1}H}-NMR-spectra, DOSY and 2D-spectra were recorded on a Bruker Avance III – 300 (^{1}H NMR: 300 MHz, ^{13}C{^{1}H}-NMR: 75 MHz) and Bruker Avance III – 600 (^{1}H NMR: 600 MHz, ^{13}C{^{1}H}-NMR: 150 MHz) NMR-spectrometers. ^{13}C{^{1}H}-NMR of the encapsulation complexes were measured on a Bruker Avance III equipped with a BBO H&F cryoprobe at the Max Planck Institute for Coal Research located in Mülheim an der Ruhr, Germany. All samples were dissolved in deuterated solvents.

DOSY NMR

For the estimation of the hydrodynamic radii, the unmodified Stokes-Einstein-equation was used.[121]

$$D = \frac{k_B T}{6\pi\eta r_H}$$

D is the measured diffusion coefficient (m^2s^{-1})

k_B is the Boltzmann constant ($1.3806485 \cdot 10^{-23}$ $m^2kg\ s^{-2}\ K^{-1}$)

T is the temperature (K)

r_H is the hydrodynamic radius of the analyte (m)

η is the viscosity of the solvent at temperature T ($kg\ m^{-1}\ s^{-1}$)

IR

Infrared spectra were measured with a FT/IR-6200 of the company JASCO and FT/IR IRAffinity-1 with ATR attachment of the company Shimadzu.

Mass spectrometry

Mass spectrometry was performed by using a UHR-QTOF maXis 4G spectrometer of the company Bruker Daltonics for high-resolution accurate mass spectrometer or by using a UltrafleXtreme from Bruker Daltonics for MALDI mass spectrometry.

Melting points

Melting points were determined with a melting point apparatus (B-540) of the company BÜCHI Labortechnik GmbH.

Centrifuge

Samples were centrifuged with a laboratory centrifuge (Allegra^{TM} 25R Centrifuge) by Beckman Coulter. The time, rpm, and temperature are stated for every experiment individually.

Freeze-dryer

For the removal of water, a laboratory freeze-dryer (Alpha 1-2) from the company Christ was used. All samples were freeze-dried overnight.

Gel permeation chromatography (GPC)

GPC (SEC) with $CHCl_3$ (≥99.8%, stabilized with 2-methyl-2-buten, HiPerSolv CHROMANORM® HPLC grade, VWR) as eluent was performed using a HPLC pump (PU-2080plus, Jasco) equipped with a refractive index detector (RI-2031plus, Jasco). The sample solvent contained 250 mg·mL^{-1} 3,5-di-*t*-4-butylhydroxytoluene (BHT, ≥99%, Fluka) as internal standard. One pre-column (8×50 mm) and four SDplus gel columns (8×300 mm, SDplus, MZ Analysentechnik) were applied at a flow rate of 1.0 mL·min^{-1} at 20 °C. The diameter of the gel particles was 5 µm, the nominal pore widths were 50, 10^2, 10^3, and 10^4 Å. Calibration was achieved using narrowly distributed poly(methyl methacrylate) standards (Polymer Standards Service). Molar masses (M_n and M_w) and molar mass distributions (M_w/M_n) were calculated by using the PSS WinGPC UniChrom software (Version 8.1.1).

Small-angle X-ray scattering (SAXS)

SAXS measurements were performed on a Xeuss 2.0 (Xenocs). The instrument was equipped with a Cu K_α X-ray source (λ = 0.154 nm) and a Pilatus3 300k (Dectris) detector. The sample-to-detector distance was varied between 1200 mm and 270 mm. The exposure time for each measurement was 3600 s. The samples were prepared in Kapton® sealed cells with a thickness of 1 mm. An empty cell was also measured for the background subtraction. Foxtrot (v.3.4.9 Xenoxs/Soleil) was used for the radial averaging, background subtraction and merging of the data. The data was fitted with SASfit (v 0.94.11, Paul Scherrer Institute).[122]

Scanning electron microscope (SEM)

The sample was initially freeze-dried overnight and then sputtered with gold in a JEOL JFC-1200 Fine Coater before it was measured with a JEOL JSM-6510.

5.3 Experimental details for section 3.1

Building blocks

Synthesis of 2,4,6-tris(4-pyridyl)-1,3,5-triazine (TPT)

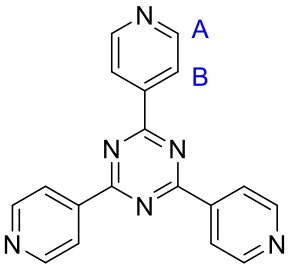

This synthesis was done in accordance to the literature procedure published by Fujita *et al*.[100]

4-Cyanopyridine (**28**) (10 g, 100 mmol, 1.0 eq.) was stirred at 160 °C. Powdered NaOH (0.40 g, 10 mmol, 0.10 eq.) was added and the reaction was stirred overnight for 18 h. The reaction was cooled to RT, washed with acetone, and dried. The resulting solid was dissolved in 2 M HCl (80 mL) and precipitated with a 5 M NaOH-solution (80 mL). The colorless solid was filtered, washed with H_2O and acetone, dried in a high vacuum oven at 80 °C yielding the product as an off-white solid (4.5 g, 45 %). If necessary, the product was sublimated (230 °C, 1 x 10^{-3} mbar).

^{1}H NMR (300 MHz, $CDCl_3$): δ = 8.97 (d, *J* = 5.8 Hz, 6H, **A**), 8.62 (s, 6H, **B**).

Synthesis of 4-hydroxymethyl-4'-methyl-2,2'-bipyridine (17)

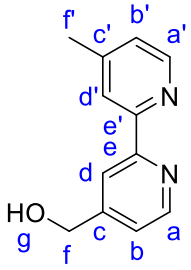

This synthesis was done in accordance to the literature procedure published by Studer *et al*.[98]

4,4'-Dimethyl-2,2'-bipyridine (**16**) (5.0 g, 27 mmol, 1.0 eq.) was dissolved in 1,4-dioxane (180 mL) and SeO_2 (3.3 g, 30 mmol, 1.1 eq.) was added. This suspension was degassed with argon for 30 min. and then refluxed for 3 d. After the reaction was cooled to room temperature, the black solid was filtered off and washed several times with chloroform, giving a yellow solution. The solvent was removed under reduced pressure and the resulting pink solid was suspended in MeOH (40 mL). $NaBH_4$ (1.1 g, 30 mmol, 1.1 eq.) dissolved in NaOH (2.0 M, 6.8 mL, 14 mmol) was added to the suspension at 0 °C. The mixture was stirred for 1 h at RT. The resulting solution was set to pH = 1 with aqueous HCl and

stirred for an additional 30 min. The red suspension was adjusted to pH = 9 with a saturated Na_2CO_3-solution and extracted with DCM (3 x 100 mL). The combined organic phases were dried over $MgSO_4$ and the solvent was removed under reduced pressure. The crude product was purified by a deactivated silica gel chromatography with cyclohexane/ethyl acetate (9/1, later 1/1), yielding **17** as a colorless solid (2.6 g, 48 %).

^{1}H NMR (300 MHz, $CDCl_3$): δ 8.60 (d, *J* = 5.0 Hz, 1H, **a**), 8.51 (d, *J* = 5.0 Hz, 1H, **a´**), 8.33 (s, 1H, **d**), 8.20 (s, 1H, **d´**), 7.30 (d, *J* = 5.0 Hz, 1H, **b**), 7.14 (d, *J* = 5.1 Hz, 1H, **b´**), 4.78 (s, 2H, **f**), 3.10 (s, 1H, **g**), 2.43 (s, 3H, **f´**).

Synthesis of 4-bromomethyl-4'-methyl-2,2'-bipyridine (18)

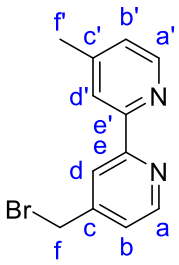

This synthesis was done in accordance to the literature procedure published by Studer *et al*.[98]

4-Hydroxymethyl-4'-methyl-2,2'-bipyridine (**17**) (2.0 g, 10 mmol, 1.0 eq.) was dissolved in HBr/H_2O (48 wt%, 100 mL). H_2SO_4 (4 mL) was added, and the reaction mixture was heated to 120 °C for 3 d. Water (25 mL) was added and the reaction was basified with Na_2CO_3 to pH = 8. The aqueous solution was extracted with DCM (8 x 50 mL) until the organic layer was colourless, dried over Na_2SO_4 and filtered. The solvent was removed under reduced pressure at 30 °C. The crude product was purified by silica gel chromatography with dichloromethane/acetone (1/1) yielding **18** as a colourless solid (1.7 g, 64 %) (again the solvent was removed under reduced pressure at 30 °C).

^{1}H NMR (300 MHz, $CDCl_3$): δ 8.59 (d, *J* = 5.0 Hz, 1H, **a**), 8.48 (d, *J* = 5.0 Hz, 1H, **a´**), 8.36 (s, 1H, **d**), 8.18 (s, 1H, **d´**), 7.28 (dd, *J* = 5.0, 1.8 Hz, 1H, **b**), 7.10 (d, *J* = 5.0 Hz, 1H, **b´**), 4.41 (s, 2H, **f**), 2.38 (s, 3H, **f´**).

*Synthesis of cage **MOC₁***

Synthesis of 4-ethoxymethyl-4'-methyl-2,2'-bipyridine (**19**)

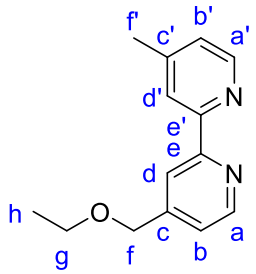

4-Bromomethyl-4'-methyl-2,2'-bipyridine (**18**) (0.55 g, 2.1 mmol, 1.0 eq.) was dissolved in EtOH (10 mL) a solution of NaH (60 wt% in mineral oil, 0.20 g, 5.1 mmol, 2.4 eq.) in EtOH (15 mL) was added in small portions. The resulting solution was stirred for 15 h until the starting material was fully converted, after that H_2O (15 mL) was added. The aqueous solution was extracted with EE (8 x 15 mL) until the organic layer was colourless and the combined organic layers were dried over anhydrous Na_2SO_4. The solution was filtered, and the solvent was removed under reduced pressure. The obtained brown oil was purified by silica gel column chromatography with DCM/MeOH (97/3) to yield **19** (0.45 g, 95 %) as a pale-yellow oil.

^{1}H NMR (600 MHz, $CDCl_3$): δ 8.61 (d, *J* = 4.9 Hz, 1H, **a**), 8.51 (d, *J* = 4.9 Hz, 1H, **a´**), 8.30 (s, 1H, **d**), 8.21 (s, 1H, **d´**), 7.32 (d, *J* = 4.6 Hz, 1H, **b**), 7.10 (d, *J* = 4.7 Hz, 1H, **b´**), 4.57 (s, 2H, **f**), 3.57 (q, *J* = 7.0 Hz, 2H, **g**), 2.41 (s, 3H, **f´**), 1.26 (t, *J* = 7.0 Hz, 3H, **h**); **^{13}C{^{1}H} NMR** (151 MHz, $CDCl_3$): δ 156.33 (**e**), 155.90 (**e´**), 149.34 (**c**), 149.05 (**c´**), 149.02 (**a**), 148.25 (**a´**), 124.82 (**b´**), 122.11 (**b**), 121.92 (**d´**), 119.47 (**d**), 71.27 (**f**), 66.49 (**g**), 21.26 (**f´**), 15.26 (**h**). **IR** (cm^{-1}): 3053.32 (w), 2974.23 (w), 2866.22 (b), 1597.06 (s), 1556.55 (m), 1456.26 (m), 1379.10 (m), 1109.07 (s,b), 991.41 (m), 821.68 (s); **HRMS** (ESI): m/z calc. 228.1263; found 229.1340 $[M+H]^+$.

Synthesis of (4-ethoxymethyl-4'-methyl-2,2'-bipyridine)-dichloropalladium(II) (**20**)

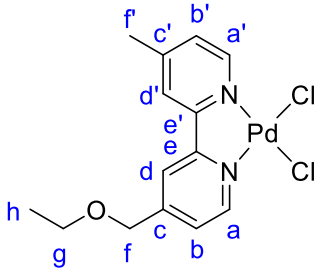

4-Ethoxymethyl-4'-methyl-2,2'-bipyridine (**19**) (0.76 g, 3.3 mmol, 1.0 eq.) was dissolved in MeCN (22 mL) and $PdCl_2$ (0.59 g, 3.3 mmol, 1.0 eq.) was added, resulting in a brown suspension which was heated at 70 °C for 15 h until the suspension turned yellow. The suspension was allowed to cool to

room temperature. The solid was filtered off and washed with cold H_2O (3 x 3 mL), cold acetone (6 × 3 mL) and dried *in vacuo* at 40 °C for 3 h yielding **20** as a yellow solid (1.1 g, 83 %).

^{1}H NMR (600 MHz, DMSO-d_6): δ 9.03 (d, *J* = 5.9 Hz, 1H, **a**), 8.92 (d, *J* = 5.9 Hz, 1H, **a´**), 8.47 (s, 1H, **d**), 8.43 (s, 1H, **d'**), 7.78 – 7.70 (m, 1H, **b**), 7.67 – 7.58 (m, 1H, **b´**), 4.70 (s, 2H, **f**), 3.61 (q, *J* = 7.0 Hz, 2H, **g**), 2.53 (s, 3H, **f´**), 1.23 (t, *J* = 7.0 Hz, 3H, **h**); **^{13}C{^{1}H} NMR** (126 MHz, DMSO-d_6): δ 156.03 (**e**), 155.55 (**e´**), 153.75 (**c**), 153.28 (**c´**), 149.35 (**a**), 148.75 (**a´**), 127.63 (**b´**), 124.44 (**d´**), 124.36 (**b**), 121.11 (**d**), 69.26 (**f**), 65.88 (**g**), 20.79 (**f´**), 14.84 (**h**); **IR** (cm^{-1}): 3115.04 (w), 3064.89 (w), 2927.94 (w), 1614.42 (m), 1419.61 (m), 1347.89 (w), 1303.88 (w), 1244.09 (w), 1163.08 (w), 1091.71 (s), 866.04 (s), 829.39 (s), 746.45 (w), 644.22 (w); **Elemental analysis:** calc. for $C_{14}H_{16}Cl_2N_2OPd$ %C: 41.46, %H: 3.98, %N: 6.91; found %C: 41.64, %H: 3.90, %N: 6.95; **Mp.**: 243.7-245.3 °C.

Synthesis of (4-ethoxymethyl-4'-methyl-2,2'-bipyridine)-dinitratopalladium(II) (21)

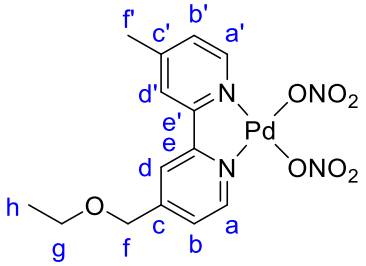

Nitrate complex **20** was prepared by adding $AgNO_3$ (0.43 g, 2.5 mmol, 2.0 eq.) to a suspension of (4-ethoxymethyl-4'-methyl-2,2'-bipyridine)-dichloropalladium(II) (**7**) (0.51 g, 1.3 mmol, 1.0 eq.) in MeCN (45 mL). The round-bottomed flask was wrapped in aluminium foil and the suspension was stirred for 17 h in the dark. The precipitated AgCl was removed by centrifugation (4400 rpm, 20 min), the resulting yellow supernatant was transferred into a round bottom flask and the solvent was removed by rotary evaporation to yield **21** as a yellow solid (0.53 g, 92 %).

^{1}H NMR (600 MHz, DMSO-d_6): δ 8.48 (s, 1H, **d**), 8.41 (s, 1H, **d´**), 8.13 (d, *J* = 6.0 Hz, 1H, **a**), 8.01 (d, *J* = 6.0 Hz, 1H, **a´**), 7.71 (d, *J* = 6.0, 1H, **b**), 7.63 (d, *J* = 6.3, 1H, **b´**), 4.72 (s, 2H, **f**), 3.61 (q, *J* = 7.0 Hz, 2H, **g**), 2.55 (s, 3H, **f´**), 1.23 (t, *J* = 7.0 Hz, 3H, **h**); **^{13}C{^{1}H} NMR** (151 MHz, DMSO-d_6): δ 155.80 (**e**), 155.54 (**c**), 155.29 (**e´**), 155.17 (**c´**), 148.61 (**a**), 148.00 (**a´**), 128.33 (**b**), 125.04 (**d**), 124.97 (**b´**), 121.55 (**d´**), 69.23 (**f**), 66.10 (**g**), 21.06 (**f´**), 15.01 (**h**). **IR** (cm^{-1}): 3122.75 (w), 2968.45 (w), 2926.01 (w), 2767.85 (w), 1614.42 (m), 1494.83 (s, b), 1257.59 (s, b), 1122.57 (m), 972.12 (s), 898.83 (m), 833.25 (m); **Elemental analysis:** calc. for $C_{14}H_{16}N_4O_7Pd$ %C: 36.66, %H: 3.52, %N: 12.21; found %C: 36.44, %H: 3.28, %N: 12.06; **Mp.**: 248.2-249.4 °C.

Synthesis of cage MOC_1

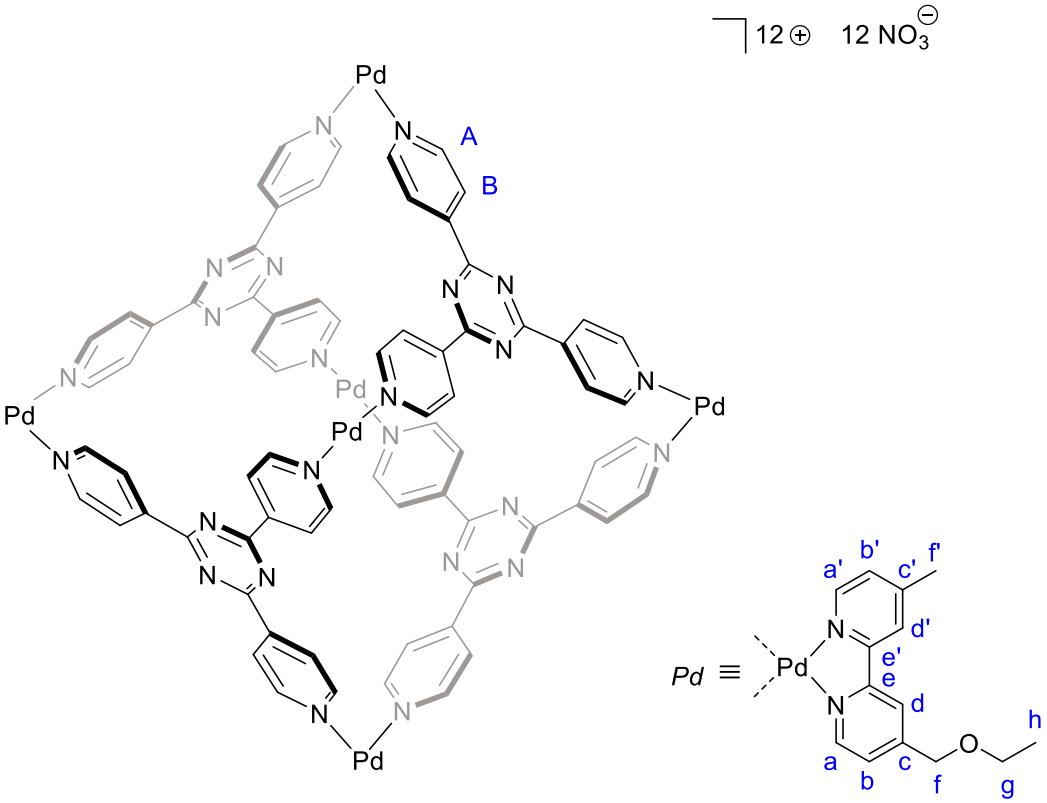

A suspension of (4-ethoxymethyl-4'-methyl-2,2'-bipyridine)-dinitratopalladium(II) (**21**) (0.30 g, 0.66 mmol, 1.0 eq.) and **TPT** (0.14 g, 0.44 mmol, 0.67 eq.) in H_2O (22 mL) was stirred at 80 °C for 2 h. Trace amounts of insoluble materials were removed by filtration using a syringe filter. The obtained clear yellow solution was evaporated under reduced pressure to give cage **MOC_1** (0.40 g, 10 mmol, 92 %) as a pale-yellow solid.

^{1}H NMR (600 MHz, D_2O): δ 9.48 (d, *J* = 6.2 Hz, 24H, **A**), 8.92 (d, *J* = 6.2 Hz, 24H, **B**), 8.42 (s, 6H, **d**), 8.36 (s, 6H, **d´**), 7.66 (d, *J* = 6.0 Hz, 6H, **a**), 7.57 (d, *J* = 6.0 Hz, 6H, **b**), 7.53 (d, *J* = 6.0 Hz, 6H, **a´**), 7.45 (d, *J* = 6.1 Hz, 6H, **b´**), 4.86 (s, 12H, **f**), 3.75 (q, *J* = 7.1 Hz, 12H, **g**), 2.63 (s, 18H, **f´**), 1.30 (t, *J* = 7.1 Hz, 18H, **h**); **^{13}C{^{1}H} NMR** (126 MHz, D_2O): δ 169.84 (**D**), 157.03 (**e´**), 156.67 (**c´**), 156.06 (**e**), 155.63 (**c**), 152.52 (**A**), 150.09 (**a**), 149.45 (**a´**), 146.43 (**C**), 128.98 (**b´**), 126.74 (**B**), 125.79 (**b**), 125.35 (**d´**), 122.08 (**d**), 69.90 (**f**), 67.50 (**g**), 21.17 (**f´**), 14.44 (**h**); **DOSY**: D= $2.16 \cdot 10^{-10}$ m^2/s **IR** (cm^{-1}): 3093.82 (w), 3427.51 (w), 3028.24 (w), 2821.86 (w), 2358.94 (w), 1622.13 (m), 1506.41 (s), 1317.38 (s,b), 1111.00 (m), 974.05 (w), 810.10 (s); **Mp.**: 298.9-301.2 °C (dec.).

Synthesis of cage ***polyMOC$_{60}$***

Synthesis of 4-methoxypolyethyleneglycolmethyl-4'-methyl-2,2'-bipyridine (**22**)

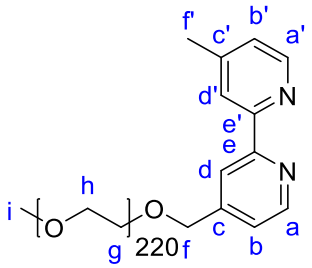

Poly(ethylene glycol) methyl ether (M_n = 10.000 Da, 5.0 g, 0.50 mmol, 1.0 eq.) was degassed with N_2 and dissolved in DCM (40 mL). The colorless solution was cooled to 0 °C. NaH (80 mg, 1.0 mmol, 4.0 eq.) was added and the reaction mixture was stirred for 1 h. 4-Bromomethyl-4'-methyl-2,2'-bipyridine (**18**) (0.14 g, 0.53 mmol, 1.1 eq.) was added and the mixture was stirred for 3 d at 0 °C before the reaction was quenched with a saturated NH_4Cl-solution (2 mL). The reaction was stirred for an additional hour and then filtered. Water (50 mL) and a saturated NH_4Cl-solution (5 mL) were added, and the aqueous phase was extracted with DCM (3 x 50 mL). The combined organic phases were dried over $MgSO_4$, filtered and the solvent was removed under reduced pressure. The crude product was dialyzed against deionized water for 4 d (MWCO: 1 kDa). After the solvent was removed the colorless solid was dissolved in hot DCM and precipitated in cold diethyl ether. After filtration **22** was obtained as a colorless solid (4.1 g, 81 %).

^{1}H NMR (600 MHz, $CDCl_3$): δ 8.62 (d, *J* = 5.1 Hz, 1H, **a**), 8.52 (d, *J* = 5.1 Hz, 1H, **a'**), 8.37 (s, 1H, **d**), 8.28 (s, 1H, **d'**), 7.39 (s, 1H, **b**), 7.17 (s, 1H, **b'**), 4.65 (s, 2H, **f**), 3.73 – 3.45 (m, 1072H, **g**, **h**), 3.32 (s, 3H, **i**), 2.44 (s, 3H, **f'**); **IR** (cm^{-1}): 2881.65 (m), 1465.90 (m), 1359.82 (w), 1340.53 (s), 1278.81 (m), 1242.16 (m), 1147.65 (m), 1099.43 (s), 1060.85 (m), 960.55 (m), 840.96 (m). **Mp.**: 60-65 °C.

Synthesis of (4-methoxypolyethyleneglycolmethyl-4'-methyl-2,2'-bipyridine)-dichloropalladium(II) (**23**)

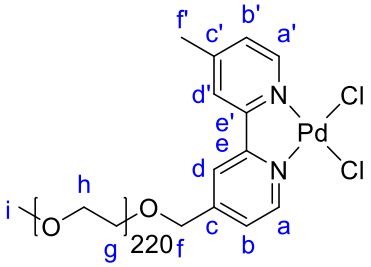

4-Methoxypolyethyleneglycolmethyl-4'-methyl-2,2'-bipyridine (**22**) (3.8 g, 0.37 mmol, 1.0 eq.) and $PdCl_2$ (66 mg, 0.37 mmol, 1.0 eq.) were suspended in MeCN (45 mL) and heated to 60 °C. After 19 h

the yellow solution was cooled to RT, filtered and the solvent was removed under reduced pressure yielding the product as a yellow solid (3.8 g, 99 %).

^{1}H NMR (600 MHz, $CDCl_3$): δ 9.01 (d, *J* = 5.8 Hz, 1H, **a**), 8.93 (d, *J* = 5.8 Hz, 1H, **a'**), 8.12 (s, 1H, **d**), 7.97 (s, 1H, **d'**), 7.39 (d, *J* = 5.9 Hz, 1H, **b**), 7.24 (d, *J* = 6.0 Hz, 1H, **b'**), 4.76 (s, 2H, **f**), 3.59 (s, 911H, **g**, **h**), 3.32 (s, 3H, **i**), 2.55 (s, 3H, **f'**); **IR** (cm^{-1}): 2881.65 (m), 2360.87 (w), 1465.90 (m), 1359.82 (w), 1340.53 (s), 1278.81 (m), 1240.23 (m), 1147.65 (m), 1097.50 (s), 1060.85 (m), 960.55 (m), 840.96 (m); **Mp.**: 60-65 °C.

Synthesis of (4-methoxypolyethyleneglycolmethyl-4'-methyl-2,2'-bipyridine)-dinitratopalladium(II) (**24**)

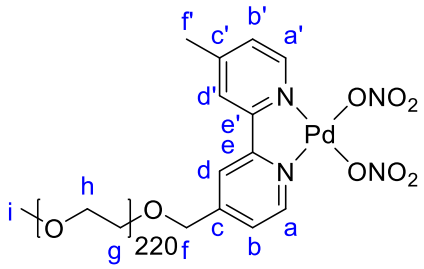

(4-methoxypolyethyleneglycolmethyl-4'-methyl-2,2'-bipyridine)-dichloro-palladium (**23**) (4.1 g, 0.40 mmol, 1.0 eq.) was dissolved in MeCN (50 mL) and $AgNO_3$ (0.15 g, 0.88 mmol, 2.2 eq.) was added, resulting in a colour change from yellow to a pale yellow. The conversion was tracked with 1 mL NMR-samples. After 19 h a full conversion of the starting material was observed and the AgCl was removed by centrifugation (4400 rpm, 1 h). The resulting yellow supernatant was transferred into a round bottom flask and the solvent was removed by rotary evaporation at 30 °C in the dark to yield a yellow solid. This solid was dissolved in DCM, precipitated from cold diethyl ether, filtered, and dried to yield **24** as a yellow solid (3.8 g, 93 %).

^{1}H NMR (600 MHz, $CDCl_3$): δ 8.22 (s, 1H, **d**), 8.11 (d, *J* = 5.9 Hz, 1H, **a**), 8.09 (s, 1H, **d'**), 8.02 (d, *J* = 5.9 Hz, 1H, **a'**), 7.55 (d, *J* = 6.0 Hz, 1H, **b**), 7.36 (d, *J* = 6.0, 1.7 Hz, 1H, **b'**), 4.79 (s, 2H, **f**), 3.57 (m, 985H, **g**, **h**), 3.30 (s, 3H, **i**), 2.56 (s, 3H, **f**); **IR** (cm^{-1}): 2881.65 (m), 1465.90 (m), 1359.82 (w), 1340.53 (s), 1278.81 (m), 1240.23 (m), 1147.65 (m), 1097.50 (s), 1060.85 (m), 960.55 (m), 840.96 (m); **Mp.**: 60-65 °C.

Synthesis of cage **polyMOC$_{60}$**

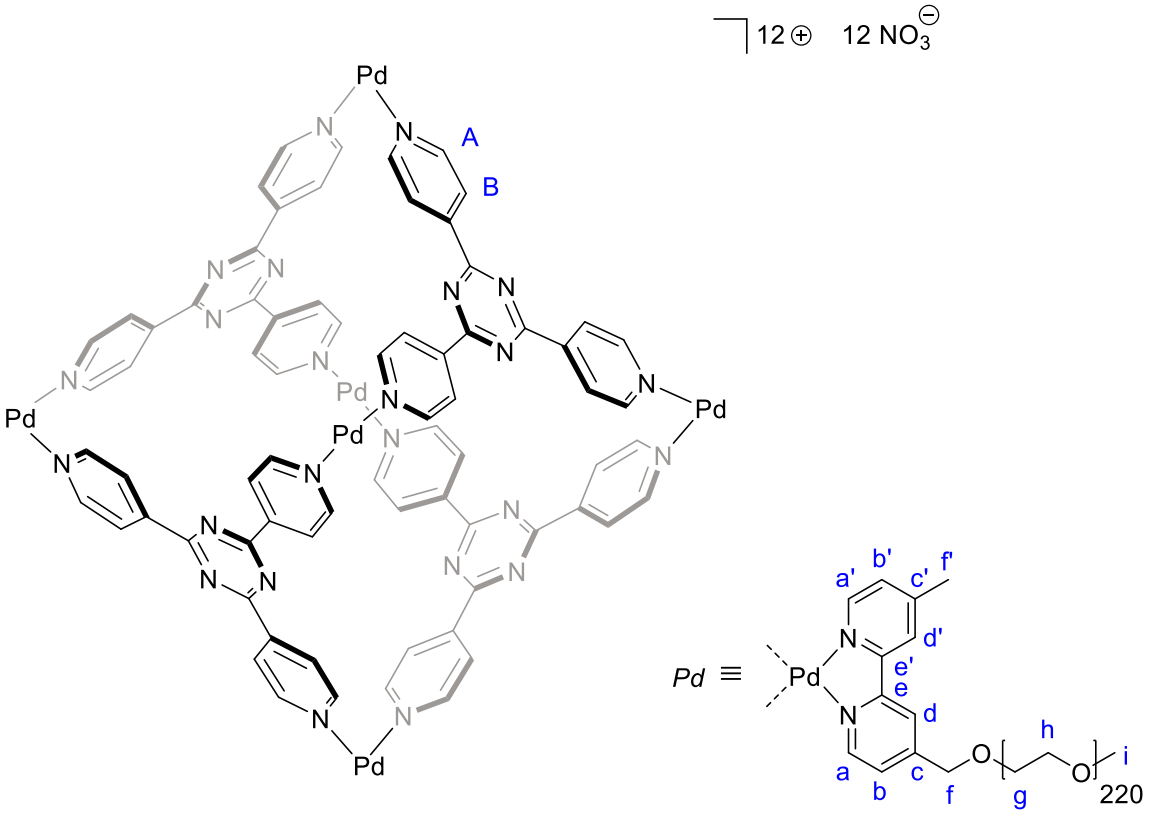

(4-methoxypolyethyleneglycolmethyl-4'-methyl-2,2'-bipyridine)-dinitrato palladium (**24**) (0.33 g, 0.032 mmol, 1.0 eq.) and 2,4,6-tris(4-pyridyl)-1,3,5-triazine (**TPT**) (9.6 mg, 0.021 mmol, 0.67 eq.) were suspended in H_2O (0.80 mL). The reaction was stirred at 80 °C for 1 d, cooled to RT, filtered and the solvent was removed under reduced pressure. The crude product was dissolved in DCM and precipitated in cold diethyl ether yielded **polyMOC$_{60}$** as a pale-yellow solid (0.29 g, 86 %).

^{1}H NMR (600 MHz, D_2O): δ 9.51 (s, 24H, **A**), 8.96 (s, 24H, **B**), 8.46 (m, 12H, **d**, **d'**), 7.57 (m, 24H, **a**, **a'**, **b**, **b'**), 3.72 (s, 5209H, **g**, **h**), 3.40 (s, 18H, **i**), 2.64 (s, 18H, **f'**); **IR** (cm^{-1}): 2881.65 (m), 1465.90 (m), 1359.82 (w), 1340.53 (s), 1278.81 (m), 1240.23 (m), 1147.65 (m), 1097.50 (s), 1060.85 (m), 960.55 (m), 840.96 (m); **Mp.**: 60-65 °C.

*Synthesis of cage **polyMOC$_{120}$***

Synthesis of 4-methoxypolyethyleneglycolmethyl-4'-methyl-2,2'-bipyridine (**25**)

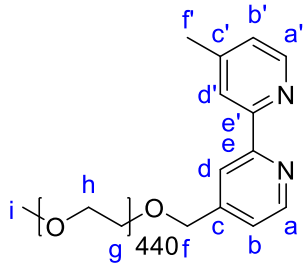

Poly(ethylene glycol) methyl ether (M_n = 20.000 Da, 5.0 g, 0.25 mmol, 1.0 eq.) was degassed with N_2 and dissolved in DCM (55 mL). The colorless solution was cooled to 0 °C. NaH (18 mg, 0.75 mmol, 3.0 eq.) was added and the reaction mixture was stirred for 1 h. 4-Bromomethyl-4'-methyl-2,2'-bipyridine (**18**) (0.072 g, 0.28 mmol, 1.1 eq.) was added and the mixture was stirred for 4 d at 0 °C before another portion of NaH (18 mg, 0.75 mmol, 3.0 eq.) was added. After additional 5 d the reaction was quenched with MeOH (2 mL). The reaction was stirred for 30 min. and then filtered. The crude product was dialyzed against deionized water for 4 d (MWCO: 1 kDa). After the solvent was removed, the colorless solid was dissolved in hot DCM and precipitated from cold diethyl ether. After filtration **25** was obtained as a colorless solid (3.8 g, 76 %).

^{1}H NMR (600 MHz, D_2O): δ 8.60 (d, *J* = 4.9 Hz, 1H, **a**), 8.49 (d, *J* = 4.8 Hz, 1H, **a'**), 8.28 (s, 1H, **d**), 8.19 (s, 1H, **d'**), 7.32 (dd, *J* = 4.9, 1.5 Hz, 1H, **b**), 7.10 (d, *J* = 5.0 Hz, 1H, **b'**), 4.63 (s, 2H, **f**), 3.60 (s, 1444H, **g**, **h**), 3.33 (s, 3H, **i**), 2.40 (s, 3H, **f'**).

Synthesis of (4-methoxypolyethyleneglycolmethyl-4'-methyl-2,2'-bipyridine)-dichloropalladium(II) (**26**)

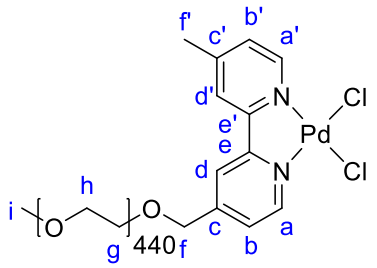

4-Methoxypolyethyleneglycolmethyl-4'-methyl-2,2'-bipyridine (**25**) (2.5 g, 0.12 mmol, 1.0 eq.) and $PdCl_2$ (22 mg, 0.12 mmol, 1.0 eq.) were suspended in MeCN (75 mL) and heated to 60 °C. After 23 h the yellow solution was cooled to RT, filtered and the solvent was removed under reduced pressure yielding **26** as a yellow solid (2.4 g, 95 %).

^{1}H NMR (600 MHz, D_2O): δ 9.06 (d, *J* = 5.9 Hz, 1H, **a**), 8.98 (d, *J* = 5.9 Hz, 1H, **a'**), 8.12 (s, 1H, **d**), 7.97 (s, 1H, **d'**), 7.40 (d, *J* = 6.0 Hz, 1H, **b**), 7.26 (s, 1H, **b'**), 4.75 (s, 2H, **f**), 3.58 (s, 1777H, **g**, **h**), 3.31 (s, 3H, **i**), 2.54 (s, 3H, **f'**).

Synthesis of (4-methoxypolyethyleneglycolmethyl-4'-methyl-2,2'-bipyridine)-dinitratopalladium(II) (**27**)

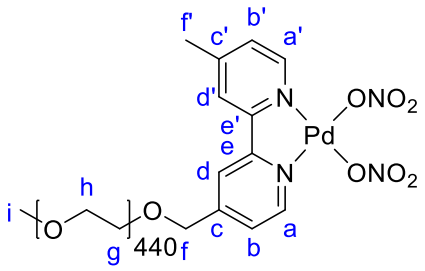

(4-methoxypolyethyleneglycolmethyl-4'-methyl-2,2'-bipyridine)-dichloro-palladium (**26**) (3.4 g, 0.17 mmol, 1.0 eq.) was dissolved in MeCN (55 mL) and $AgNO_3$ (0.1 g, 0.58 mmol, 3.4 eq.) was added, resulting in a colour change from yellow to a pale yellow. The conversion was tracked with 1 mL NMR-samples. After 23 h a full conversion of the starting material was observed and the AgCl was removed by centrifugation (4400 rpm, 90 min.). The resulting yellow supernatant was transferred into a round bottom flask and the solvent was removed by rotary evaporation at 30 °C in the dark to yield a yellow solid. This solid was dissolved in DCM, precipitated in cold diethyl ether, filtered, and dried to yield **27** as a yellow solid (3.1 g, 91 %).

^{1}H NMR (600 MHz, D_2O): δ 8.21 (s, 1H, **d**), 8.15 (d, *J* = 5.9 Hz, 1H, **a**), 8.07 (d, *J* = 5.9 Hz, 1H, **a'**), 8.06 (s, 1H, **d'**), 7.52 (d, *J* = 5.4 Hz, 1H, **b**), 7.37 (d, *J* = 6.1 Hz, 1H, **b'**), 4.76 (s, 2H, **f**), 3.57 (s, 1661H, **g**, **h**), 3.30 (s, 3H, **i**), 2.56 (s, 3H, **f'**).

Synthesis of cage **polyMOC$_{120}$**

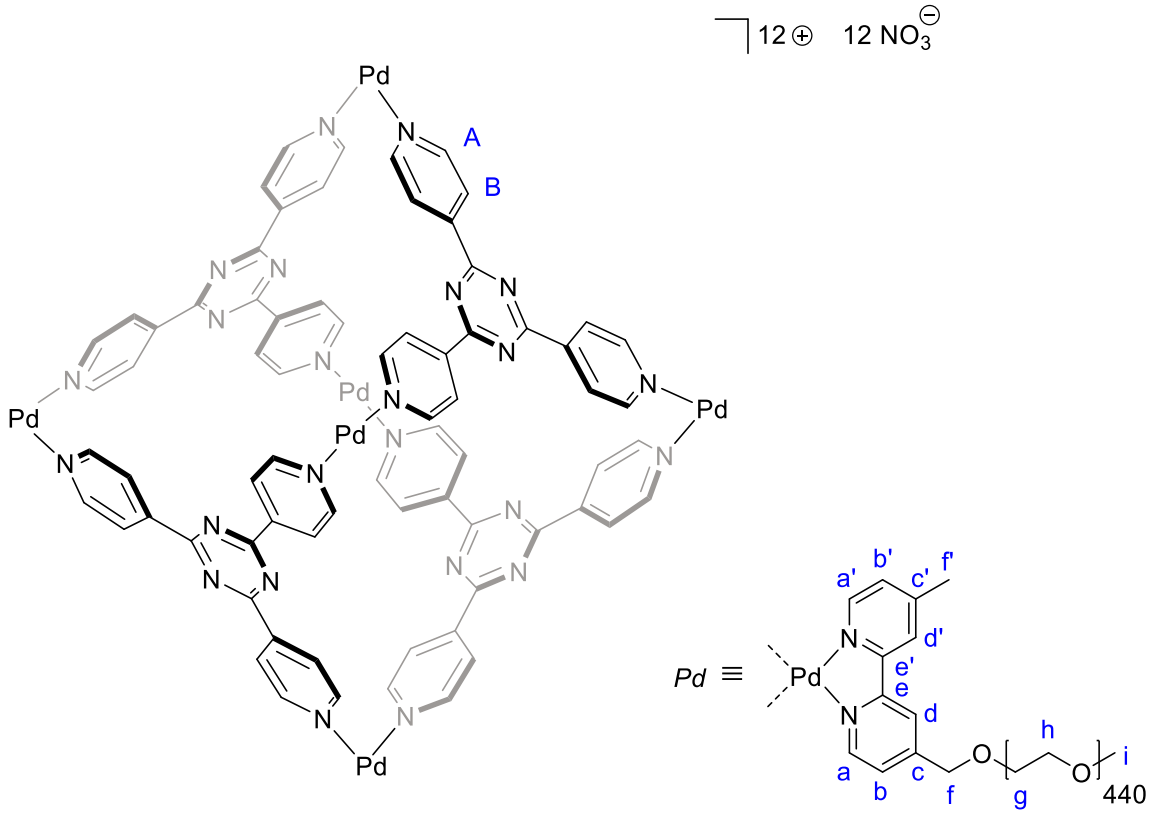

(4-methoxypolyethyleneglycolmethyl-4'-methyl-2,2'-bipyridine)-dinitrato palladium (**27**) (0.38 g, 0.019 mmol, 1.0 eq.) and 2,4,6-tris(4-pyridyl)-1,3,5-triazine (**TPT**) (3.9 mg, 0.013 mmol, 0.67 eq.) were suspended in H_2O (0.80 mL). The reaction was stirred at 80 °C for 1 d, cooled to RT, filtered and the solvent was removed under reduced pressure yielding **polyMOC$_{120}$** as a pale-yellow solid (0.30 g, 78 %).

^{1}H NMR (600 MHz, D_2O): δ 9.52 (s, 24H, **A**), 8.96 (s, 24H, **B**), 8.46 (m, 12H, **d**, **d'**), 7.78 – 7.45 (m, 24H, **a**, **a'**, **b**, **b'**), 3.72 (s, 10549H, **g**, **h**), 3.40 (s, 18H, **i**), 2.64 (s, 18H, **f'**).

*Encapsulations with **MOC$_1$***

For each of the following encapsulation experiments 1 mL of a 5 mM cage solution (in D_2O) of cage **MOC$_1$** was added to 5 eq. of the respective guest molecule. The resulting mixture was stirred at 80 °C for 2 h. After removal of residual guests by filtration, ^{1}H NMR spectra of the solution were measured. The yields of the inclusion complexes were determined by comparison of the integral ratio between host and guest in the ^{1}H NMR spectra.

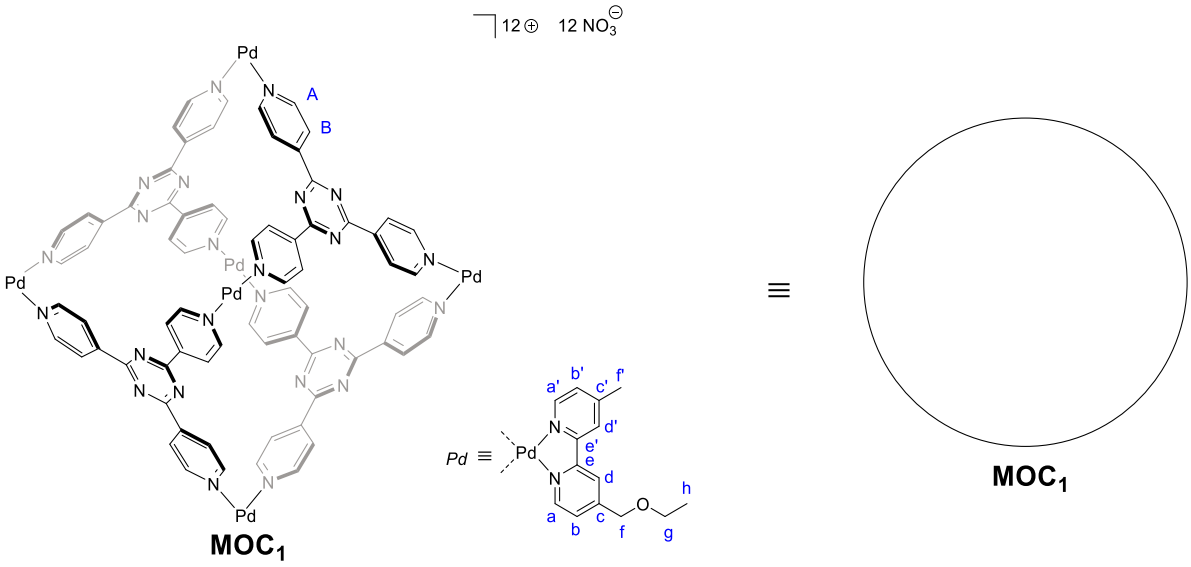

For the following encapsulation experiments cage **MOC₁** will be depicted as shown above plus its corresponding guest.

Encapsulation experiments of Steroids

Cage MOC₁•(progesterone)

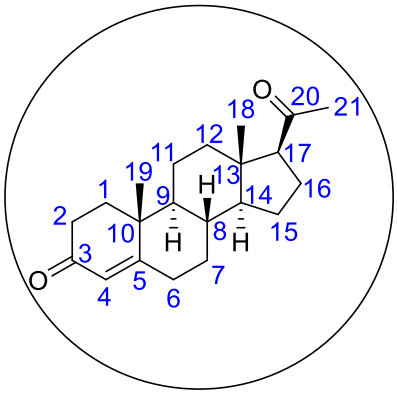

^{1}H NMR (600 MHz, D_2O): δ 9.57 (dd, *J* = 12.3, 6.0 Hz, 24H, **A**), 8.97 (dt, *J* = 6.6, 3.2 Hz, 24H, **B**), 8.43 (s, 6H, **d**), 8.36 (s, 6H, **d´**), 7.72 (d, *J* = 5.9 Hz, 6H, **a**), 7.58 (dd, *J* = 8.0, 6.0 Hz, 12H, **b, a´**), 7.48 – 7.44 (m, 6H, **b´**), 4.86 (s, 12H, **f**), 3.76 (q, *J* = 7.0 Hz, 12H, **g**), 2.99 (s, 1H, **4**), 2.63 (s, 18H, **f'**), 2.24 – 2.13 (m, 4H, **21**), 2.00 (d, *J* = 0.7 Hz, 1H, **17**), 1.67 (s, 1H, cannot be assigned), 1.30 (t, *J* = 7.0 Hz, 19H, **h**, cannot be assigned unambiguously), 0.94 (s, 1H, cannot be assigned unambiguously), 0.66 (s, 2H, **6** or **7**), 0.57 (s, 1H, cannot be assigned unambiguously), 0.34 (s, 2H, **16**), 0.20 (d, *J* = 11.7 Hz, 1H, cannot be assigned unambiguously), -0.20 (s, 1H, **8** or **14**), -0.48 (s, 1H, **12**), -0.62 – -0.87 (m, 8H, **9**, **11**, **15**, **19**), -1.22 (s, 4H, **18**), -1.48 (s, 1H, **8** or **21**); **^{13}C{^{1}H} NMR** (151 MHz, D_2O): δ 213.44 (**20**), 201.03 (**3**), 173.74 (**5**), 169.81 (**D**), 156.98 (**e´**), 156.59 (**c´**), 156.02 (**e**), 155.57 (**c**), 152.82 (**A**), 150.18 (**a**), 149.55 (**a´**), 145.78 (**C**), 128.92 (**b**), 126.55 (**B**), 125.69 (**b´**), 125.30 (**d**), 121.99 (**d´**), 121.43 (**4**), 69.86 (**f**), 67.45 (**g**), 62.77 (**17**), 55.59 (**14**), 53.80 (**9**), 42.39 (**13**), 37.58 (**12**), 37.35 (**10**), 34.80 (**1 or 8**), 32.87 (**1 or 8**),

32.80 (**2**), 31.25 (**6**, **7**), 31.15 (**21**), 22.33 (**15 or 16**), 21.91 (**15 or 16**), 21.14 (**f´**), 19.05 (**11**), 14.66 (**19**), 14.40 (**h**), 11.00 (**18**); **DOSY** (D_2O, 298 K): D = $2.01 \cdot 10^{-10}$ m^2/s; **IR** (cm^{-1}): 2358.94 (w), 1616.35 (w), 1506.41 (m), 1373.32 (m), 1338.60 (m), 1267.23 (w), 1114.86 (w), 962.48 (b), 810.10 (m); **Mp.**: 296.8-298.4 °C.

Cage MOC_1•(drospirenone)

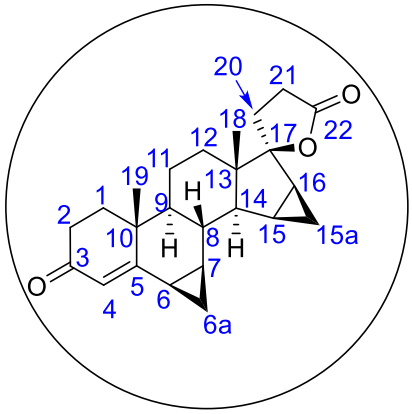

MOC_1•(drospirenone)

The assignment was done based on the work of Baldessari *et al.*[123]

^{1}H NMR (600 MHz, D_2O): δ 9.58 (dd, *J* = 21.8, 6.1 Hz, 24H, **A**), 8.99 (dd, *J* = 34.7, 6.0 Hz, 24H, **B**), 8.59 – 8.39 (m, 6H, **d**), 8.36 (d, *J* = 1.7 Hz, 6H, **d´**), 7.69 (d, *J* = 6.0 Hz, 6H, **a**), 7.57 (m, 12H, **b**, **a´**), 7.48 (m, 6H, **b´**), 5.21 (s, 1H, **4**), 4.86 (s, 12H, **f**), 3.76 (q, *J* = 7.1 Hz, 12H, **g**), 2.63 (s, 18H, **f´**), 2.31 (s, 1H, **21**), 1.82 – 1.57 (m, 3H, **2**, **21**), 1.30 (t, *J* = 7.0 Hz, 18H, **h**), 0.87 (d, *J* = 43.6 Hz, 2H, **20**), -0.02 (d, *J* = 59.6 Hz, 2H, cannot be assigned unambiguously), -0.21 (s, 1H, cannot be assigned unambiguously), -0.30 – -0.71 (m, 4H, cannot be assigned unambiguously), -0.83 (d, *J* = 46.7 Hz, 3H, cannot be assigned unambiguously), -0.98 (s, 3H, **19**), -1.12 (s, 5H, **18**), -1.31 (s, 1H, **6a**), -1.60 (s, 1H, **15a**); **^{13}C{^{1}H} NMR** (151 MHz, D_2O): δ 200.91 (**3**), 179.31 (**22**), 174.23 (**5**), 169.92 (**D**), 157.00 (**e´**), 156.63 (**c´**), 156.05 (**e**), 155.61 (**c**), 152.90 (d, *J* = 18.0 Hz, **A**), 150.18 (**a**), 149.55 (**a´**), 145.79 (**C**), 128.95 (**b´**), 126.62 (d, *J* = 42.7 Hz, **B**), 125.72 (**b**), 125.34 (**d´**), 124.42 (**5**), 122.03 (**d**), 95.74 (**17**), 69.89 (**f**), 67.48 (**g**), 51.19 (**14** or **9**), 50.76 (**9 or 24**), 40.40 (**13**), 36.61 (**10**), 36.10 (**12**), 35.59 (**11**), 33.26 (**8**), 31.62 (**20**), 30.54 (**1** or **2**), 29.47 (**2 or 1**), 23.81 (**16**), 21.17 (**f´**), 19.77 (**18** or **7**), 19.50 (**7 or 18**), 18.31 (**6**), 17.04 (**6a**), 16.25 (**19**), 14.84 (**15**), 14.44 (**h**), 8.57 (**15a**); **DOSY** (D_2O, 298 K): D = $2.13 \cdot 10^{-10}$ m^2/s; **IR** (cm^{-1}): 2966.52 (w), 2937.59 (w), 2357.01 (w), 1604.77 (s), 1388.75 (s), 1323 (s), 1288.45 (m), 1114.86 (m), 1074.35 (m), 1047.35 (m), 1001.06 (w), 989.48 (w), 920.05 (m), 767.67 (w), 702.09 (w), 626.87 (s); **Mp.**: 298.5-300.3°C.

Cage MOC_1•(testosterone)

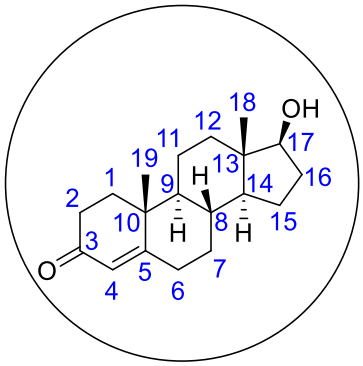

MOC_1•(testosterone)

The assignment was done based on the work of Kamo *et al*.[124]

^{1}H NMR (600 MHz, D_2O): δ 9.61 – 9.53 m, 24H, **A**), 8.99 – 8.95 (m, 24H, **B**), 8.43 (s, 6H, **d**), 8.37 (s, 6H, **d´**), 7.71 (d, *J* = 5.9 Hz, 6H, **a**), 7.60 – 7.56 (m, 6H, **b, a´**), 7.46 (d, *J* = 6.2 Hz, 6H, **b´**), 4.86 (s, 12H, **f**), 3.76 (q, *J* = 7.0 Hz, 12H, **g**), 3.16 – 3.11 (m, 1H, **4**), 2.63 (s, 18H, **f´**), 1.93 (s, 1H, **17**), 1.51 – 1.48 (m, 2H, **2**), 1.30 (t, *J* = 7.0 Hz, 18H, **h**), 0.87 (m, 4H, **6**, **16**), 0.71 (s, 1H, cannot be assigned unambiguously), 0.51 (d, 2H, **7**), 0.23 (s, 1H, cannot be assigned unambiguously), -0.04 (s, 1H, cannot be assigned unambiguously), -0.30 – -0.84 (m, 13H, **18**, **19** cannot be assigned unambiguously), -1.04 – -1.25 (m, 2H, **9**, **14**); **^{13}C{^{1}H} NMR** (151 MHz, D_2O): δ 200.81 (**3**), 174.12 (**5**), 169.82 (**D**), 156.98 (**e´**), 156.60 (**c´**), 156.02 (**e**), 155.57 (**c**), 152.82 (d, *J* = 6.9 Hz, **A**), 150.18 (**a**), 149.55 (**a´**), 145.77 (**C**), 128.92 (**b´**), 126.57 (d, *J* = 8.3 Hz, **B**), 125.69 (**b**), 125.31 (**d´**), 122.00 (**d**), 121.31 (**4**), 80.06 (**17**), 69.87 (**f**), 67.45 (**g**), 54.16 (**9**), 50.08 (**14**), 41.43 (**13**), 37.48 (**10**), 35.43 (**12**), 34.75 (**1**), 33.07 (**6**), 32.70 (**2**), 31.13 (**8**), 29.25 (**16**), 21.28 (**15**), 21.14 (**f´**), 19.01 (**11**), 14.84 (**19**), 14.41 (**h**), 9.19 (**18**); **DOSY** (D_2O, 298 K): D = $2.06 \cdot 10^{-10}$ m^2/s; **IR** (cm^{-1}): 2360.87 (m), 2320.37 (w), 1618.28 (w), 1485.63 (s), 1330.88 (s), 1313.52 (s), 1265.30 (m), 1105.21 (w), 1062.78 (w), 968.27 (b), 808.17 (s); **Mp.**: 298.4-301.6 °C.

Cage MOC_1•(cortisone)

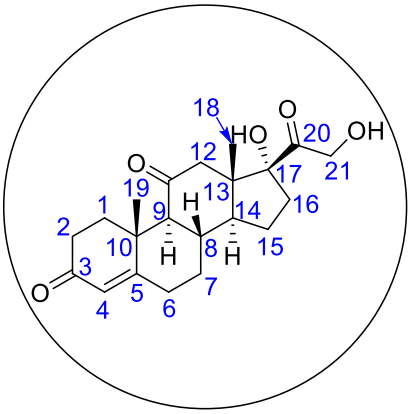

MOC_1•(cortisone)

^{1}H-NMR (600 MHz, D_2O): δ 9.57 (dd, *J* = 8.1, 6.0 Hz, 24H, **A**), 9.12 – 8.85 (m, 24H, **B**), 8.43 (s, 6H, **d**), 8.36 (s, 6H, **d´**), 7.69 (d, *J* = 6.0 Hz, 6H, **a**), 7.63 – 7.54 (m, 12H, **b,a´**), 7.48 – 7.45 (m, 6H, **b´**), 4.86 (s, 12H, **f**), 4.16 (d, *J* = 19.5 Hz, 2H, **9**), 3.76 (q, *J* = 7.1 Hz, 12H, **g**), 2.63 (s, 18H, **f´**), 2.18 (s, *J* = 27.1 Hz, 1H, **12**), 1.79 (d, *J* = 15.7 Hz, 1H, **6**), 1.56 (s, 3H, **1, 16**), 1.30 (t, *J* = 7.0 Hz, 18H, **h**), 1.20 – 0.61 (m, 8H, **21, 13**, **14**, **15**, **16**), 0.04 (d, *J* = 142.2 Hz, 8H, **6, 19**), -0.65 (s, 5H, **18**); **DOSY** (D_2O, 298 K): D= $2.53 \cdot 10^{-10}$ m^2/s **Mp.**: 297.7 °C-299.4 °C.

Cage MOC_1•(estradiol)

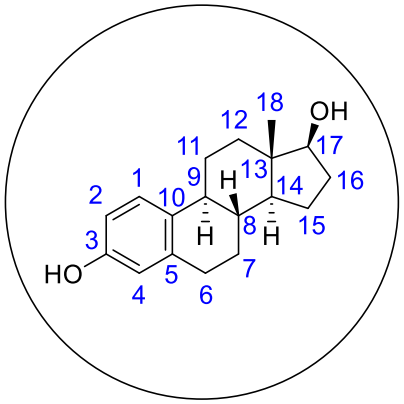

MOC_1•(estradiol)

^{1}H-NMR (600 MHz, D_2O): δ 9.57 – 9.54 (m, 24H, **A**), 8.97 (d, *J* = 5.7 Hz, 24H, **B**), 8.44 – 8.42 (m, 6H, **d**), 8.38 – 8.34 (m, 6H, **d´**), 7.61 (d, *J* = 6.0 Hz, 6H, **a**), 7.59 – 7.55 (m, 6H, **b**), 7.48 (d, *J* = 6.0 Hz, 6H, **a´**), 7.46 – 7.42 (m, 6H, **b´**), 5.12 (s, 1H, **1**), 4.96 (d, *J* = 20.5 Hz, 1H, **2**), 4.86 (s, 12H, **f**), 4.69 – 4.59 (m, 1H, **4**), 3.76 (q, *J* = 7.1 Hz, 12H, **g**), 3.44 (s, 1H, **17**), 2.63 (s, 18H, **f´**), 1.94 (s, 1H, **6α** or **β**), 1.30 (t, *J* = 7.0 Hz, 18H, **h**), 0.90 (s, 1H, **11α**), 0.75 (s, 1H, **9**), 0.39 (s, 3H, **7β**, **12β**, **16α**), 0.15 (s, 1H, **11β**), -0.01 (s, 1H, **15α**), -0.11

(s, 1H, **16β**), -0.27 (s, 3H, **18**), -0.43 – -0.63 (m, 4H, **7α,8,12α,15β**), -1.08 (s, 1H, **14**); **^{13}C{^{1}H}-NMR**: N/A**;** **Mp.**: 297.5 °C-300.1 °C.

Encapsulation experiments of drugs

Cage MOC_1•(ibuprofen)$_2$

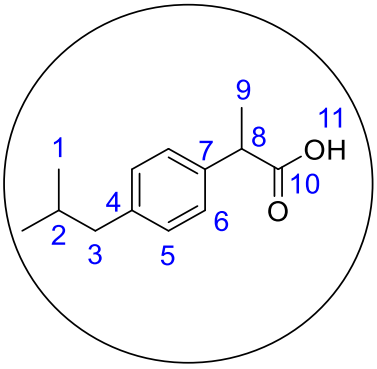

MOC_1•(ibuprofen)$_2$

^{1}H NMR (600 MHz, D_2O): δ 9.60 (d, *J* = 6.1 Hz, 24H, **A**), 9.00 – 8.95 (m, 24H, **B**), 8.43 (s, 6H, **d**), 8.36 (s, 6H, **d'**), 7.70 (d, *J* = 6.0 Hz, 6H, **a**), 7.59 – 7.54 (m, 12H, **b**, **a'**), 7.45 (d, 6H, **b'**), 5.25 (s, 4H, **6**), 4.86 (s, 12H, **f**), 4.52 (s, 4H, **5**), 3.75 (q, *J* = 7.1 Hz, 12H, **g**), 2.88 – 2.83 (m, 2H, **8**), 2.63 (s, 18H, **f'**), 1.30 (t, *J* = 7.0 Hz, 18H, **h**), 1.23 – 1.10 (m, 4H, **3**), 0.43 (d, *J* = 6.9 Hz, 6H, **9**), 0.18 (s, 2H, **2**), -0.61 (s, 12H, **1**); **^{13}C{^{1}H} NMR** (151 MHz, D_2O): δ 177.04 (**10**), 169.53 (**D**), 156.98 (**e´**), 156.65 (**c´**), 156.02 (**e**), 155.62 (**c**), 152.89 (**A**), 150.17 (**a**), 149.54 (**a´**), 145.56 (**C**), 138.32 (**4**), 137.23 (**7**), 128.94 (**b´**), 127.17 (**5**), 126.44 (**B**), 125.71 (**b**), 125.34 (**d´**), 125.10 (**6**), 122.03 (**d**), 69.86 (**f**), 67.47 (**g**), 44.48 (**8**), 43.61 (**3**), 28.89 (**2**), 21.15 (**f´**), 20.59 (**1**), 18.14 (**9**), 14.41 (**h**); **DOSY** (D_2O, 298 K): D = 2.13·10^{-10} m^2/s; **IR** (cm^{-1}): 2985.81 (m), 2970.38 (m), 2885.51 (m), 2355.08 (w), 1375.25 (w), 1228.66 (w), 1220.94 (w), 1074.35 (s), 1056.99 (s), 864.11 (w); **Mp.**: 300.1-302.4 °C.

Cage MOC_1•(paracetamol)

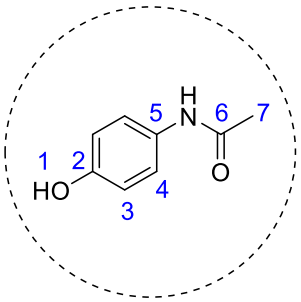

MOC_1•(paracetamol)

^{1}H-NMR (600 MHz, D_2O): δ 9.52 – 9.48 (m, 24H, **A**), 8.93 – 8.89 (m, 24H, **B**), 8.41 (s, 6H, **d**), 8.36 – 8.33 (m, 6H, **d´**), 7.64 (d, *J* = 6.0 Hz, 6H, **a**), 7.59 – 7.55 (m, 6H, **b**), 7.51 (d, *J* = 5.9 Hz, 6H, **a´**), 7.48 – 7.43 (m,

6H, **b´**), 6.91 (d, *J* = 8.4 Hz, 8H, **4**), 6.53 (d, *J* = 8.3 Hz, 8H, **3**), 4.85 (s, 12H, **f**), 3.76 (q, *J* = 7.1 Hz, 12H, **g**), 2.63 (s, 18H, **f´**), 1.88 (s, 12H, **6**), 1.30 (t, *J* = 7.1 Hz, 18H, **h**); **DOSY**: $3.52 \cdot 10^{-10}$ m^2/s.

Cage MOC_1•(melatonin)

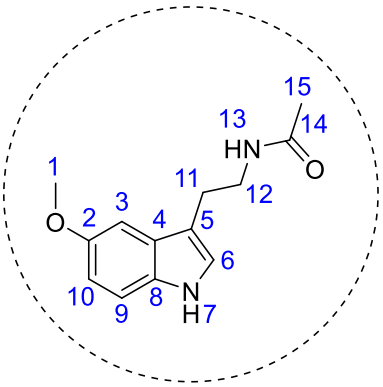

MOC_1•(melatonin)

^{1}H-NMR (600 MHz, D_2O): δ 9.58 (d, *J* = 6.1 Hz, 24H, **A**), 8.90 (s, 24H, **B**), 8.41 (s, 6H, **d**), 8.37 – 8.18 (m, 6H, **d´**), 7.63 (d, *J* = 6.0 Hz, 6H, **a**), 7.58 – 7.54 (m, 6H, **b**), 7.50 (d, *J* = 6.0 Hz, 6H, **a´**), 7.47 – 7.42 (m, 6H, **b´**), 6.25 – 5.11 (m, 15H, **3, 6, 9, 10**), 4.85 (s, 12H, **f**), 3.75 (q, *J* = 7.0 Hz, 12H, **g**), 3.01 – 2.42 (m, 20H, **1,12**), 2.62 (s, 18H, **f´**), 2.13 – 1.73 (m, 10H, **11**), 1.30 (t, *J* = 7.1 Hz, 18H, **h**), 1.03 – 0.58 (m, 9H, **15**).

Encapsulation experiments of various molecules

Cage MOC_1•(phenolphthalein)

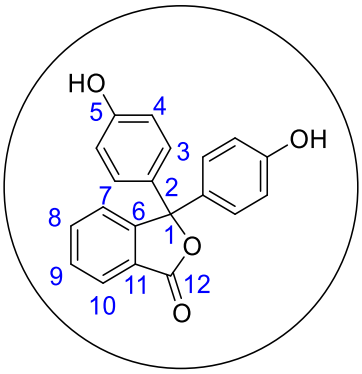

MOC_1•(phenolphthalein)

^{1}H NMR (600 MHz, D_2O): δ 9.45 – 9.41 (m, 24H, **A**), 8.82 – 8.78 (m, 24H, **B**), 8.35 – 8.32 (m, 6H, **d**), 8.29 – 8.26 (m, 6H, **d´**), 7.58 (d, *J* = 6.0 Hz, 6H, **a**), 7.50 – 7.47 (m, 6H, **b**), 7.45 (d, *J* = 6.0 Hz, 6H, **a´**), 7.38 – 7.33 (m, 6H, **b´**), 6.88 (s, 1H, **10**), 6.50 (s, 1H, **9**), 6.34 (s, 1H, **8**), 5.62 (s, 1H, **7**), 5.22 (s, 4H, **4**), 5.12 (s, 4H, **3**), 4.77 (s, 12H, **f**), 3.66 (q, *J* = 7.0 Hz, 12H, **g**), 2.54 (s, 18H, **f´**), 1.21 (t, *J* = 7.0 Hz, 18H, **h**); **DOSY** (D_2O, 298 K): D = $1.88 \cdot 10^{-10}$ m^2/s.

Cage MOC_1•(*umbelliferone*)

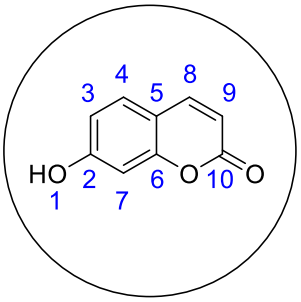

MOC_1•(umbelliferone)

^{1}H-NMR (600 MHz, D_2O): δ 9.66 – 9.30 (m, 24H, **A**), 9.05 – 8.89 (m, 24H, **B**), 8.43 – 8.40 (m, 6H, **d**), 8.37 – 8.34 (m, 6H, **d´**), 7.65 (d, *J* = 6.0 Hz, 6H, **a**), 7.59 – 7.55 (m, 6H, **b**), 7.52 (d, *J* = 5.9 Hz, 6H, **a´**), 7.47 – 7.43 (m, 6H, **b´**), 6.90 (s, 1H, **8**), 6.43 (s, 1H, **4**), 5.86 (s, 1H, **3**), 5.69 (s, 1H, **7**), 5.25 (s, 0H, **9**), 4.85 (s, 12H, **f**), 3.75 (q, *J* = 7.1 Hz, 12H, **g**), 3.36 (s, 2H, **1**), 2.62 (s, 18H, **f´**), 1.30 (t, *J* = 7.1 Hz, 18H, **h**); **DOSY**: $1.86 \cdot 10^{-10}$ m^2/s.

Cage MOC_1•(flavone)

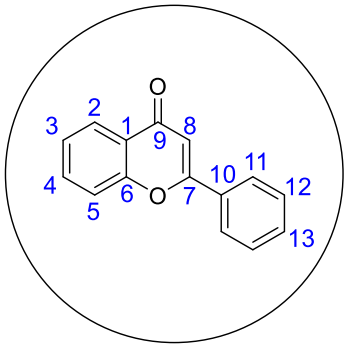

MOC_1•(flavone)

^{1}H-NMR (600 MHz, D_2O): δ 9.58 – 9.28 (m, 24H, **A**), 8.92 – 8.80 (m, 24H, **B**), 8.33 (s, 6H, **d**), 8.29 – 8.24 (m, 6H, **d´**), 7.52 (d, *J* = 6.0 Hz, 6H, **a**), 7.47 (d, *J* = 5.9 Hz, 6H, **b**), 7.39 (d, *J* = 6.0 Hz, 6H, **a´**), 7.37 – 7.33 (m, 6H, **b´**), 7.26 – 7.19 (m, 4H, **2, 3**), 6.99 – 6.88 (m, 2H, **2**), 6.63 (s, 2H, **5**), 6.41 – 6.19 (m, 4H, **11**), 6.15 – 5.88 (m, 8H, **3, 12, 13**), 5.09 (s, 2H, **8**), 4.76 (s, 12H, **f**), 3.66 (q, J = 7.1 Hz, 12H, **g**), 2.53 (s, 18H, **f´**), 1.21 (t, *J* = 7.0 Hz, 18H, **h**).

NMR shows signs of decomposition.

Co-encapsulation of Cage MOC_1•(caffeine and pyrene)

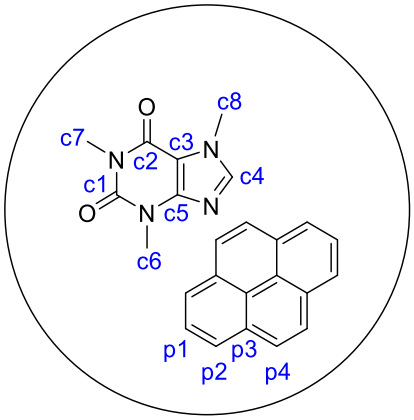

MOC_1•(caffeine and **pyrene)**

^{1}H-NMR (600 MHz, D_2O): δ 9.41 – 9.38 (m, 35H, **A**), 8.79 (s, 24H, **B**), 8.23 (s, 12H, **d**), 8.17 (s, 12H, **d´**), 7.48 (d, *J* = 5.9 Hz, 11H, **a**), 7.41 (s, 12H, **b**), 7.35 (d, *J* = 5.9 Hz, 10H, **a´**), 7.29 (d, *J* = 6.0 Hz, 13H, **b´**), 6.47 (d, *J* = 8.0 Hz, 2H, **p1**), 6.14 (d, *J* = 7.6 Hz, 4H, **p2**), 5.75 (s, 4H, **p4**), 4.68 (s, 25H, **f**), 3.58 (q, *J* = 7.0 Hz, 33H, **g**), 2.45 (s, 38H, **f´**), 1.53 (s, 3H, **c8**), 1.12 (t, *J* = 7.1 Hz, 35H, **h**), 0.17 (s, 3H, **c6**), 0.00 (s, 3H, **c7**).

Encapsulations with polyMOC$_{60}$

The following encapsulation experiments were done using cage **polyMOC$_{60}$**

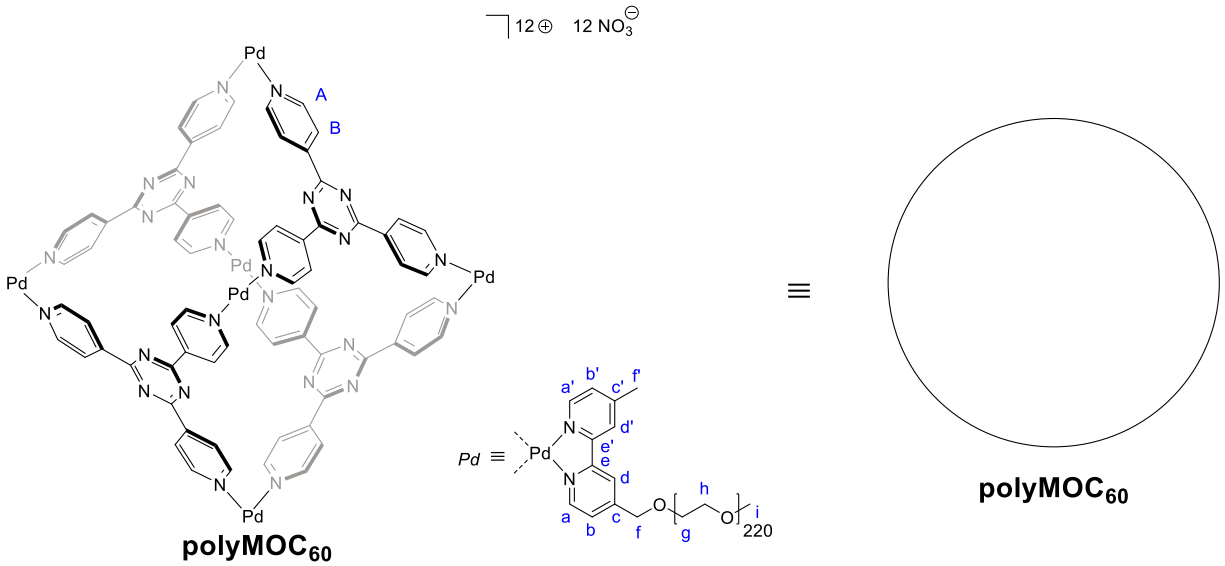

polyMOC$_{60}$ **polyMOC$_{60}$**

For the following encapsulation experiments cage **polyMOC$_{60}$** will be depicted as shown above plus its corresponding guest.

Cage polyMOC$_{60}$•(progesterone)

Cage **polyMOC$_{60}$** (0.15 g, 0.0024 mmol, 1.0 eq.) was dissolved in H_2O (0.8 mL) and progesterone (7.4 mg, 0.024 mmol, 10 eq.) was added. The solution was stirred at 50 °C for 1 h. After removal of residual guests by filtration, the solvent was evaporated under reduced pressure to yield **polyMOC$_{60}$•(progesterone)** as a yellow solid (0.13 g, 87 %).

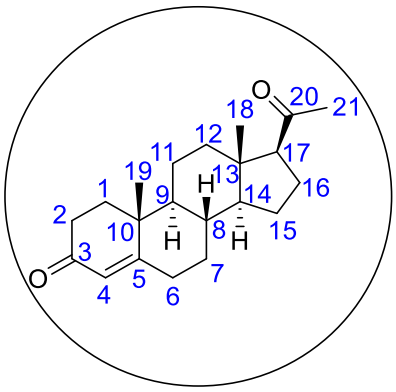

polyMOC$_{60}$•(progesterone)

^{1}H NMR (600 MHz, D_2O): δ 9.61 (s, 24H, **A**), 9.00 (s, 24H, **B**), 8.46 (m, 12H, **d**, **d'**), 7.61 (t, *J* = 77.4 Hz, 24H, **a**, **a'**, **b**, **b'**), 3.72 (s, 5016H, **g**, **h**), 3.40 (s, 18H, **i**), 2.64 (s, 18H, **f'**), 2.18 (s, 4H, **21**), 2.05 (d, *J* = 7.1 Hz, 1H, **17**), 1.17 (s, 1H, could not be assigned due to overlaps in the spectrum), 0.67 (s, 3H, **6 or 7**), 0.44 (s, 3H, **12**, last proton could not be assigned due to overlaps), -0.66 (s, 8H, **9**, **11**, **15**, **19**), -1.15 (s, 4H, **18**); **IR** (cm^{-1}): 2879.72 (m), 1660.71 (w), 1465.90 (m), 1359.82 (w), 1340.53 (s), 1278.81 (m), 1240.23 (m), 1143.79 (m), 1097.50 (s), 1058.92 (m), 960.55 (m), 840.96 (m); **Mp.**: 60-65 °C.

Cage polyMOC$_{60}$•(ibuprofen)$_2$

Cage **polyMOC$_{60}$** (0.15 g, 0.0024 mmol, 1.0 eq.) was dissolved in H_2O (0.8 mL) and ibuprofen (4.9 mg, 0.024 mmol, 10 eq.) was added. The solution was stirred at 50 °C for 1 h. After removal of residual guests by filtration, the solvent was evaporated under reduced pressure to **polyMOC$_{60}$•(ibuprofen)$_2$** as a yellow solid (0.14 g, 93 %).

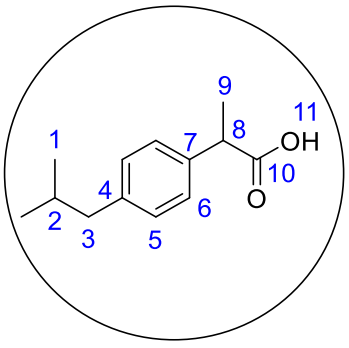

polyMOC$_{60}$•(ibuprofen)$_2$

^{1}H NMR (600 MHz, D_2O): δ 9.64 (s, 24H, **A**), 9.03 (s, 24H, **B**), 8.49 (d, *J* = 53.8 Hz, 12H, **d**, **d'**), 7.62 (t, *J* = 74.8 Hz, 24H, **a**, **a'**, **b**, **b'**), 5.69 (s, 4H, **6**), 3.75 (s, 5889H, **g**, **h**), 3.43 (s, 18H, **i**), 3.02 (s, 2H, **8**), 2.67 (s, 18H, **f'**), 1.32 (s, 4H, **3**), 0.72 (s, 6H, **9**), 0.36 (s, 2H, **2**), -0.41 (s, 12H, **1**); **IR** (cm^{-1}): 2881.65 (m), 2360.87 (w), 1521.84 (w), 1465.90 (m), 1359.82 (w), 1342.46 (s), 1278.81 (m), 1242.16 (m), 1143.79 (m), 1097.50 (s), 1058.92 (m), 962.48 (m), 840.96 (m); **Mp.**: 60-65 °C.

Cage polyMOC$_{60}$•(phenolphthalein)

Cage **polyMOC$_{60}$** (0.25 g, 0.0039 mmol, 1.0 eq.) was dissolved in H_2O (1.2 mL) and phenolphthalein (0.40 mg, 0.0020 mmol, 0.50 eq.) was added. The solution was stirred at 50 °C for 2 h. After removal of residual guests by filtration, the solvent was evaporated under reduced pressure to yield **polyMOC$_{60}$•(phenolphthalein)** as a yellow solid (0.24 g, 96 %).

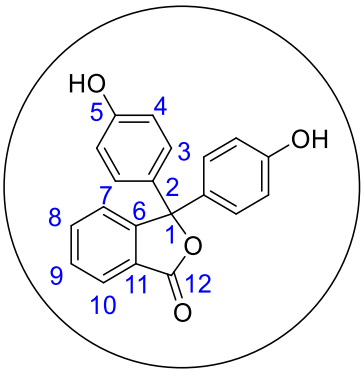

polyMOC$_{60}$•(phenolphthalein)

^{1}H NMR (600 MHz, D_2O): 9.45 (s, 24H, **A**), 8.83 (s, 24H, **B**), 8.37 (d, *J* = 52.9 Hz, 12H, **d**, **d'**), 7.62 – 7.33 (m, 24H, **a**, **a'**, **b**, **b'**), 3.63 (s, 5424H, **g, h**), 3.31 (s, 18H, **i**), 2.55 (s, 18H, **f'**); **IR** (cm^{-1}): 2883.58 (m), 1465.90 (m), 1359.82 (w), 1340.53 (s), 1278.81 (m), 1240.23 (m), 1147.65 (m), 1097.50 (s), 1060.85 (m), 960.55 (m), 840.96 (m); **Mp.**: 60-65 °C.

Release

General procedure

All sonication experiments were performed with a Vibra cell VCX 500 sonicator with a frequency of 20 kHz, an amplitude of 30 % and a full wave probe (13 mm). For each sonication experiment a 5 $mg \cdot mL^{-1}$ cage solution (in H_2O) was degassed with N_2 in a suslick vessel and cooled with an ice-water bath. A sequence of 1 s on and 1 s off was chosen, if not stated otherwise. Samples were taken out using a degassed syringe. The solution was exposed to N_2 during the whole sonication.

Cage **polyMOC$_{60}$**

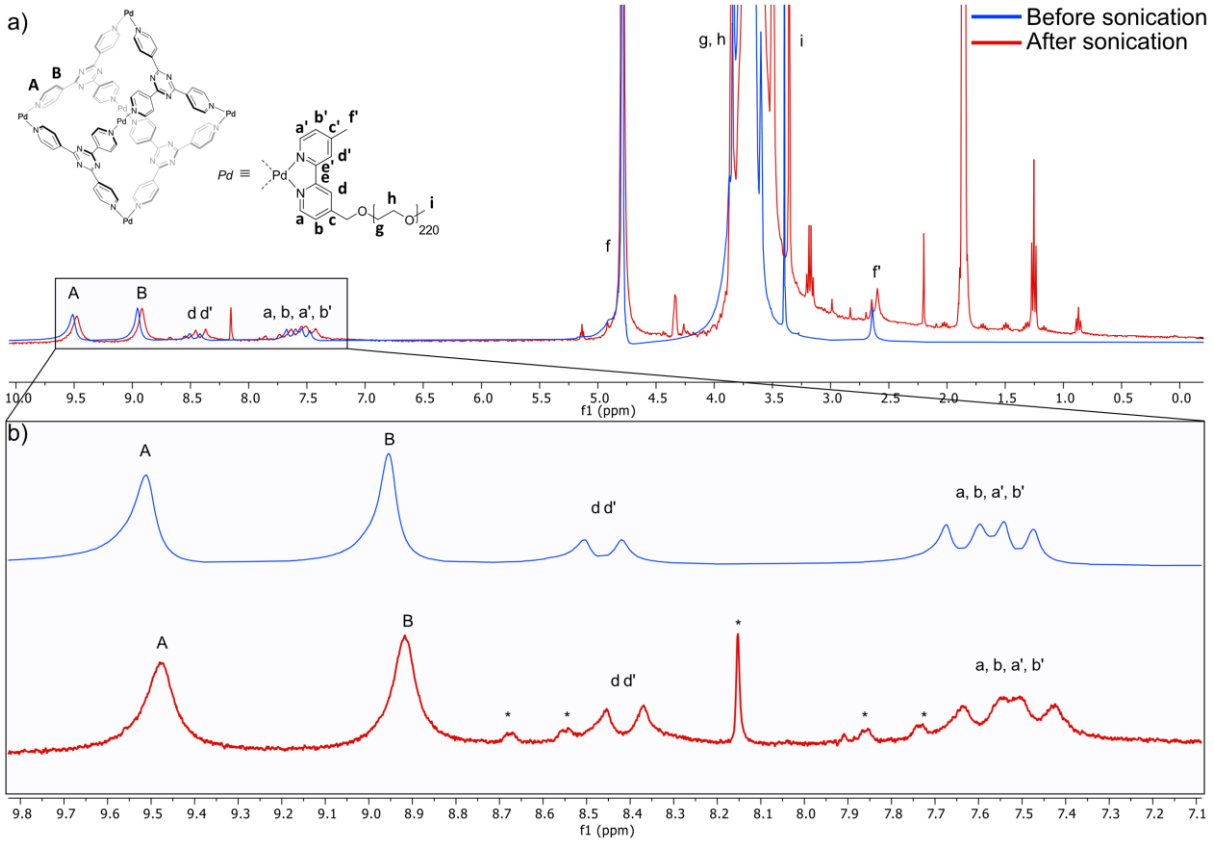

*Figure 63: ^{1}H NMR (D_2O) of cage **polyMOC$_{60}$** before (blue) and after sonication (red) with a) the complete spectral range and b) the enlarged region for characteristic signals of the supramolecular host. Sonicated for 1 h (1 s on, 2 s off). The ^{1}H NMR after the sonication was baseline corrected using a Whittaker Smoother: filter=45, smooth factor=16384, the unedited spectrum is additionally provided in the "Spectra encapsulation and release studies" section. The asterisks indicate fragmented cage, an accurate assignment was not always possible.*

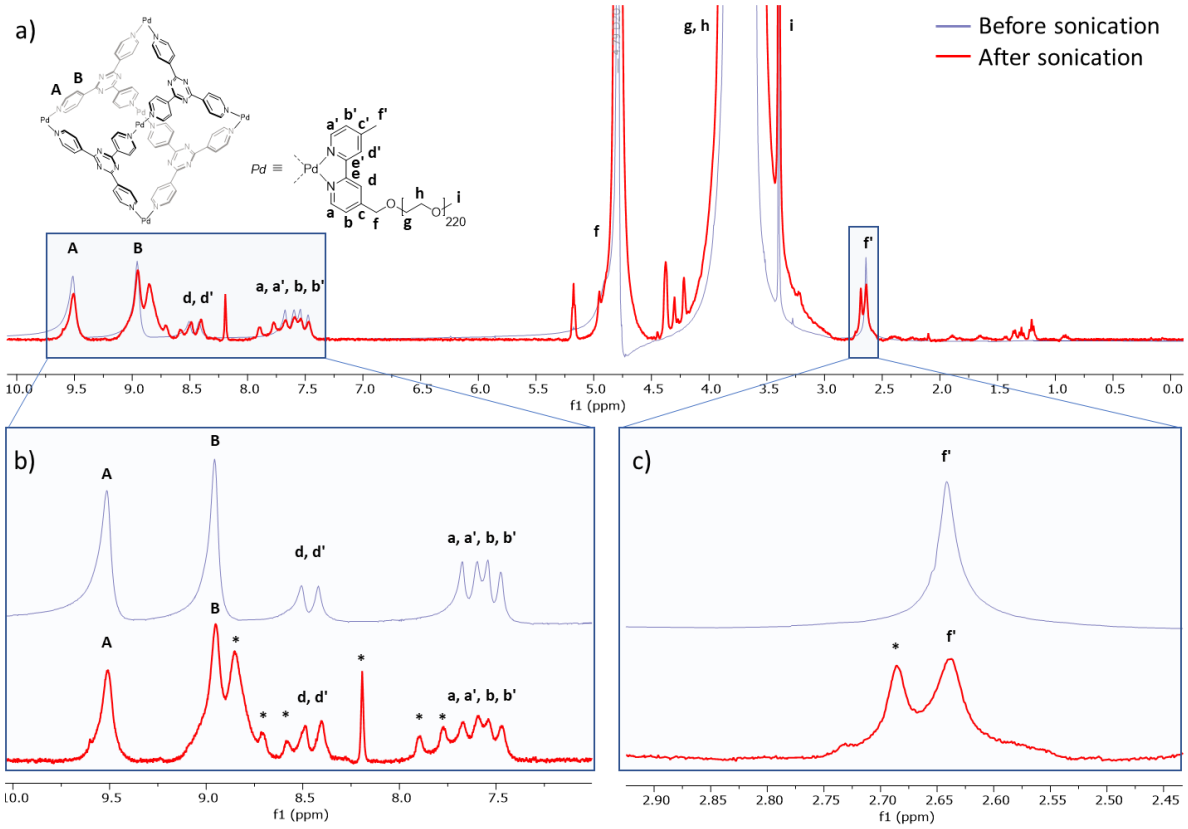

*Figure 64: ^{1}H NMR (D_2O) of cage **polyMOC$_{60}$** before (blue) and after sonication (red) with a) the complete spectral range and b+c) the enlarged region for characteristic signals of the supramolecular host. Sonicated for 3 h (1 s on, 1 s off). The ^{1}H NMR after the sonication was baseline corrected using a Whittaker Smoother: filter=45, smooth factor=16384, the unedited spectrum is additionally provided in the "Spectra encapsulation and release studies" section. The asterisks indicate the fragmented cage, an accurate assignment of the resulting signals was not always possible.*

Cage polyMOC$_{60}$•(progesterone)

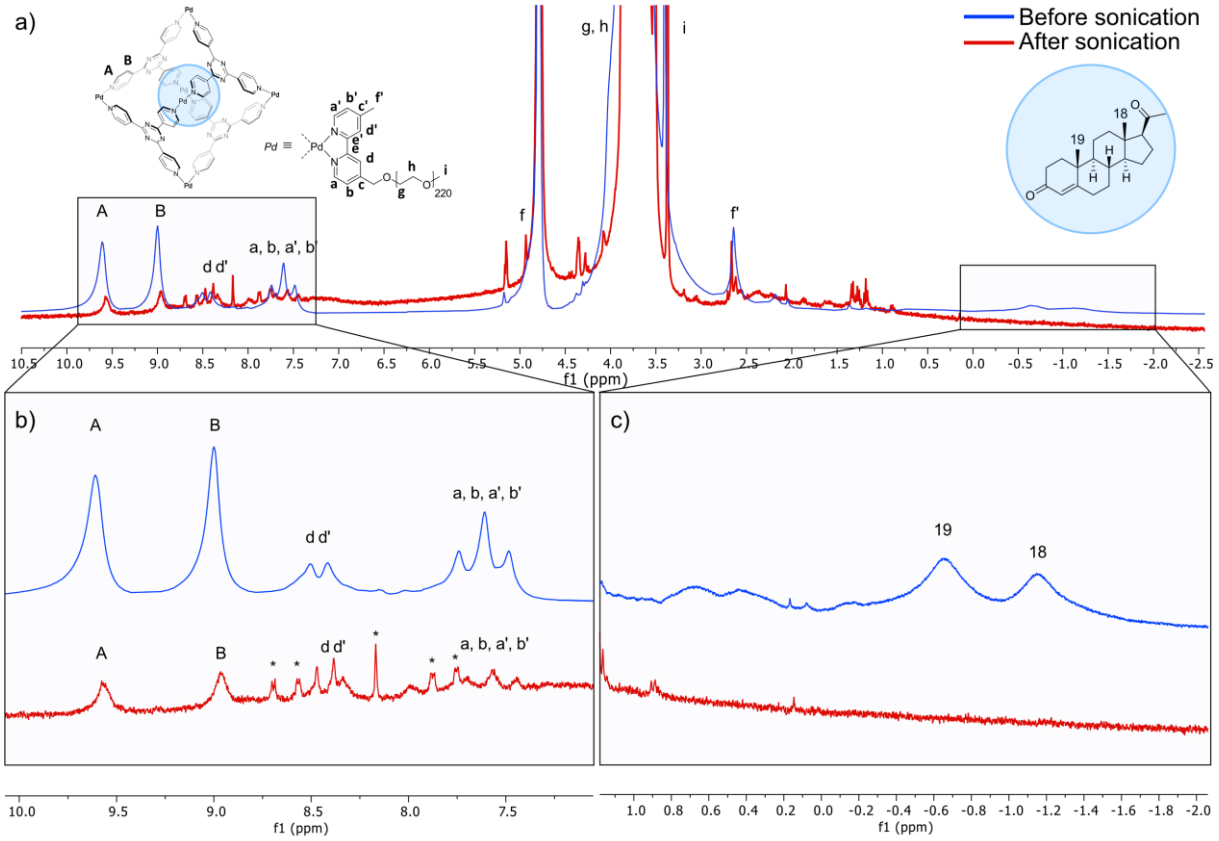

*Figure 65: ^{1}H NMR (D_2O) of cage **polyMOC$_{60}$•(progesterone)** before (blue) and after sonication (red) with a) the complete spectral range, b) the enlarged region for characteristic signals of the supramolecular host and c) the region showing guest encapsulation and release. Sonicated for 3 h (1 s on, 1 s off). The asterisks indicate the fragmented cage, an accurate assignment of the resulting signals was not always possible; c) the release of progesterone can be observed.*

Cage **polyMOC$_{60}$•(ibuprofen)$_2$**

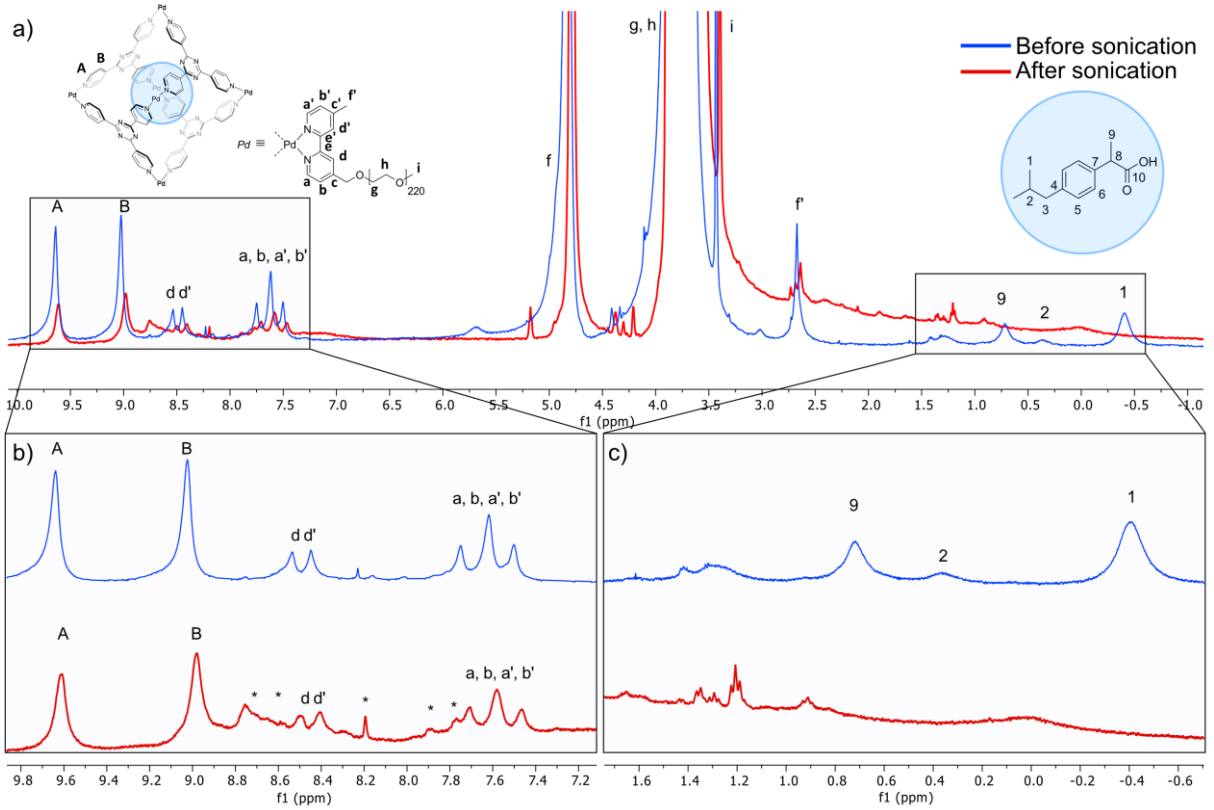

*Figure 66: ^{1}H NMR (D_2O) of cage **polyMOC$_{60}$•(ibuprofen)$_2$** before (blue) and after sonication (red) with a) the complete spectral range, b) the enlarged region for characteristic signals of the supramolecular host and c) the region showing guest encapsulation and release. Sonicated for 3 h. (1 s on, 1 s off). The asterisks indicate the fragmented cage, where an accurate assignment of the resulting signals was not always possible. For c), the release of ibuprofen can be observed.*

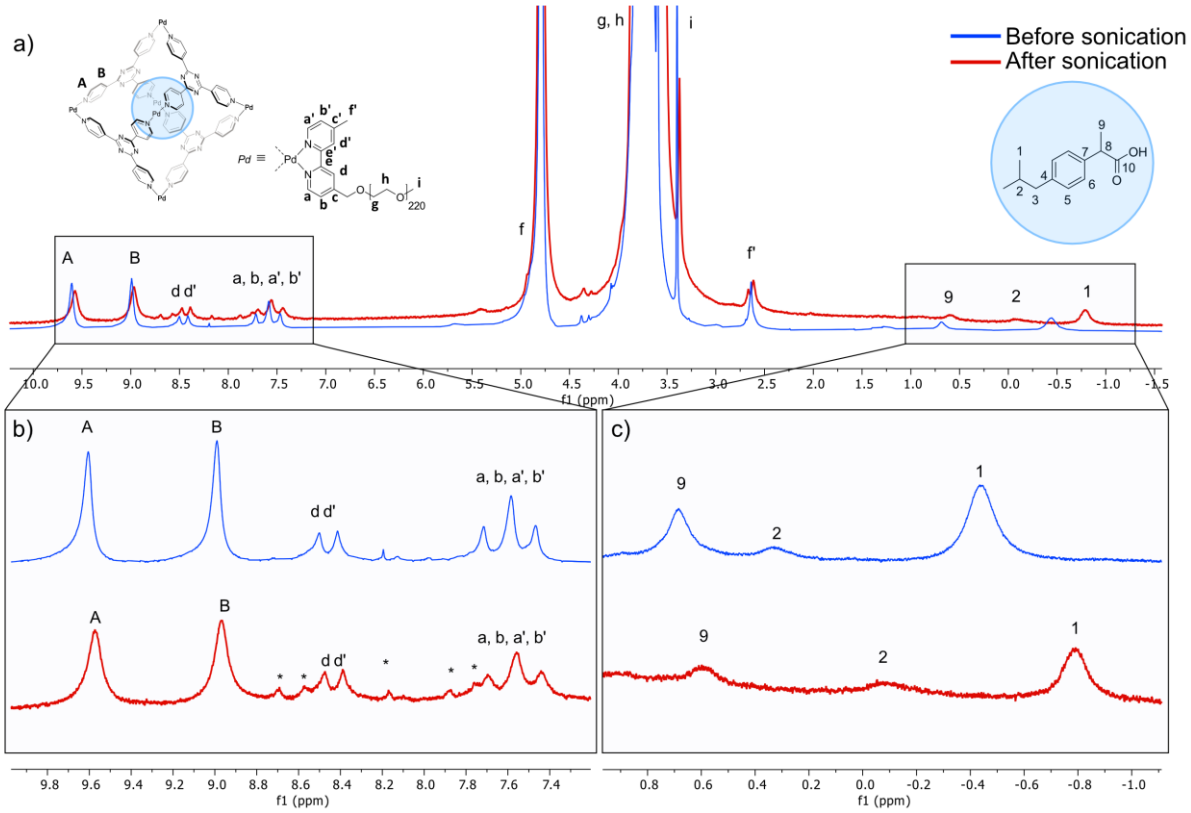

*Figure 67: ^{1}H NMR (D_2O) of cage **polyMOC$_{60}$•(ibuprofen)$_2$** before (blue) and after sonication (red) with a) the complete spectral range, b) the enlarged region for characteristic signals of the supramolecular host and c) the region showing guest encapsulation. Sonicated for 15 min. (1 s on, 2 s off). The asterisks indicate the fragmented cage. An accurate assignment of the resulting signals was not always possible. b) Some fragmentation of cage **polyMOC$_{60}$** can be observed, c) indicates that no guest was released.*

Cage polyMOC$_{60}$•(phenolphthalein)

Cage **polyMOC$_{60}$•(phenolphthalein)** (0.20 g, 3.1 µmol) was dissolved in a 1 mM carbonate buffer (10 mL) in a suslick vessel, degassed with N_2 and cooled with an ice-water bath. The solution was sonicated for a total of 6 h (1 sec on, 1 sec off). Every 30 min a sample was taken with a degassed syringe and diluted to a 20 µM solution with carbonate buffer. For the UV-Vis spectra a 1-cm quartz cell (3.0 mL) was used. The absorbance for phenolphthalein at 529 nm was monitored. An increase is observable at 529 nm but at the same time the absorbance for the whole UV-Vis spectra increases. This might be due to the high concentration of the carbonate buffer during the sonication resulting in an unwanted decomposition or side reaction of cage **polyMOC$_{60}$**.

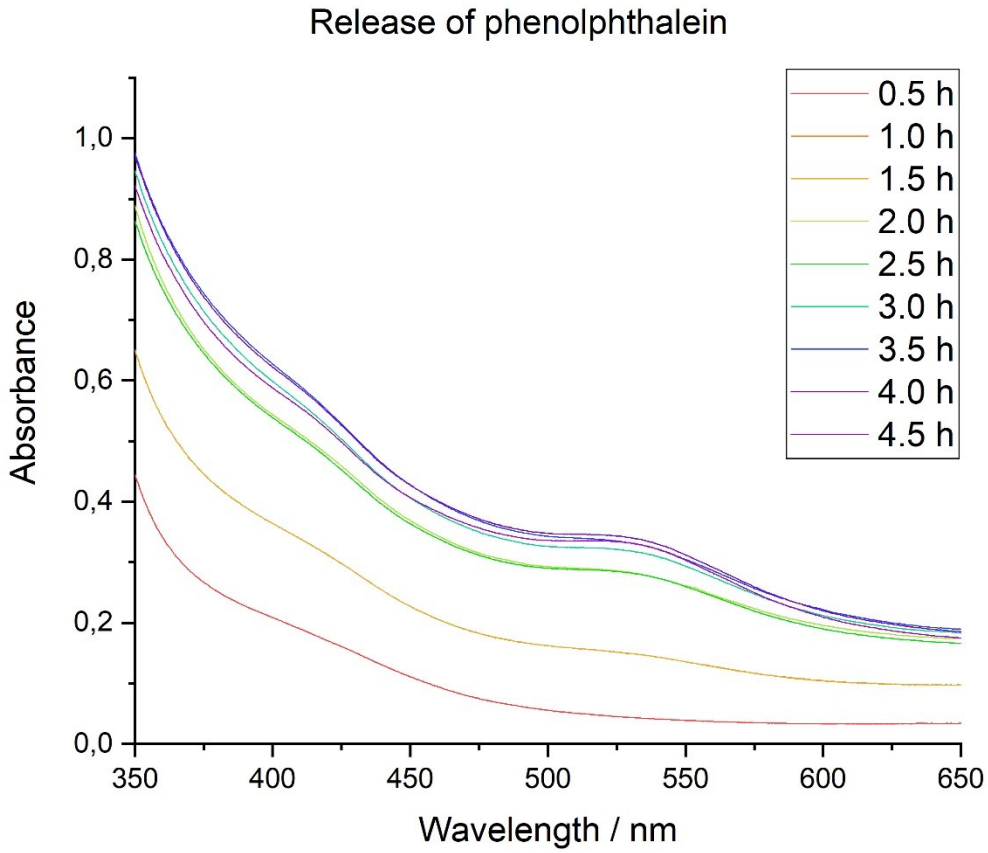

*Figure 68: UV-Vis spectra of the sonication of cage **polyMOC$_{60}$•(phenolphthalein)** (20 µM) in carbonate buffer (1 mM).*

Cage **polyMOC$_{120}$**

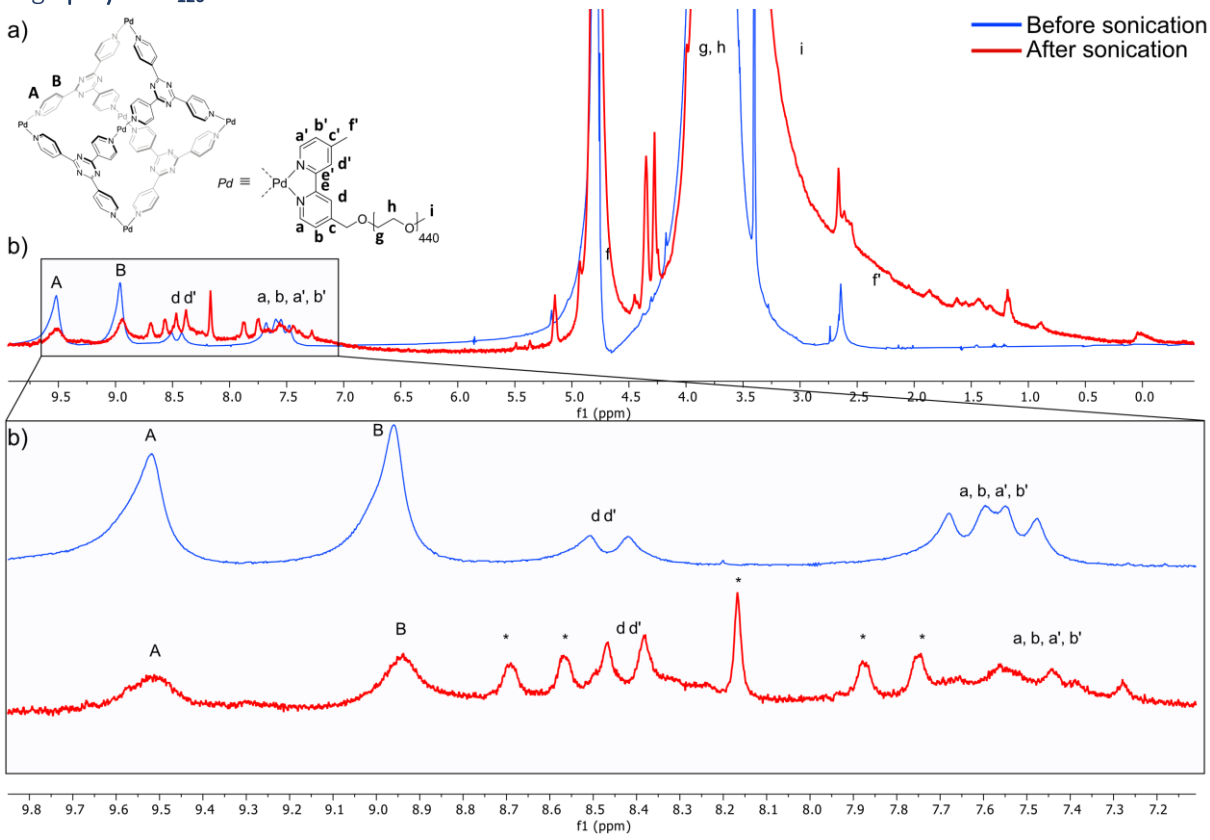

*Figure 69: ^{1}H NMR (D_2O) of cage **polyMOC$_{120}$** before (blue) and after sonication (red) with a) the complete spectral range and b) the enlarged region for characteristic signals of the supramolecular host. Sonicated for 1 h. (1 s on, 1 s off). For the ^{1}H NMR after the sonication a baseline correction with a polynomial fit: filter=67, polynomial order=5 was employed. The unedited spectrum is additionally provided in the "NMR encapsulation and release studies" section. The asterisks indicate fragmented cage **polyMOC$_{120}$**. An accurate assignment of the resulting signals was not possible for all signals.*

Cage MOC_1

For the sonication experiments with cage **MOC_1** a 1 mg mL^{-1} cage solution in H_2O was used instead of 5 mg mL^{-1}. This solution was degassed with N_2 in a suslick vessel and cooled with an ice-water bath. A sequence of 1 sec on and 1 sec off was chosen. Samples were taken out by a degassed syringe. The solution was exposed to N_2 during the whole sonication.

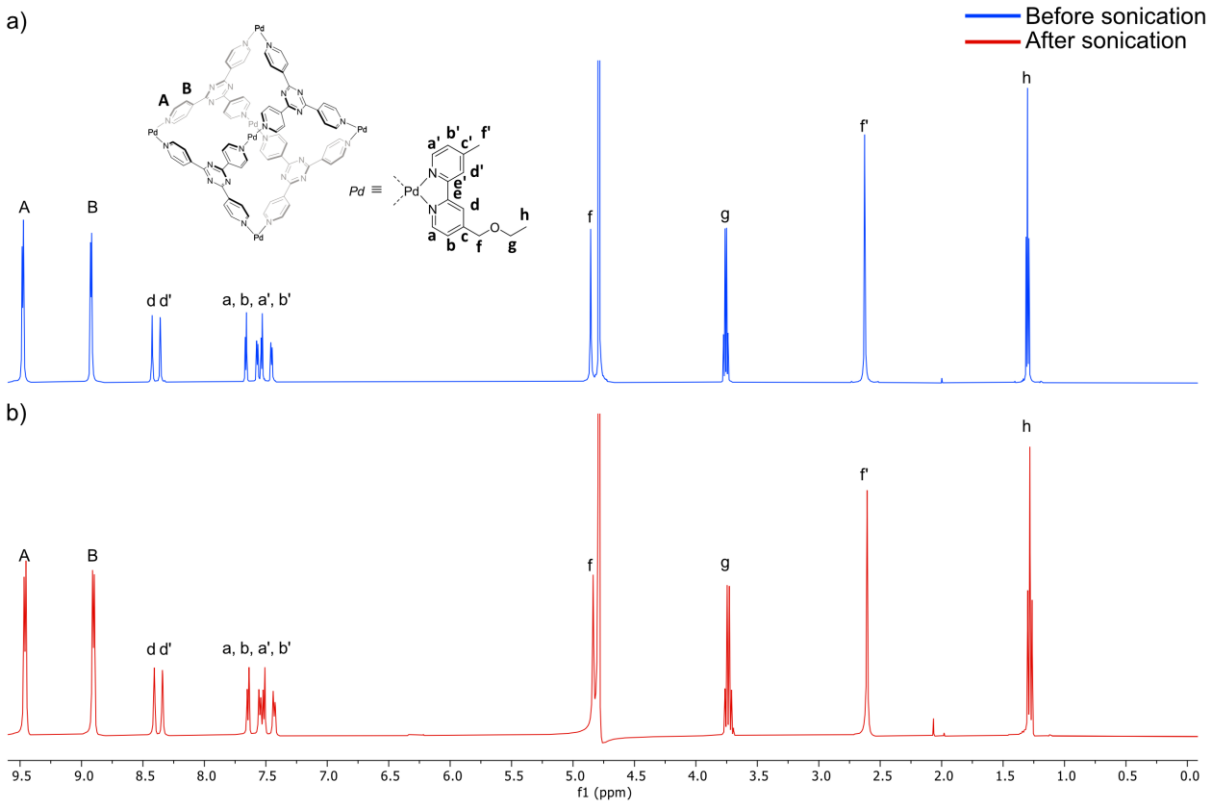

*Figure 70: a) ^1H NMR (D_2O) of cage **MOC_1** before (blue) and b) after sonication (red). Sonicated for 3 h (1 s on, 1 s off). No fragmentation of cage **MOC_1** can be observed.*

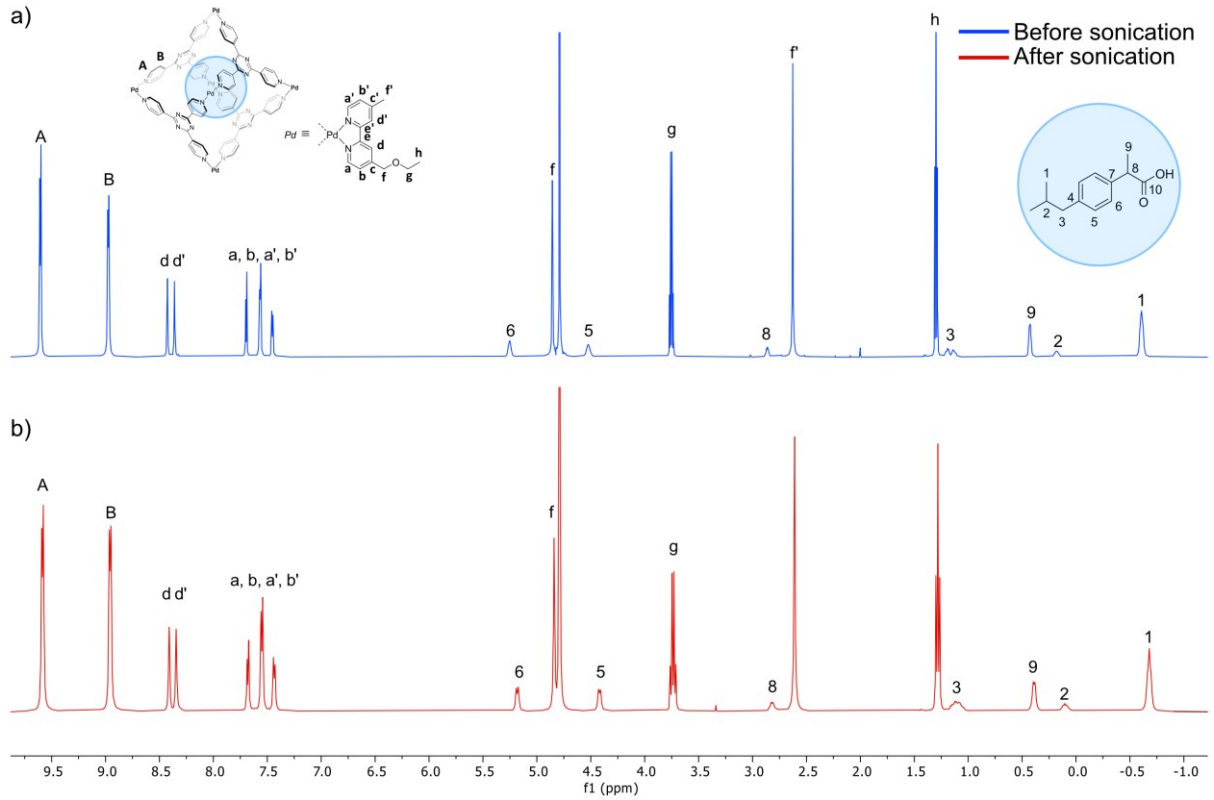

*Figure 71: a) ^{1}H NMR (D_2O) of the cage **MOC_1•(ibuprofen)$_2$** before (blue) and b) after sonication (red). Sonicated for 2 h (1 s on, 1 s off). It can be seen that no guest was released.*

GPC elugrams in $CHCl_3$

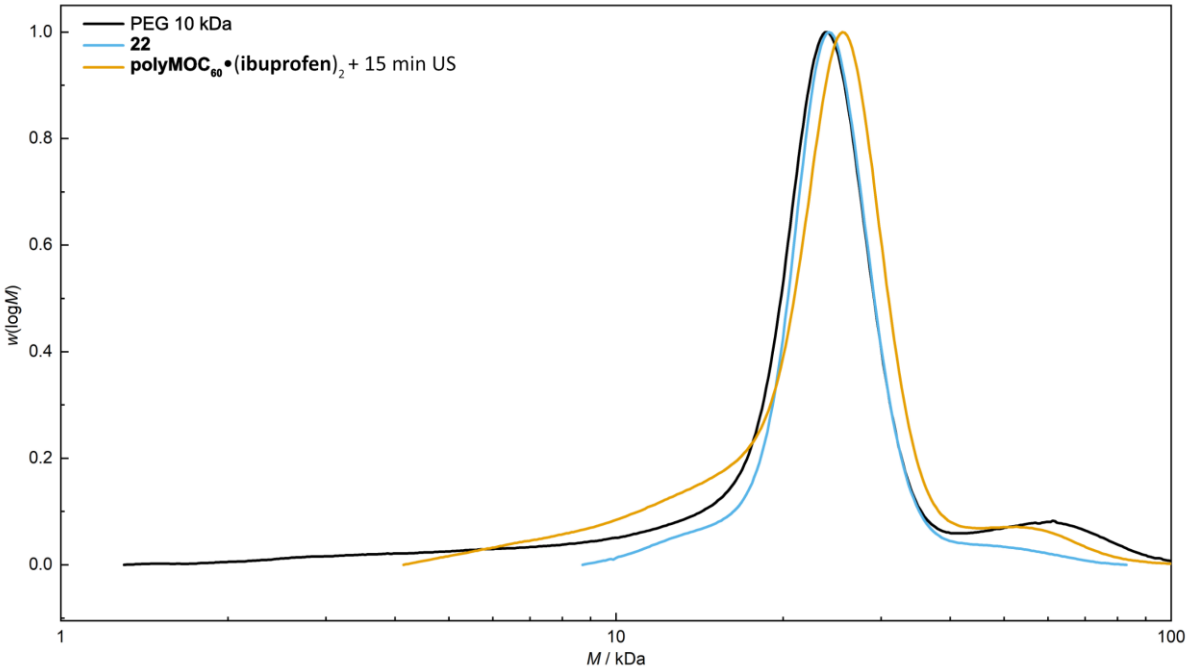

*Figure 72: GPC elugrams were obtained in $CHCl_3$ via the RI detector; pristine PEG 10 kDa, cage building block **22** were not sonicated and **polyMOC$_{60}$•(ibuprofen)$_2$** was sonicated for only 15 min.*

5.4 Experimental details for section 3.2

Synthesis

Synthesis of **CMP**

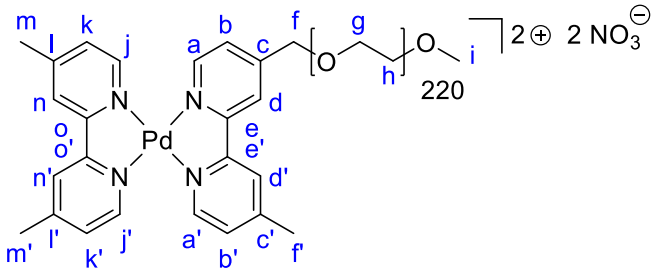

(4-Methoxypolyethyleneglycolmethyl-4'-methyl-2,2'-bipyridine)-dinitrato palladium (**24**) (0.10 g, 10 µmol, 1.0 eq.) and 4,4'-dimethyl-2,2'-bipyridine **16** (2.1 mg, 10 µmol, 1.2 eq.) were dissolved in an acetone/water (2 mL, 3/1) mixture. The yellow solution was heated in the dark at 70 °C. After 23 hours the reaction was cooled to RT, the solvent was removed under reduced pressure and dissolved in a MeOH/MeCN (4 mL, 1/1) mixture. After heating for 1 h at 70 °C the reaction was filtered, and the solvent was removed under reduced pressure. The yellow solid was dissolved in MeOH (0.5 mL) and precipitated from cold diethyl ether to yield complex **CMP** as a colorless solid (69 mg, 67 %).

^{1}H NMR (600 MHz, D_2O): δ 8.70 (s, 1H), 8.60 – 8.52 (m, 3H), 8.48 (s, 1H), 8.39 (s, 1H), 8.31 (s, 2H), 7.89 (s, 1H), 7.77 – 7.66 (m, 3H), 4.95 (s, 3H), 3.72 (m, 1072H), 3.39 (s, 3H), 2.67 (s, 9H); **IR** (cm^{-1}): 2881.65 (m), 1465.90 (m), 1359.82 (w), 1342.46 (m), 1278.81 (m), 1240.23 (w), 1147.65 (w), 1105.21 (s), 1060.85 (m), 960.55 (m), 840.96 (m); **Mp.**: 59-65 °C.

Synthesis of **MP_{15}**

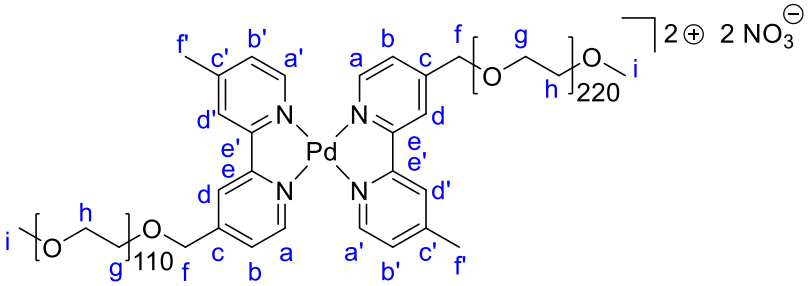

(4-Methoxypolyethyleneglycolmethyl-4'-methyl-2,2'-bipyridine)-dinitrato palladium (**24**) (0.15 g, 14 µmol, 1.0 eq.) and 4-methoxypolyethyleneglycolmethyl-4'-methyl-2,2'-bipyridine **29** (75 mg, 14 µmol, 1.0 eq.) were dissolved in an acetone/water (3 mL, 3/1) mixture. The yellow solution was heated in the dark at 60 °C. After 23 hours the reaction was cooled to RT, the solvent was removed under reduced pressure and dissolved in a MeOH/MeCN (6 mL, 1/1) mixture. After heating for 1 h at 70 °C the reaction

was filtered, and the solvent was removed under reduced pressure. The yellow solid was dissolved in MeOH (1.5 mL) and precipitated from cold diethyl ether to yield complex **MP_{15}** as a colorless solid (131 mg, 58 %).

^{1}H NMR (600 MHz, D_2O): δ 8.67 (s, 2H), 8.55 (s, 2H), 8.42 (s, 2H), 8.32 (s, 2H), 7.85 (s, 2H), 7.71 (s, 2H), 3.72 (s, 1486H), 3.40 (s, 6H), 2.65 (s, 6H); **IR** (cm^{-1}): 2881.65 (m), 1465.90 (m), 1359.82 (w), 1340.46 (m), 1278.81 (m), 1240.23 (w), 1147.65 (w), 1105.21 (s), 1060.85 (m), 960.55 (m), 840.96 (m); **Mp.**: 57-66 °C.

Synthesis of MP_{20}

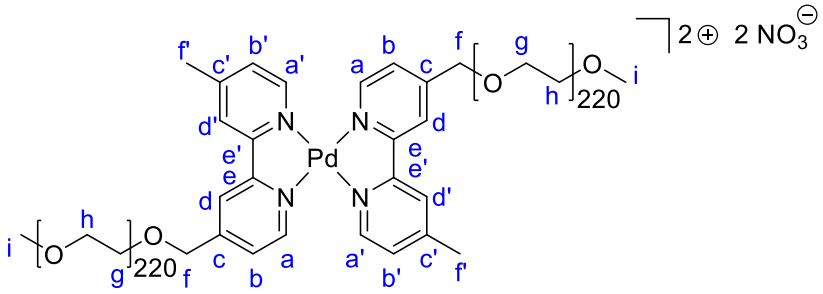

(4-Methoxypolyethyleneglycolmethyl-4'-methyl-2,2'-bipyridine)-dinitrato palladium (**24**) (50 mg, 4.9 µmol, 1.0 eq.) and 4-methoxypolyethyleneglycolmethyl-4'-methyl-2,2'-bipyridine (**22**) (49 mg, 4.9 µmol, 1.0 eq.) were dissolved in an acetone/water (1 mL, 3/1) mixture. The yellow solution was heated in the dark at 60 °C. After 23 hours the reaction was cooled to RT, the solvent was removed under reduced pressure and dissolved in a MeOH/MeCN (2 mL, 1/1) mixture. After heating for 1 h at 70 °C the reaction was filtered, and the solvent was removed under reduced pressure. The yellow solid was dissolved in MeOH (0.5 mL) and precipitated from cold diethyl ether to yield complex **MP_{20}** as a colorless solid (74 mg, 74 %).

^{1}H NMR (600 MHz, D_2O): δ 8.72 (d, *J* = 6.1 Hz, 2H), 8.59 (d, *J* = 6.1 Hz, 2H), 8.50 (s, 2H), 8.41 (s, 2H), 7.90 (d, J = 6.1 Hz, 2H), 7.78 (d, *J* = 6.1 Hz, 2H), 4.96 (s, 6H), 4.01 – 3.54 (m, 1880H), 3.39 (s, 6H), 2.69 (s, 6H); **IR** (cm^{-1}): 2881.65 (m), 1465.90 (m), 1359.82 (w), 1342.46 (m), 1278.81 (m), 1240.23 (w), 1147.65 (w), 1105.21 (s), 1060.85 (m), 960.55 (m), 840.96 (m); **Mp.**: 58-65 °C.

Calculations

The CoGEF[113] and FMPES[125] computations were done using the B3LYP functional with the 6-31G* basis set. For Pd^{2+}, the LanL2DZ ECP[126] was used. To account for dispersion effects, Grimme's D3[127] dispersion correction was applied. Electronic structure computations were performed with Terachem[128] and applied graphics card acceleration.[129] All calculations were conducted by Dr. Jan Meisner.

We used the $[Pd(py)_2(bipy)]^{2+}$ model complex surrounded by 8 water molecules placed around the Pd complex. These water molecules are essential to fill up the coordination sphere of the Pd ion after dissociation of the nitrogen ligands. The total system is double positively charged, and the dissociation process assumed to be closed shell. Two different pulling modes have been used for both CoGEF and FMPES computations (Figure 73).

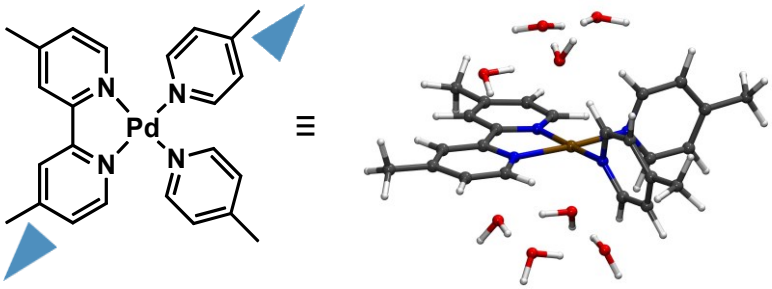

Figure 73: Model system used in this study. The blue triangles indicate the atoms pulled away from each other in the CoGEF and FMPES computations. Depicted is the trans pulling force.

CoGEF simulations were performed in Terachem with a step size of 0.01 Angstrøm. The computations were stopped after the pyridine ligands have been dissociated completely.

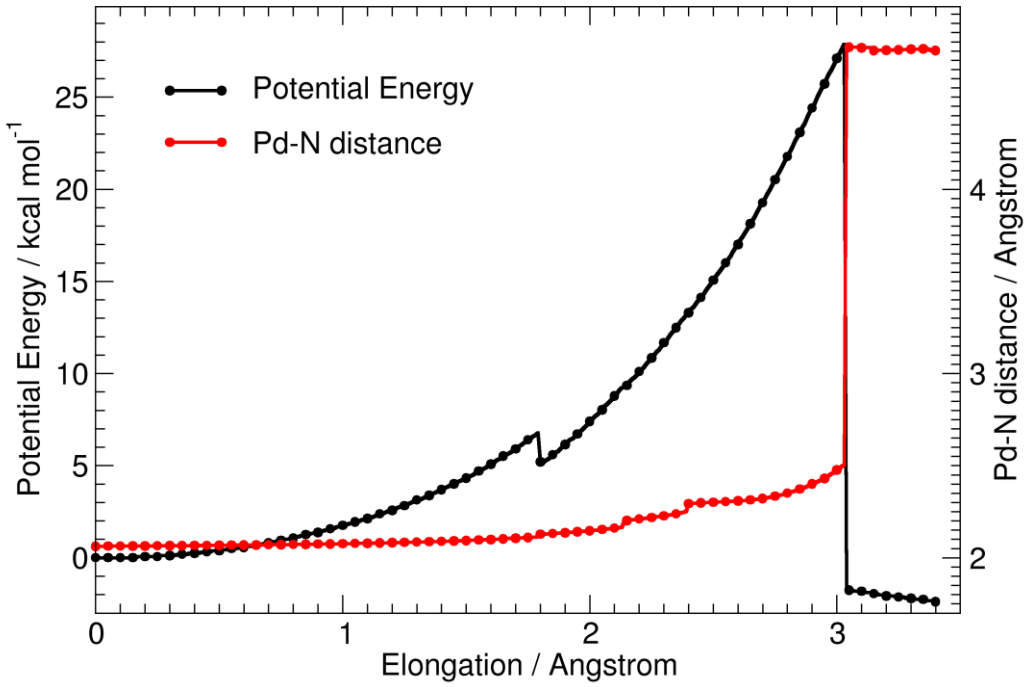

Figure 74: CoGEF simulations for the mechanochemical dissociation. The force was applied in cis-direction. Dissociation can be observed at 27.8 kcal mol^{-1}. Just every fifth point was shown for clarity.

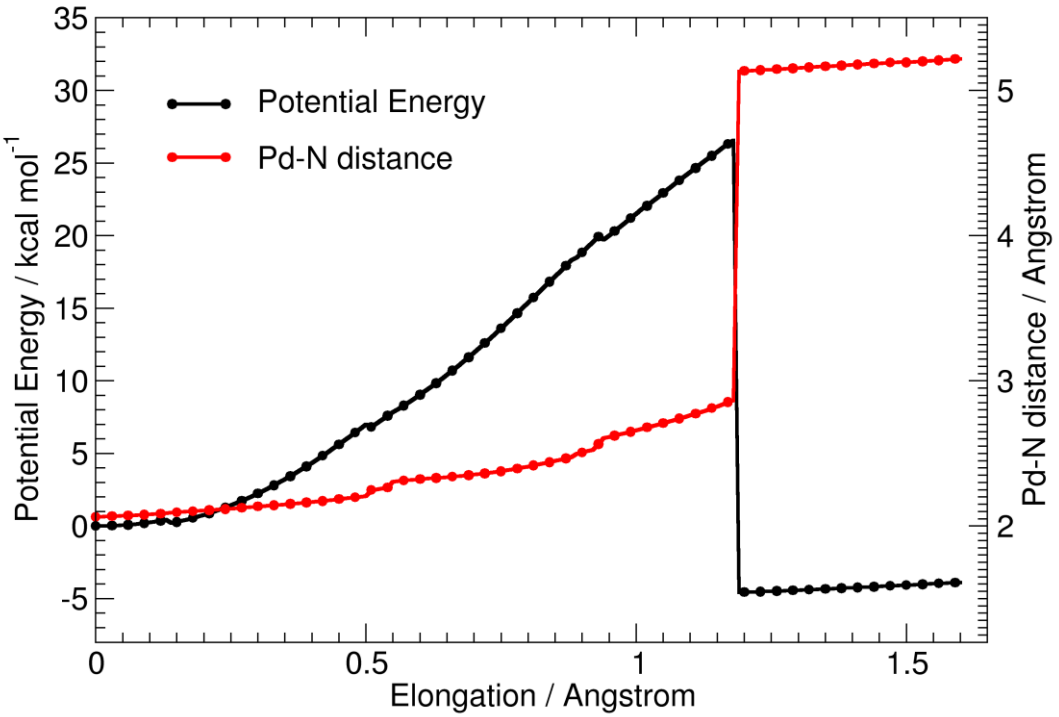

Figure 75: CoGEF simulations for the mechanochemical dissociation. The force was applied in trans-direction. Dissociation can be observed at 26.5 kcal mol^{-1}. Just every fifth point was shown for clarity.

To obtain free energy barriers with the FMPES approach, the stationary points had to be optimized for every force in steps of 0.1 nN. For this, the DL-FIND optimization library[130a] was coupled to Terachem via the Chemshell[130b] interface. In case of trans-pulling, we could not locate transition state structures below 0.4 nN. Above 2.3 nN, the reactant is not a stable minimum structure, and the pyridine ligand immediately dissociates. For cis-pulling, the reactant is not a stable minimum structure above 1.2 nN (Figure 76). The nature of the stationary points has been validated by the correct number of negative eigenvalues of the corresponding Hessian matrix: zero for reactants and one for transition state structures. Free energy barriers have been computed using the standard rigid rotor-harmonic oscillator models computed on the corresponding stationary points on the FMPES. To avoid divergence of the vibrational entropic contribution to the free energy, frequencies below 100 cm^{-1} were set to this value for the computation of their vibrational contribution (but not the zero point energy).

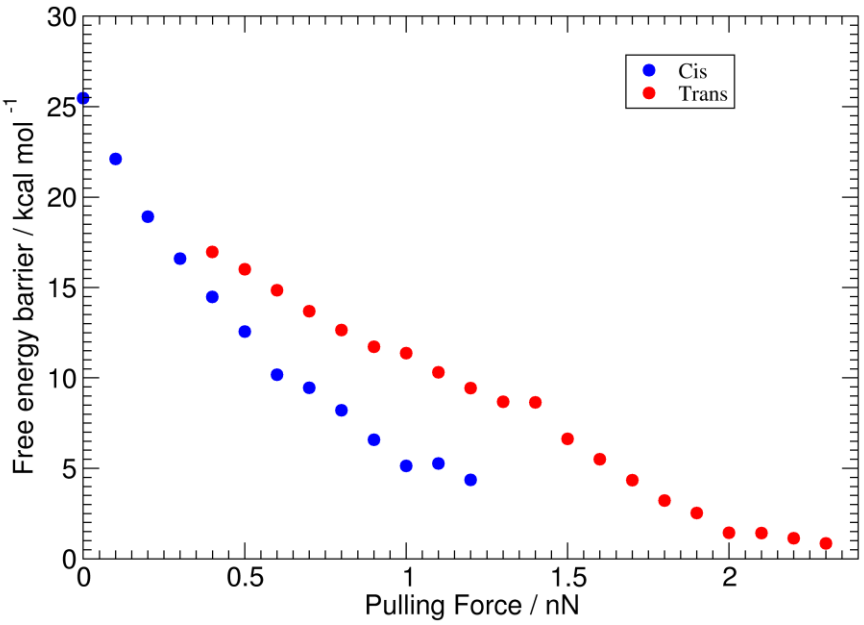

Figure 76: To compute the free energy barrier heights the force-modified potential energy surface approach was used. At 0.5 nN-PES, the barrier heights are 12.6 kcal mol^{-1} (cis-pulling) and 16.0 kcal mol^{-1} (trans-pulling). At a force of 1.0 nN, the free energy barrier is 5.1 kcal mol^{-1} (cis) and 11.4 kcal mol^{-1} (trans).

We assume that the CoGEF results are robust with respect to the used basis set. However, we increased the accuracy of the potential energy for the barriers using the FMPES method and performed single-point energy calculations on all stationary points (*i.e.*, reactant and transition state structures) using the def2-TZVP basis set and the corresponding ECP for Pd, as implemented in Turbomole V7.2.1.[131]

Table S1: Free energy barriers computed using B3LYP+D3/6-31G level of theory (not shown in the main text) and free energy barriers with potential energy corrections with B3LYP+D3/def2-ZTVP level of theory.*

Force / nN	Free energy barrier / kcal mol^{-1}			
	cis-pulling		*trans*-pulling	
	B3LYP+D3/def2-TZVP//6-31G*	B3LYP+D3/6-31G*	B3LYP+D3/def2-TZVP//6-31G*	B3LYP+D3/6-31G*
0.0	25.47	20.20		
0.1	22.10	16.97		
0.2	18.91	14.16		
0.3	16.59	11.71		

0.4	14.48	9.50	16.96	13.95
0.5	12.56	7.66	16.01	12.96
0.6	10.17	6.71	14.85	11.79
0.7	9.45	5.03	13.69	10.57
0.8	8.21	4.25	12.64	9.52
0.9	6.57	2.88	11.72	8.46
1.0	5.13	1.64	11.37	8.08
1.1	5.26	0.99	10.31	7.11
1.2	4.36	0.12	9.44	6.36
1.3			8.68	5.67
1.4			8.64	5.47
1.5			6.63	3.94
1.6			5.51	3.01
1.7			4.34	2.06
1.8			3.21	1.27
1.9			2.52	0.77
2.0			1.43	0.64
2.1			1.42	0.58
2.2			1.14	0.39
2.3			0.85	0.13

xyz-coordinates of the model used for CoGEF and FMPES computations

Energy = 0.00 kcal/mol

C 1.338477 -2.386908 -1.595531

C 1.973193 -1.878663 -0.454936

C 0.077465 -2.956050 -1.498129

N -0.570382 -3.027429 -0.318856

C 0.018416 -2.547732 0.795099

C -0.858850 -6.250372 -1.095324

N -1.440508 -5.713102 -0.005778

C -1.318472 -6.333064 1.186711

C -0.602264 -7.512433 1.319551

C 0.014363 -8.092913 0.203070

C -0.132813 -7.430292 -1.020728

H 0.318013 -7.828130 -1.924083

H -1.829547 -5.878878 2.027598

H -0.527733 -7.975419 2.298300

C 1.278003 -1.970363 0.757454

H 1.712957 -1.591638 1.676625

H 1.822824 -2.343056 -2.565593

H -0.429160 -3.369704 -2.361748

C 3.352648 -1.286817 -0.524926

H 3.502313 -0.532162 0.252311

H 3.541786 -0.833601 -1.502034

H 4.104514 -2.071752 -0.373475

C 0.777019 -9.382876 0.314212

H 0.082171 -10.232071 0.315553

H 1.346175 -9.425662 1.247820

H 1.463764 -9.513759 -0.526174

C -3.794197 0.187758 -0.382114

C -5.151631 0.080544 -0.066395

C -3.000764 -0.951206 -0.412529

N -3.499333 -2.163525 -0.148668

C -4.816911 -2.307416 0.147555

C -5.264966 -3.693677 0.354227

N -4.311075 -4.642972 0.178567

C -4.632755 -5.939400 0.271306

C -5.922386 -6.353243 0.568067

C -6.923583 -5.401291 0.791006

C -6.569515 -4.053713 0.672553

H -7.322483 -3.289130 0.820522

H -3.835017 -6.647745 0.102311

H -6.138682 -7.414425 0.629983

C -5.653154 -1.198977 0.201877

H -6.702519 -1.320043 0.443190

H -3.346196 1.151484 -0.599056

H -1.946696 -0.899544 -0.640994

C -6.051573 1.283884 -0.043367

H -6.879478 1.146898 0.657675

H -6.482933 1.447811 -1.038928

H -5.499063 2.186922 0.230374

C -8.322218 -5.810360 1.157517

H -8.645300 -6.674407 0.568744

H -9.031245 -4.992762 1.005300

H -8.363682 -6.101731 2.214370

Pd -2.426939 -3.903609 -0.118950

O -2.509598 -2.682843 2.836233

H -2.397188 -1.718311 2.674508

H -1.958066 -2.920219 3.616974

H -2.254130 -3.777604 -3.543955

O -1.832445 -4.679140 -3.652475

H -1.567838 -4.741008 -4.584169

H -0.996353 -5.718989 -2.030191

H -0.565744 -2.628927 1.704620

O -3.447291 -5.146379 3.272514

H -3.438564 -4.207060 2.975669

H -4.338039 -5.307026 3.621450

O -1.412894 -4.155111 4.871038

H -0.594040 -4.562804 4.546586

H -2.126109 -4.731897 4.510996

O -3.020845 -2.351782 -3.151944

H -3.149680 -1.827587 -3.959013

H -3.918206 -2.736483 -2.942960

O -1.855187 -0.080663 2.217637

H -1.207413 0.242422 2.865585

H -2.589879 0.551342 2.276252

O -3.951039 -6.100597 -2.726281

H -3.152828 -5.718550 -3.173094

H -4.354508 -6.690102 -3.383293

O -5.265991 -3.726970 -2.596401

H -4.874622 -4.642669 -2.619217

H -5.873838 -3.697011 -3.352256

5.5 Experimental details for section 3.3

Ibuprofen-based linker

Synthesis of cross-linker **36**

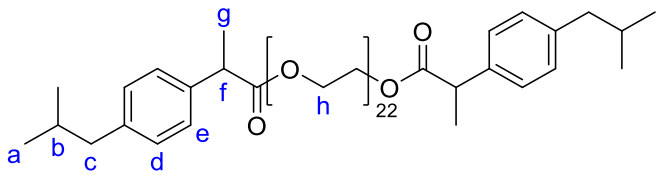

Ibuprofen (0.10 g, 0.50 mmol, 2.0 eq.) and PEG (M_n = 1.000 Da, 0.25 g, 0.25 mmol, 1.0 eq.) were suspended in DCM (3.0 mL). The reaction was cooled to 0 °C before DMAP (6.0 mg, 50 µmol, 0.20 eq.) and EDC (0.10 g, 0.50 mmol, 2.0 eq.) were added successively. The reaction was then stirred for 16 h at room temperature before a saturated $NaHCO_3$ solution (20 mL) was added. The phases were separated, and the aqueous phase was extracted with DCM (3 x 20 mL). The combined organic phases were washed once with citric acid (5 %, 20 mL), dried over Na_2SO_4, filtrated and the solvent was removed under reduced pressure to yield a colorless oil (230 mg, 67 %) which was used without further purification.

^{1}H NMR (300 MHz, $CDCl_3$): δ 7.20 (d, *J* = 8.0 Hz, 4H, **e**), 7.08 (d, *J* = 8.0 Hz, 2H, **d**), 4.32 – 4.11 (m, 4H, 7.2 Hz, **f**), 3.78 – 3.52 (m, 84H, **h**), 2.44 (d, *J* = 6.9 Hz, 4H, **c**), 1.84 (dp, *J* = 13.8, 6.9 Hz, 2H, **b**), 1.48 (d, *J* = 7.1 Hz, 6H, **g**), 0.89 (d, *J* = 6.9 Hz, 12H, **b**).

Synthesis of hydrogel 37b

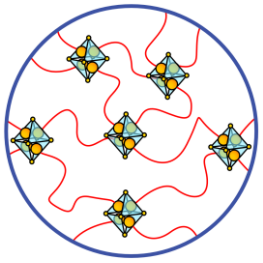

37b

HG_{ibu} with 20 wt%

Cage **2c** (or **MOC_1**) (15 mg, 4.1 µmol, 1.0 eq.) and polymer **36** (11 mg, 8.2 µmol, 2.0 eq.) were dissolved in D_2O (110 µl) and stirred over night at 50 °C in the dark. No gel was formed after 24 h.

HG_{ibu} with 25 wt%

Cage **2c** (or **MOC_1**) (15 mg, 4.1 µmol, 1.0 eq.) and polymer **36** (11 mg, 8.2 µmol, 2.0 eq.) were dissolved in DMSO (80 µl) and stirred for 3 days at 70 °C. No gel was formed.

Synthesis of cross-linker 35

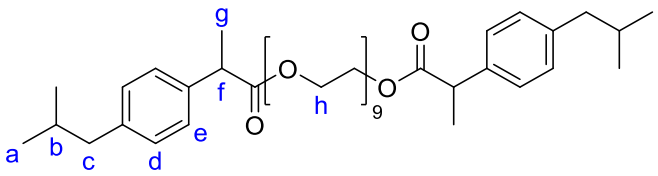

Ibuprofen (0.22 g, 1.1 mmol, 2.0 eq.) and PEG (M_n = 400 Da, 0.21 g, 0.53 mmol, 1.0 eq.) were suspended in DCM (5.0 mL). DMAP (6.0 mg, 50 µmol, 0.10 eq.) and EDC (0.20 g, 1.0 mmol, 2.0 eq.) were added successively. The reaction was then stirred for 23 h at room temperature. The organic phase was transferred into a separation funnel and washed with citric acid (1 %, 3 x 20 mL). The combined aqueous phases were extracted with DCM (3 x 20 mL), dried over Na_2SO_4 and filtrated. The solvent was removed under reduced pressure to yield a colorless oil (230 mg, 67 %) which was used without further purification.

^{1}H NMR (300 MHz, $CDCl_3$): δ (300 MHz, $CDCl_3$): δ 7.20 (d, *J* = 8.0 Hz, 4H, **e**), 7.08 (d, *J* = 8.0 Hz, 2H, **d**), 4.36 – 4.12 (m, 4H, 7.2 Hz, **f**), 3.76 – 3.51 (m, 32H, **h**), 2.44 (d, *J* = 7.2 Hz, 4H, **c**), 1.84 (dt, *J* = 13.8, 6.9 Hz, 2H, **b**), 1.48 (d, *J* = 7.2 Hz, 6H, **g**), 0.89 (d, *J* = 6.9 Hz, 12H, **b**).

Synthesis of of hydrogel **37a**

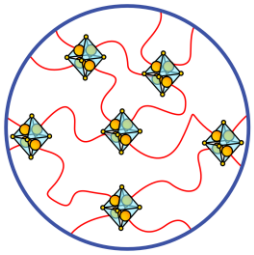

37a

HG_{ibu} with 20 wt%

Cage **2c** (or **MOC_1**) (20 mg, 5.5 µmol, 1.0 eq.) and polymer **35** (8.5 mg, 11 µmol, 2.0 eq.) were dissolved in D_2O (110 µL) and stirred over night at 60 °C in the dark. No gel was formed after 24 h.

Triazole-based linker

Synthesis of 1-adamantanemethanol (**40**)

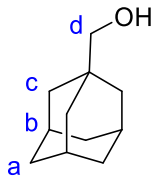

$LiAlH_4$ (0.97 g, 24 mmol, 1.2 eq.) was submitted into a N_2 degassed flask and suspended in THF (80 mL). The reaction was cooled to 0 °C and 1-Adamantanecarboxylic acid **38** (3.9 g, 21 mmol, 1.0 eq.) was added in portions. The suspension was stirred for 15 h at RT before subsequently water (4 mL), NaOH (15 %, 4mL) and water (4 mL) was added. This suspension was stirred for 15 min before it was filtered and dried over Na_2SO_4. The solvent was removed under reduced pressure and the resulting solid was purified by column chromatography CyHex/EE (9/1) to yield 1-adamantanemethanol **40** (3.2 g, 93 %) as a colorless solid.

^{1}H NMR (300 MHz, $CDCl_3$): δ 3.20 (s, 2H, **d**), 1.99 (s, 3H, **b**), 1.80 – 1.46 (m, 12H, **a**, **c**).

Synthesis of 1-adamantylmethyl methanesulfonate (**41**)

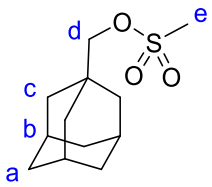

To a solution of alcohol **40** (2.7 g, 16 mmol, 1.0 eq.) and triethylamine (2.5 ml, 18 mmol, 1.1 eq.) MsCl (1.4 ml, 18 mmol, 1.1 eq.) was added at 0 °C. The reaction was warmed to RT and stirred for 6 h before it was neutralized with a 1 M HCl solution. The DCM was removed under reduced pressure and the resulting aqueous phase was extracted with EE (3 x 20mL). The combined organic phases were washed with water (2 x 30 mL), brine (30 mL) and dried over Na_2SO_4. The solvent was removed under reduced pressure to yield **41** (3.9 g, 99 %) as a colorless solid.

^{1}H NMR (300 MHz, $CDCl_3$): δ 3.78 (s, 2H, **d**), 2.99 (s, 3H, **e**), 2.02 (s, 3H, **b**), 1.79 – 1.46 (m, 12H, **a**, **c**).

Synthesis of 1-adamantanylmethylazide (**42**)

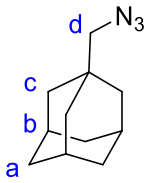

To a solution of 1-adamantylmethyl methanesulfonate **41** (0.49 g, 2.0 mmol, 1.0 eq.) in DMSO (10 ml) was added NaN_3 (0.52 g, 8.0 mmol, 4.0 eq.) and the mixture was heated to 130 °C for 16 h. After full conversion, the reaction was cooled to RT and water (10 mL) was added. The mixture was extracted with EE (2 x 25 mL) and the combined organic phases were washed with water (30 mL) and brine (30 mL), and then dried over Na_2SO_4. After filtration, the solvent was removed under reduced pressure and the crude product was purified by column chromatography to yield azide **42** (0.28 g, 73 %) as a colorless oil.

^{1}H NMR (300 MHz, $CDCl_3$): δ 2.95 (s, 2H, **d**), 2.00 (s, 3H, **b**), 1.77 – 1.49 (m, 12H, **a**, **c**).

Synthesis of bis-propargyl-polyethyleneglycol$_5$ **44**

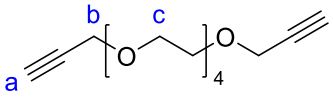

Poly(ethylene glycol) (**43**) (M_n = 200 Da, 0.71 ml, 4.0 mmol, 1.0 eq.) was degassed with N_2 and dissolved in THF (10 mL). The solution was cooled to 0 °C, NaH (0.48 g, 12 mmol, 3.0 eq.) was added and stirred for 1 h. Propargyl bromide (3.6 ml, 24 mmol, 6.0 eq.) was added and the reaction was stirred at RT for 24 h. After completion water (30 mL) was added and THF was removed under reduced pressure. The aqueous phase was extracted with DCM (3 x 25mL), dried over Na_2SO_4, filtered and the solvent was removed under reduced pressure. The crude product was purified by column chromatography CyHex/EE (1/1) and later EE to yield **44** (0.86 g, 80 %) as a light-yellow oil.

^{1}H NMR (300 MHz, $CDCl_3$): δ 4.20 (d, *J* = 2.4 Hz, 4H, **b**), 3.74 – 3.61 (m, 16H, **c**), 2.42 (t, *J* = 2.4 Hz, 2H, **a**).

Synthesis of triazole based linker **45**

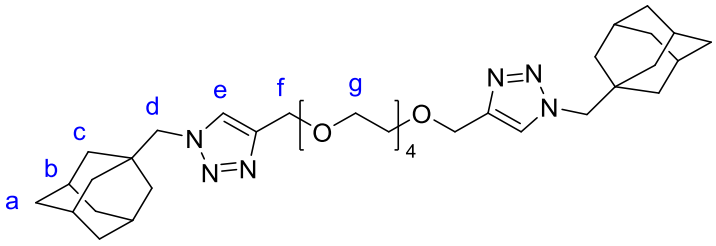

Alkyne **44** (54 mg, 0.20 mmol, 1.0 eq.) and azide **42** (81 mg, 0.42 mmol, 2.1 eq.) were submitted into a schlenk flask under inert conditions and dissolved in THF (4.0 mL). $CuSO_4$ (2.5 mg, 0.16 mmol, 0.80 eq.) in water (1 mL) was added and the blue suspension was stirred vigorously for 30 min. before ascorbic acid (5.9 mg, 30 µmol, 0.15 eq.) was subsequently added, resulting in a yellow suspension. Full conversion was observed after 17 h and DCM (10 mL) was added. The organic phase was washed with $NaHCO_3$ (3 x 10 mL). dried over Na_2SO_4, filtered and the solvent was removed under reduced pressure yielding **45** as a light-yellow oil (0.12 g, 90 %). The product was used without further purification.

^{1}H NMR (300 MHz, $CDCl_3$): δ 7.47 (s, 2H, **e**), 4.70 (s, 4H, **f**), 4.00 (s, 4H, **d**), 3.72 – 3.51 (m, 16H, **g**), 1.99 (s, 6H, **b**), 1.83 – 1.35 (m, 24H, **a**, **c**)

Synthesis of triazole connected cage 46

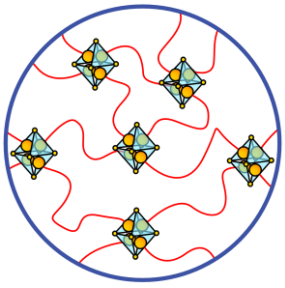

46

TPT (13 mg, 40 µmol, 4.0 eq.) and 2,2'-bipyridine (23 mg, 60 µmol, 6.0 eq.) were submitted into a reaction flask in D_2O (0.25 ml) and stirred for 1 h at 60 °C. The suspension was cooled to RT and linker **45** (triazole) (13 mg, 20 µmol, 2.0 eq.) was added. Stirring was continued over night at 60 °C but no gel was formed.

Adamantyl-based linker

Synthesis of 1,8-bis-(adamantyl-1-methoxy)-octane (51)

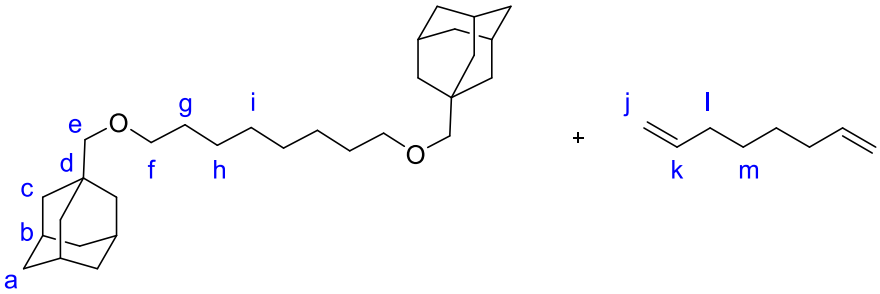

1-adamantanemethanol **40** (0.19 g, 1.1 mmol, 2.1 eq.) was submitted into a N_2 degassed schlenk tube and dissolved in DMF (1.0 mL). The solution was cooled to 0 °C, NaH (46 mg, 1.1 mmol, 2.1 eq.) was added and stirred for 30 min. 1,8-Dibromooctane (0.1 g, 0.55 mmol, 1.0 eq.) was added and the reaction stirred for 18 h at RT before water (5 mL) and EE (5 mL) were added. The phases were separated, and the organic phase was washed with a brine (3 x 20 mL). The combine aqueous phases were extracted with EE (3 x 20 mL), dried over $MgSO_4$ and filtered before the solvent was removed under reduced pressure. The crude product was purified by column chromatography CyHex/EE (99/1) to yield **51** as a colorless oil (0.10 g, 46 %). Main product/side product in a proportion of 2/1.

^{1}H NMR (300 MHz, $CDCl_3$): δ 5.92 – 5.70 (m, 1H, **k**), 5.08 – 4.86 (m, 2H, **j**), 3.36 (t, *J* = 6.6 Hz, 4H, **f**), 2.95 (s, 4H, **e**), 2.10 – 1.98 (m, 2H, **l**), 1.95 (s, 6H, **b**), 1.76 – 1.61 (m, 12H, **c**), 1.53 (s, 16H, **a**, **g**), 1.41 – 1.22 (m, 10H, **h**, **i, m**).

Section for ***HG$_1$***

Synthesis of poly[oxy(ethane-1,2-diyl)]bis(oxy)bis(methylene)bis(4-methyl-2,2'-bipyridine) (**54**)

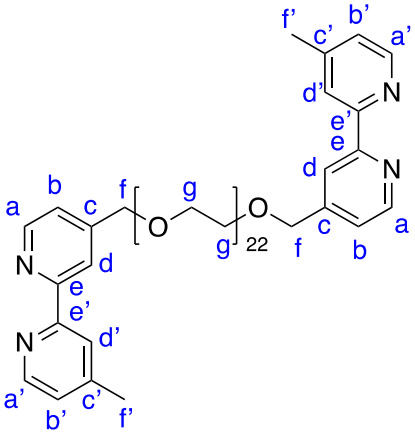

Poly(ethylene glycol) (M_n = 1.000 Da, 0.40 g, 0.40 mmol, 1.0 eq.) was degassed with N_2 and dissolved in THF (15 mL). The solution was cooled to 0 °C, NaH (64 mg, 1.6 mmol, 4.0 eq.) was added and stirred for 1 h. 4-Bromomethyl-4'-methyl-2,2'-bipyridine (**18**) (0.21 g, 0.80 mmol, 2.0 eq.) was added and the reaction stirred at 0 °C for 4 d. H_2O (5 mL) and a saturated NH_4Cl-solution (5 mL) were added to quench the reaction. The phases were separated, and the organic phase was washed with a saturated NH_4Cl-solution (3 x 30 mL). The combined aqueous phases were extracted with DCM (3 x 20 mL). The organic phase was dried over Na_2SO_4, filtered, and the solvent was removed under reduced pressure at 30 °C. The obtained colorless wax was purified by silica gel column chromatography with EE and then DCM/MeOH (9/1) to yield **54** (0.40 g, 74 %) as a colorless oil/wax.

^{1}H NMR (600 MHz, $CDCl_3$): δ 8.61 (d, *J* = 5.0 Hz, 2H, **a**), 8.50 (d, *J* = 4.9 Hz, 2H, **a'**), 8.28 (s, 2H, **d**), 8.20 (s, 2H, **d'**), 7.33 (d, *J* = 5.0 Hz, 2H, **b**), 7.11 (d, *J* = 4.9 Hz, 2H, **b'**), 4.64 (s, 4H, **f**), 3.71 – 3.57 (m, 92H, **g**), 2.41 (s, 6H, **f'**); **^{13}C{^{1}H} NMR** (151 MHz, $CDCl_3$): δ 156.34 (**e**), 155.87 (**e'**), 149.35 (**c**), 149.04 (**a'**), 148.74 (**a**), 148.20 (**c'**), 124.82 (**b'**), 122.07 (**b**), 121.92 (**d'**), 119.41 (**d**), 71.83 (**f**), 70.77 – 70.27 (**g**), 21.26 (**f'**). **IR** (cm^{-1}): 2866.22 (m), 1597.06 (w), 1456.26 (w), 1348.24 (w), 1280.73 (w), 1242.16 (w), 1097.50 (s), 947.05 (m), 840.96 (m); **MALDI**: m/z 1043.742, 1087.777, 1131.810, 1175.844, 1219.876, 1307.942, 1351.975, 1396.009, 1440.042, 1484.076, 1528.109 ($[M+H^+]^+$ for n = 15-25), 1109.757, 1153.798, 1197.828, 1373.962, 1417.996 ($[M+Na^+]^+$ for n = 16-23).

Synthesis of {poly[oxy(ethane-1,2-diyl)]bis(oxy)bis(methylene)bis(4-methyl-2,2'-bipyridine)}-bis(dichloropalladium(II)) (**58**)

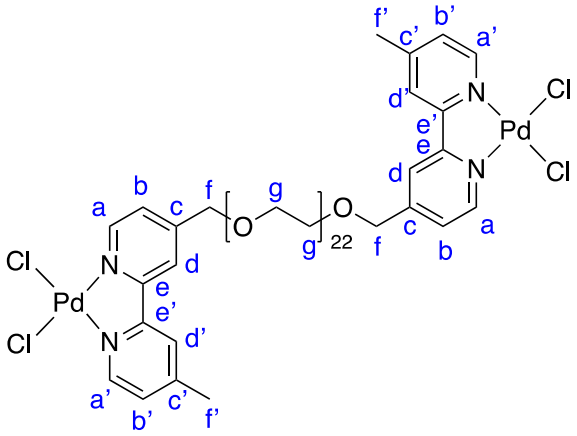

$PdCl_2$ (0.11 g, 0.60 mmol, 2.0 eq.) was suspended in MeCN (15 mL) and **54** (0.40 g, 0.30 mmol, 1.0 eq.) was added. The suspension was heated to 60 °C. After 16 h, the yellow solution was cooled to RT, filtered, and the solvent was removed under reduced pressure, yielding **58** as a yellow oil/wax (0.48 g, 93 %).

^{1}H NMR (600 MHz, $CDCl_3$): δ 8.68 (d, *J* = 5.9 Hz, 2H, **a**), 8.59 (d, *J* = 6.0 Hz, 2H, **a'**), 8.13 (s, 2H, **d**), 8.03 (s, 2H, **d'**), 7.33 (d, *J* = 5.9 Hz, 2H, **b**), 7.15 (d, *J* = 6.0 Hz, 2H, **b'**), 4.79 (s, 4H, **f**), 3.82 – 3.48 (m, 97H, **g**), 2.55 (s, 6H, **f'**); **^{13}C{^{1}H} NMR** (151 MHz, $CDCl_3$): δ 155.43 (**e**), 155.16 (**e'**), 153.97 (**c**), 153.51 (**c'**), 149.34 (**a**), 149.01 (**a'**), 127.35 (**b'**), 125.00 (**d'**), 123.83 (**b**), 121.47 (**d**), 70.74 (**f**), 70.43 (**g**), 21.91 (**f'**); **IR** (cm^{-1}): 2866.22 (m), 1618.28 (w), 1448.54 (w), 1348.24 (w), 1298.09 (w), 1246.02 (w), 1093.64 (s), 947.05 (m), 835.18 (m); **MALDI**: m/z 1131.759, 1219.821, 1263.854, 1307.887 ($[M+H^+]^+$ for n = 9-13 or ($[M-(PdCl_2)_2+H^+]^+$ for n = 16-20), 1368.765, 1492.544, 1546.636, 1678.733, 1713.709, 1765.796 ($[M+NH_4^+]^+$ for n = 14-23).

Synthesis of {poly[oxy(ethane-1,2-diyl)]bis(oxy)bis(methylene)bis(4-methyl-2,2'-bipyridine)}-bis(dinitratopalladium(II)) (**62**)

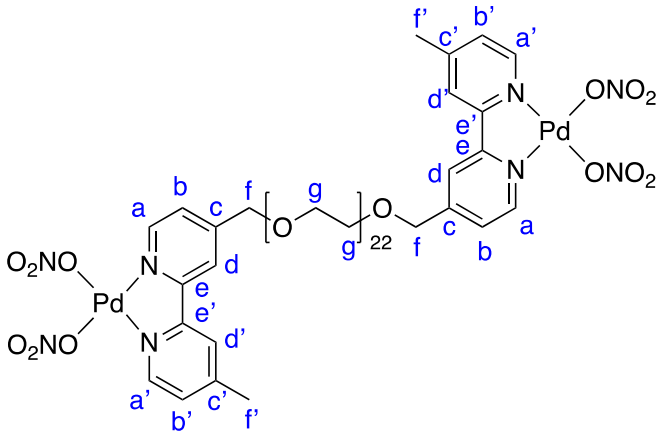

58 (0.48 g, 0.28 mmol, 1.0 eq.) was dissolved in MeCN (24 mL). To the yellow solution, $AgNO_3$ (0.19 g, 1.1 mmol, 4.0 eq.) was added, resulting in an immediate color change to a pale yellow. The solution was stirred in the dark at RT. The conversion was tracked with 1 mL NMR-samples. After 24 h, a full conversion of the starting material was observed, and the AgCl was removed by centrifugation (10.000 rpm, 2 h, at 15 °C). The resulting yellow supernatant was filtered using a syringe filter and transferred into a round-bottom flask. The solvent was removed by rotary evaporation at 30 °C in the dark to yield **62** as a yellow oil/wax (0.48 g, 96 %).

^{1}H NMR (600 MHz, $CDCl_3$): δ 8.24 (d, *J* = 6.1 Hz, 2H, **d**), 8.12 (d, *J* = 6.0 Hz, 2H, **d'**), 8.08 (s, 2H, **a**), 7.98 (s, 2H, **a'**), 7.57 (d, *J* = 6.1 Hz, 2H, **b**), 7.41 (d, *J* = 6.0 Hz, 2H, **b'**), 4.80 (s, 4H, **f**), 3.79 – 3.57 (m, 94H, **g**), 2.60 (s, 6H, **f'**); **^{13}C{^{1}H} NMR** (151 MHz, $CDCl_3$): δ 155.85 (**e**, **e'**), 155.63 (**c**), 155.31 (**c'**), 149.15 (**a'**), 148.85 (**a**), 128.23 (**b'**), 124.80 (**b**, **d'**), 121.12 (**d**), 70.79 (**f**), 70.50 (**g**), 21.78 (**f'**); **IR** (cm^{-1}): 2866.22 (m), 1620.21 (w), 1500.62 (s), 1348.24 (w), 1294.24 (m), 1261.45 (s), 1093.64 (s), 972.12 (s), 835.18 (m); **MALDI**: m/z 1192.527, 1236.569, 1280.596, 1368.649, 1456.706, 1500.733, 1544.762 ($[M+MeCN+H^+]^+$ for n = 7-15 or $[M-2(PdNO_3)_2+NH_4^+]^+$ for n = 18-26), 1654.576, 1742.632, 1874.716, 1918.745, 1961.771, 2005.799 ($[M+Na^+]^+$ for n = 18-26).

Self-assembly of HG_1

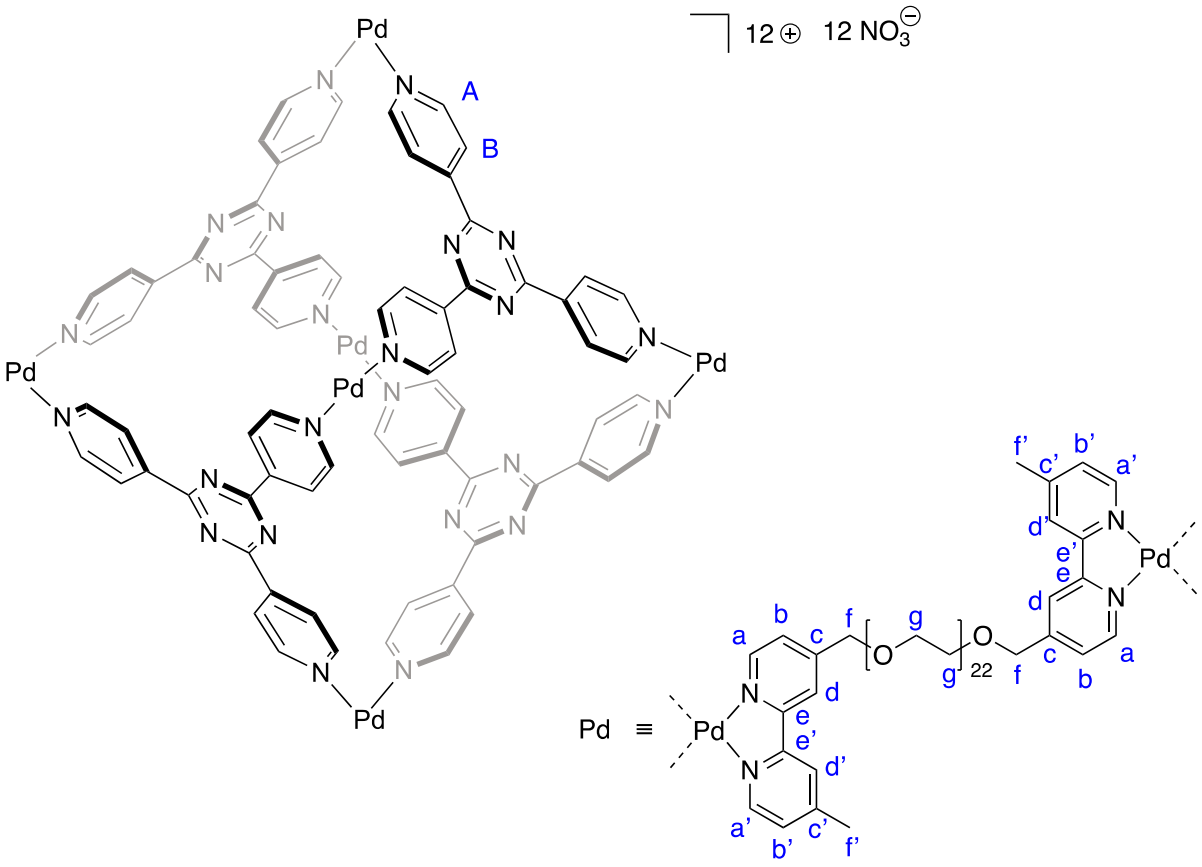

HG_1 with 5 wt%

In a small reaction vial, **62** (9.6 mg, 5.3 µmol, 1.0 eq.) was dissolved in D_2O (200 µL). Then **TPT** (2.2 mg, 7.1 µmol, 1.3 eq.) was added. The reaction was heated to 50 °C and stirred. No hydrogel was formed.

HG_1 with 10 wt%

In a small reaction vial, **62** (22 mg, 12 µmol, 1.0 eq.) was dissolved in D_2O (266 µL). Then **TPT** (5.0 mg, 16 µmol, 1.3 eq.) was added. The reaction was heated to 50 °C and stirred for approximately 1 hour before the reaction formed a firm yellow gel.

HG_1 with 20 wt%

In a small reaction vial, **62** (19 mg, 11 mmol, 1.0 eq.) was dissolved in D_2O (94 µL). Then **TPT** (4.4 mg, 14 mmol, 1.3 eq.) was added. The reaction was heated to 50 °C and stirred for about 2 hours before it formed a firm yellow gel.

If necessary, hydrogels could be purified by rinsing them with small amounts of D_2O. This was, in most cases, enough to obtain a pure sample.

^{1}H NMR (300 MHz, D_2O): δ 9.63 – 9.47 (m, 24H, **A**), 9.11 – 8.87 (m, 24H, **B**), 8.57 – 8.35 (m, 12H, **d**, **d'**), 7.75 – 7.41 (m, 24H, **a**, **a'**, **b**, **b'**), 4.91 (s, 18H, **f**), 3.96 – 3.56 (m, 270H **g**), 2.63 (s, 18, **f'**); **IR** (cm^{-1}): 2868.15 (m), 1620.21 (w), 1573.91 (w), 1519.91 (s), 1336.67 (s), 1089.78 (s), 813.96 (s), 675.09 (s).

*Section for **HG$_3$***

Synthesis of poly[oxy(ethane-1,2-diyl)]bis(oxy)bis(methylene)bis(4-methyl-2,2'-bipyridine) (**55**)

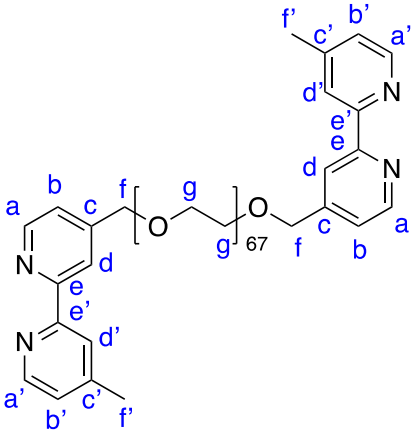

Poly(ethylene glycol) (Mn = 3.000 Da, 0.60 g, 0.20 mmol, 1.0 eq.) was degassed with N_2 and dissolved in DCM (7 mL). The solution was cooled to 0 °C, NaH (32 mg, 0.80 mmol, 4.0 eq.) was added and stirred for 1 h. 4-Bromomethyl-4'-methyl-2,2'-bipyridine (**18**) (0.11 g, 0.40 mmol, 2.0 eq.) was added and the reaction stirred at 0 °C for 4 d. H_2O (5 mL) and a saturated NH_4Cl-solution (5 mL) were added to quench the reaction. The phases were separated, and the organic phase was washed with a saturated NH_4Cl-solution (3 x 30 mL). The combined aqueous phases were extracted with DCM (3 x 20 mL). The organic phase was dried over Na_2SO_4, filtered, and the solvent was removed under reduced pressure at 30 °C. The obtained colorless solid was purified by silica gel column chromatography with EE and then DCM/MeOH (9/1) to yield **55** (0.43 g, 64 %) as a colorless solid.

^{1}H NMR (300 MHz, $CDCl_3$): δ 8.65 (d, *J* = 5.0 Hz, 2H, **a**), 8.55 (d, *J* = 5.0 Hz, 2H, **a'**), 8.35 (s, 2H, **d**), 8.27 (s, 2H, **d'**), 7.39 (d, *J* = 5.1 Hz, 2H, **b**), 7.17 (d, *J* = 5.2 Hz, 2H, **b'**), 4.68 (s, 4H, **f**), 3.64 (d, *J* = 1.4 Hz, 297H, **g**), 2.46 (s, 6H, **f'**); **IR** (cm^{-1}): 2881.65 (m), 1597.06 (w), 1465.90 (w), 1342.46 (m), 1278.81 (w), 1240.23 (w), 1105.21 (s), 960.55 (m), 840.96 (m); **MP.**: 46.5–47.5 °C; **MALDI**: m/z 2782.603, 2826.634, 2870.659, 2914.686, 2958.712, 3002.736, 3046.761, 3090.790, 3222.864, 3398.964, 3575.063, 3619.088, 3707.136, 3751.162, 3795.184, 3839.203, 3883.238, 3927.257 ($[M+Na^+]^+$ for n = 54-80).

Synthesis of {poly[oxy(ethane-1,2-diyl)]bis(oxy)bis(methylene)bis(4-methyl-2,2'-bipyridine)}-bis(dichloropalladium(II)) (59)

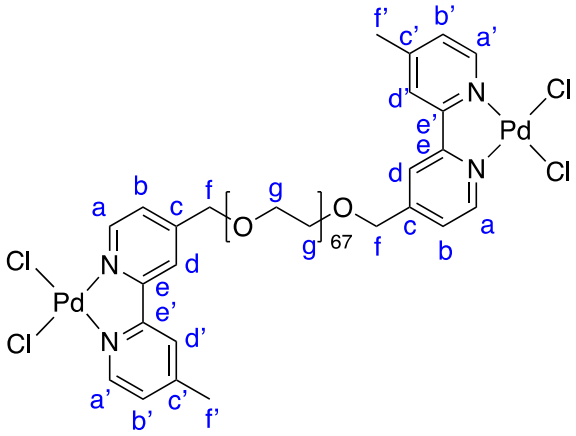

$PdCl_2$ (45 mg, 0.26 mmol, 2.0 eq.) was suspended in MeCN (10 ml) and **55** (0.43 g, 0.13mmol, 1.0 eq.) was added. The suspension was heated to 60 °C. After 16 h, the yellow solution was cooled to RT, filtered, and the solvent was removed under reduced pressure, yielding **59** as a yellow solid (0.45 g, 94 %).

^{1}H NMR (300 MHz, $CDCl_3$): δ 8.93 (d, *J* = 5.4Hz, 2H, **a**), 8.85 (d, *J* = 5.5 Hz, 2H, **a'**), 8.18 (s, 2H, **d**), 8.04 (s, 2H, **d'**), 7.40 (d, *J* = 5.4 Hz, 2H, **b**), 7.23 (d, *J* = 5.5 Hz, 2H, **b'**), 4.83 (s, 4H, **f**), 3.62 (s, 304H, **g**), 2.59 (s, 6H, **f'**); **IR** (cm^{-1}): 2881.65 (m), 1465.90 (w), 1342.46 (m), 1278.81 (w), 1240.23 (w), 1097.50 (s), 960.55 (m), 840.96 (m); **MP.**: 46.5–47.5 °C; **MALDI**: m/z 2870.697, 2914.713, 2958.742, 3002.767, 3046.789, 3091.832, 3135.852, 3265.892, 3309.914, 3531.522, 3665.337, 3840.423, 3924.708, 4012.247 ($[M+Na^+]^+$ for n = 48-70), 3173.747, 3746.912, 3791.896, 3876.141, 3967.781 ($[M+NH_4^+]^+$ for n = 55-73).

Synthesis of {poly[oxy(ethane-1,2-diyl)]bis(oxy)bis(methylene)bis(4-methyl-2,2'-bipyridine)}-bis(dinitratopalladium(II)) (63)

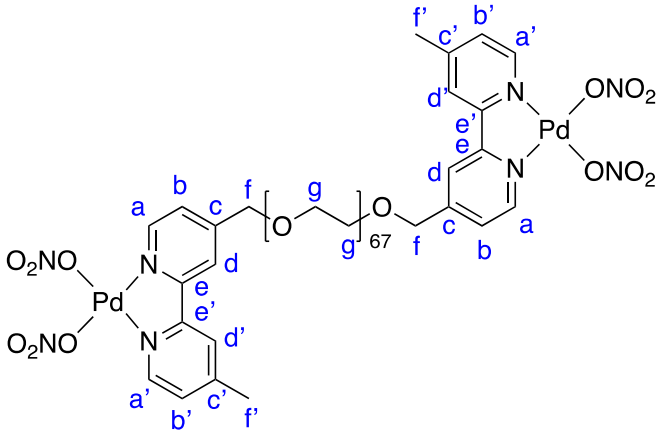

59 (0.45 g, 0.12 mmol, 1.0 eq.) was dissolved in MeCN (20 mL). To the yellow solution, $AgNO_3$ (82 mg, 0.48 mmol, 4.0 eq.) was added, resulting in an immediate color change to a pale yellow. The solution was stirred in the dark at RT. The conversion was tracked with 1 mL NMR-aliquots. After 24 h, a full conversion of the starting material was observed, and the AgCl was removed by centrifugation (10.000 rpm, 2 h, at 15 °C). The resulting yellow supernatant was filtered using a syringe filter and transferred into a round-bottom flask. The solvent was removed by rotary evaporation at 30 °C in the dark to yield **63** as a yellow solid (0.46 g, 99 %).

^{1}H NMR (300 MHz, $CDCl_3$): δ 8.23 (s, 2H, **d**), 8.13 (d, *J* = 5.9 Hz, 2H, **d'**), 8.09 (s, 2H, **a**), 8.05 (d, *J* = 5.9 Hz, 2H, **a'**), 7.57 (d, *J* = 5.9, 2H, **b**), 7.40 (d, *J* = 5.9, 2H, **b'**), 4.81 (s, 4H, **f**), 3.90 – 3.36 (m, 323H, **g**), 2.61 (s, 6H, **f'**). **IR** (cm^{-1}): 2881.65 (m), 1504.48 (w), 1465.90 (w), 1342.46 (m), 1265.30 (m), 1240.23 (w), 1105.21 (s), 960.55 (m), 840.96 (m); **MP.**: 46.5–47.5 °C; **MALDI**: m/z 2826.667, 2914.738, 3002.668, 3046.517, 3090.550, 3134.321, 3178.770, 3399.021, 3530.150, 3574.207, 3618.115, 3706.183, 3746.159, 3794.225, 3838.402, 3877.348, 3921.372 ($[M+H^+]^+$ for n = 45-70).

Self-assembly of HG_3

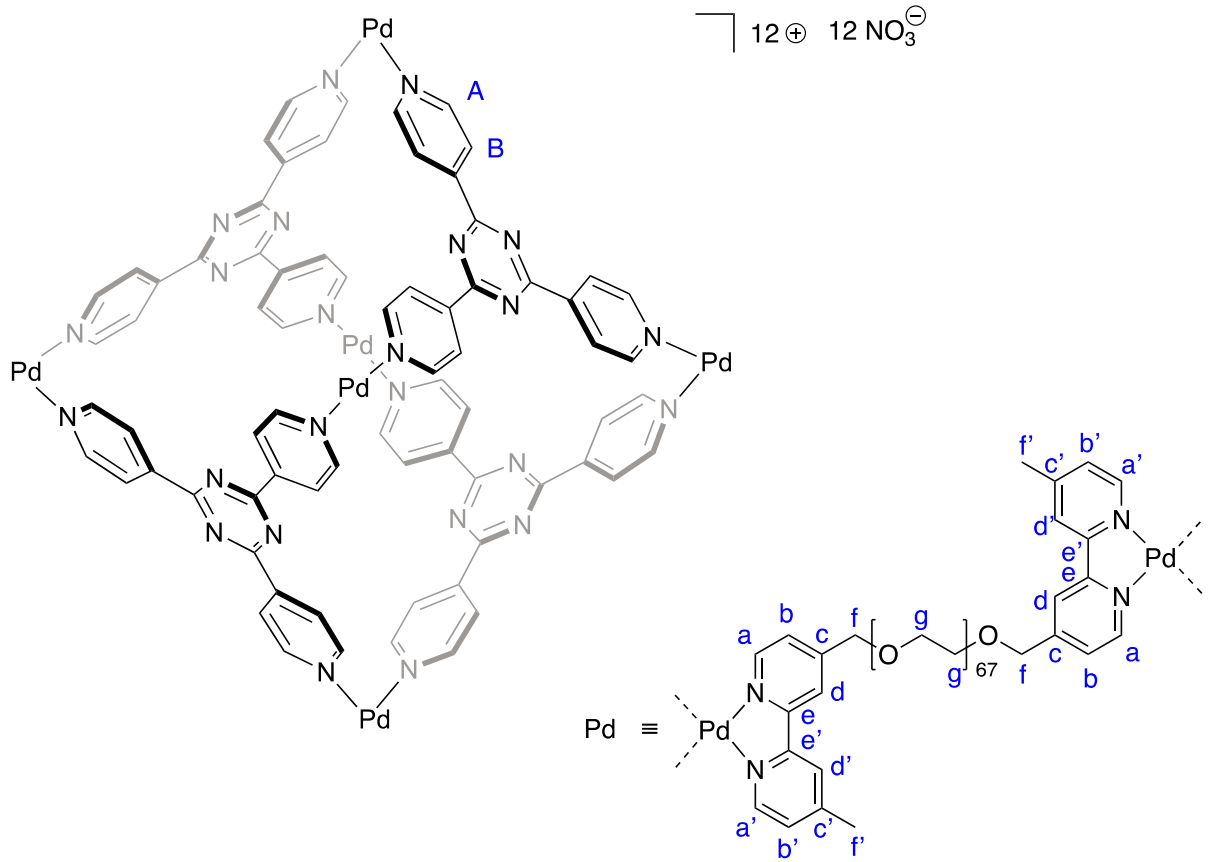

HG_3 with 5 wt%

In a small reaction vial, **63** (20 mg, 5.2 µmol, 1.0 eq.) was dissolved in D_2O (420 µL). Then **TPT** (2.2 mg, 6.9 µmol, 1.3 eq.) was added. The reaction was heated to 60 °C and stirred for more than 12 h. No hydrogel was initially formed. However, after two weeks, a firm yellow hydrogel was formed.

HG_3 with 10 wt%

In a small reaction vial, **63** (20 mg, 5.2 µmol, 1.0 eq.) was dissolved in D_2O (200 µL). Then **TPT** (2.2 mg, 6.9 µmol, 1.3 eq.) was added. The reaction was heated to 60 °C and stirred for approximately 1 h before the reaction formed a firm yellow gel.

HG_3 with 20 wt%

In a small reaction vial, **63** (44 mg, 12 µmol, 1.0 eq.) was dissolved in D_2O (275 µL). Then **TPT** (7.2 mg, 23 µmol, 2.0 eq.) was added. The reaction was heated to 60 °C and stirred for 1 h before the reaction formed a firm yellow gel.

If necessary, hydrogels could be purified by rinsing them with small amounts of D_2O. This was, in most cases, enough to obtain a pure sample.

^{1}H NMR (300 MHz, D_2O): δ 9.66 – 9.41 (m, 24H, **A**), 9.09 – 8.87 (m, 24H, **B**), 8.57 – 8.36 (m, 12H, **d**, **d'**), 7.74 – 7.42 (m, 24H, **a**, **a'**, **b**, **b'**), 4.00 – 3.35 (m, 735H, **g**), 2.64 (s, 18, **f'**); **IR** (cm^{-1}): 2870.08 (w), 1614.42 (w), 1506.41 (w), 1456.26 (w), 1338.60 (m), 1093.62 (s), 947.05 (m), 815.89 (m), 677.01 (m).

*Section for **HG_6***

Synthesis of poly[oxy(ethane-1,2-diyl)]bis(oxy)bis(methylene)bis(4-methyl-2,2'-bipyridine) (**56**)

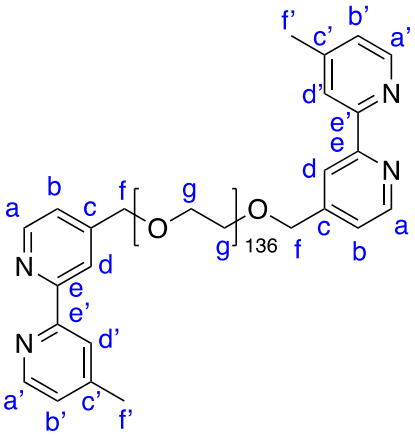

Poly(ethylene glycol) (Mn = 6.000 Da, 1.2 g, 0.20 mmol, 1.0 eq.) was degassed with N_2 and dissolved in DCM (16 mL). The solution was cooled to 0 °C, NaH (40 mg, 1.0 mmol, 5.0 eq.) was added and stirred for 1 h. 4-Bromomethyl-4'-methyl-2,2'-bipyridine (**18**) (0.11 g, 0.41 mmol, 2.1 eq.) was added and the reaction stirred at 0 °C for 3 d. A saturated NH_4Cl-solution (20 mL) was added to quench the reaction.

The phases were separated, and the organic phase was washed with a saturated NH_4Cl-solution (3 x 30 ml). The combined aqueous phases were extracted with DCM (3 x 30 mL). The organic phase was dried over Na_2SO_4, filtered, and the solvent was removed under reduced pressure at 30 °C. After the solvent was removed, the colorless solid was dissolved in small amounts of hot DCM and precipitated into cold diethyl ether. After filtration, **56** was obtained as a colorless solid (1.0 g, 79 %).

^{1}H NMR (600 MHz, $CDCl_3$): δ 8.62 (d, *J* = 4.9 Hz 2H, **a**), 8.51 (d, *J* = 4.9 Hz, 2H, **a'**), 8.29 (s, 2H, **d**), 8.21 (s, 2H, **d'**), 7.34 (d, *J* = 4.9 Hz, 2H, **b**), 7.13 (d, *J* = 4.9 Hz, 2H, **b'**), 4.65 (s, 4H, **f**), 3.77 – 3.46 (m, 575H, **g**), 2.42 (s, 6H, f'). **IR** (cm^{-1}): 2881.65 (m), 1465.90 (w), 1342.46 (m), 1278.81 (m), 1240.23 (w), 1145.72 (m), 1099.43 (s), 1060.85 (m), 960.55 (m), 840.96 (m); **MP.**: 52.4–52.7 °C; **MALDI**: m/z 5735.4, 5823.6, 5867.9, 5911.8, 5955.6, 5999.7, 6044.1, 6087.9, 6131.9, 6176.0, 6220.0, 6264.1, 6352.1, 6484.5, 6881.2, 7145.7, 7234.1, 7277.8, 7366.0, 7410.3, 7454.3, 7498.3, 7542.3, 7586.4, 7630.5, 7674.6, 7718.7, 7762.5, 7806.1 ($[M+Na^+]^+$ for n = 121-168).

Synthesis of {poly[oxy(ethane-1,2-diyl)]bis(oxy)bis(methylene)bis(4-methyl-2,2'-bipyridine)}-bis(dichloropalladium(II)) (60)

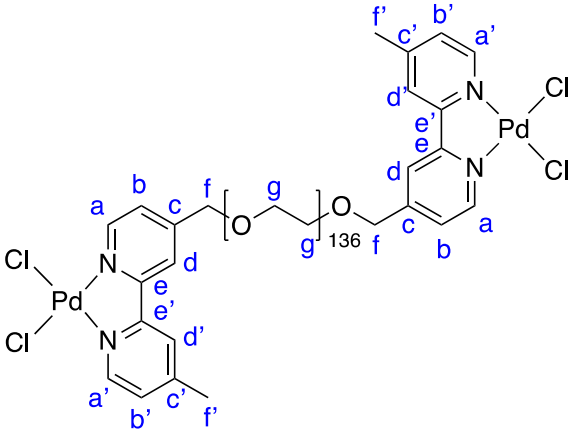

$PdCl_2$ (50 mg, 0.28 mmol, 2.0 eq.) was suspended in MeCN (25 mL) and **56** (0.90 g, 0.14 mmol, 1.0 eq.) was added. The suspension was heated to 50 °C. After 19 h, the yellow solution was cooled to RT, filtered, and the solvent was removed under reduced pressure, yielding **60** as a yellow solid (0.90 g, 95 %).

^{1}H NMR (600 MHz, $CDCl_3$): δ 8.97 (d, *J* = 5.9 Hz, 2H, **a**), 8.89 (d, *J* = 5.8 Hz, 2H, **a'**), 8.15 (s, 2H, **d**), 8.02 (s, 2H, **d'**), 7.40 (d, *J* = 5.9 Hz, 2H, **b**), 7.24 (d, *J* = 5.8 Hz, 2H, **b'**), 4.80 (s, 4H, **f**), 3.82 – 3.45 (m, 782H, **g**), 2.58 (s, 6H, **f'**); **IR** (cm^{-1}): 2877.79 (m), 1465.90 (w), 1342.46 (s), 1278.81 (w), 1240.23 (w), 1145.72 (m), 1097.50 (s), 1060. 85 (m), 960.55 (m), 840.96 (m); **MP.**: 52.2-53.3 °C; **MALDI**: m/z 6127.7, 6219.3,

6262.5, 6347.9, 6484.0, 6527.6, 6703.3, 6968.3, 7100.6, 7232.0, 7320.5, 7407.6, 7451.8, 7539.4 ($[M+Na^+]^+$ for n = 122-153).

Synthesis of {poly[oxy(ethane-1,2-diyl)]bis(oxy)bis(methylene)bis(4-methyl-2,2'-bipyridine)}-bis(dinitratopalladium(II)) (64)

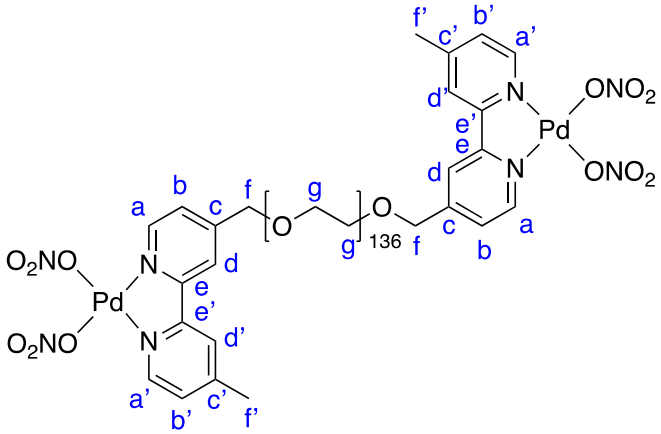

60 (0.85 g, 0.13 mmol, 1.0 eq.) was dissolved in MeCN (30 mL). To the yellow, solution $AgNO_3$ (91 mg, 0.53 mmol, 4.0 eq.) was added, resulting in an immediate color change to a pale yellow. The solution was stirred in the dark at RT. The conversion was tracked with 1 mL NMR-aliquots. After 16 h, full conversion of the starting material was observed, and the AgCl was removed by centrifugation (10.000 rpm, 2 h, at 15 °C). The resulting yellow supernatant was filtered using a syringe filter and transferred into a round-bottom flask. The solvent was removed by rotary evaporation at 30 °C in the dark to yield **64** as a yellow solid (0.84 g, 92 %).

^{1}H NMR (600 MHz, $CDCl_3$): δ 8.20 (s, 2H, **d**), 8.17 (d, *J* = 6.0 Hz, 2H, **a**), 8.09 (d, *J* = 6.0 Hz, 2H, **a'**), 8.05 (s, 2H, **d'**), 7.54 (d, *J* = 6.0 Hz, 2H, **b**), 7.40 (d, *J* = 6.0 Hz, 2H, **b'**), 4.79 (s, 4H, **f**), 3.80 – 3.48 (m, 690H, **g**), 2.61 (s, 6H, **f'**); **IR** (cm^{-1}): 2881.65 (m), 1504.48 (w), 1465.90 (w), 1342.46 (m), 1278.81 (m), 1240.23 (w), 1099.43 (s), 960.55 (m), 840.96 (m); **MP.**: 52.1-52.9 °C; **MALDI**: m/z 6082.9, 6127.3, 6215.1, 6303.3, 6347.6, 6391.3, 6436.1, 6479.7, 6523.8, 6567.6, 6788.6, 7009.2, 7097.5, 7141.2, 7186.0, 7229.5, 7273.9, 7317.9, 7361.6, 7406.1, 7450.1, 7493.7, 7538.3, 7582.3, 7626.4, 7669.5 ($[M+H^+]^+$ for n = 118-155).

Self-assembly of of HG_6

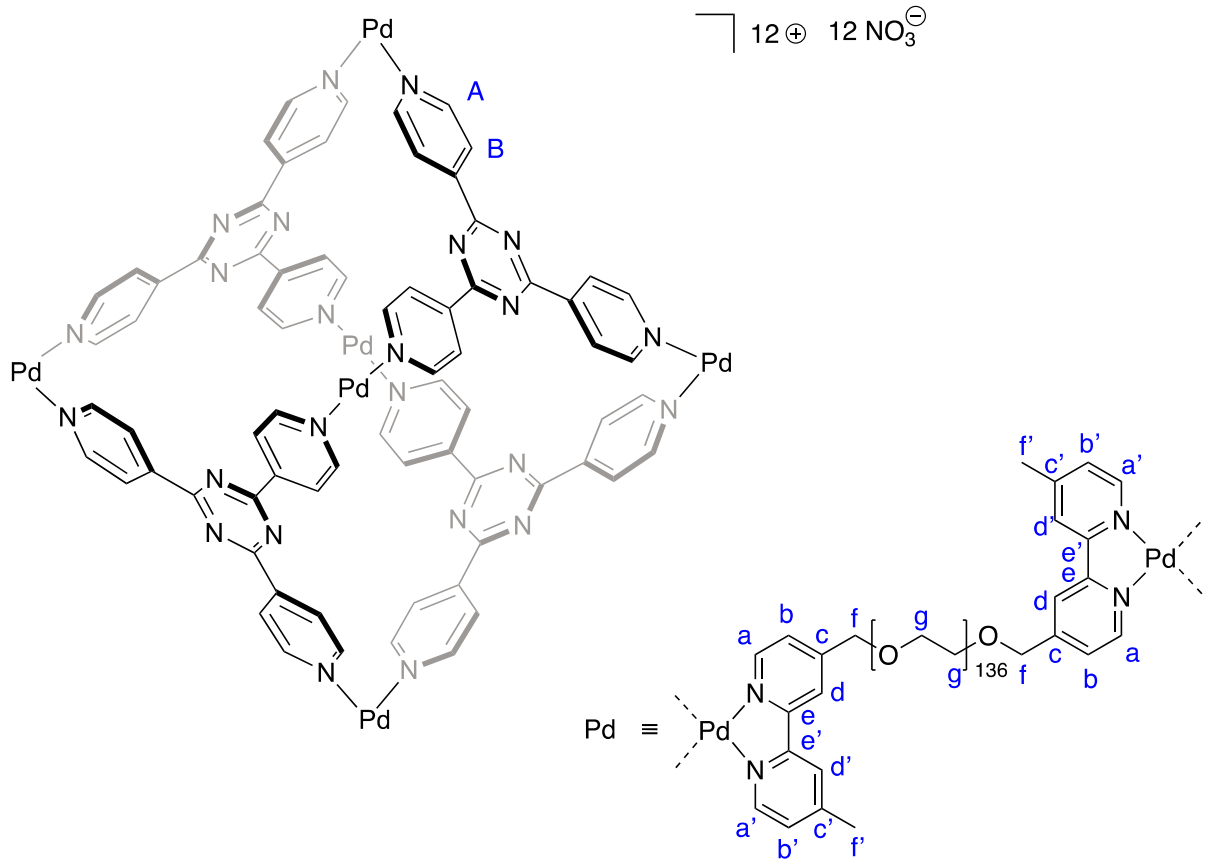

HG_6 with 5 wt%

In a small reaction vial, **64** (20 mg, 2.9 µmol, 1.0 eq.) was dissolved in D_2O (402 µL). Then **TPT** (1.2 mg, 3.9 µmol, 1.3 eq.) was added. The reaction was heated to 70 °C and stirred over night before the reaction formed a firm yellow gel.

HG_6 with 10 wt%

In a small reaction vial, **64** (20 mg, 2.9 µmol, 1.0 eq.) was dissolved in D_2O (191 µL). Then **TPT** (1.2 mg, 3.9 µmol, 1.3 eq.) was added. The reaction was heated to 70 °C and stirred for 4 h before the reaction formed a firm yellow gel.

HG_6 with 20 wt%

In a small reaction vial, **64** (40 mg, 5.9 µmol, 1.0 eq.) was dissolved in D_2O (170 µL). Then **TPT** (2.4 mg, 7.9 µmol, 1.3 eq.) was added. The reaction was heated to 70 °C and stirred for 4 h before the reaction formed a firm yellow gel.

If necessary, hydrogels could be purified by rinsing them with small amounts of D_2O. This was, in most cases, enough to obtain a pure sample.

^{1}H NMR (300 MHz, D_2O): δ 9.49 (s, 24H, **A**), 9.14 – 8.89 (m, 24H, **B**), 8.55 – 8.37 (m, 12H, **d**, **d'**), 7.71 – 7.41 (m, 24H, **a**, **a'**, **b**, **b'**), 4.02 – 2.91 (m, 1462H, **g**), 2.63 (s, 18, **f'**); **IR** (cm^{-1}): 2881.65 (w), 1614.42 (w), 1465.90 (w), 1342.46 (m), 1278.81 (w), 1242.16 (w), 1101.35 (s), 962.48 (m).

*Encapsulations with **HG$_1$***

General procedure A for hydrogel encapsulation

For the encapsulation of the guests, a 10 wt% hydrogel was synthesized as described above. Approximately 80 mg of the hydrogel was suspended in 500 µL D_2O and 1.0 eq. (in relation to the used dinitratopalladium-complex) of the guest was added. The reaction was stirred overnight at 50 °C. ^{1}H NMR spectra were measured, and the yield of the encapsulation was determined by the comparison of the host and the guest.

General procedure B for hydrogel encapsulation

For the encapsulation of the guests, a 10 wt% hydrogel was prepared as described above, but 0.66 eq. (in relation to the used dinitratopalladium-complex) of the guest were added instantly. The reaction was stirred overnight at 60 °C. ^{1}H NMR spectra were measured, and the yield of the encapsulation was determined by the comparison of the host and the guest.

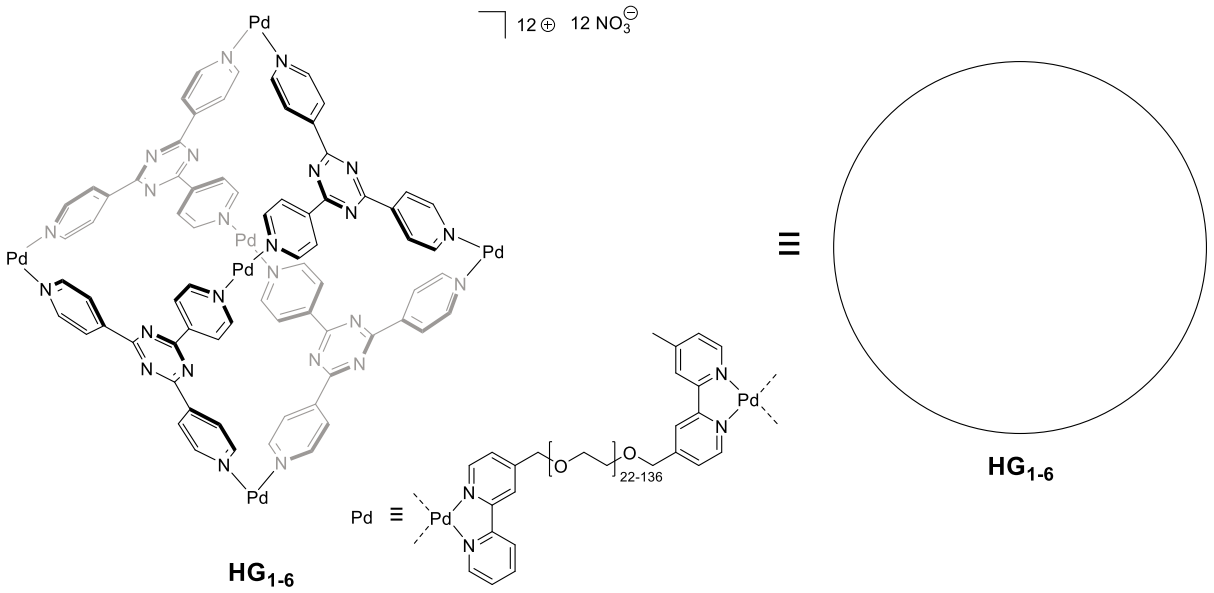

For the following encapsulation experiments cage **HG$_{1-6}$** will be depicted as shown above plus its corresponding guest.

Guest encapsulation with HG_1

HG_1•(ibuprofen)$_2$

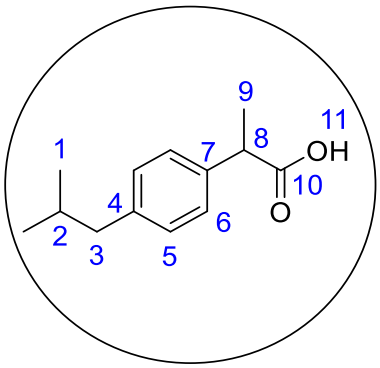

HG_1•(ibuprofen)$_2$

The ^{1}H NMR revealed that per cage two molecules of ibuprofen can be encapsulated. The encapsulation was quantitative.

^{1}H NMR (600 MHz, D_2O): δ 9.62 (s, 24H, **A**), 8.98 (s, 24H, **B**), 8.55 – 8.35 (m, 12H, **d**, **d'**), 7.75 – 7.41 (m, 24H, **a**, **a'**, **b**, **b'**), 5.22 (s, 4H, **6**), 4.79 (s, 4H, **f**), 4.46 (s, 4H, **5**), 3.91 – 3.53 (m, 320H, **g**), 2.86 (s, 2H, **8**), 2.64 (s, 18H, **f'**), 1.21 – 1.06 (m, 4H, **3**), 0.42 (s, 6H, **9**), 0.13 (s, 2H, **2**), -0.66 (s, 12H, **1**).

*Encapsulations with **HG₃***

Guest encapsulation with HG₃

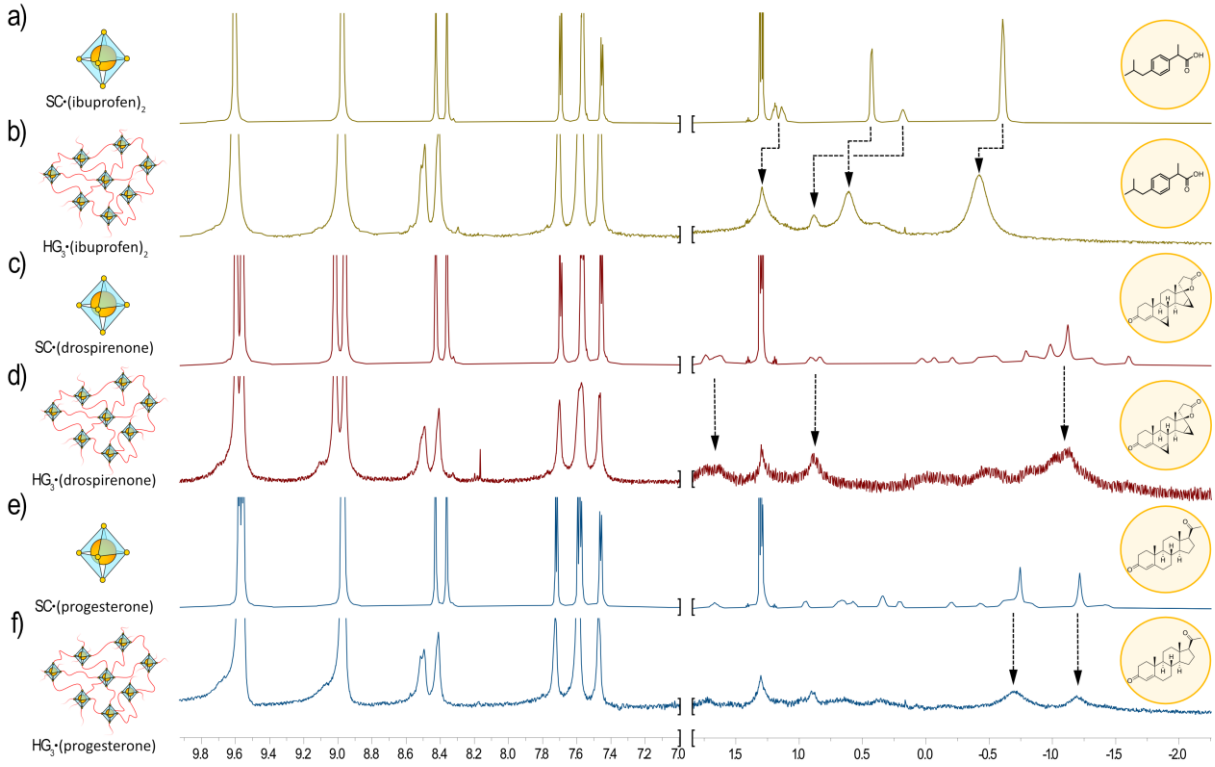

*Figure 77: ^{1}H NMR (600 MHz, D_2O) of different encapsulated guests. (a) Reference cage **SC•**(ibuprofen)$_2$, (b) 10 wt % hydrogel **HG₃•**(ibuprofen)$_2$; (c) reference cage **SC•**(drospirenone); (d) 10 wt % hydrogel **HG₃•**(drospirenone), (e) reference cage **SC•**(progesterone), (f) 10 wt % hydrogel **HG₃•**(progesterone). The chemical shift of the encapsulated guests in **HG₃** is in all cases nearly identical to our previously reported reference cage **SC.***

HG₃•(ibuprofen)$_2$

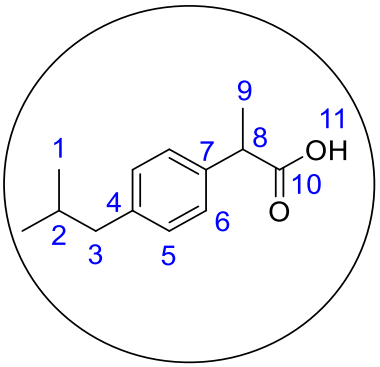

HG$_3$•(ibuprofen)$_2$

The ^{1}H NMR revealed that per cage two molecules of ibuprofen are encapsulated. The encapsulation was quantitative.

^{1}H NMR (600 MHz, D_2O): δ 9.60 (s, 24H, **A**), 8.98 (s, 24H, **B**), 8.68 – 8.30 (m, 12H, **d**, **d'**), 7.81 – 7.29 (m, 24H, **a**, **a'**, **b**, **b'**), 5.56 (s, 4H, **6**), 3.93 – 3.50 (m, 970H, **g**), 2.98 (s, 2H, **8**), 2.64 (s, 18H, **f'**), 1.29 (s, 4H, **3**), 0.88 (s, 2H, **2**), 0.61 (s, 6H, **9**), -0.42 (s, 12H, **1**).

HG_3•(progesterone)

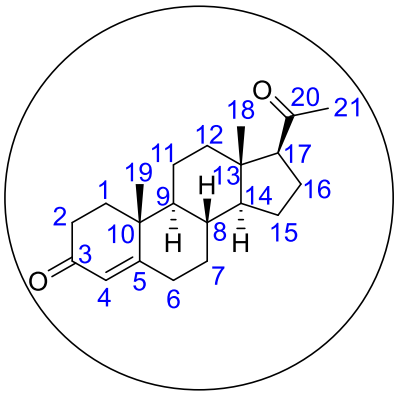

HG_3•(progesterone)

The ^{1}H NMR revealed that per cage one molecule of progesterone are encapsulated. The encapsulation was quantitative.

^{1}H NMR (600 MHz, D_2O): δ 9.57 (s, 24H, **A**), 8.97 (s, 24H, **B**), 8.56 – 8.37 (m, 12H, **d**, **d'**), 7.80 – 7.41 (m, 24H, **a**, **a'**, **b**, **b'**), 3.96 – 3.41 (m, 700H, **g**), 2.64 (s, 18H, **f'**), 2.16 (s, 3H, **21**, cannot be assigned unambiguously), 1.30 (s, 3H, cannot be assigned unambiguously), -0.70 (s, 8H, **11**, **12**, **19**, cannot be assigned unambiguously), -1.19 (s, 5H, **9**, **18**, cannot be assigned unambiguously).

HG_3•(drospirenone)

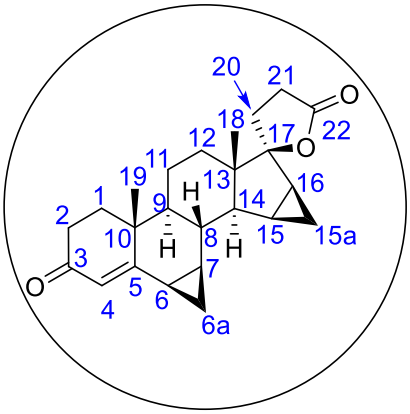

HG_3•(drospirenone)

The ^{1}H NMR revealed that per cage one molecule of drospirenone is encapsulated. The encapsulation was quantitative.

^{1}H NMR (300 MHz, D_2O): δ 9.67 – 9.46 (m, 24H, **A**), 9.17 – 8.88 (m, 24H, **B**), 8.58 – 8.36 (m, 12H, **d**, **d'**), 7.81 – 7.37 (m, 24H, **a**, **a'**, **b**, **b'**), 3.95 – 3.50 (m, 960H, **g**), 2.63 (s, 18H, **f'**), 2.35 (s, 1H, **21,** cannot be assigned unambiguously), 1.63 (s, 3H, **2**, **21**), 1.30 (s, 2H, cannot be assigned unambiguously), 0.89 (s, 2H, **20**, cannot be assigned unambiguously), 0.13 – -1.30 (m, 23H, 6a, 15a, 18, 19, cannot be assigned unambiguously).

*Encapsulations with **HG$_6$***

Guest encapsulation with **HG$_6$**

HG$_6$•(ibuprofen)$_2$

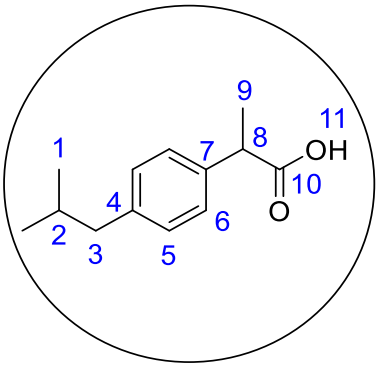

HG$_6$•(ibuprofen)$_2$

The ^{1}H NMR revealed that per cage two molecules of ibuprofen are encapsulated. The encapsulation was quantitative.

^{1}H NMR (300 MHz, D_2O): δ 9.62 (s, 24H, A), 8.99 (s, 24H, **B**), 8.73 – 8.34 (m, 12H, **d**, **d'**), 7.92 – 7.35 (m, 24H, **a**, **a'**, **b**, **b'**), 5.63 (s, 4H, **6**), 4.18 – 3.35 (m, 1712H, **g**), 3.01 (s, 2H, **8**), 2.65 (s, 18H, **f'**), 1.31 (s, 4H, **3**), 0.66 (s, 6H, **9**), 0.40 (s, 2H, **2**), -0.38 (s, 12H, **1**).

General sonication procedure

Sonication experiments were performed with a Vibra-Cell VCX 500 immersion probe sonicator from Sonics & Materials with a frequency of 20 kHz, an amplitude of 30 %, and a full wave probe (13 mm). In each sonication experiment, a 10 wt% hydrogel was submerged in H_2O, degassed with N_2 in a Suslick vessel, and cooled with an ice-water bath. A pulse sequence of 1 s “on” and 1 s “off” (or 1 s “on” and 2 s “off”) was chosen and is stated for every experiment. Consequently, the effective sonication time was either 1/2 or 1/3 of the duration of the sonication experiment. The solution was exposed to N_2 during the whole sonication. For each experiment, only the effective sonication time is reported.

Release

Sonication of HG_1

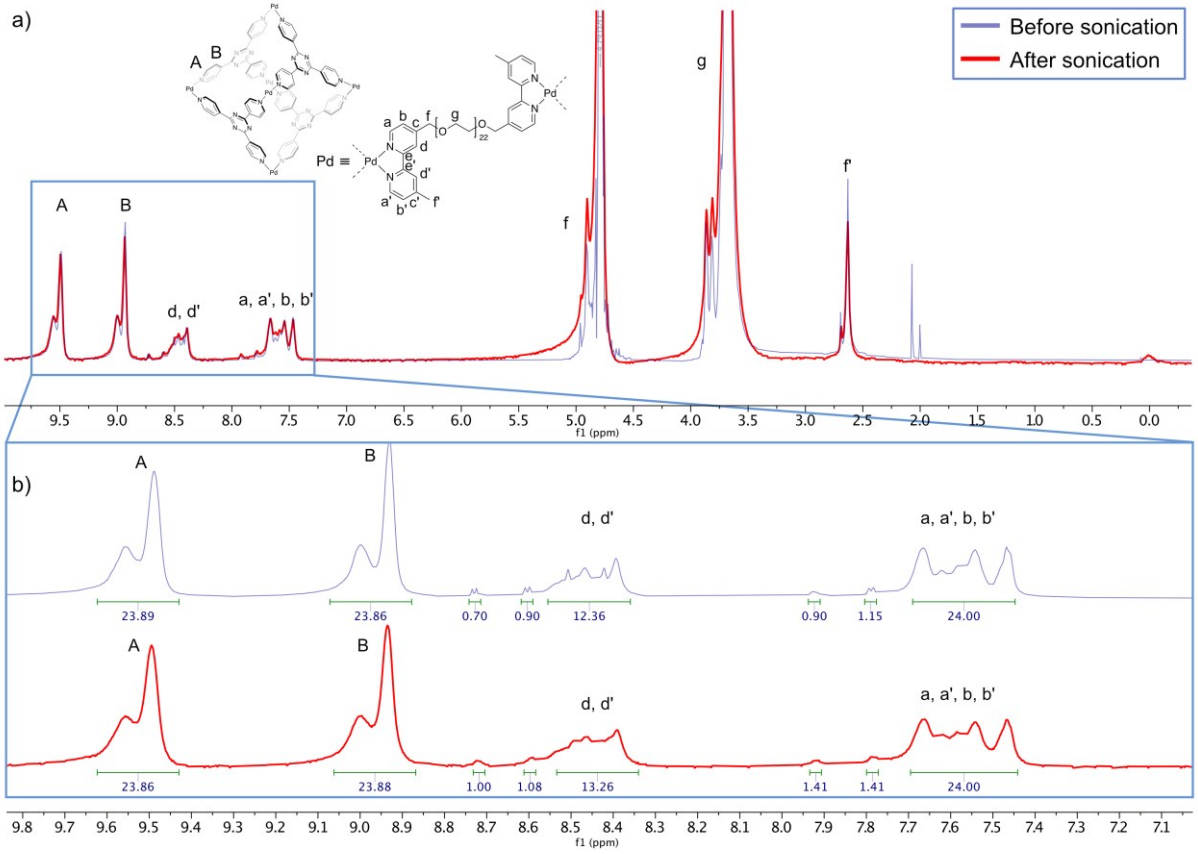

*Figure 78: ^{1}H NMR (D_2O) of hydrogel **HG_1** before (blue) and after sonication (red). The concentration during the sonication was 2.5 mg mL^{-1}. The reaction was sonicated for 3 h (1 s on, 1 s off). A small amount of defragmentation could be observed for this hydrogel. The full spectra are reproduced in the “Spectra encapsulation and sonication” section.*

Sonication of $HG_1 \bullet (ibuprofen)_2$

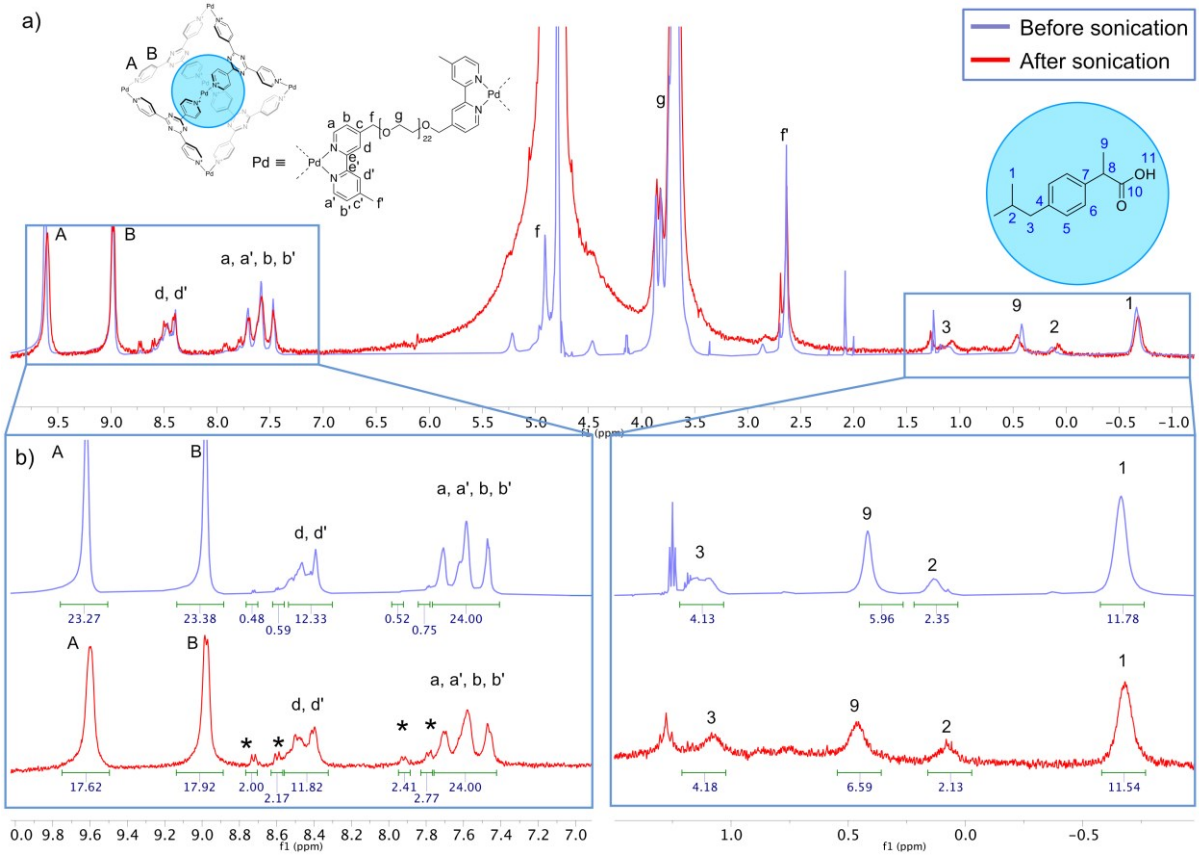

*Figure 79: ^1H NMR (D_2O) of hydrogel **$HG_1 \bullet (ibuprofen)_2$** before (blue) and after sonication (red). The concentration during the sonication was 2.5 mg mL^{-1}. The reaction was sonicated for 2 h (1 s on, 2 s off). A small amount of defragmentation could be observed but no observable release was achieved for this hydrogel. The full spectra are reproduced in the "Spectra encapsulation and sonication" section.*

Sonication of HG_3

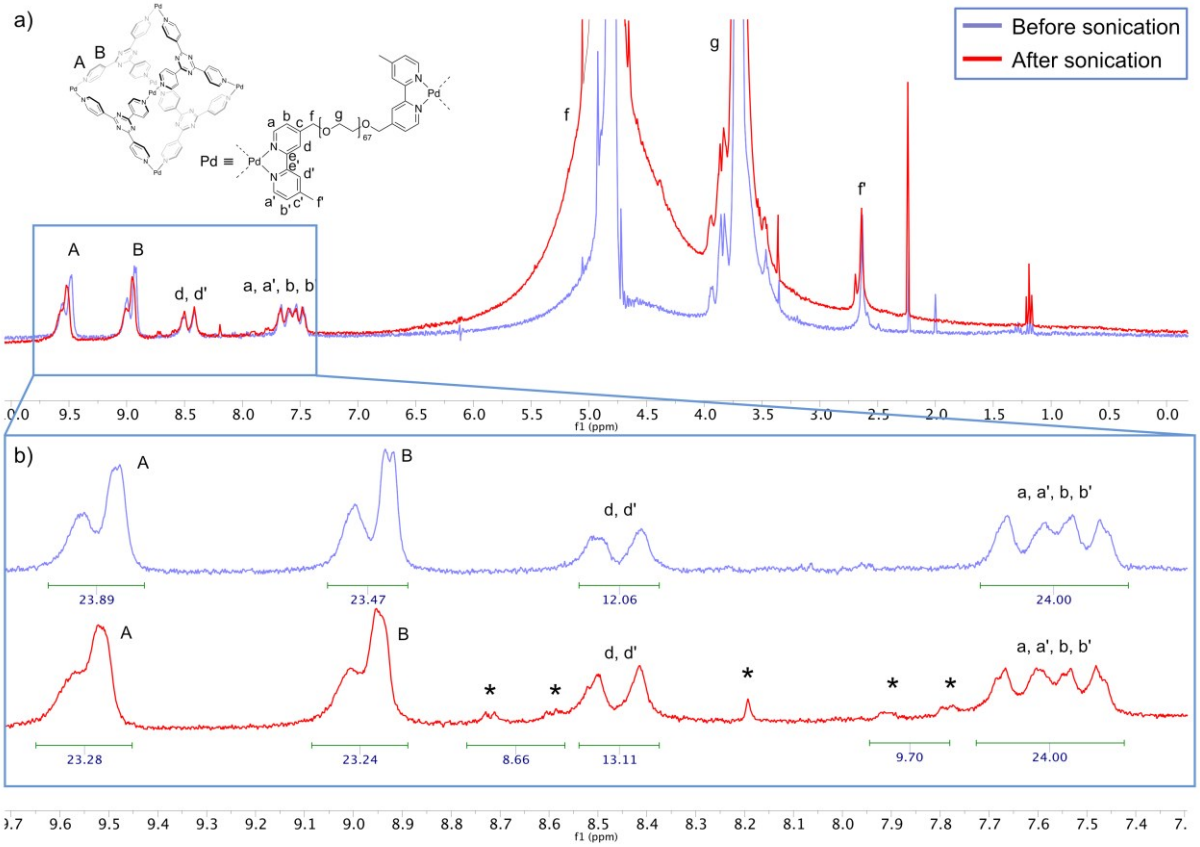

*Figure 80: ^1H NMR (D_2O) of hydrogel Sonication of **HG_3** before (blue) and after sonication (red). The concentration during the sonication was 2.5 mg/ml. The reaction was sonicated for 2 h (1 s on, 1 s off). Defragmentation could be observed. The full spectra are reproduced in the "Spectra encapsulation and sonication" section.*

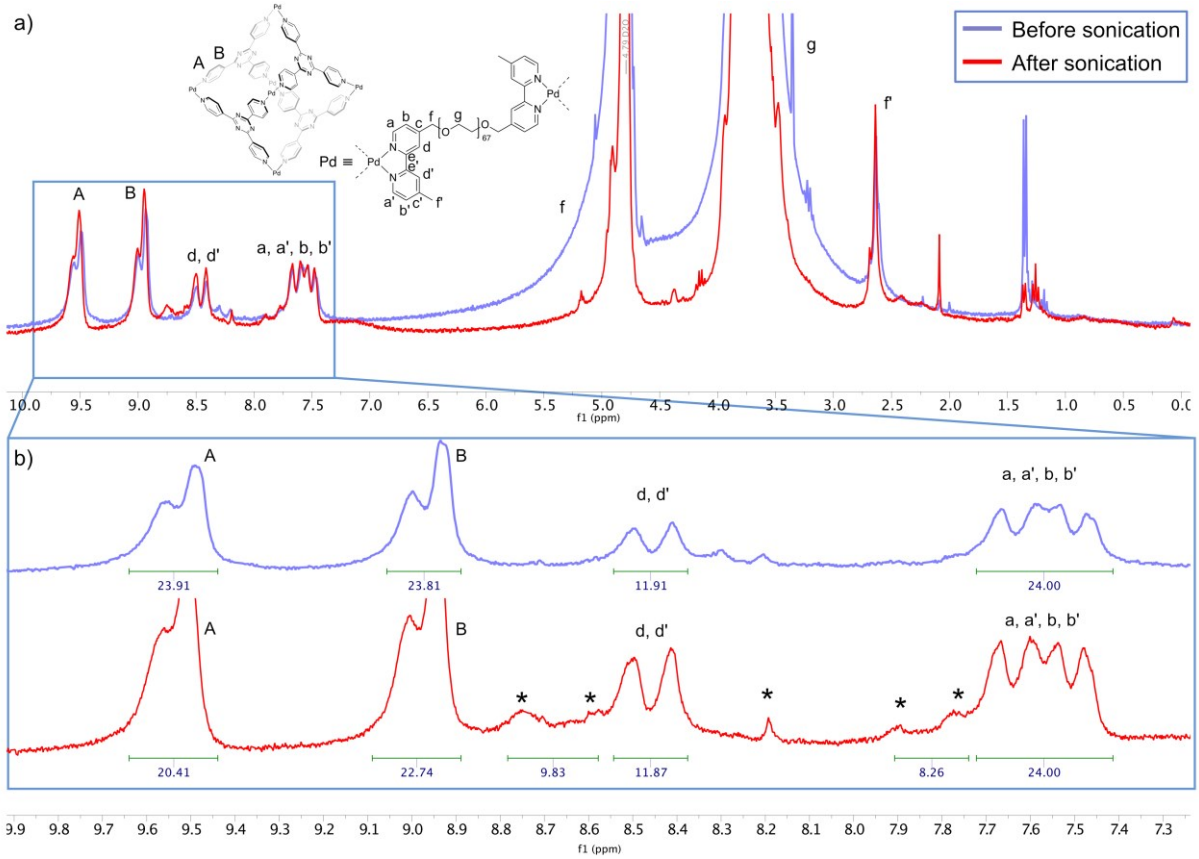

*Figure 81: ^{1}H NMR (D_2O) of hydrogel **HG_3** before (blue) and after sonication (red). The concentration during the sonication was 1.0 mg mL^{-1}. The reaction was sonicated for 3 h. (1 s on, 1 s off). Defragmentation could be observed. The single spectra are reproduced in the "Spectra encapsulation and sonication" section.*

Sonication of HG_3•(ibuprofen)$_2$

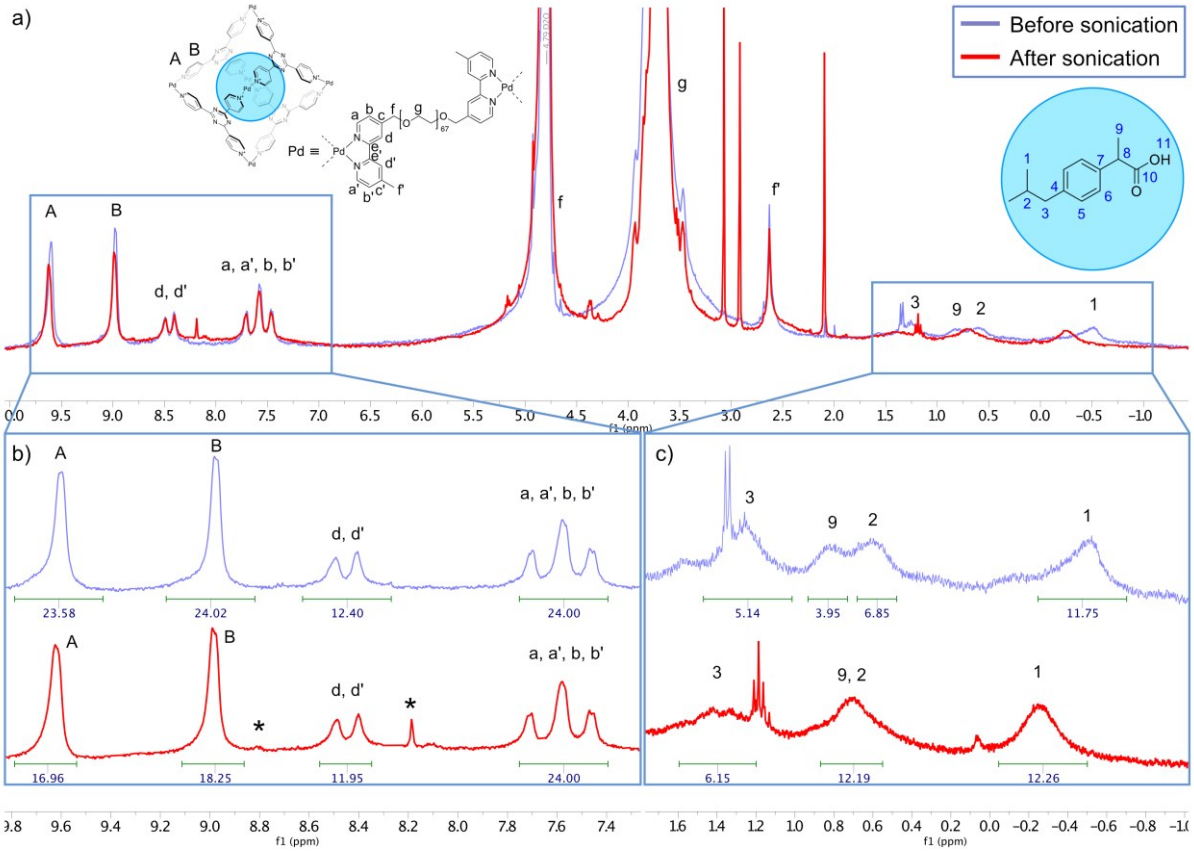

*Figure 82: ^{1}H NMR (D_2O) of hydrogel **HG_3•(ibuprofen)$_2$** before (blue) and after sonication (red). The concentration during the sonication was 1.0 mg mL^{-1}. The reaction was sonicated for 3 h (1 s on, 1 s off). A small amount of defragmentation could be observed but guest release could not be observed. The single spectra are reproduced in the "Spectra encapsulation and sonication" section.*

Sonication of HG_6

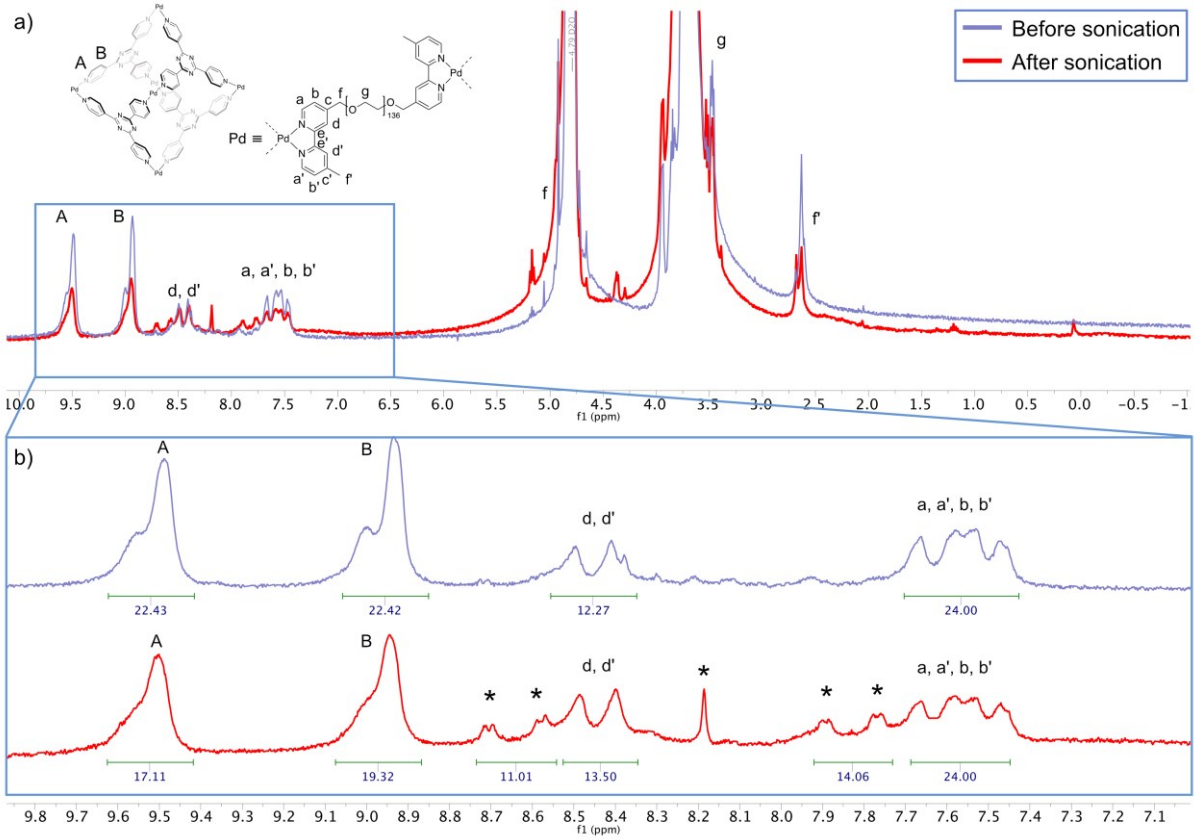

*Figure 83: ^1H NMR (D_2O) of hydrogel **HG_6** before (blue) and after sonication (red). The concentration during the sonication was 1.0 mg mL^{-1}. The reaction was sonicated for 3 h (1 s on, 1 s off). Defragmentation could be observed. The single spectra are reproduced in the "Spectra encapsulation and sonication" section.*

Sonication of HG_6•(ibuprofen)$_2$

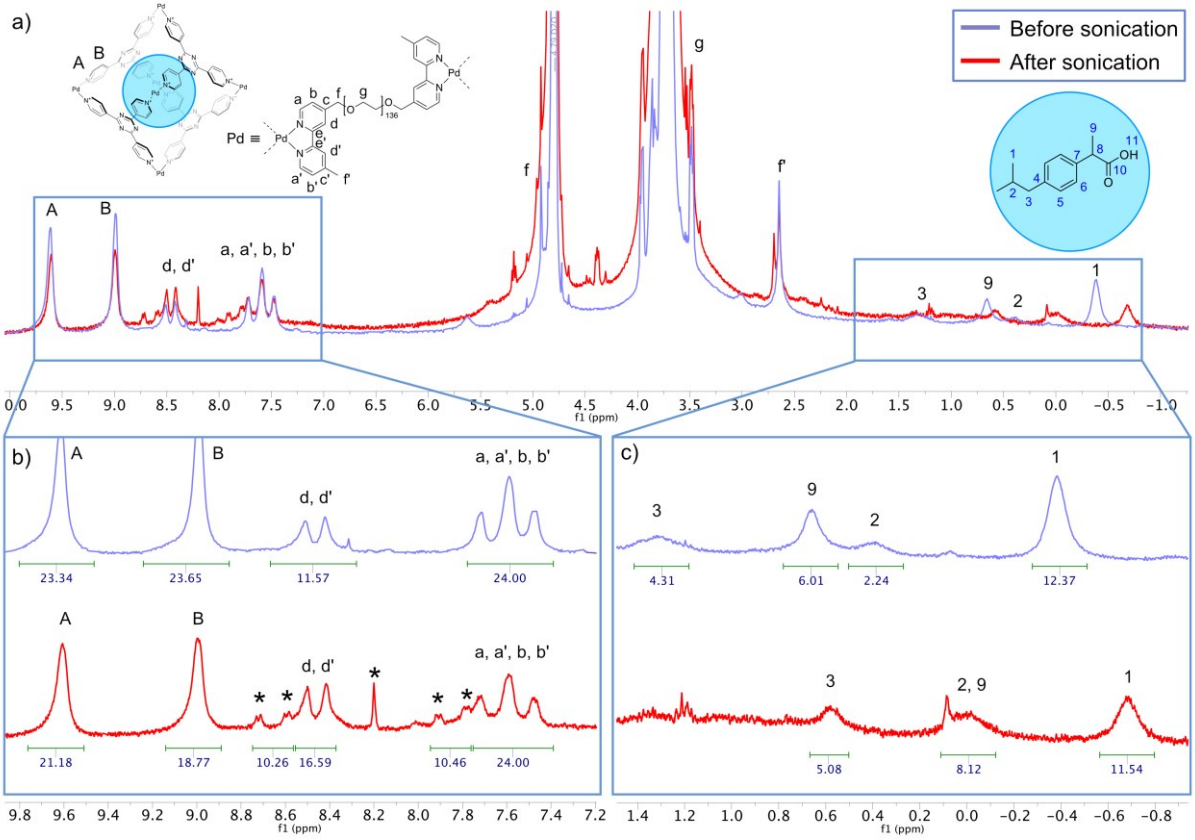

*Figure 84: ^{1}H NMR (D_2O) of hydrogel **HG_6•(ibuprofen)$_2$** before (blue) and after sonication (red). The concentration during the sonication was 1.0 mg mL^{-1}. The reaction was sonicated for 3 h (1 s on, 1 s off). Defragmentation could be observed but no guest release. The single spectra are reproduced in the "Spectra encapsulation and sonication" section.*

Comparison of all sonication experiments

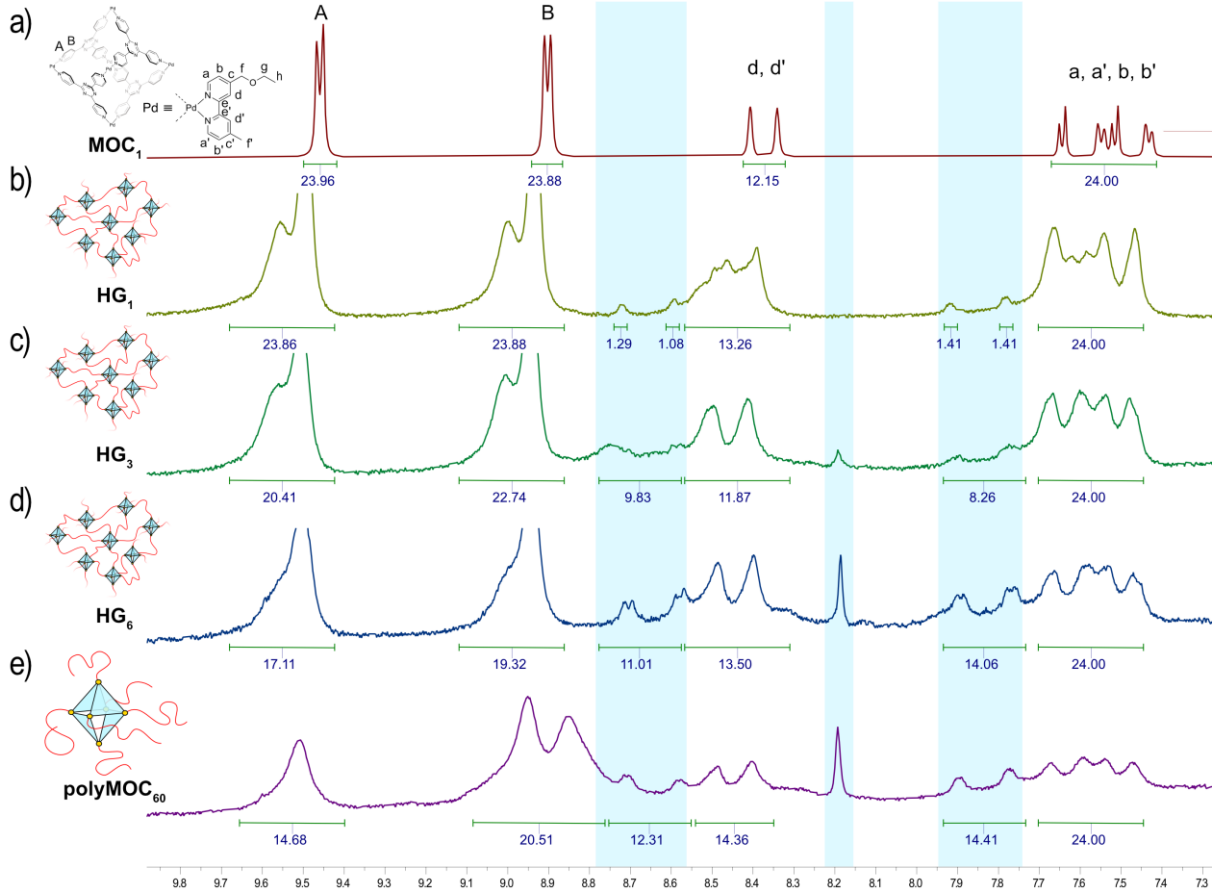

*Figure 85: ^{1}H NMR (600 MHz, D_2O) after 3 h of sonication with a sequence of 1 s on and 1 s off (only the "on" time is reported). Highlighted in blue indicates the cage fragmentation. a) Sonicated **MOC_1** shows no susceptibility to ultrasound. b) Sonicated **HG_1** shows a small amount of fragmentation. c) Increased activation was observed for **HG_3**. d) highest activation rate was achieved for **HG_6**. e) For reference the previous reported star shaped cage **$polyMOC_{60}$** with a similar activation rate as **HG_6**.*

Sonication of HG_6 with reference

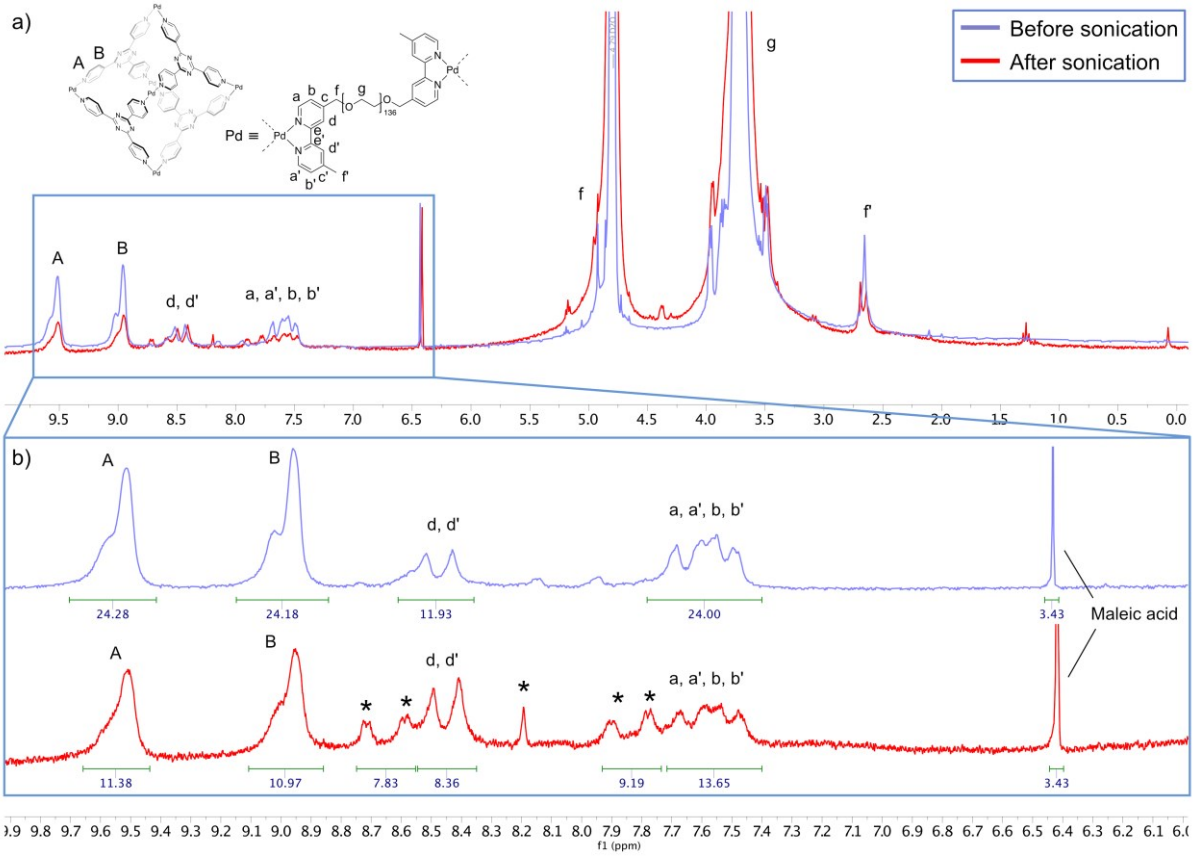

*Figure 86: ^1H NMR (D_2O) of hydrogel **HG_6** before (blue) and after sonication (red). The concentration during the sonication was 1.0 mg mL^{-1}. The external reference has a concentration of c = 0.02 mol L^{-1}. The reaction was sonicated for 3 h (1 s on, 1 s off). Defragmentation could be observed. The single spectra are reproduced in the "Spectra encapsulation and sonication" section.*

Sonication of HG_6•(ibuprofen)$_2$ with reference

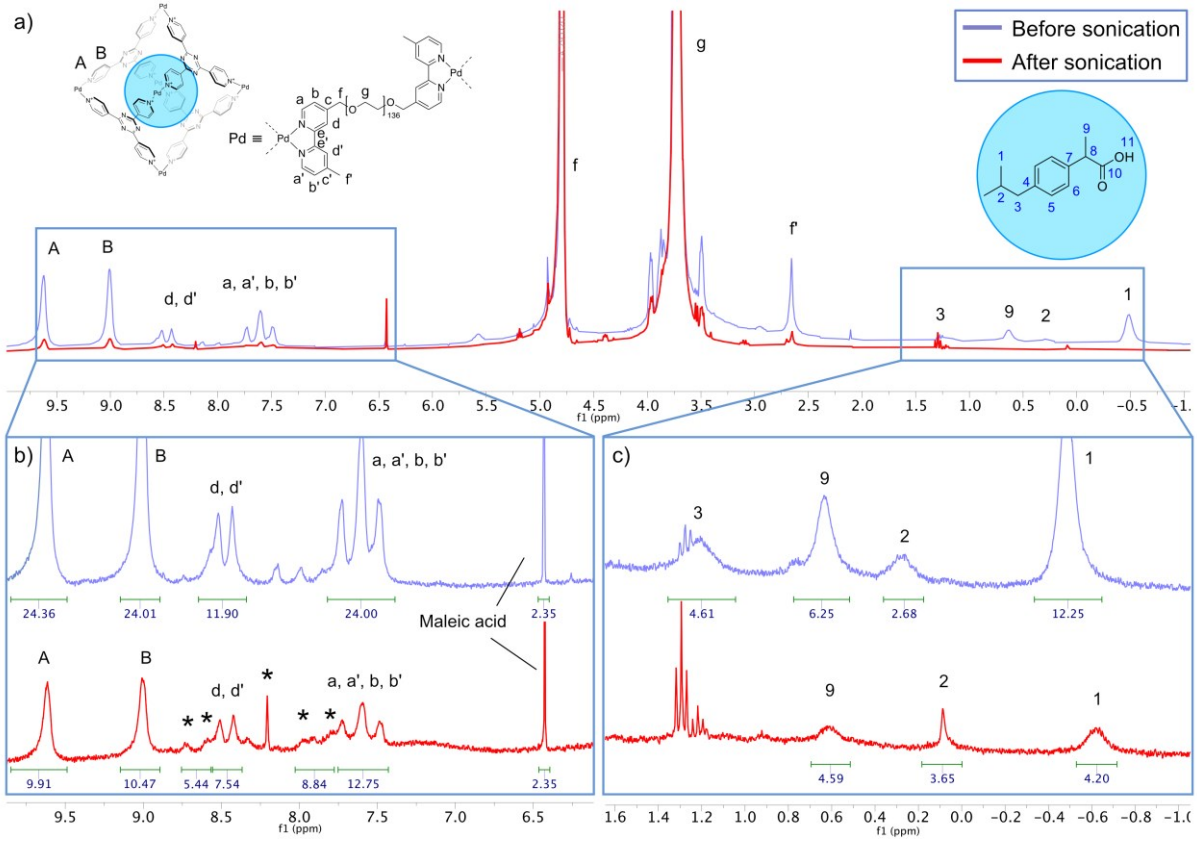

*Figure 87: ^{1}H NMR (D_2O) of hydrogel **HG_6•(ibuprofen)$_2$** before (blue) and after sonication (red). The concentration during the sonication was 1.0 mg mL^{-1}. The external reference has a concentration of c = 0.02 mol L^{-1}. The reaction was sonicated for 3 h (1 s on, 1 s off). Defragmentation and release could be observed. The single spectra are reproduced in the "Spectra encapsulation and sonication" section.*

Self-healing

HG_1

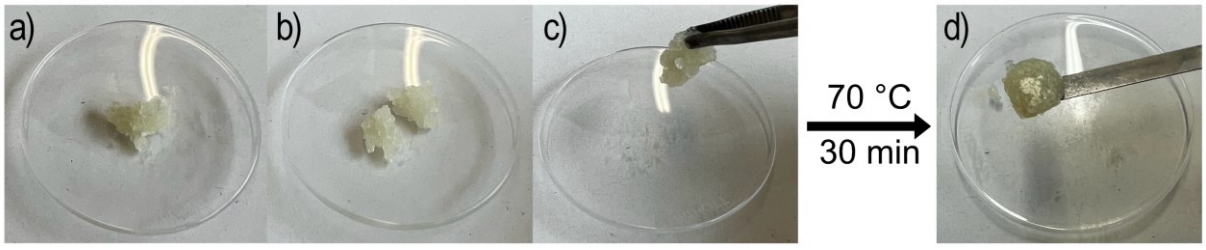

Figure 88: a) A small amount of the hydrogel was placed on the glass. b) The hydrogel was cut into two halves. c) After reassembling the pieces, they immediately supported their own weight. d) The hydrogel returned to its original form after 30 minutes of heating at 70 °C.

HG_3

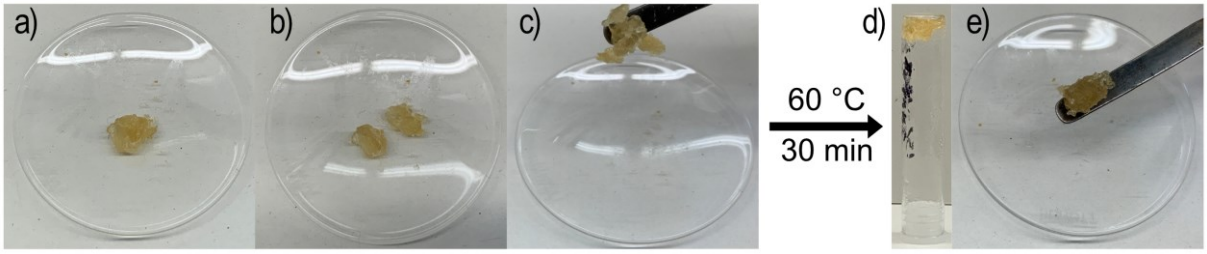

Figure 89: a) A small amount of the hydrogel was placed on the glass. b) The hydrogel was cut into two halves. c) After bringing the pieces back together they supported instantly their own weight. d) The hydrogel returned to its original form after 30 minutes of heating at 60 °C.

HG_6

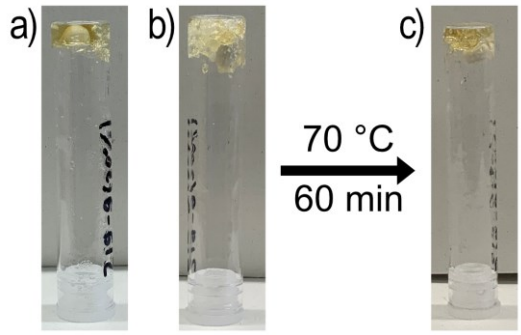

Figure 90: a) The hydrogel was cooled to RT. b) The stirring bar was removed, and the hydrogel was mechanically mixed thoroughly. c) The sample was heated for 60 min at 70 °C and turned into its original form.

Swelling experiments

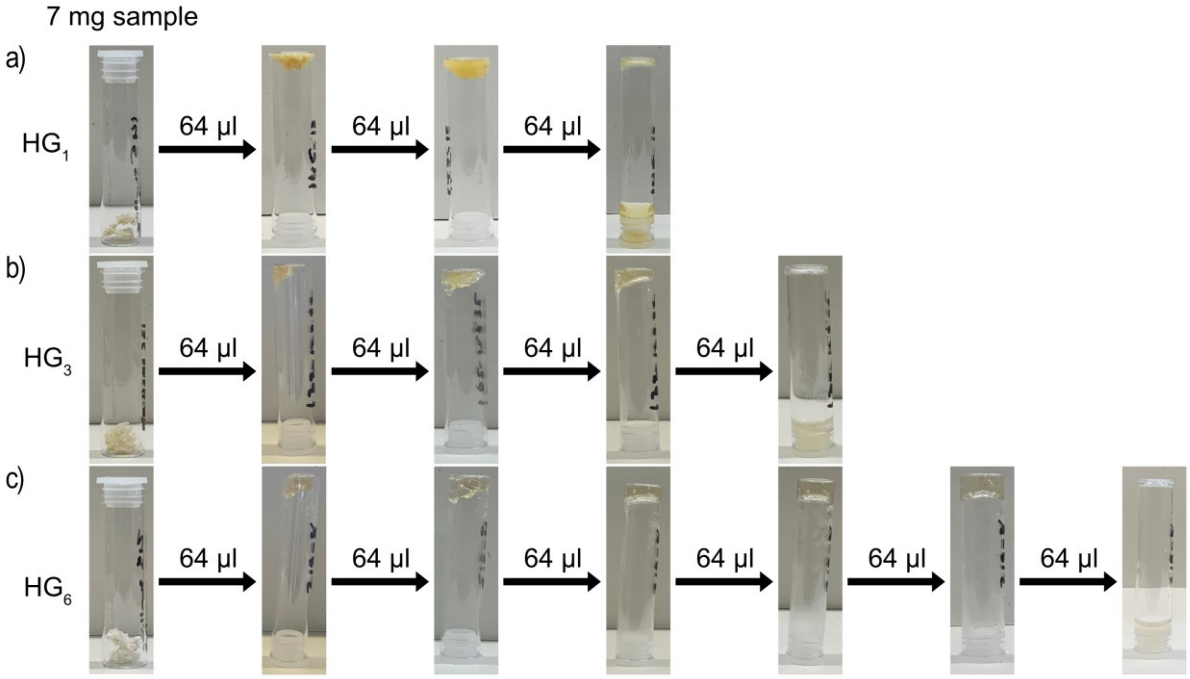

Figure 91: Depicted are the swelling experiments for each hydrogel. Each hydrogel was freeze-dried, and 7 mg were submitted into a vial. Onto each sample, 64 µL of H_2O was added once per day and equilibrated. a) The short hydrogel was capable of absorbing 18 times of its own mass in H_2O before it collapsed. b) For the medium hydrogel, this property could be increased to 27 times. c) The longest hydrogel could absorb 45 times its own mass in H_2O.

SEM

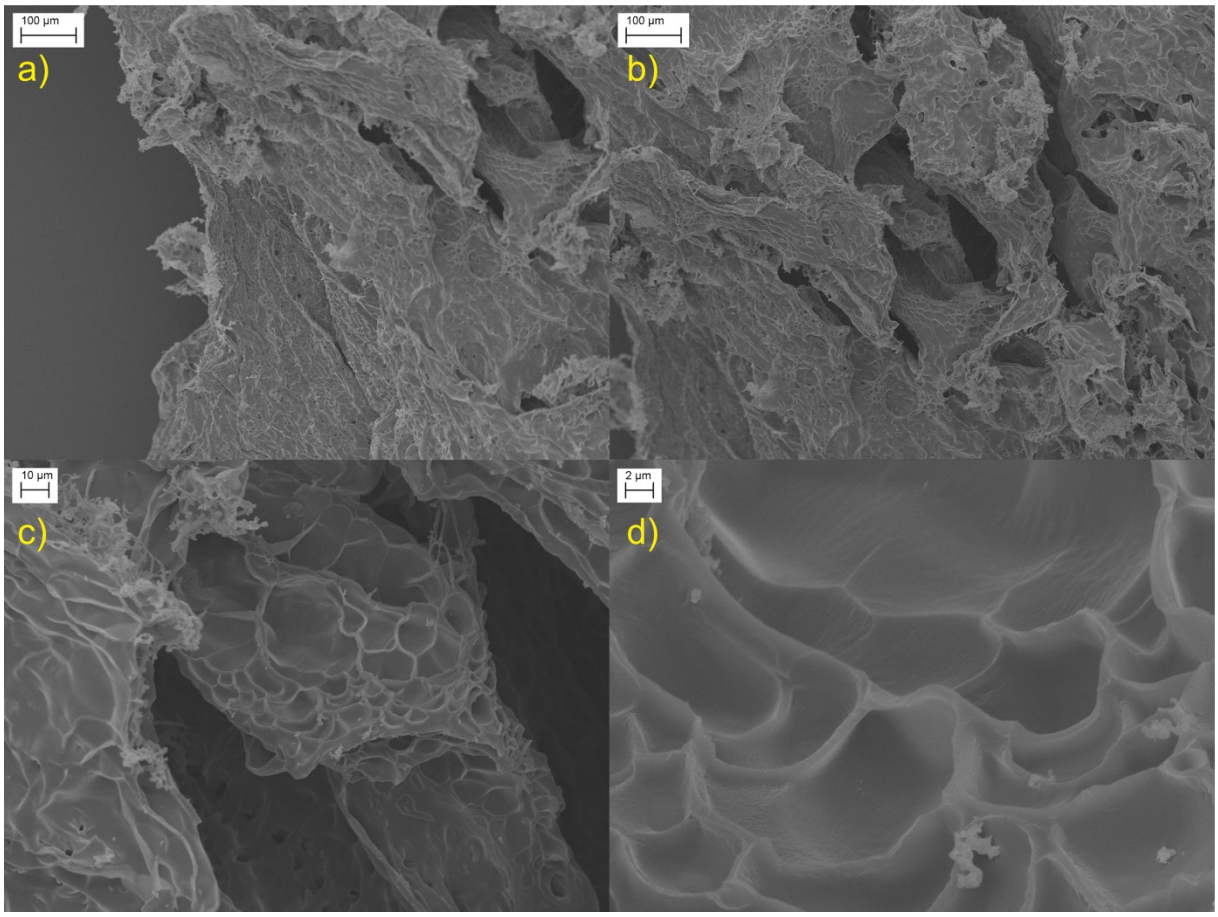

Figure 92: SEM images with different magnification.

SEM measurements were performed to visualize the tertiary structure of the hydrogel. Therefore, a sample of 100 mg of a 20 wt% hydrogel **HG$_3$** was allowed to swell over 3 days in 400 µL of D_2O. This sample was then freeze-dried for 3 hours to yield a colorless solid. The first two SEM-images show the sponge-like structure of the freeze-dried hydrogel. In the magnified pictures c) and d), it is observable that the pores are between 1 and 5 µm wide and appear to have a smooth surface. This structure of the pores results in an increase in the network surface area, which is needed for the immobilization of the solvent.

SAXS

The internal structure of the hydrogels was investigated by SAXS. First, we studied the freeze-dried aerogel-like samples. Figure 93 shows the SAXS profile of **HG$_1$**. The scattering profiles are characterized by three distinct features: A linear increase in scattering intensity at low *q* and two well-separated correlation peaks in the mid to high *q* region. We aimed to describe the scattering profiles with the simplest possible model with the smallest number of fitting parameters. The low *q* region can be well described by a simple power law. The peaks in the mid and high *q* region were described by broad peak functions. The resulting fit functions to describe our SAXS data are then given by:

$$(q) = I_B + cq^{-\alpha} + \sum_{n=1} \frac{I_{0n}}{1+(|q-q_n|\xi_n)^{m_n}} \qquad \text{(S1)}$$

Here, $I(q)$ corresponds to the measured scattering intensity where q is the magnitude of the scattering vector $\vec{q}$, I_B to the background scattering, the second term is the power law contribution with the intensity c, and the last term is the sum of individual broad peak contributions with a number n corresponding to the number of broad peaks used. For n = 1, the resulting fit function consists only of the background, power law, and one broad peak. α is the power law contribution exponent. The broad peak contributions consist of the peak intensities I_{0_n}, the peak positions q_n, the correlation lengths ξ_n and the scaling exponents m_n.

In Figure 93, we show the fit to the data based on equation S1 as a black solid line as well as the individual fit contributions. As can be seen, the sum of the power law (– – –) and the two broad peaks (• • • and – • –) describes the scattering profile very well. The power law exponent is close to a value of α = 4 (Porod scattering), which is typical for scattering from sharp interfaces. The broad peak contributions describe internal inhomogeneities that appear on characteristic length scales. The structure peak at smallest q is attributed to the average distance between crosslinker points in the network.

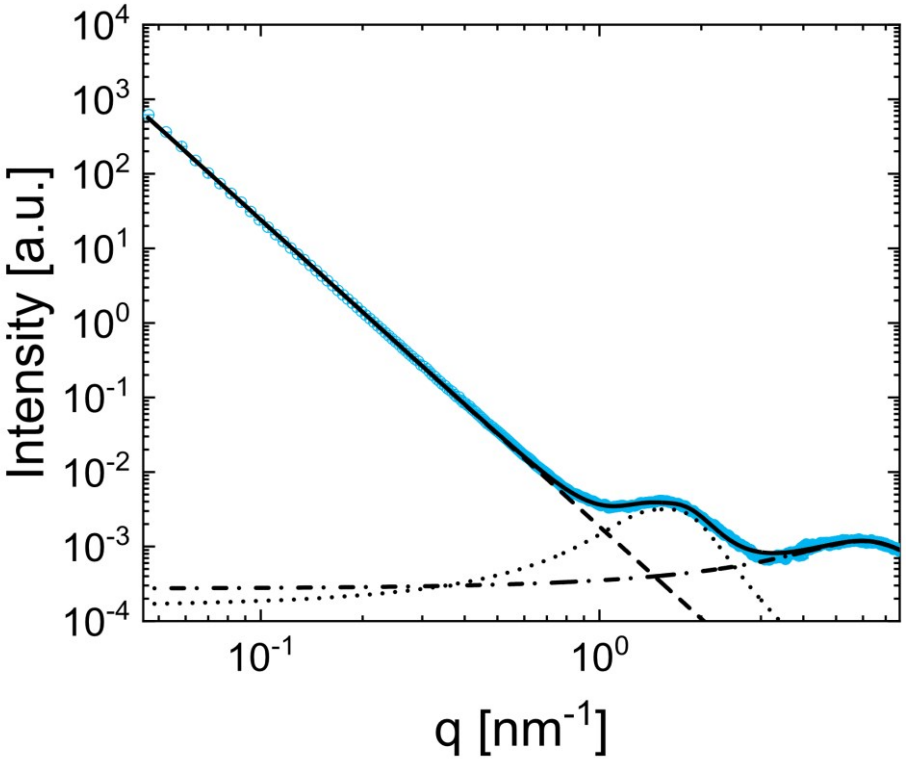

*Figure 93: SAXS profile o **HG$_1$** (freeze-dried) with the three fit contributions shown separately. The power law (– – –), the first broad peak (• • •) and the second broad peak (– • –). The black solid line is the full fit (sum of the three contributions) according to equation S1.*

Figure 94 compares the SAXS profiles of the three freeze-dried samples, **HG$_1$**, **HG$_3$** and **HG$_6$**. Generally, the shapes of the profiles are very similar, and the fits according to the model given by equation S1 describe the measured data well. The corresponding fit parameters are listed in Table S and the corresponding real space distances are listed in Table S2. To calculate the real space distance d_n from the values of q_n the following equation was used:

$$d_n = \frac{2\pi}{q_n} \qquad \text{(S2)}$$

When the SAXS profile of **HG$_1$** is compared to **HG$_3$** and **HG$_6$**, the most obvious change is the shift of the first structure peak to lower q. This means that the average distance between the crosslinking points is increasing with the increasing length of the poly(ethylene glycol) chains.

The broad peak at highest q, at approximately 6 nm^{-1} shifts only slightly to higher q for the samples with longer poly(ethylene glycol) chains.

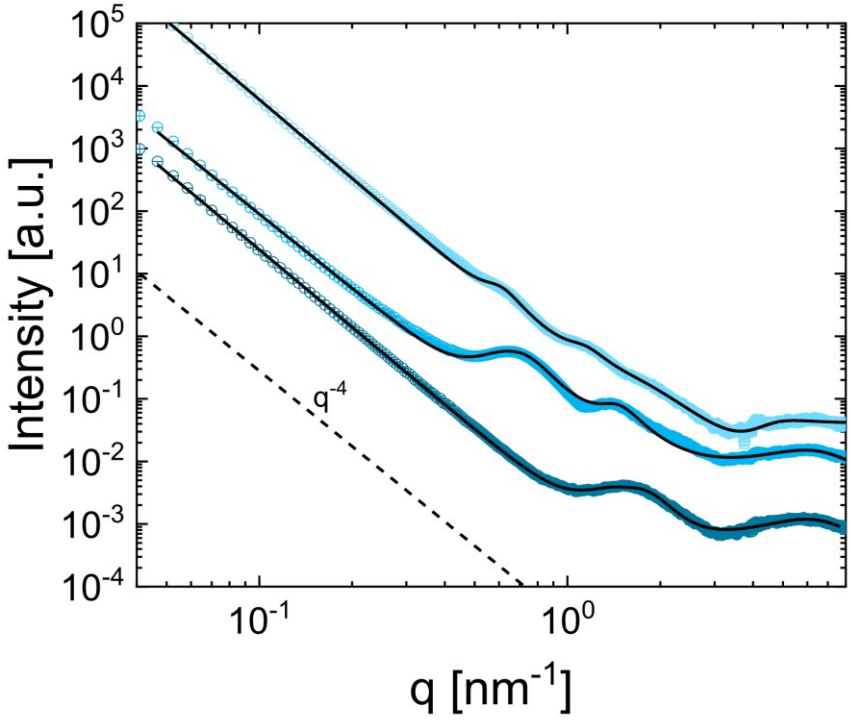

*Figure 94: SAXS profiles of the hydrogels **HG$_1$** (dark blue), **HG$_3$** (blue) and **HG$_6$** (light blue) after freeze-drying with corresponding fits according to equation S1 (black solid lines). The scattering profiles are shifted by fixed multipliers for better visibility.*

Table S2: Fitting parameters obtained from analysis of the SAXS profiles of freeze-dried hydrogels. The q values correspond to the position of the broad peaks, the values ξ to the peak width (correlation length) and α is the exponent of the power law contribution.

Sample	q_1 [nm^{-1}]	q_2 [nm^{-1}]	q_3 [nm^{-1}]	q_4 [nm^{-1}]	ξ_1 [nm]	ξ_2 [nm]	ξ_3 [nm]	ξ_4 [nm]	α
HG$_1$	1.56	-	-	5.97	1.90	-	-	0.32	4.11
HG$_3$	0.64	1.30	-	6.18	5.34	3.99	-	0.44	3.33
HG$_6$	0.60	1.11	1.51	6.48	9.78	4.61	1.33	0.44	4.18

Table S3: Corresponding real space distances calculated from the positions of the broad peaks from the fit of the SAXS profiles of freeze-dried hydrogels.

Sample	d_1 [nm]	d_2 [nm]	d_3 [nm]	d_4 [nm]
HG$_1$	4.03	-	-	1.05
HG$_3$	9.79	4.82	-	1.02
HG$_6$	10.54	5.62	4.17	0.97

Figure 95 shows SAXS profiles of the freeze-dried as well as the hydrated (20 wt%) sample **HG$_1$**. The high and low *q* regions are very similar in both profiles and again, a broad peak at approximately 6 nm^{-1} and a power law contribution at lowest *q* are visible. In the mid *q* range, the hydrogel sample does not

show a clear correlation peak and rather a plateau is observed. This region can be described by a Lorentzian (Ornstein-Zernike-like) contribution, that is obtained for m_n = 2 in the broad peak contribution in equation S1. This indicates dynamic network fluctuations in the solvated hydrogel sample. Table S4 lists the most relevant results from the SAXS analysis.

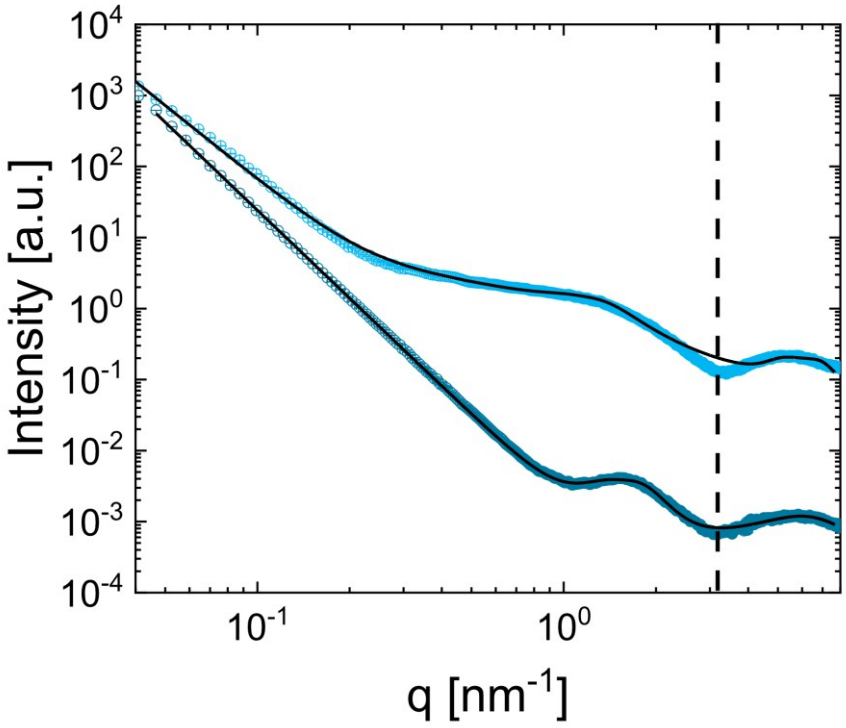

*Figure 95: SAXS profile of **HG$_1$** after freeze-drying (dark blue) and the corresponding hydrogel, 20 wt% **HG$_1$** (light blue). The black solid lines are fits according to equation S1. The profiles are shifted by fixed multipliers for better visibility.*

*Table S4: Peak positions from analysis of the SAXS data recorded from **HG$_1$** after freeze-drying and with 20 wt% water. The corresponding length in real space, d, are also listed.*

Sample	q_1 [nm^{-1}]	q_4 [nm^{-1}]	d_1 [nm]	d_4 [nm]
HG$_1$	1.56	5.97	4.03	1.05
20 wt% **HG$_1$**	1.16	6.02	5.42	1.04

The impact of sonication on sample **HG$_3$** was also studied by SAXS. Figure 96 compares the SAXS profiles prior to (blue) and after (red) sonication. For the sonicated sample, broad peaks stay in the same position but lose significantly in intensity. The high *q* peak vanishes completely. This is in good agreement with the NMR analysis of the mechanochemical activation.

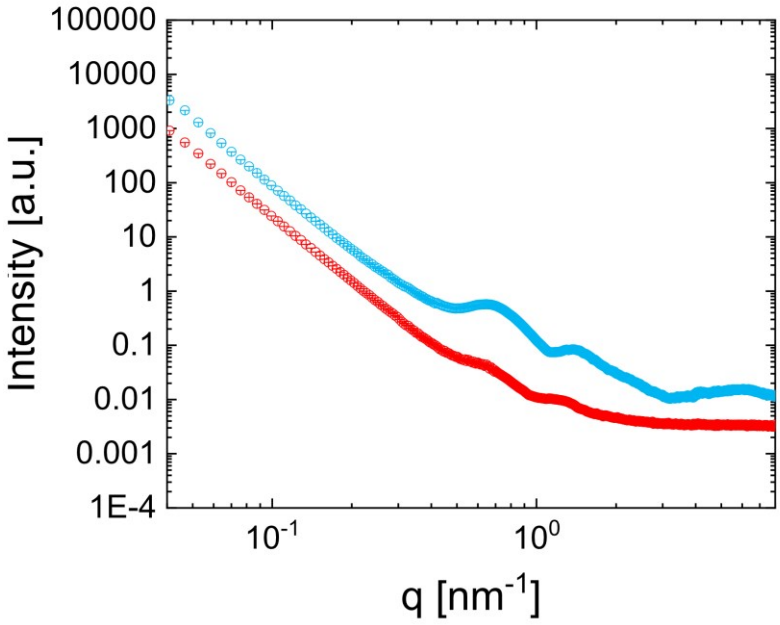

*Figure 96: SAXS profiles of **HG$_3$** before sonication (blue) and after sonication 3 h of sonication with a sequence of 1 s on and 1 s off (only the "on" time is reported) (red). The scattering profiles are shifted by fixed multipliers for better visibility.*

6 Spectra

6.1 Spectra for section 3.1

Section for the synthesis

2,4,6-Tris(4-pyridyl)-1,3,5-triazine **TPT**

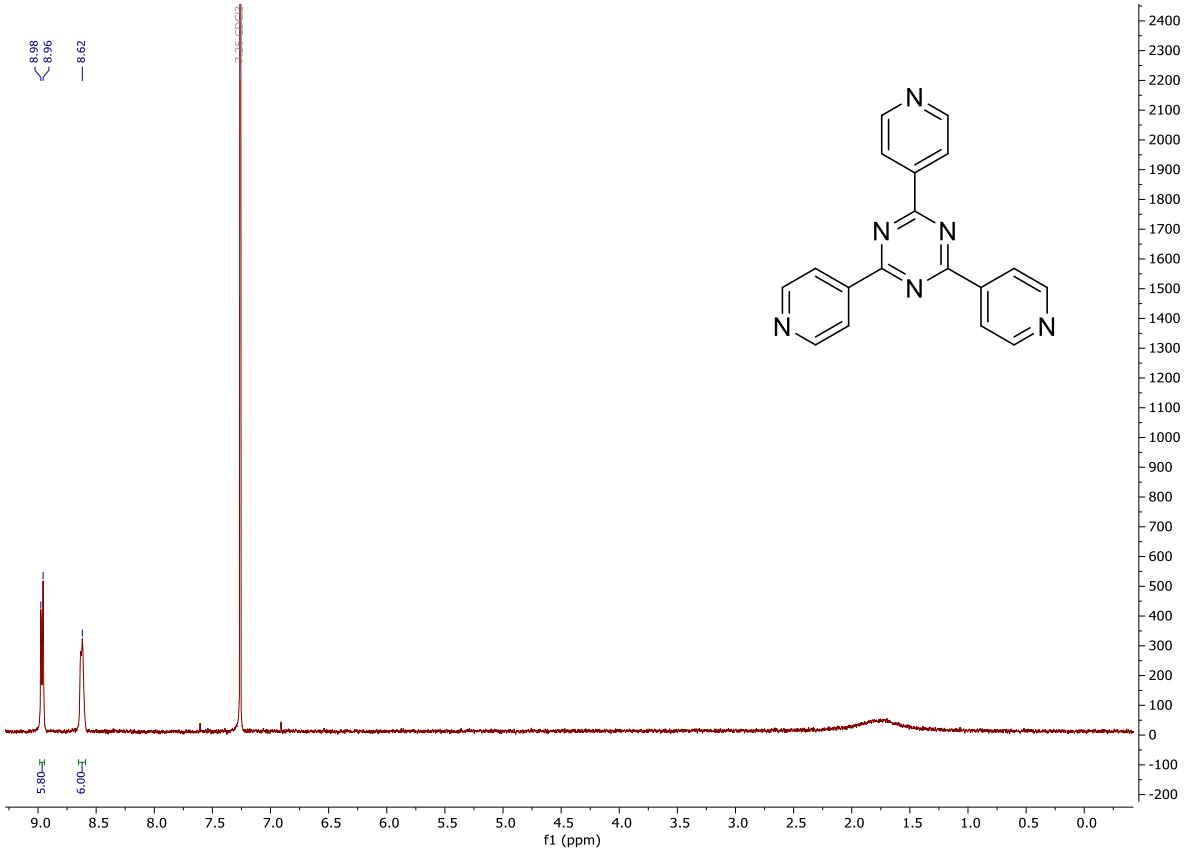

*Figure 97: ^{1}H NMR (300 MHz, $CDCl_3$) of 2,4,6-tris(4-pyridyl)-1,3,5-triazine (**TPT**).*

4-Hydroxymethyl-4’-methyl-2,2’-bipyridine **17**

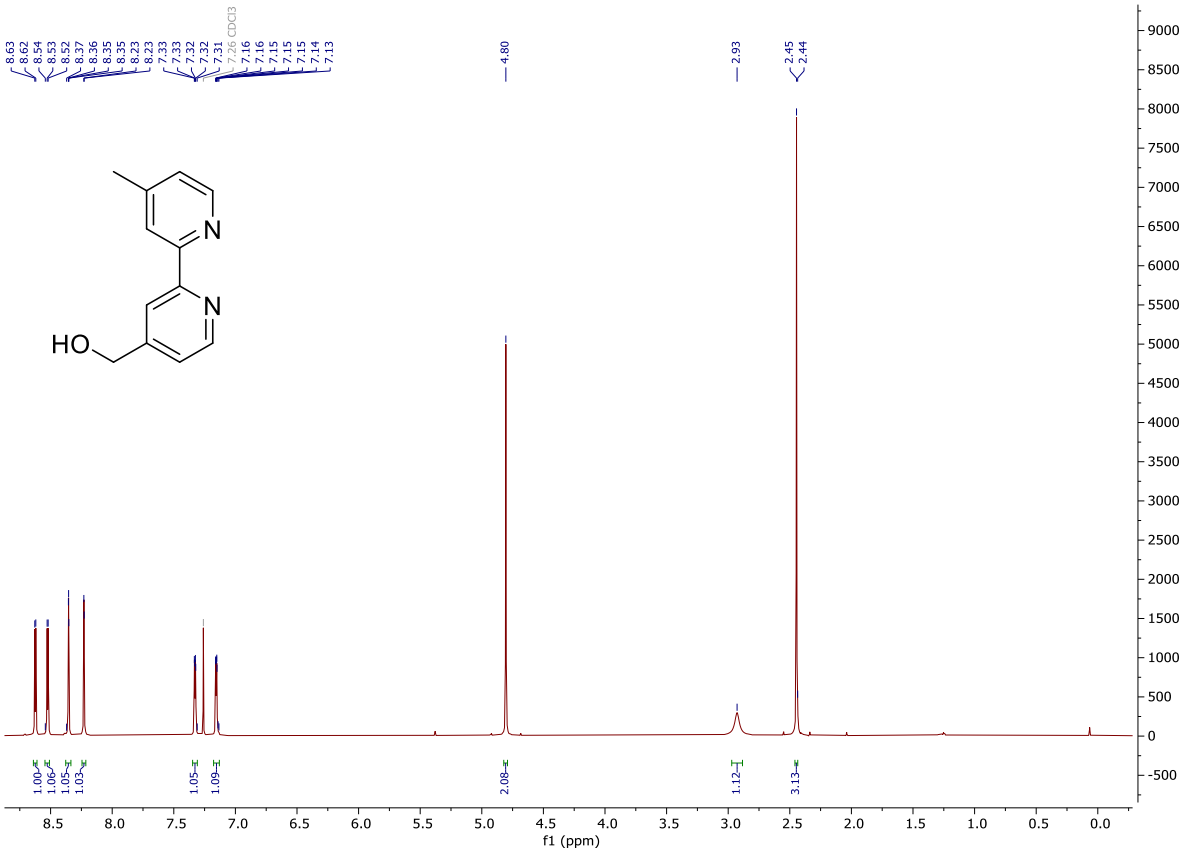

*Figure 98: ^{1}H NMR (300 MHz, $CDCl_3$) of 4-hydroxymethyl-4’-methyl-2,2’-bipyridine (**17**).*

4-Bromomethyl-4’-methyl-2,2’-bipyridine **18**

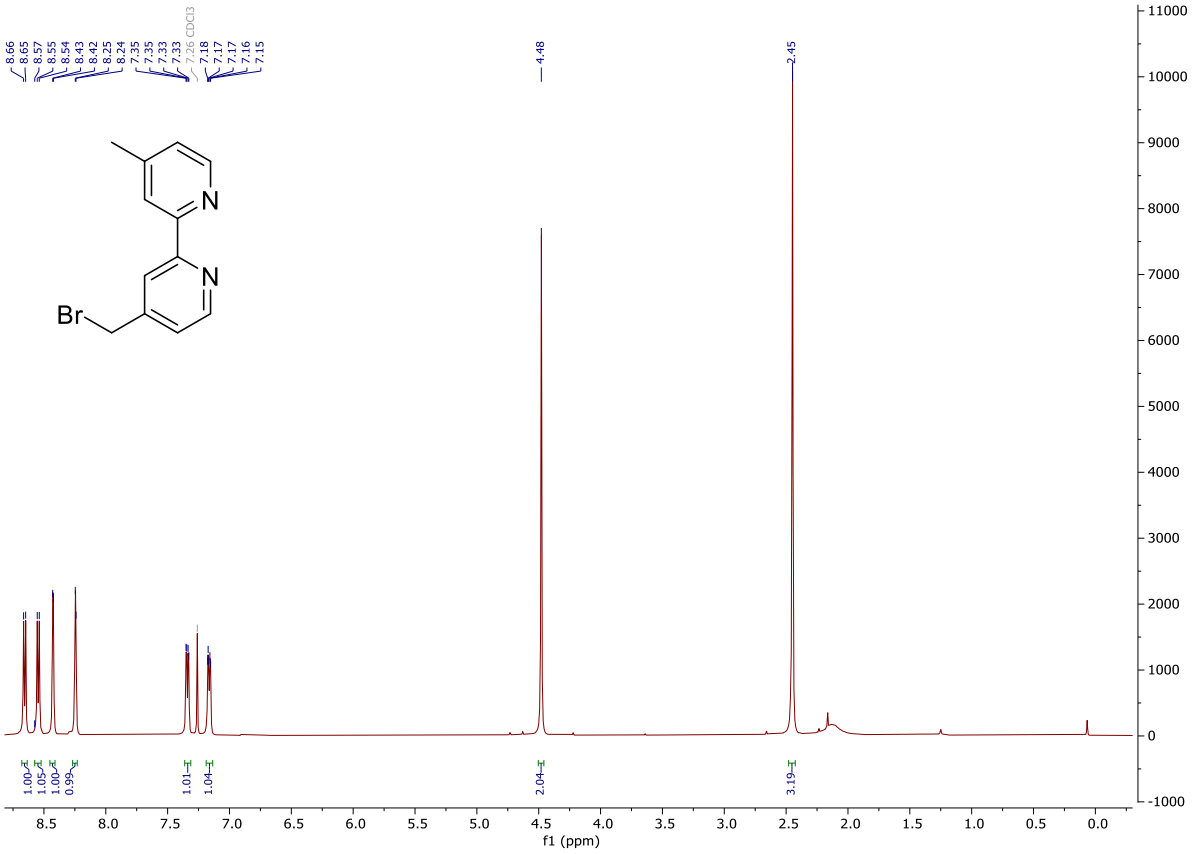

*Figure 99: ^{1}H NMR (300 MHz, $CDCl_3$) of 4-bromomethyl-4’-methyl-2,2’-bipyridine (**18**).*

4-Ethoxymethyl-4'-methyl-2,2'-bipyridine **19**

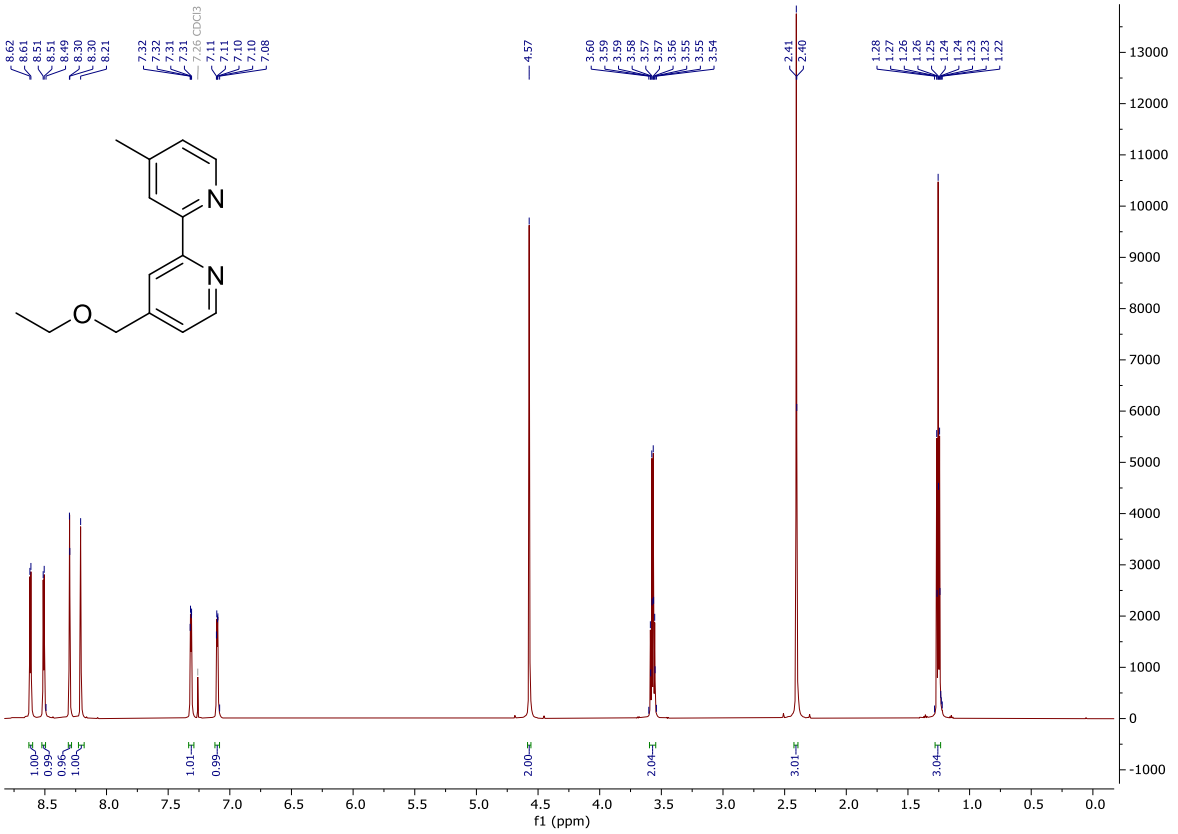

*Figure 100: ^{1}H NMR (300 MHz, $CDCl_3$) of 4-ethoxymethyl-4'-methyl-2,2'-bipyridine (**19**).*

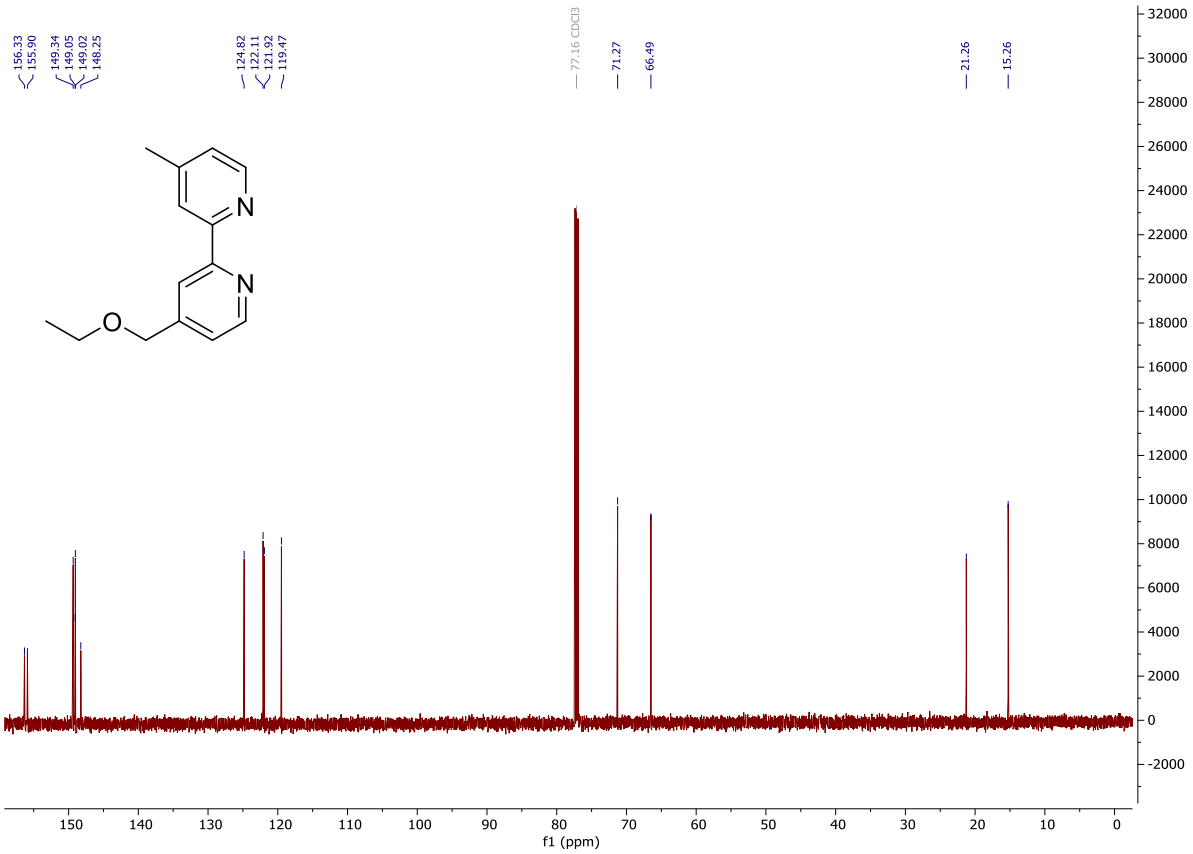

*Figure 101: $^{13}C\{^{1}H\}$ NMR (151 MHz, $CDCl_3$) of 4-ethoxymethyl-4'-methyl-2,2'-bipyridine (**19**).*

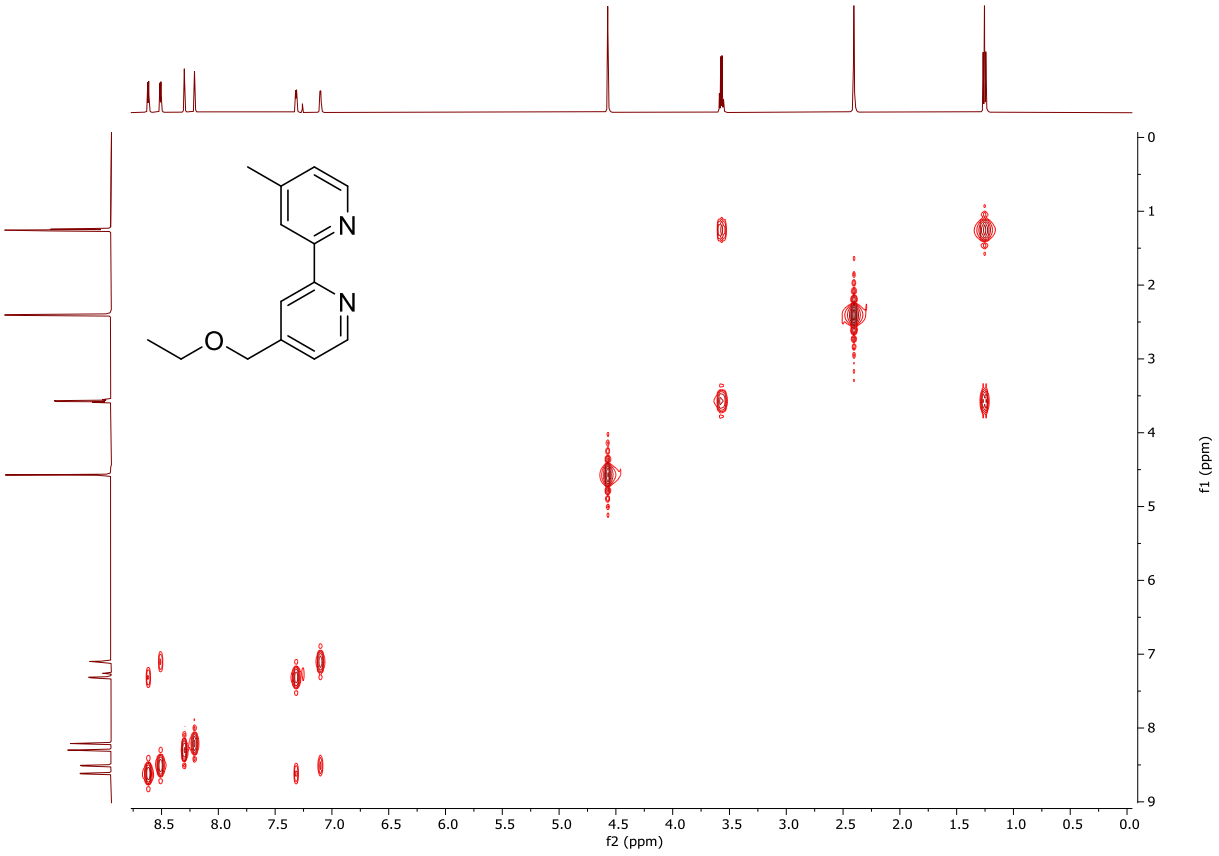

*Figure 102: ^{1}H-^{1}H COSY NMR (600 MHz, $CDCl_3$) of 4-ethoxymethyl-4'-methyl-2,2'-bipyridine (**19**).*

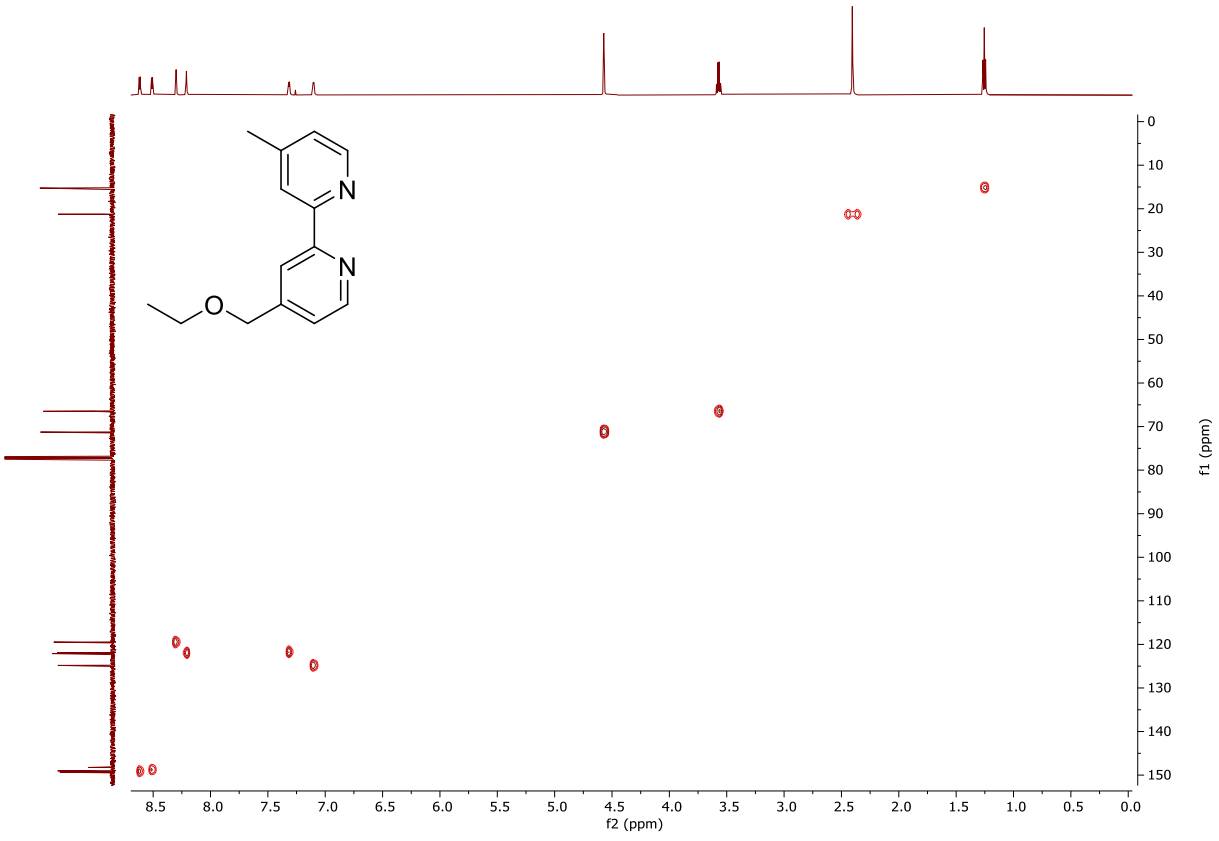

*Figure 103: ^{1}H-{^{13}C} HSQC NMR (600 MHz, $CDCl_3$) of 4-ethoxymethyl-4'-methyl-2,2'-bipyridine (**19**).*

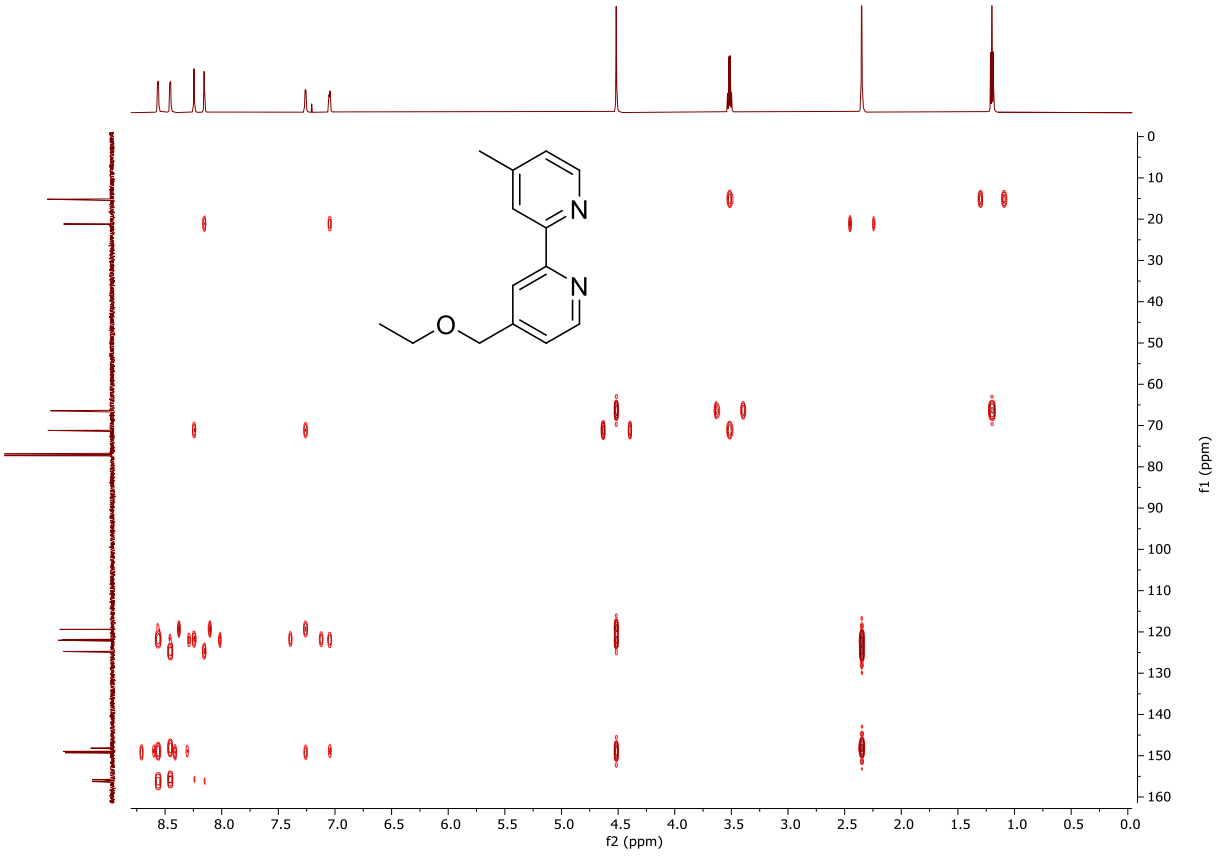

*Figure 104: ^{1}H-{^{13}C} HMBC NMR (600 MHz, $CDCl_3$) of 4-ethoxymethyl-4'-methyl-2,2'-bipyridine (**19**).*

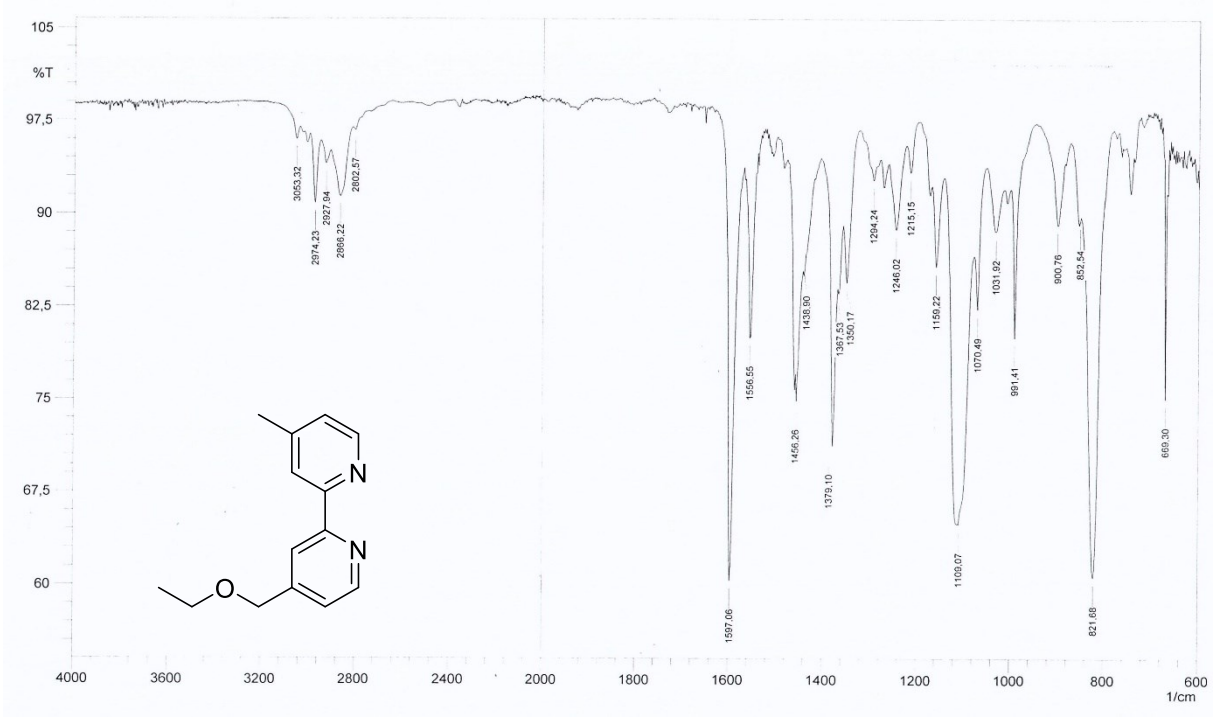

*Figure 105: IR spectrum of 4-ethoxymethyl-4'-methyl-2,2'-bipyridine (**19**).*

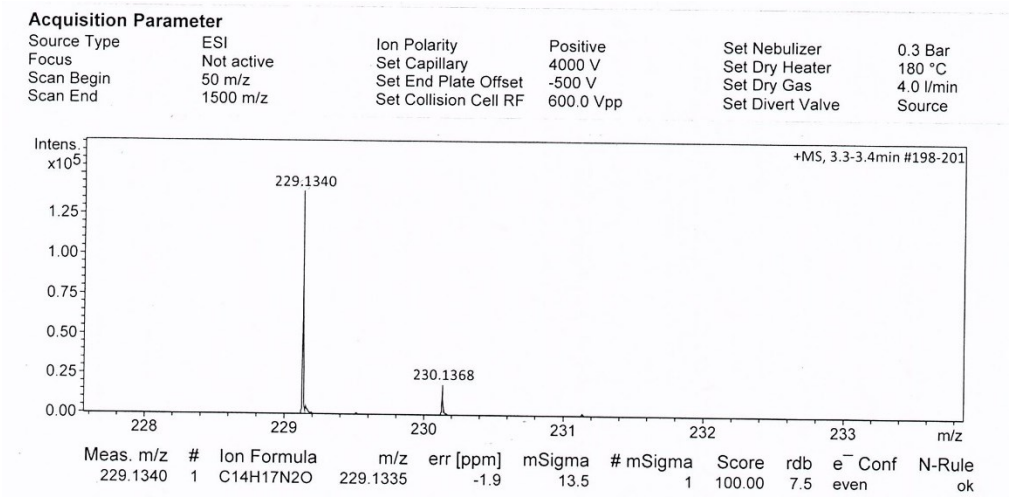

*Figure 106: HRMS (ESI) spectrum of 4-ethoxymethyl-4'-methyl-2,2'-bipyridine (**19**).*

(4-Ethoxymethyl-4'-methyl-2,2'-bipyridine)-dichloropalladium(II) (**20**)

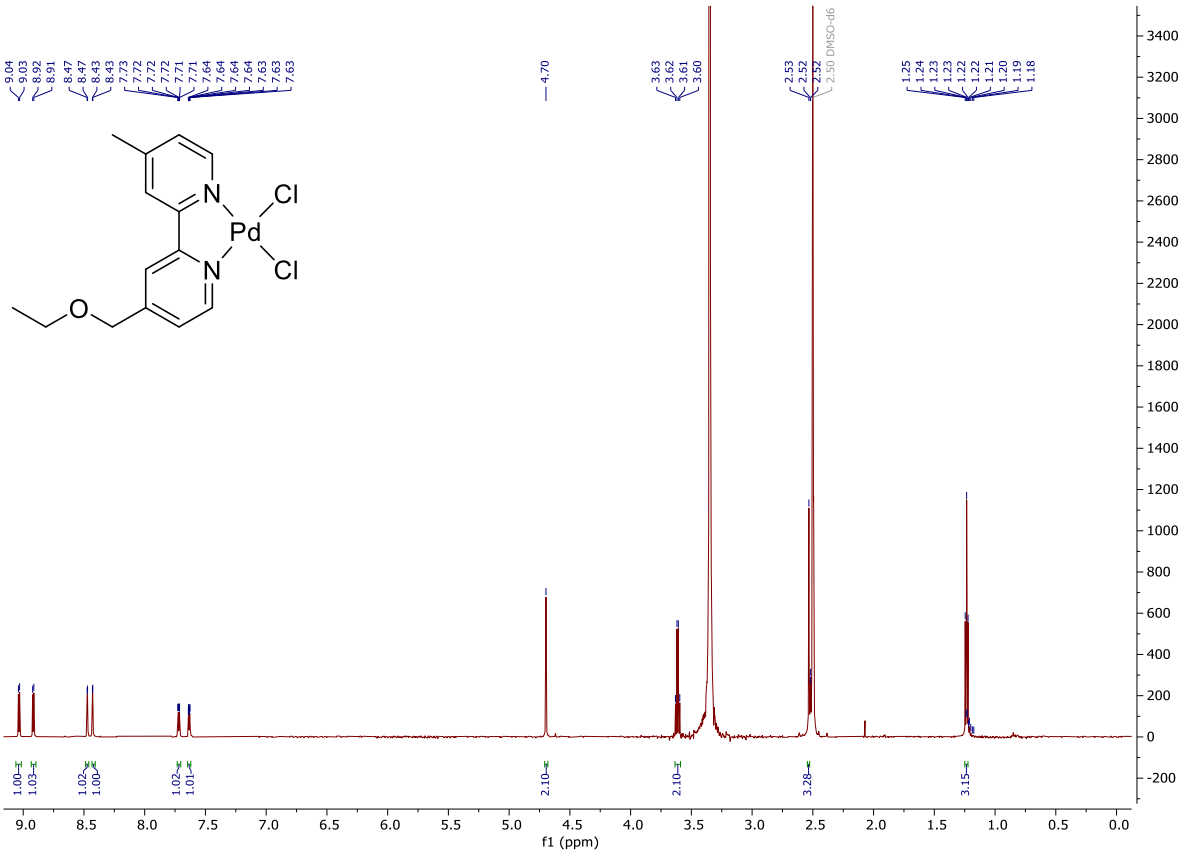

*Figure 107: ^{1}H NMR (600 MHz, DMSO-d_6) of (4-ethoxymethyl-4'-methyl-2,2'-bipyridine)-dichloropalladium(II) (**20**).*

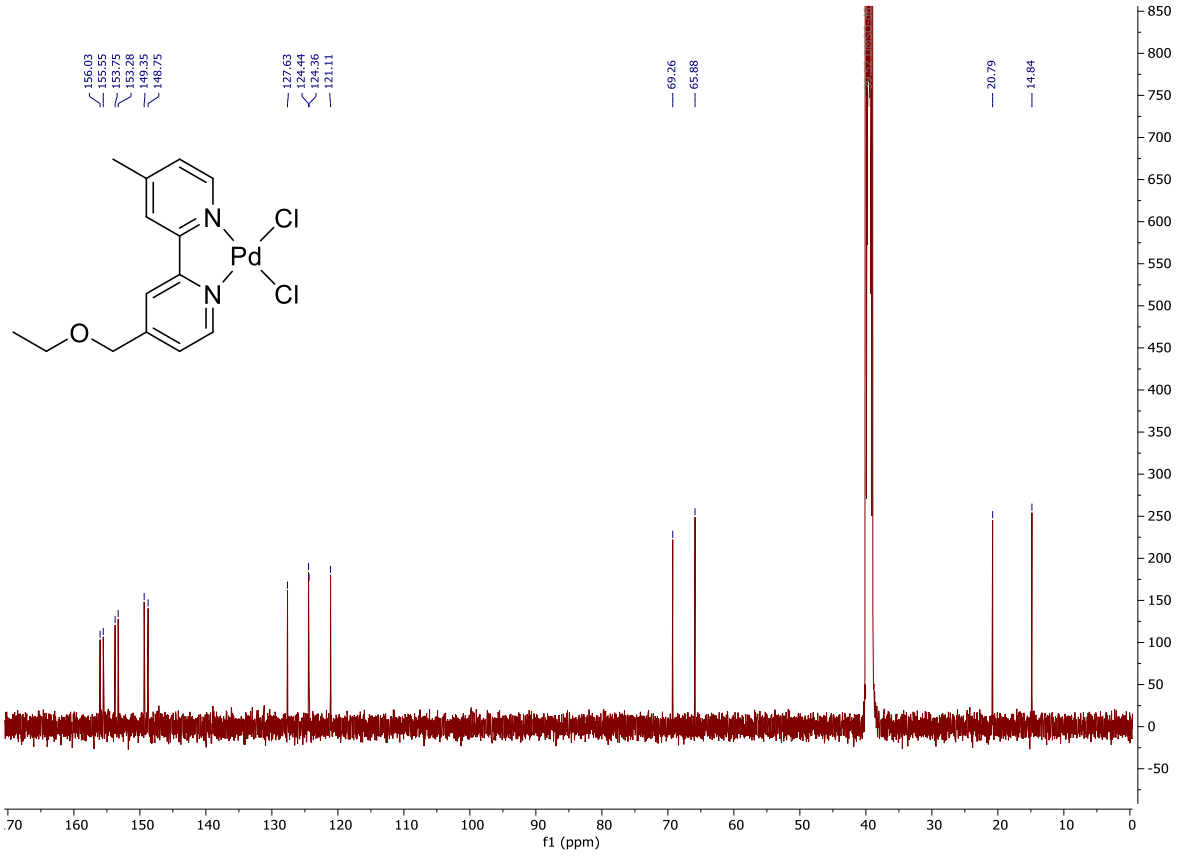

*Figure 108: $^{13}C\{^{1}H\}$ NMR (126 MHz, DMSO-d_6) of (4-ethoxymethyl-4'-methyl-2,2'-bipyridine)-dichloropalladium(II) (**20**).*

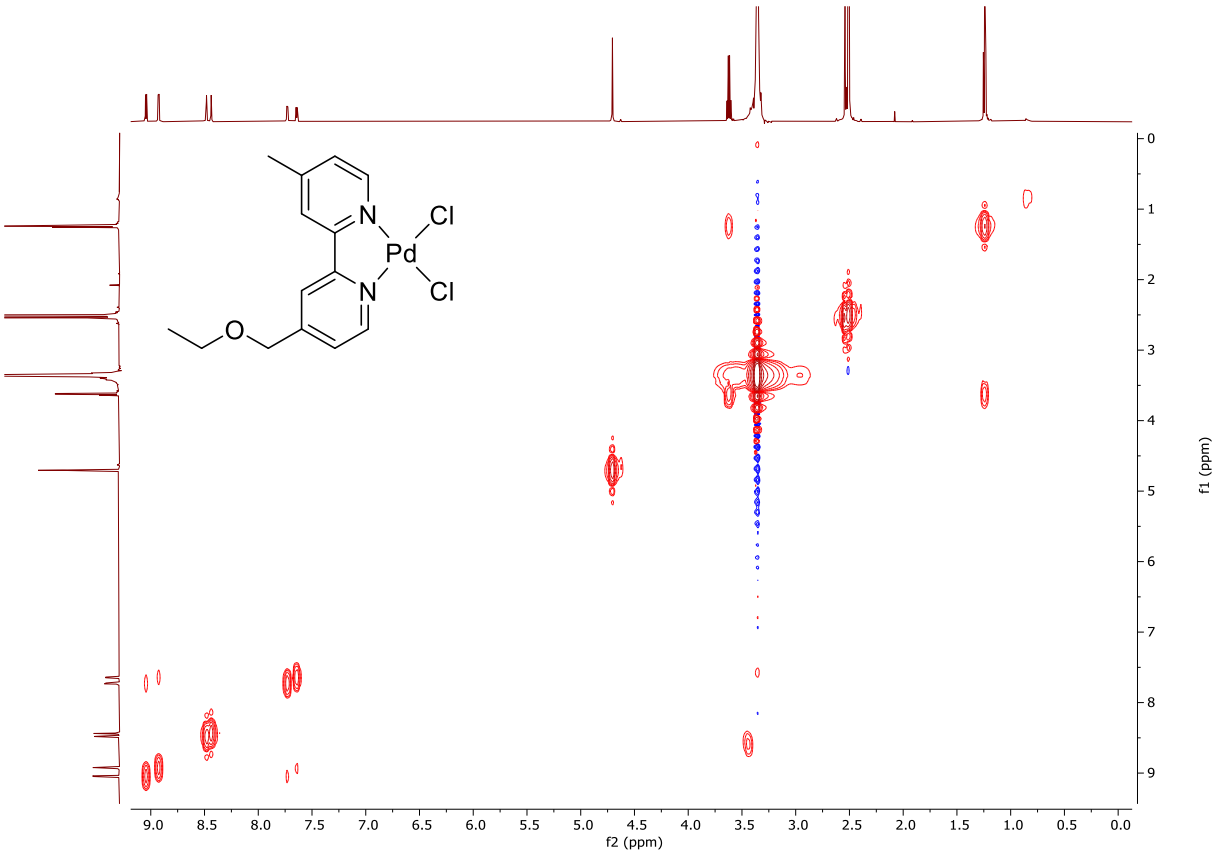

*Figure 109: ^{1}H-^{1}H COSY NMR (600 MHz, DMSO-d_6) of (4-ethoxymethyl-4'-methyl-2,2'-bipyridine)-dichloropalladium(II) (**20**).*

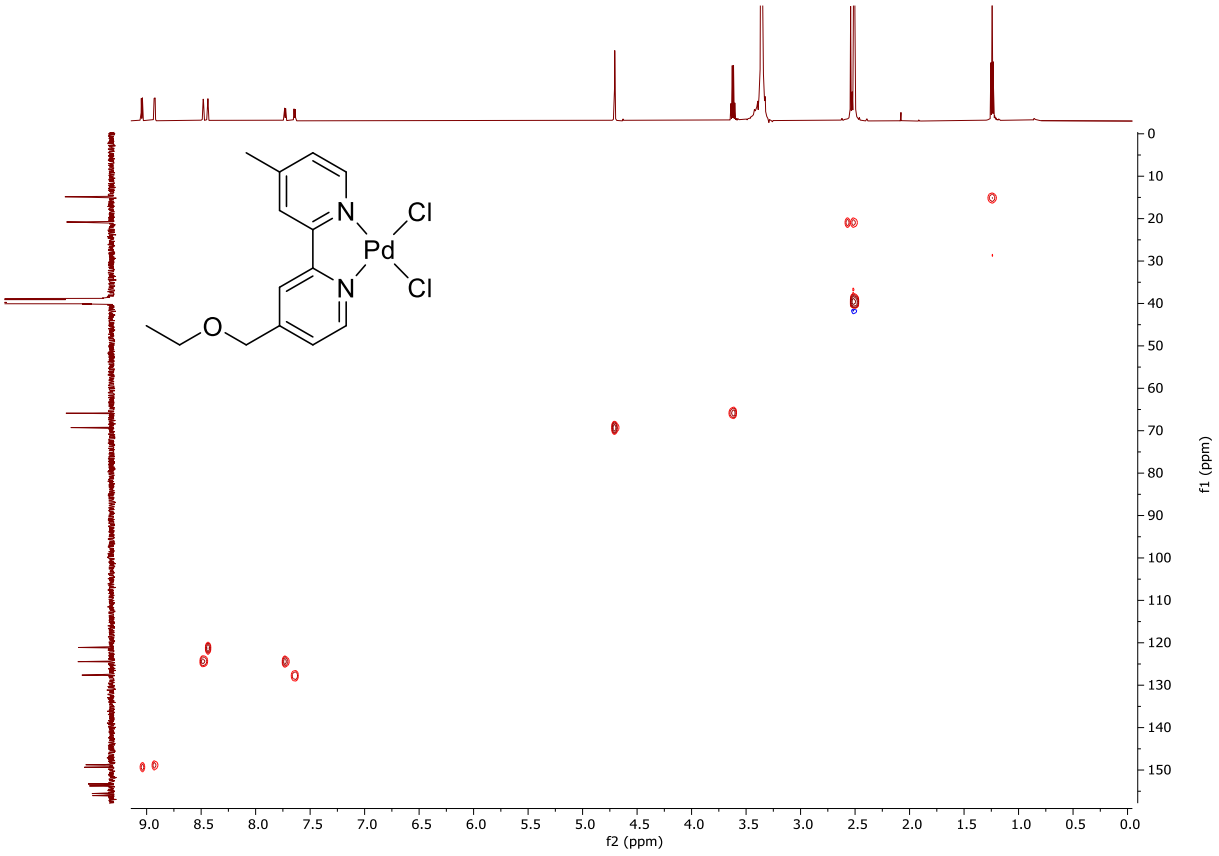

*Figure 110: ^{1}H-{^{13}C} HSQC NMR (600 MHz, DMSO-d_6) of (4-ethoxymethyl-4'-methyl-2,2'-bipyridine)-dichloropalladium(II) (**20**).*

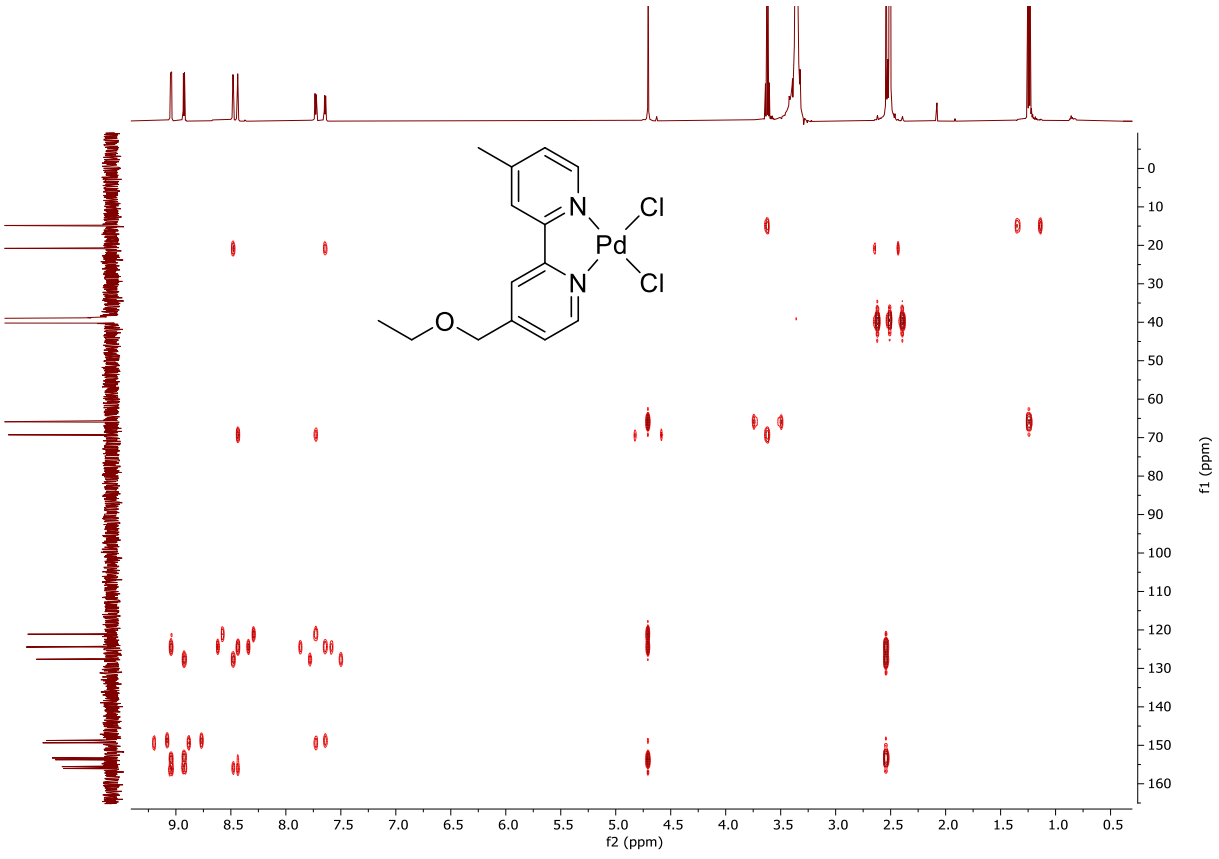

*Figure 111: ^{1}H-{^{13}C} HMBC NMR (600 MHz, $CDCl_3$) of (4-ethoxymethyl-4'-methyl-2,2'-bipyridine)-dichloropalladium(II) (**20**).*

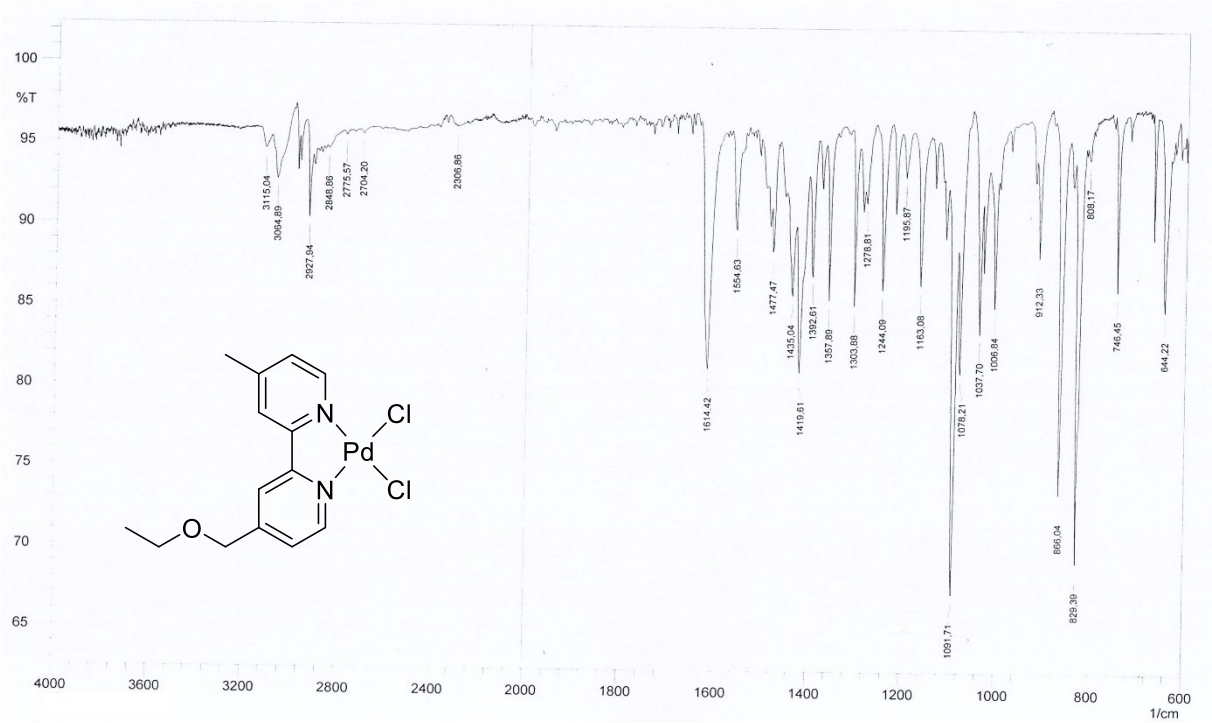

*Figure 112: IR spectrum of (4-ethoxymethyl-4'-methyl-2,2'-bipyridine)-dichloropalladium(II) (**20**).*

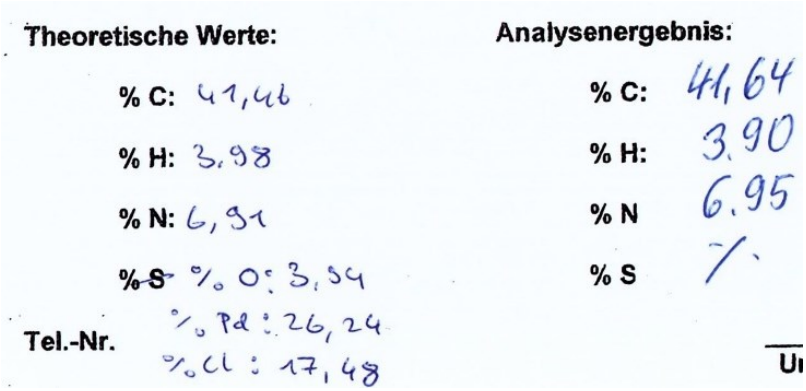

*Figure 113: Elemental analysis of (4-ethoxymethyl-4'-methyl-2,2'-bipyridine)-dichloropalladium(II) (**20**).*

(4-Ethoxymethyl-4'-methyl-2,2'-bipyridine)-dinitratopalladium(II) (**21**)

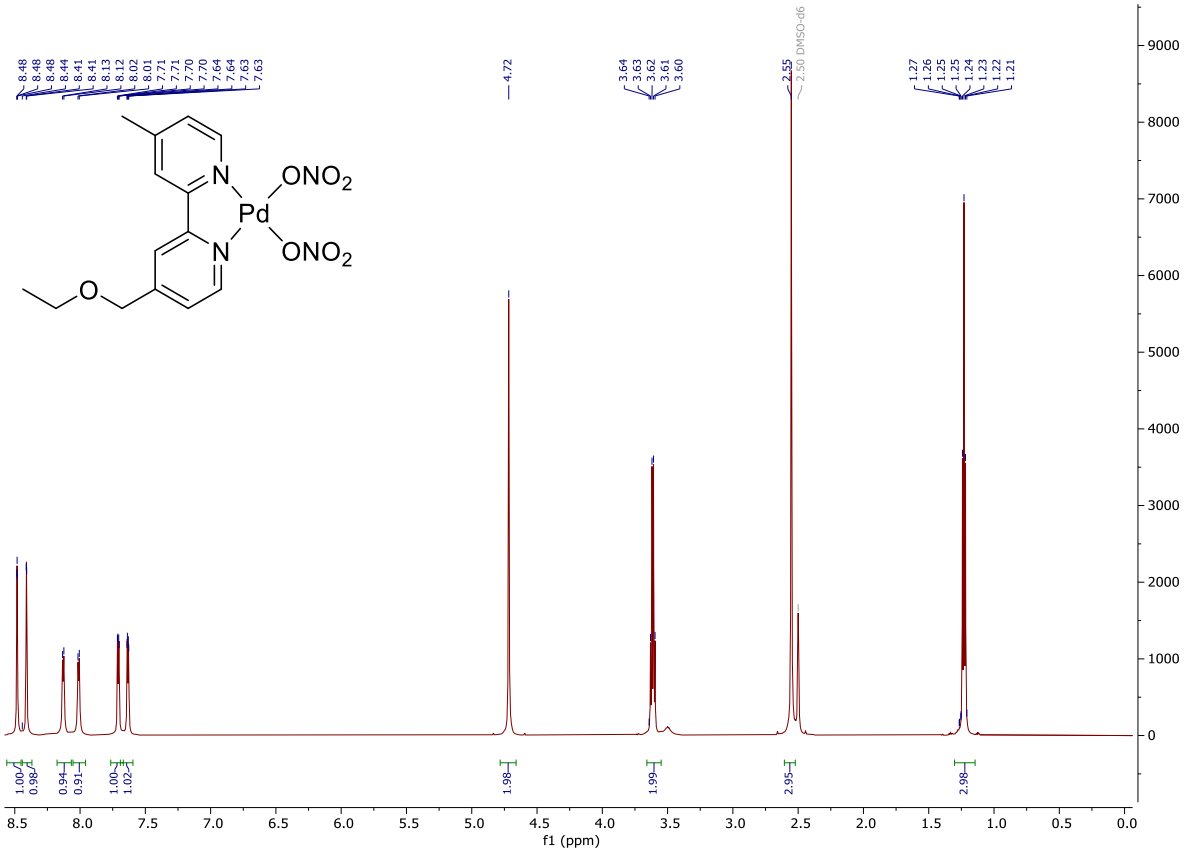

*Figure 114: ^{1}H NMR (600 MHz, DMSO-d_6) of (4-ethoxymethyl-4'-methyl-2,2'-bipyridine)-dinitratopalladium(II) (**21**).*

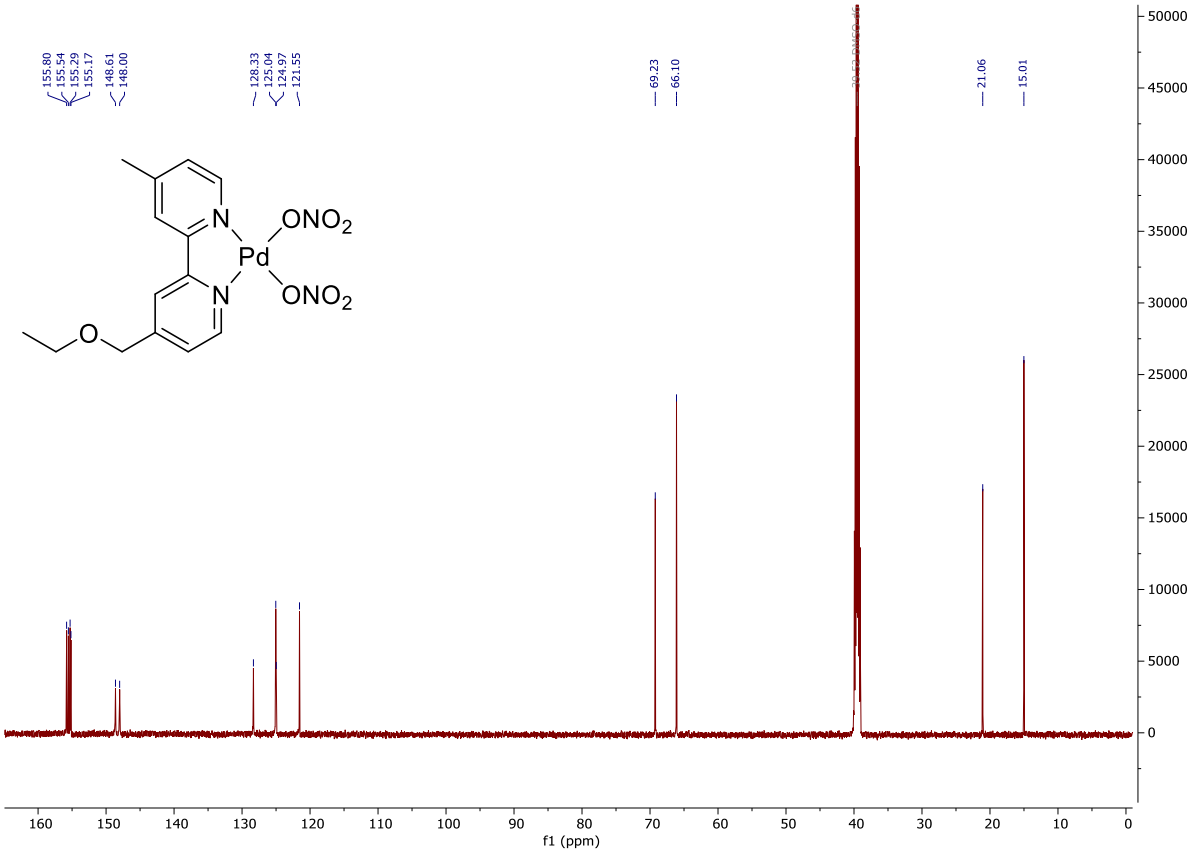

*Figure 115: $^{13}C\{^{1}H\}$ NMR (151 MHz, DMSO-d_6) of (4-ethoxymethyl-4'-methyl-2,2'-bipyridine)-dinitratopalladium(II) (**21**).*

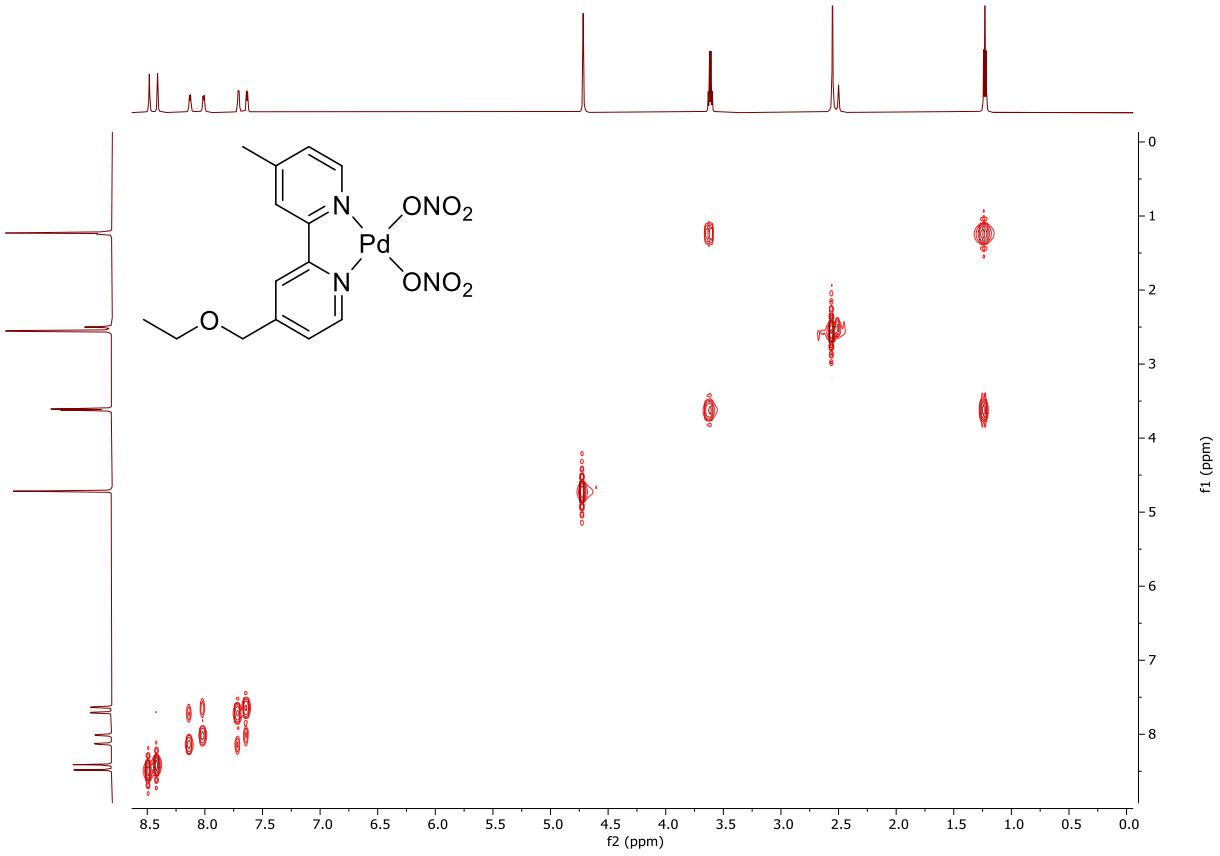

*Figure 116: ^{1}H-^{1}H COSY NMR (600 MHz, DMSO-d_6) of (4-ethoxymethyl-4'-methyl-2,2'-bipyridine)-dinitratopalladium(II) (**21**).*

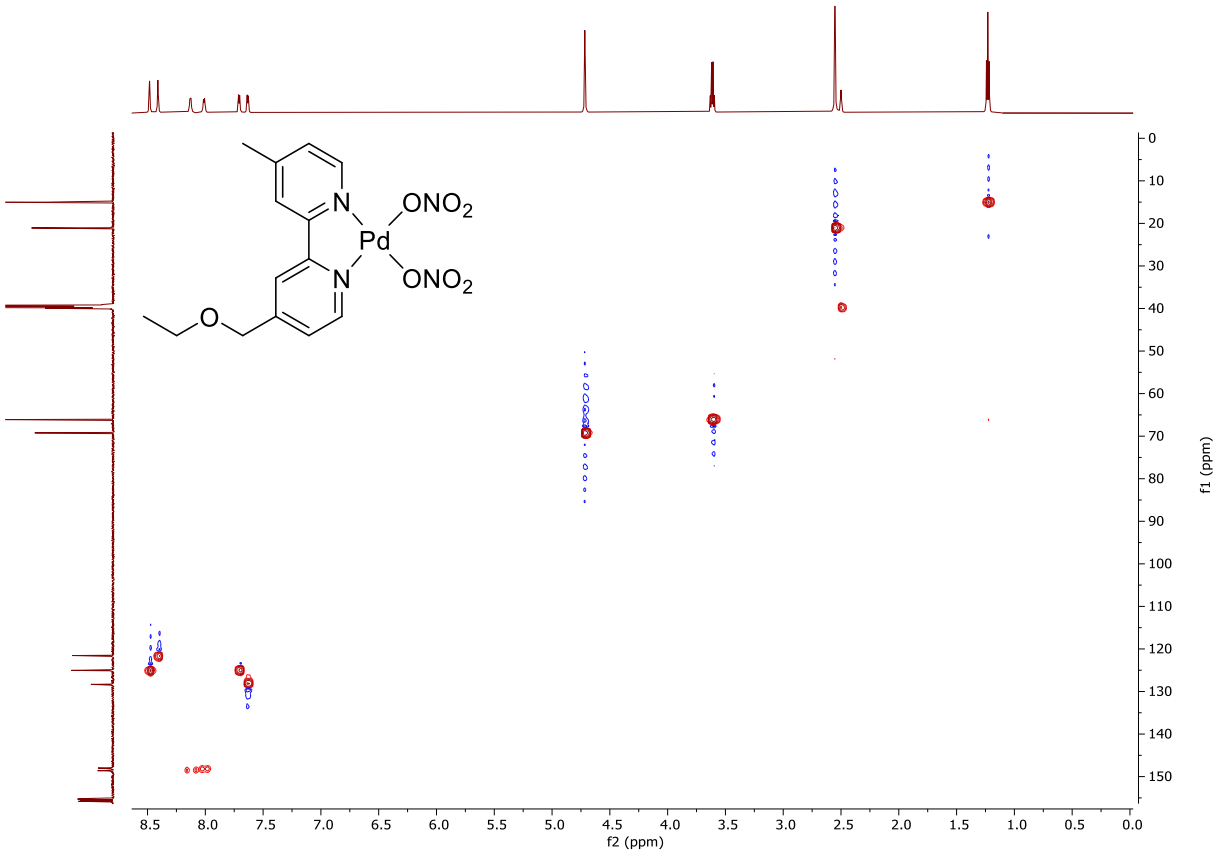

*Figure 117: ^{1}H-{^{13}C} HSQC NMR (600 MHz, DMSO-d_6) of (4-ethoxymethyl-4'-methyl-2,2'-bipyridine)-dinitratopalladium(II) (**21**).*

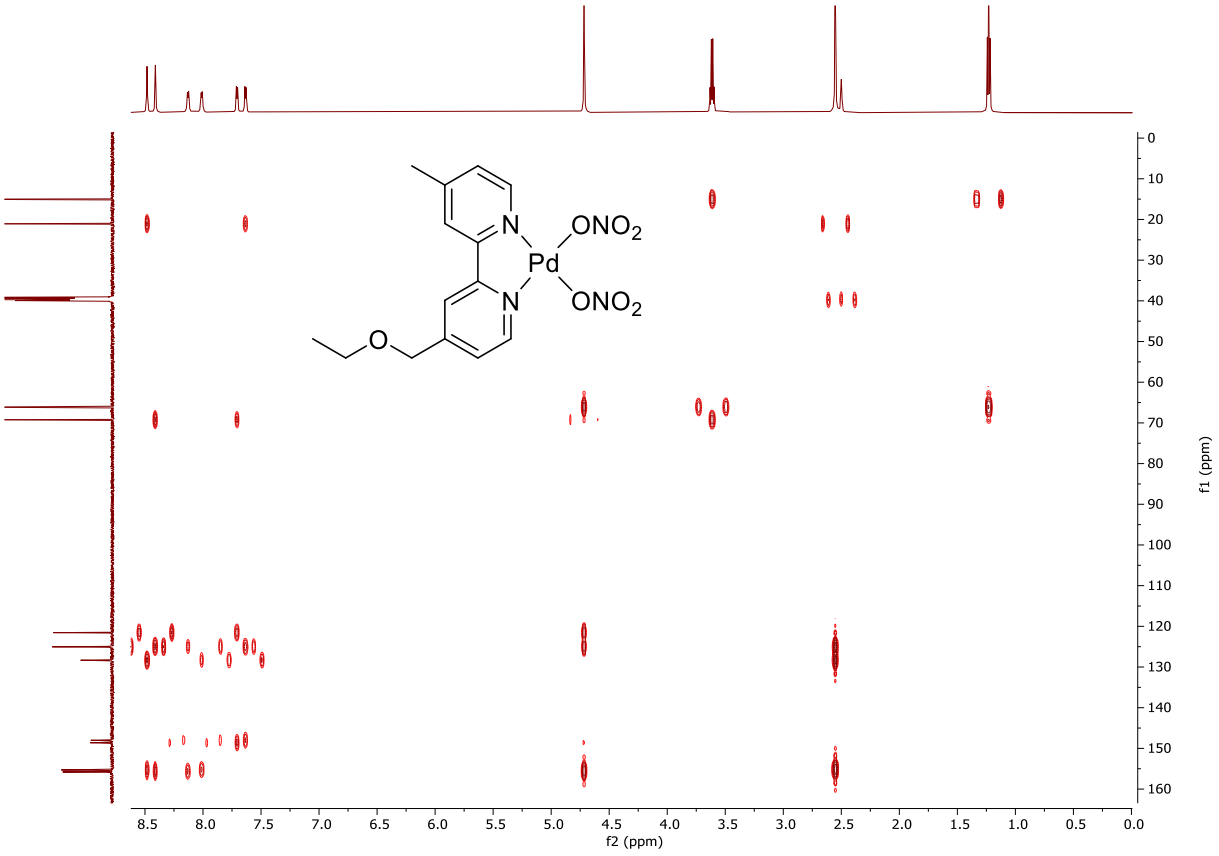

*Figure 118: ^{1}H-{^{13}C} HMBC NMR (600 MHz, DMSO-d_6) of (4-ethoxymethyl-4'-methyl-2,2'-bipyridine)-dinitratopalladium(II) (**21**).*

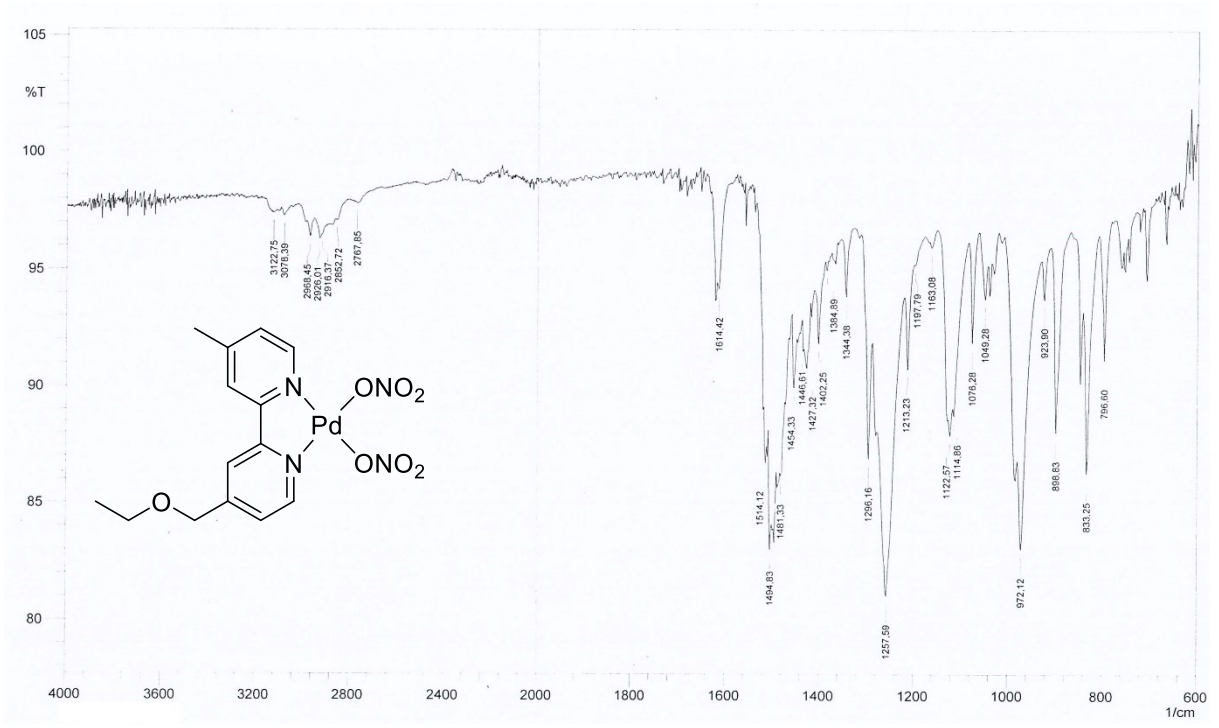

*Figure 119: IR spectrum of (4-ethoxymethyl-4'-methyl-2,2'-bipyridine)-dinitratopalladium(II) (**21**).*

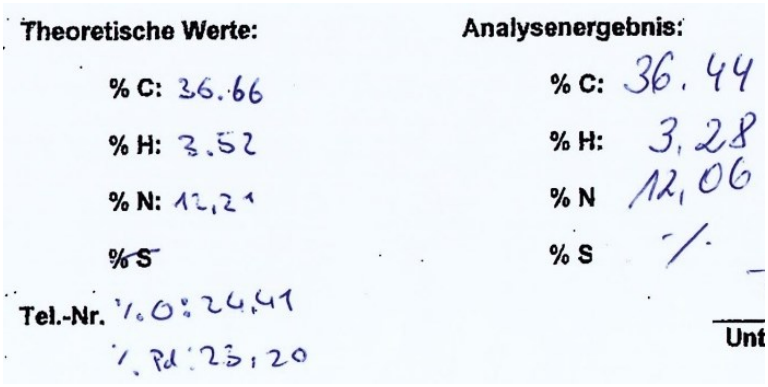

*Figure 120: Elemental analysis of (4-ethoxymethyl-4'-methyl-2,2'-bipyridine)-dinitratopalladium(II) (**21**).*

Cage MOC_1

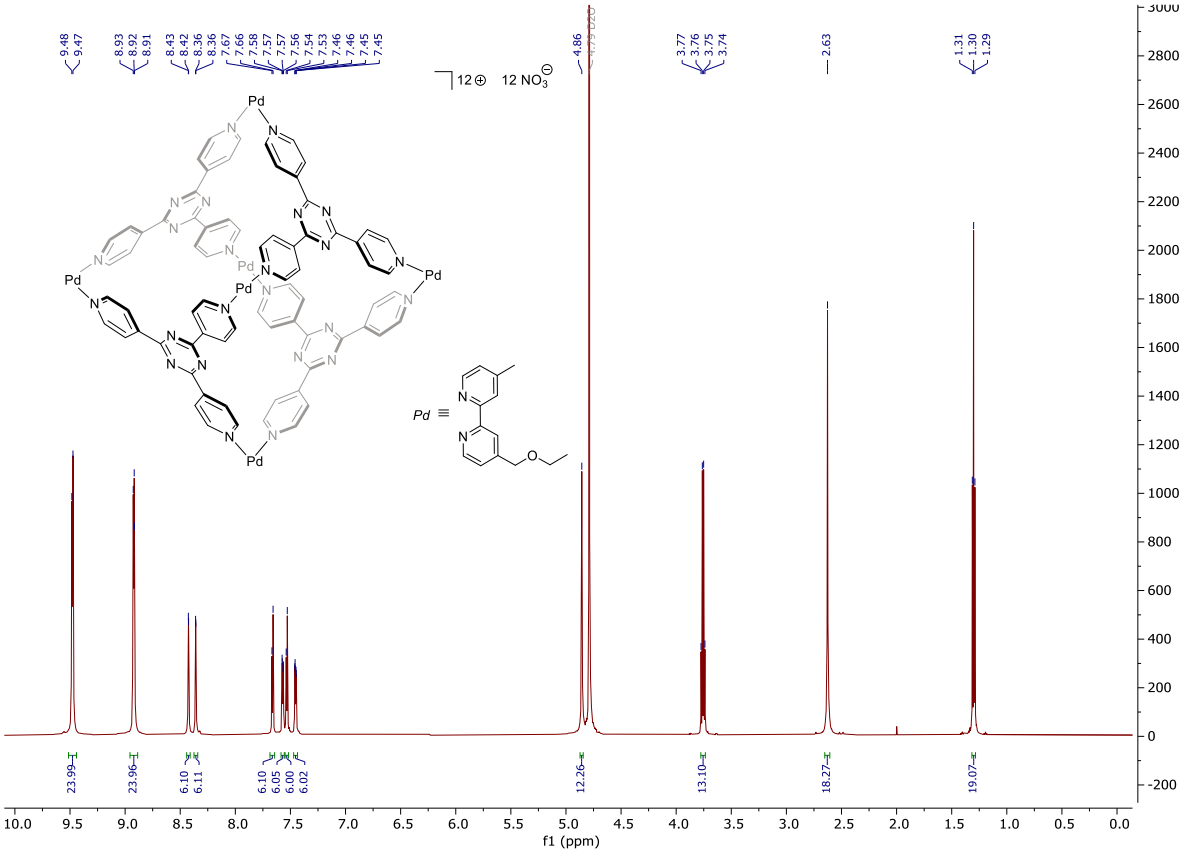

*Figure 121: ^1H NMR (600 MHz, D_2O) of cage **MOC_1**.*

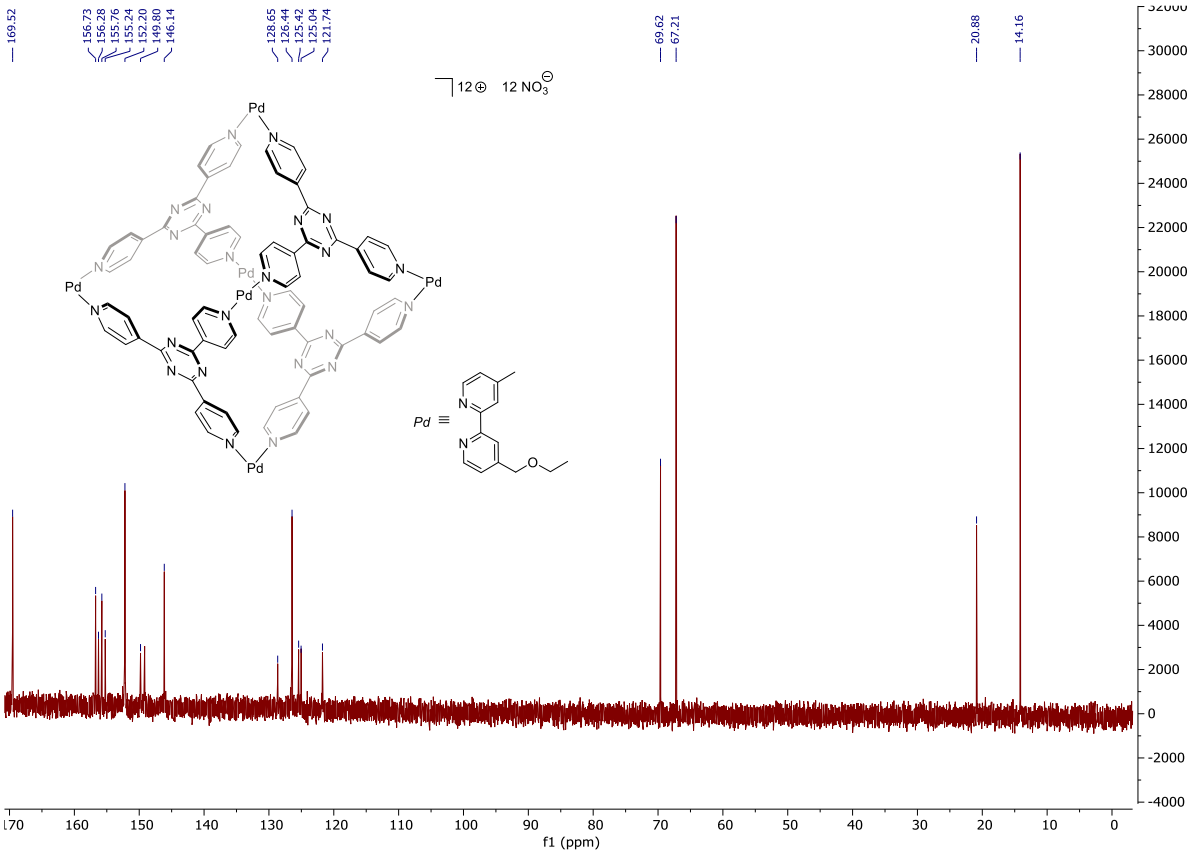

*Figure 122: $^{13}C\{^{1}H\}$ NMR (151 MHz, D_2O) of cage **MOC₁**.*

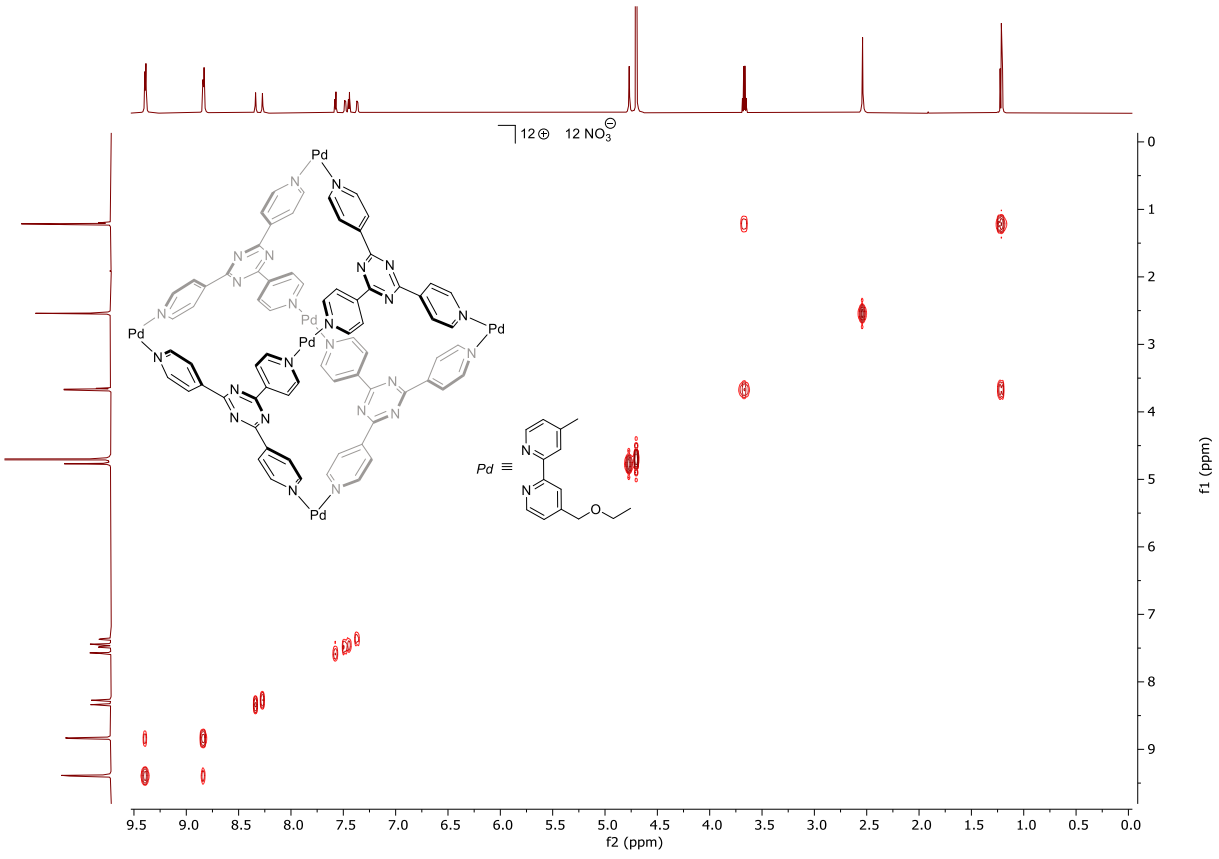

*Figure 123: ^{1}H-^{1}H COSY NMR (600 MHz, D_2O) of cage **MOC₁**.*

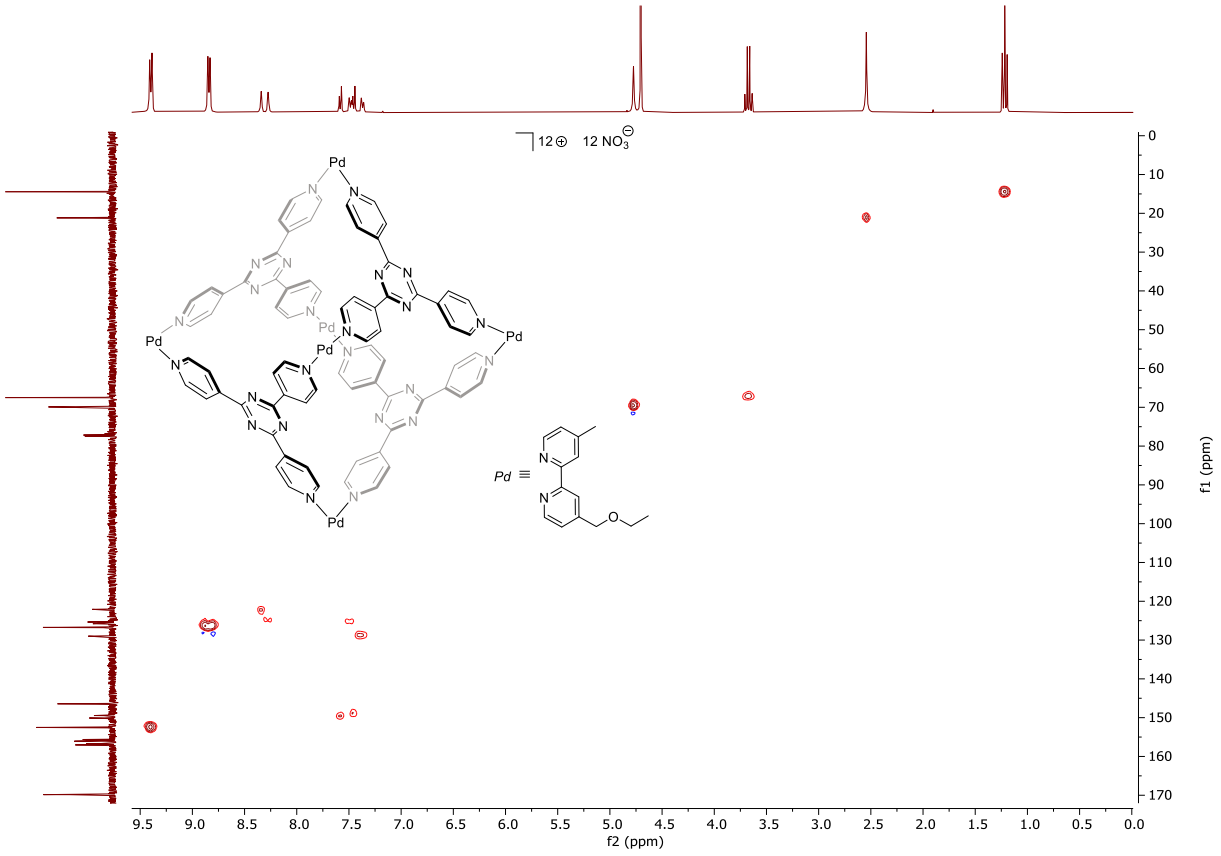

*Figure 124: ^{1}H-{^{13}C} HSQC NMR (600 MHz, D_2O) of cage **MOC_1**.*

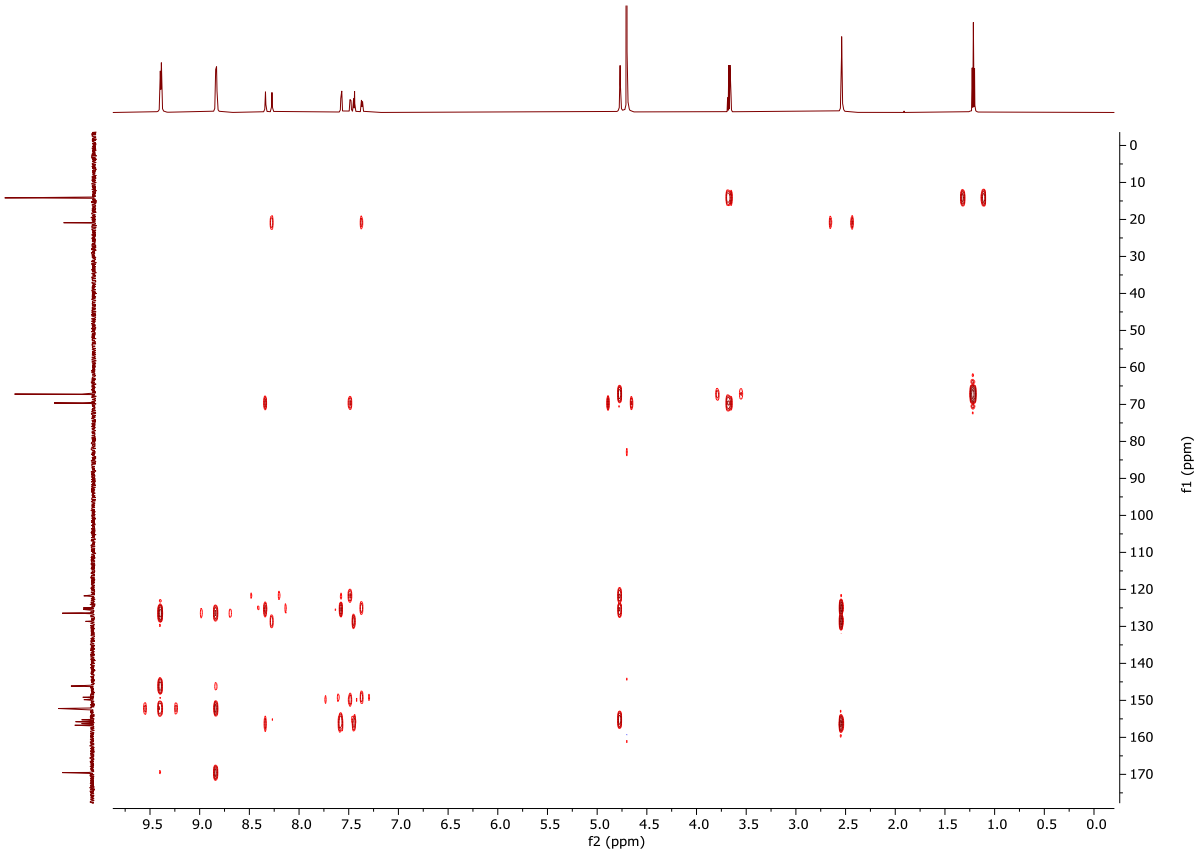

*Figure 125: ^{1}H-{^{13}C} HMBC NMR (600 MHz, D_2O) of cage **MOC_1**.*

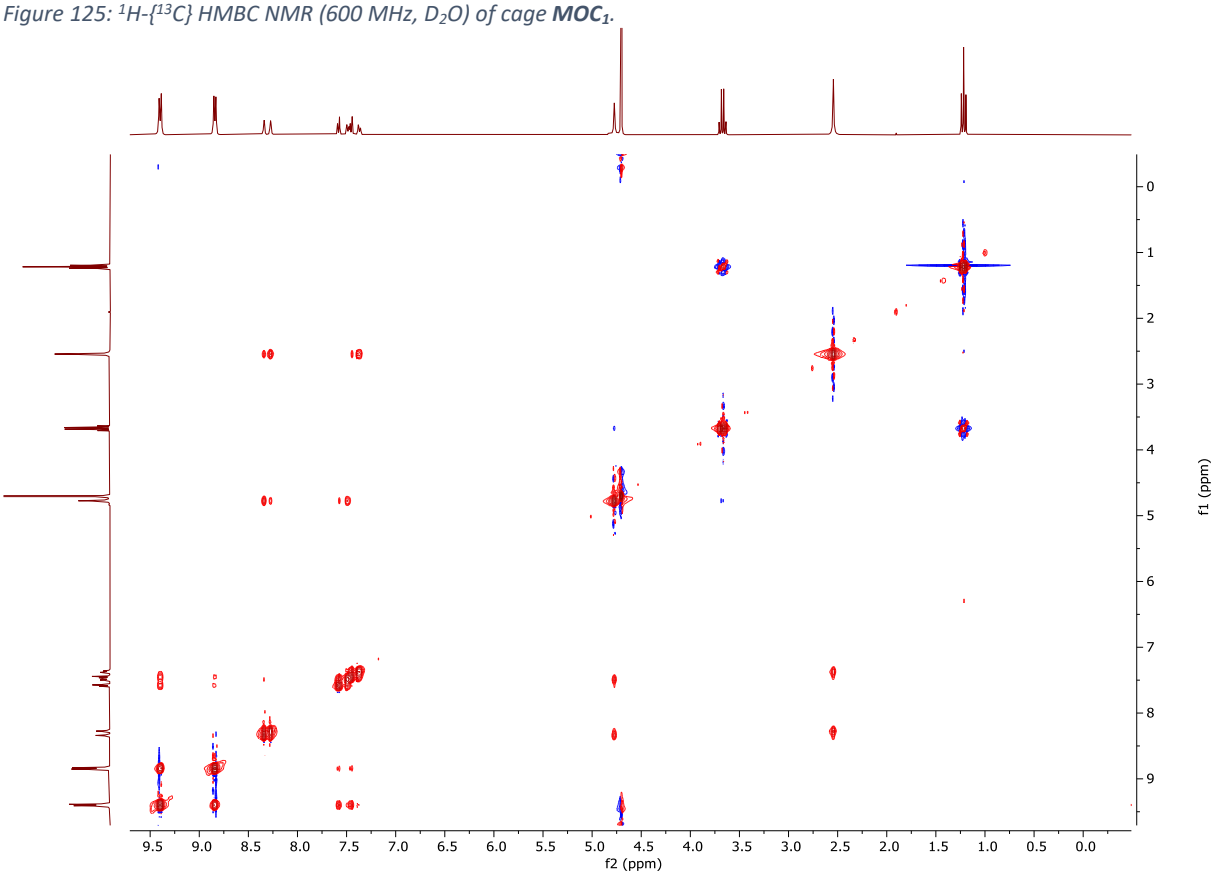

*Figure 126: ^{1}H-^{1}H NOESY NMR (300 MHz, D_2O) of cage **MOC_1**. Baseline correction with Whittaker Smoother: Filter=1, Smooth factor=256.*

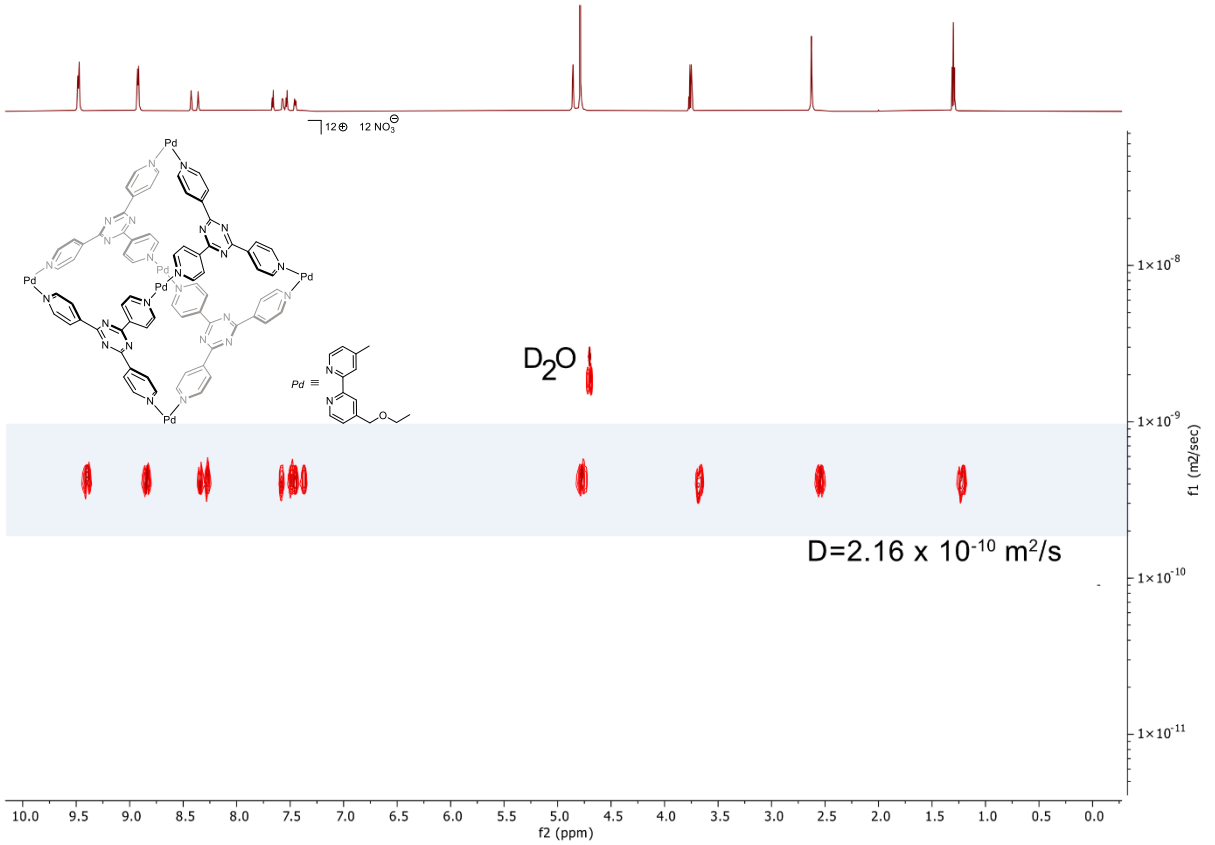

*Figure 127: DOSY NMR (600 MHz, D_2O) of cage **MOC_1**.*

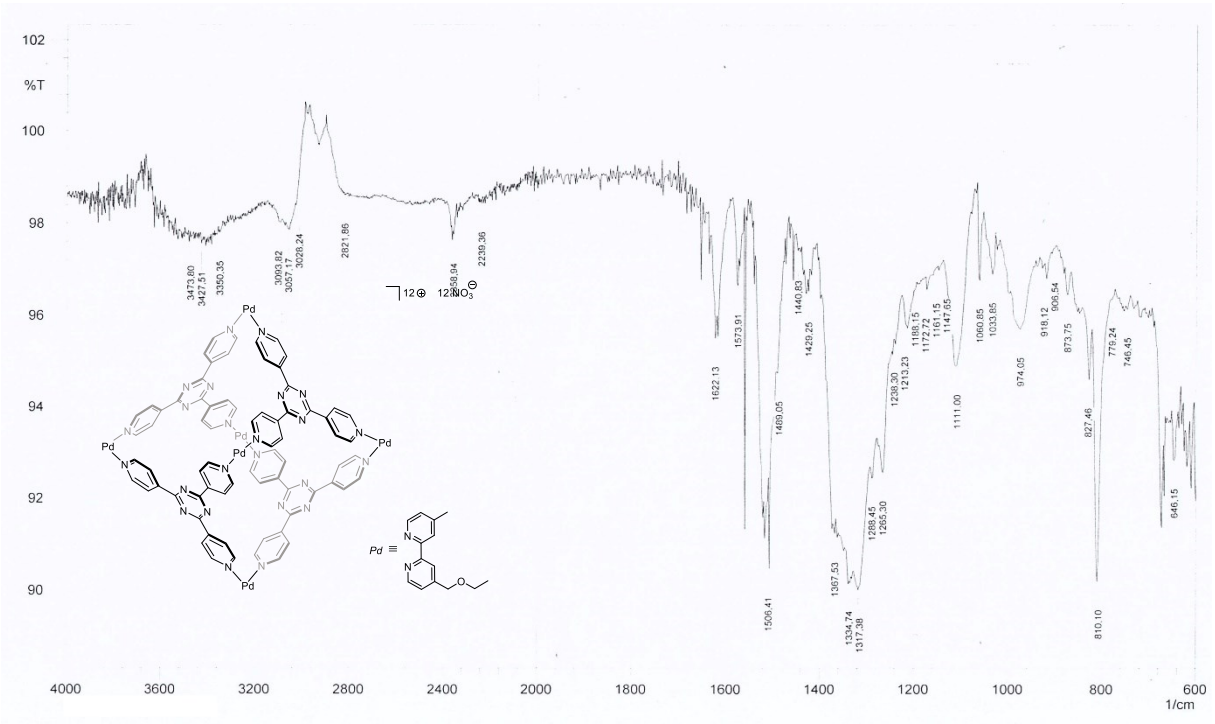

*Figure 128: IR spectrum of cage **MOC_1**.*

4-Methoxypolyethyleneglycolmethyl-4’-methyl-2,2’-bipyridine (**22**)

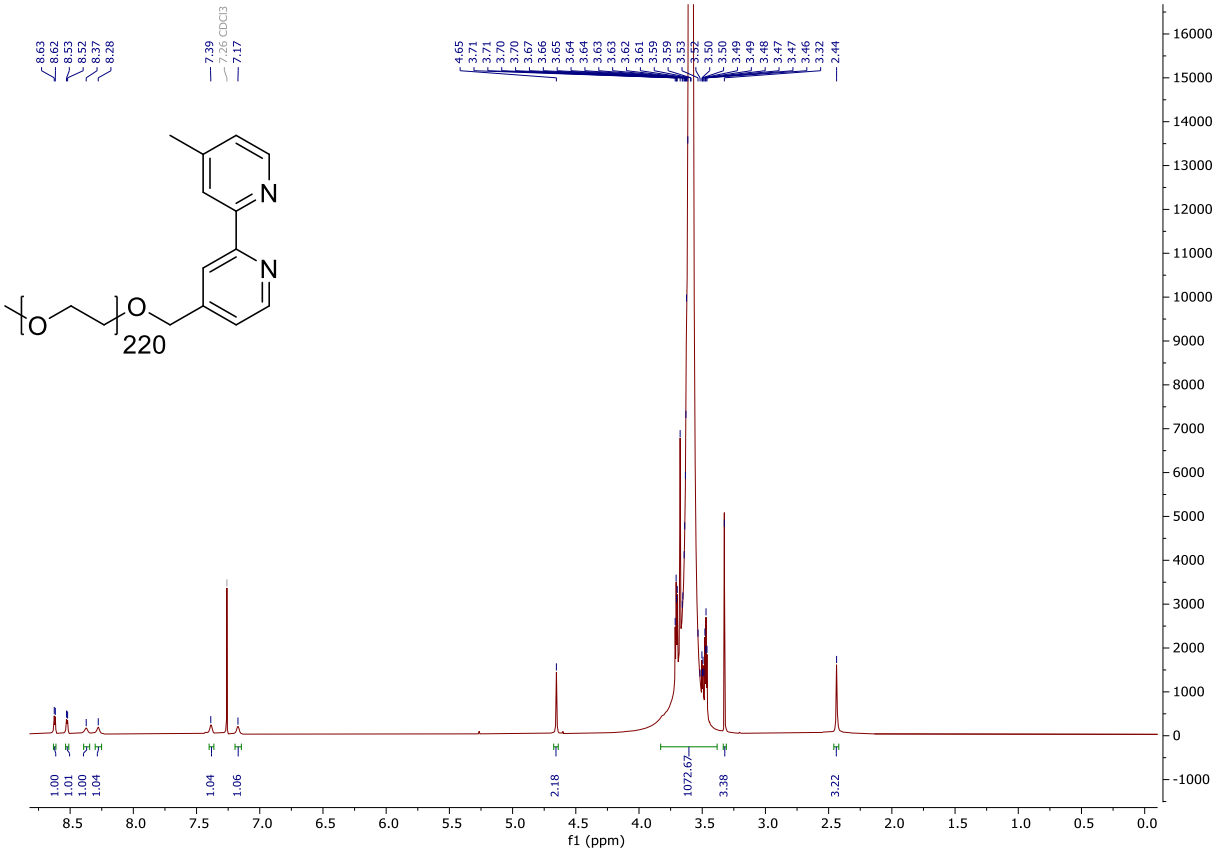

*Figure 129: ^{1}H NMR (600 MHz, D_2O) of 4-methoxypolyethyleneglycolmethyl-4’-methyl-2,2’-bipyridine (**22**).*

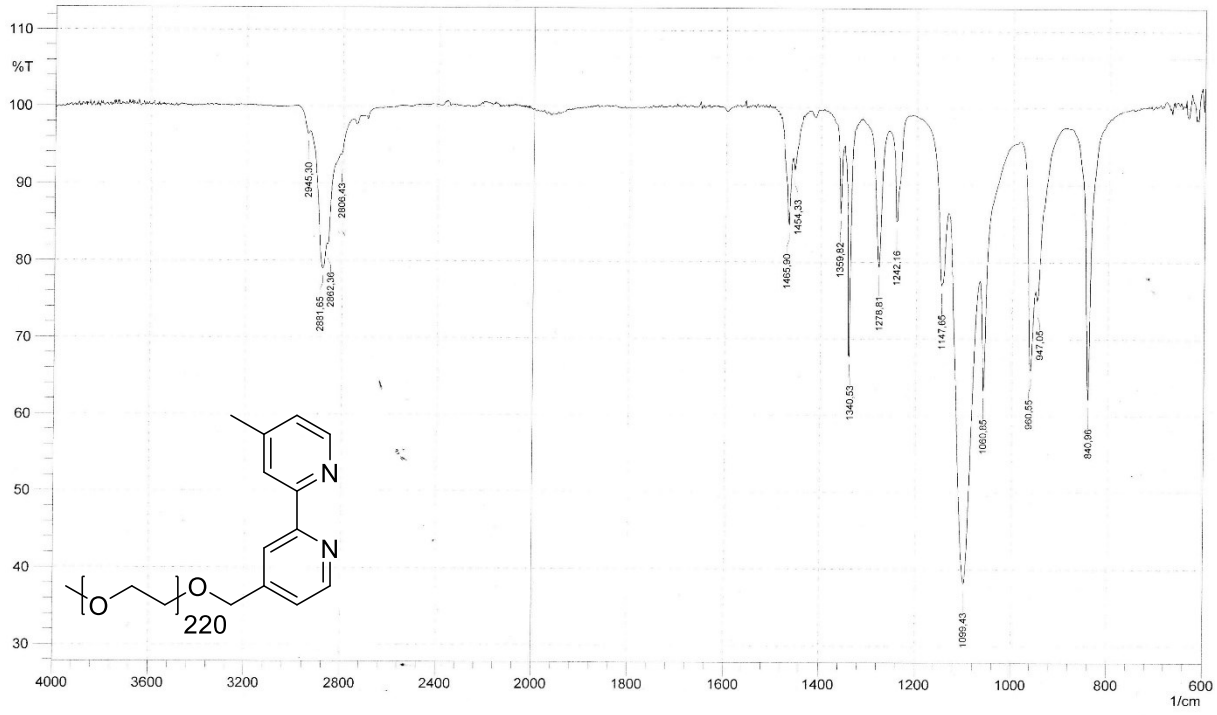

*Figure 130: IR spectrum of 4-methoxypolyethyleneglycolmethyl-4’-methyl-2,2’-bipyridine (**22**).*

(4-Methoxypolyethyleneglycolmethyl-4‘-methyl-2,2‘-bibyridine)-dichloropalladium(II) (**23**)

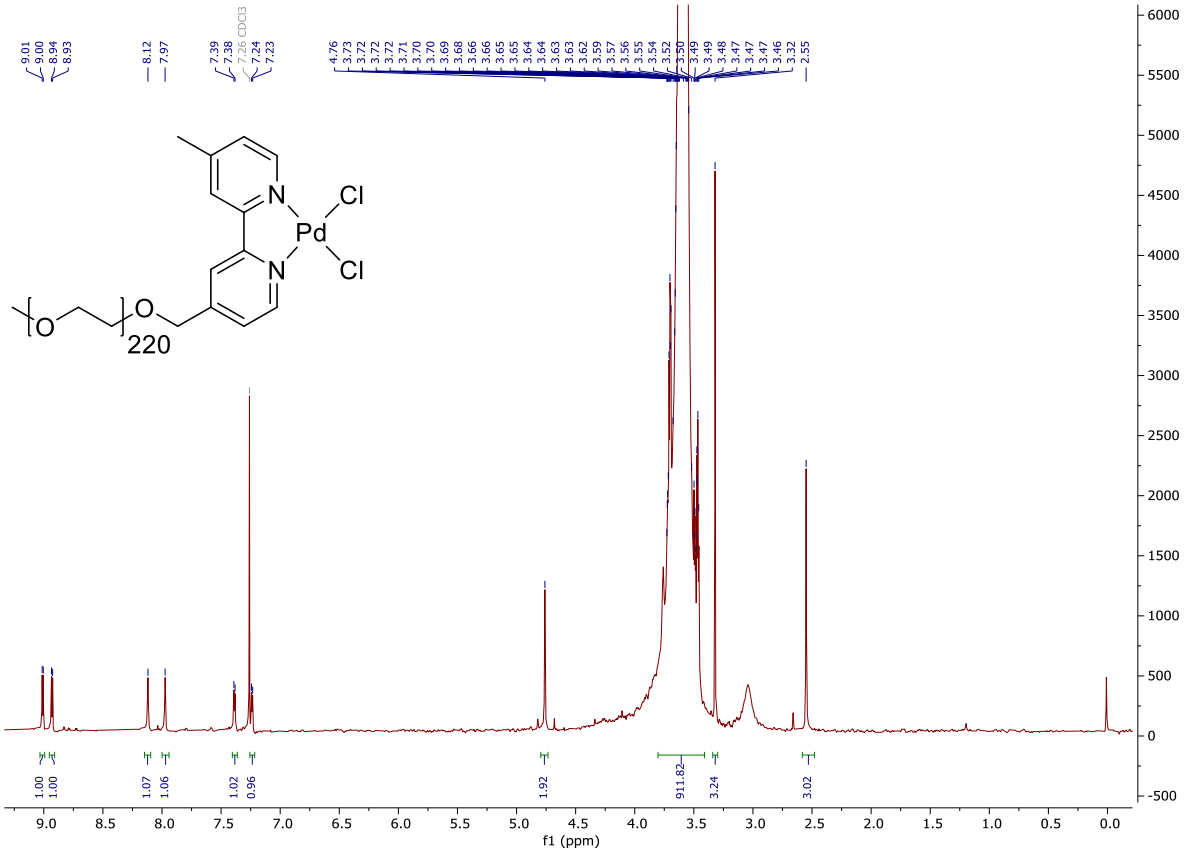

*Figure 131: ^{1}H NMR (600 MHz, $CDCl_3$) of (4-methoxypolyethyleneglycolmethyl-4’-methyl-2,2’-bipyridine)-dichloropalladium(II) (**23**).*

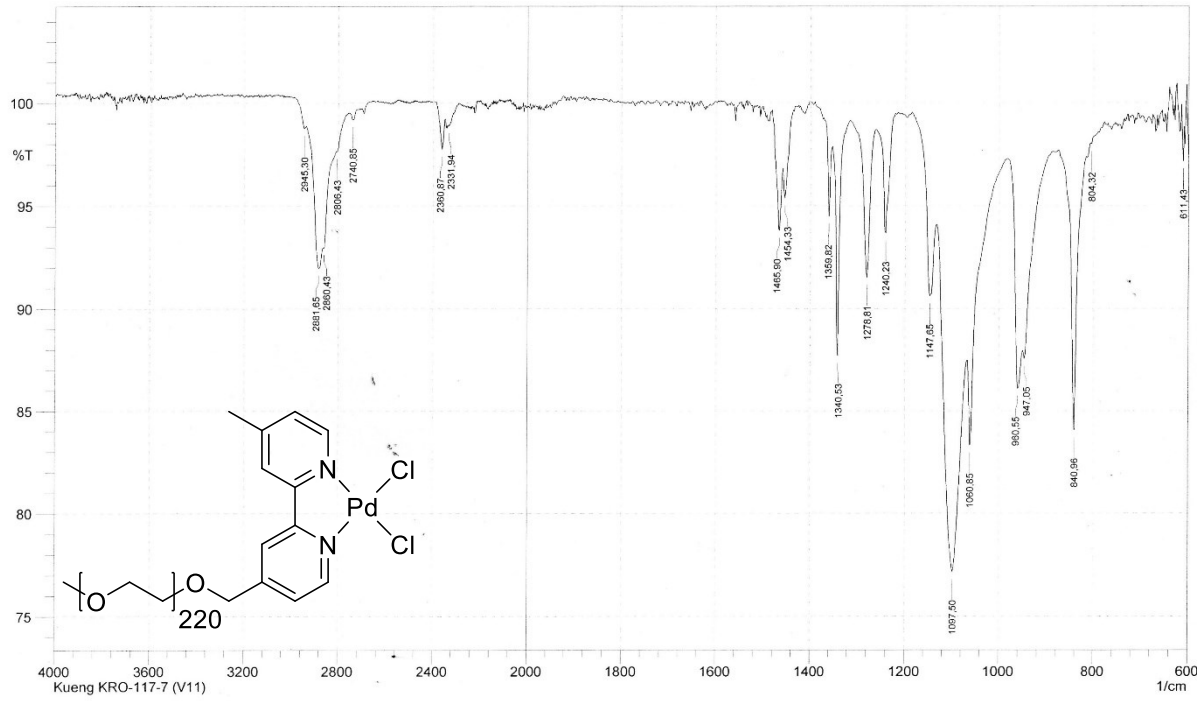

*Figure 132: IR spectrum of (4-methoxypolyethyleneglycolmethyl-4’-methyl-2,2’-bipyridine)-dichloropalladium(II) (**23**).*

(4-Methoxypolyethyleneglycolmethyl-4'-methyl-2,2'-bipyridine)-dinitratopalladium(II) (**24**)

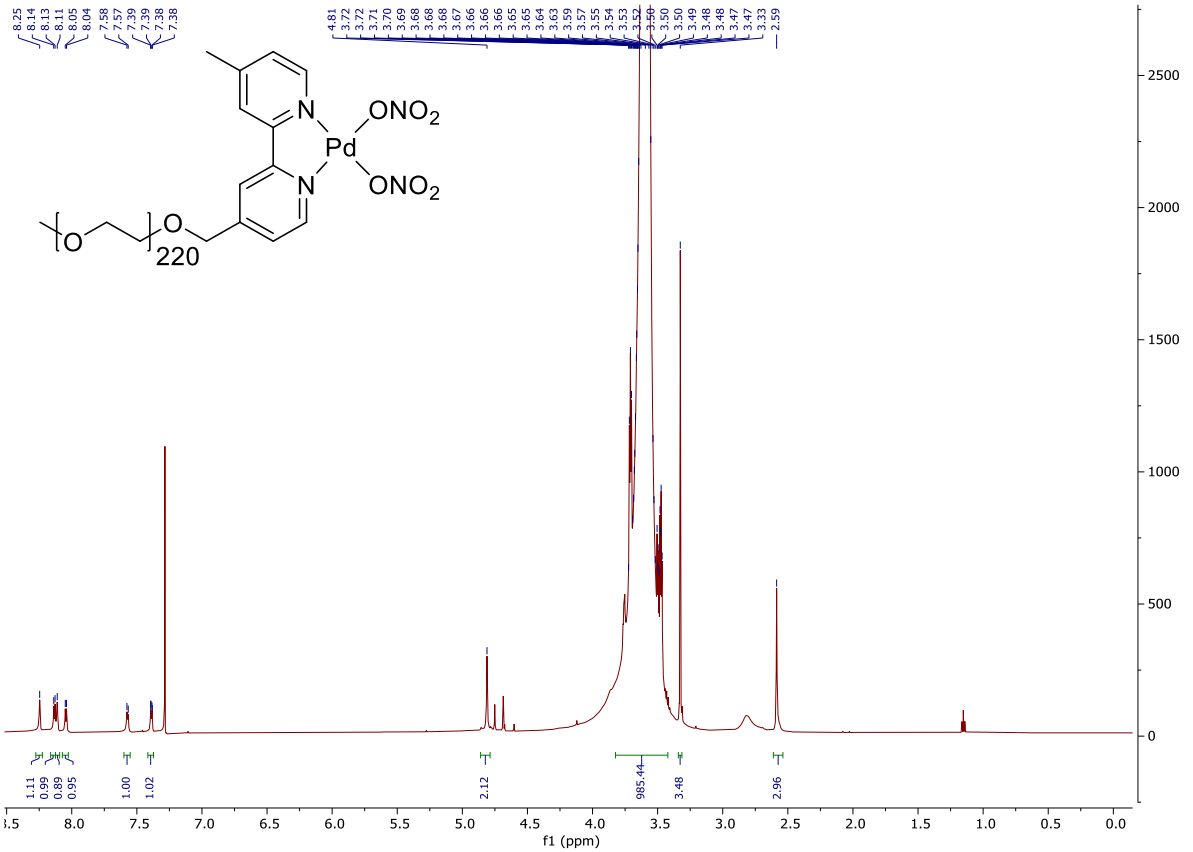

*Figure 133: ^{1}H NMR (600 MHz, $CDCl_3$) of (4-methoxypolyethyleneglycolmethyl-4'-methyl-2,2'-bipyridine)-dinitratopalladium(II) (**24**).*

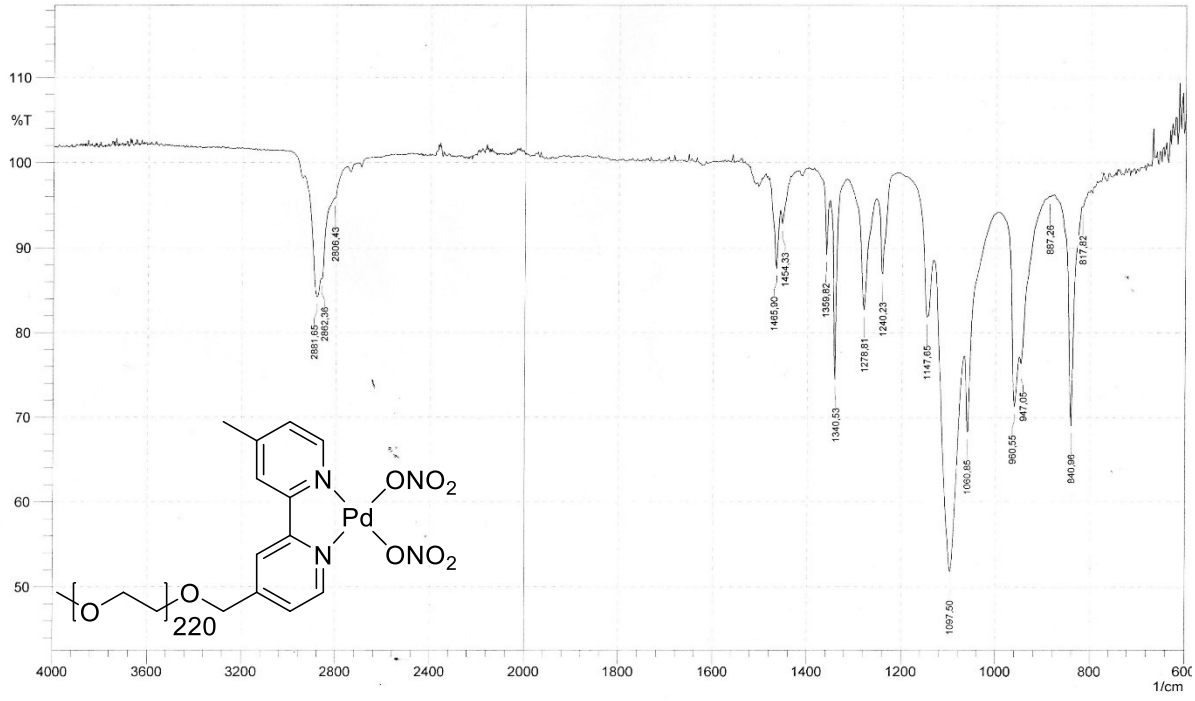

*Figure 134: IR spectrum of (4-methoxypolyethyleneglycolmethyl-4'-methyl-2,2'-bipyridine)-dinitratopalladium(II) (**24**).*

Cage **polyMOC$_{60}$**

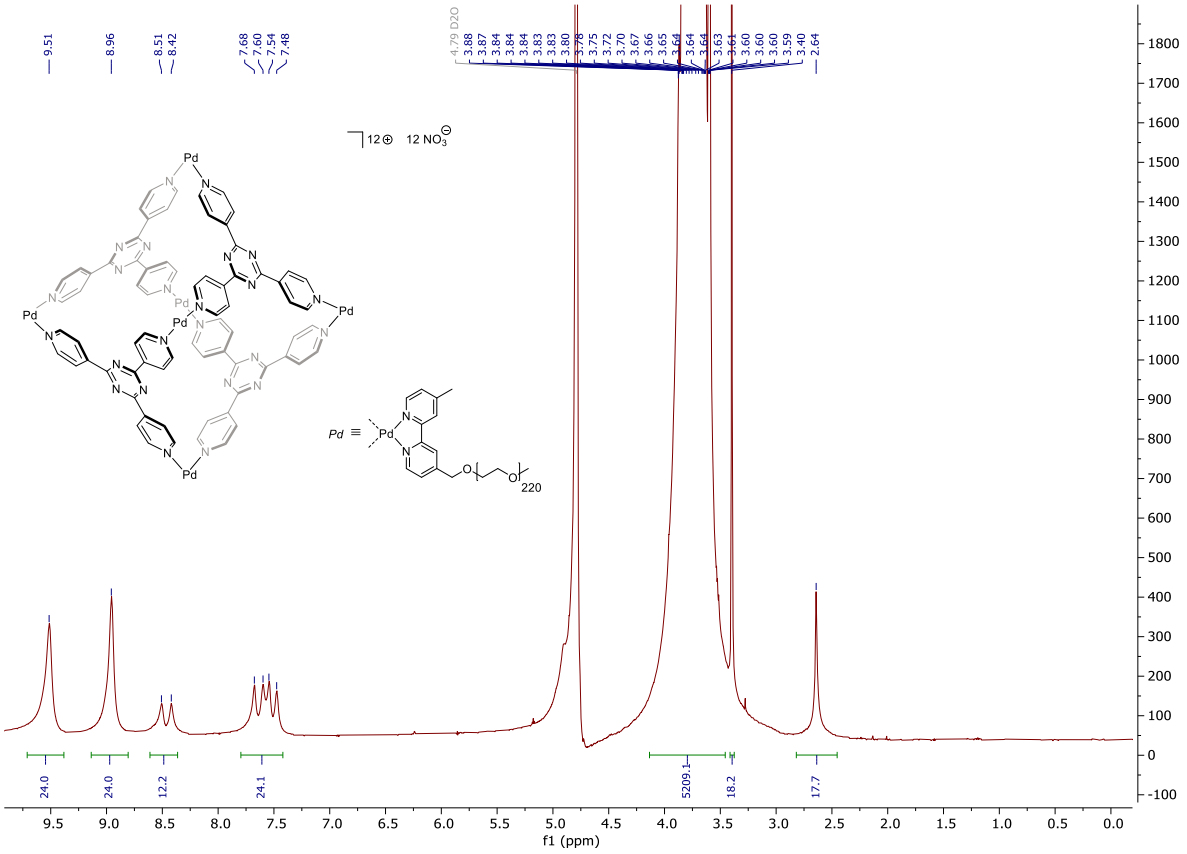

*Figure 135: ^{1}H NMR (600 MHz, D_2O) of cage **polyMOC$_{60}$**.*

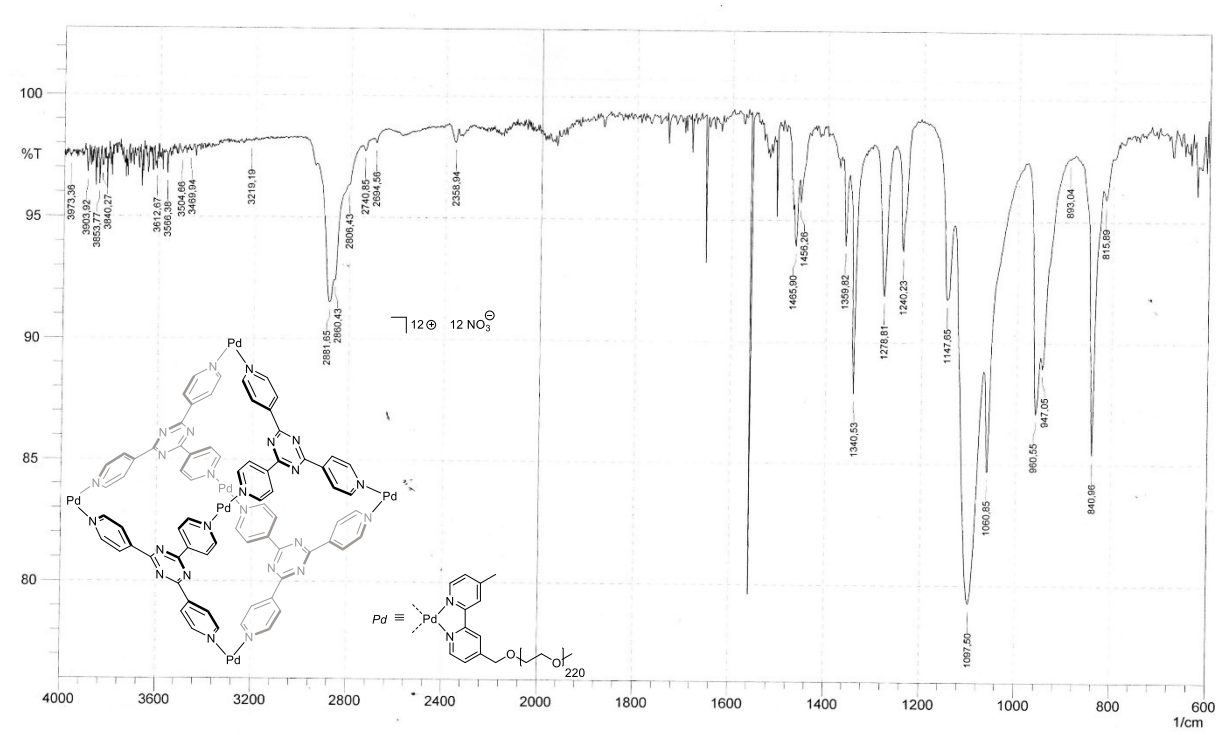

*Figure 136: IR spectrum of cage **polyMOC$_{60}$**.*

4-Methoxypolyethyleneglycolmethyl-4'-methyl-2,2'-bipyridine (**25**)

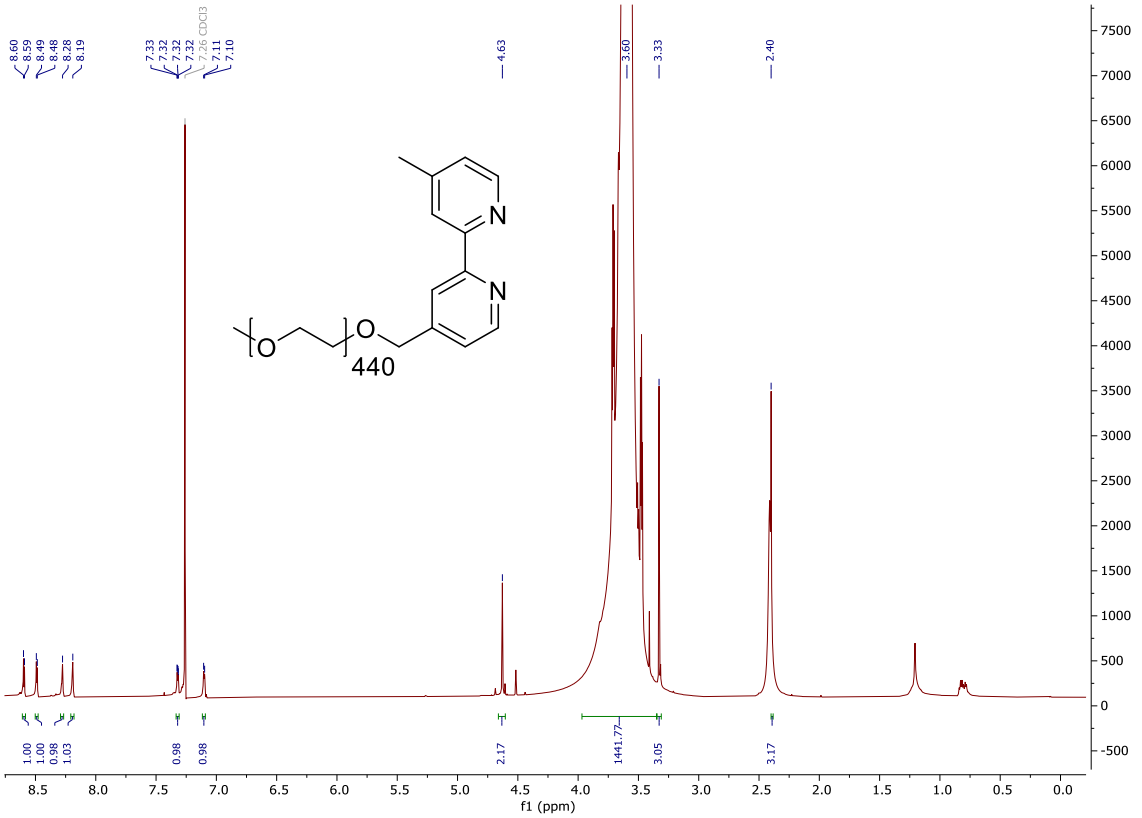

*Figure 137 ^{1}H NMR (600 MHz, $CDCl_3$) of 4-methoxypolyethyleneglycolmethyl-4'-methyl-2,2'-bipyridine (**25**).*

(4-Methoxypolyethyleneglycolmethyl-4'-methyl-2,2'-bibyridine)-dichloropalladium(II) (**26**)

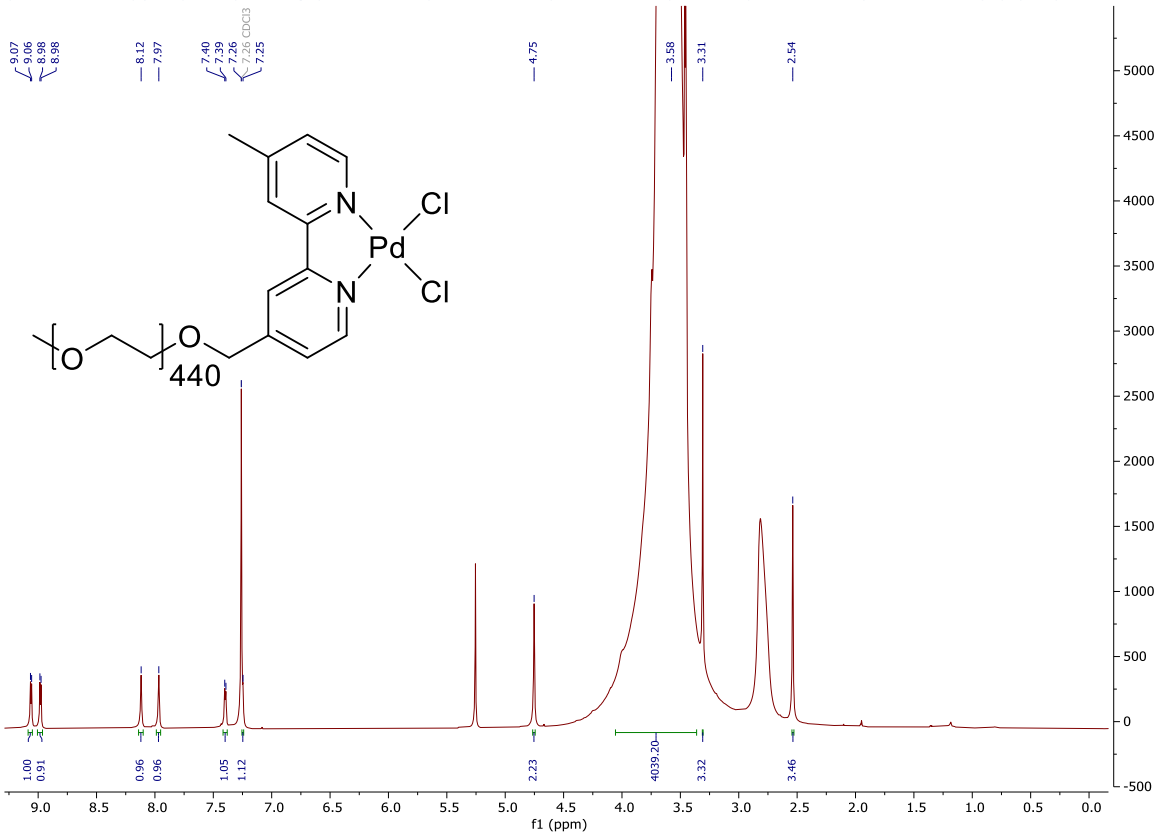

*Figure 138: ^{1}H NMR (600 MHz, $CDCl_3$) of (4-methoxypolyethyleneglycolmethyl-4'-methyl-2,2'-bipyridine)-dichloropalladium(II) (**26**).*

(4-Methoxypolyethyleneglycolmethyl-4’-methyl-2,2’-bipyridine)-dinitratopalladium(II) (**27**)

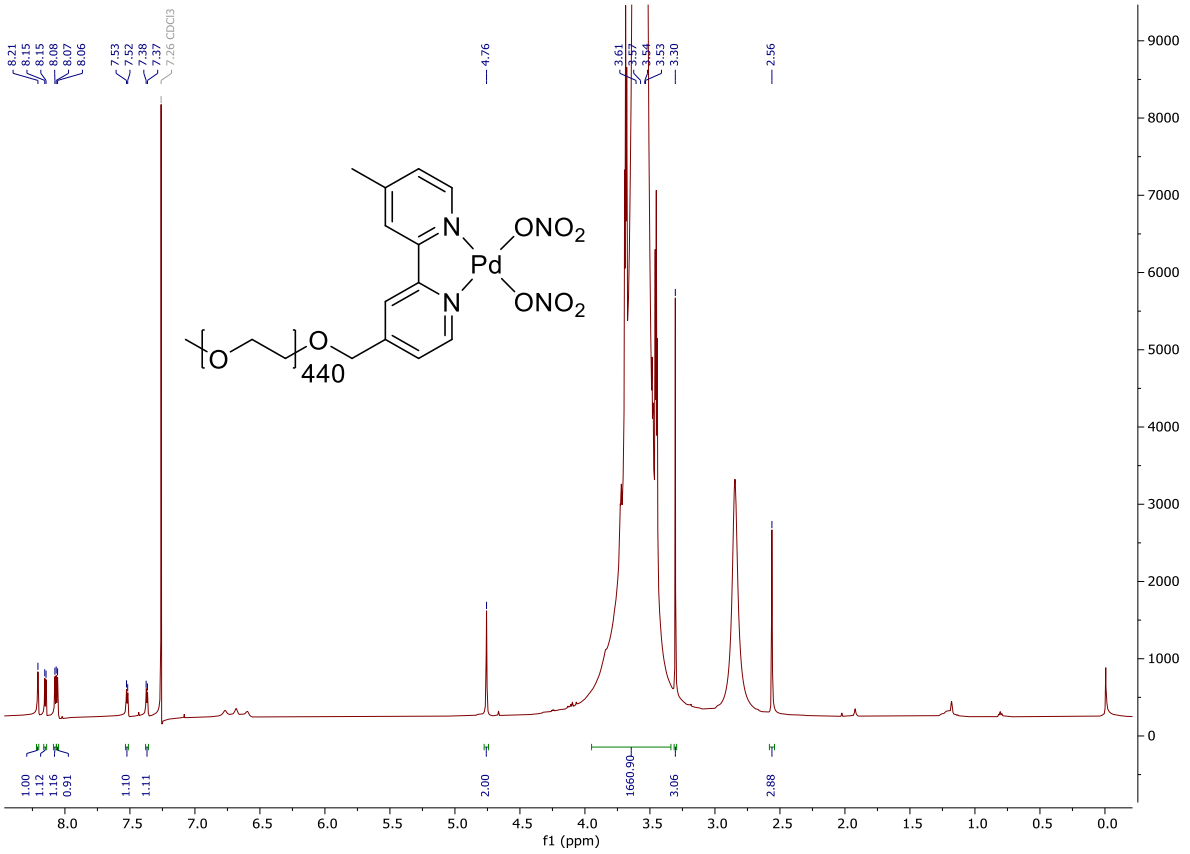

*Figure 139: ^{1}H NMR (600 MHz, $CDCl_3$) of (4-methoxypolyethyleneglycolmethyl-4’-methyl-2,2’-bipyridine)-dinitratopalladium(II) (**27**).*

Cage **polyMOC$_{120}$**

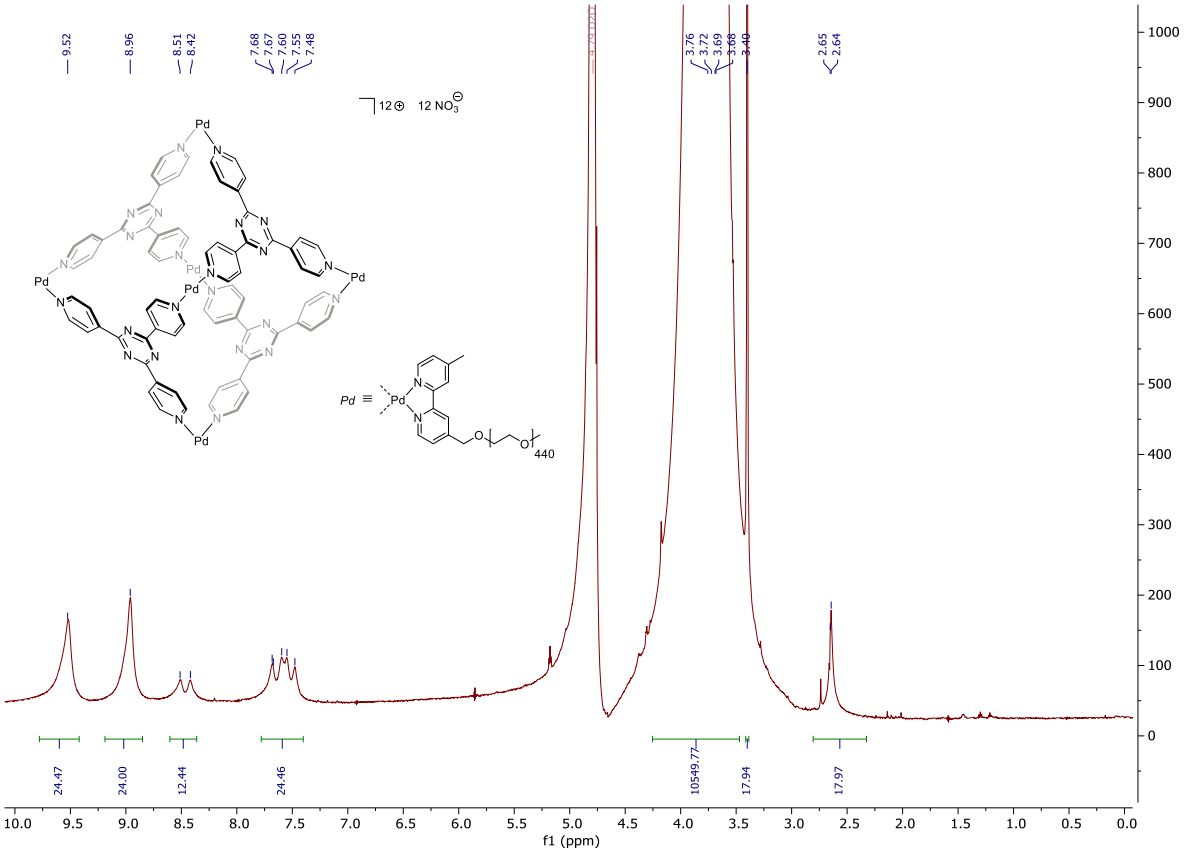

*Figure 140: ^{1}H NMR (600 MHz, D_2O) of cage **polyMOC$_{120}$**.*

Section for encapsulation

Encapsulation with **MOC_1**

Steroids

Progesterone

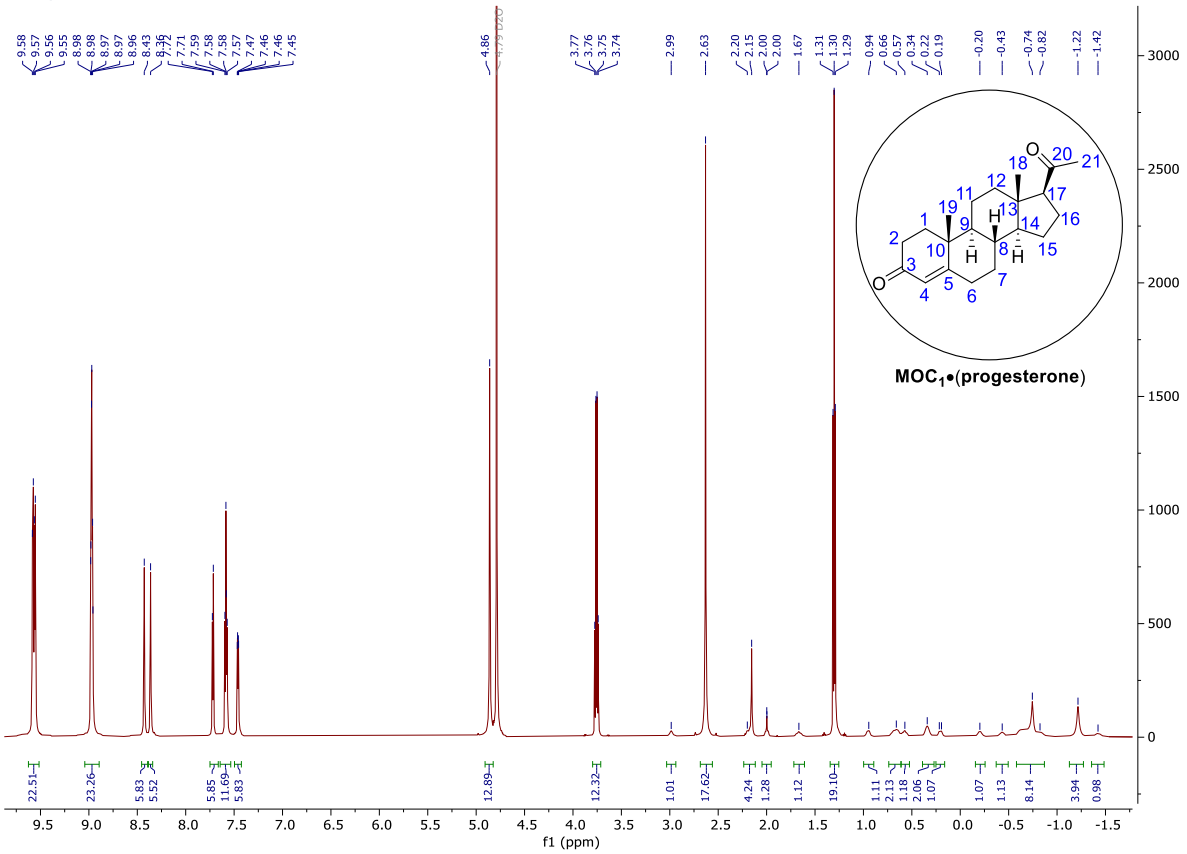

*Figure 141: ^{1}H NMR (600 MHz, D_2O) of **MOC_1•(progesterone)**.*

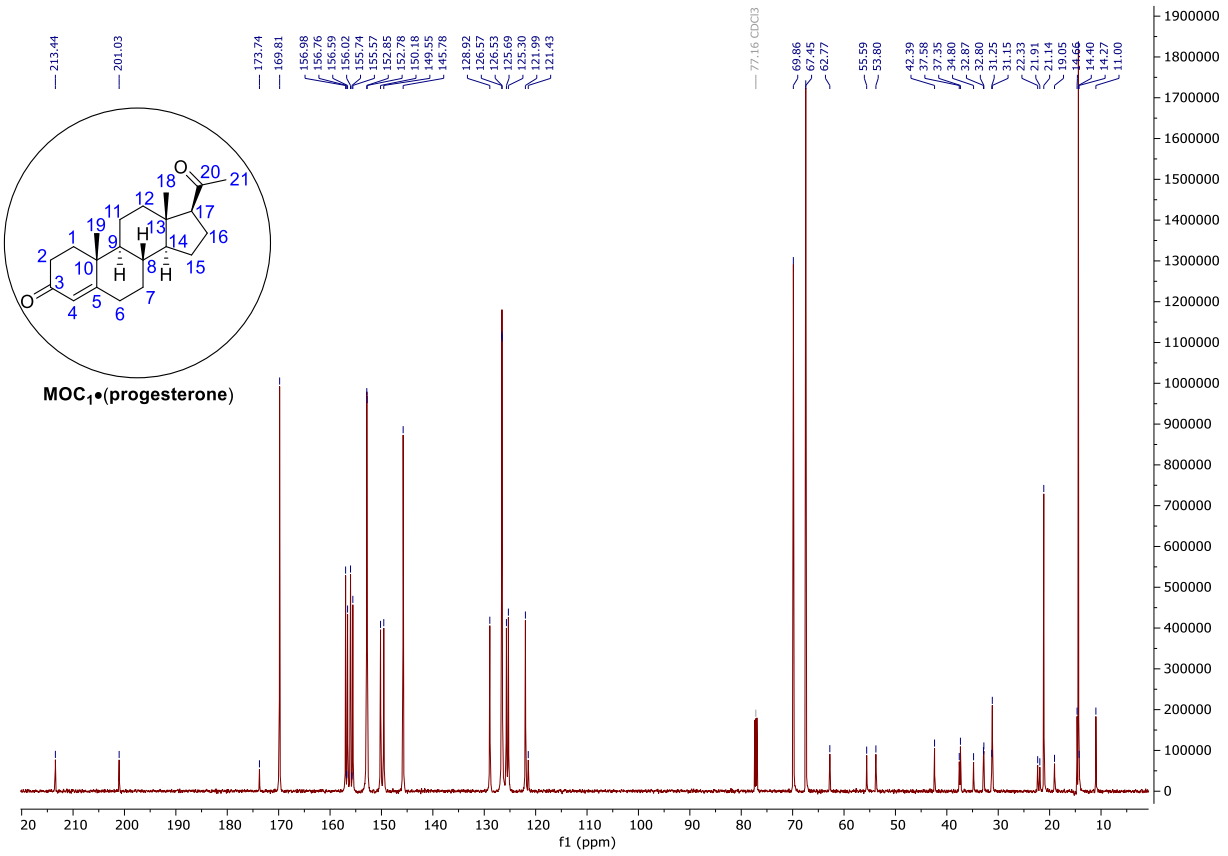

*Figure 142: $^{13}C\{^{1}H\}$ NMR (151 MHz, D_2O) of **MOC_1•(progesterone)**.*

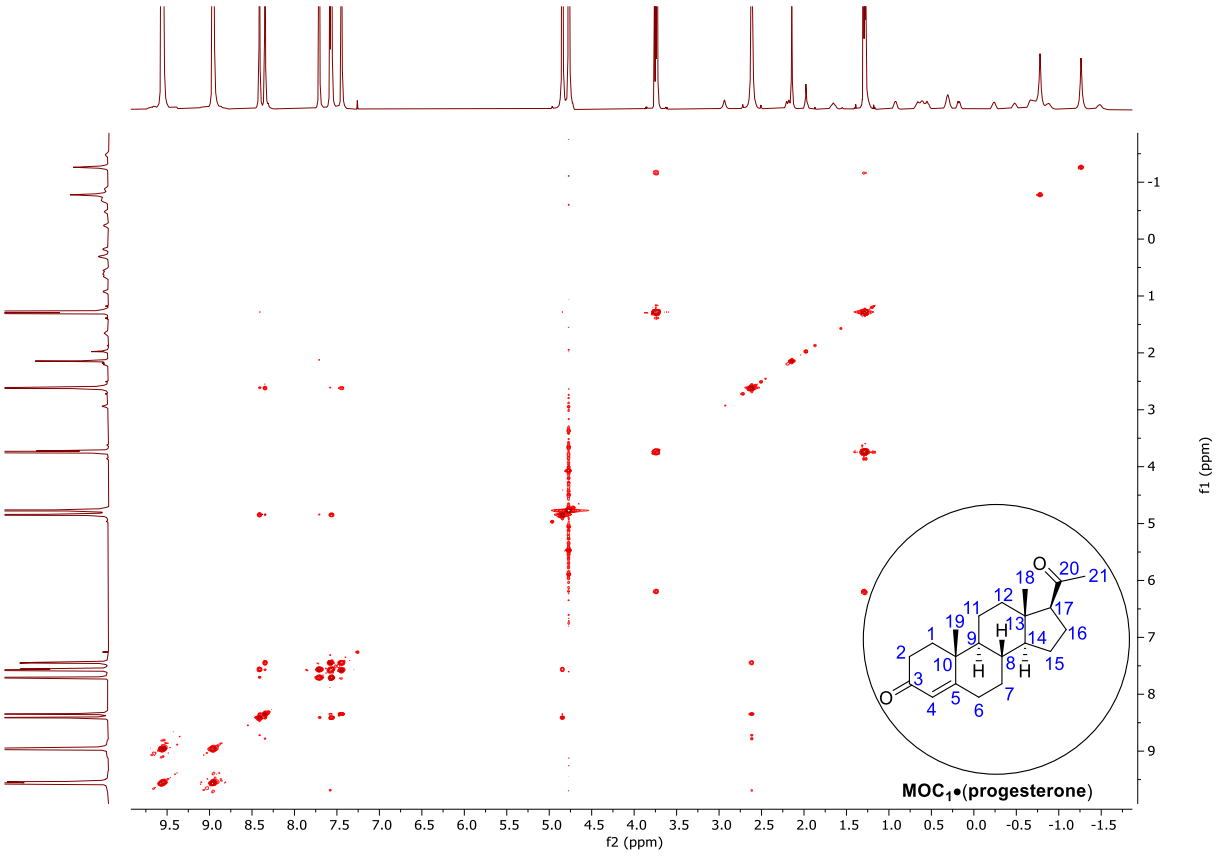

*Figure 143: ^{1}H-^{1}H COSY NMR (600 MHz, D_2O) of **MOC_1•(progesterone)**.*

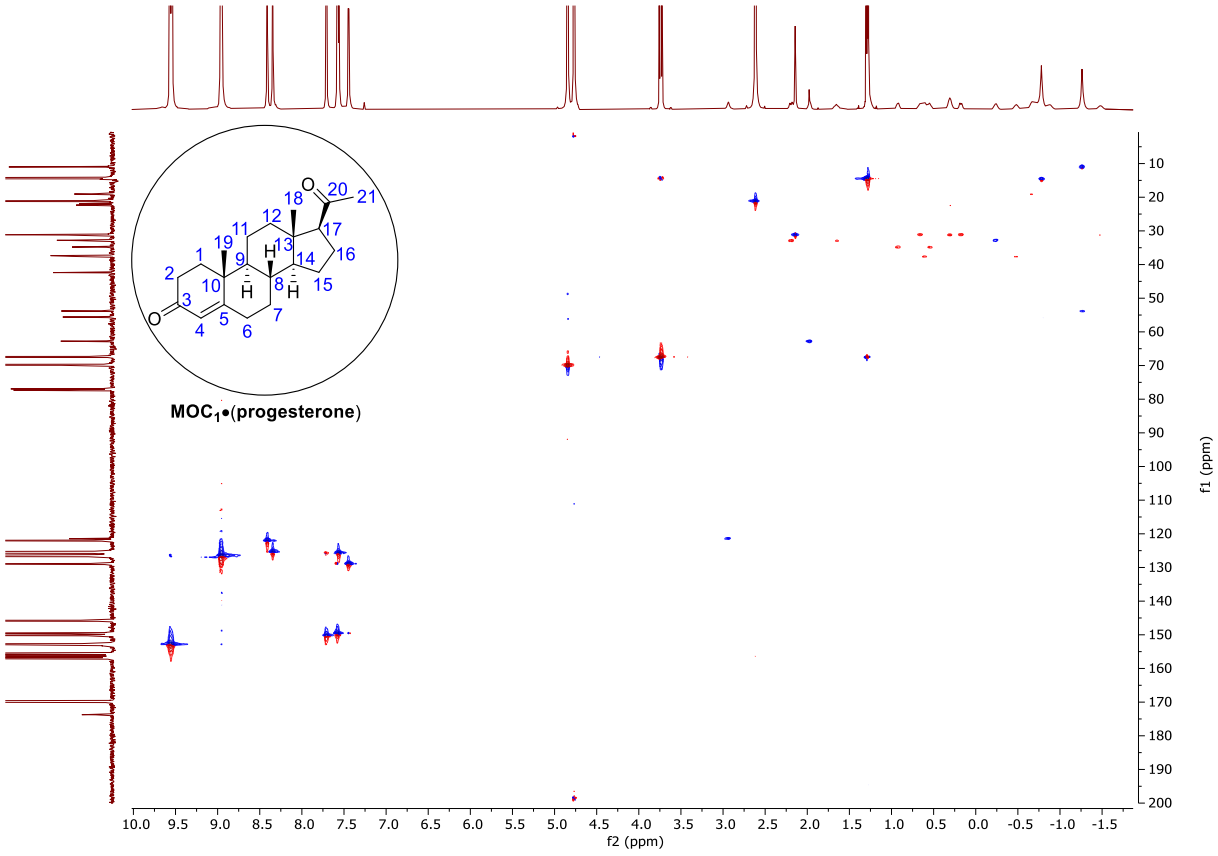

*Figure 144: ^{1}H-{^{13}C} HSQC NMR (600 MHz, D_2O) of **MOC_1•(progesterone)**.*

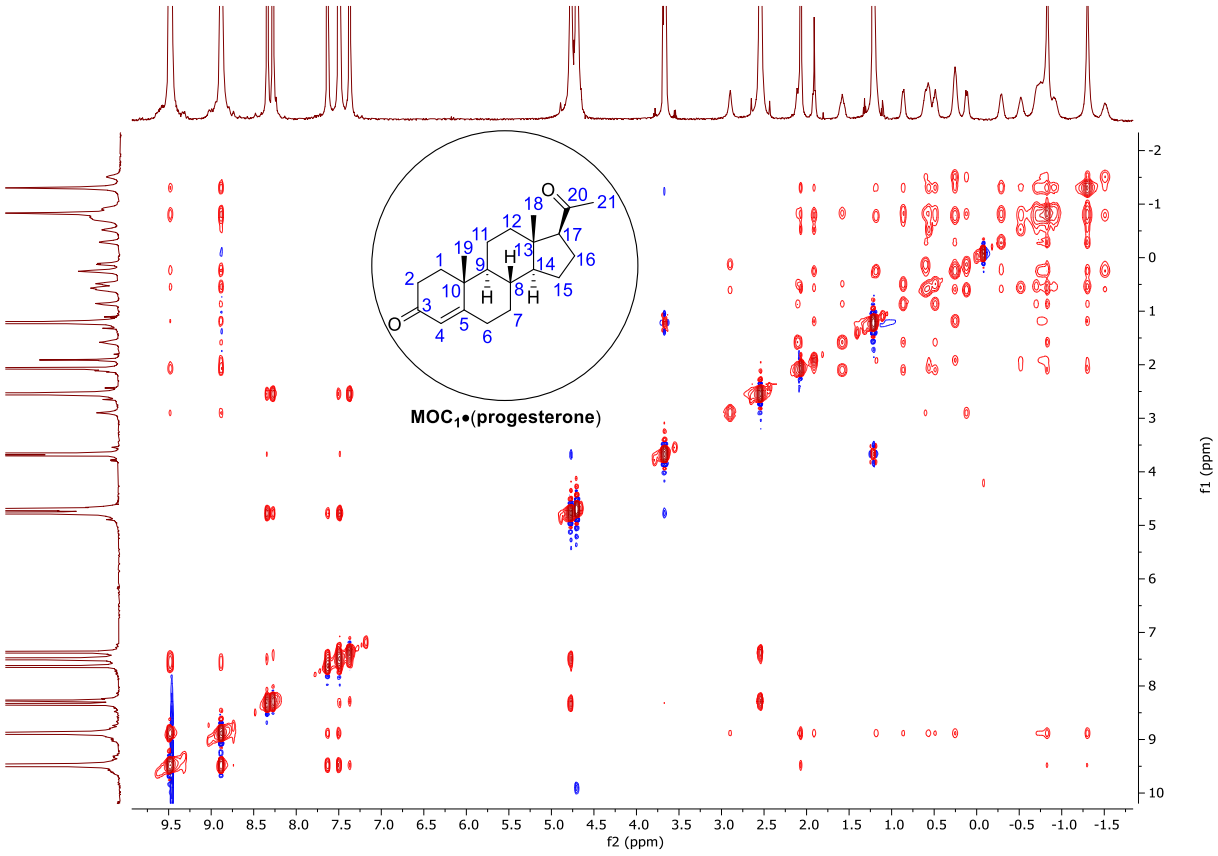

*Figure 145: ^{1}H NOESY NMR (600 MHz, D_2O) of **MOC_1•(progesterone)**.*

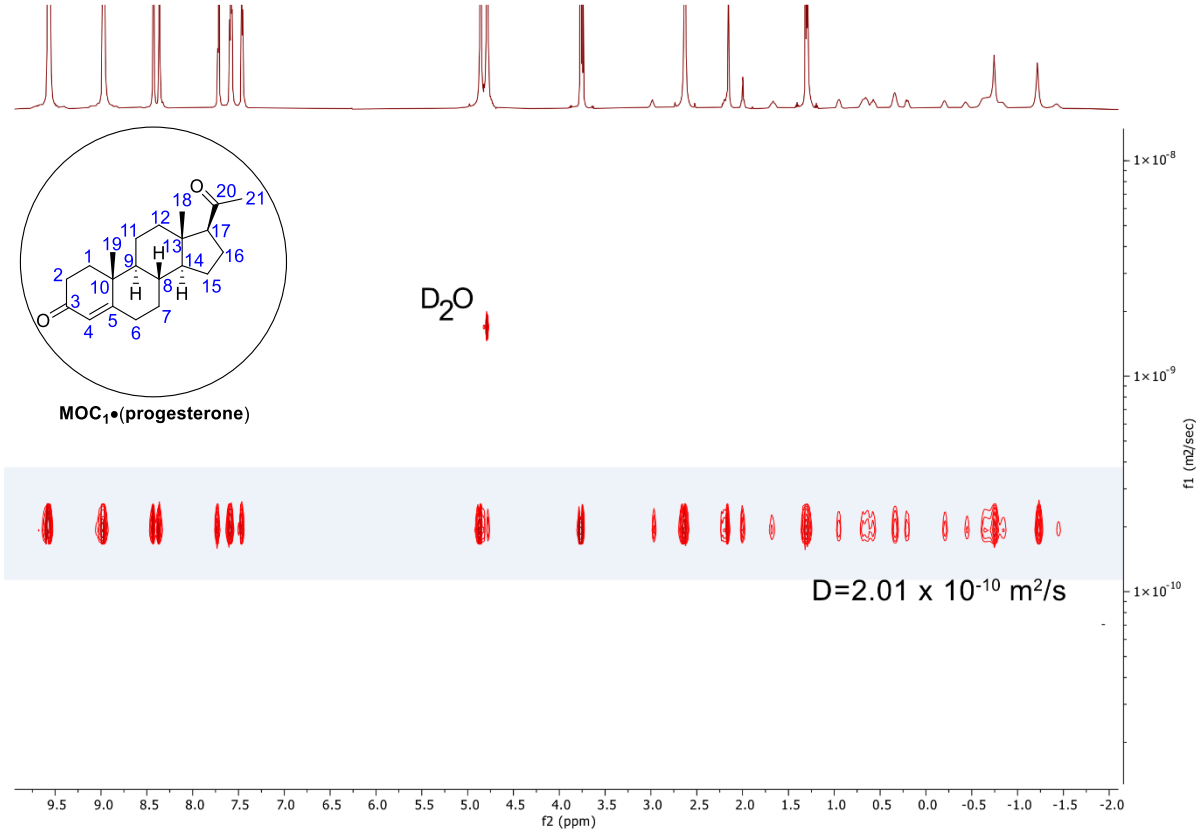

*Figure 146: DOSY NMR (600 MHz, D_2O) of **MOC₁•(progesterone)**.*

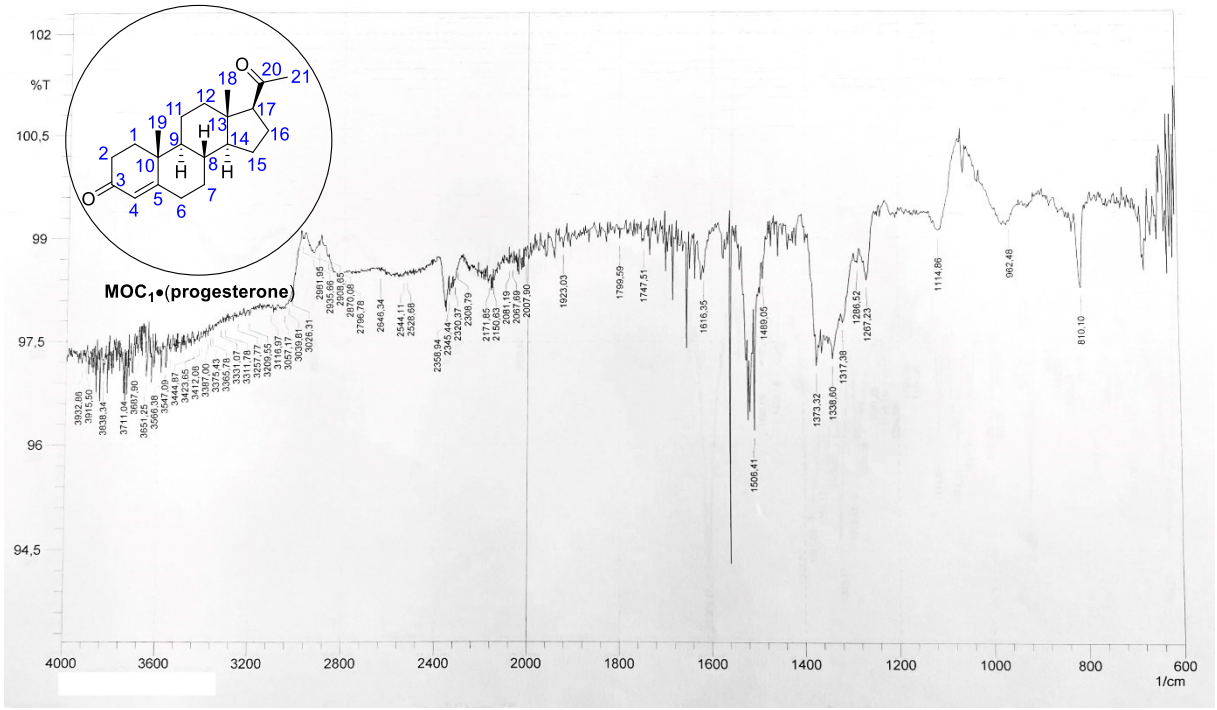

*Figure 147: IR spectrum of **MOC₁•(progesterone)**.*

Drospirenone

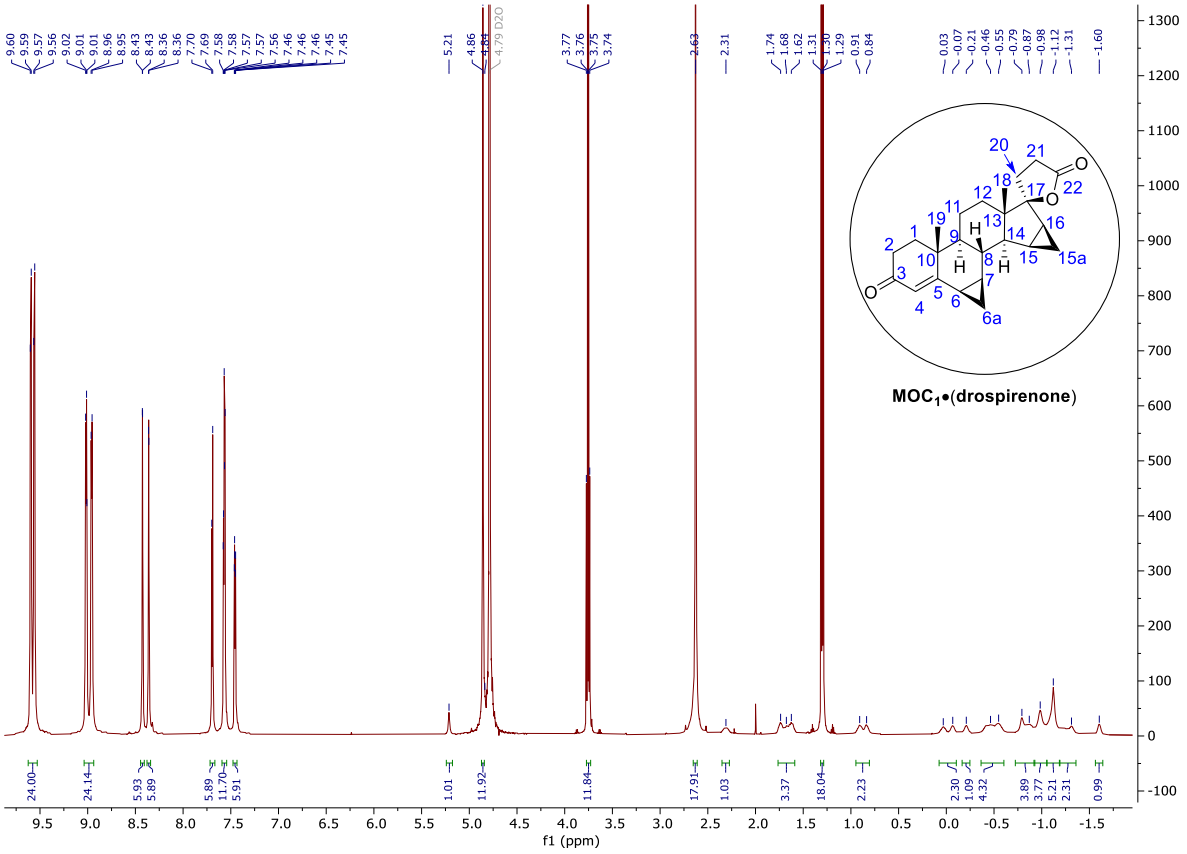

*Figure 148: ^{1}H NMR (600 MHz, D_2O) of **MOC₁•(drospirenone)**.*

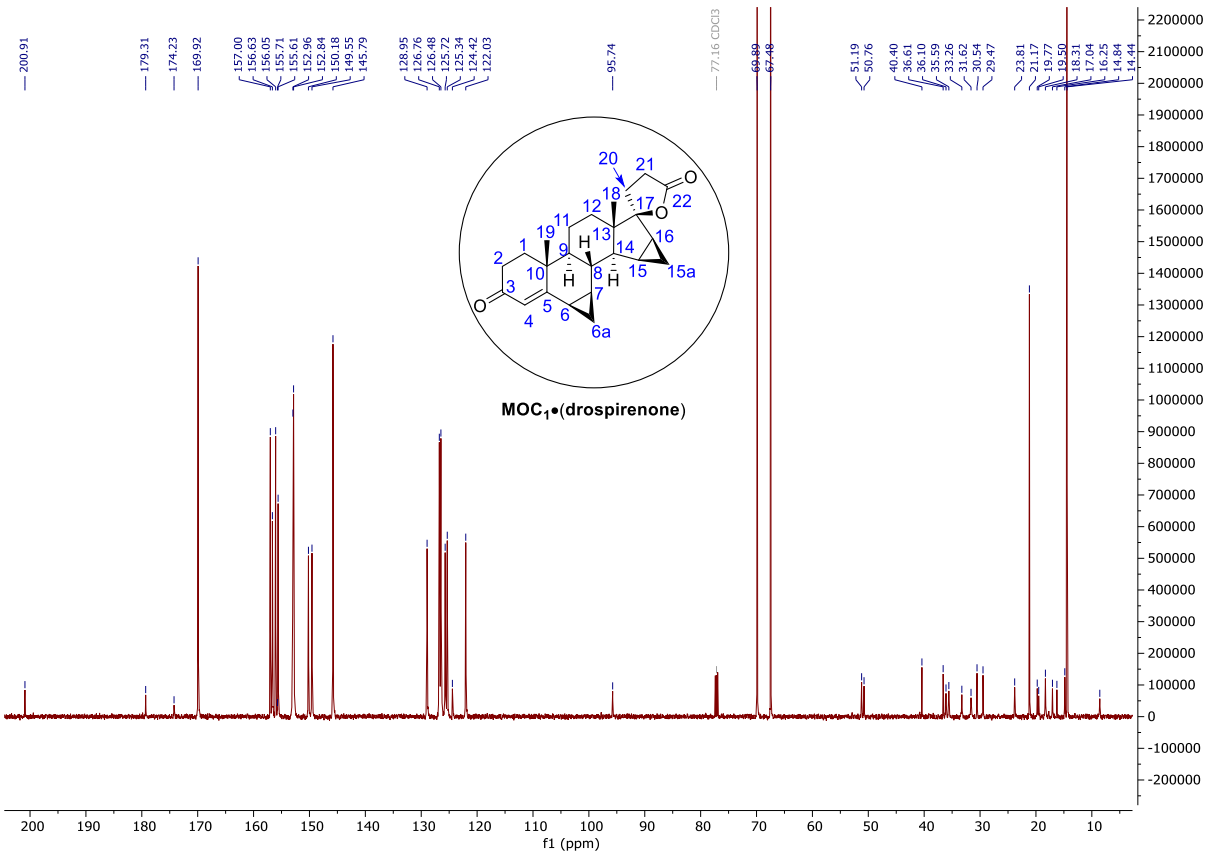

*Figure 149: $^{13}C\{^{1}H\}$ NMR (151 MHz, D_2O) of **MOC₁•(drospirenone)**.*

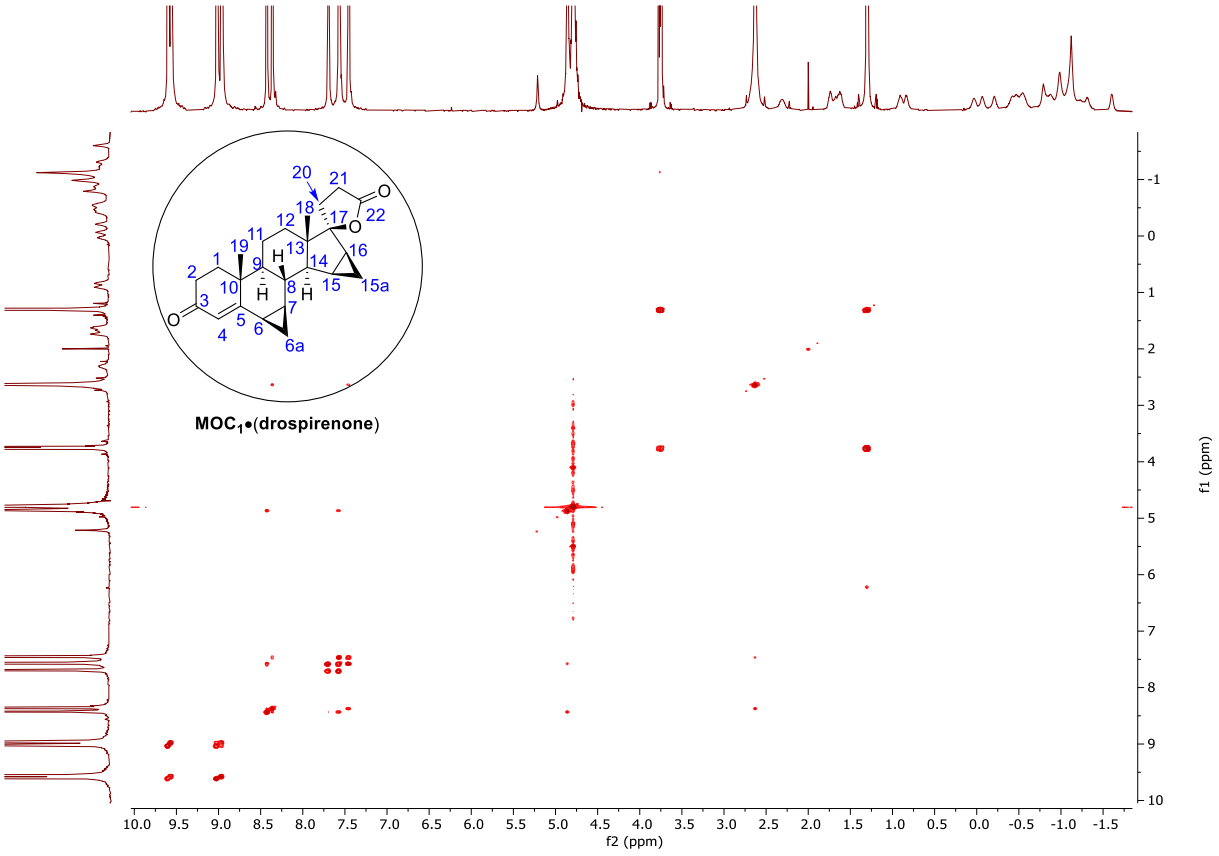

*Figure 150: ^{1}H-^{1}H COSY NMR (600 MHz, D_2O) of **MOC_1•(drospirenone)**.*

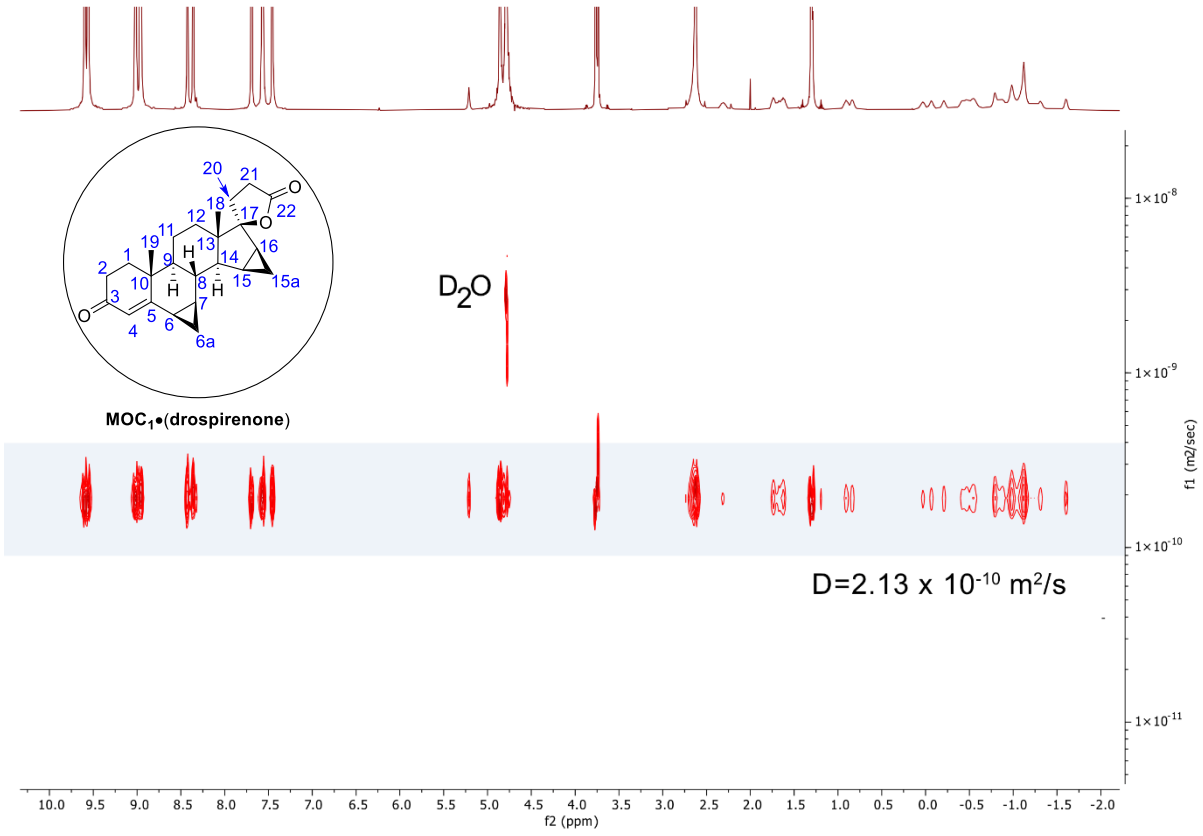

*Figure 151: DOSY NMR (600 MHz, D_2O) of **MOC_1•(drospirenone)**.*

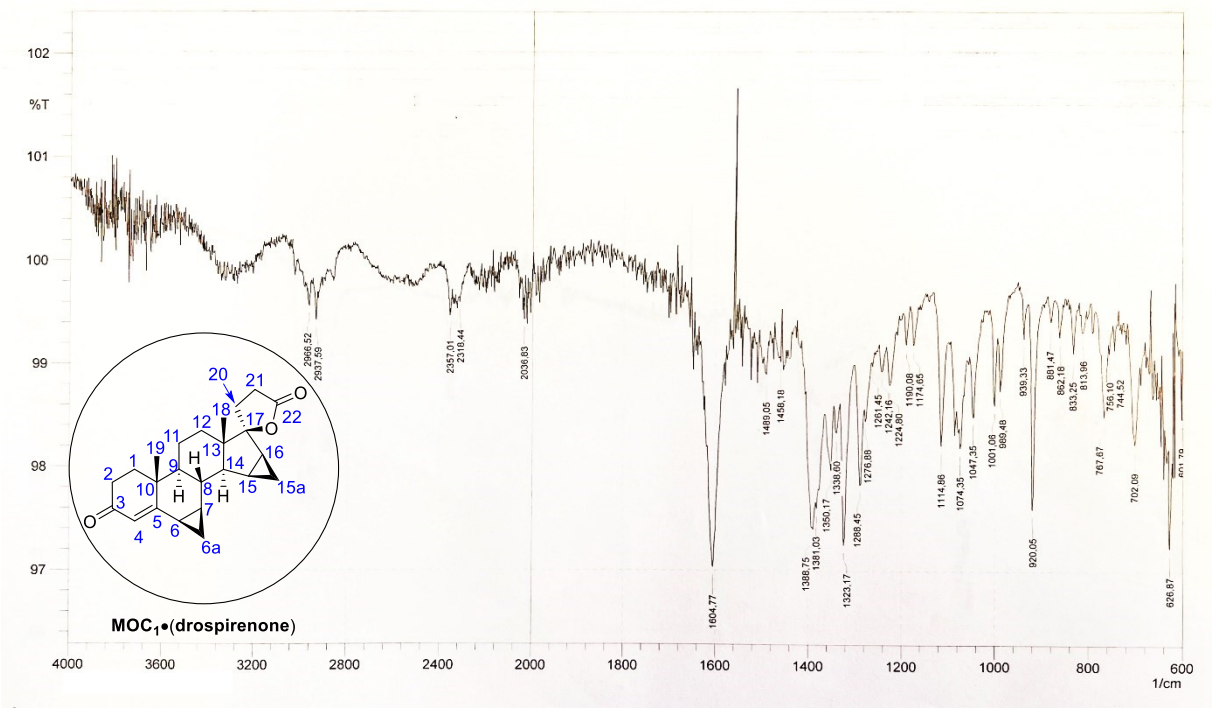

*Figure 152: IR spectrum of **MOC₁•(drospirenone)**.*

Testosterone

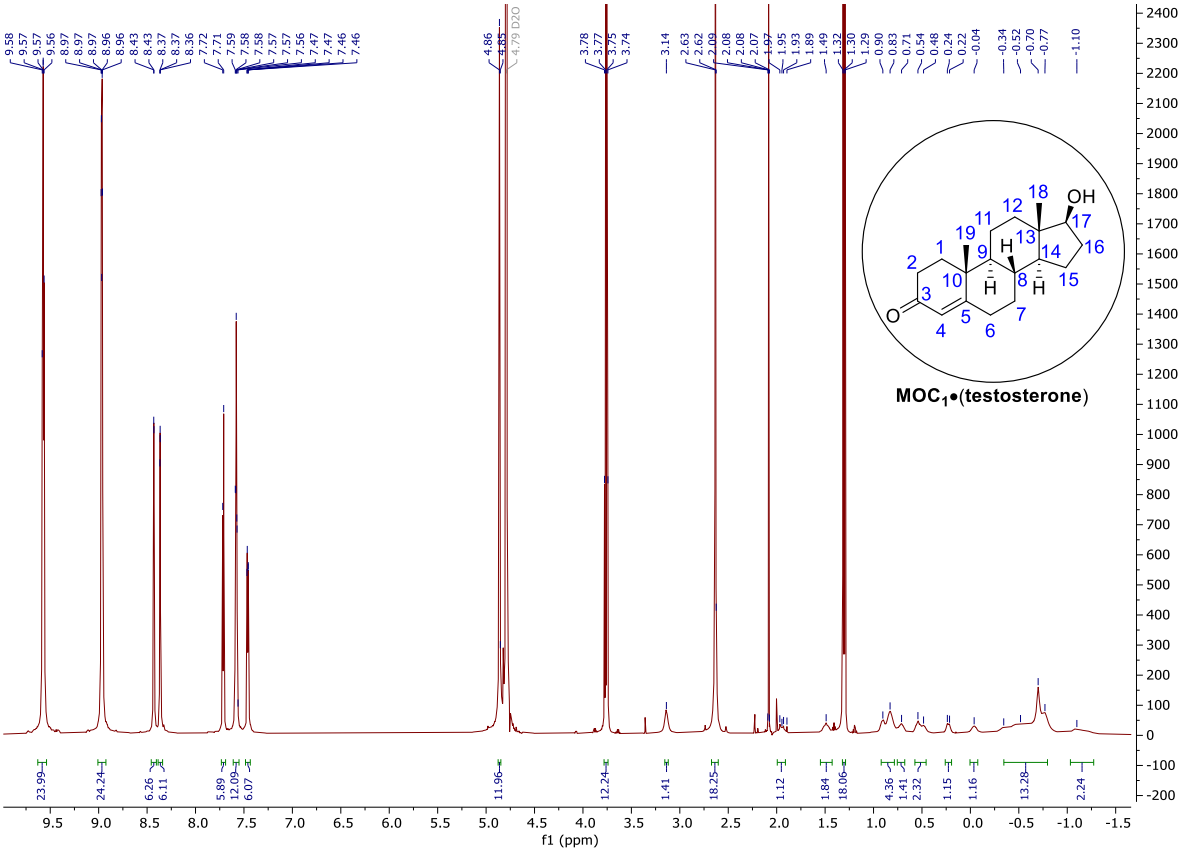

*Figure 153: ^{1}H NMR (600 MHz, D_2O) of **MOC₁•(testosterone)**.*

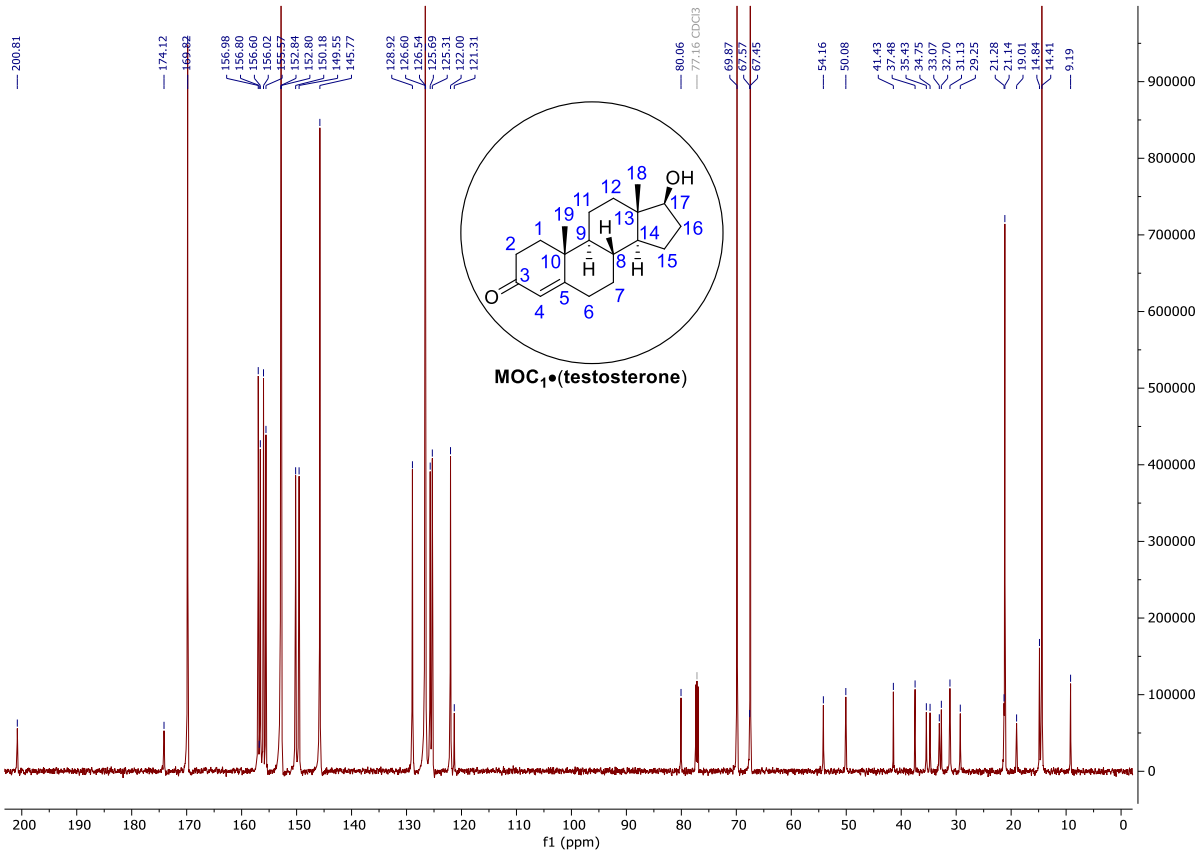

*Figure 154: $^{13}C\{^{1}H\}$ NMR (151 MHz, D_2O) of **MOC_1•(testosterone)**.*

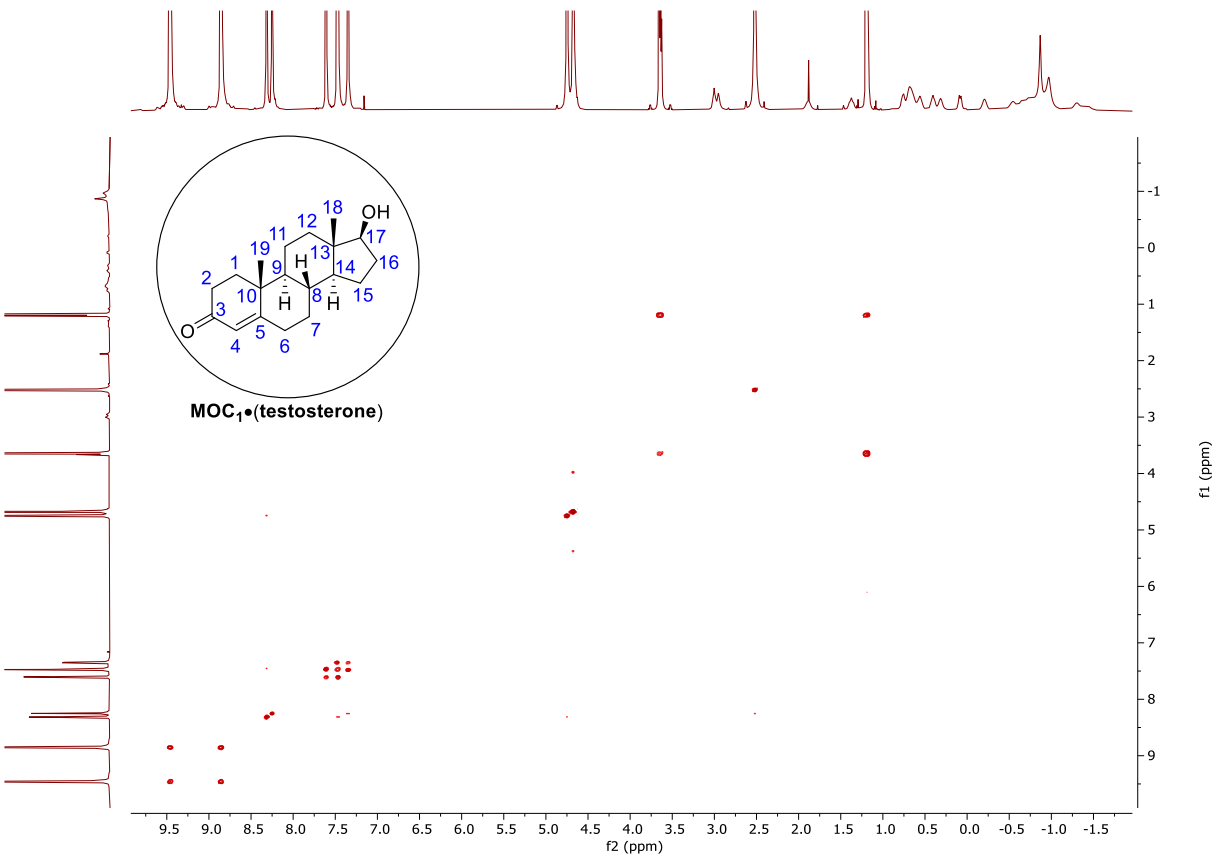

*Figure 155: ^{1}H-^{1}H COSY NMR (600 MHz, D_2O) of **MOC_1•(testosterone)**.*

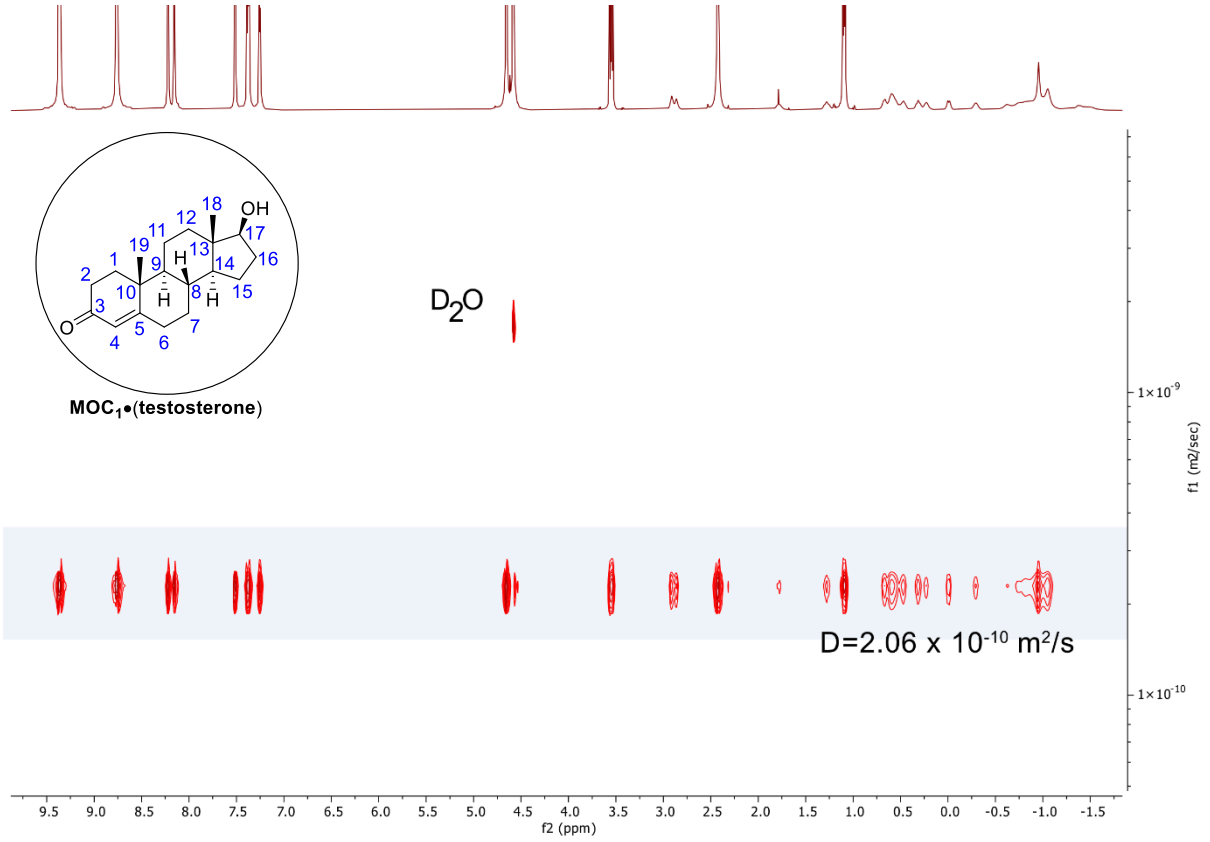

*Figure 156: DOSY NMR (600 MHz, D_2O) of **MOC_1•(testosterone)**.*

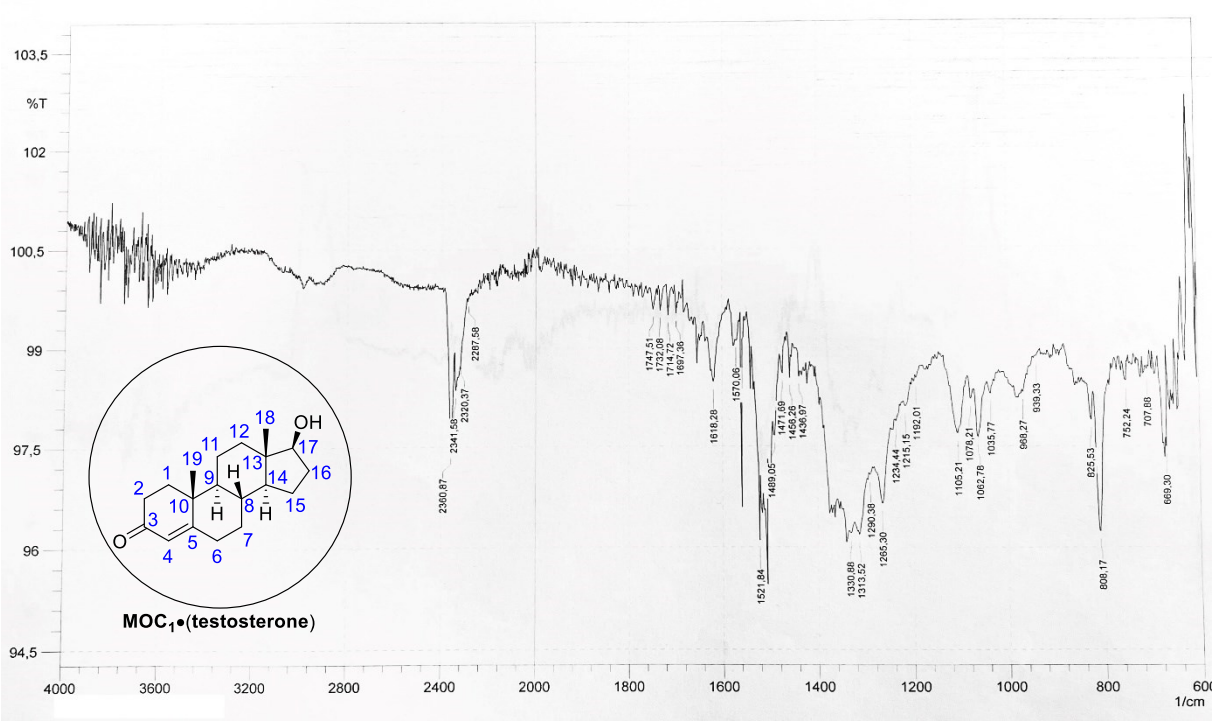

*Figure 157: IR spectrum of **MOC_1•(testosterone)**.*

Cortisone

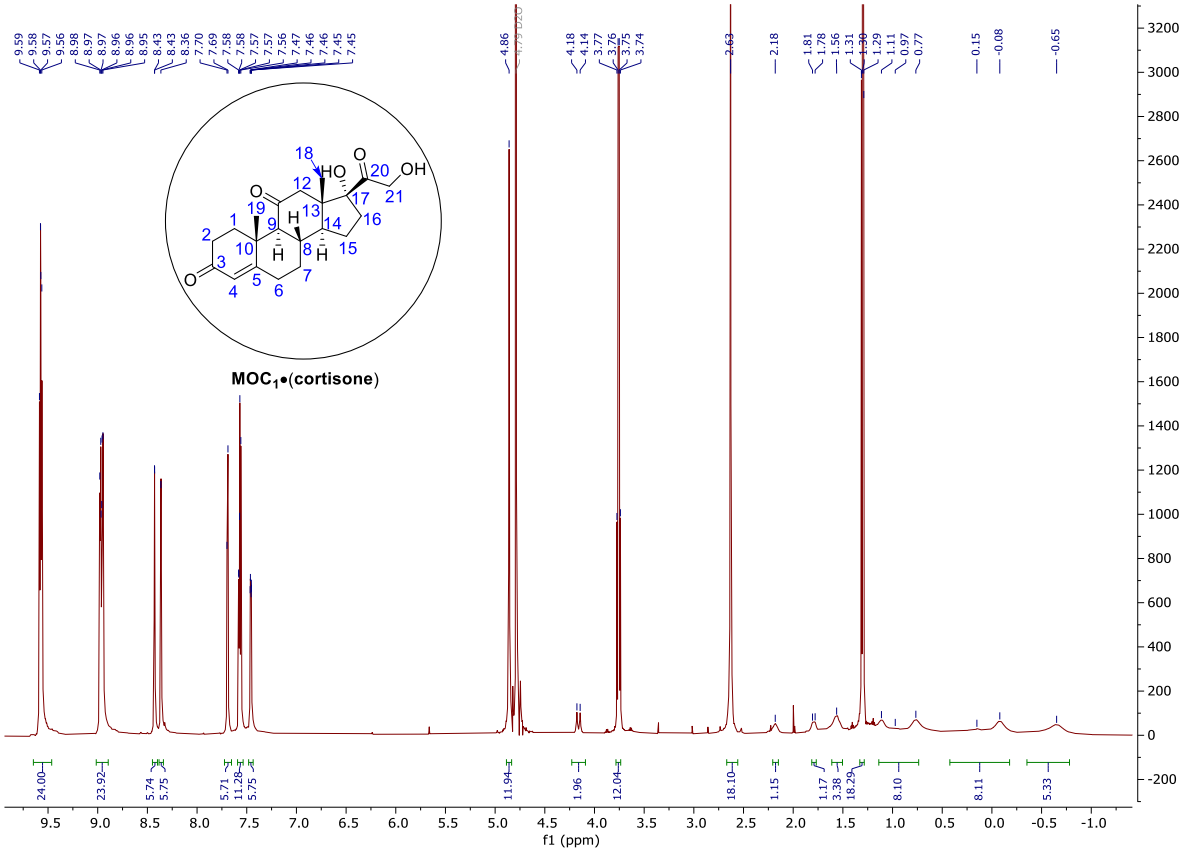

*Figure 158: ^{1}H NMR (600 MHz, D_2O) of **MOC_1•(cortisone)**.*

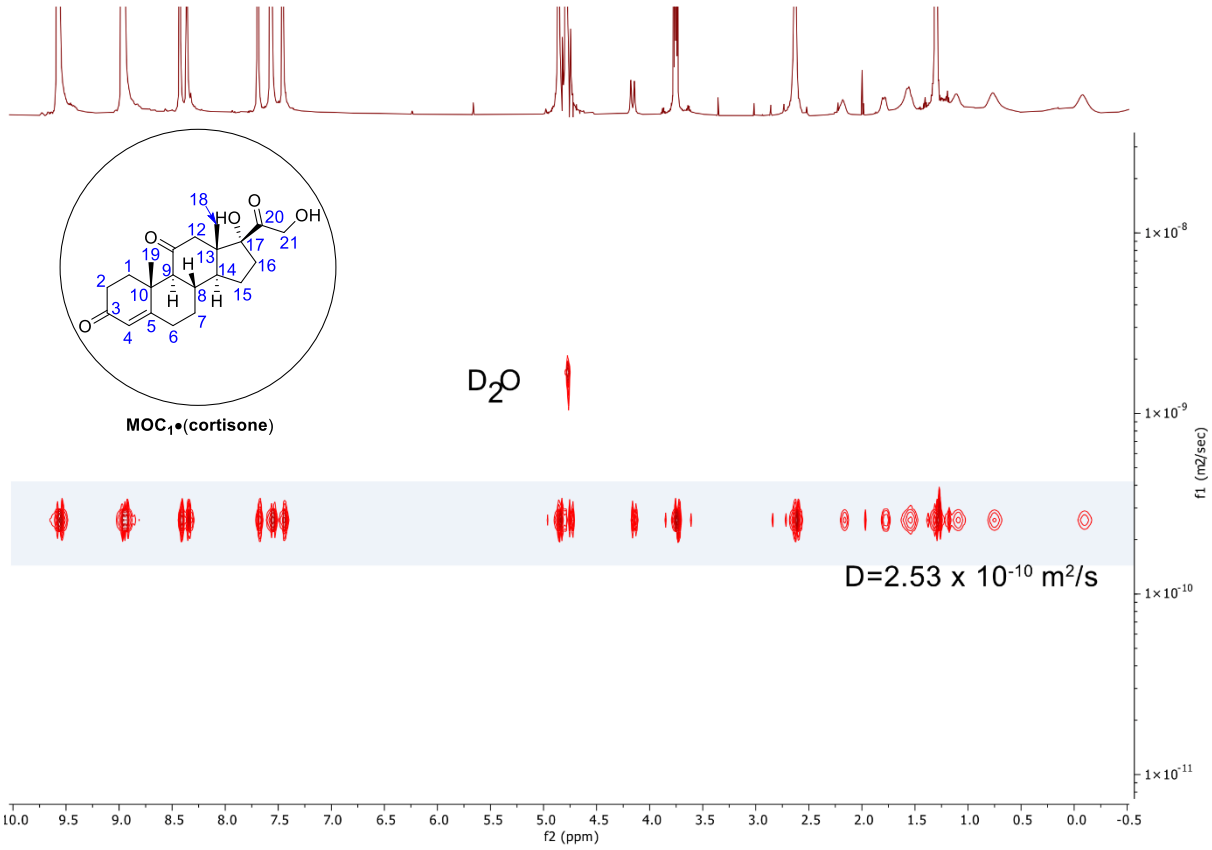

*Figure 159: DOSY NMR (600 MHz, D_2O) of **MOC_1•(cortisone)**.*

Estradiol

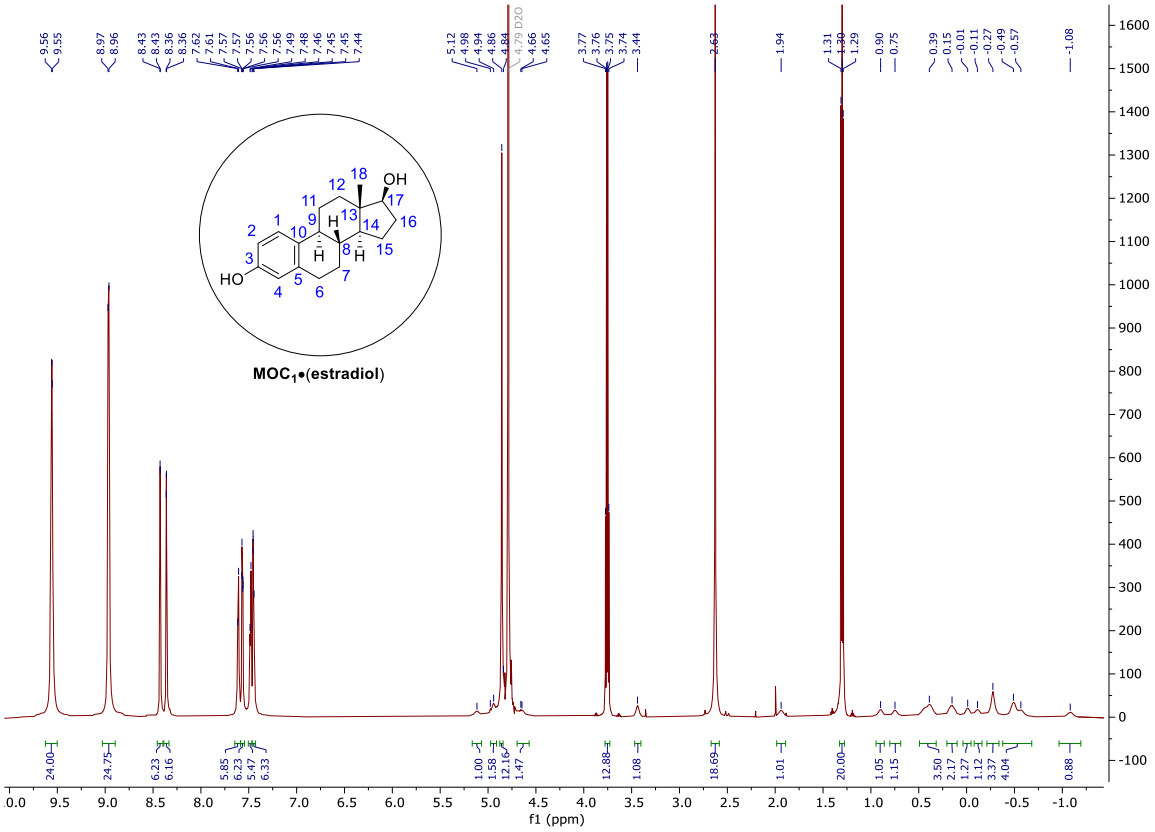

*Figure 160: ^{1}H NMR (600 MHz, D_2O) of **MOC_1•(estradiol)**.*

Drugs

Ibuprofen

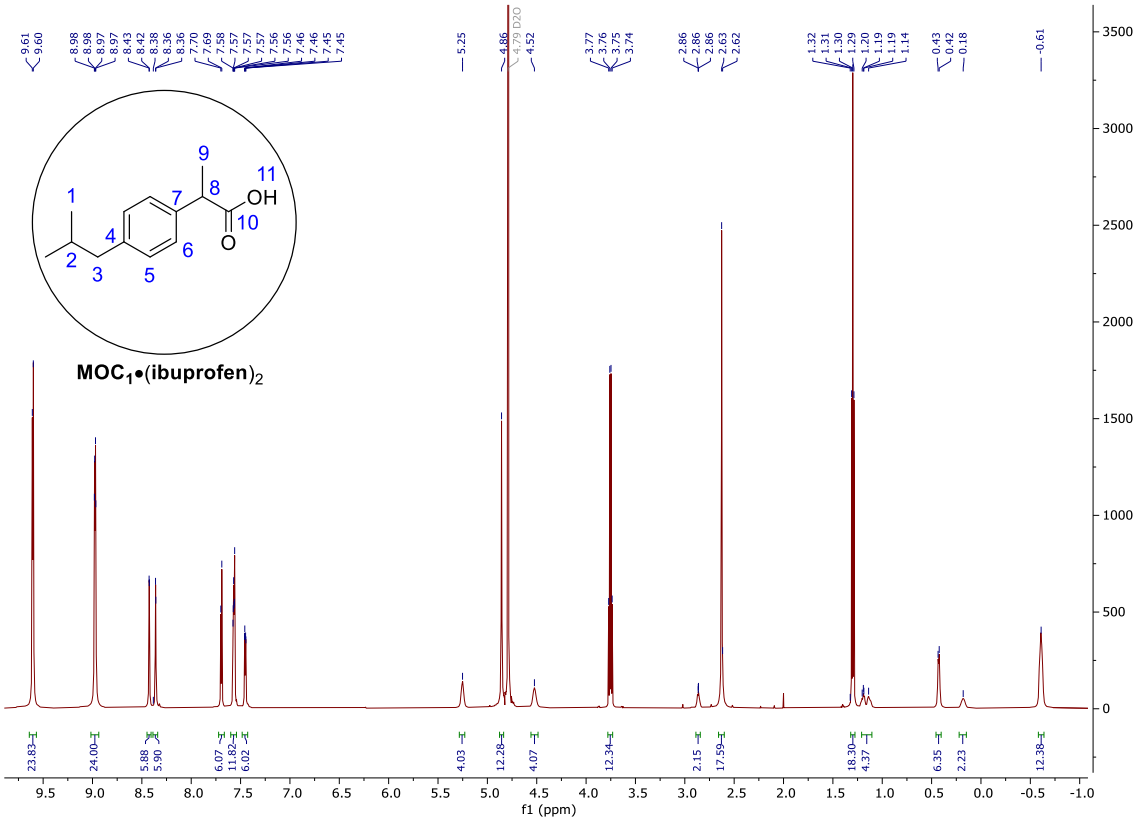

*Figure 161: ^{1}H NMR (600 MHz, D_2O) of **MOC_1•(ibuprofen)$_2$**.*

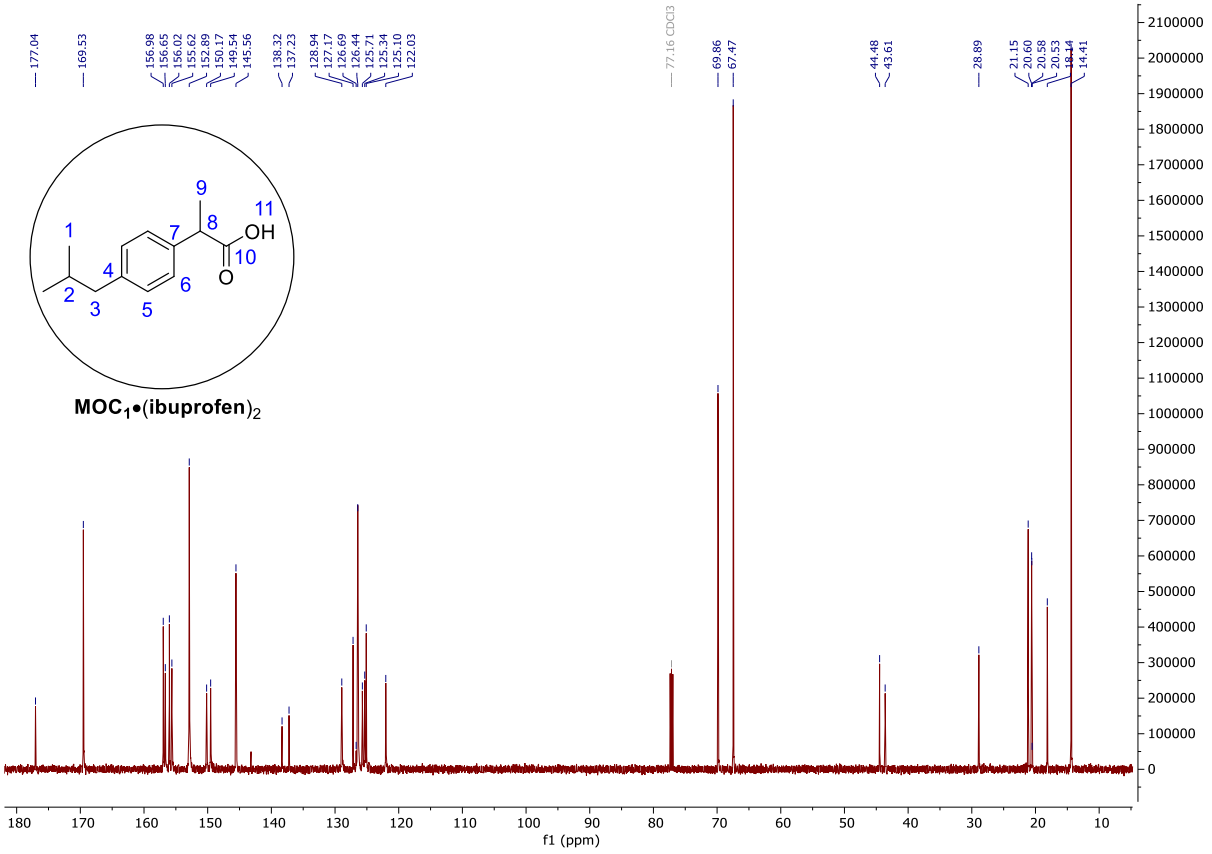

*Figure 162: $^{13}C\{^{1}H\}$ NMR (151 MHz, D_2O) of **MOC_1•(ibuprofen)$_2$**.*

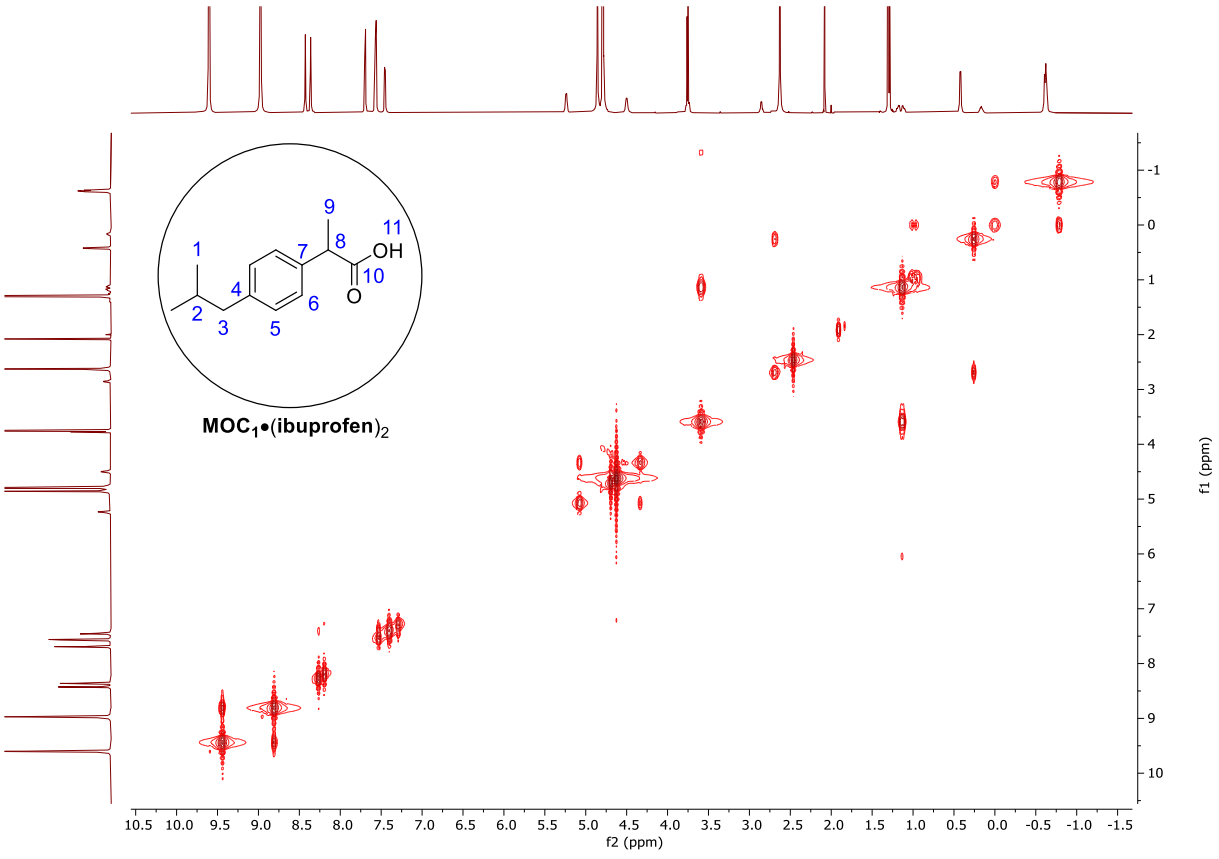

*Figure 163: ^{1}H-^{1}H COSY NMR (600 MHz, D_2O) of **MOC_1•(ibuprofen)$_2$**.*

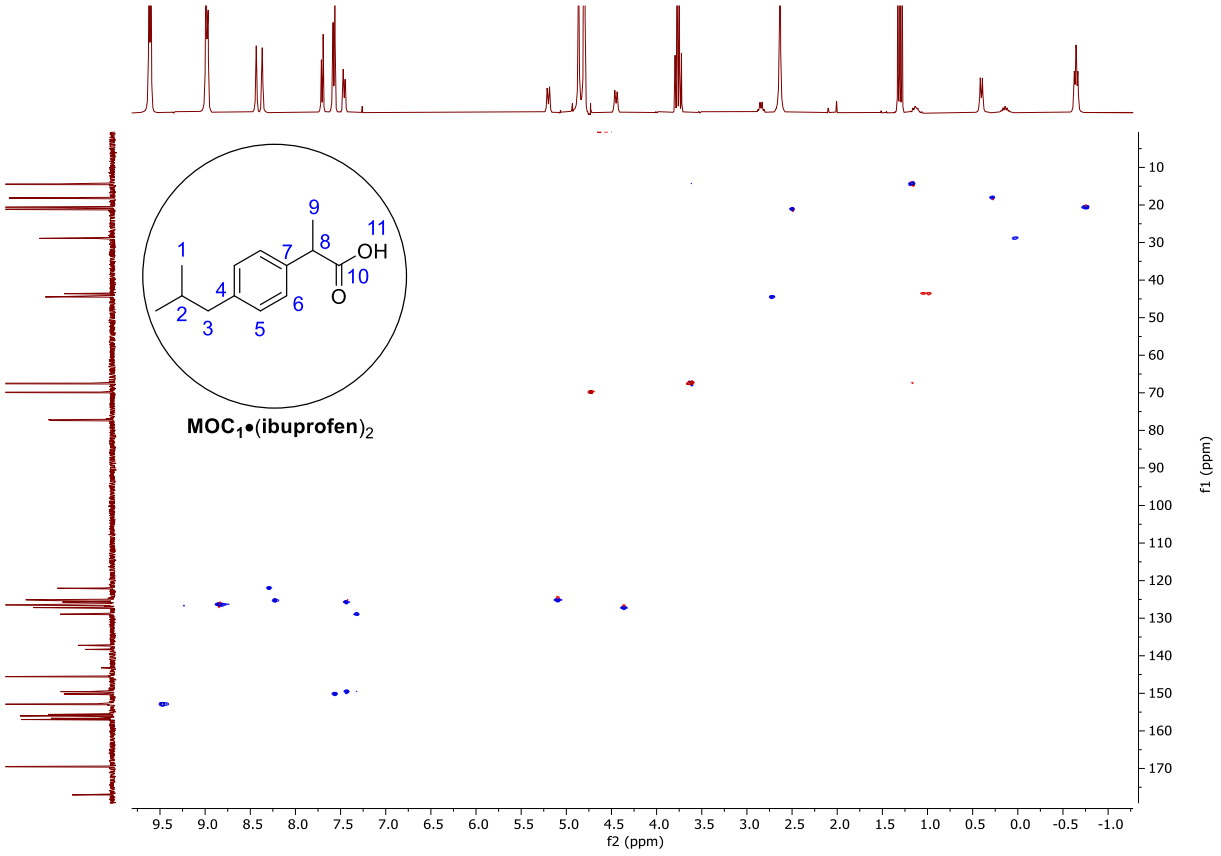

*Figure 164: ^{1}H-{^{13}C} HSQC NMR (600 MHz, D_2O) of **MOC_1•(ibuprofen)$_2$**.*

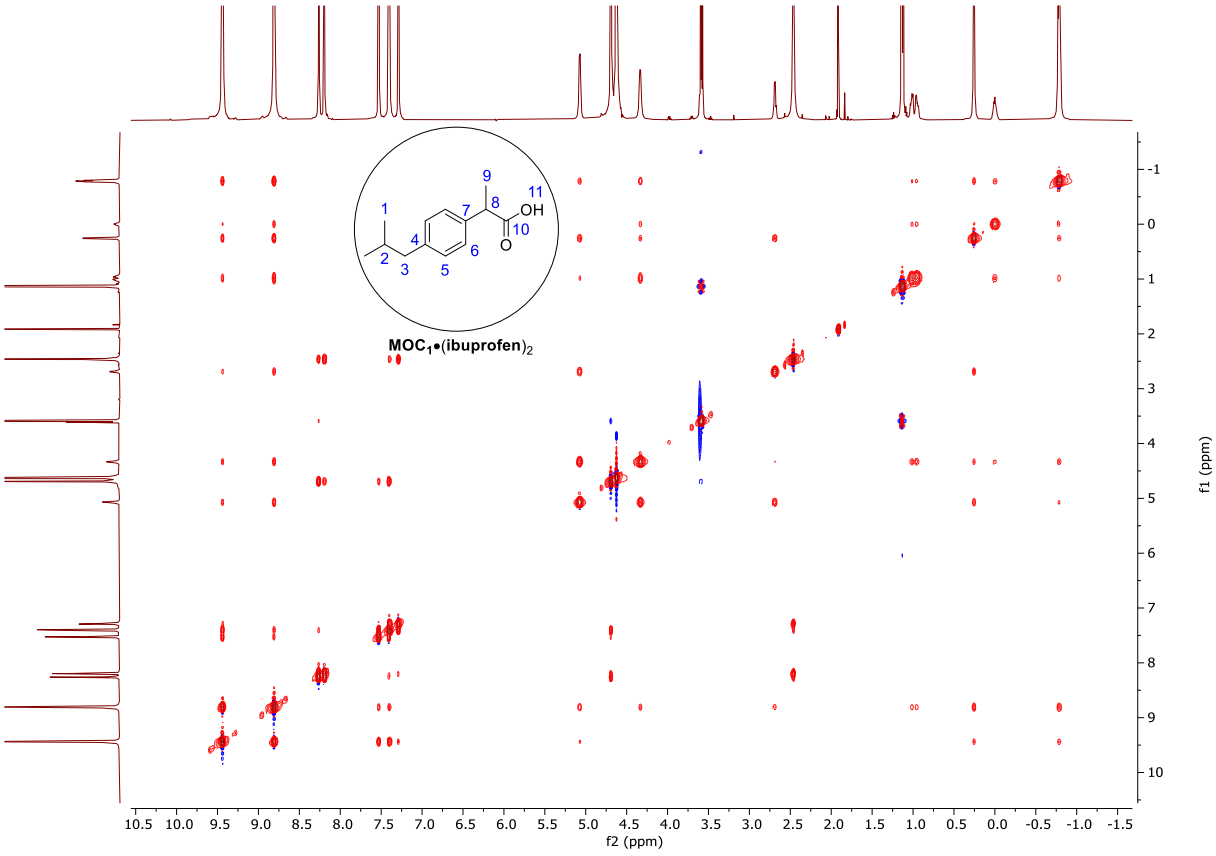

*Figure 165: ^{1}H NOESY NMR (600 MHz, D_2O) of **MOC$_1$•(ibuprofen)$_2$**.*

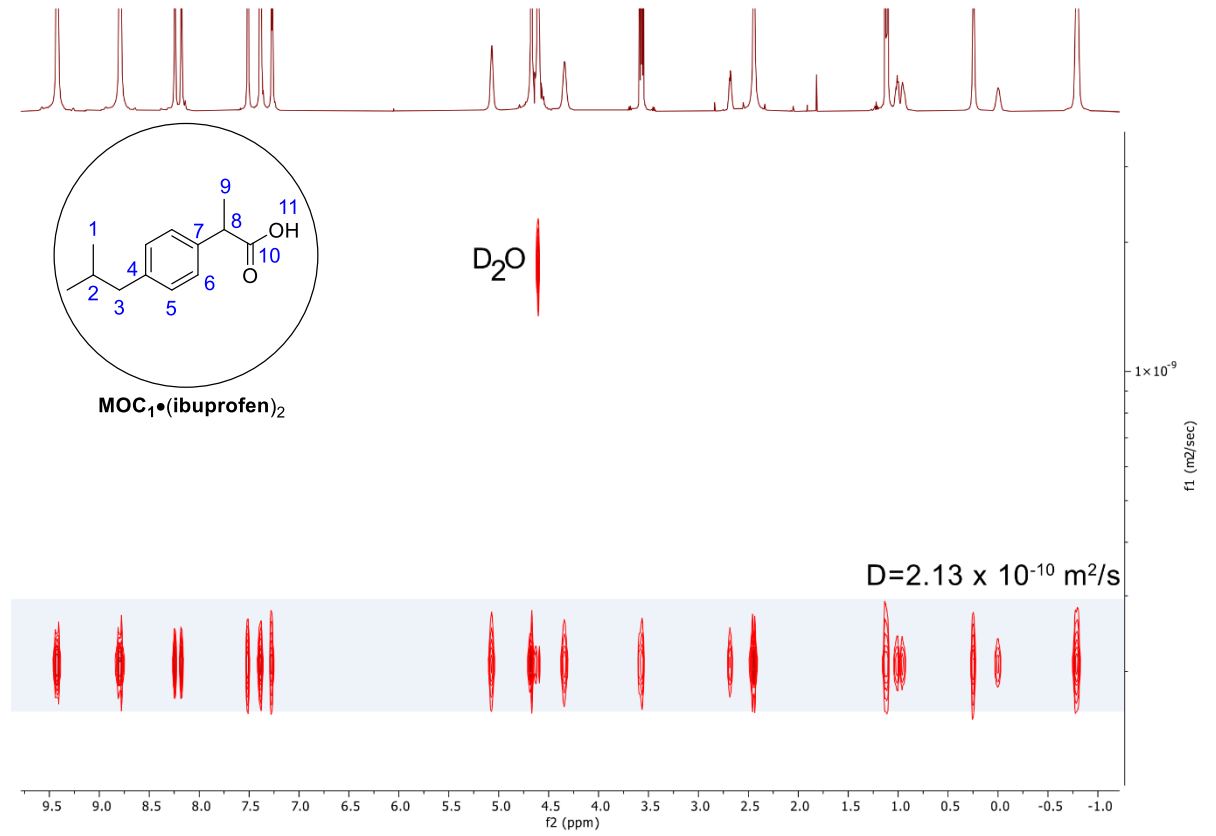

*Figure 166: DOSY NMR (600 MHz, D_2O) of **MOC$_1$•(ibuprofen)$_2$**.*

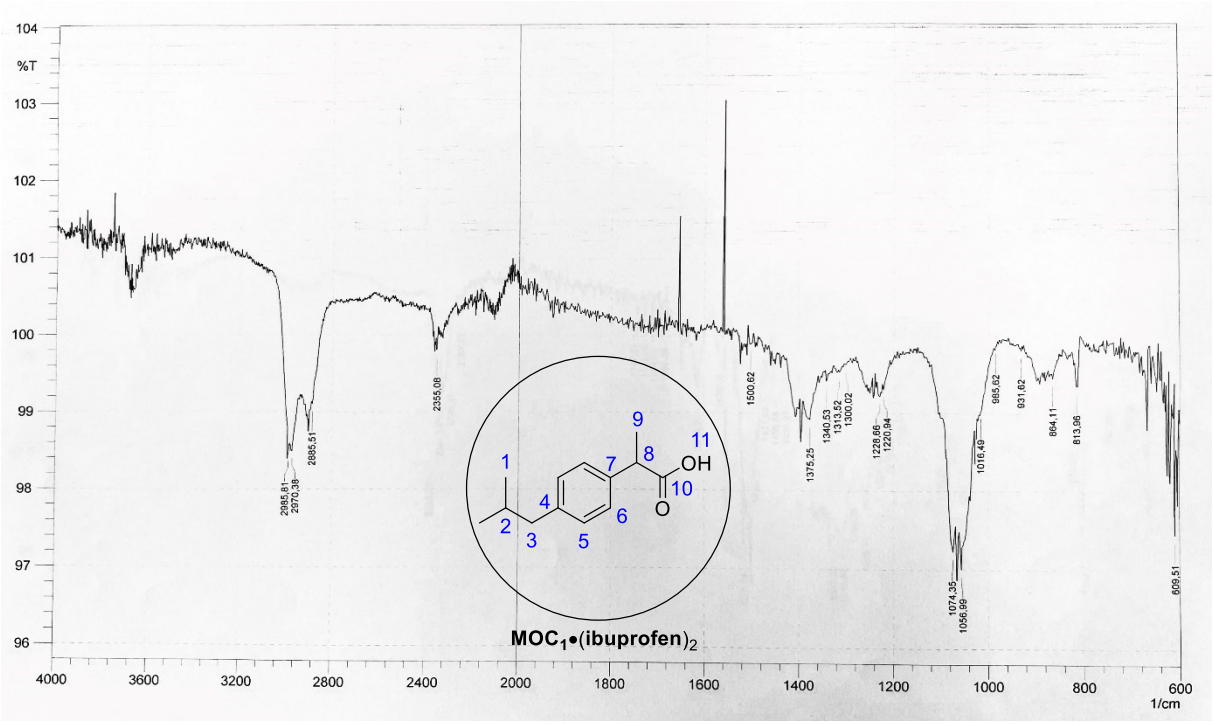

*Figure 167: IR spectrum of **MOC₁•(ibuprofen)₂**.*

Paracetamol

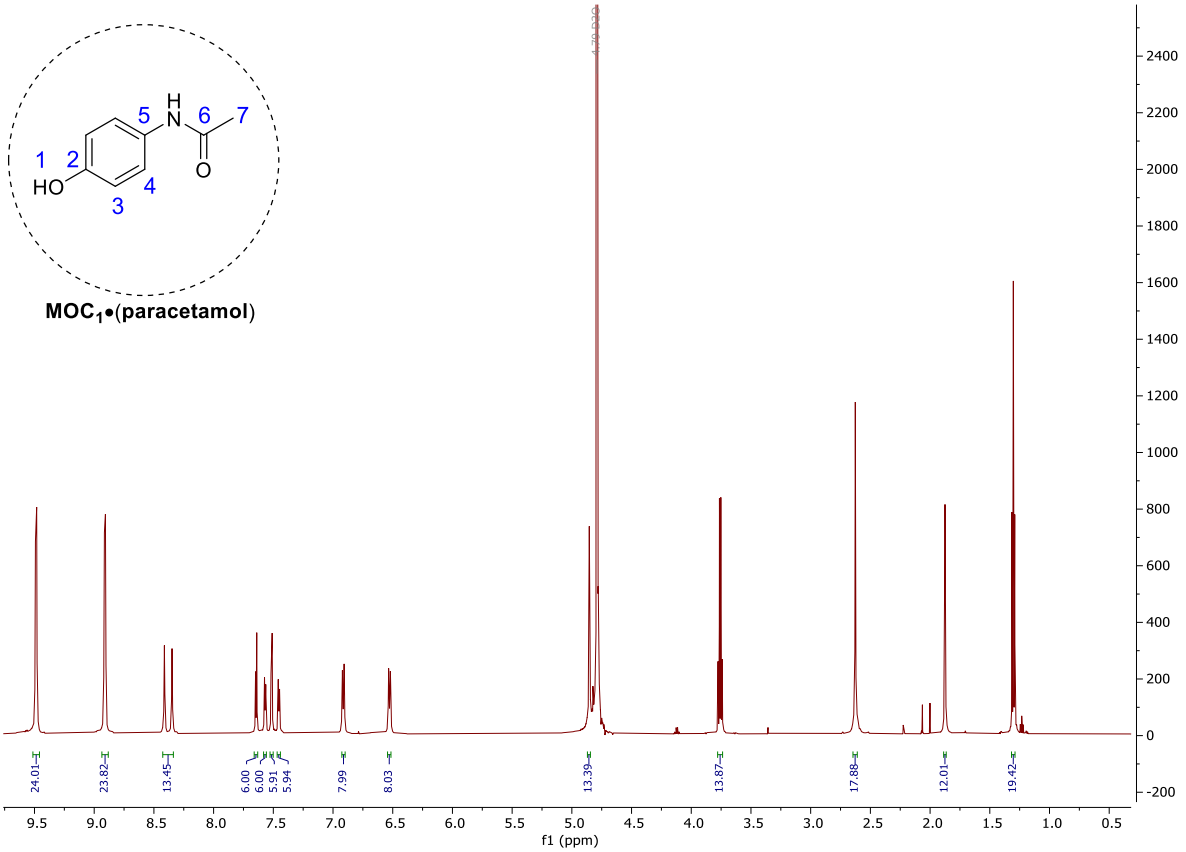

*Figure 168: ^{1}H NMR (600 MHz, D_2O) of **MOC₁•(paracetamol)**.*

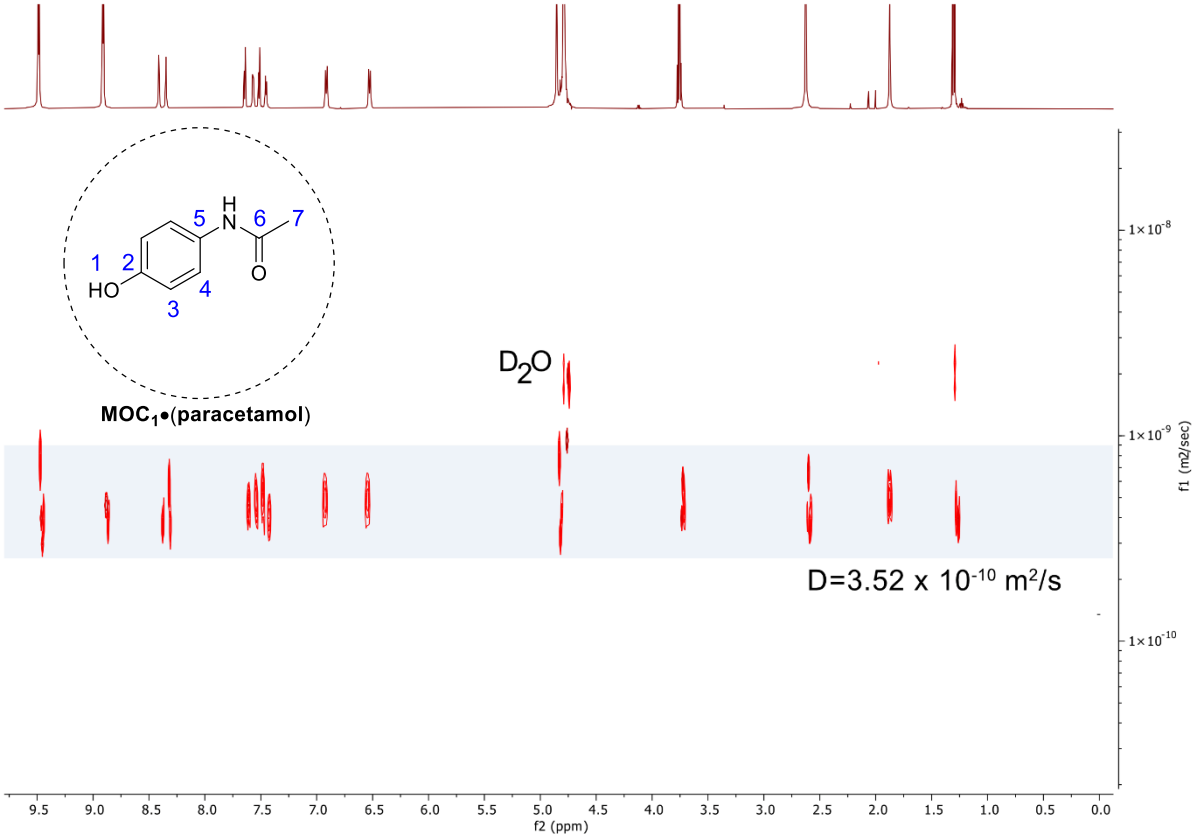

*Figure 169: DOSY NMR (600 MHz, D_2O) of **MOC_1•(paracetamol)**. No match.*

Melatonin

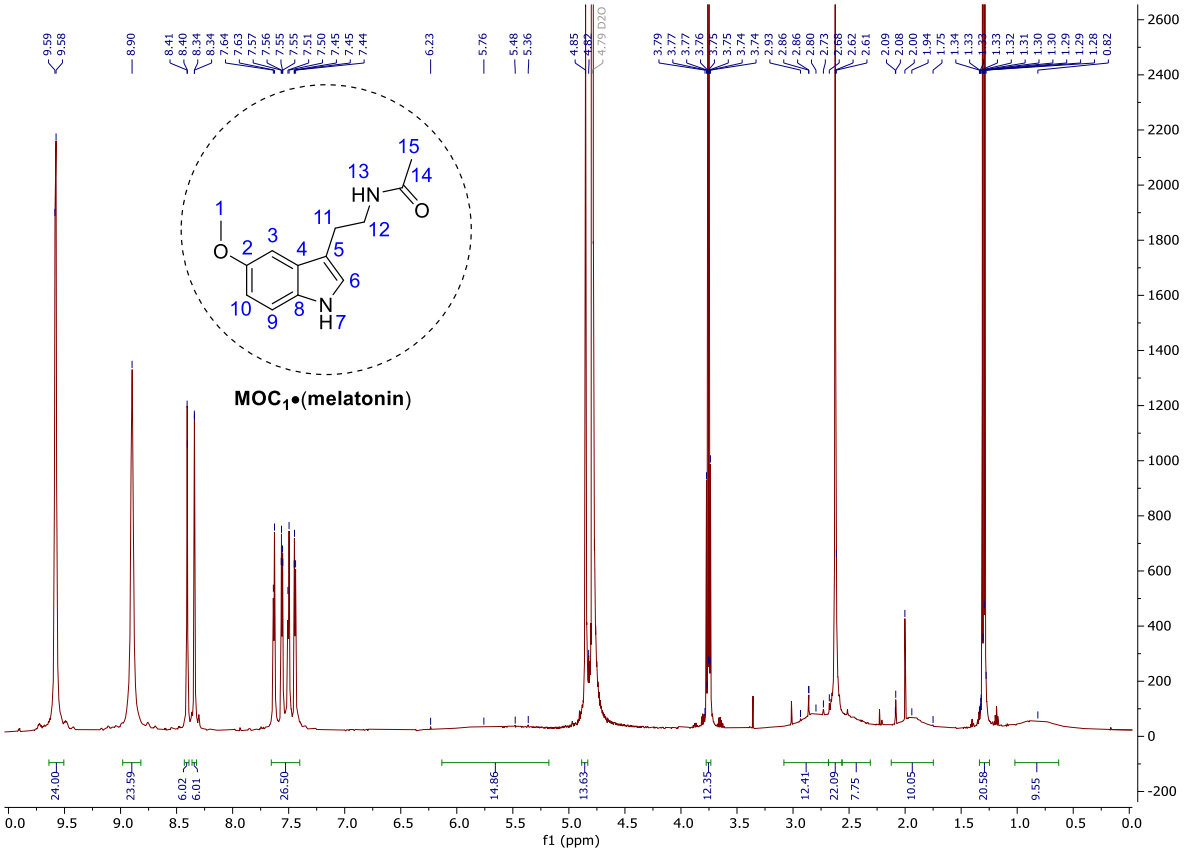

*Figure 170: ^1H NMR (600 MHz, D_2O) of **MOC_1•(melatonin)**.*

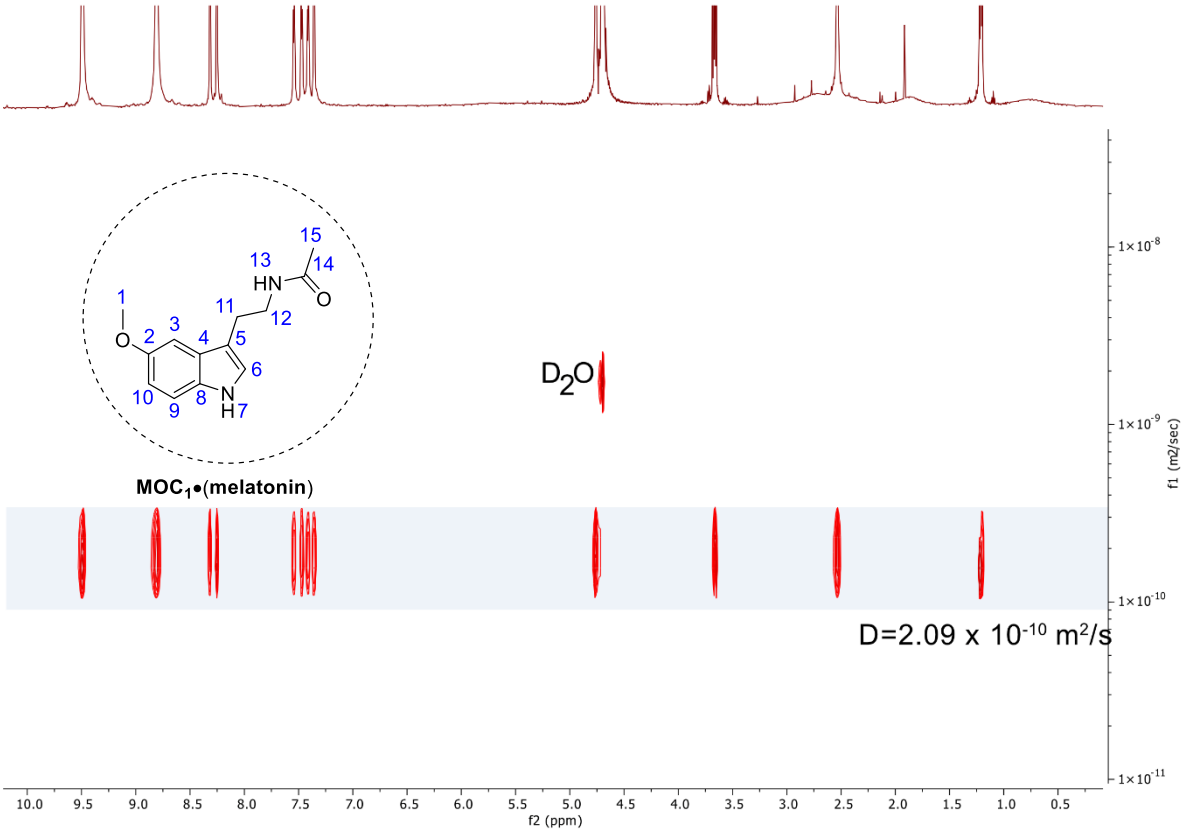

*Figure 171: DOSY NMR (600 MHz, D_2O) of **MOC_1•(melatonin)**.*

Other molecules

Phenolphthalein

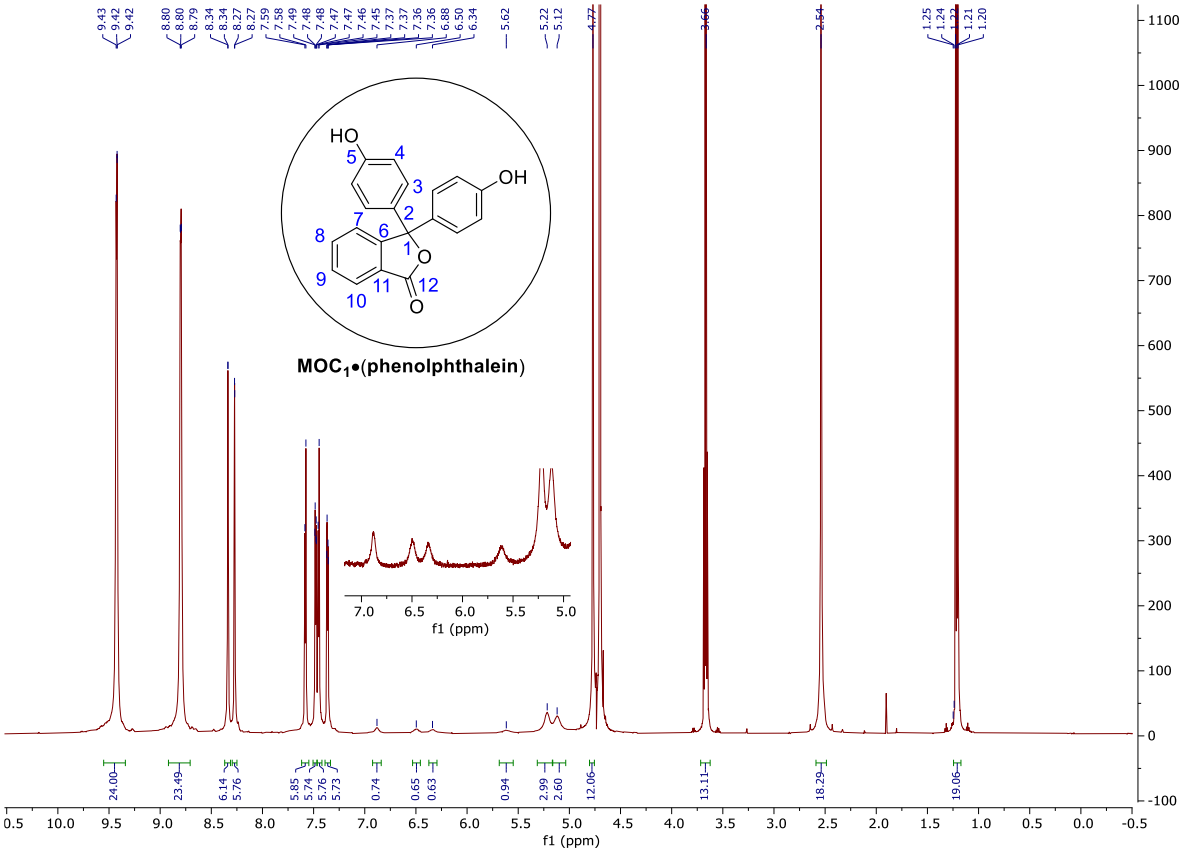

*Figure 172: ^{1}H NMR (600 MHz, D_2O) of **MOC_1•(phenolphthalein)**.*

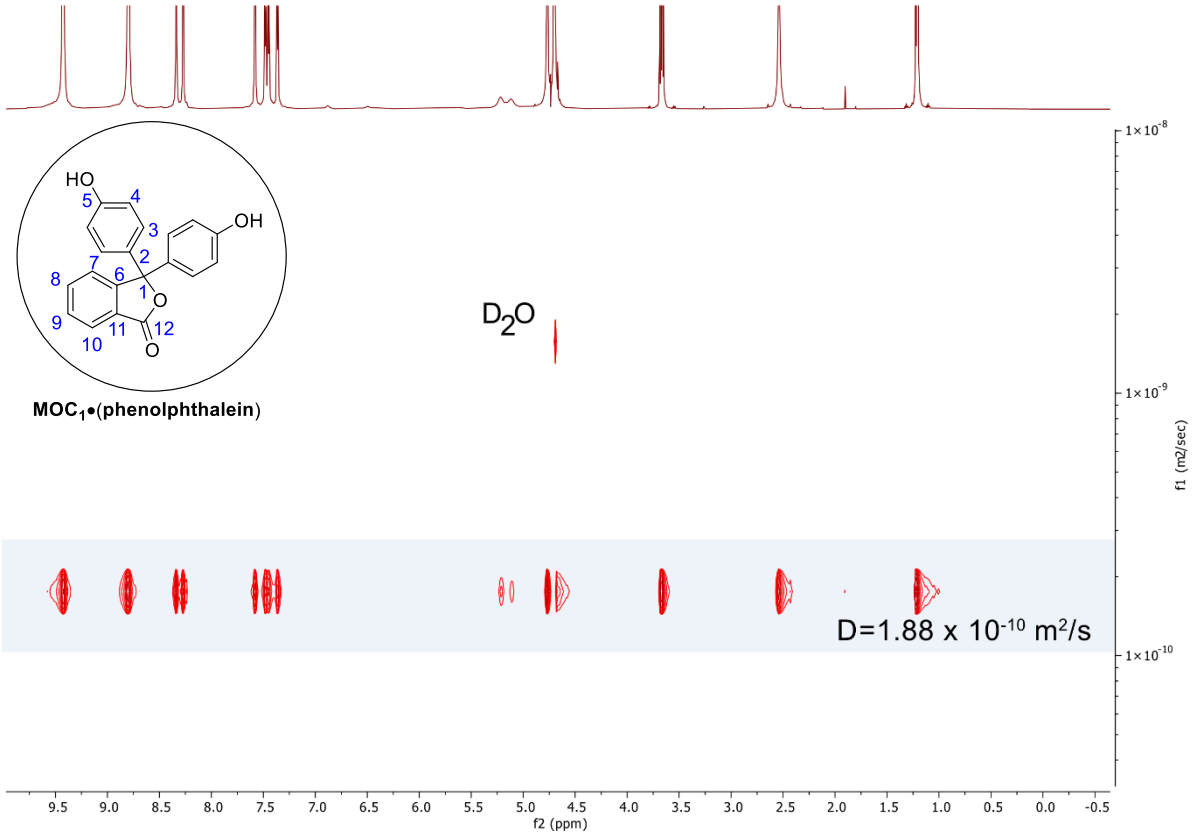

*Figure 173: DOSY NMR (600 MHz, D_2O) of **MOC_1•(phenolphthalein)**.*

Umbelliferone

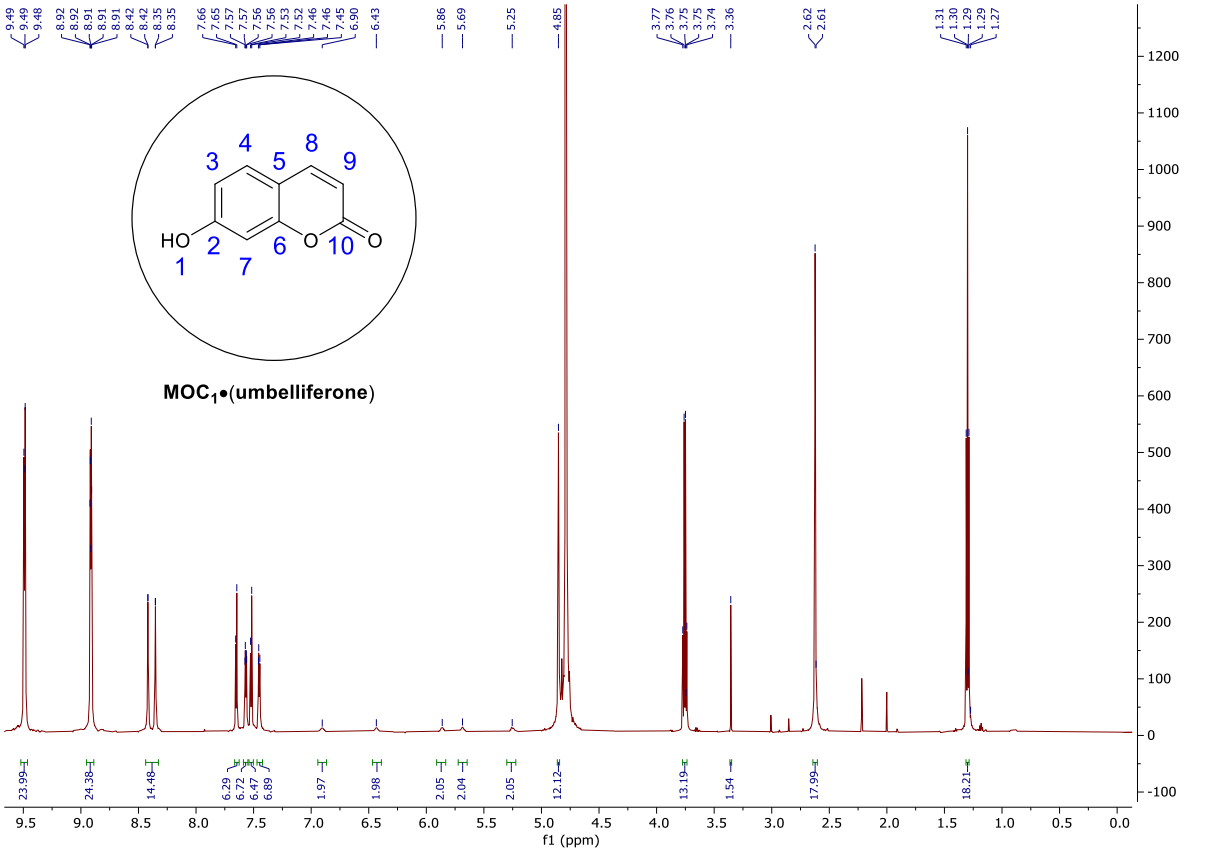

*Figure 174: ^{1}H NMR (600 MHz, D_2O) of **MOC_1•(umbelliferone)**.*

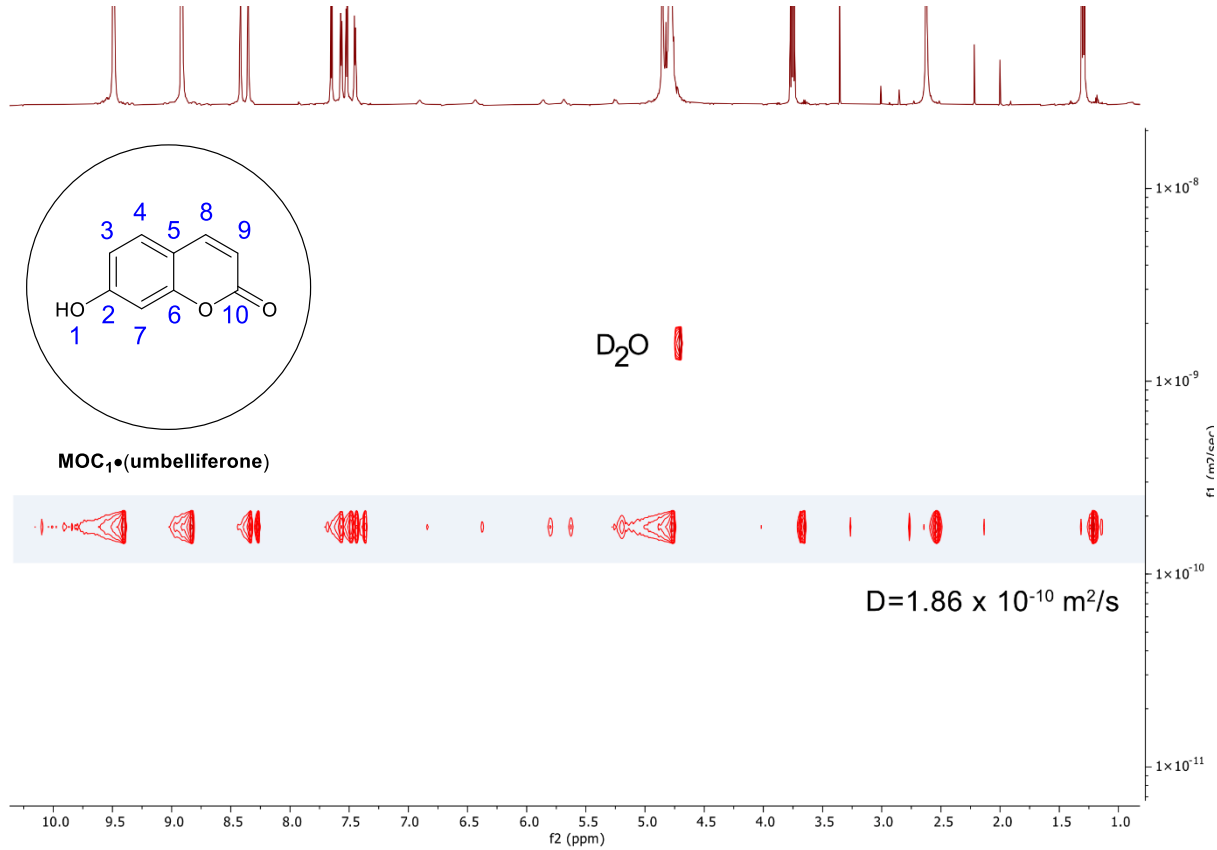

*Figure 175: DOSY NMR (600 MHz, D_2O) of **MOC_1•(umbelliferone)**.*

Flavone

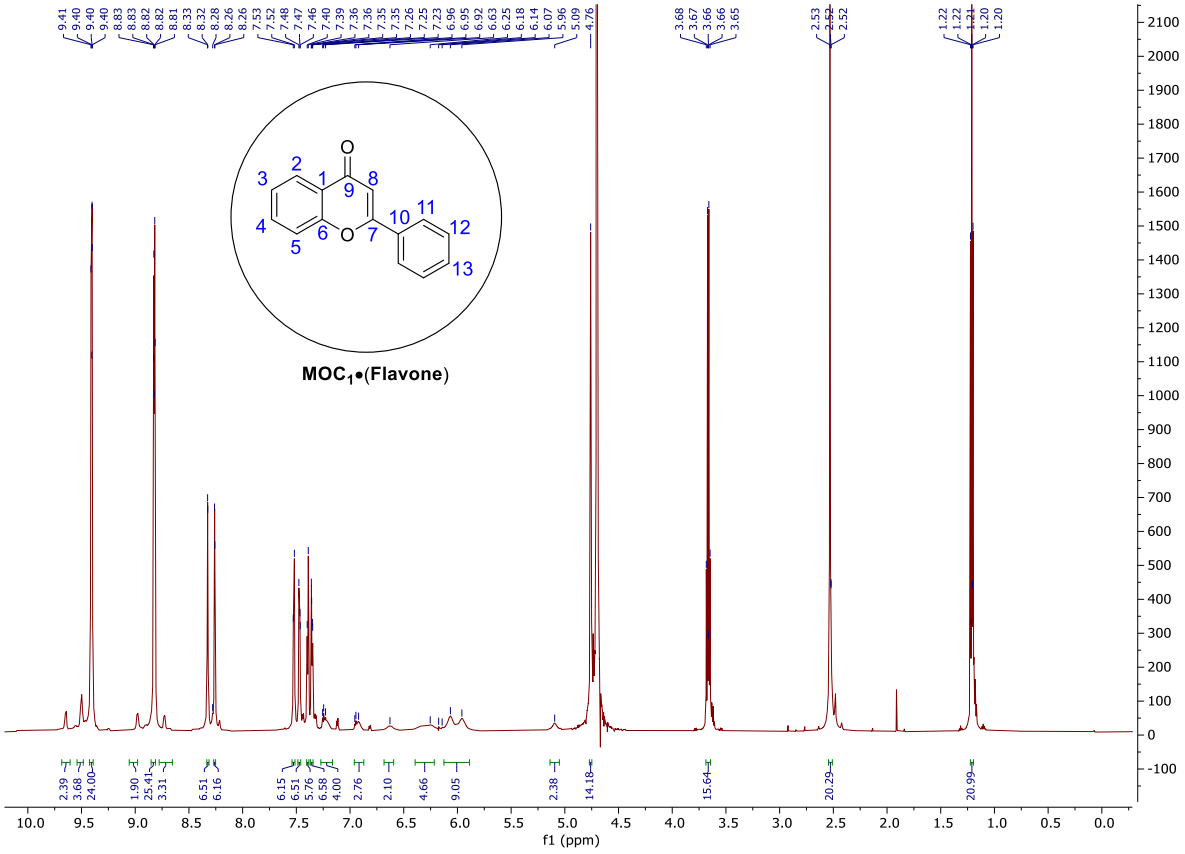

*Figure 176: ^{1}H NMR (600 MHz, D_2O) of **MOC_1•(flavone)**.*

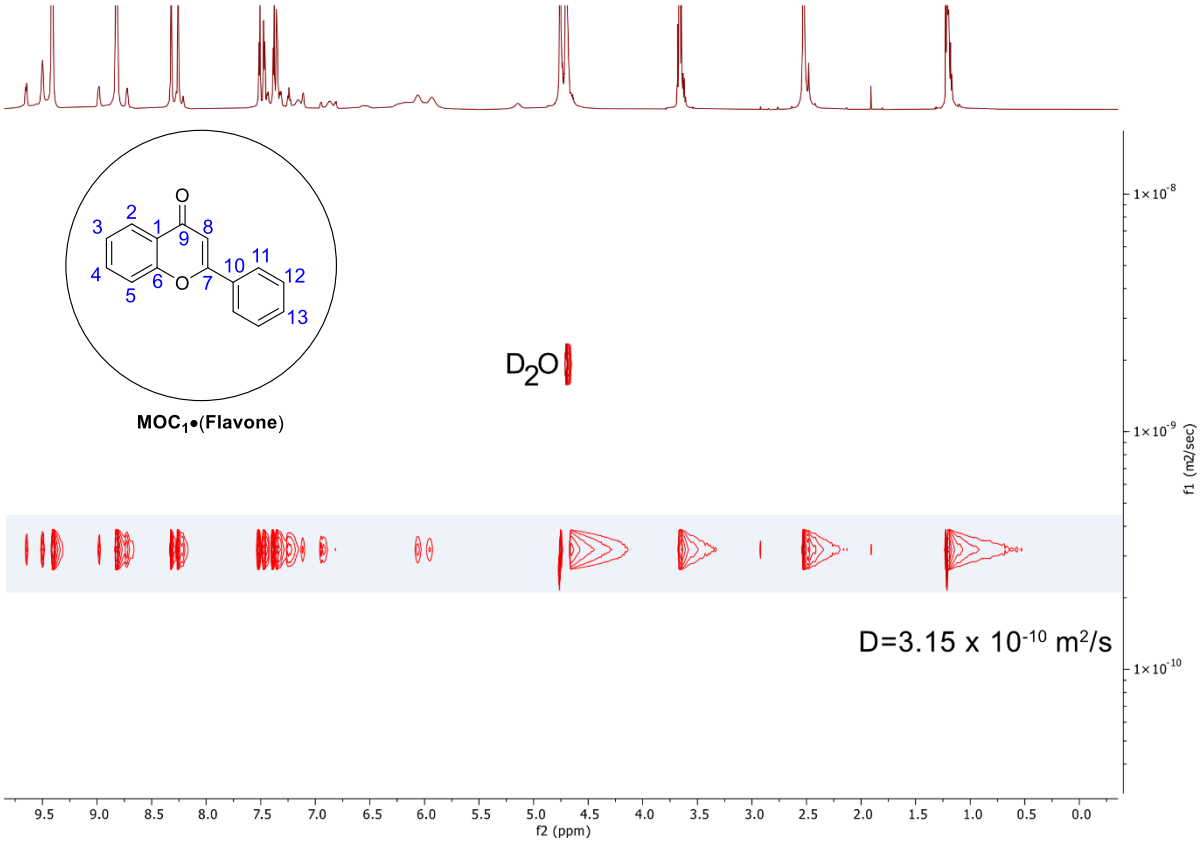

*Figure 177: DOSY NMR (600 MHz, D_2O) of **MOC_1•(flavone)**.*

caffeine and pyrene

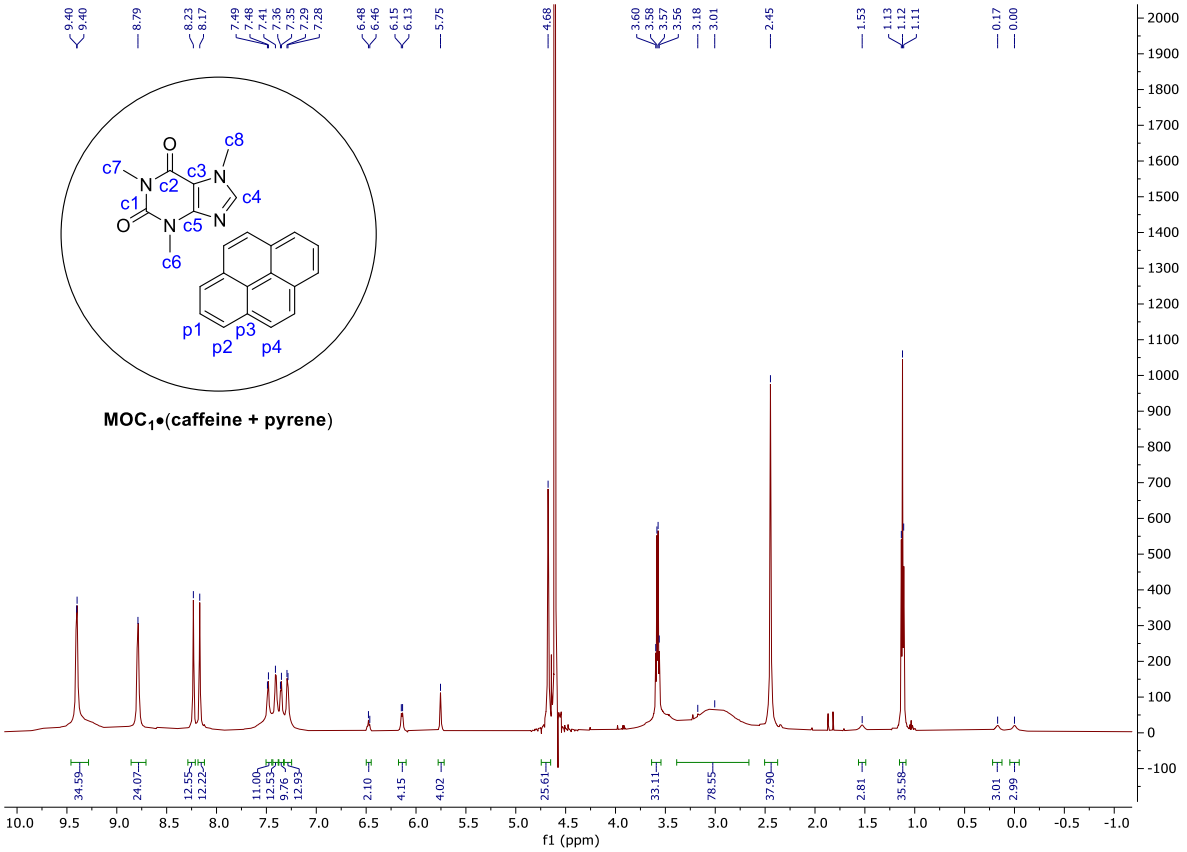

*Figure 178: ^{1}H NMR (600 MHz, D_2O) of **MOC_1•(caffeine and pyrene)**.*

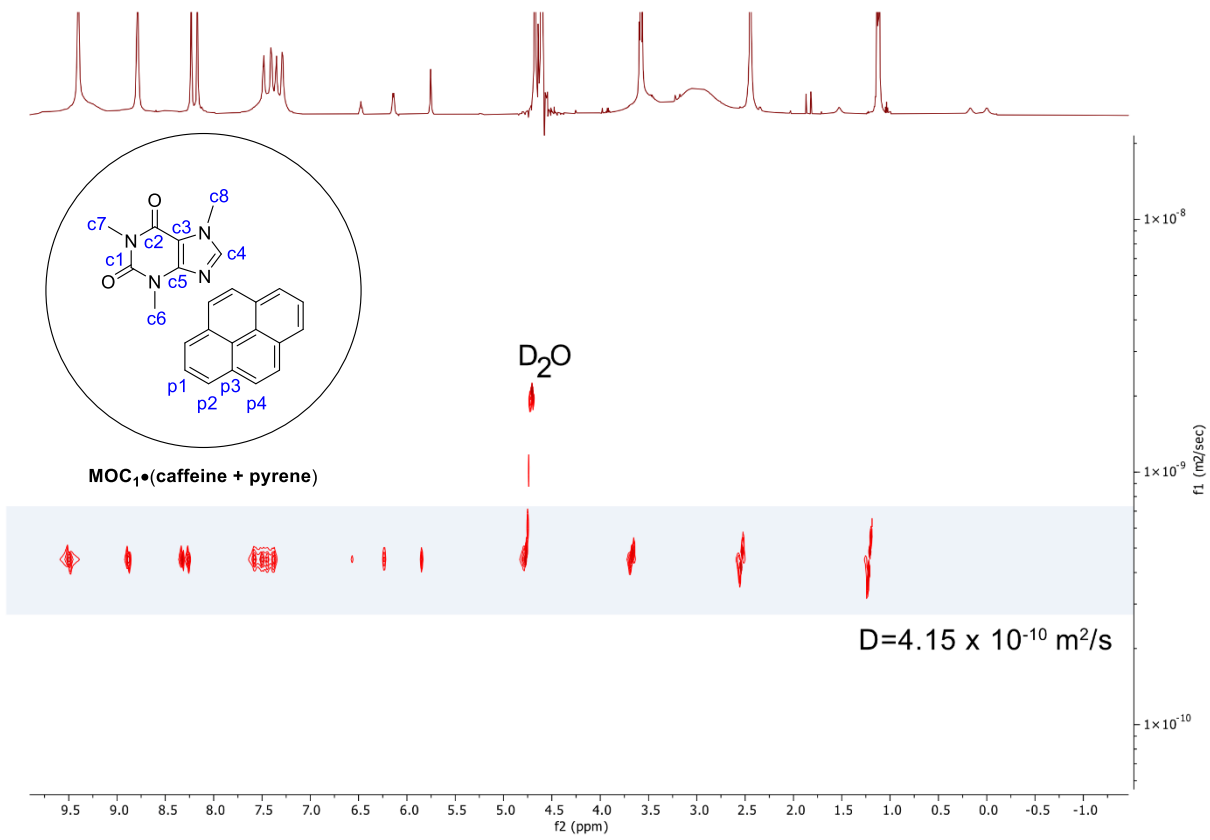

*Figure 179: DOSY NMR (600 MHz, D_2O) of **MOC_1•(caffeine and pyrene)**.*

*Encapsulation with **polyMOC$_{60}$***

Progesterone

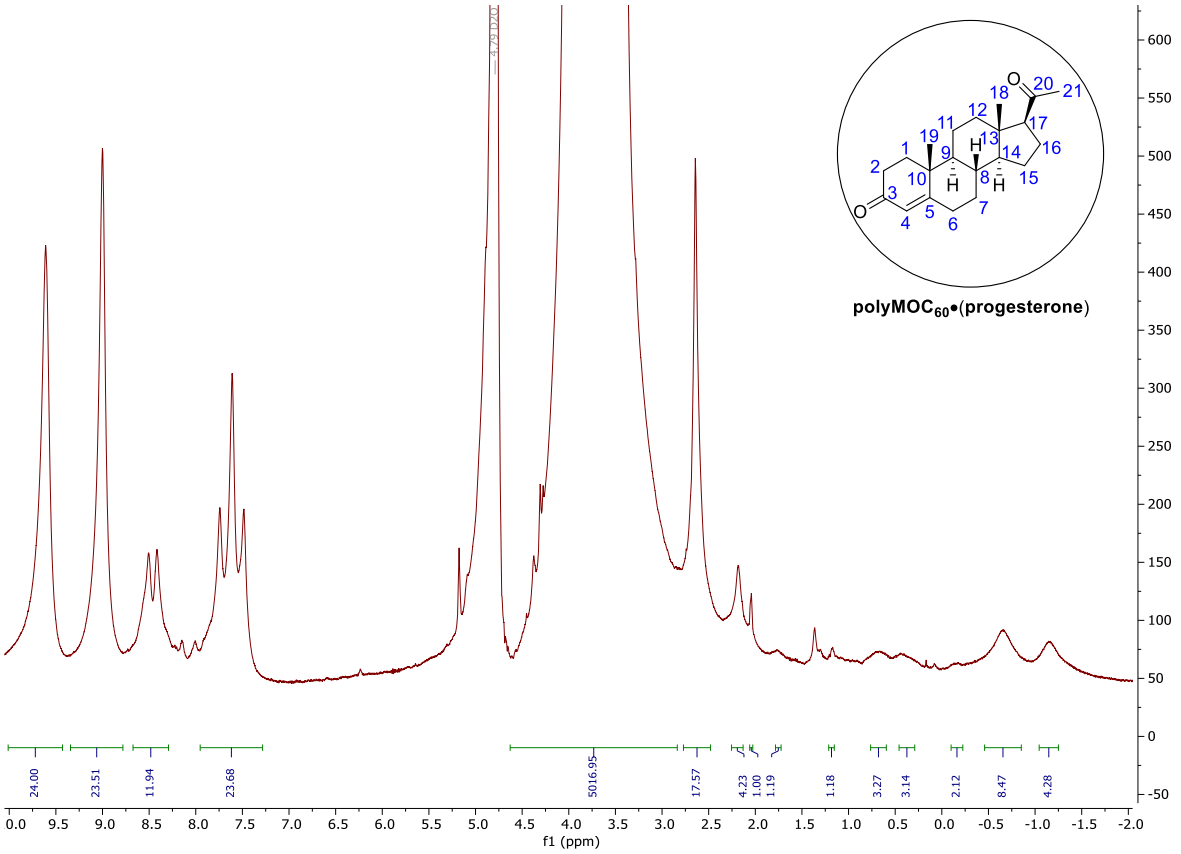

*Figure 180: ^{1}H NMR (600 MHz, D_2O) of **polyMOC$_{60}$•(progesterone)**.*

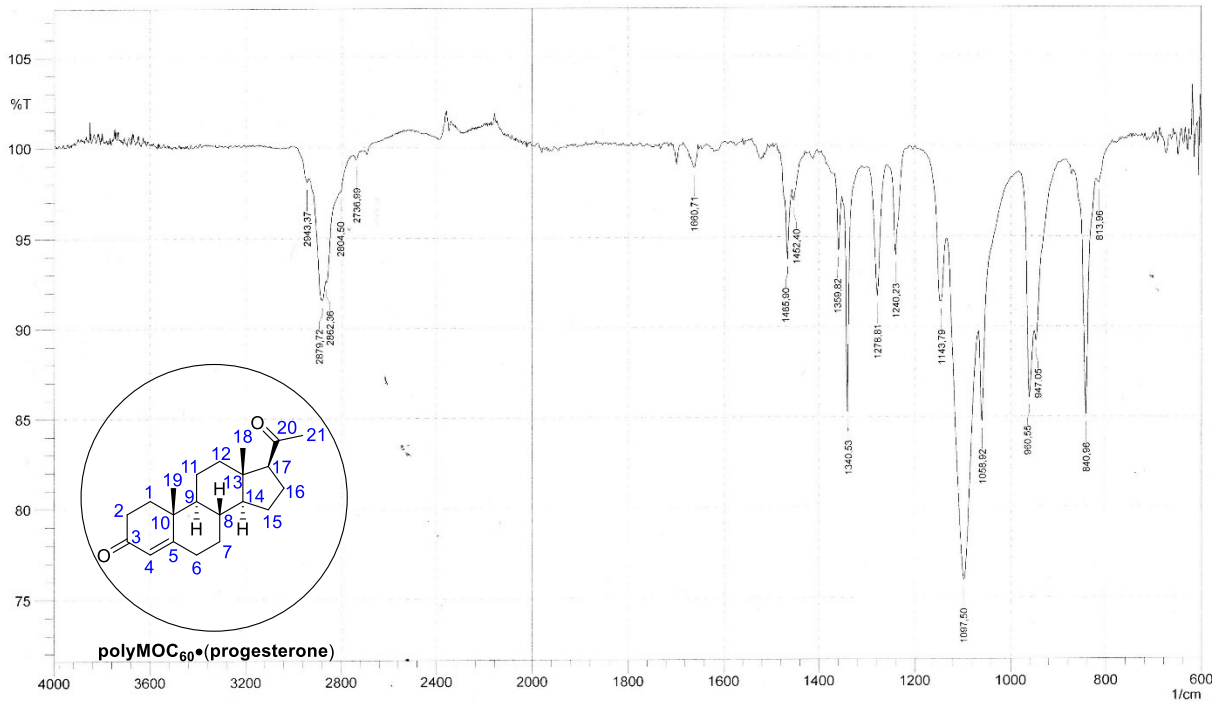

*Figure 181: IR spectrum **polyMOC$_{60}$•(progesterone)** before sonication.*

Ibuprofen

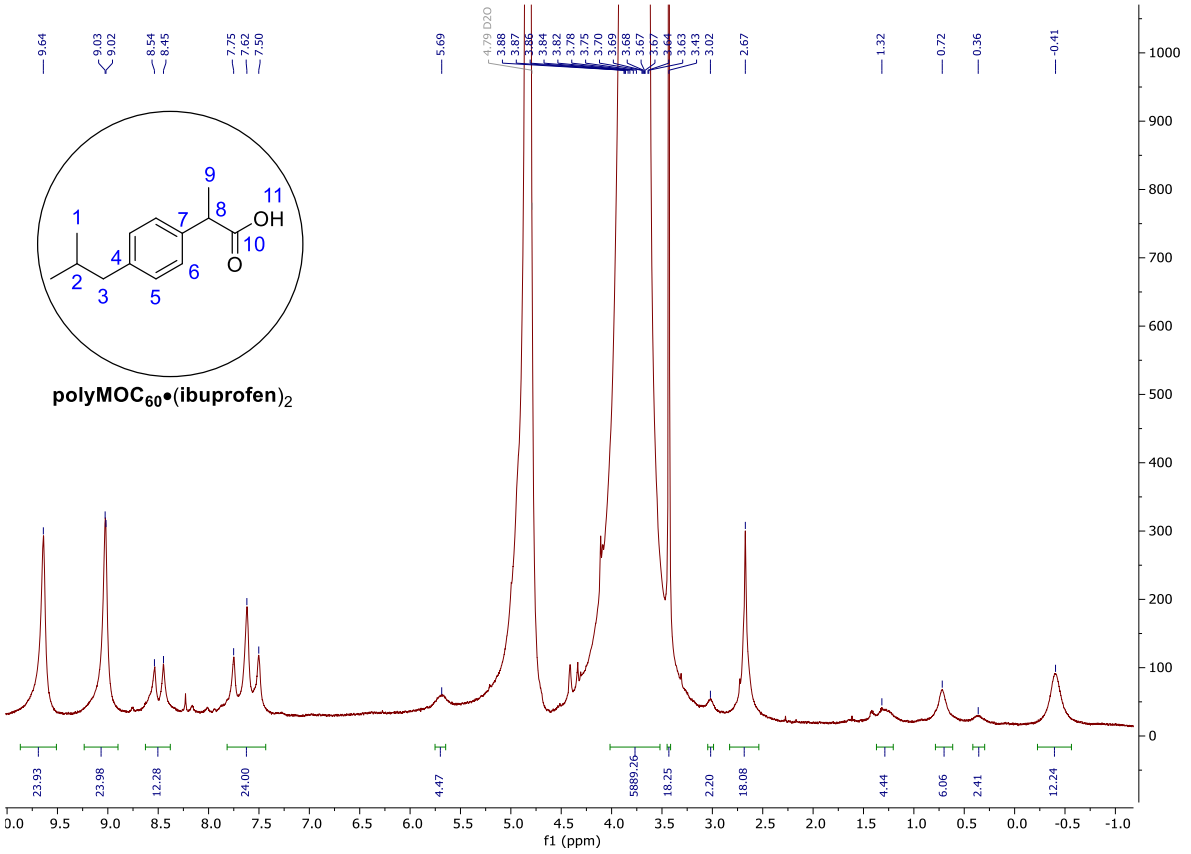

*Figure 182: ^{1}H NMR (600 MHz, D_2O) of **polyMOC$_{60}$•(ibuprofen)$_2$**.*

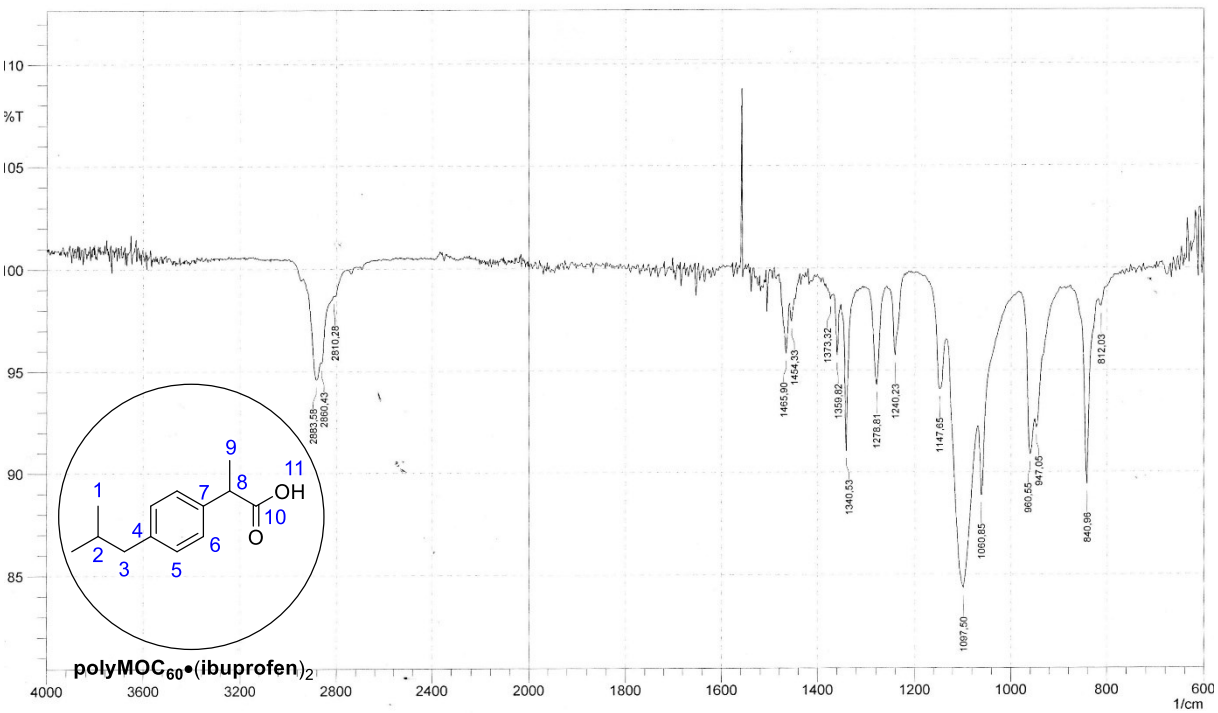

*Figure 183: IR spectrum of **polyMOC$_{60}$•(ibuprofen)$_2$** before sonication.*

Phenolphthalein

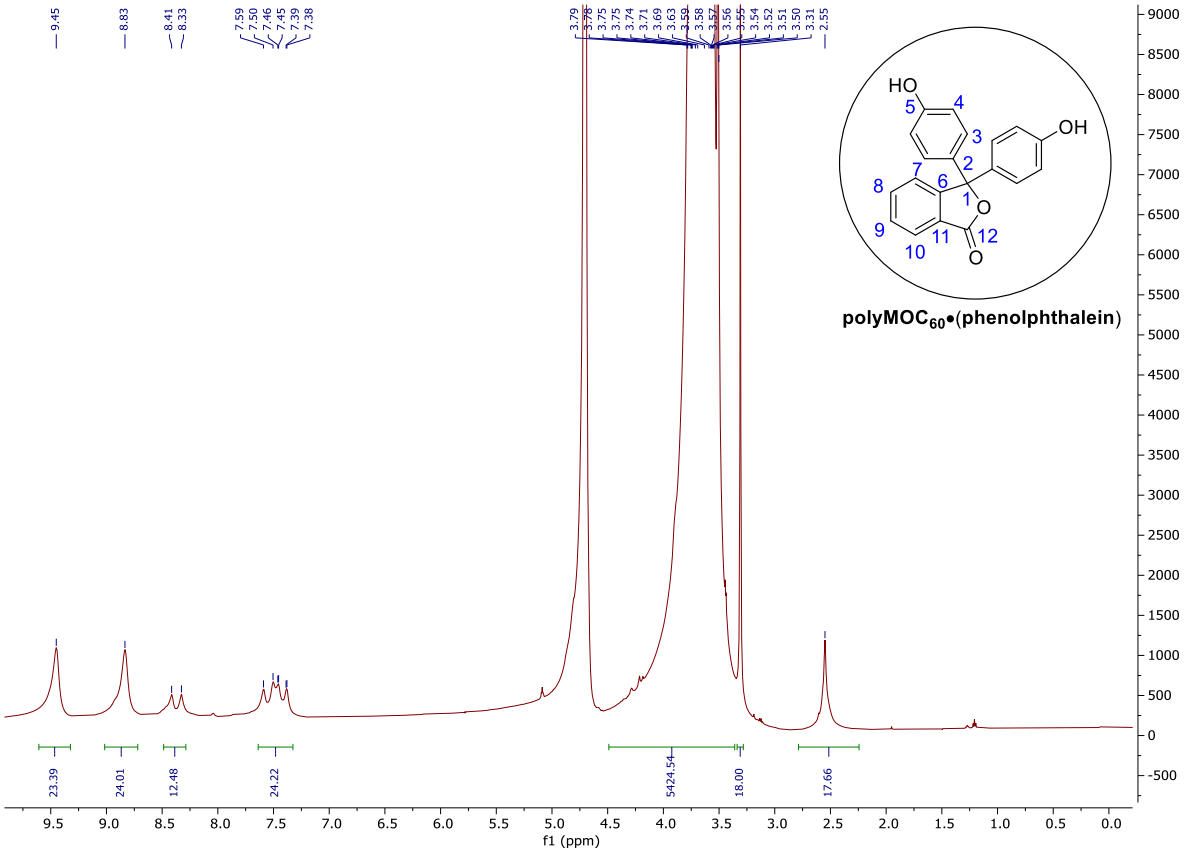

*Figure 184: ^{1}H NMR (600 MHz, D_2O) of **polyMOC$_{60}$•(phenolphthalein)**.*

Section for mechanochemical activation

Cage **polyMOC$_{60}$** empty

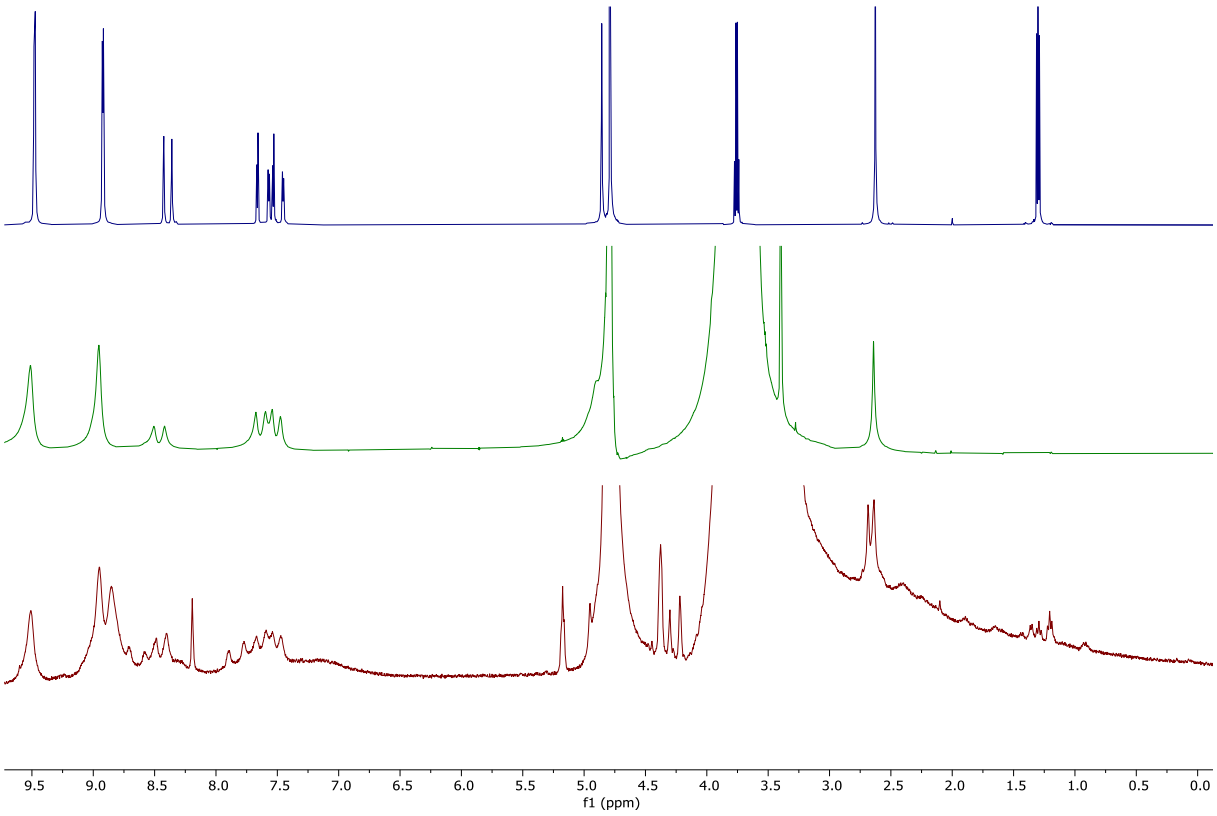

*Figure 185: ^{1}H NMR: Cage **MOC$_1$** (top), cage **polyMOC$_{60}$** before sonication (mid), cage **polyMOC$_{60}$** after sonication (bottom).*

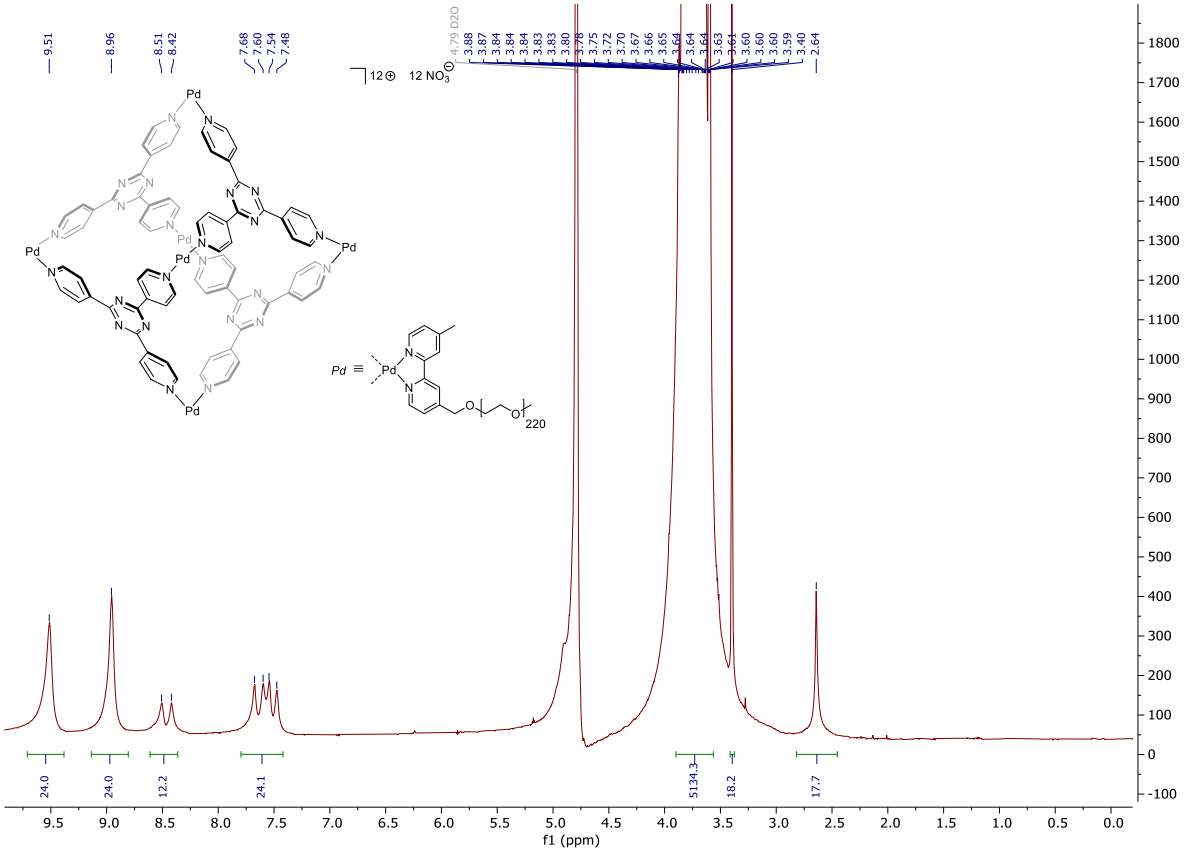

*Figure 186: ^{1}H NMR (600 MHz, D_2O) of cage **polyMOC$_{60}$** before sonication.*

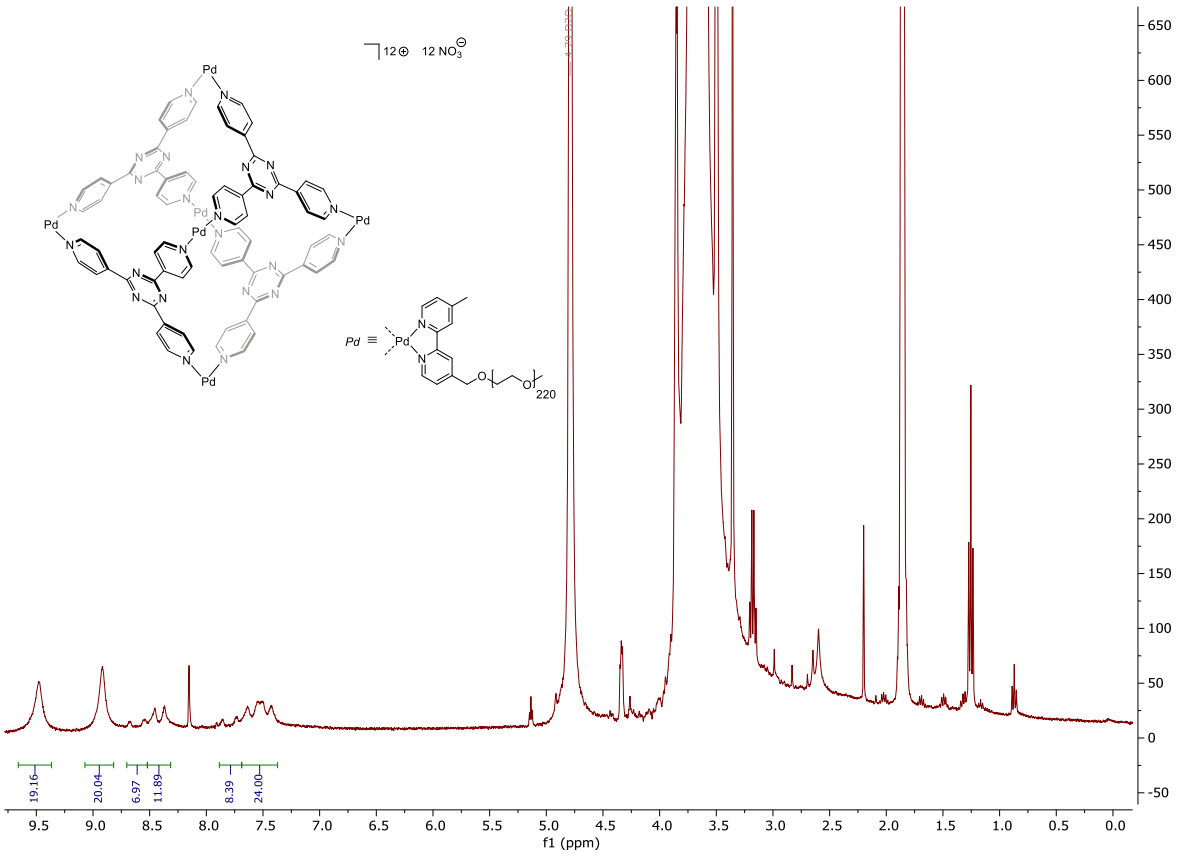

*Figure 187: ^{1}H NMR (400 MHz, D_2O) of cage **polyMOC$_{60}$** after 1 h sonication.*

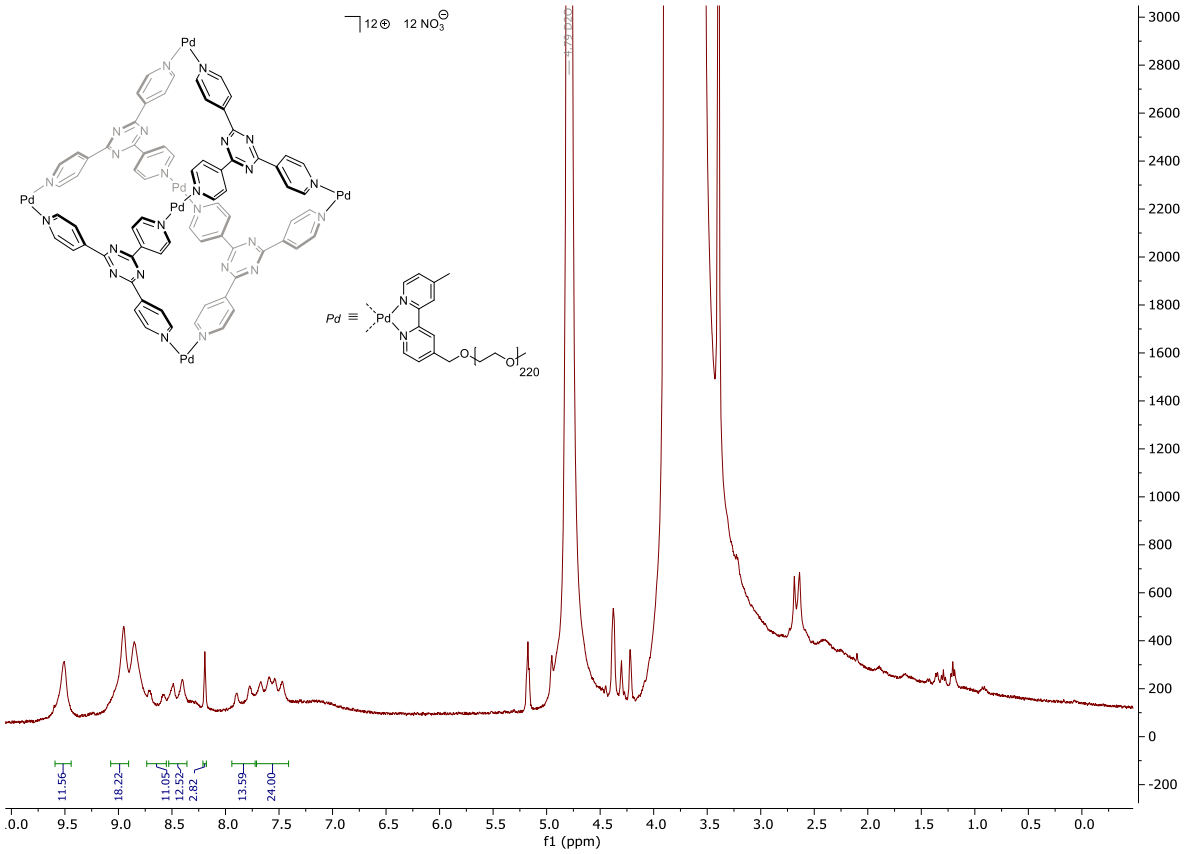

*Figure 188: ^{1}H NMR (400 MHz, D_2O) of cage **polyMOC$_{60}$** after 3 h sonication.*

Cage **polyMOC$_{120}$** empty

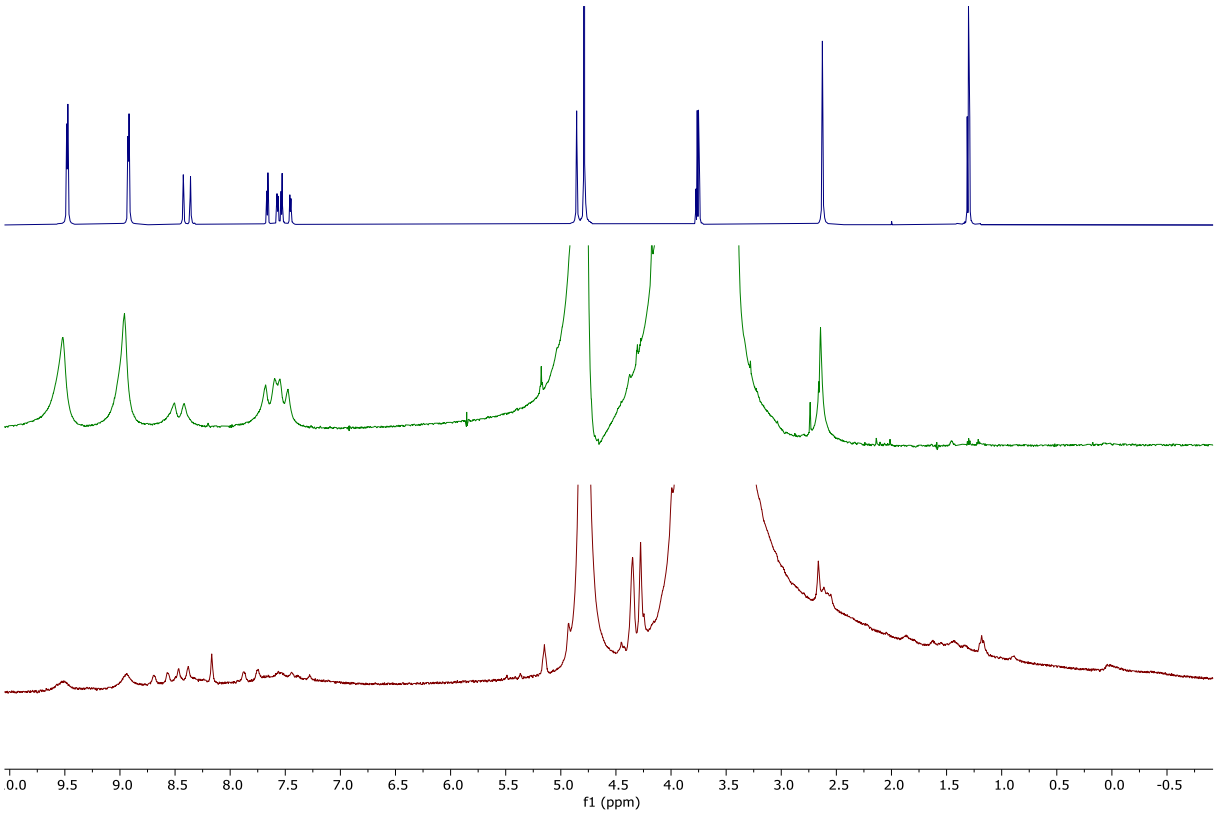

*Figure 189: ^{1}H NMR: Cage **MOC$_1$** (top), cage **polyMOC$_{120}$** before sonication (mid), cage **polyMOC$_{120}$** after sonication (bottom).*

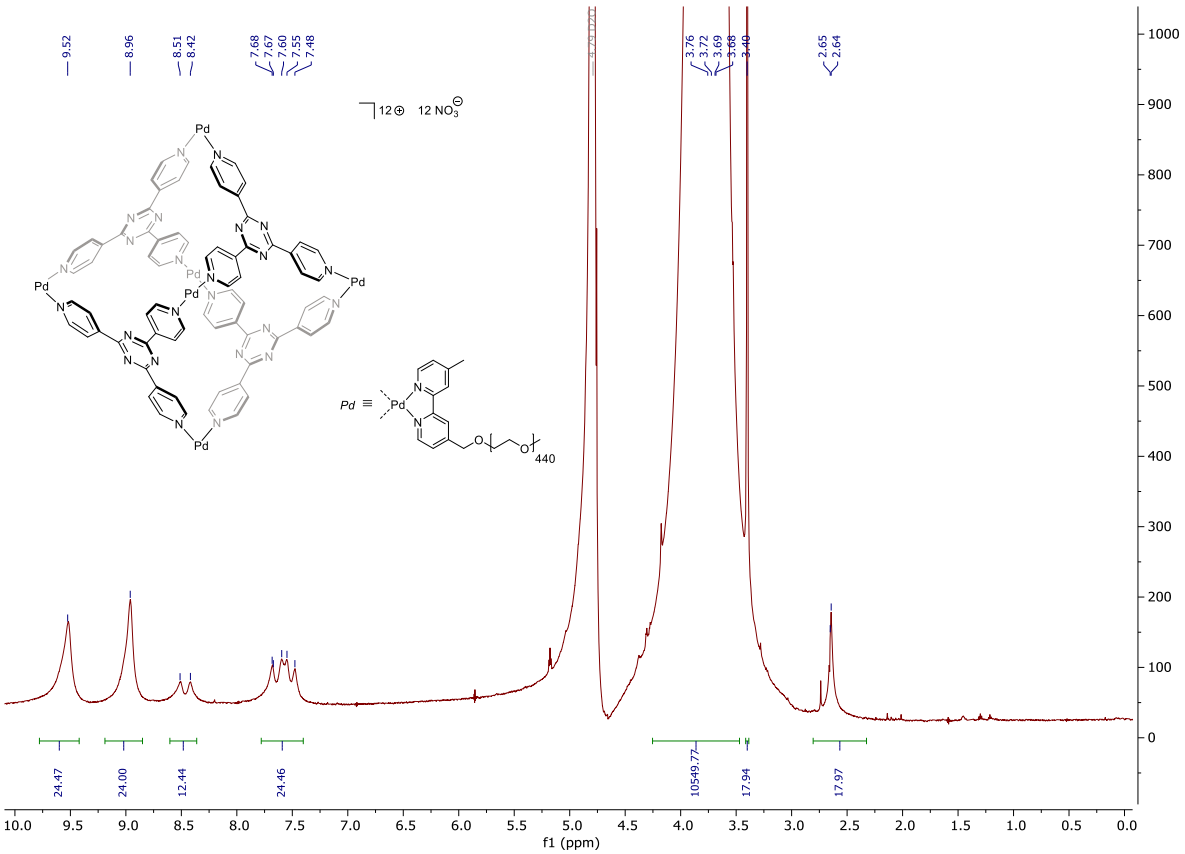

*Figure 190: ^{1}H NMR (600 MHz, D_2O) of cage **polyMOC$_{120}$** before sonication.*

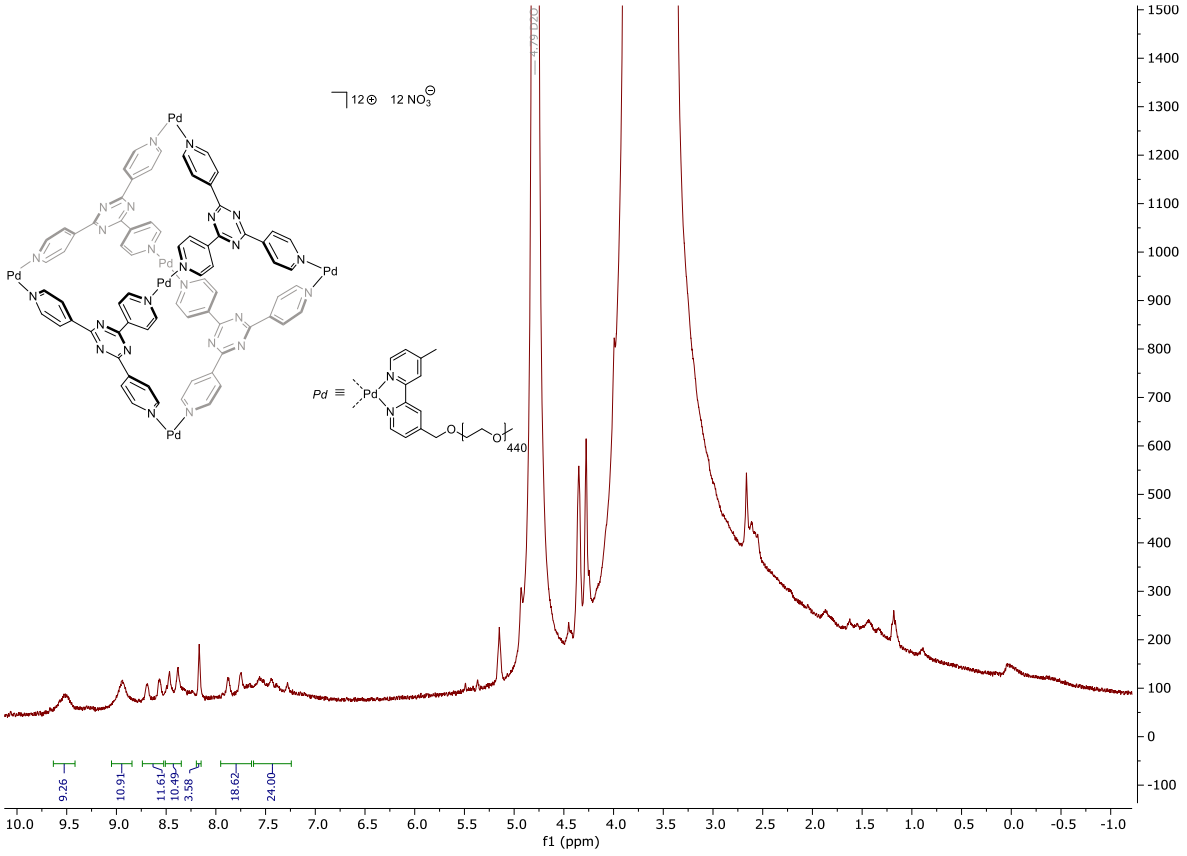

*Figure 191: ^{1}H NMR (400 MHz, D_2O) of cage **polyMOC$_{120}$** after 1 h sonication.*

PolyMOC$_{60}$•(progesterone)

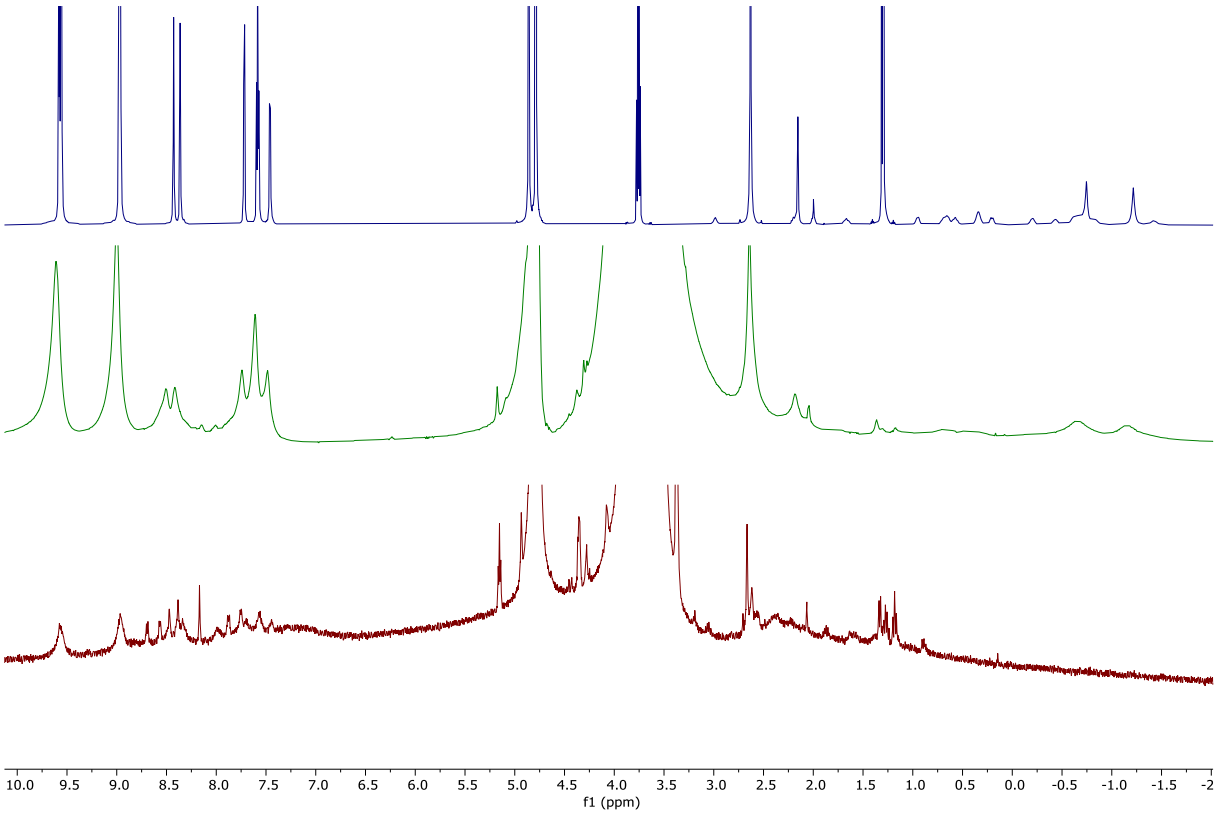

*Figure 192: ^{1}H NMR: Cage **MOC$_1$•(progesterone)** (top), cage **polyMOC$_{60}$•(progesterone)** before sonication (mid), cage **polyMOC$_{60}$•(progesterone)** after sonication (bottom).*

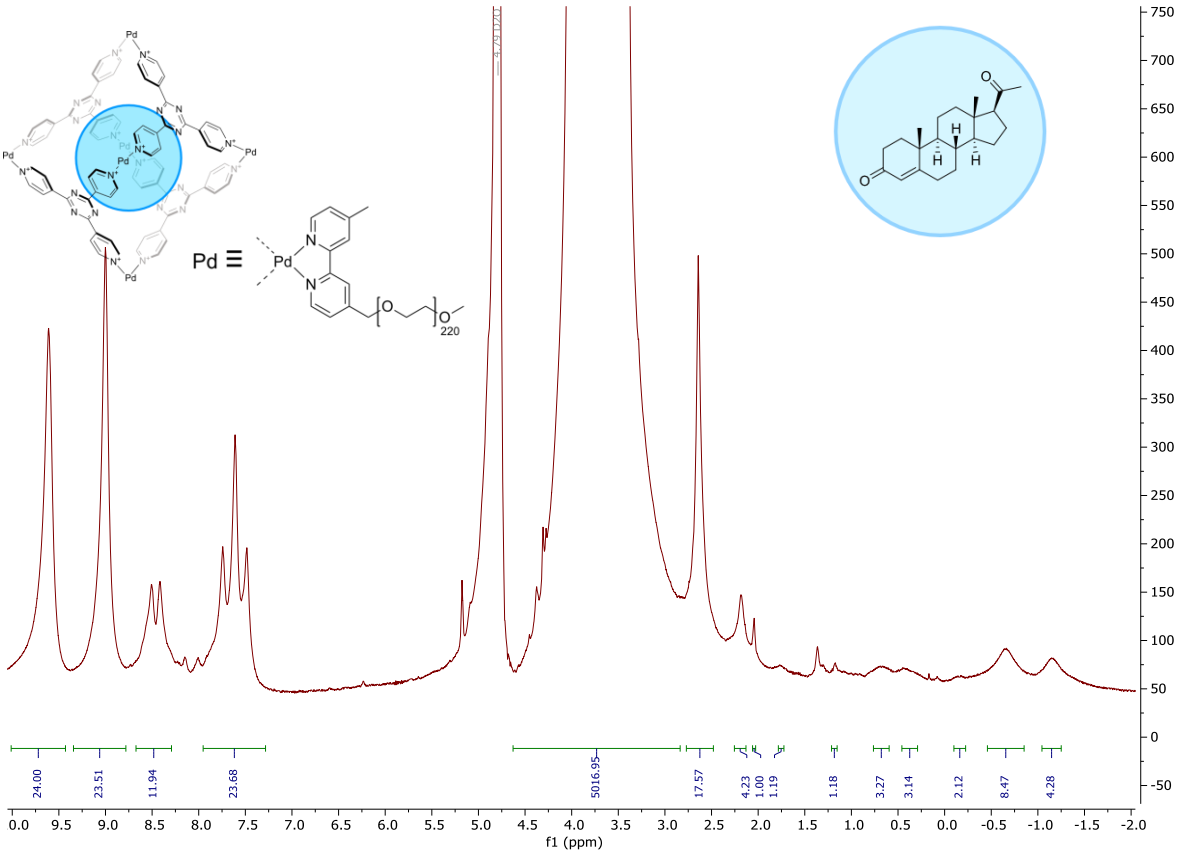

*Figure 193: ^{1}H NMR (600 MHz, D_2O) of **polyMOC$_{60}$•(progesterone)** before sonication.*

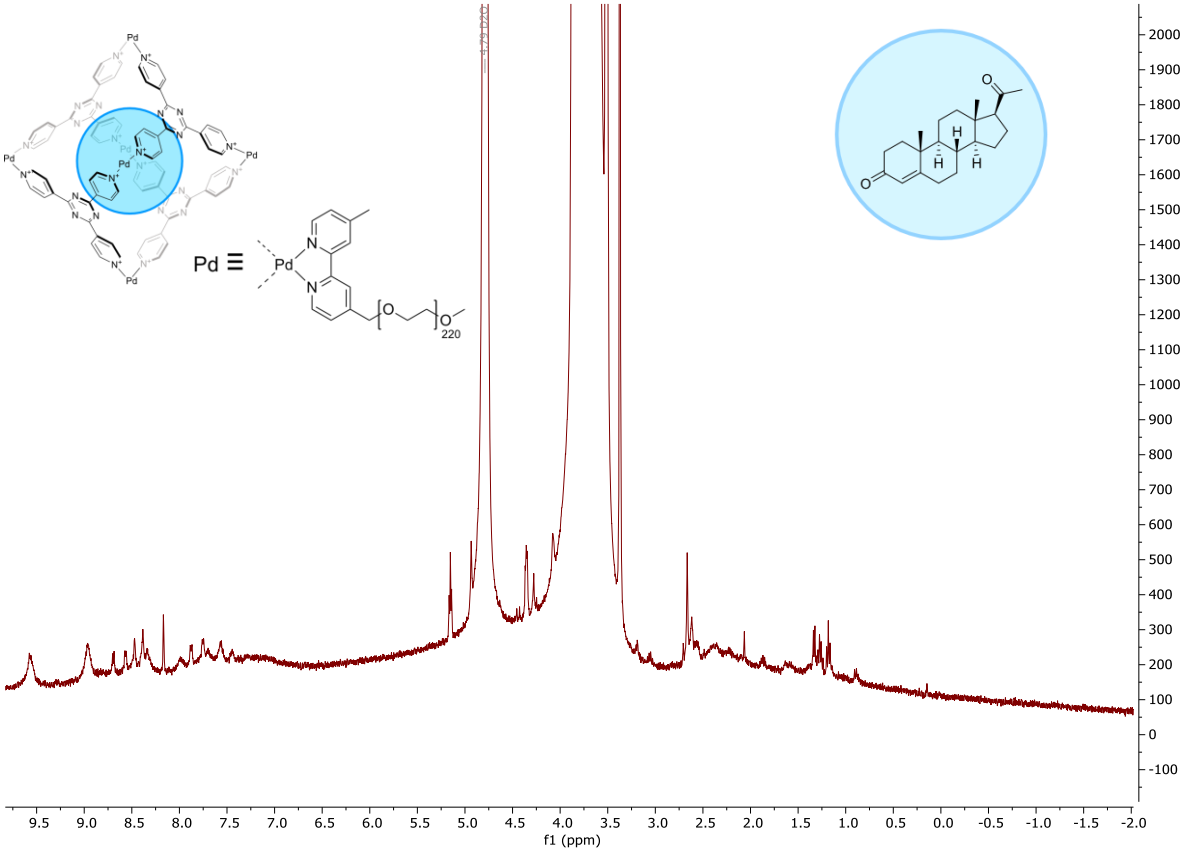

*Figure 194: ^{1}H NMR (400 MHz, D_2O) of **polyMOC$_{60}$•(progesterone)** after sonication.*

PolyMOC$_{60}$•(ibuprofen)$_2$

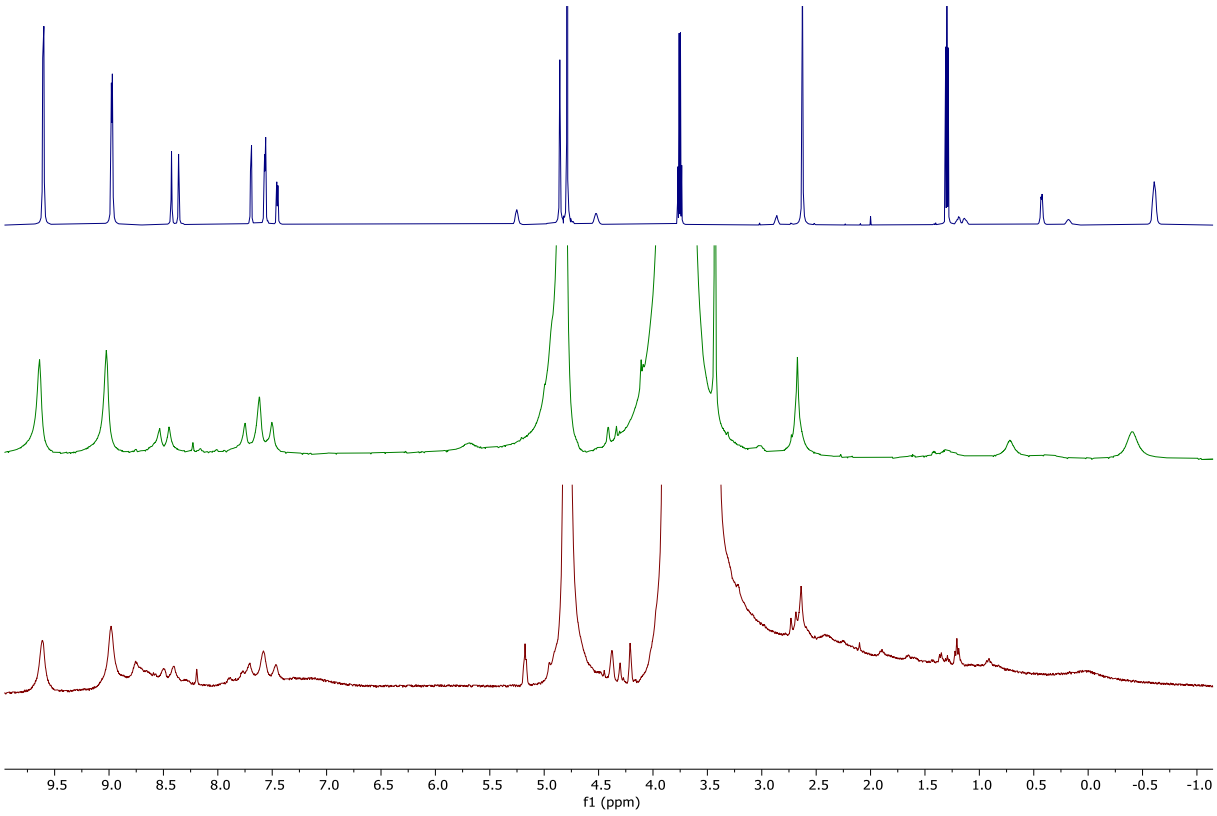

*Figure 195: ^{1}H NMR: **MOC$_1$•(ibuprofen)$_2$** (top), **polyMOC$_{60}$•(ibuprofen)$_2$** before sonication (mid), **polyMOC$_{60}$•(ibuprofen)$_2$** after sonication (bottom).*

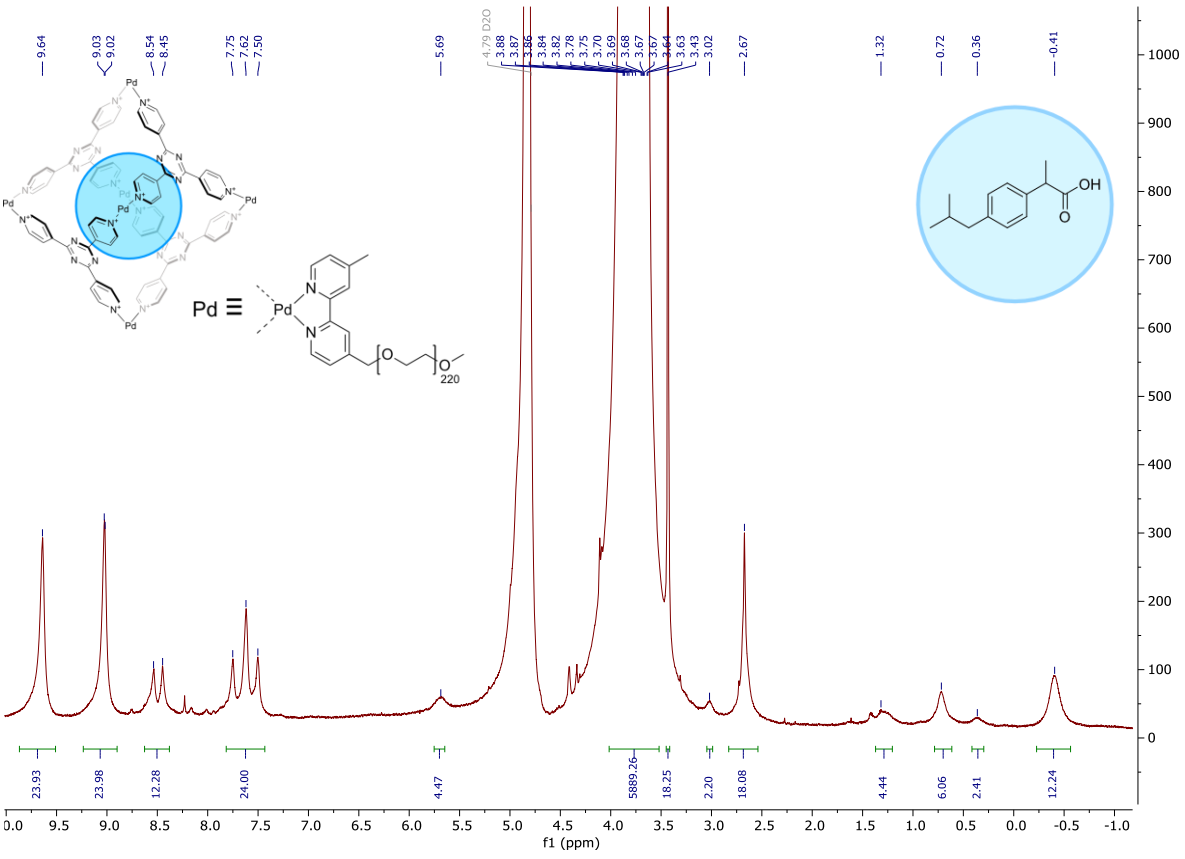

*Figure 196: ^{1}H NMR (600 MHz, D_2O) of **polyMOC$_{60}$•(ibuprofen)$_2$** before sonication.*

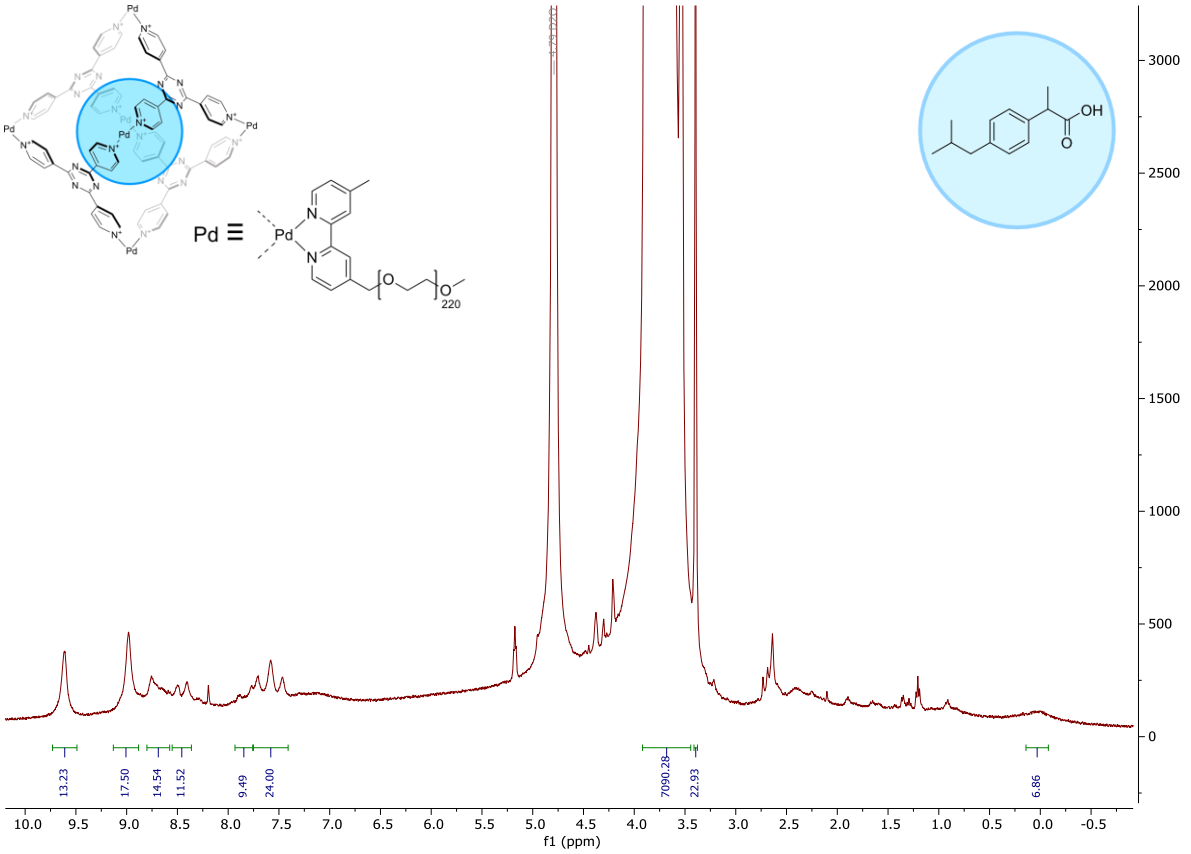

*Figure 197: ^{1}H NMR (400 MHz, D_2O) of **polyMOC$_{60}$•(ibuprofen)$_2$** after sonication.*

6.2 Spectra for section 3.2

*Synthesis of mechonophore **CMP***

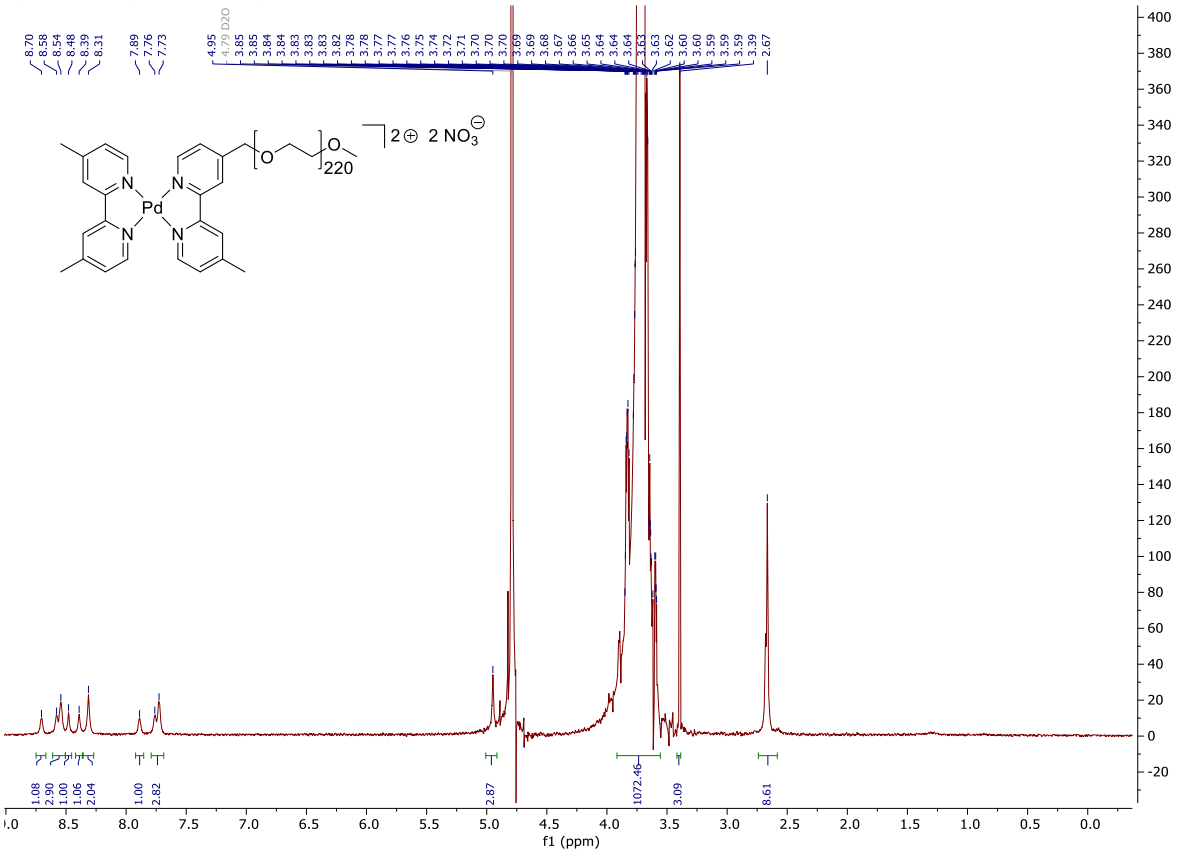

*Figure 198: ^{1}H NMR (600 MHz, D_2O) of control mechanophore C**MP**.*

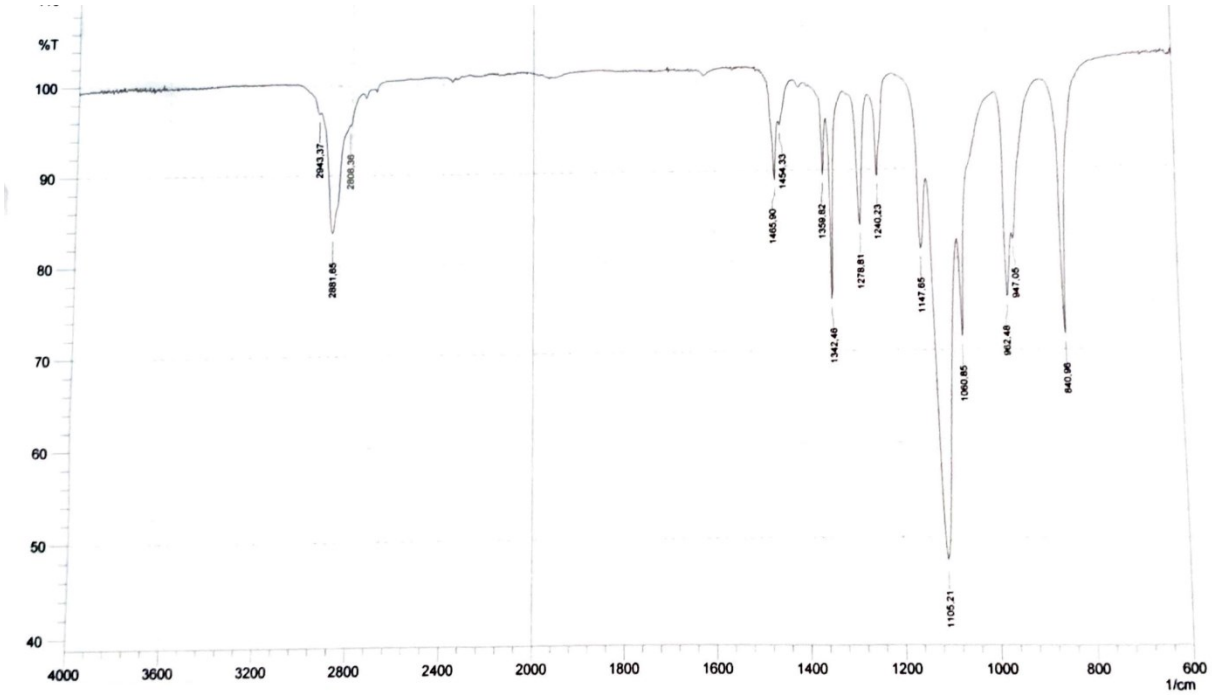

*Figure 199: IR spectrum of mechanophore **CMP**.*

*Synthesis of mechonophore **MP$_{15}$***

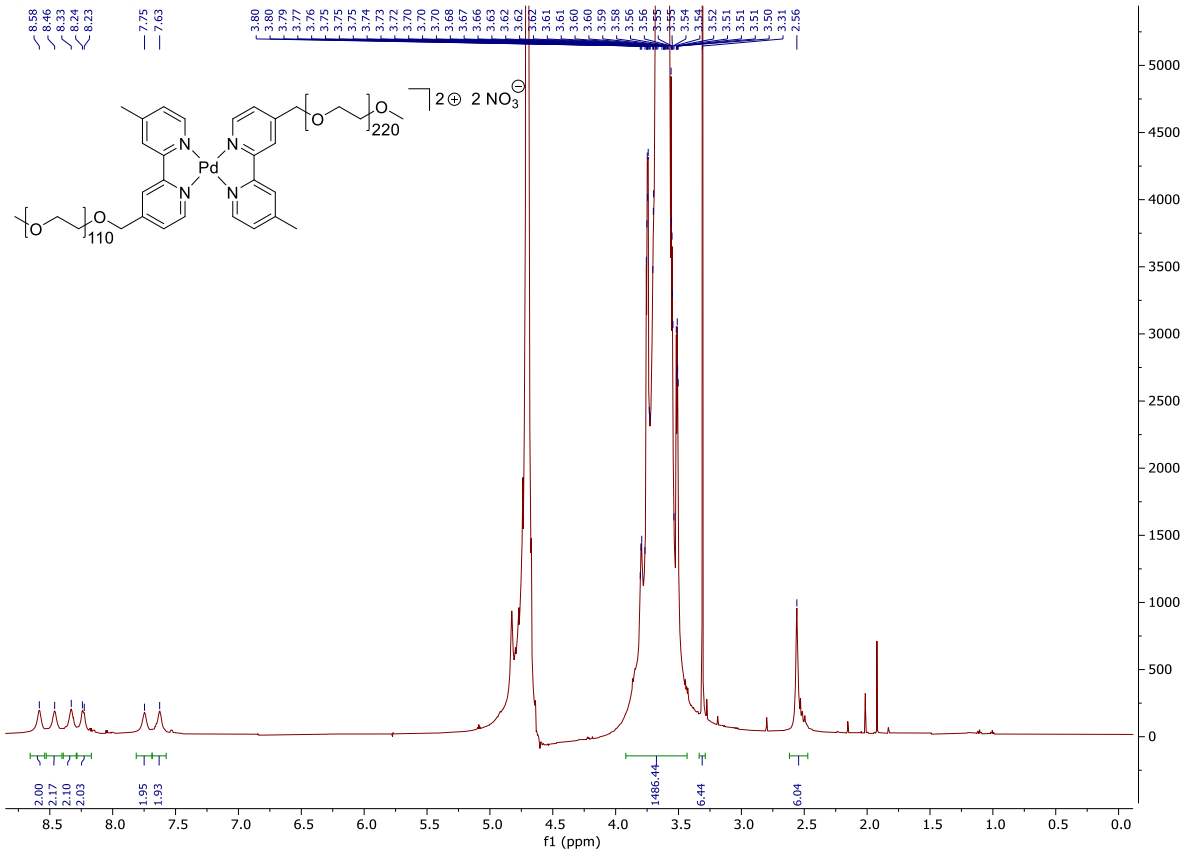

*Figure 200: ^{1}H NMR (600 MHz, D_2O) of mechanophore **MP$_{15}$**.*

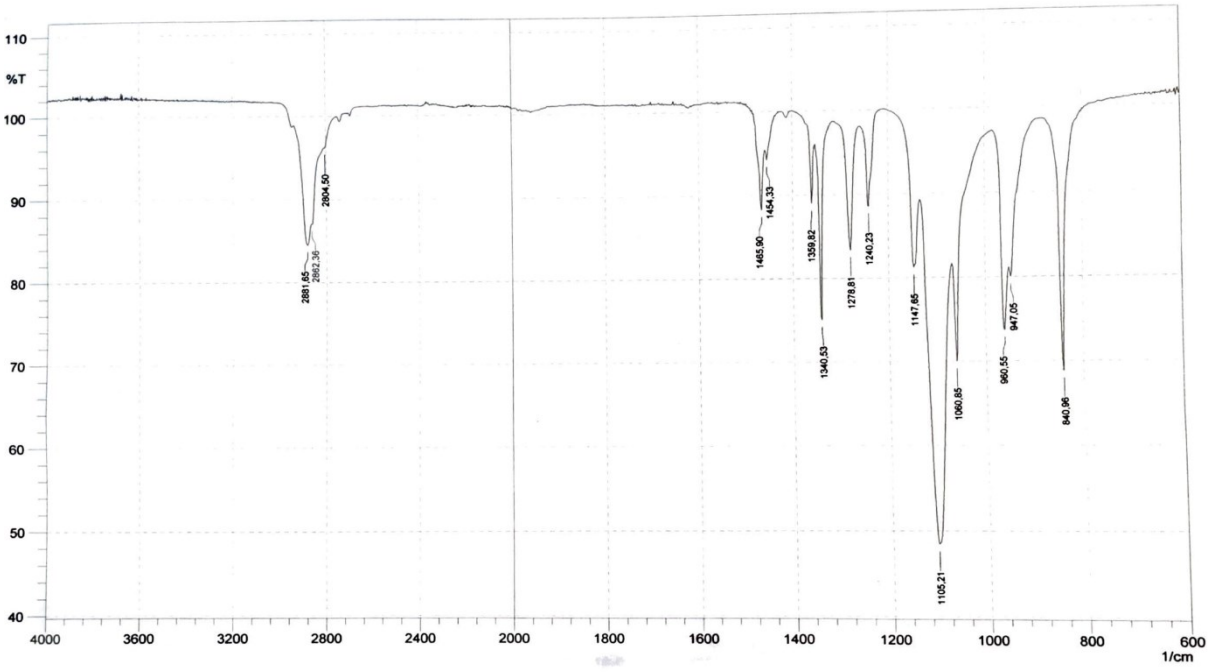

*Figure 201: IR spectrum of mechanophore **MP$_{15}$**.*

Synthesis of mechanophore MP_{20}

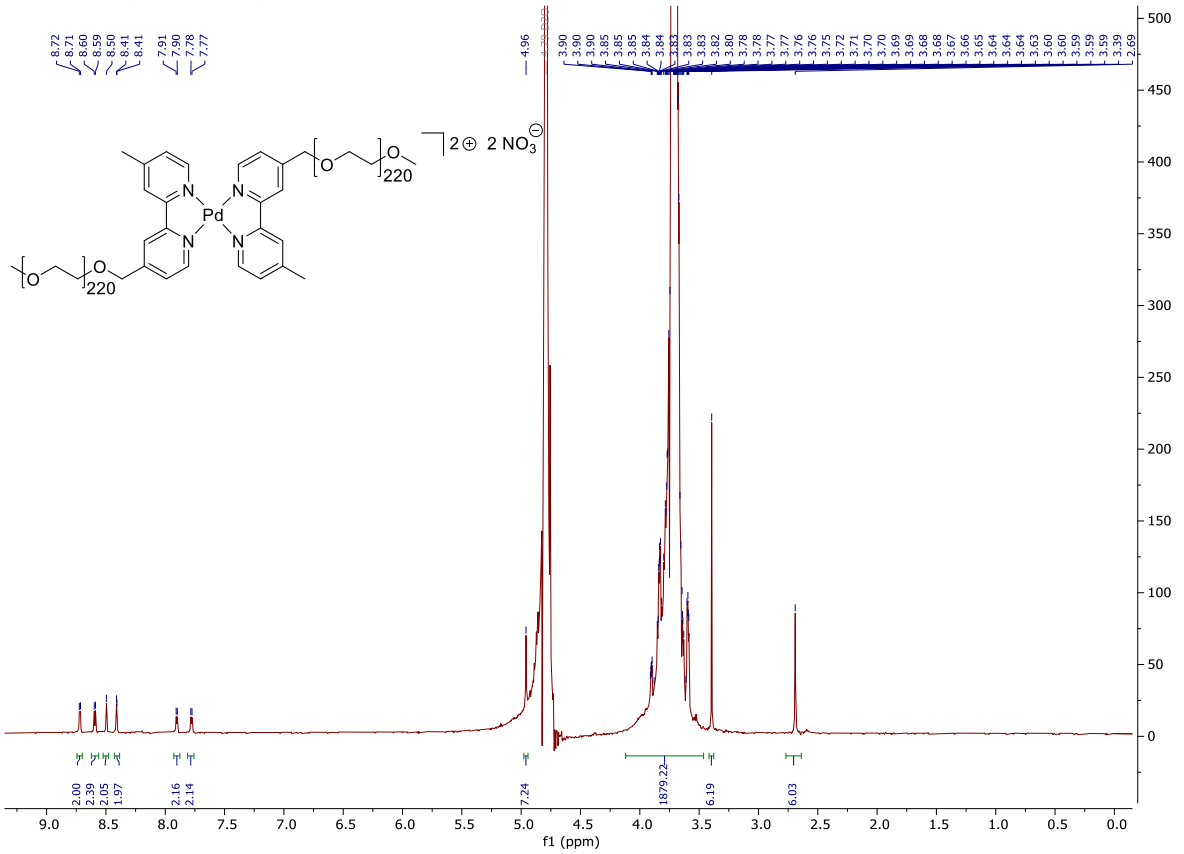

*Figure 202: ^{1}H NMR (600 MHz, D_2O) of mechanophore **MP_{20}**.*

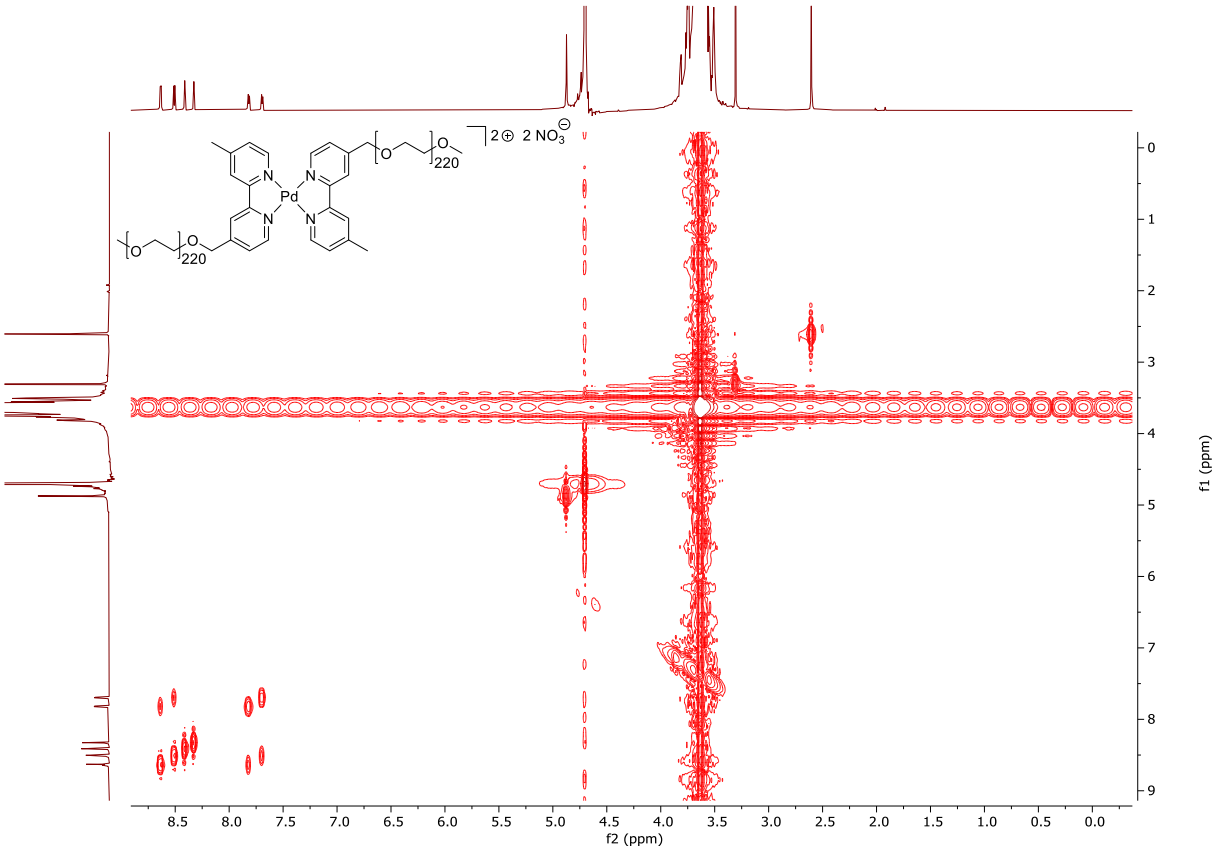

*Figure 203: ^{1}H-^{1}H COSY NMR (600 MHz, D_2O) of mechanophore **MP_{20}**.*

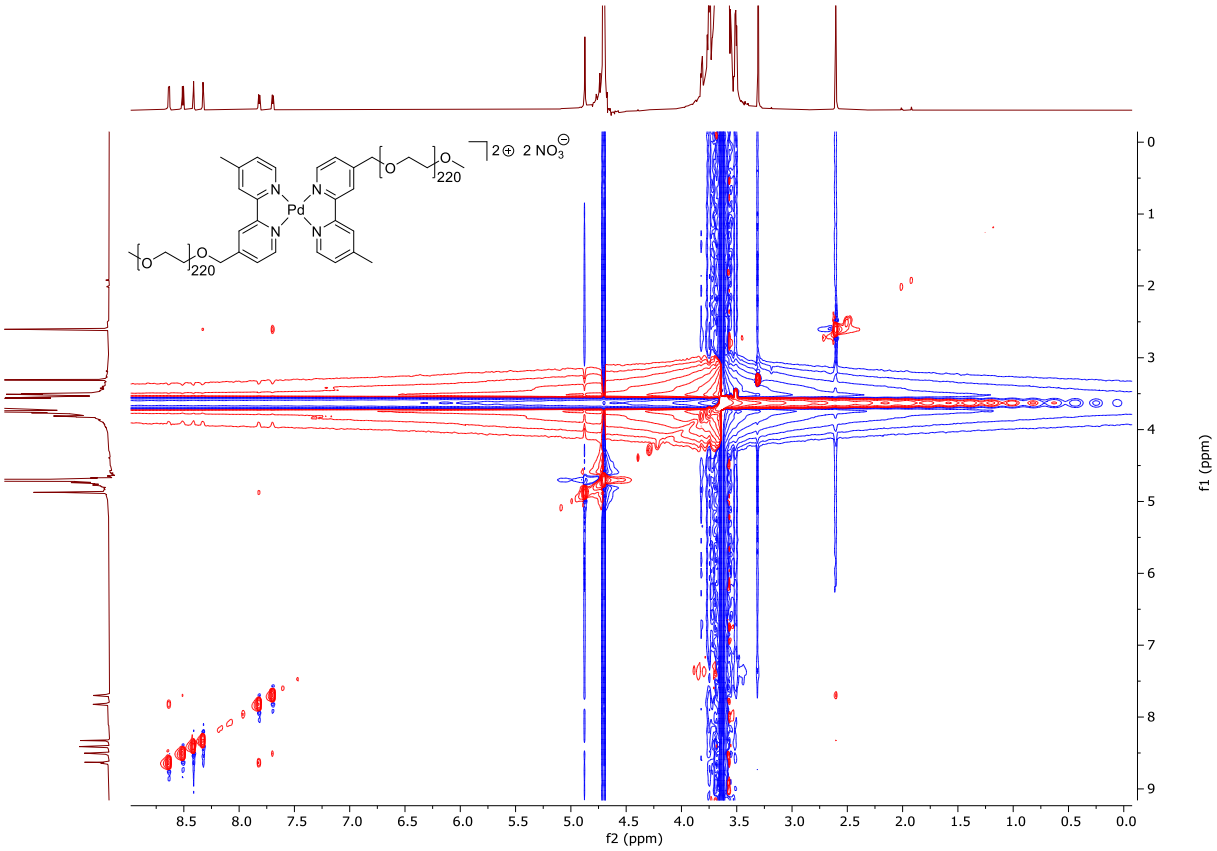

*Figure 204: ^{1}H-^{1}H NOESY NMR (600 MHz, D_2O) of mechanophore **MP_{20}**.*

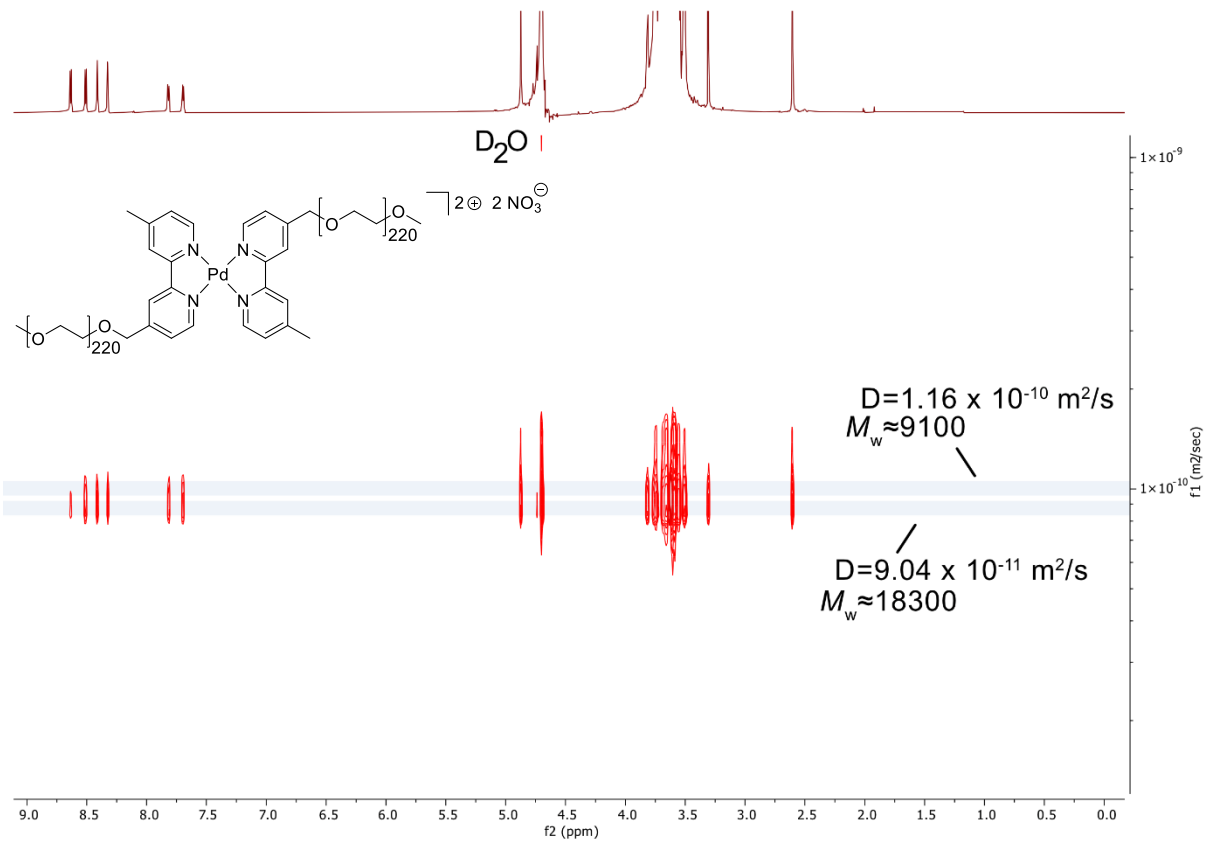

*Figure 205: DOSY NMR (600 MHz, D_2O) of mechanophore **MP_{20}**.*

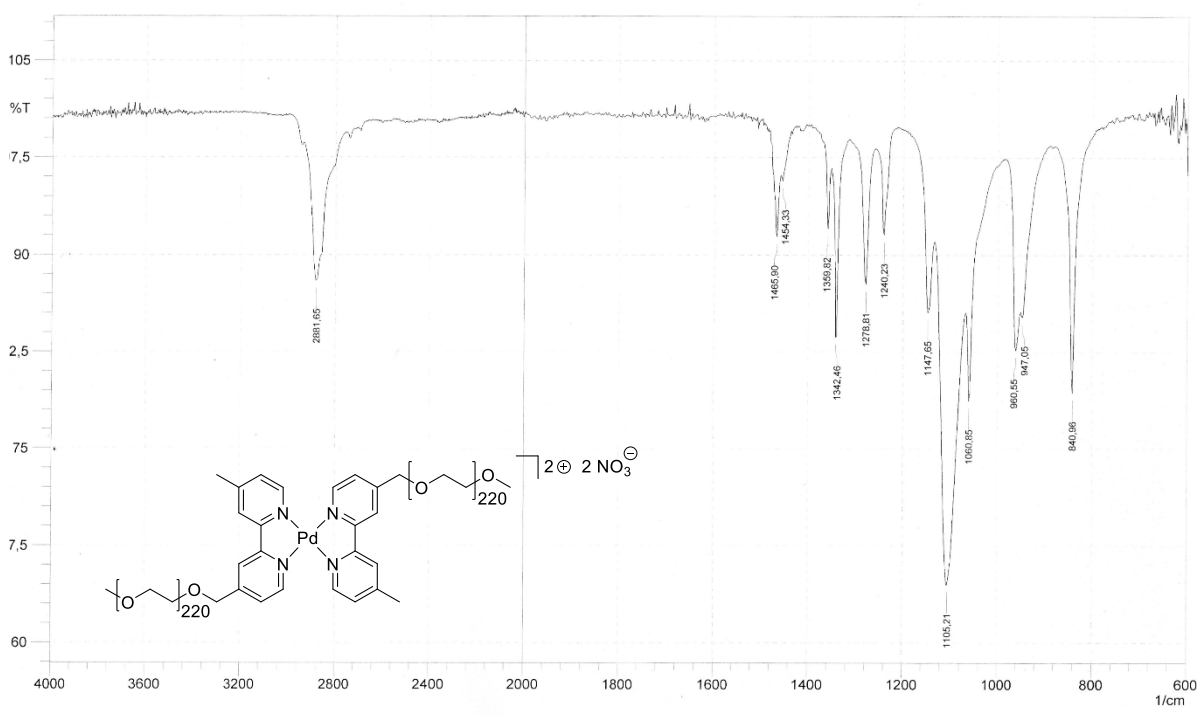

Figure 206: IR spectrum of mechanophore ***MP$_{20}$***.

6.3 Spectra for section 3.3

Section for the synthesis

ibuprofen based cross-linker **36**

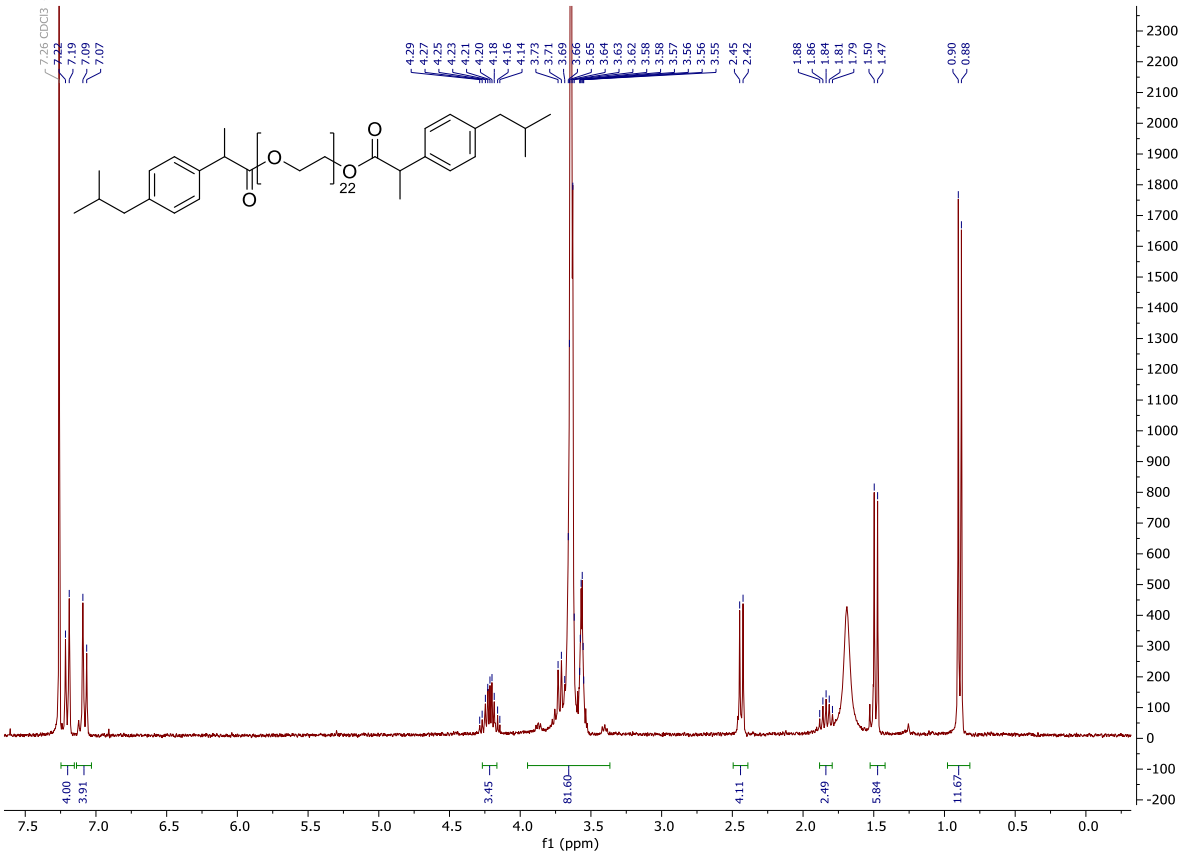

*Figure 207: ^{1}H NMR (300 MHz, $CDCl_3$) of linker **36**.*

ibuprofen based cross-linker **35**

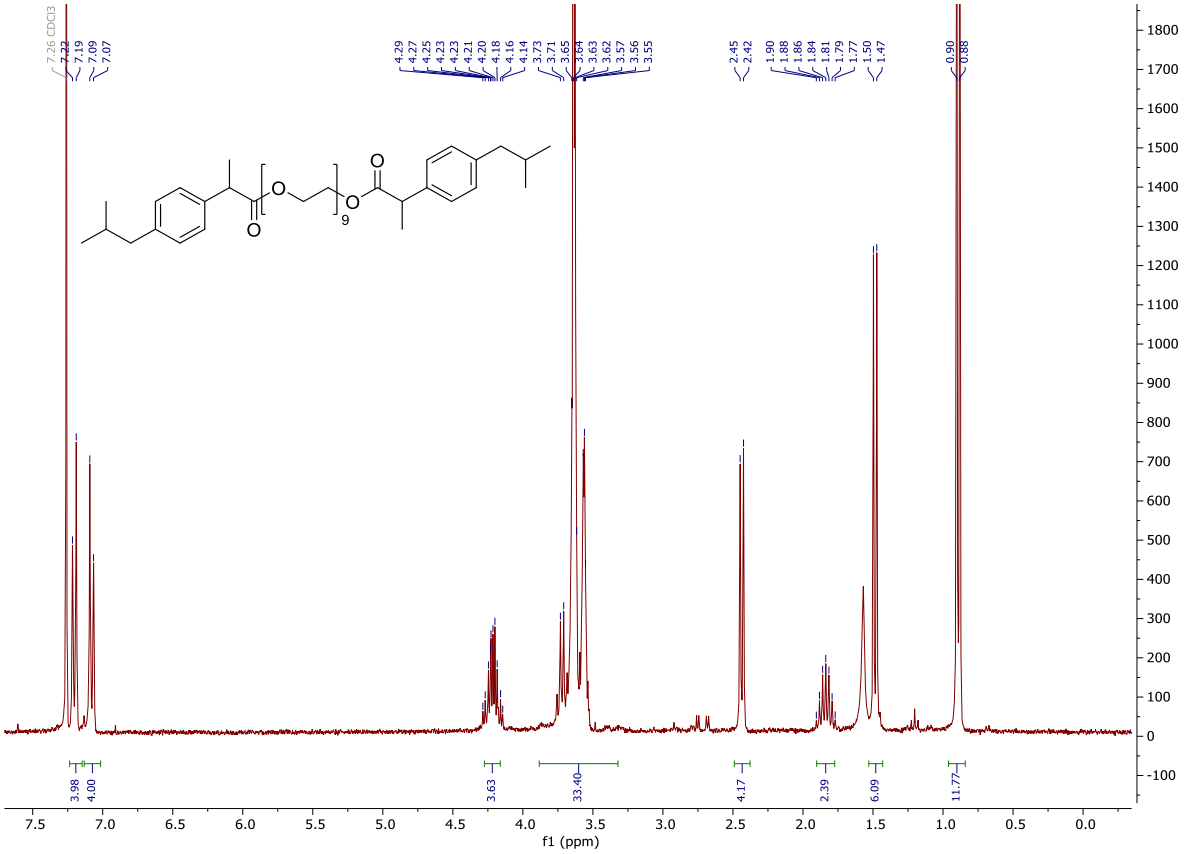

*Figure 208: ^{1}H NMR (300 MHz, $CDCl_3$) of linker **35**.*

1-adamantanemethanol (**40**)

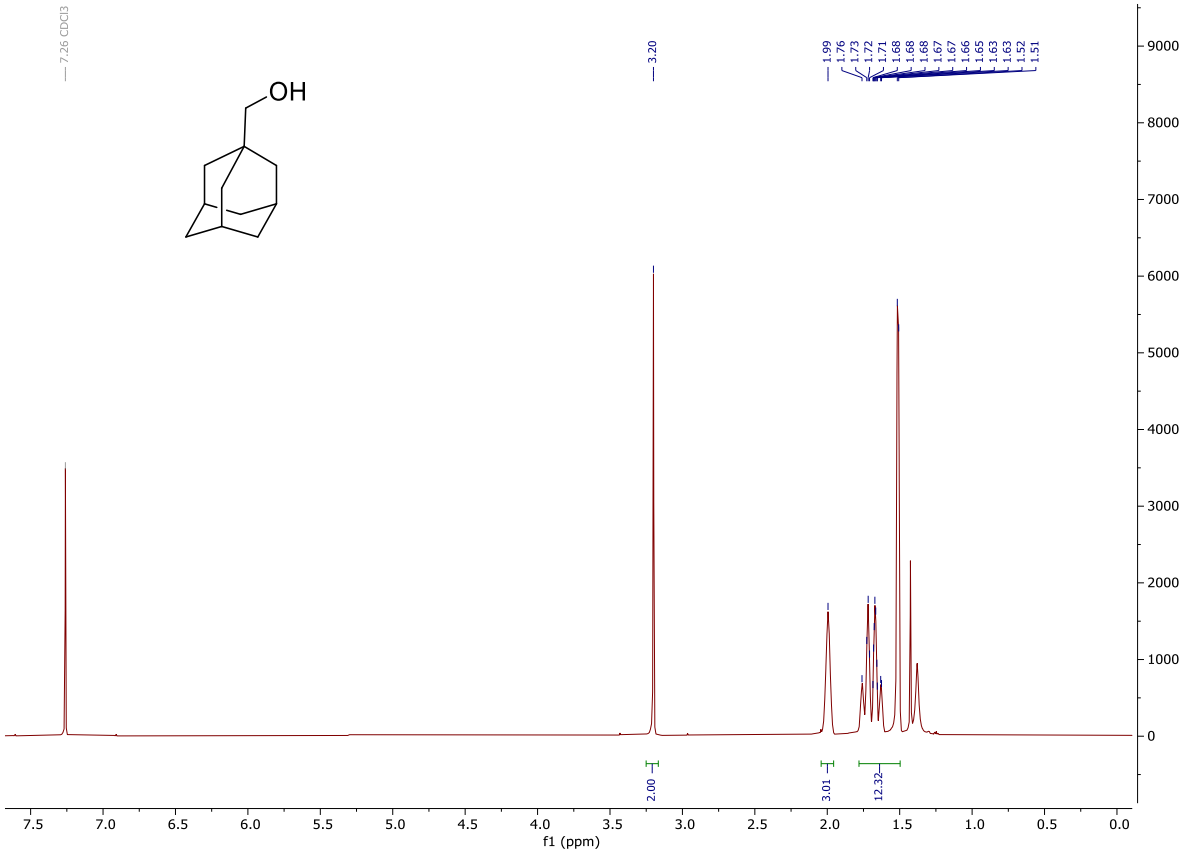

*Figure 209: ^{1}H NMR (300 MHz, $CDCl_3$) of 1-adamantanemethanol (**40**).*

1-adamantylmethyl methanesulfonate (**41**)

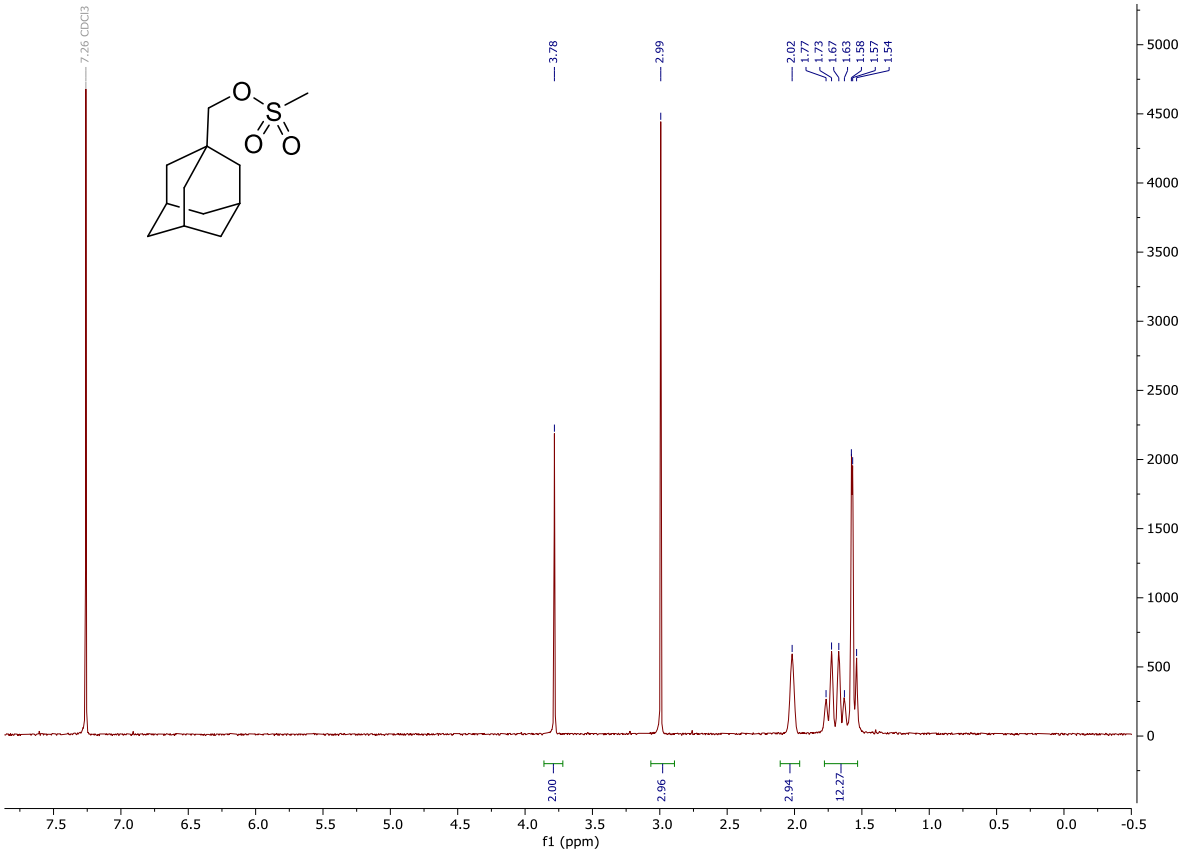

*Figure 210: ^{1}H NMR (300 MHz, $CDCl_3$) of 1-adamantyl methanesulfonate (**41**).*

1-adamantylmethyl azide (**42**)

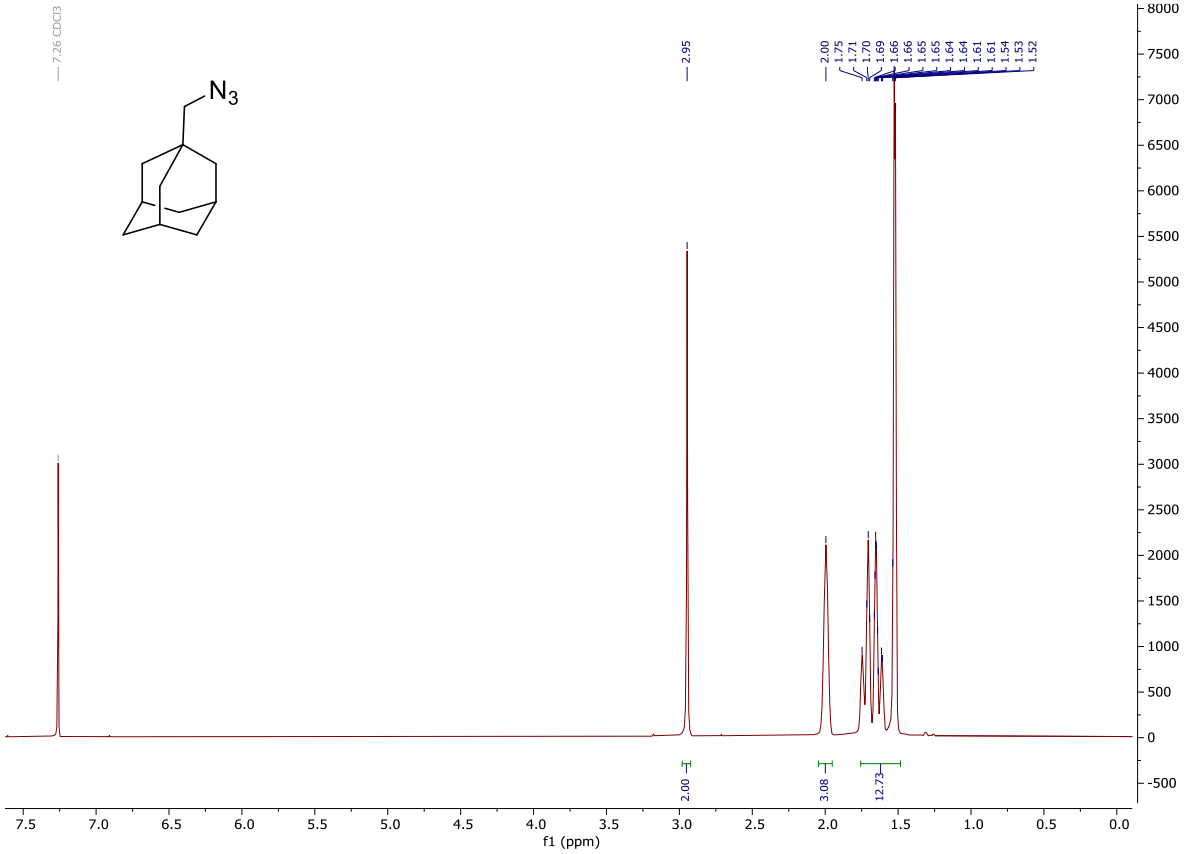

*Figure 211: ^{1}H NMR (300 MHz, $CDCl_3$) of 1-adamantylmethyl azide (**42**).*

Bis-propargyl-polyethyleneglycol$_5$ **44**

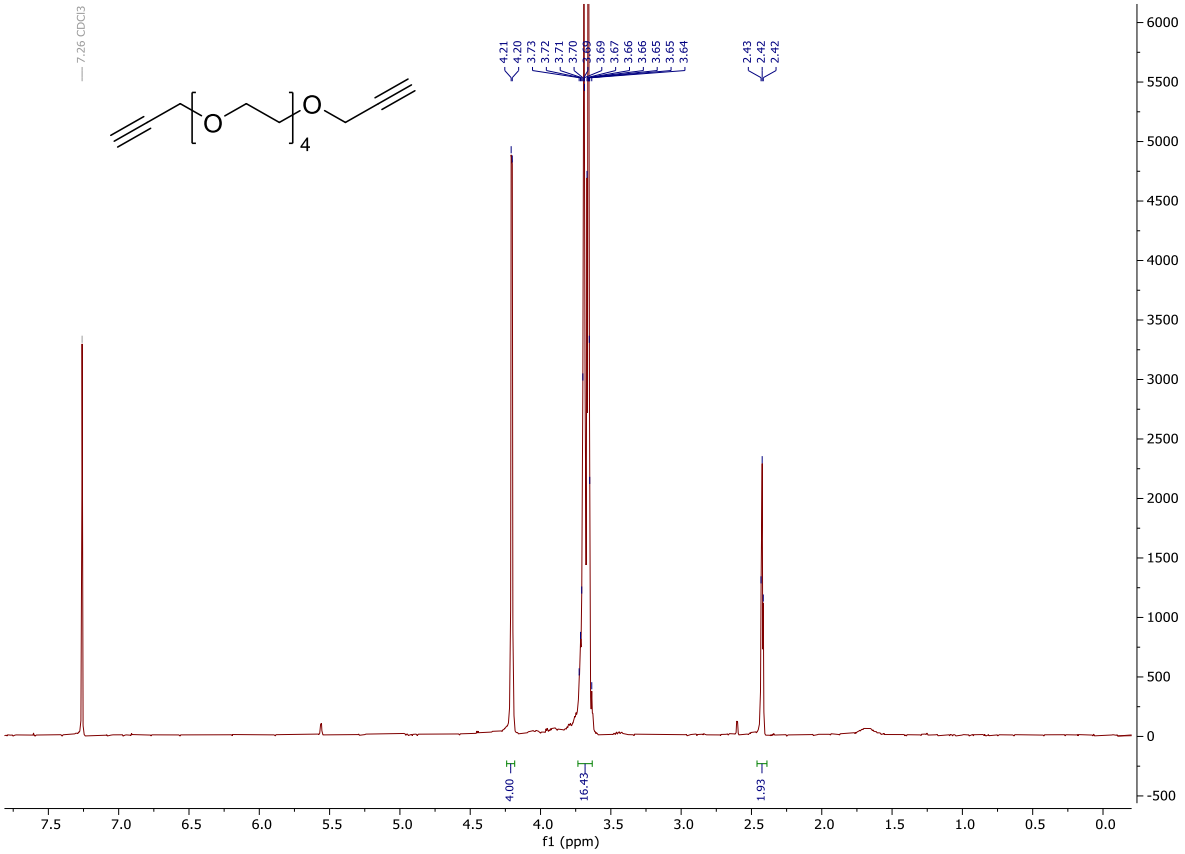

*Figure 212: ^{1}H NMR (300 MHz, $CDCl_3$) of bis-propargyl-polyethyleneglycol$_5$ **44**.*

Triazole **45**

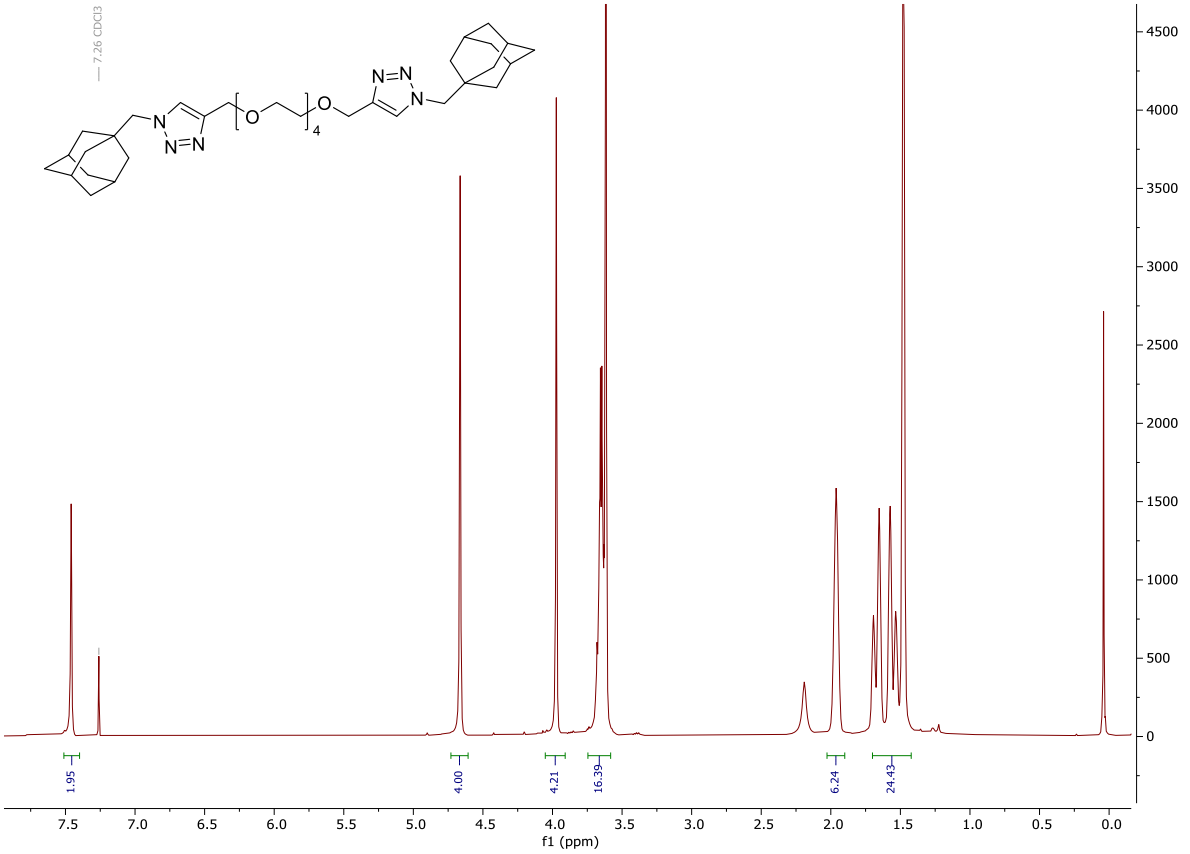

*Figure 213: ^{1}H NMR (300 MHz, $CDCl_3$) of triazole **45**.*

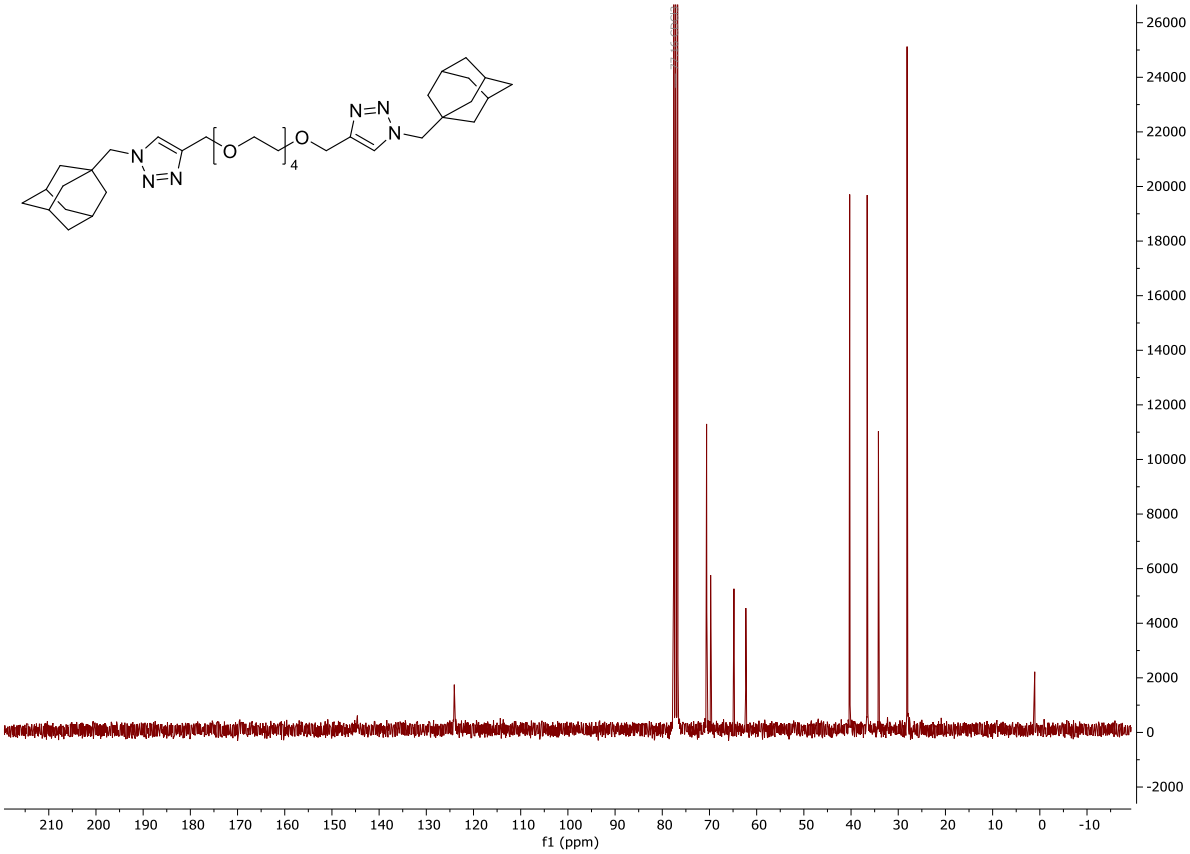

*Figure 214: $^{13}C\{^{1}H\}$ NMR (75 MHz, $CDCl_3$) of triazole **45**.*

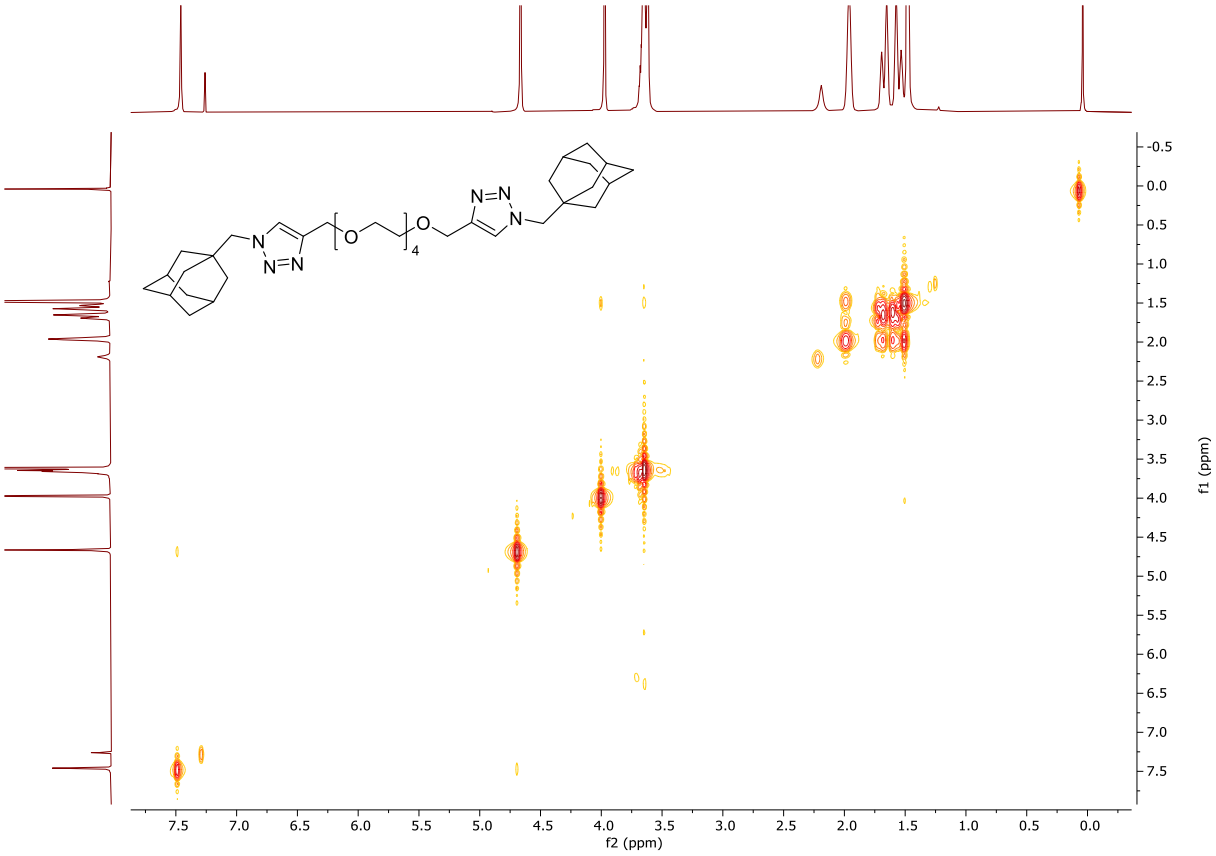

*Figure 215: ^{1}H-^{1}H COSY NMR (300 MHz, $CDCl_3$) of triazole **45**.*

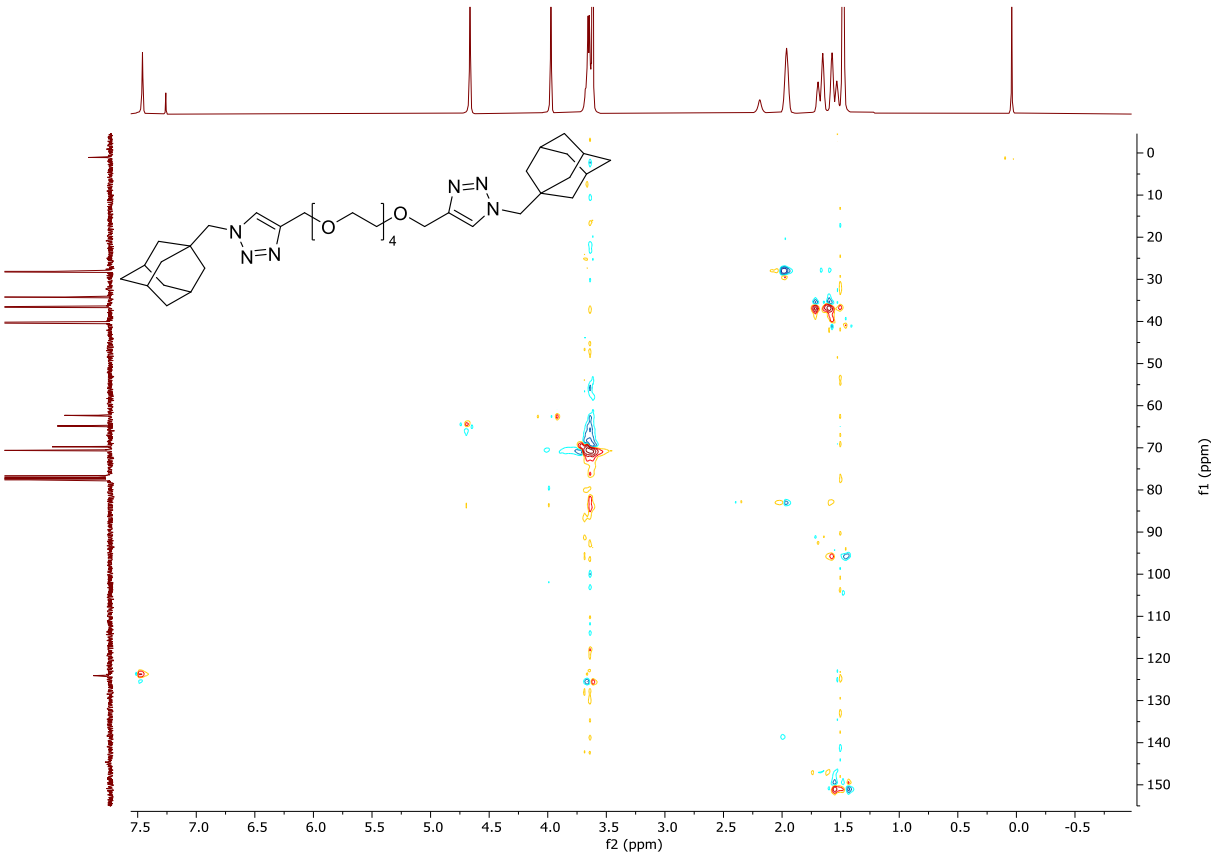

*Figure 216: ^{1}H-{^{13}C} HSQC NMR (300 MHz, $CDCl_3$) of triazole **45**.*

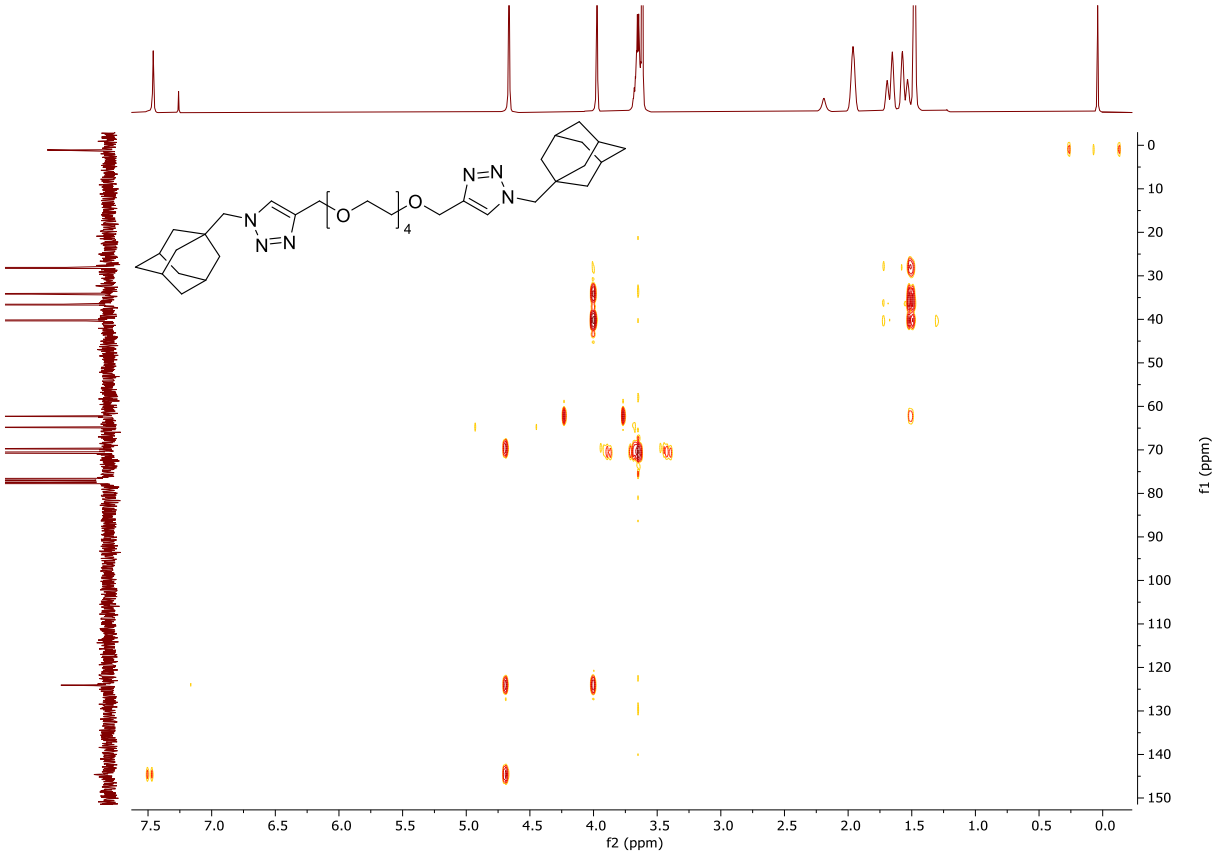

*Figure 217: ^{1}H-{^{13}C} HMBC NMR (300 MHz, $CDCl_3$) of triazole **45**.*

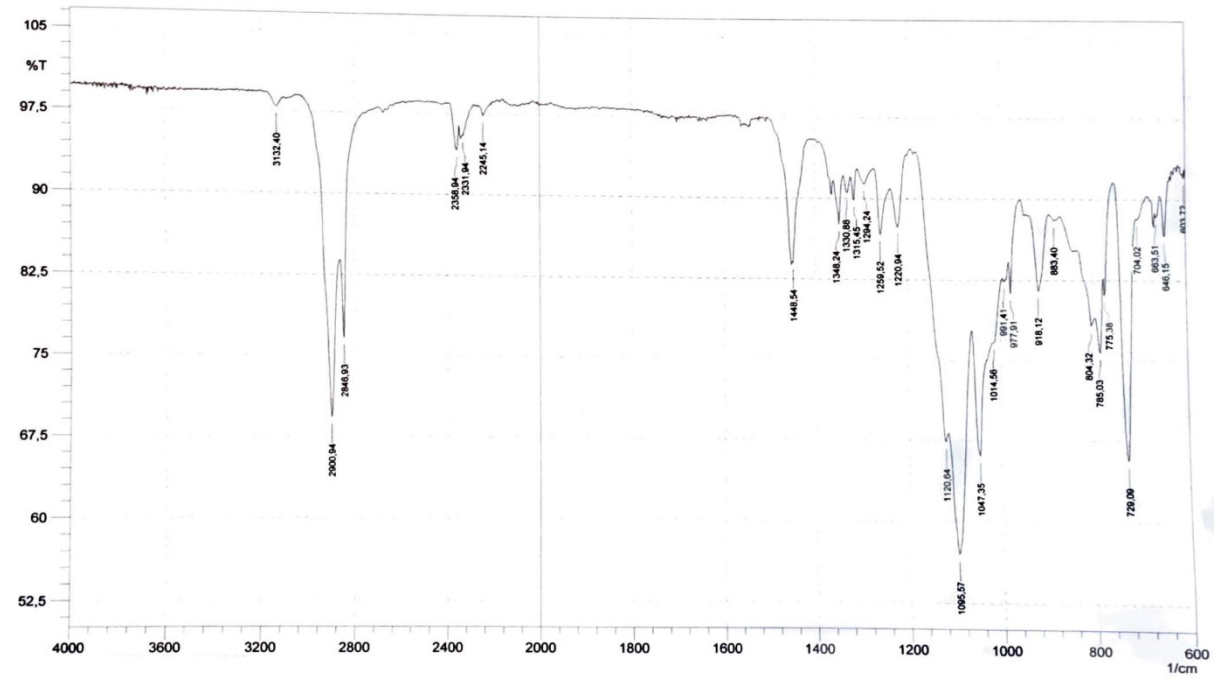

*Figure 218: IR spectrum of triazole **45**.*

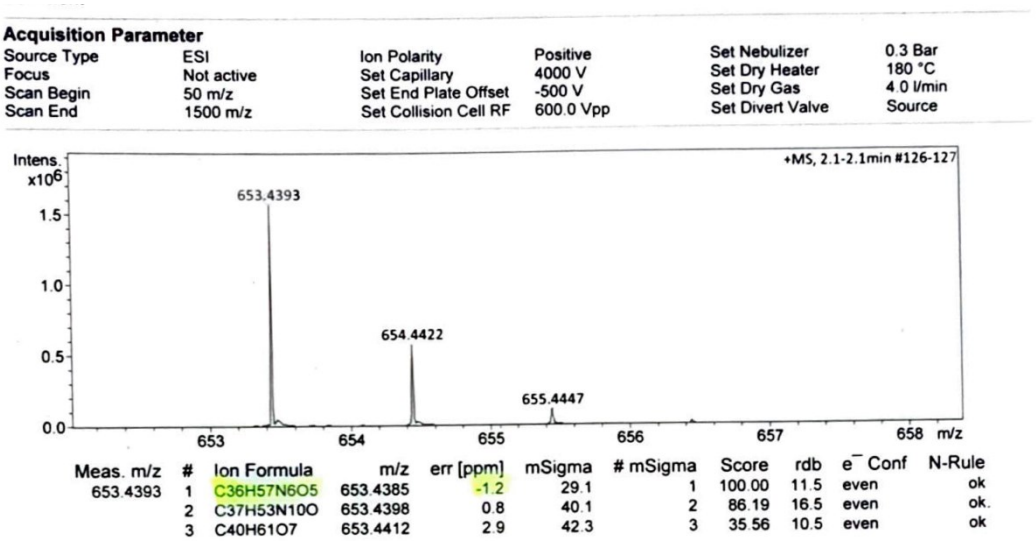

*Figure 219: HRMS (ESI) spectrum of triazole **45**.*

1,8 Bis-(adamantyl-1-methoxy)-octane (**51**)

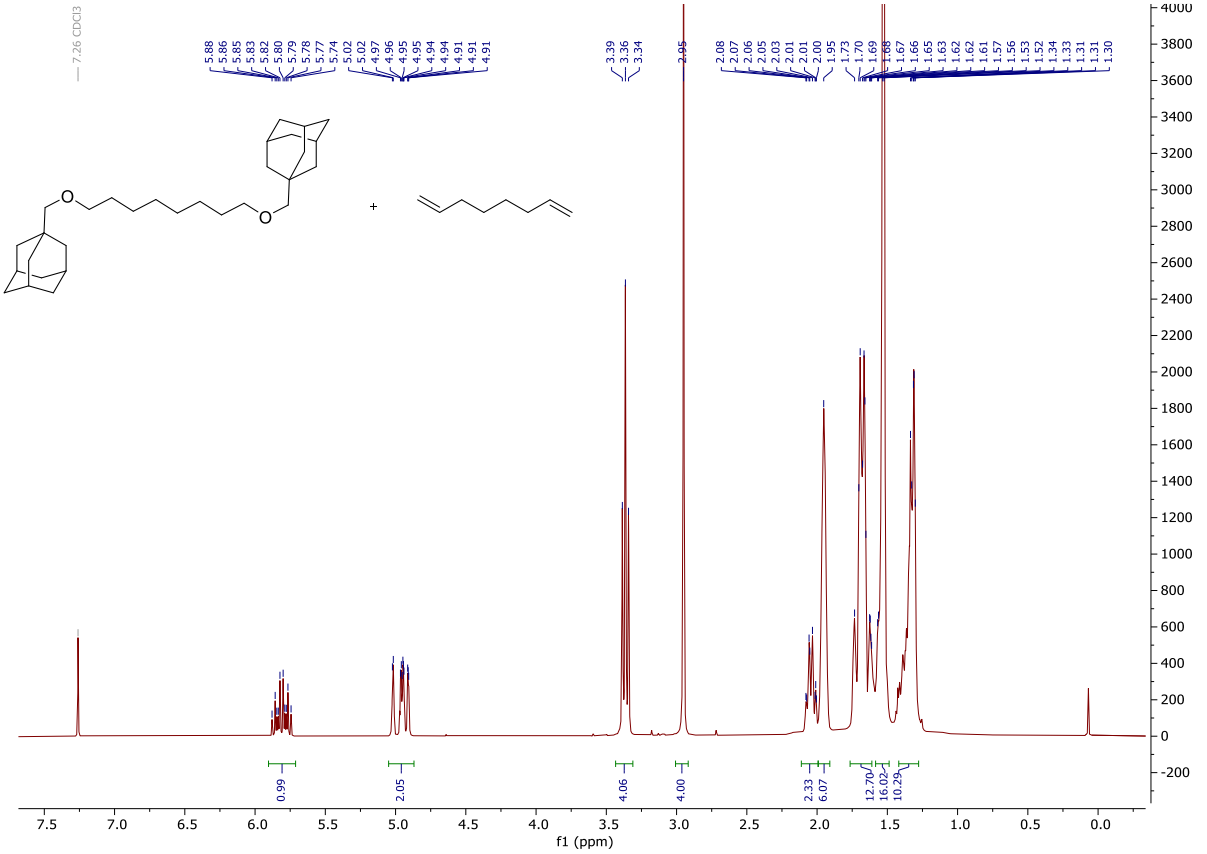

*Figure 220: ^{1}H NMR (300 MHz, $CDCl_3$) of 1,8 bis-(adamantyl-1-methoxy)-octane (**51**). Side product is 1,7-octadien.*

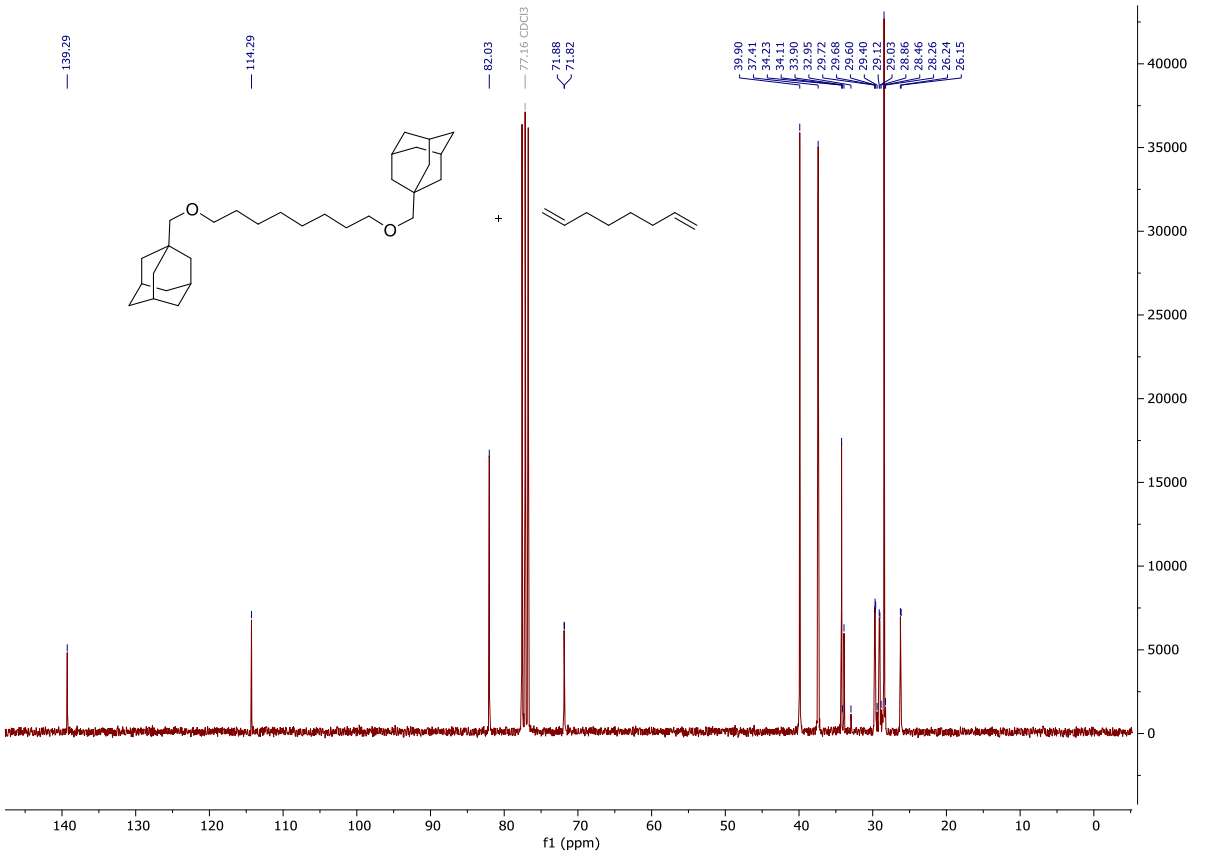

*Figure 221: $^{13}C\{^{1}H\}$ NMR (75 MHz, $CDCl_3$) of 1,8 bis-(adamantyl-1-methoxy)-octane (**51**).*

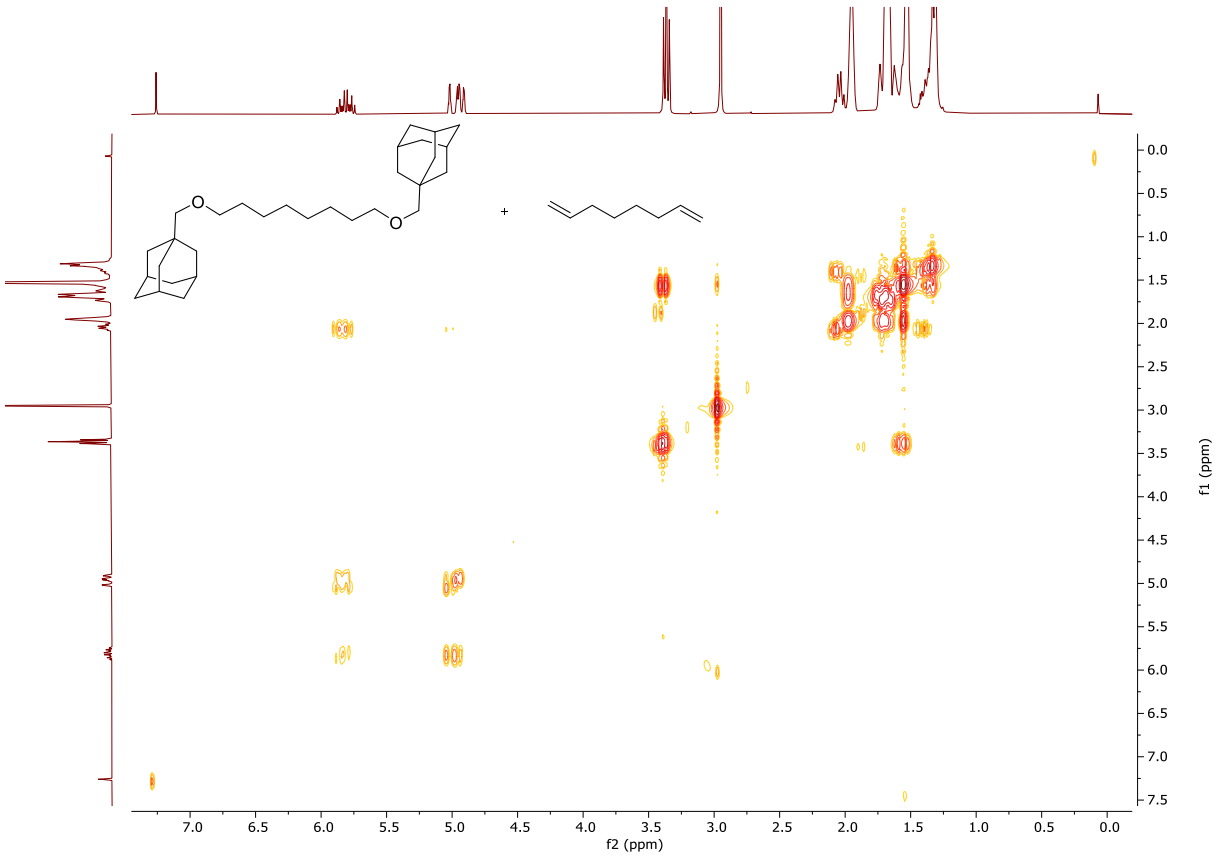

*Figure 222: ^{1}H-^{1}H COSY NMR (300 MHz, $CDCl_3$) of 1,8 bis-(adamantyl-1-methoxy)-octane (**51**).*

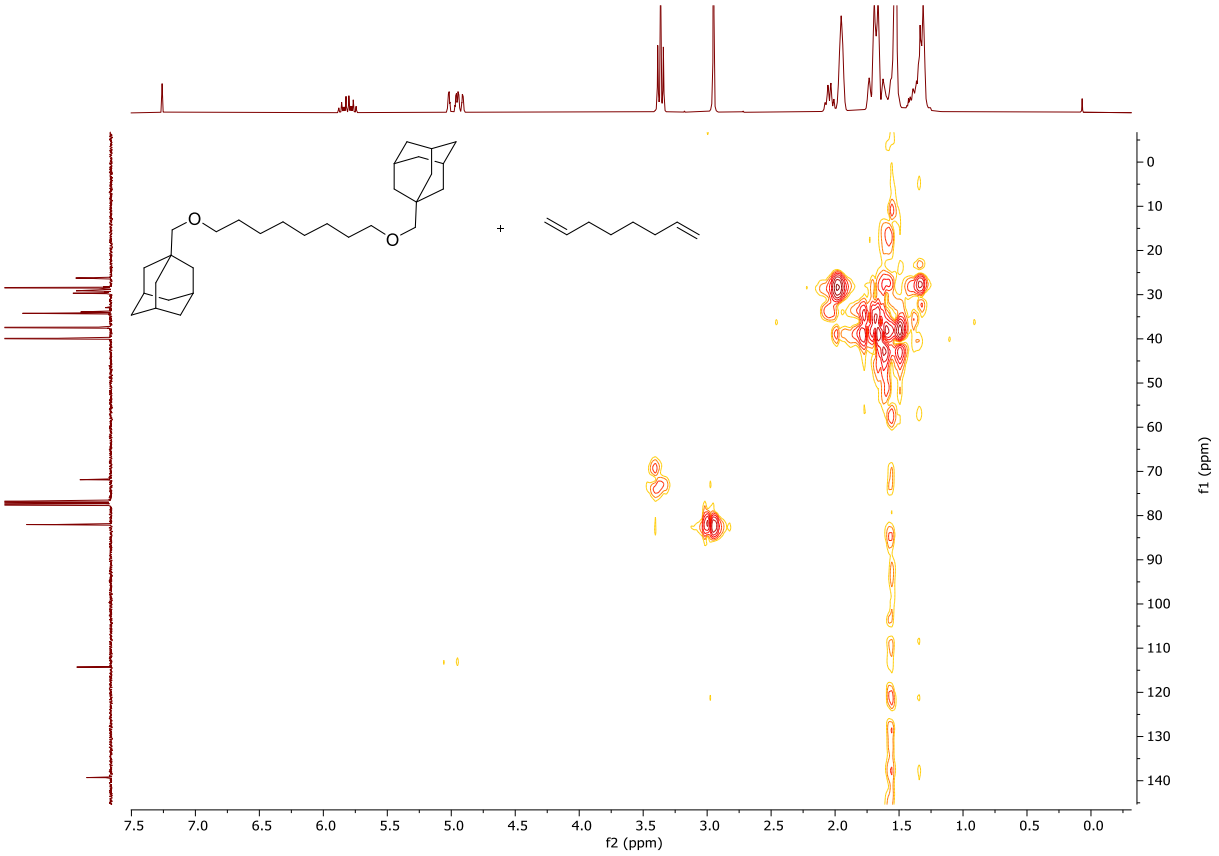

*Figure 223: ^{1}H-{^{13}C} HSQC NMR (300 MHz, $CDCl_3$) of 1,8 bis-(adamantyl-1-methoxy)-octane (**51**).*

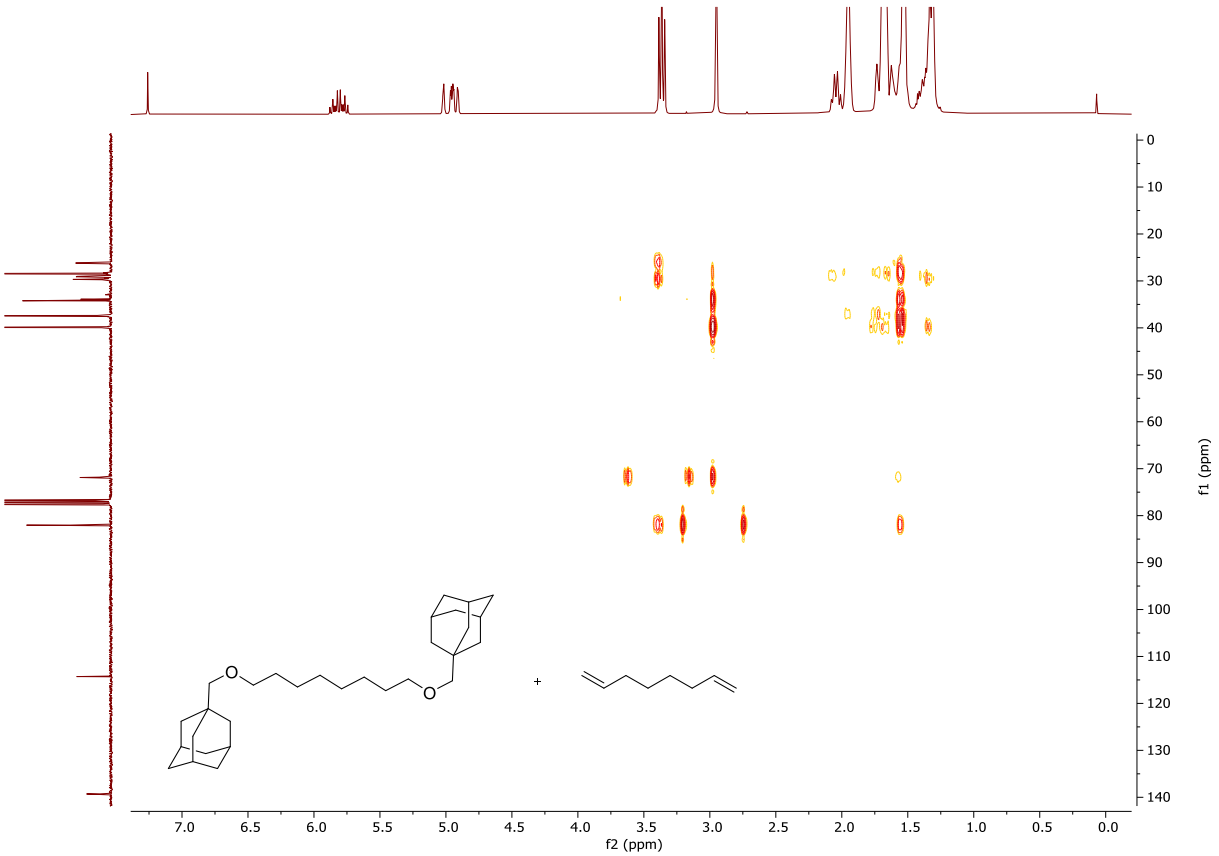

*Figure 224: ^{1}H-{^{13}C} HMBC NMR (300 MHz, $CDCl_3$) of 1,8 bis-(adamantyl-1-methoxy)-octane (**51**).*

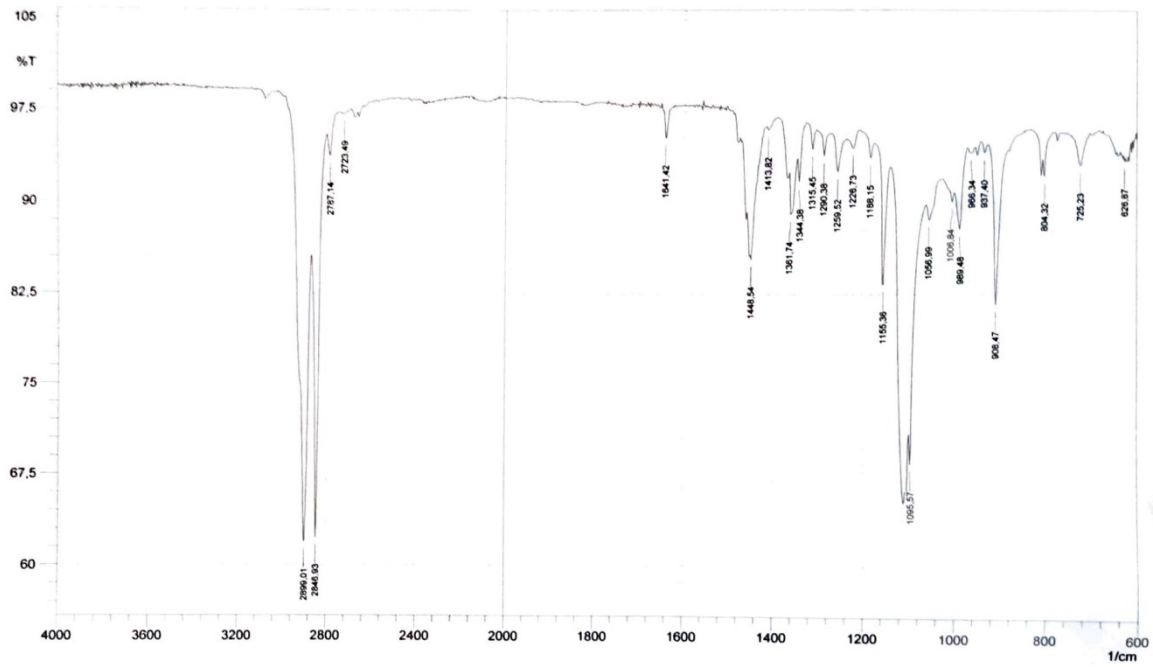

*Figure 225: IR spectrum of 1,8 bis-(adamantyl-1-methoxy)-octane (**51**).*

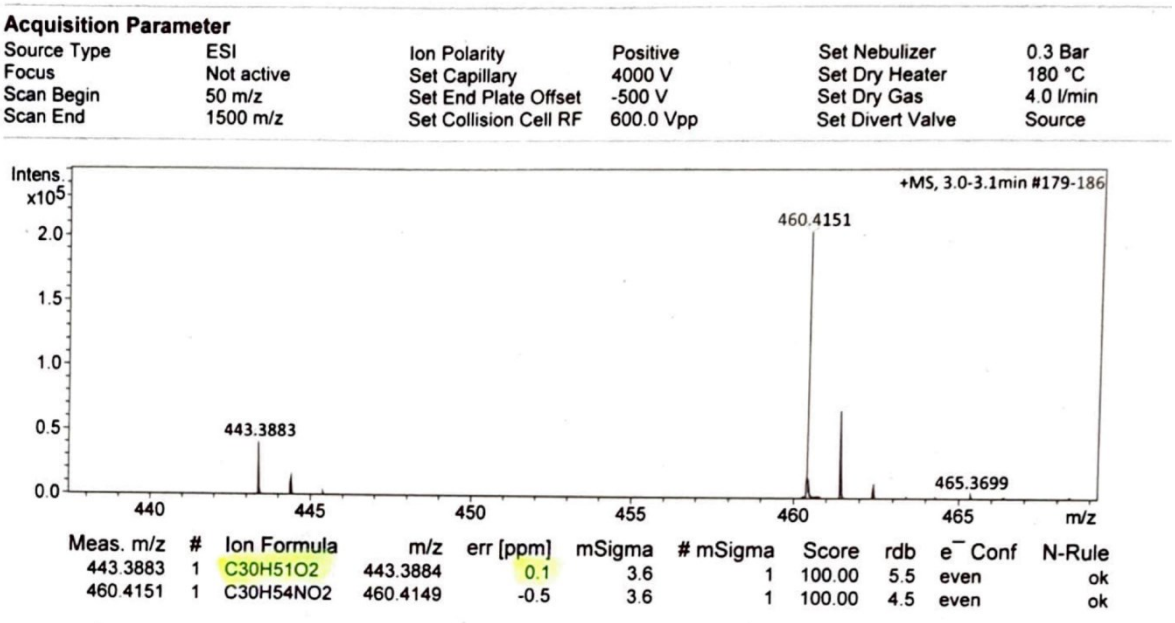

*Figure 226: HRMS (ESI) spectrum of 1,8 bis-(adamantyl-1-methoxy)-octane (**51**).*

Synthesis of HG_1 and its precursors

Poly[oxy(ethane-1,2-diyl)]bis(oxy)bis(methylene)bis(4-methyl-2,2'-bipyridine) (**54**)

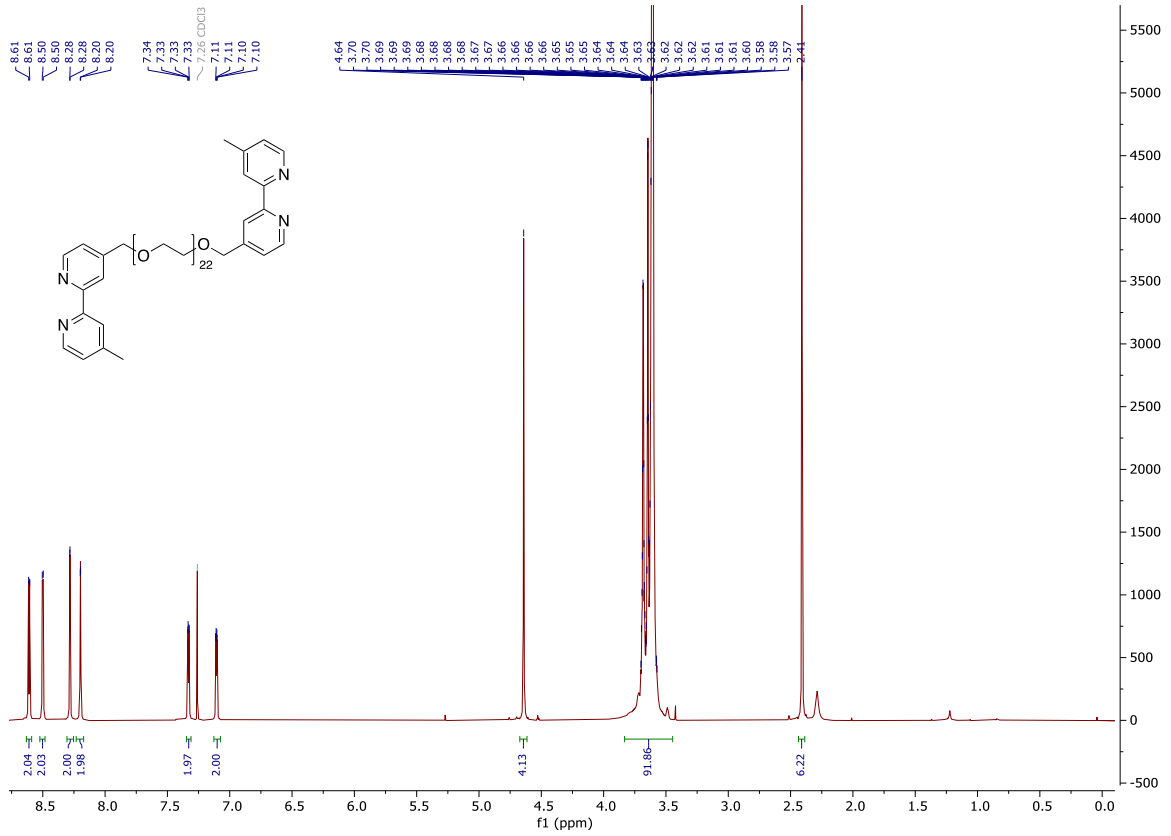

*Figure 227: ^{1}H NMR (600 MHz, $CDCl_3$) of poly[oxy(ethane-1,2-diyl)]bis(oxy)bis(methylene)bis(4-methyl-2,2'-bipyridine) (**54**).*

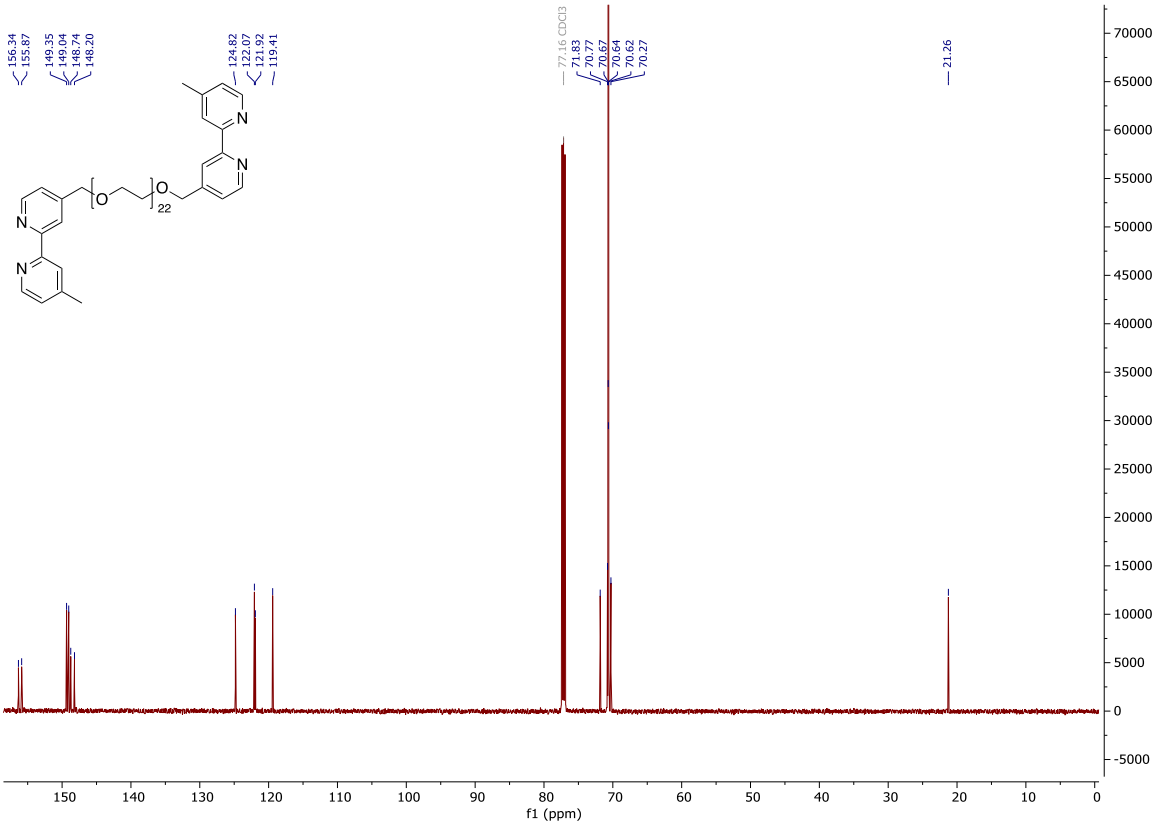

*Figure 228: $^{13}C\{^{1}H\}$ NMR (151 MHz, $CDCl_3$) of poly[oxy(ethane-1,2-diyl)]bis(oxy)bis(methylene)bis(4-methyl-2,2'-bipyridine) (**54**).*

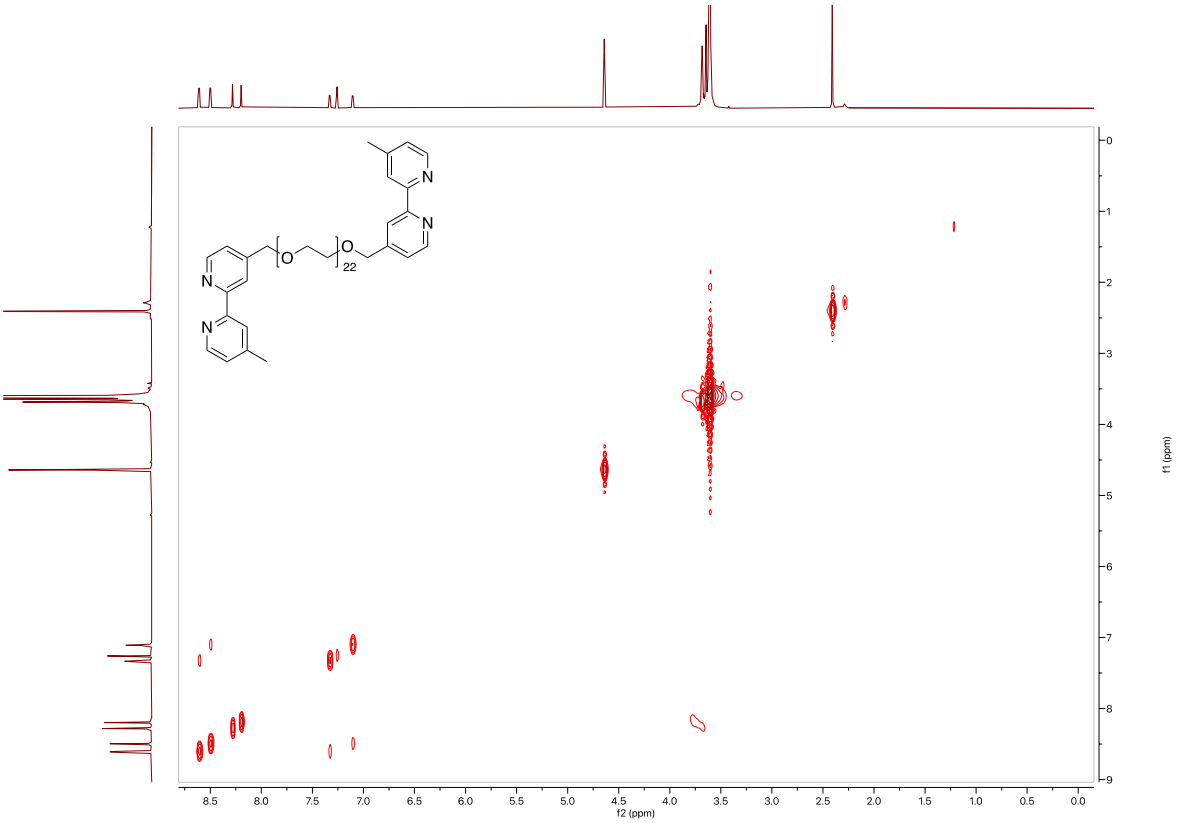

*Figure 229: ^{1}H-^{1}H COSY NMR (600 MHz, $CDCl_3$) of poly[oxy(ethane-1,2-diyl)]bis(oxy)bis(methylene)bis(4-methyl-2,2'-bipyridine) (**54**).*

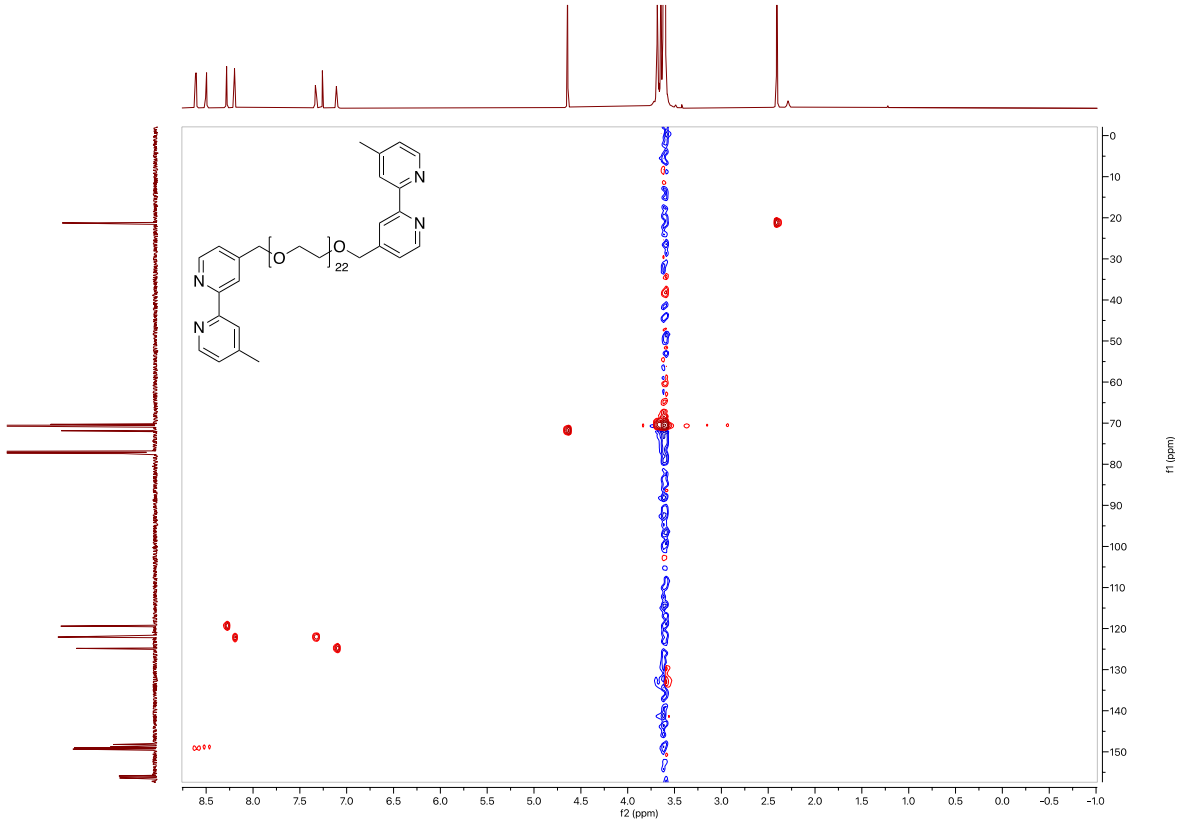

*Figure 230: ^{1}H-{^{13}C} HSQC NMR (600 MHz, $CDCl_3$) of poly[oxy(ethane-1,2-diyl)]bis(oxy)bis(methylene)bis(4-methyl-2,2'-bipyridine) (**54**).*

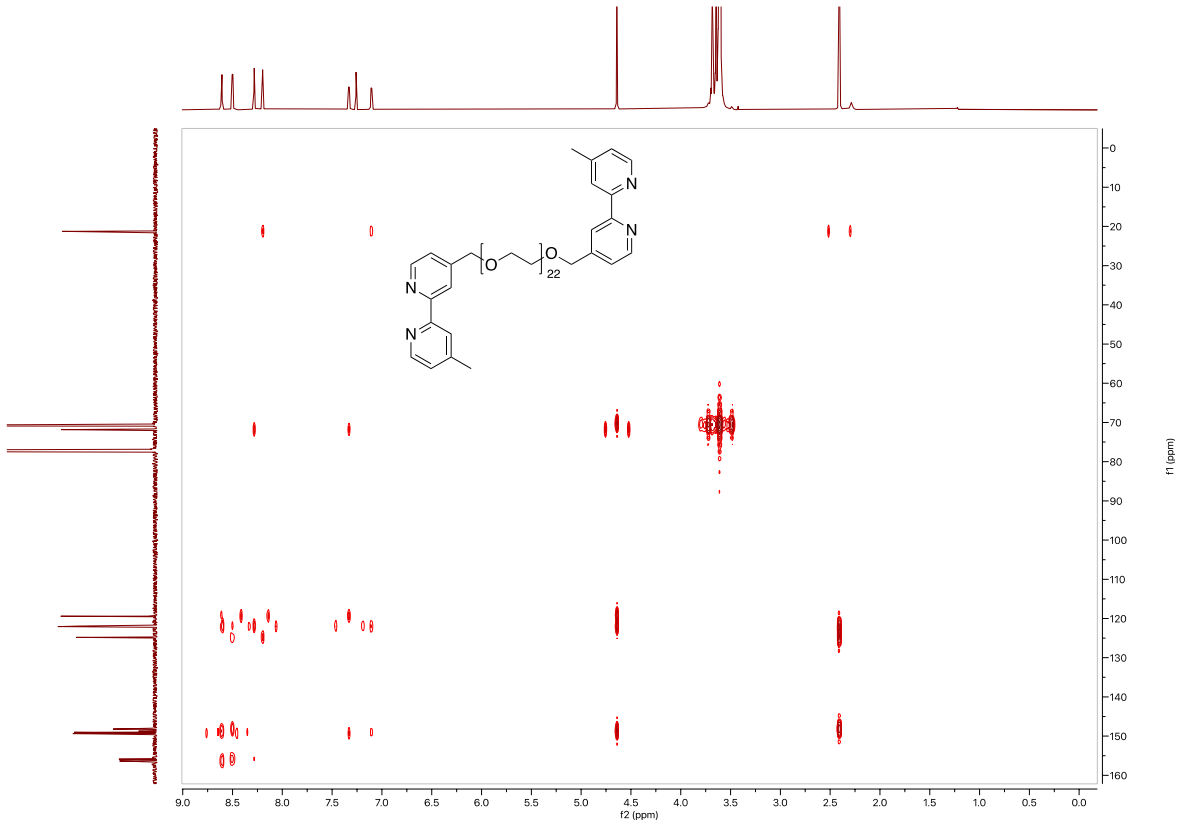

*Figure 231: ^{1}H-{^{13}C} HMBC NMR (600 MHz, $CDCl_3$) of poly[oxy(ethane-1,2-diyl)]bis(oxy)bis(methylene)bis(4-methyl-2,2'-bipyridine) (**54**).*

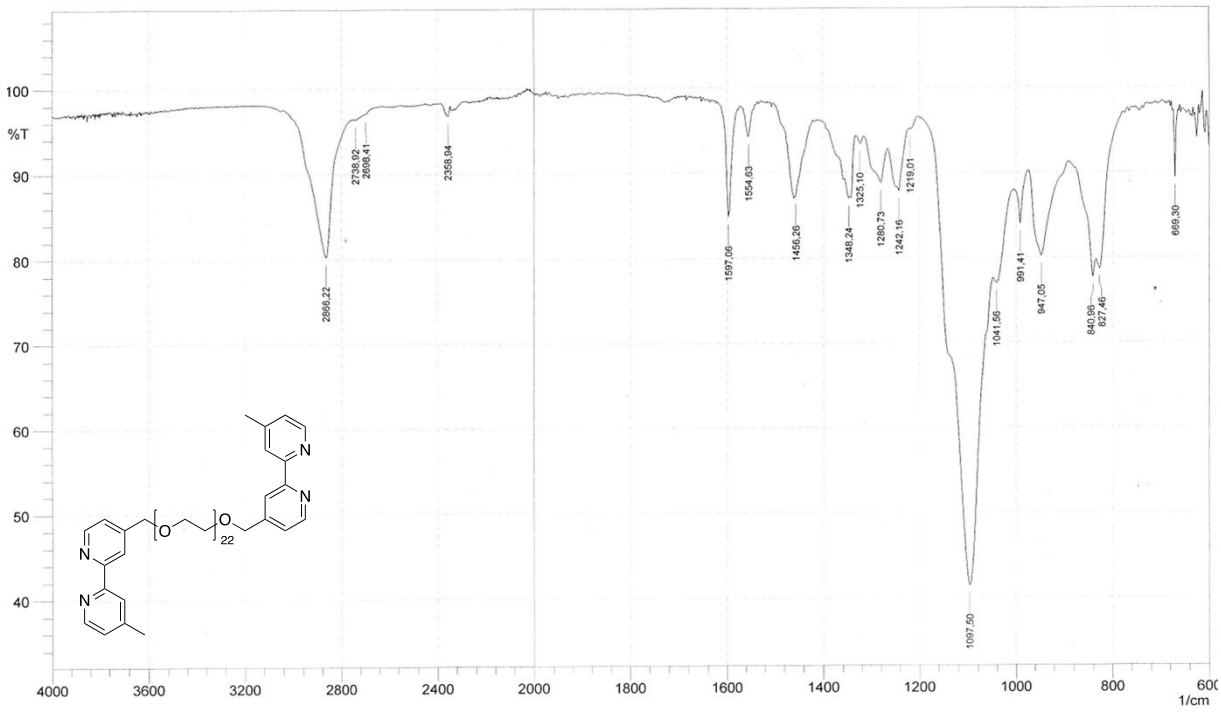

*Figure 232: IR spectrum of poly[oxy(ethane-1,2-diyl)]bis(oxy)bis(methylene)bis(4-methyl-2,2'-bipyridine) (**54**).*

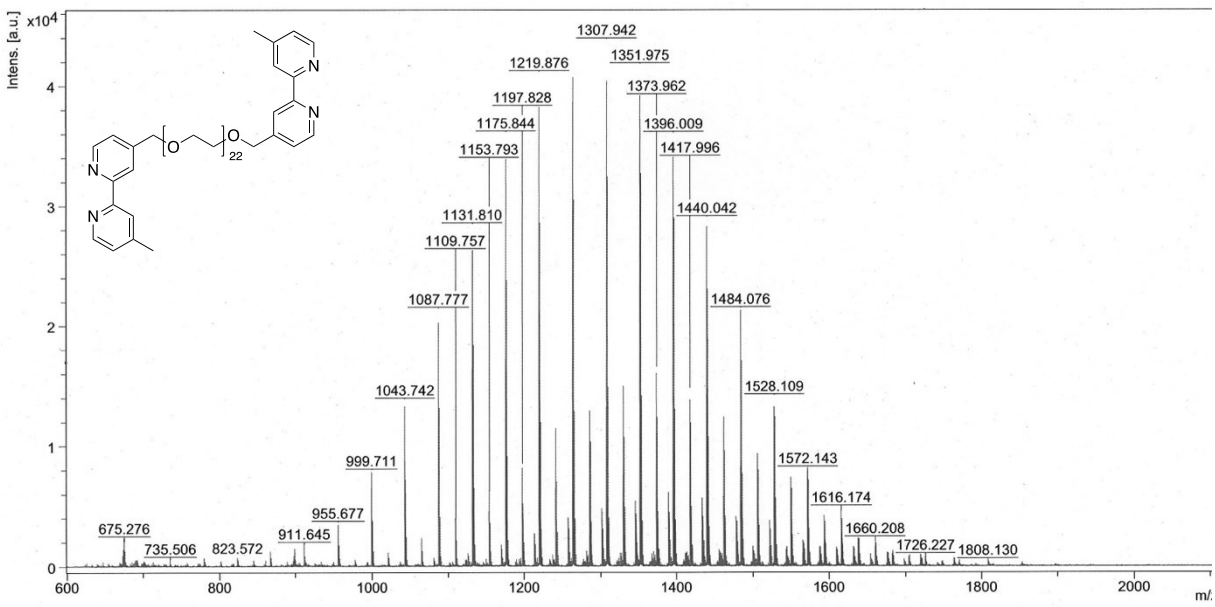

*Figure 233: MALDI spectrum of poly[oxy(ethane-1,2-diyl)]bis(oxy)bis(methylene)bis(4-methyl-2,2'-bipyridine) (**54**).*

{Poly[oxy(ethane-1,2-diyl)]bis(oxy)bis(methylene)bis(4-methyl-2,2'-bipyridine)}-bis(dichloropalladium(II)) (**58**)

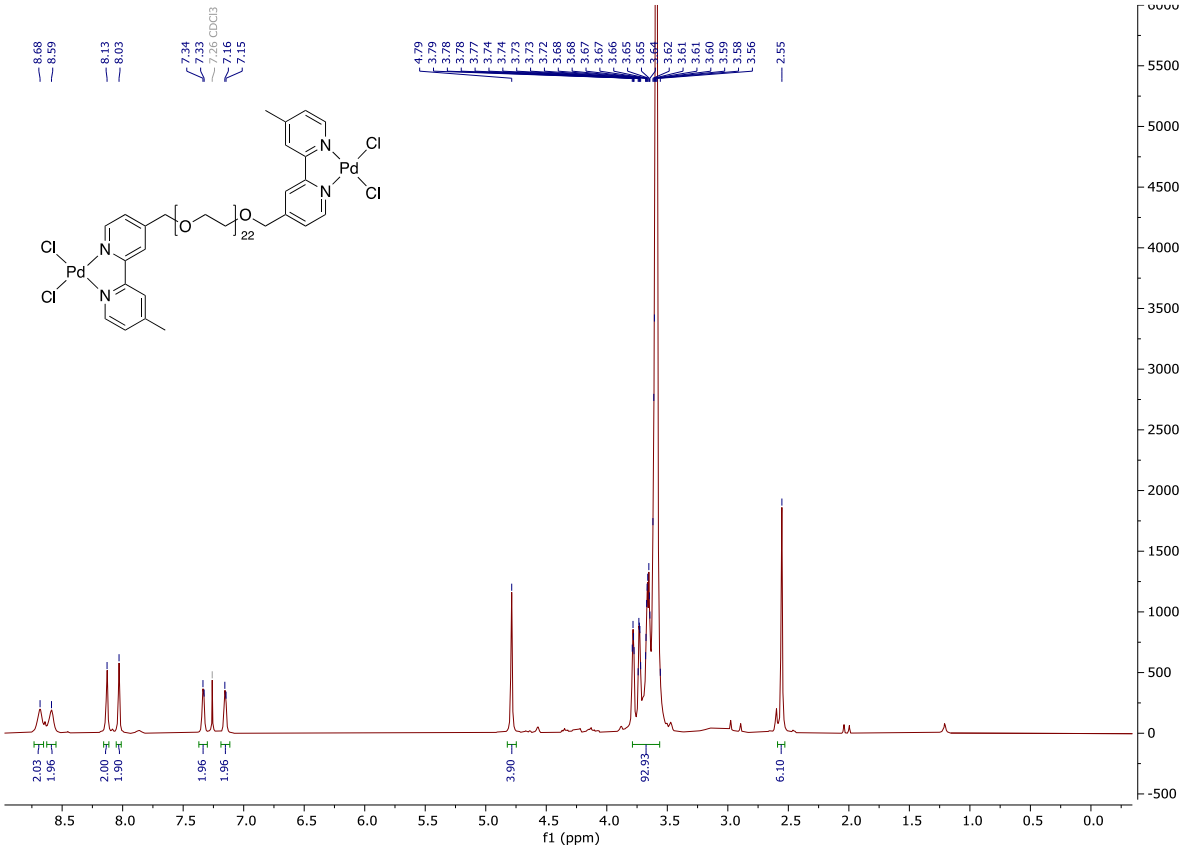

*Figure 234: ^{1}H NMR (600 MHz, $CDCl_3$) of {Poly[oxy(ethane-1,2-diyl)]bis(oxy)bis(methylene)bis(4-methyl-2,2'-bipyridine)}-bis(dichloropalladium(II)) (**58**).*

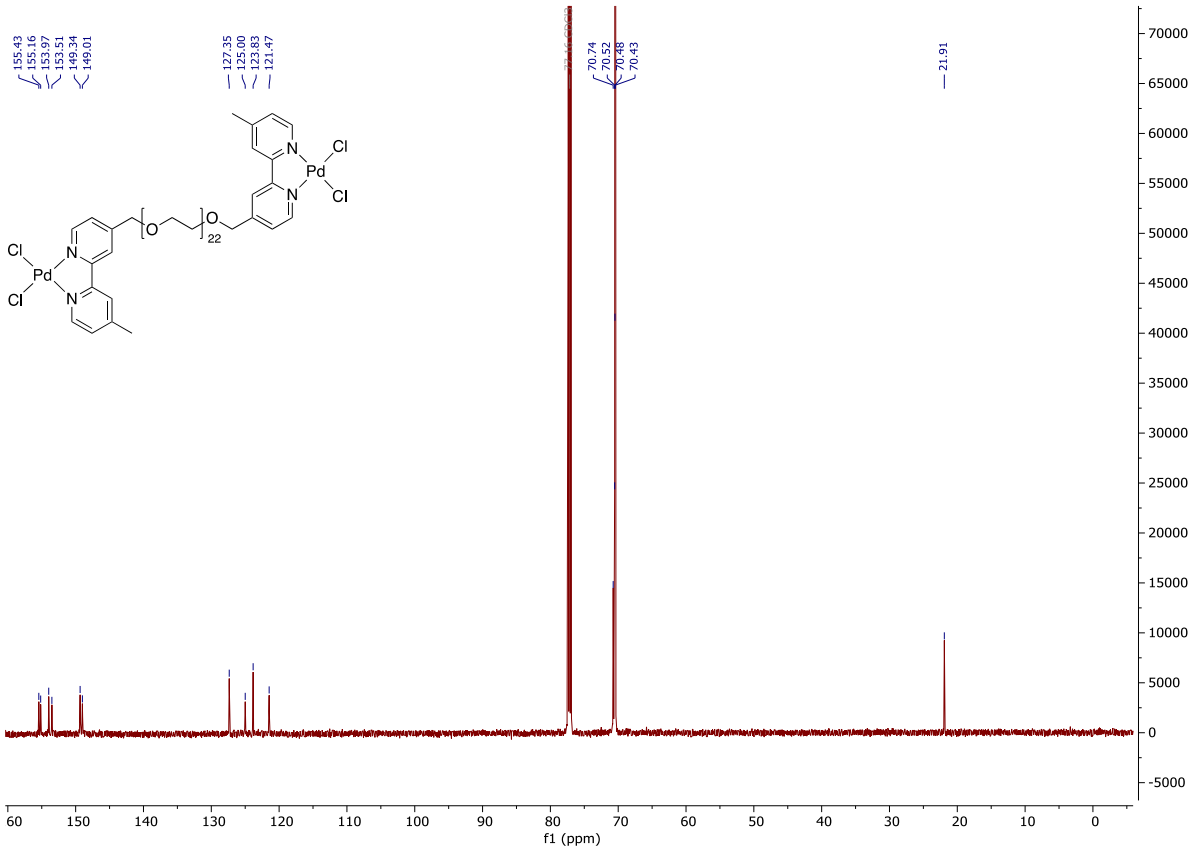

*Figure 235: $^{13}C\{^{1}H\}$ NMR (151 MHz, $CDCl_3$) of {Poly[oxy(ethane-1,2-diyl)]bis(oxy)bis(methylene)bis(4-methyl-2,2'-bipyridine)}-bis(dichloropalladium(II)) (**58**).*

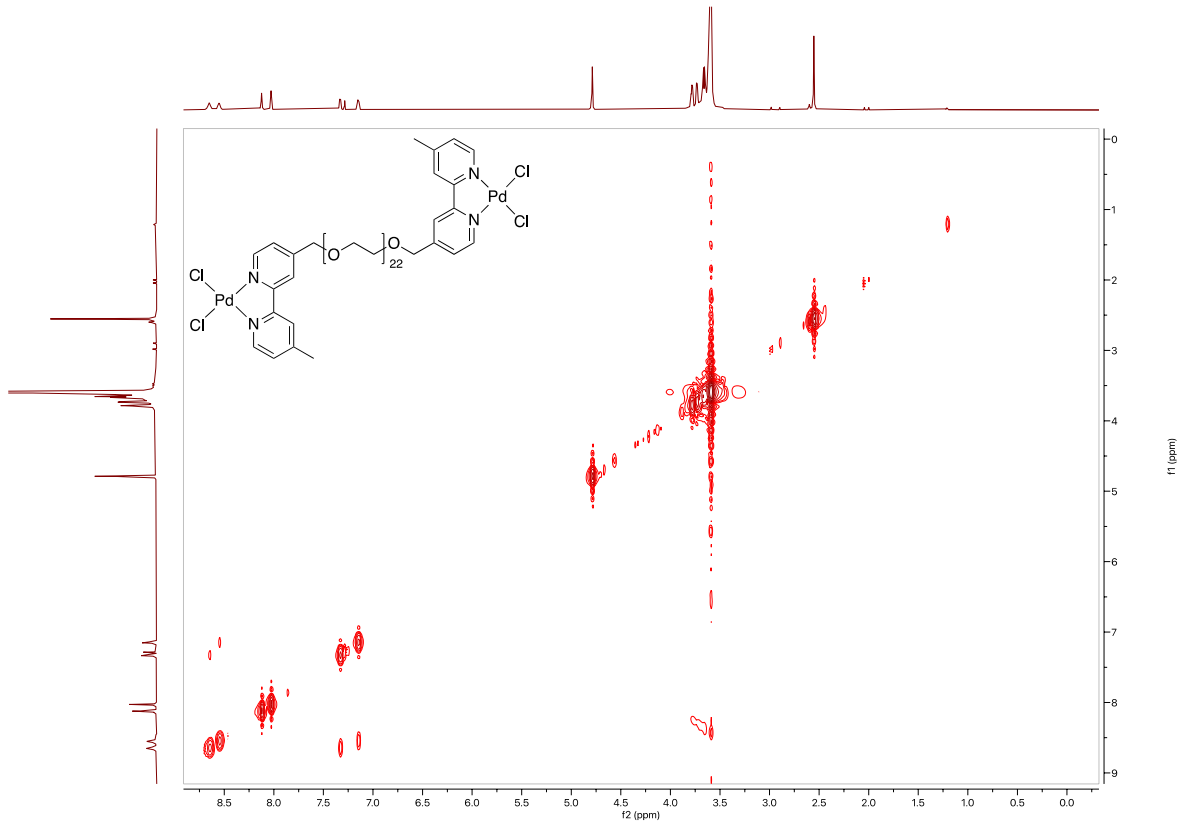

*Figure 236: ^{1}H-^{1}H COSY NMR (600 MHz, $CDCl_3$) of {Poly[oxy(ethane-1,2-diyl)]bis(oxy)bis(methylene)bis(4-methyl-2,2'-bipyridine)}-bis(dichloropalladium(II)) (**58**).*

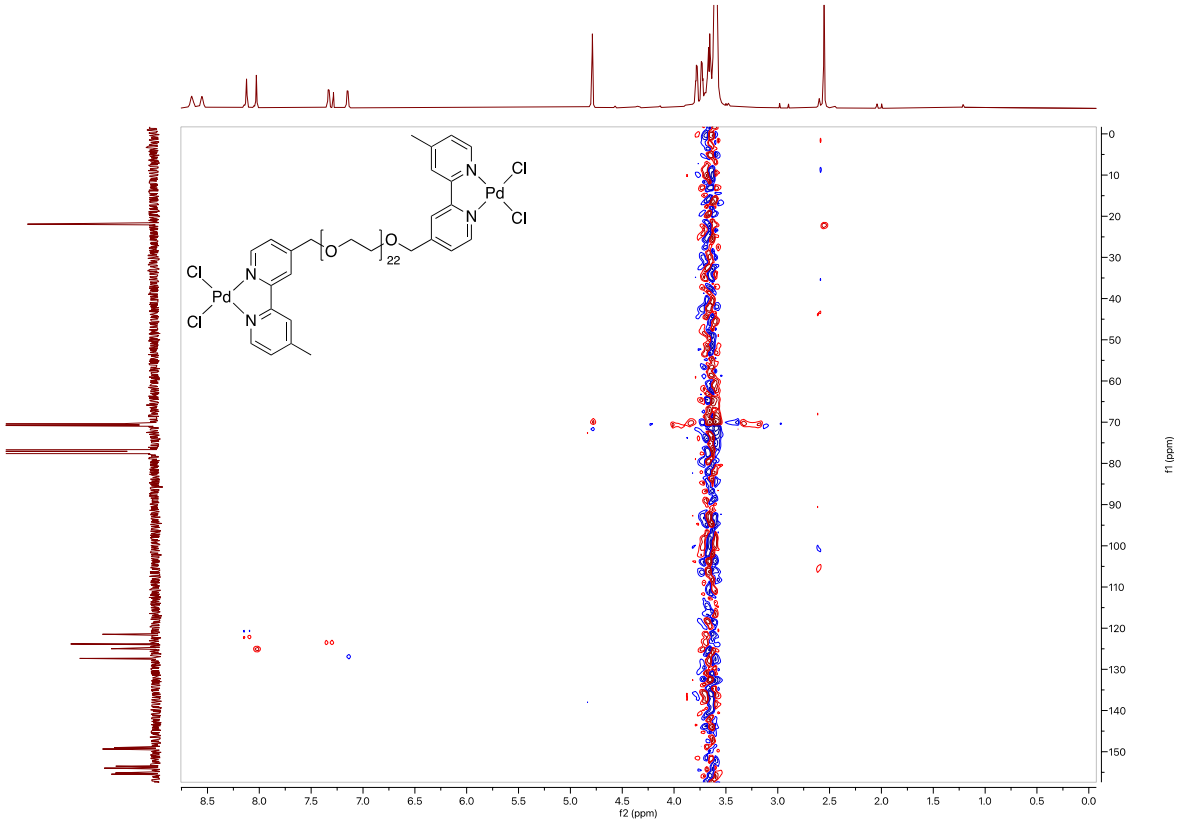

*Figure 237: ^{1}H-{^{13}C} HSQC NMR (600 MHz, $CDCl_3$) of {Poly[oxy(ethane-1,2-diyl)]bis(oxy)bis(methylene)bis(4-methyl-2,2'-bipyridine)}-bis(dichloropalladium(II)) (**58**).*

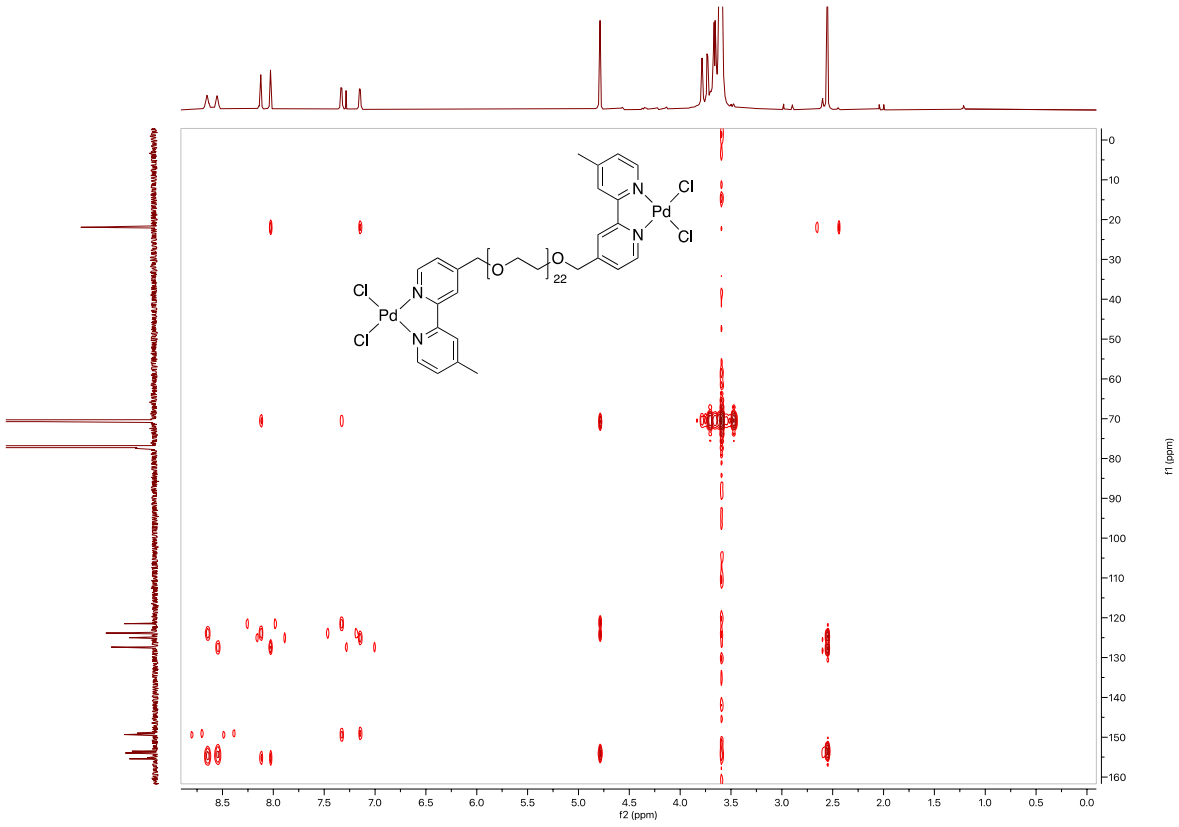

*Figure 238: ^{1}H-{^{13}C} HMBC NMR (600 MHz, $CDCl_3$) of {Poly[oxy(ethane-1,2-diyl)]bis(oxy)bis(methylene)bis(4-methyl-2,2'-bipyridine)}-bis(dichloropalladium(II)) (**58**).*

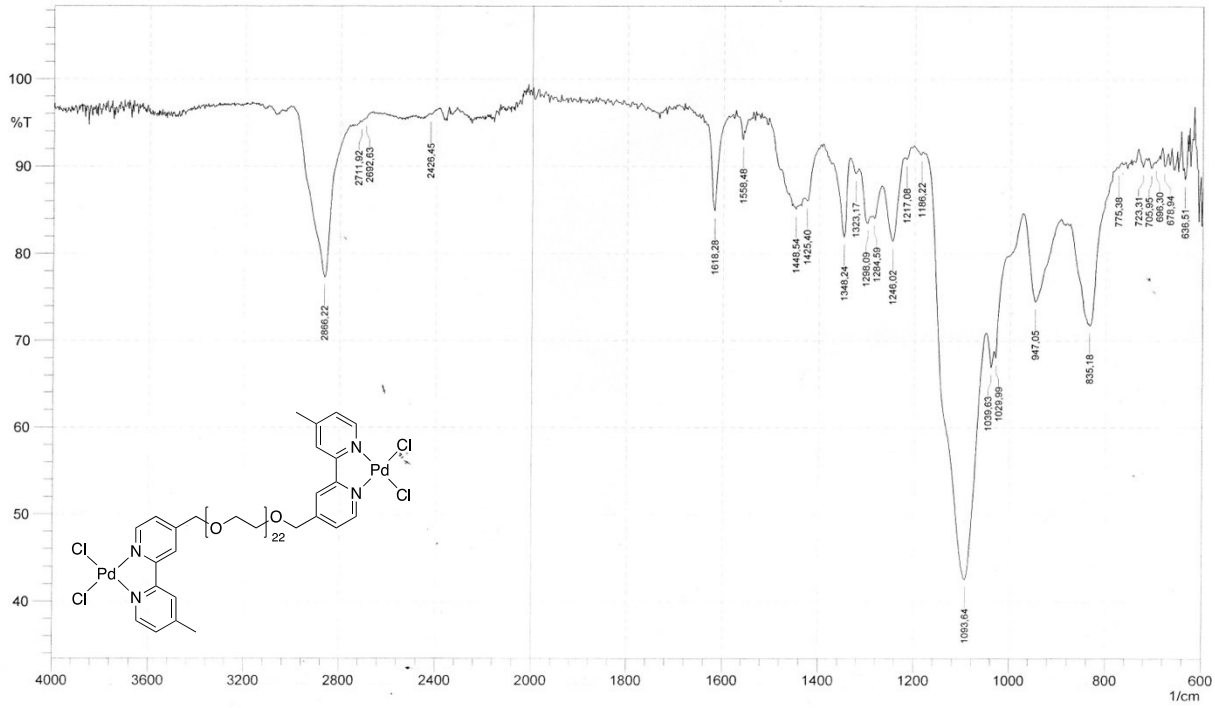

*Figure 239: IR spectrum of {Poly[oxy(ethane-1,2-diyl)]bis(oxy)bis(methylene)bis(4-methyl-2,2'-bipyridine)}-bis(dichloropalladium(II)) (**58**).*

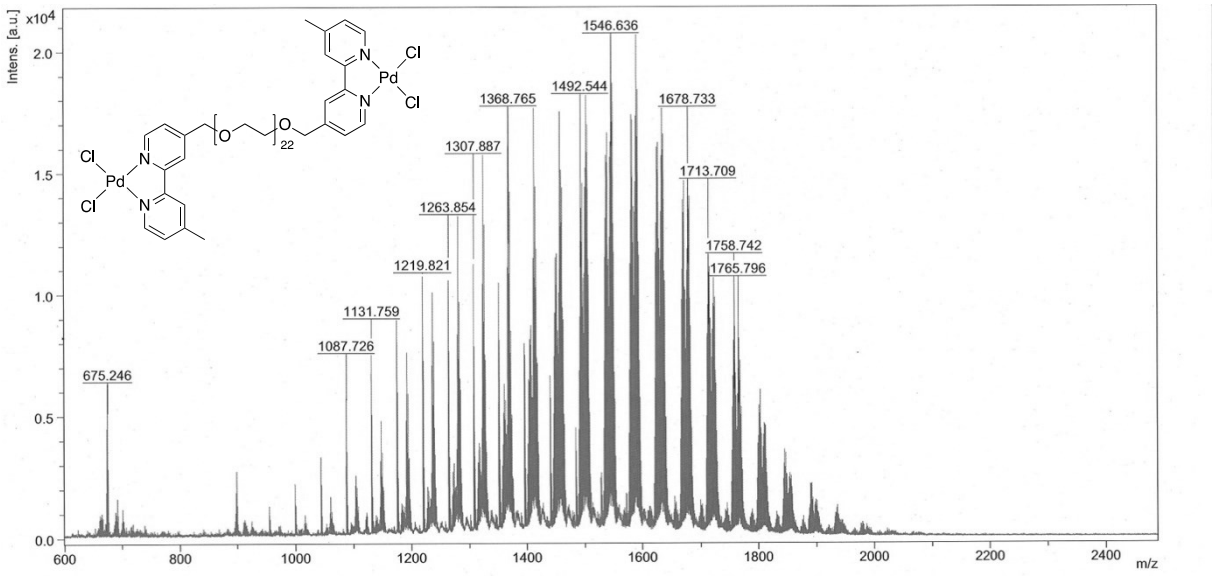

*Figure 240: MALDI spectrum of {Poly[oxy(ethane-1,2-diyl)]bis(oxy)bis(methylene)bis(4-methyl-2,2'-bipyridine)}-bis(dichloropalladium(II)) (**58**).*

{Poly[oxy(ethane-1,2-diyl)]bis(oxy)bis(methylene)bis(4-methyl-2,2'-bipyridine)}-bis(dinitratopalladium(II)) (**62**)

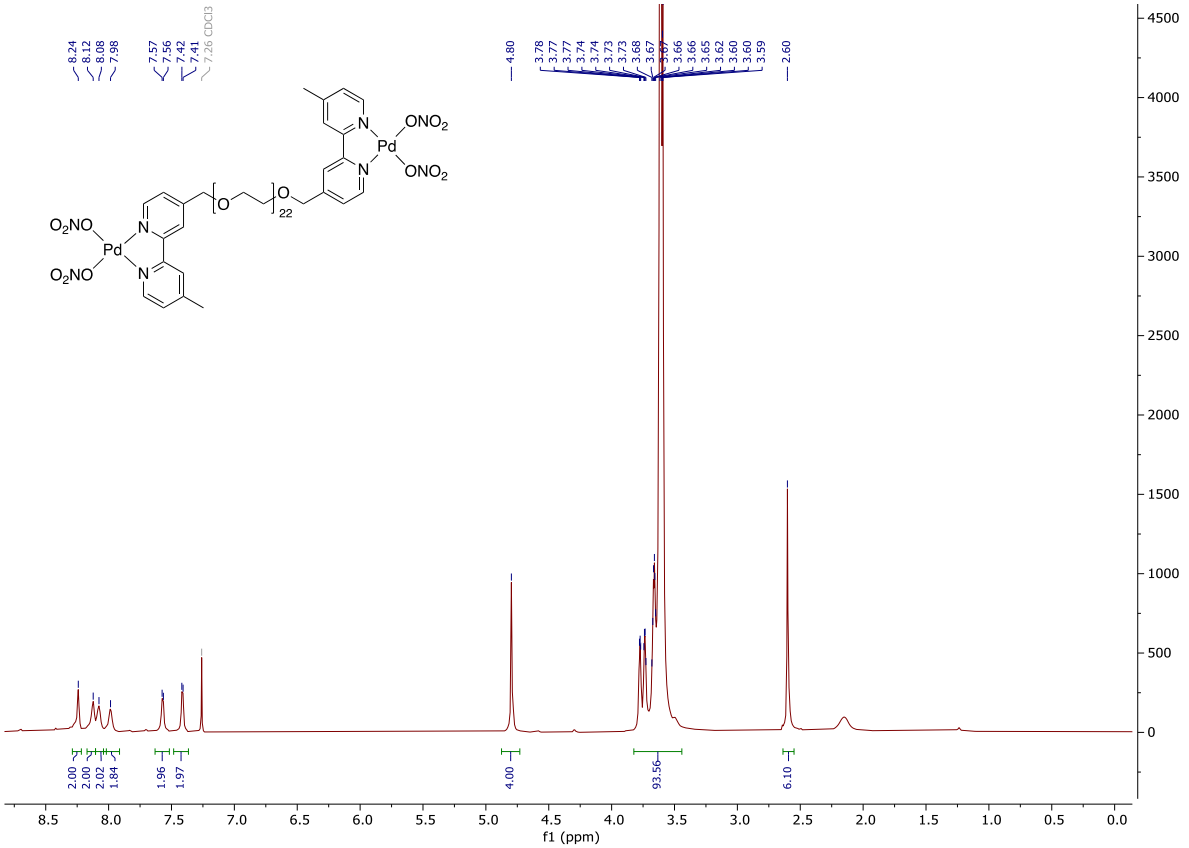

*Figure 241: ^{1}H NMR (600 MHz, $CDCl_3$) of {Poly[oxy(ethane-1,2-diyl)]bis(oxy)bis(methylene)bis(4-methyl-2,2'-bipyridine)}-bis(dinitratopalladium(II)) (**62**).*

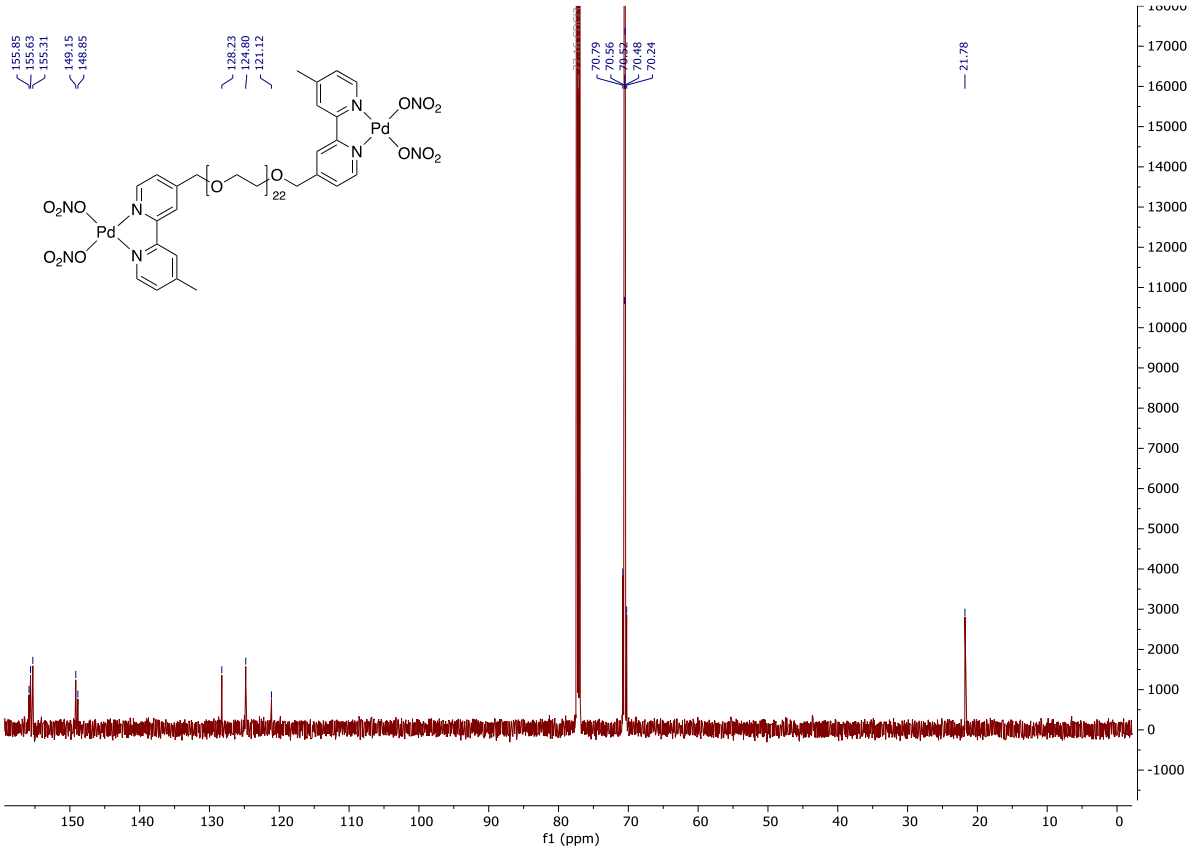

*Figure 242: $^{13}C\{^{1}H\}$ NMR (151 MHz, $CDCl_3$) of {Poly[oxy(ethane-1,2-diyl)]bis(oxy)bis(methylene)bis(4-methyl-2,2'-bipyridine)}-bis(dinitratopalladium(II)) (**62**).*

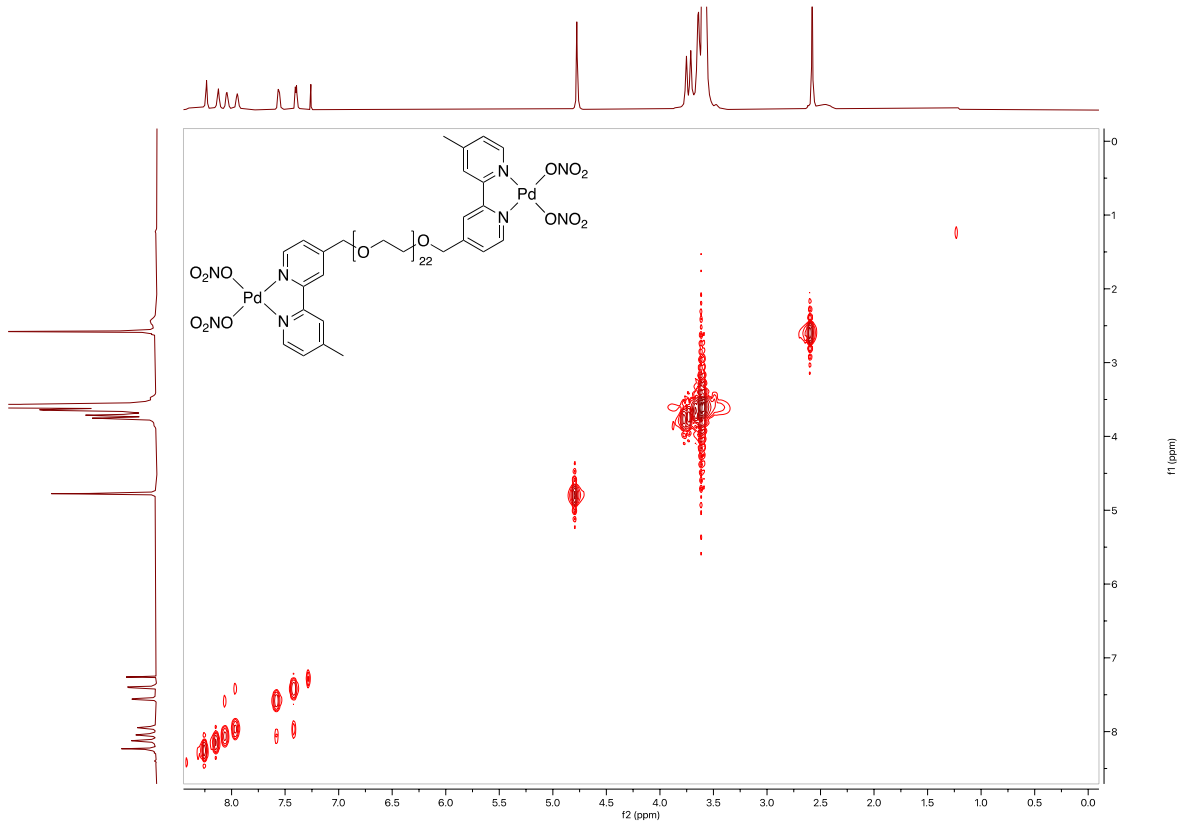

*Figure 243: ^{1}H-^{1}H COSY NMR (600 MHz, $CDCl_3$) of {Poly[oxy(ethane-1,2-diyl)]bis(oxy)bis(methylene)bis(4-methyl-2,2'-bipyridine)}-bis(dinitratopalladium(II)) (**62**).*

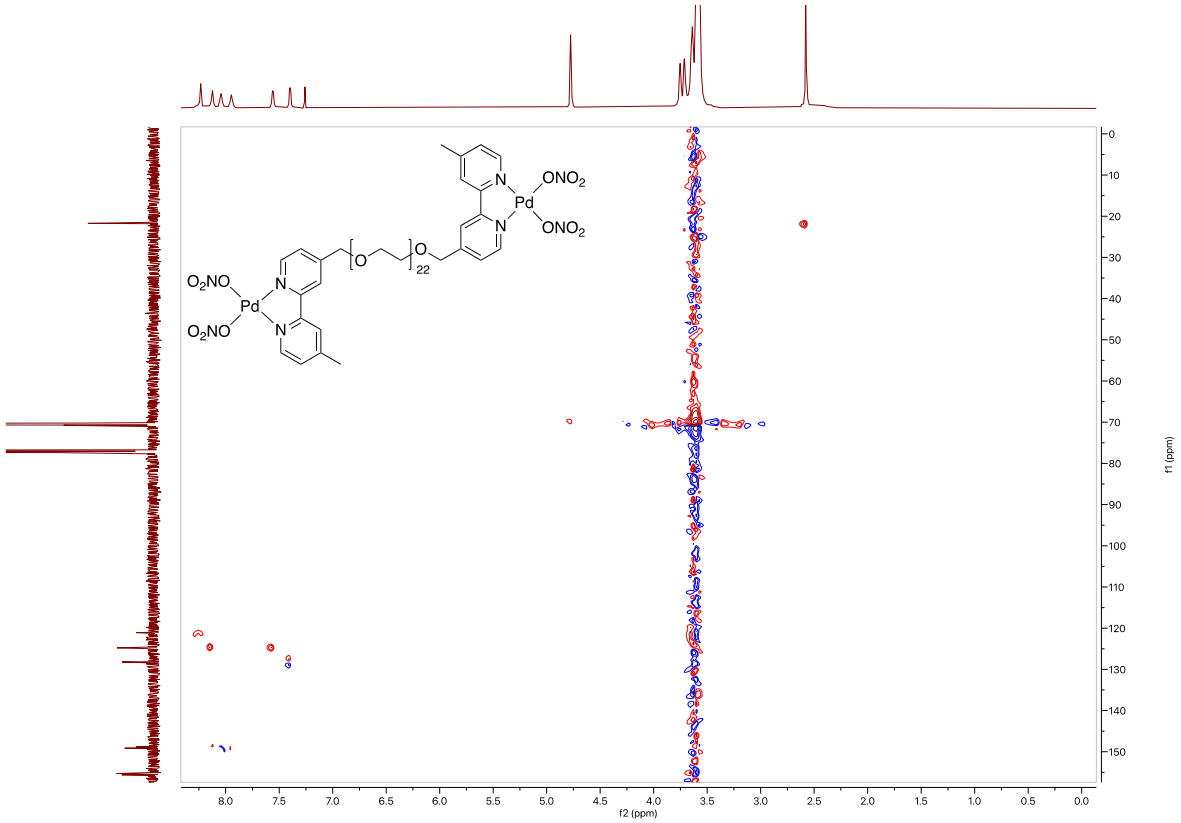

*Figure 244: ^{1}H-{^{13}C} HSQC NMR (600 MHz, $CDCl_3$) of {Poly[oxy(ethane-1,2-diyl)]bis(oxy)bis(methylene)bis(4-methyl-2,2'-bipyridine)}-bis(dinitratopalladium(II)) (**62**).*

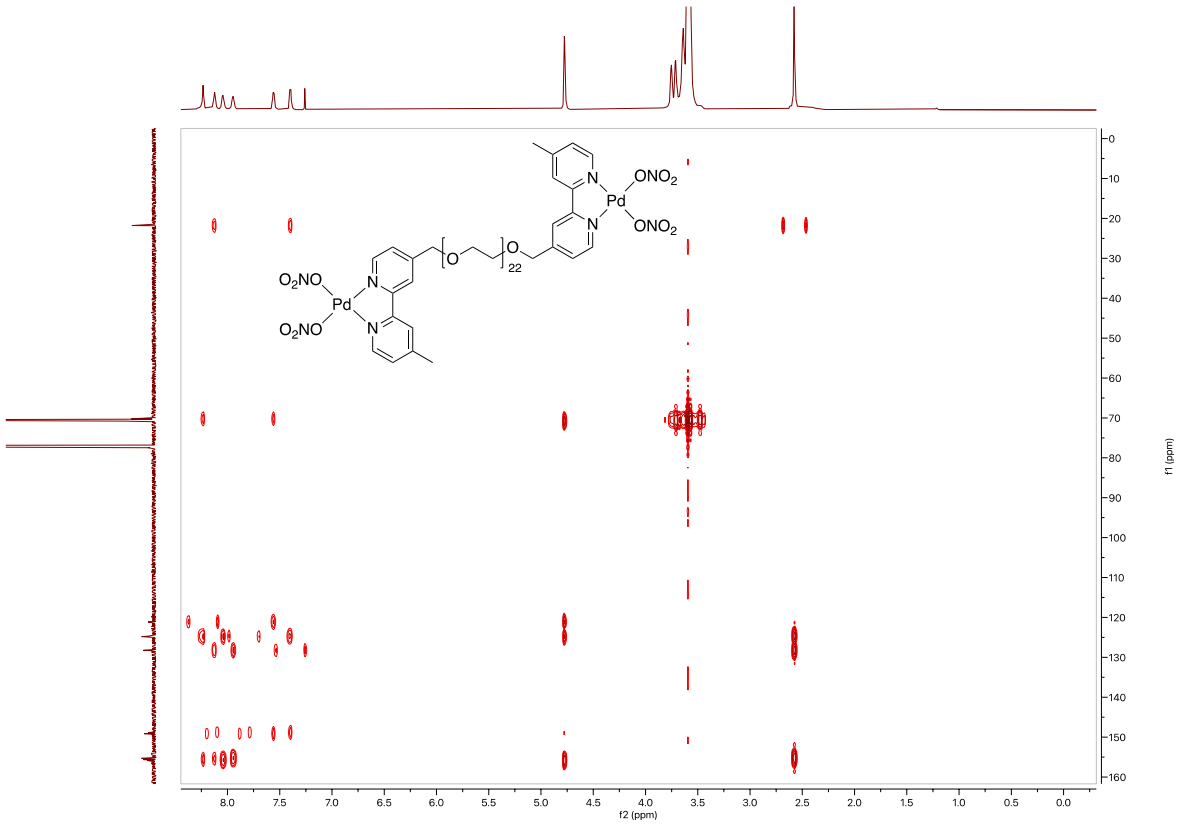

*Figure 245: ^{1}H-{^{13}C} HMBC NMR (600 MHz, $CDCl_3$) of {Poly[oxy(ethane-1,2-diyl)]bis(oxy)bis(methylene)bis(4-methyl-2,2'-bipyridine)}-bis(dichloropalladium(II)) (**62**).*

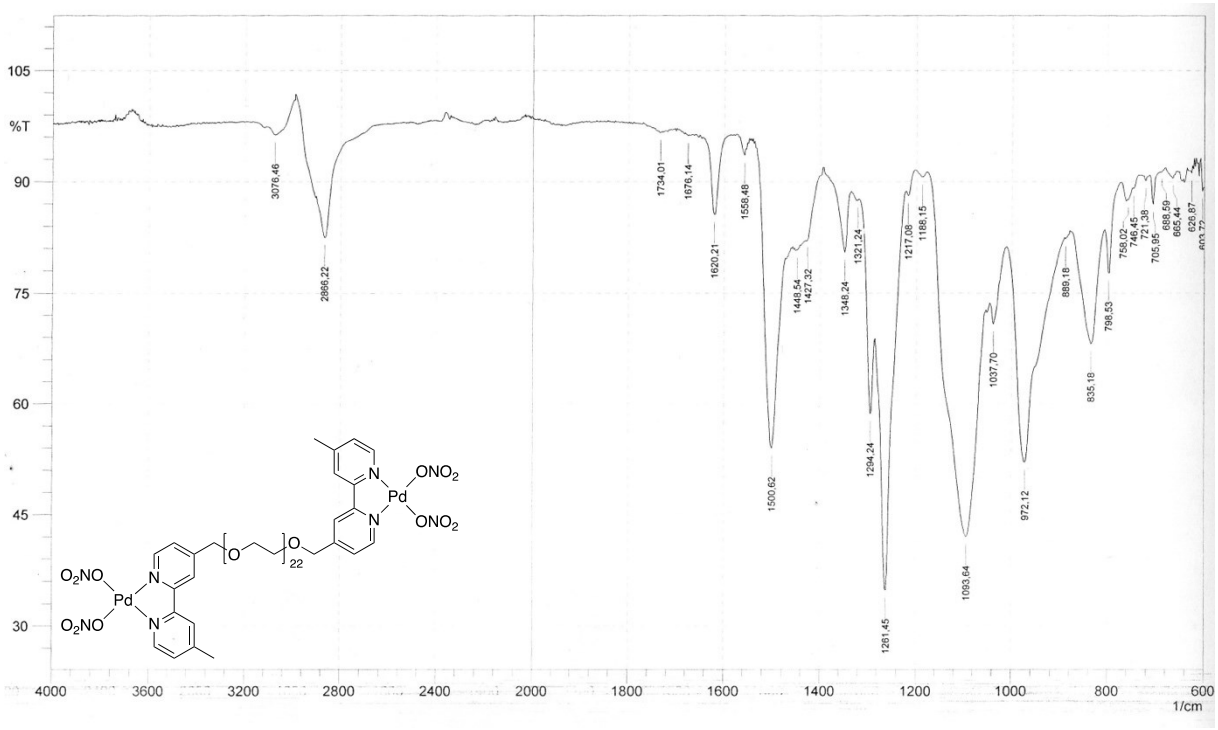

*Figure 246: IR spectrum of {Poly[oxy(ethane-1,2-diyl)]bis(oxy)bis(methylene)bis(4-methyl-2,2'-bipyridine)}-bis(dinitratopalladium(II)) (**62**).*

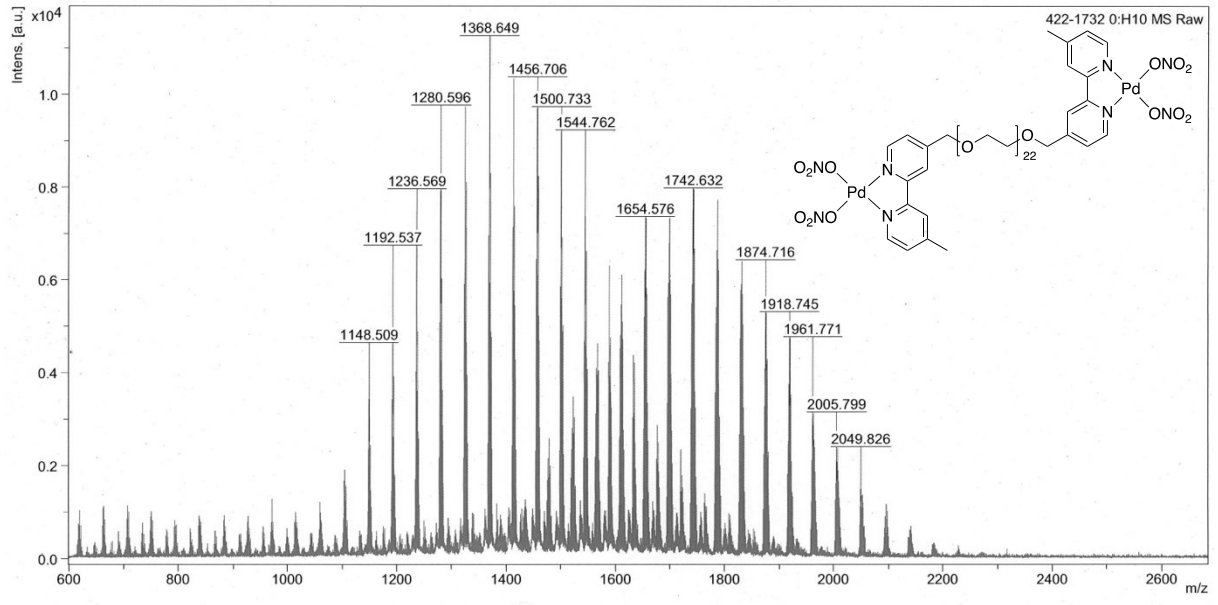

*Figure 247: MALDI spectrum of {Poly[oxy(ethane-1,2-diyl)]bis(oxy)bis(methylene)bis(4-methyl-2,2'-bipyridine)}-bis(dinitratopalladium(II)) (**62**).*

HG_1

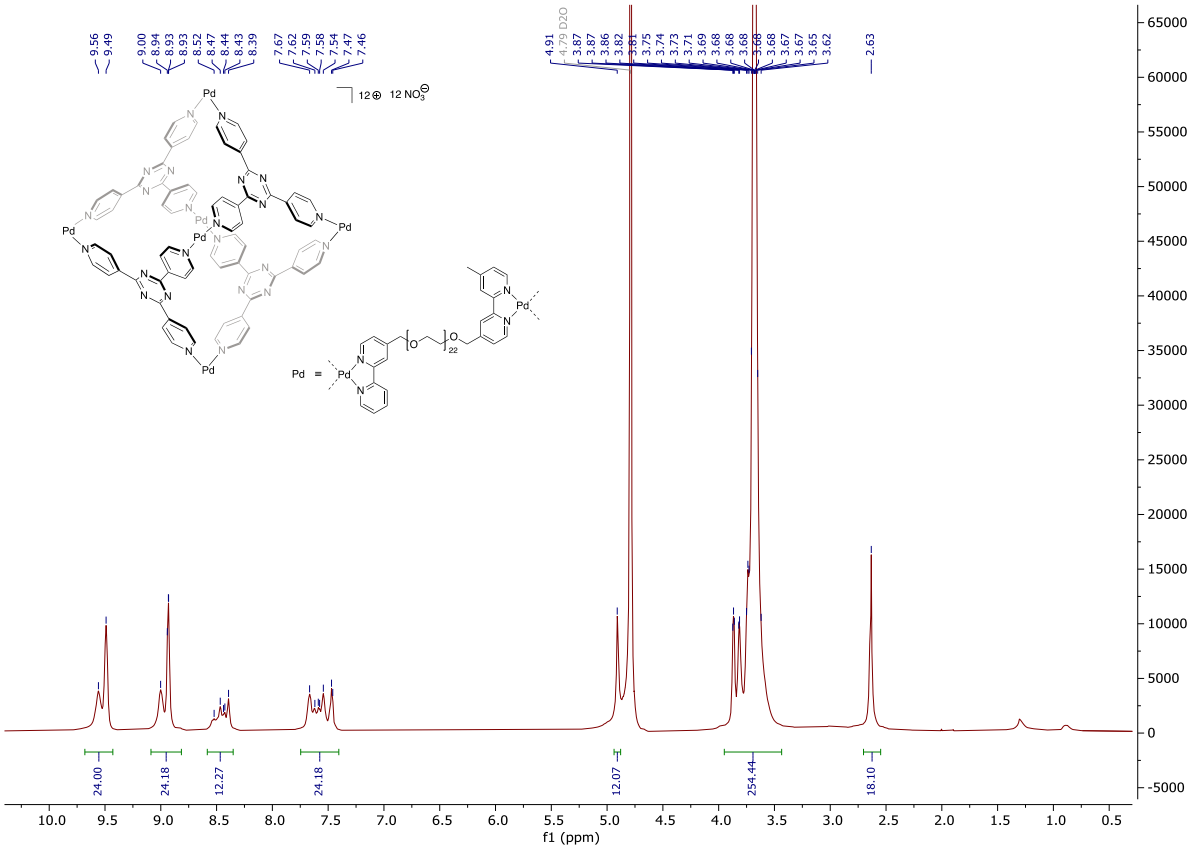

*Figure 248: ^{1}H NMR (600 MHz, D_2O) of **HG_1**.*

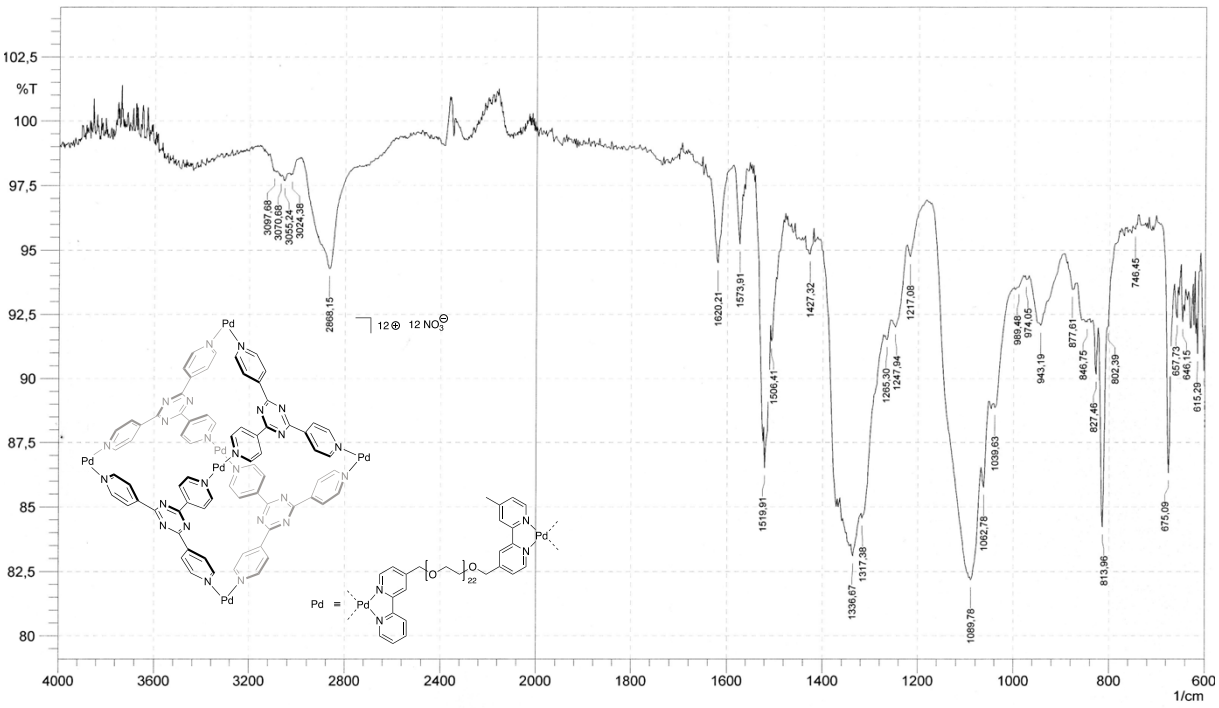

*Figure 249: IR spectrum of the freeze-dried **HG_1**.*

Synthesis of HG_3 and its precursors

Poly[oxy(ethane-1,2-diyl)]bis(oxy)bis(methylene)bis(4-methyl-2,2'-bipyridine) (**55**)

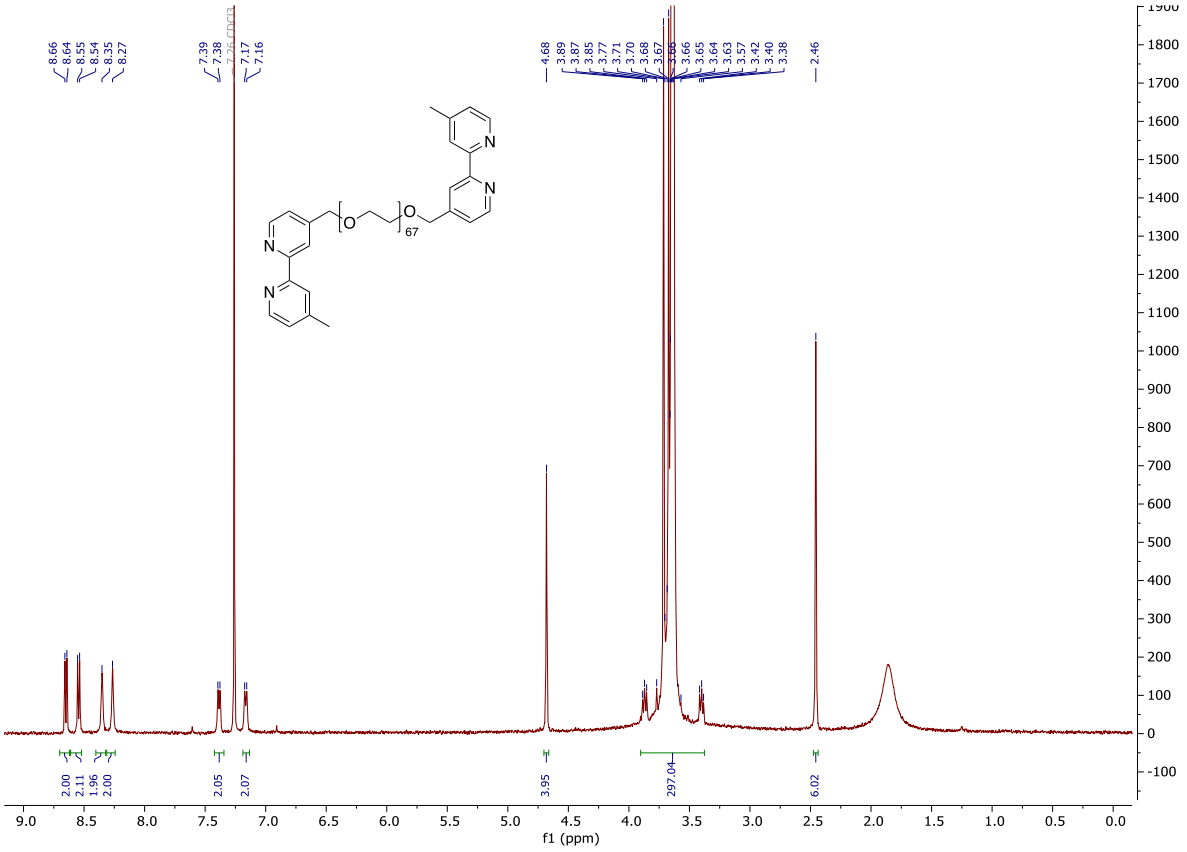

*Figure 250: ^{1}H NMR (300 MHz, $CDCl_3$) of poly[oxy(ethane-1,2-diyl)]bis(oxy)bis(methylene)bis(4-methyl-2,2'-bipyridine) (**55**).*

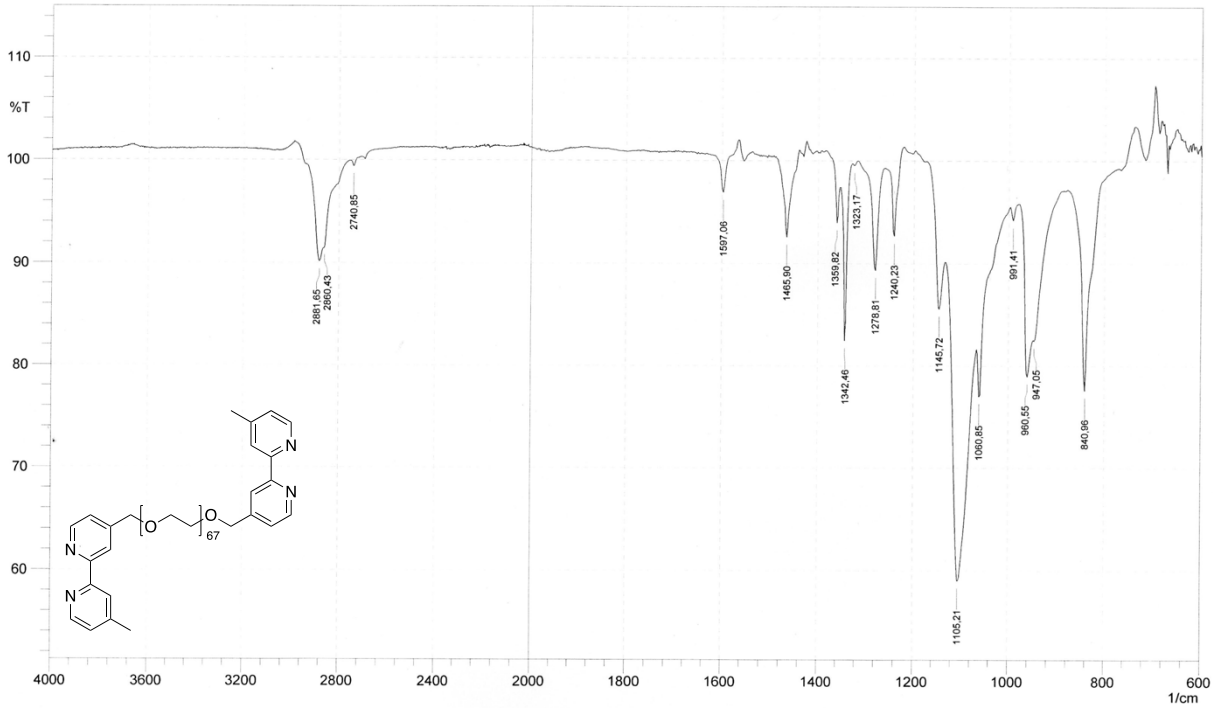

*Figure 251: IR spectrum of poly[oxy(ethane-1,2-diyl)]bis(oxy)bis(methylene)bis(4-methyl-2,2'-bipyridine) (**55**).*

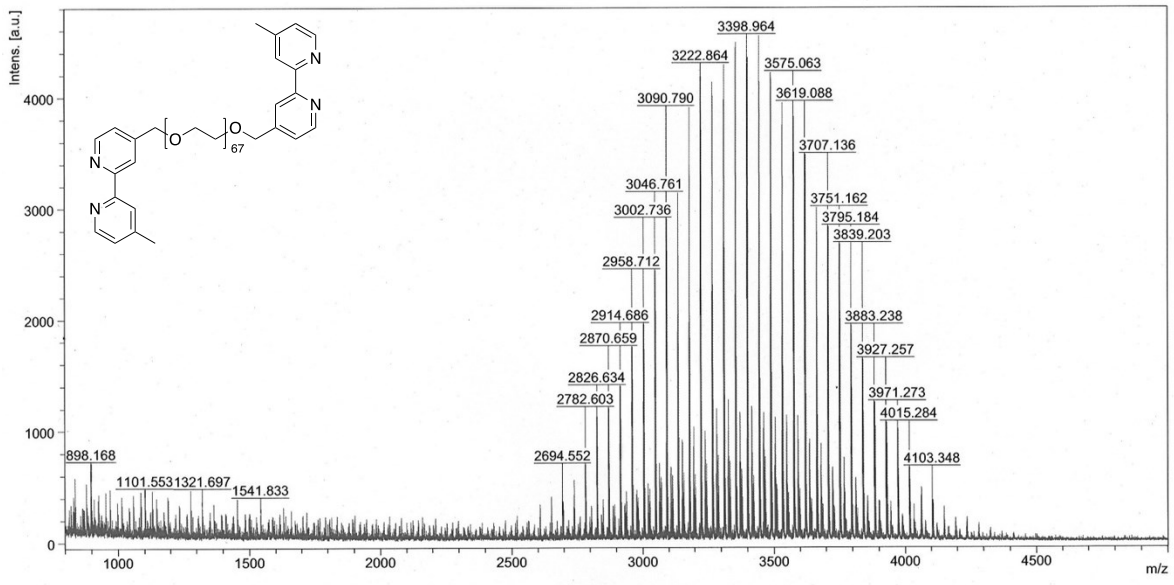

*Figure 252: MALDI spectrum of poly[oxy(ethane-1,2-diyl)]bis(oxy)bis(methylene)bis(4-methyl-2,2'-bipyridine) (**55**).*

{Poly[oxy(ethane-1,2-diyl)]bis(oxy)bis(methylene)bis(4-methyl-2,2'-bipyridine)}-bis(dichloropalladium(II)) (55)

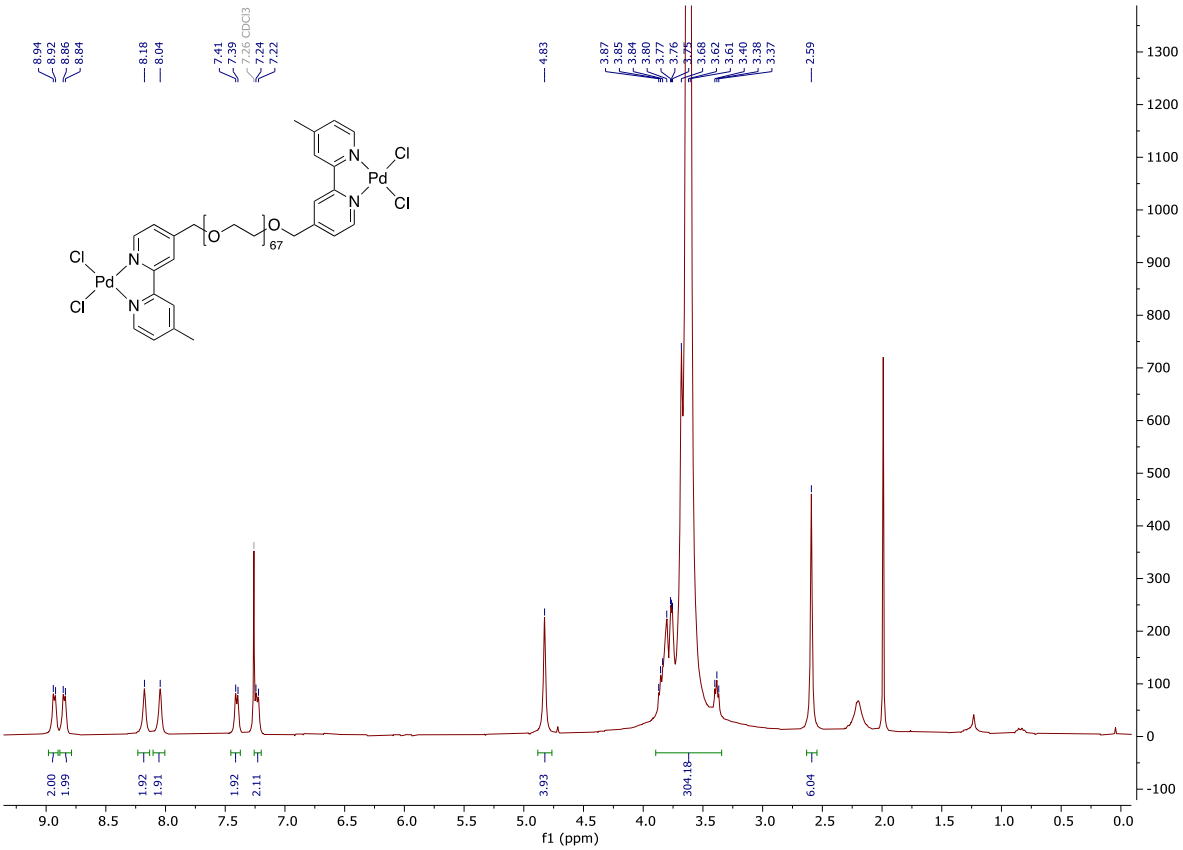

*Figure 253: ^{1}H NMR (300 MHz, $CDCl_3$) of {Poly[oxy(ethane-1,2-diyl)]bis(oxy)bis(methylene)bis(4-methyl-2,2'-bipyridine)}-bis(dichloropalladium(II)) (**59**).*

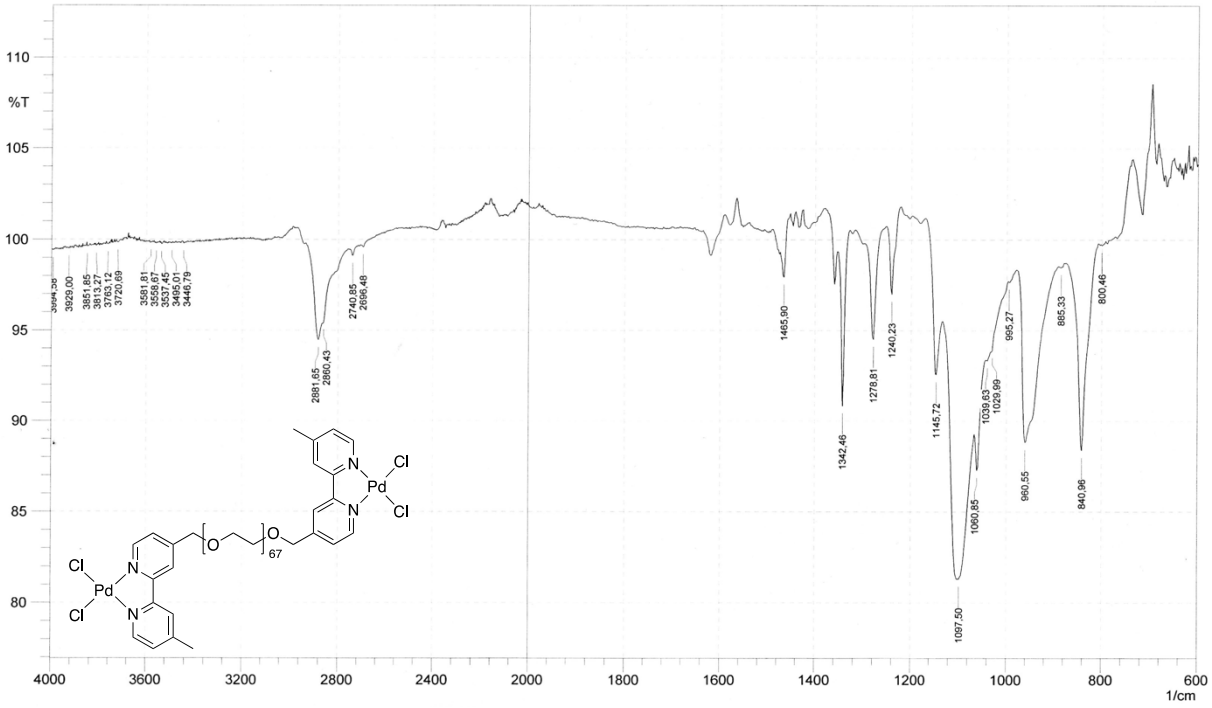

*Figure 254: IR spectrum of {Poly[oxy(ethane-1,2-diyl)]bis(oxy)bis(methylene)bis(4-methyl-2,2'-bipyridine)}-bis(dichloropalladium(II)) (**59**).*

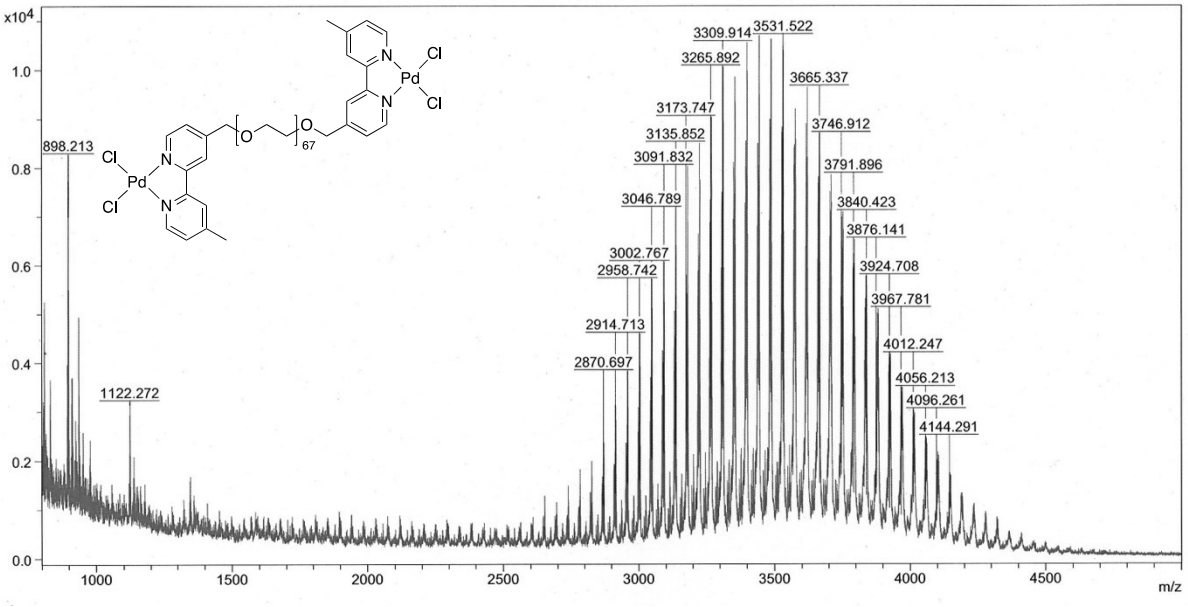

*Figure 255: MALDI spectrum of {Poly[oxy(ethane-1,2-diyl)]bis(oxy)bis(methylene)bis(4-methyl-2,2'-bipyridine)}-bis(dichloropalladium(II)) (**59**).*

{Poly[oxy(ethane-1,2-diyl)]bis(oxy)bis(methylene)bis(4-methyl-2,2'-bipyridine)}-bis(dinitratopalladium(II)) (**63**)

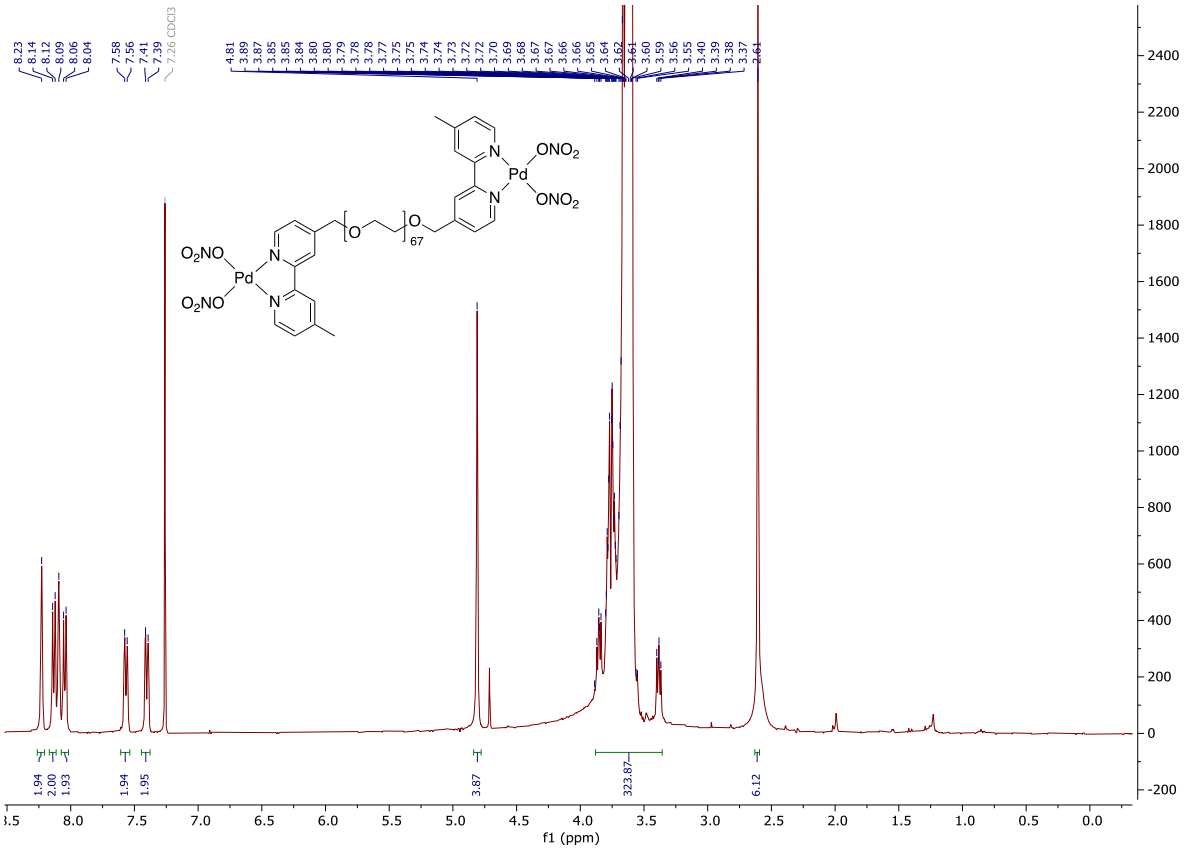

*Figure 256: ^{1}H NMR (300 MHz, $CDCl_3$) of {Poly[oxy(ethane-1,2-diyl)]bis(oxy)bis(methylene)bis(4-methyl-2,2'-bipyridine)}-bis(dinitratopalladium(II)) (**63**).*

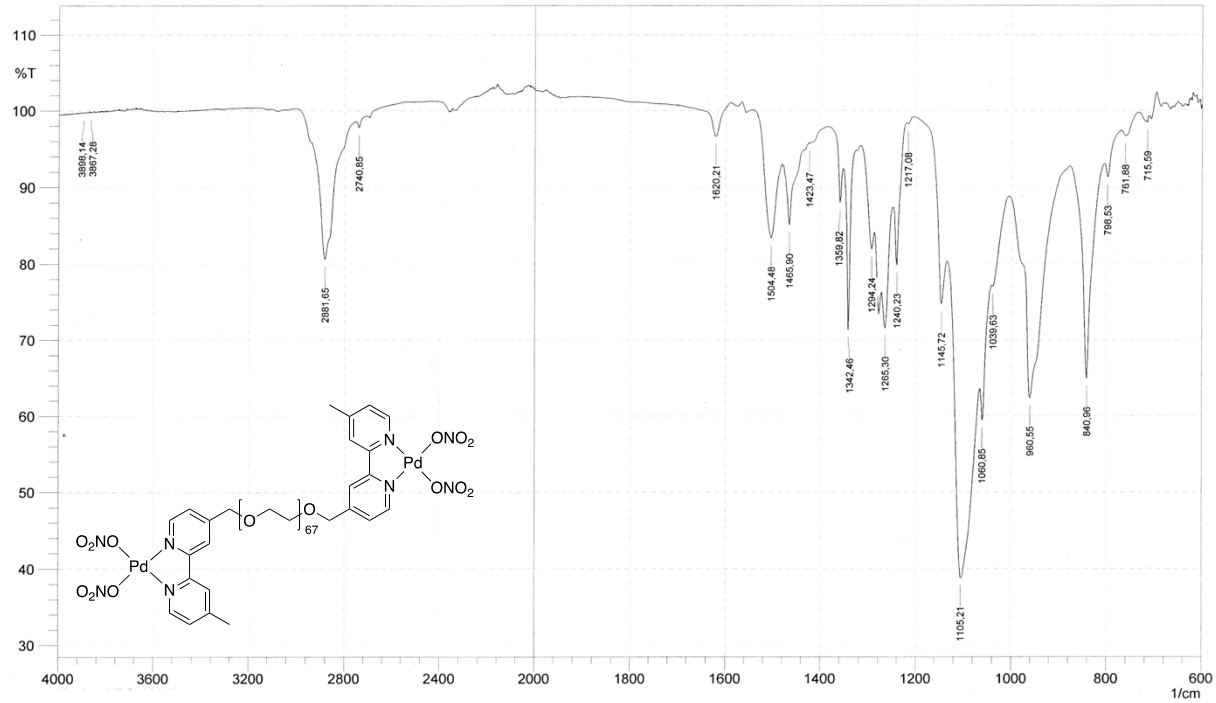

*Figure 257: IR spectrum of {Poly[oxy(ethane-1,2-diyl)]bis(oxy)bis(methylene)bis(4-methyl-2,2'-bipyridine)}-bis(dinitratopalladium(II)) (**63**).*

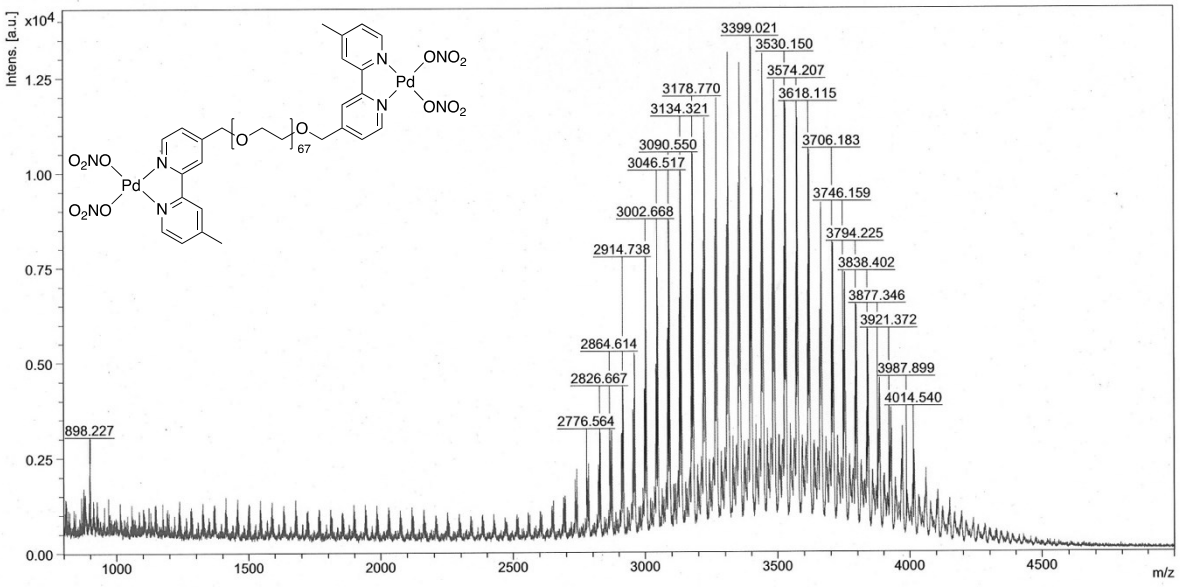

*Figure 258: MALDI spectrum of {Poly[oxy(ethane-1,2-diyl)]bis(oxy)bis(methylene)bis(4-methyl-2,2'-bipyridine)}-bis(dinitratopalladium(II)) (**63**).*

HG_3

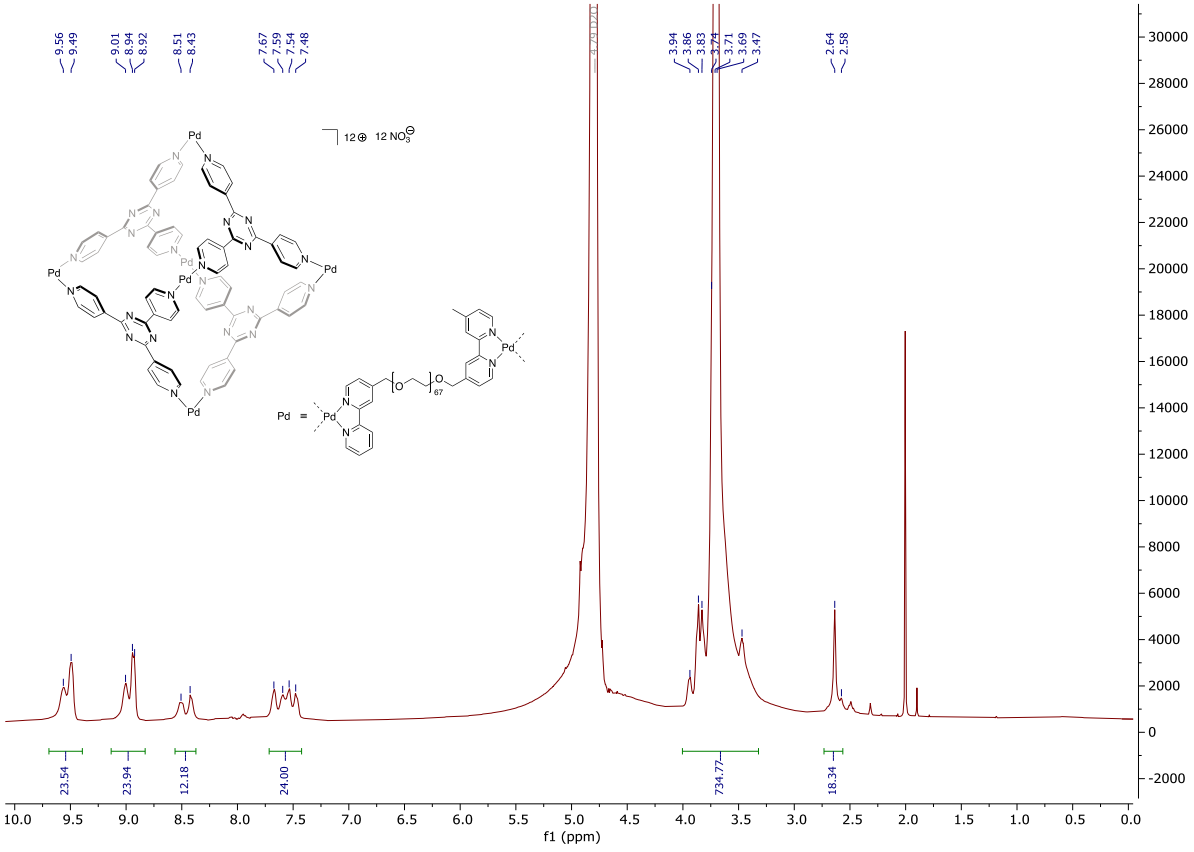

*Figure 259: ^{1}H NMR (300 MHz, D_2O) of **HG_3**.*

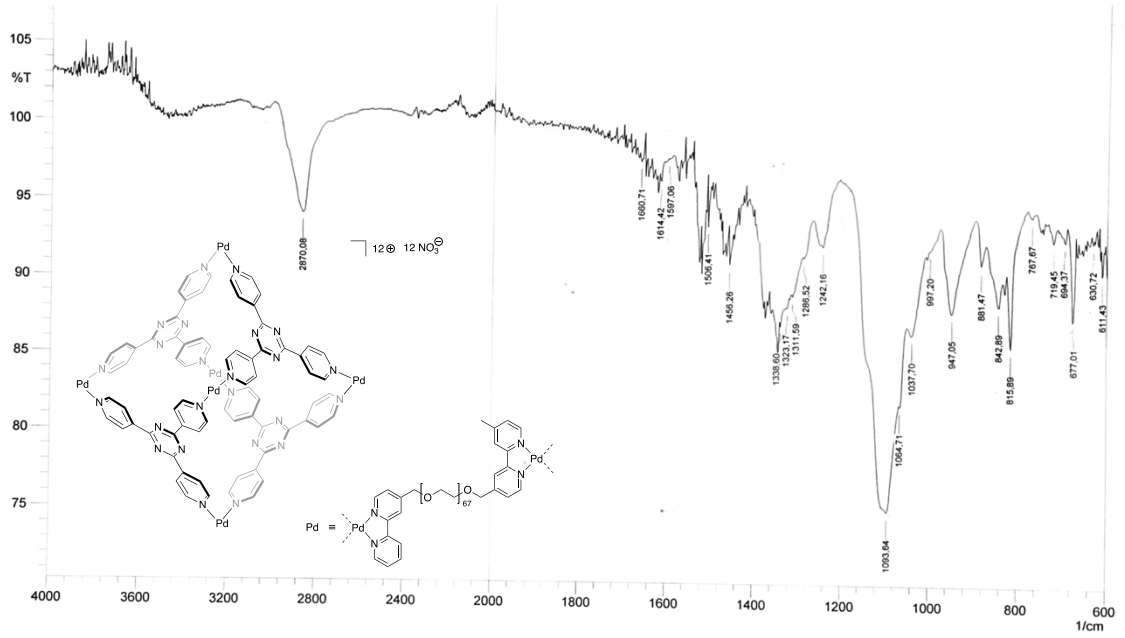

*Figure 260: IR spectrum of the freeze-dried **HG$_3$**.*

Synthesis of **56** and its precursors

Poly[oxy(ethane-1,2-diyl)]bis(oxy)bis(methylene)bis(4-methyl-2,2'-bipyridine) (**56**)

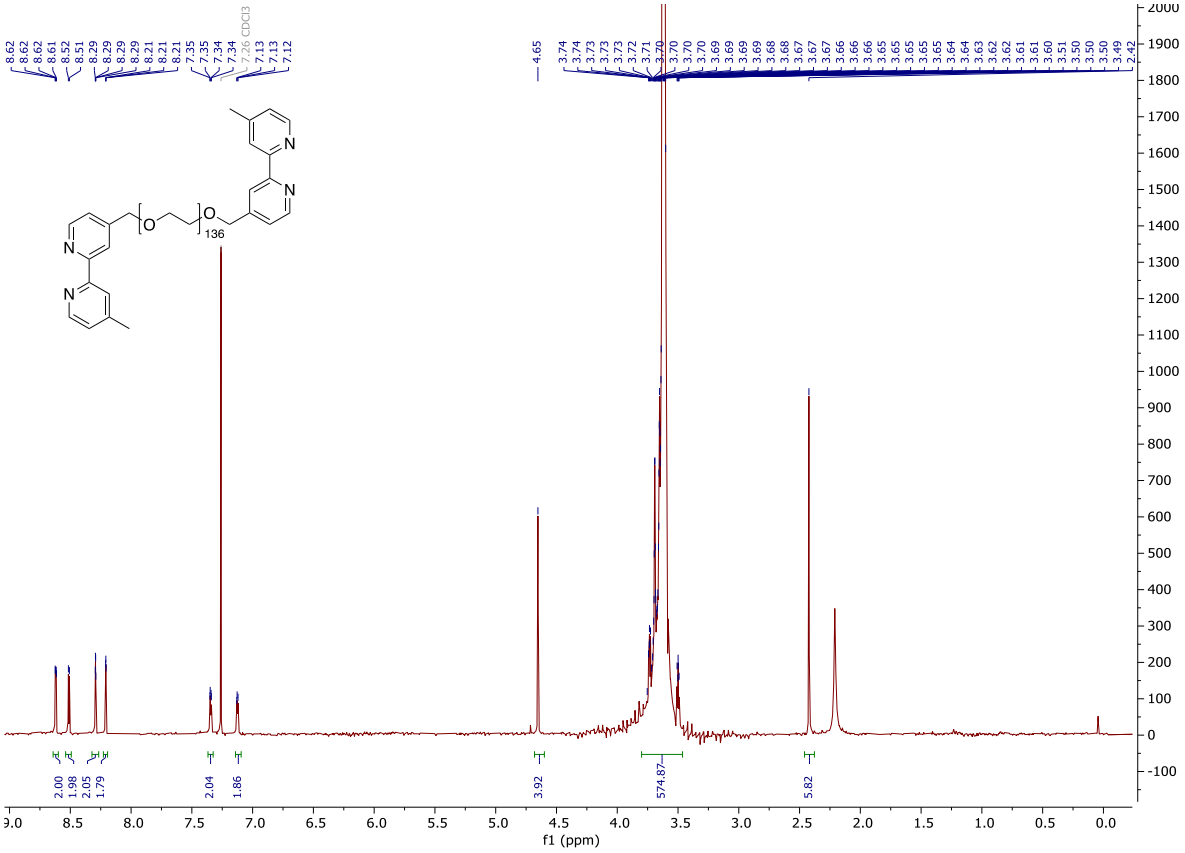

*Figure 261: ^{1}H NMR (600 MHz, $CDCl_3$) of poly[oxy(ethane-1,2-diyl)]bis(oxy)bis(methylene)bis(4-methyl-2,2'-bipyridine) (**56**).*

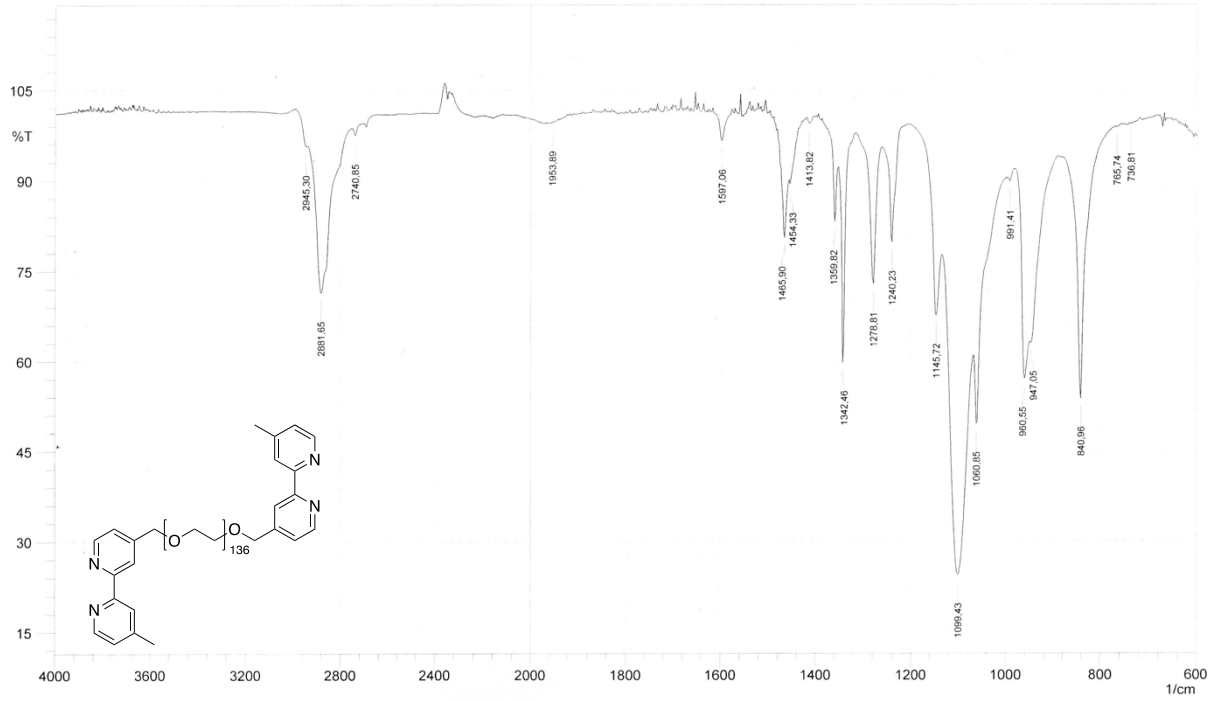

*Figure 262: IR spectrum of poly[oxy(ethane-1,2-diyl)]bis(oxy)bis(methylene)bis(4-methyl-2,2'-bipyridine) (**56**).*

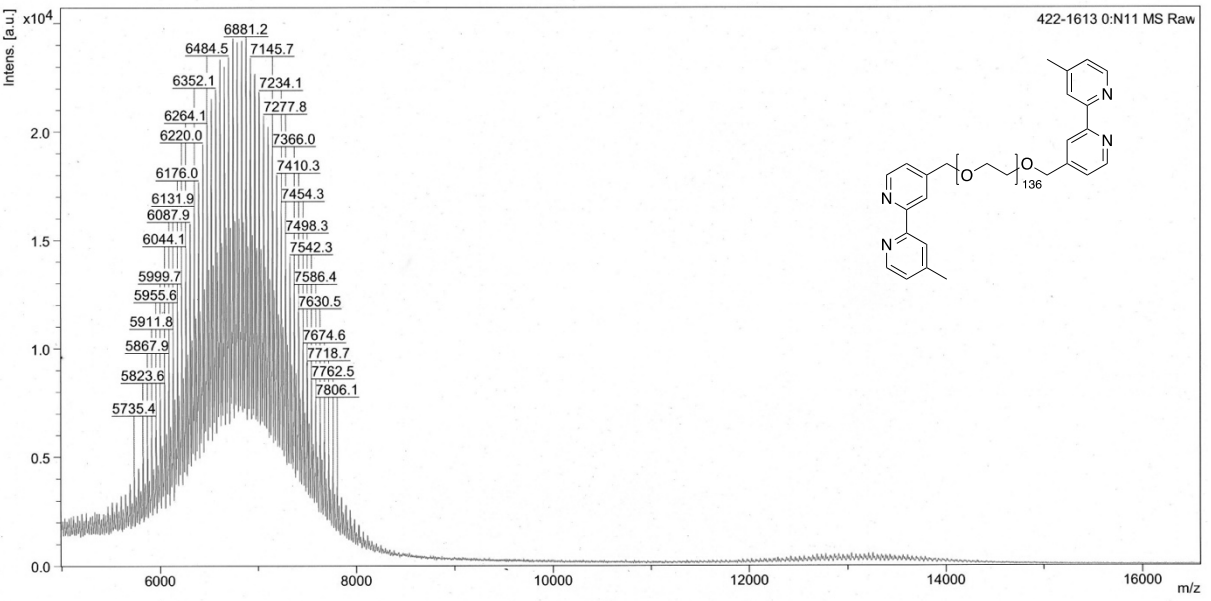

*Figure 263: MALDI spectrum of poly[oxy(ethane-1,2-diyl)]bis(oxy)bis(methylene)bis(4-methyl-2,2'-bipyridine) (**56**).*

{Poly[oxy(ethane-1,2-diyl)]bis(oxy)bis(methylene)bis(4-methyl-2,2'-bipyridine)}-bis(dichloropalladium(II)) (**60**)

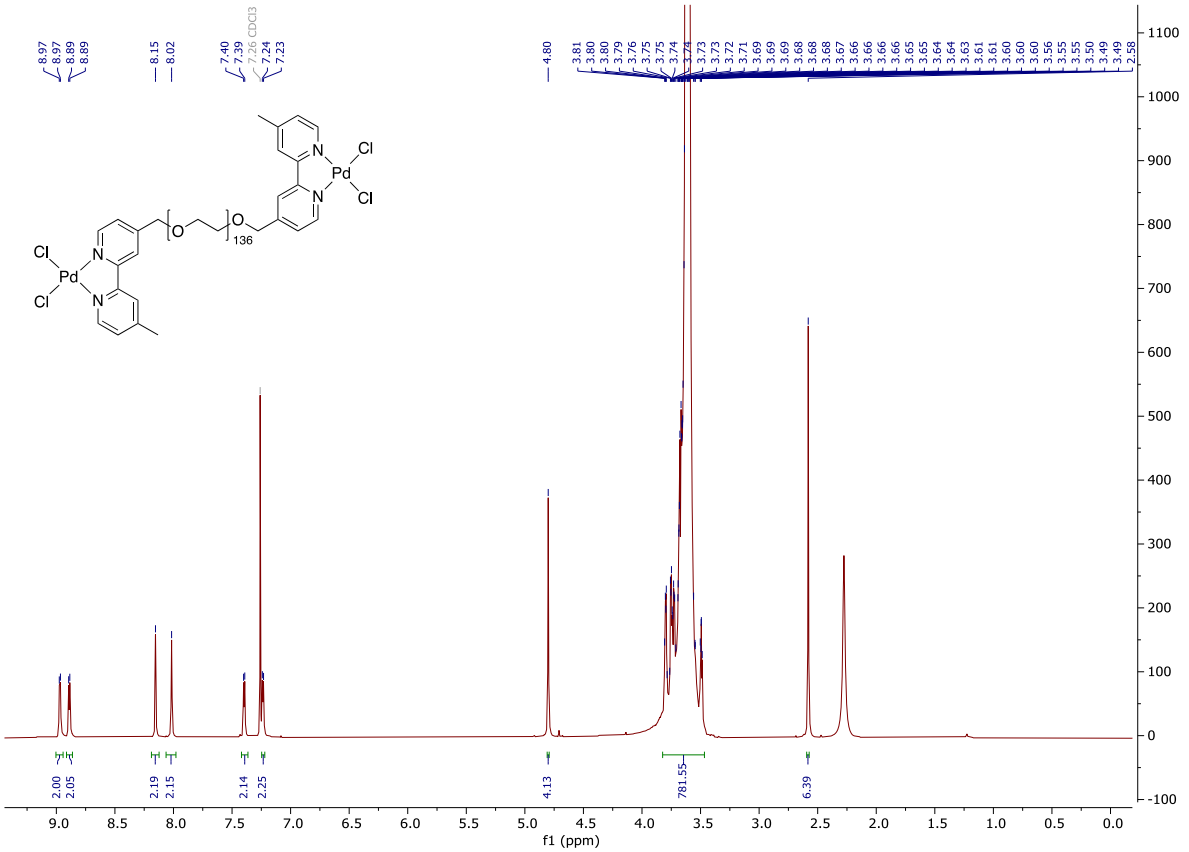

*Figure 264: ^{1}H NMR (600 MHz, $CDCl_3$) of {poly[oxy(ethane-1,2-diyl)]bis(oxy)bis(methylene)bis(4-methyl-2,2'-bipyridine)}-bis(dichloropalladium(II)) (**60**).*

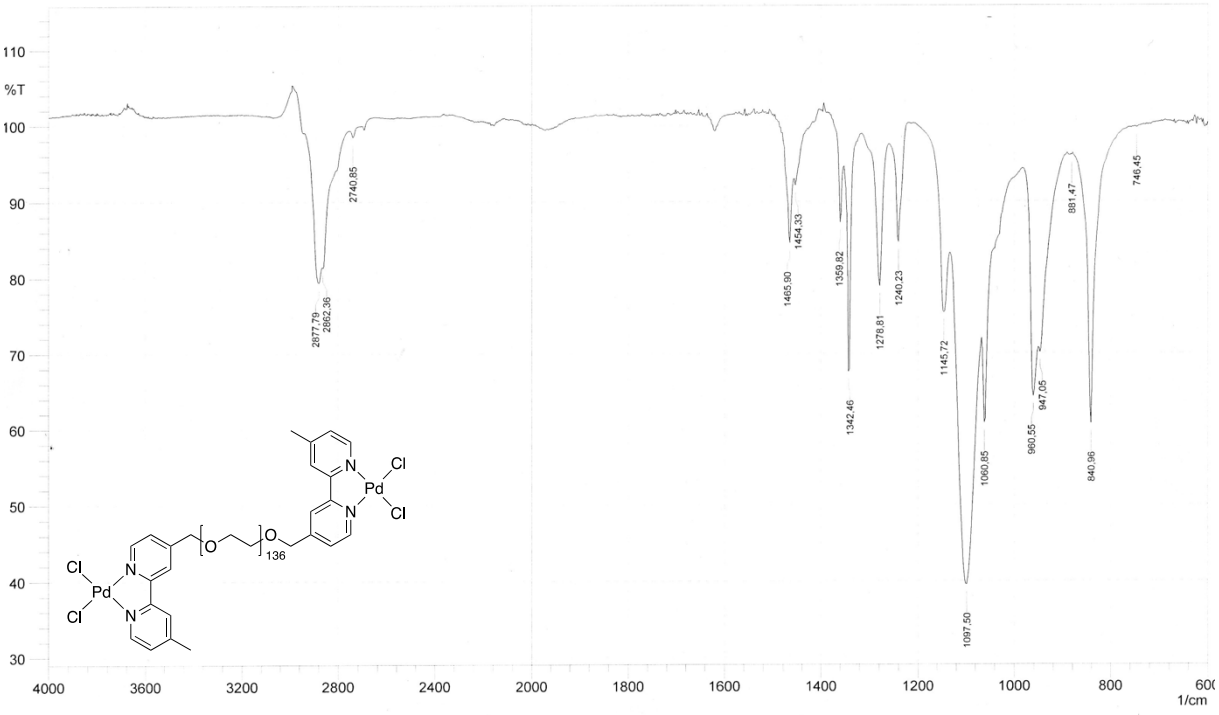

*Figure 265: IR spectrum of {poly[oxy(ethane-1,2-diyl)]bis(oxy)bis(methylene)bis(4-methyl-2,2'-bipyridine)}-bis(dichloropalladium(II)) (**60**).*

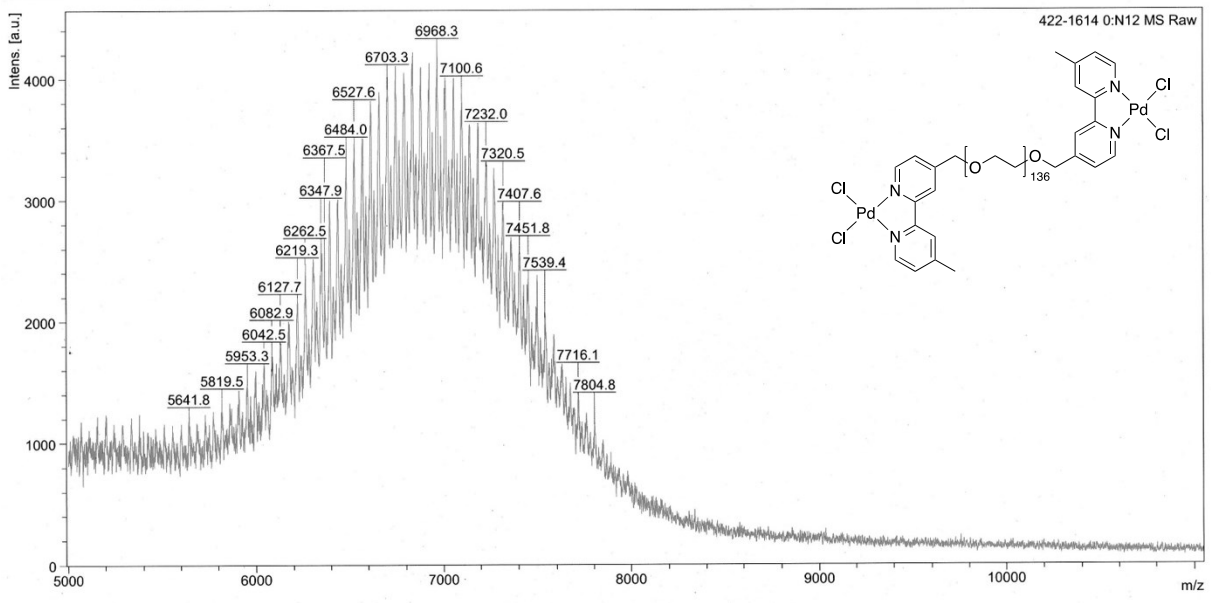

*Figure 266: MALDI spectrum of poly[oxy(ethane-1,2-diyl)]bis(oxy)bis(methylene)bis(4-methyl-2,2'-bipyridine) (**60**).*

{Poly[oxy(ethane-1,2-diyl)]bis(oxy)bis(methylene)bis(4-methyl-2,2'-bipyridine)}-bis(dinitratopalladium(II)) (**64**)

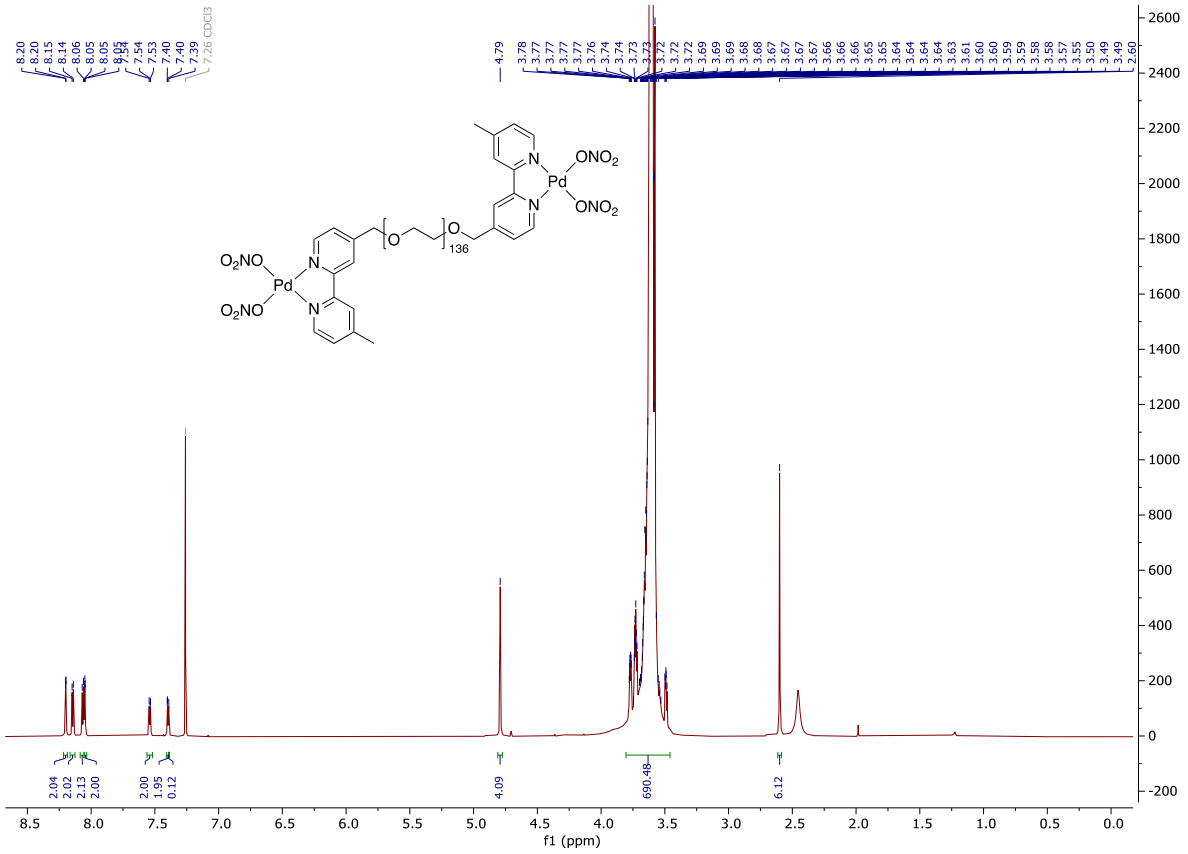

*Figure 267: ^{1}H NMR (600 MHz, $CDCl_3$) of {Poly[oxy(ethane-1,2-diyl)]bis(oxy)bis(methylene)bis(4-methyl-2,2'-bipyridine)}-bis(dinitratopalladium(II)) (**64**).*

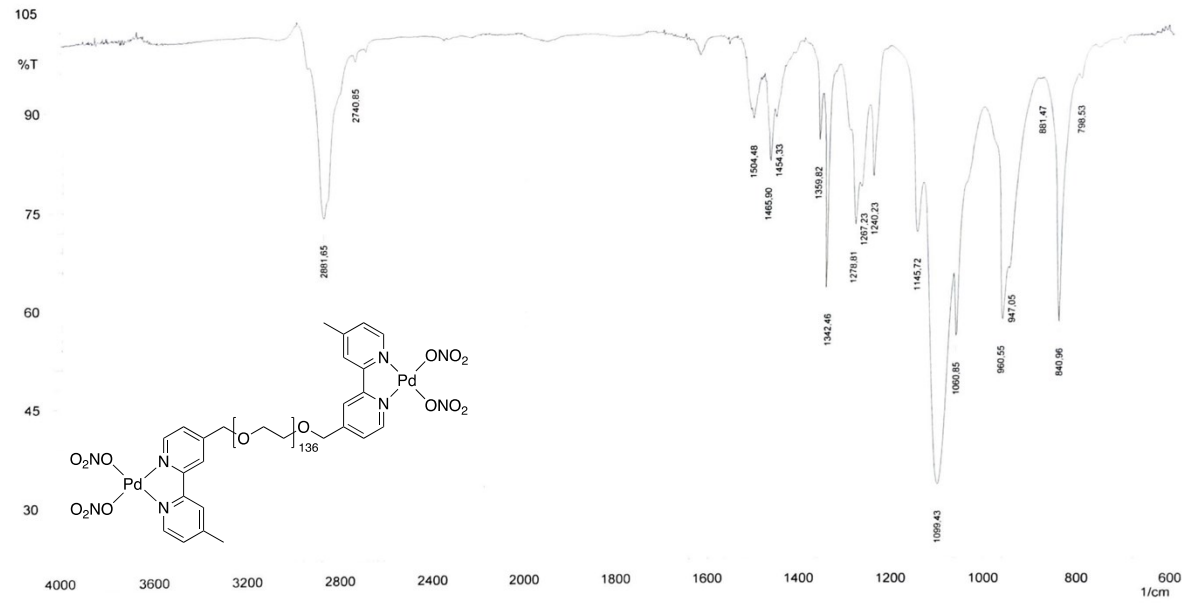

*Figure 268: IR spectrum of {poly[oxy(ethane-1,2-diyl)]bis(oxy)bis(methylene)bis(4-methyl-2,2'-bipyridine)}-bis(dinitratopalladium(II)) (**64**).*

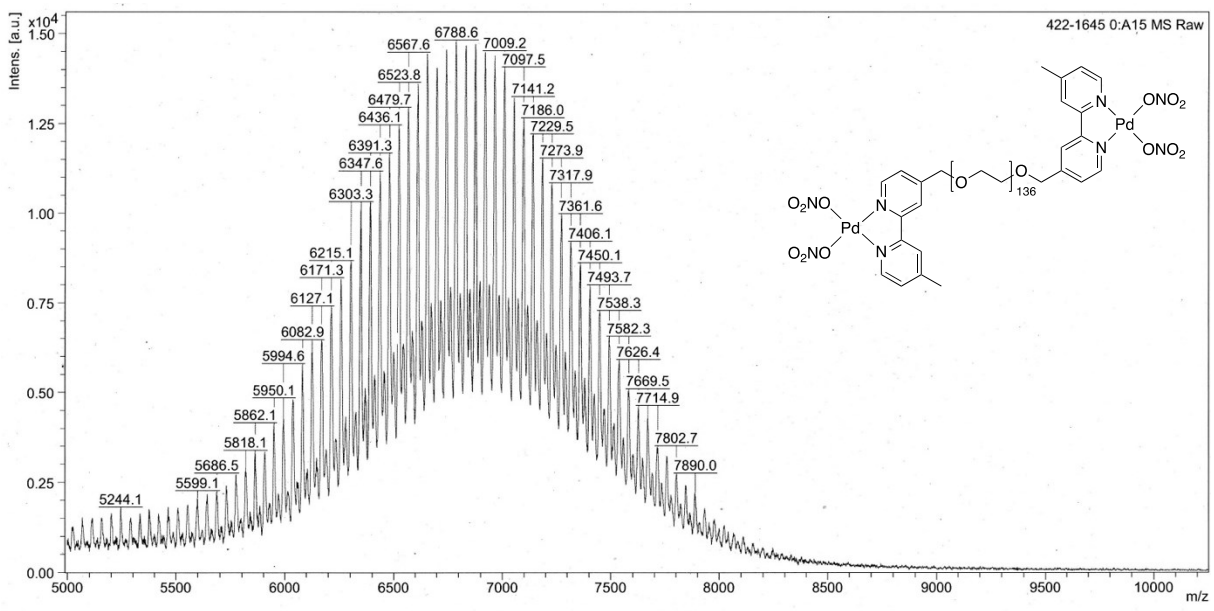

*Figure 269: MALDI spectrum of {Poly[oxy(ethane-1,2-diyl)]bis(oxy)bis(methylene)bis(4-methyl-2,2'-bipyridine)}-bis(dinitratopalladium(II)) (**64**).*

HG_6

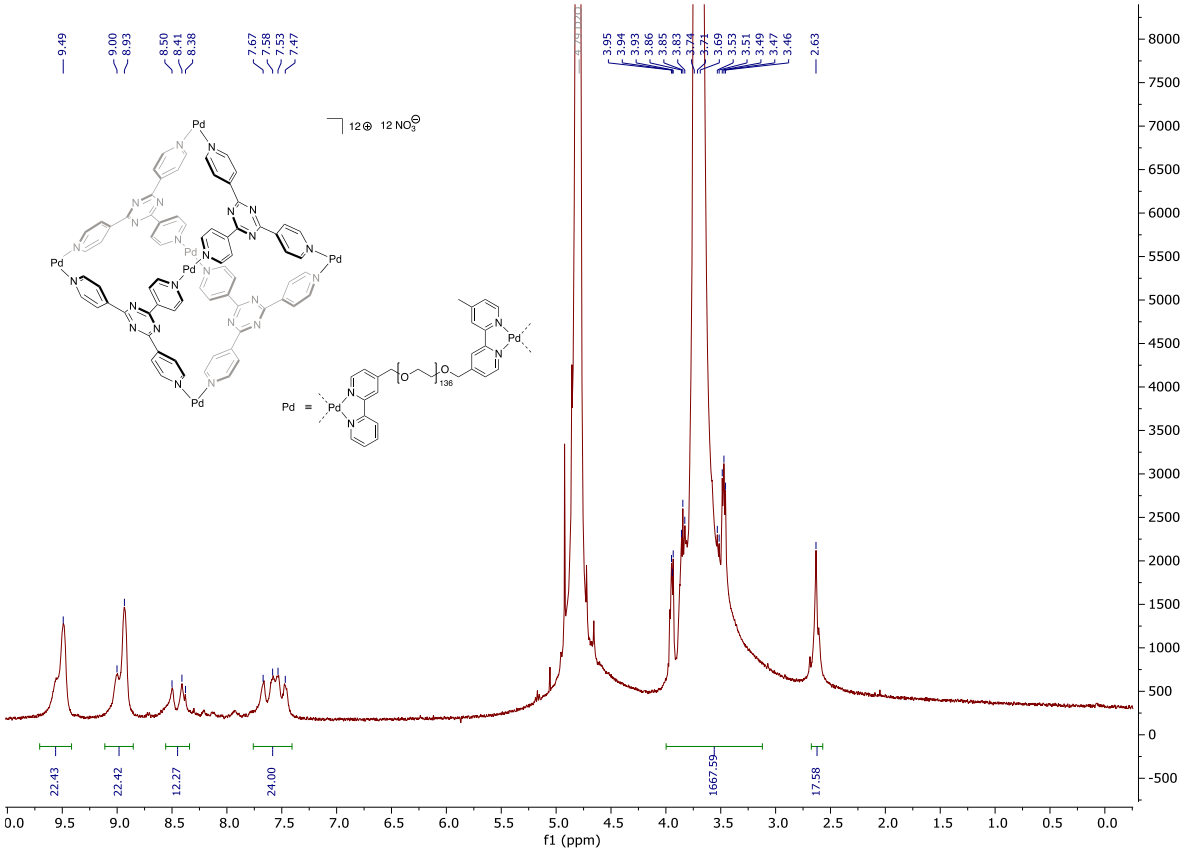

*Figure 270: ^{1}H NMR (300 MHz, D_2O) of **HG_6**.*

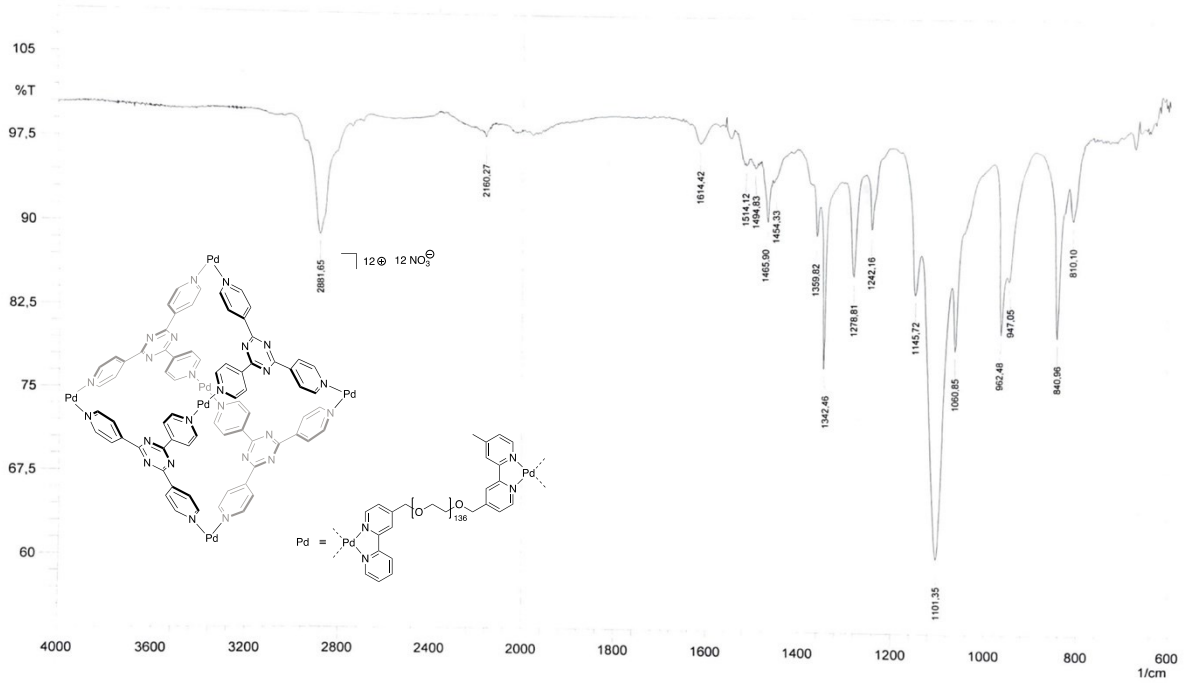

*Figure 271: IR spectrum of the freeze-dried **HG_6**.*

Section for encapsulation

HG_1

Ibuprofen

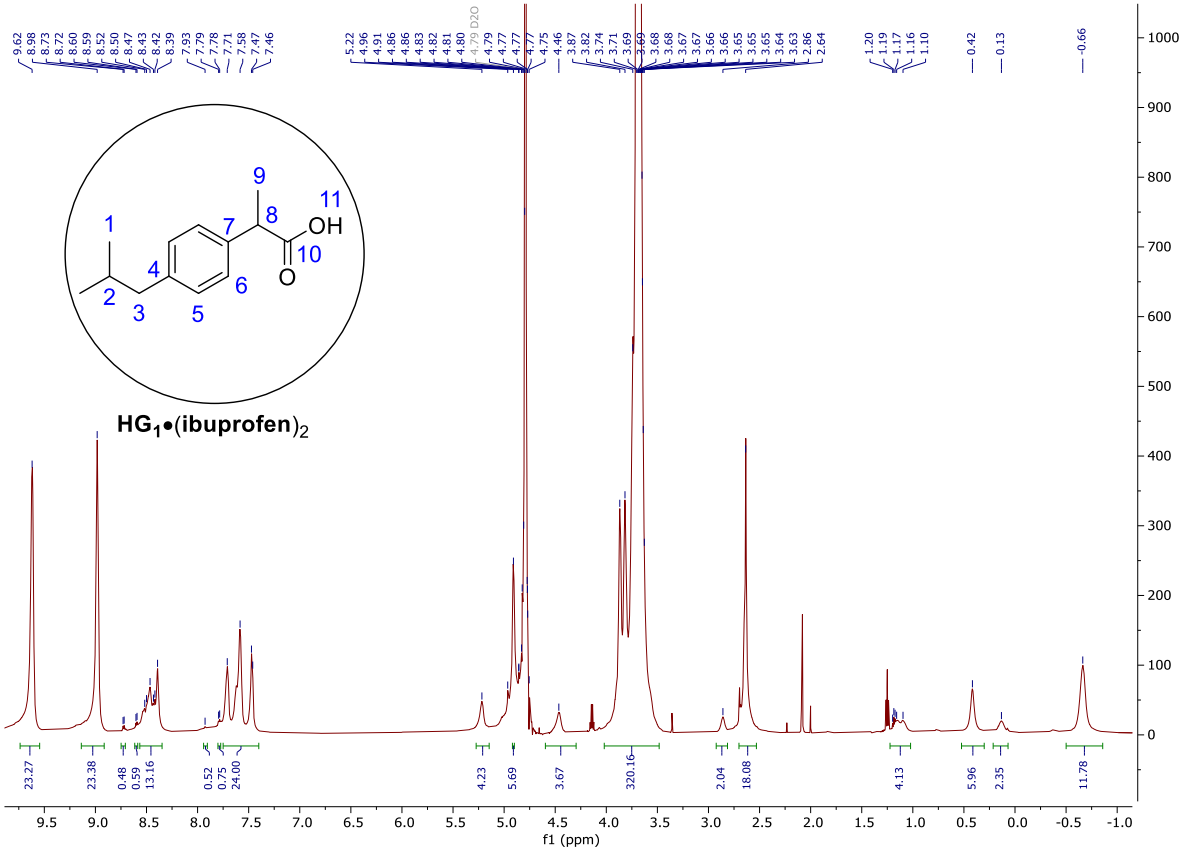

*Figure 272: ^1H NMR (600 MHz, D_2O) of **HG_1•(ibuprofen)$_2$**.*

HG_3

Ibuprofen

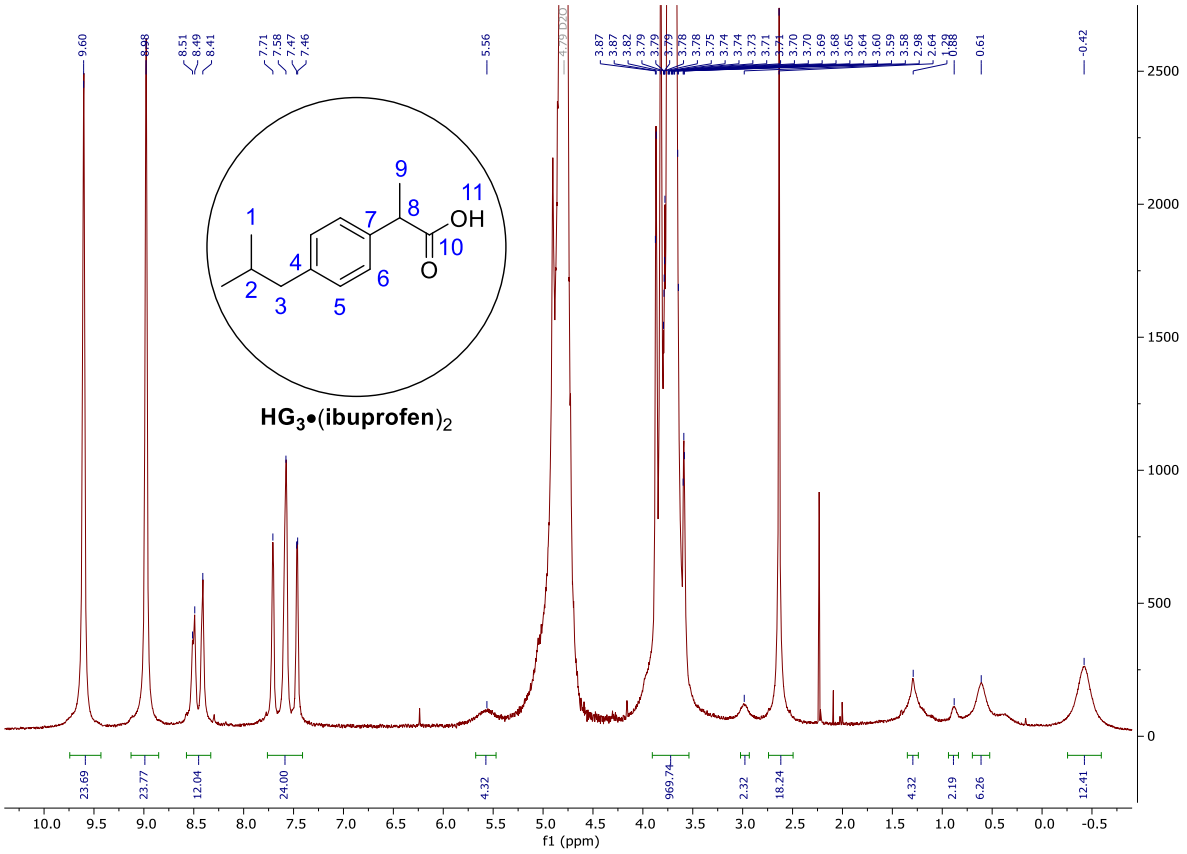

*Figure 273: ^1H NMR (600 MHz, D_2O) of **HG_3•(ibuprofen)$_2$**.*

Progesterone

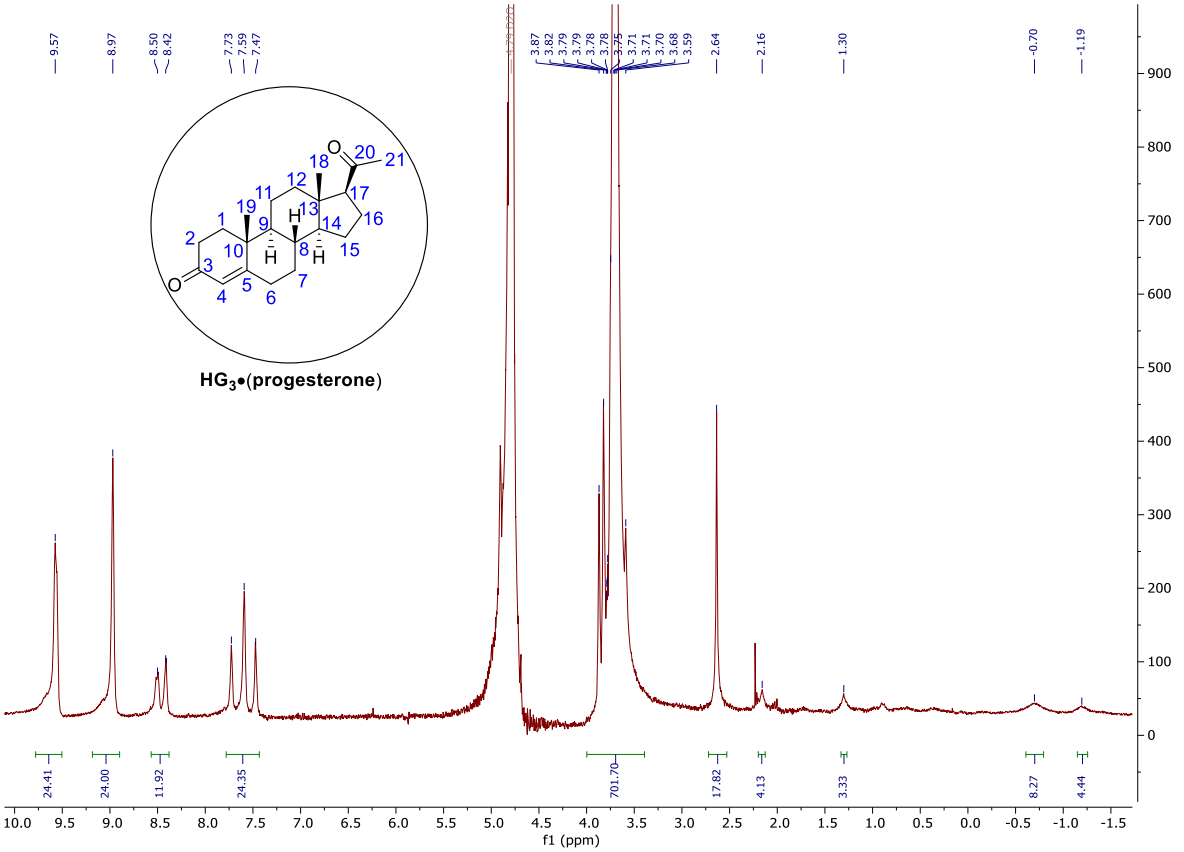

*Figure 274: ^{1}H NMR (600 MHz, D_2O) of **HG_3•(progesterone)**.*

Drospirenone

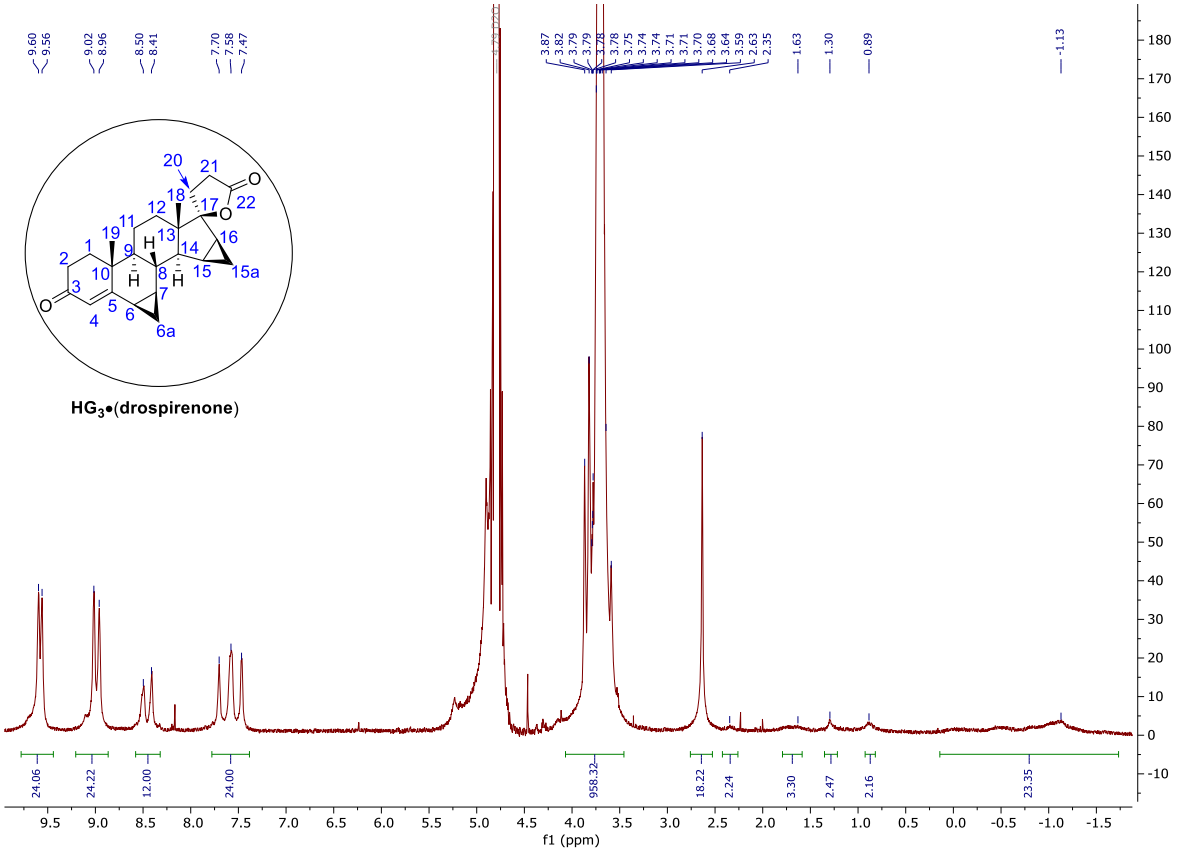

*Figure 275: ^{1}H NMR (600 MHz, D_2O) of **HG_3•(drospirenone)**.*

HG_6

Ibuprofen

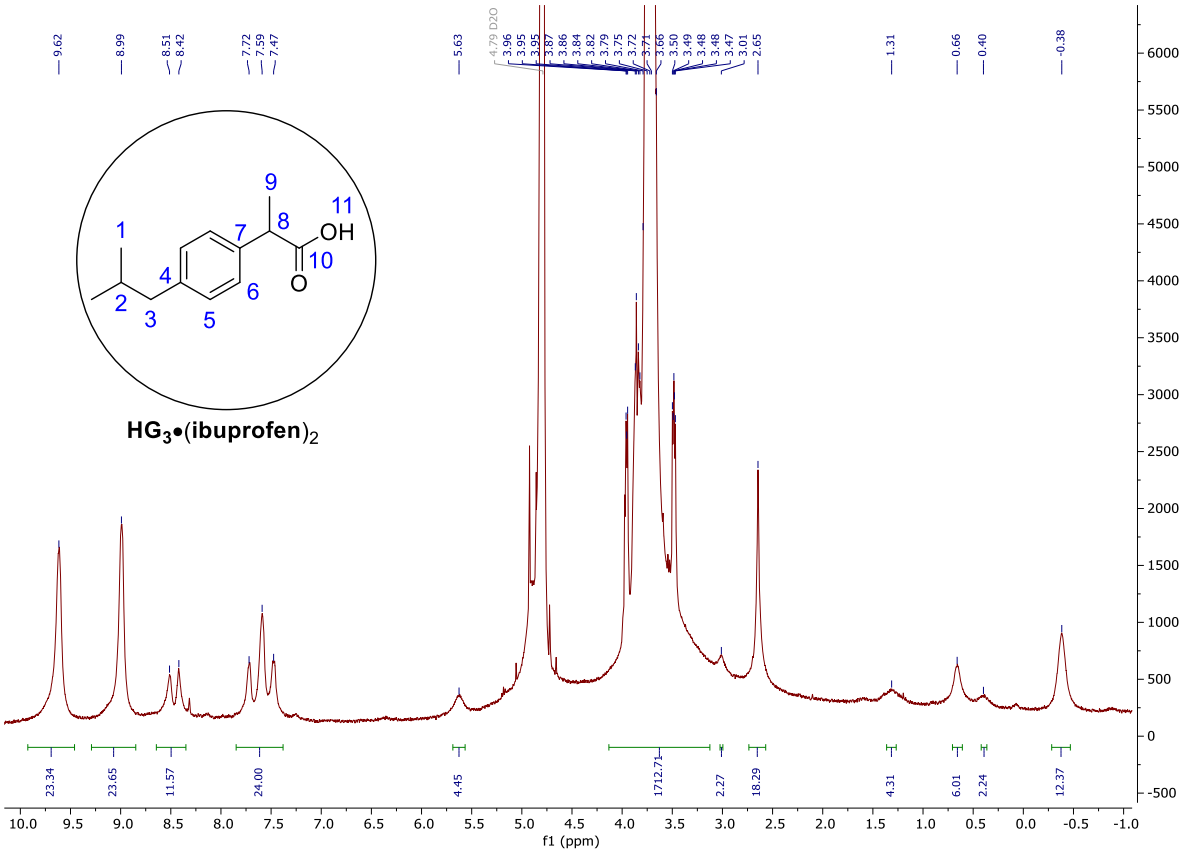

*Figure 276: ^1H NMR (300 MHz, D_2O) of **HG_3•(ibuprofen)$_2$**.*

Section for mechanochemical activation

HG_1

Empty

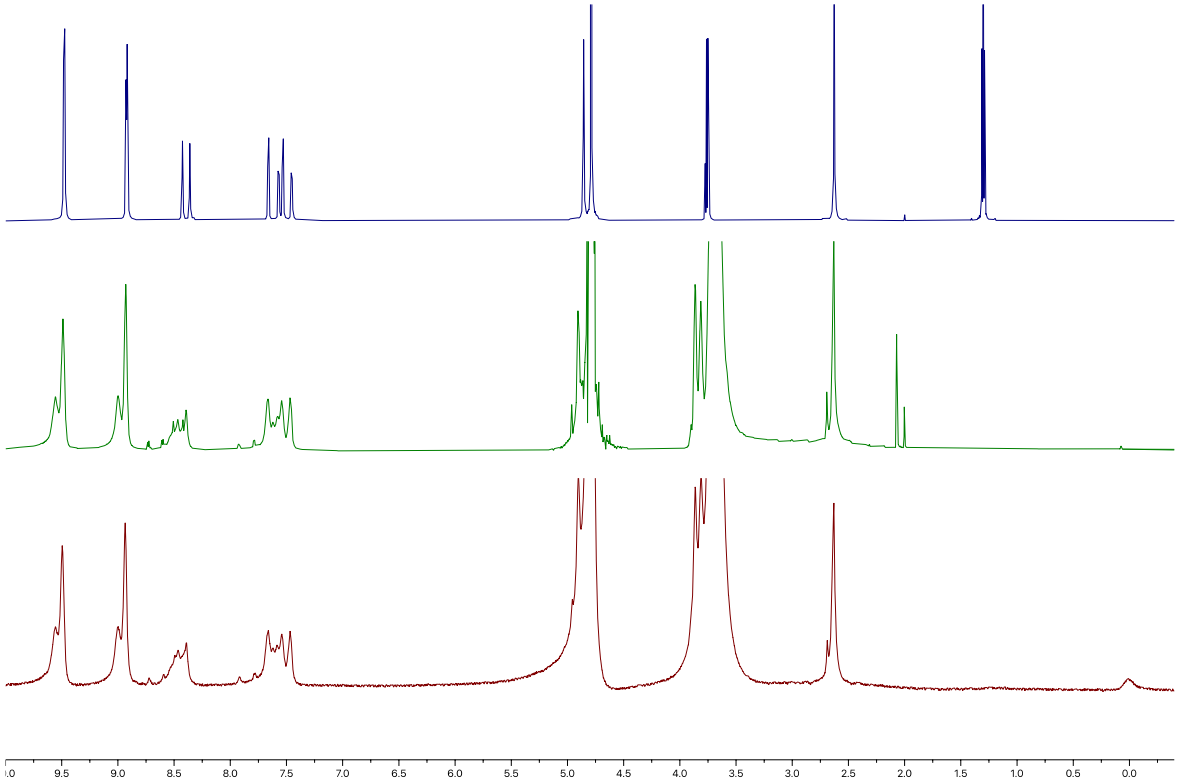

*Figure 277: ^{1}H NMR: Previously reported **MOC_1** (top), **HG_1** before sonication (mid), **HG_1** after sonication (bottom).*

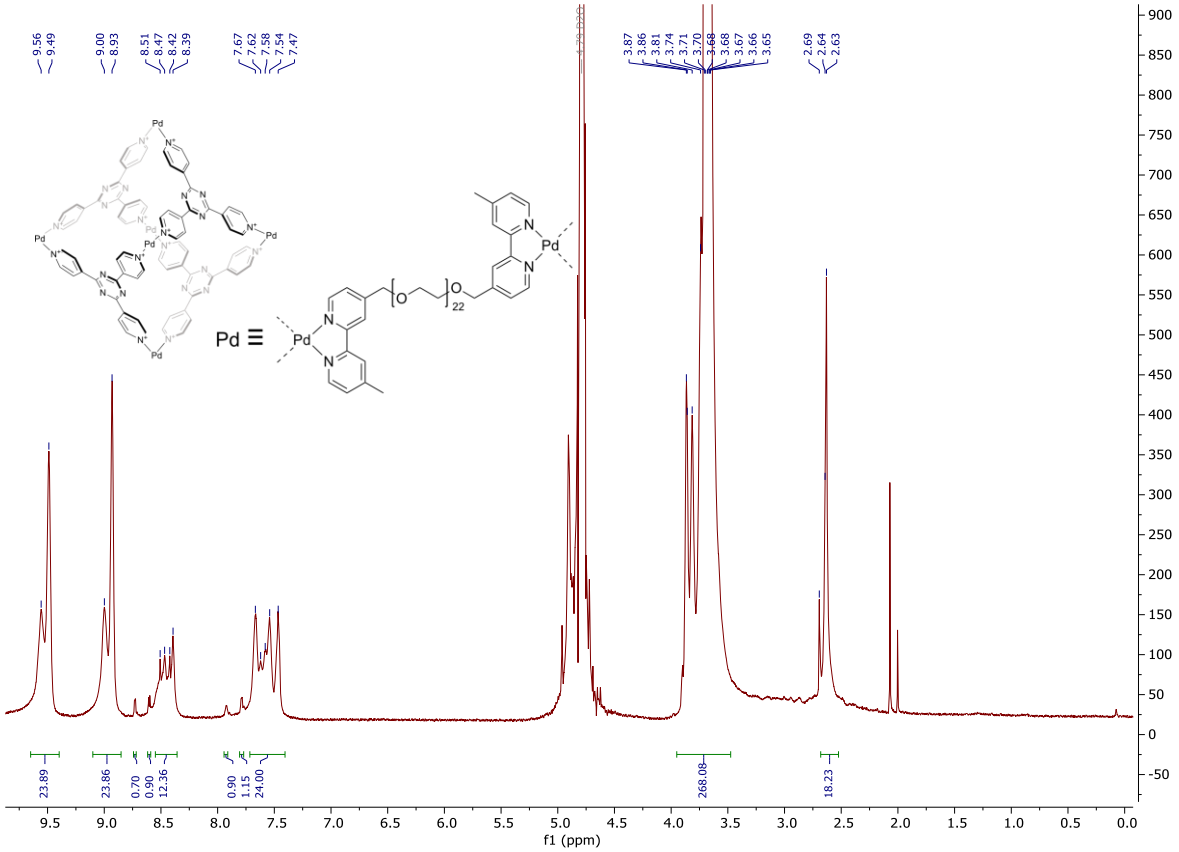

*Figure 278: ^{1}H NMR (600 MHz, D_2O) of **HG_1** before sonication.*

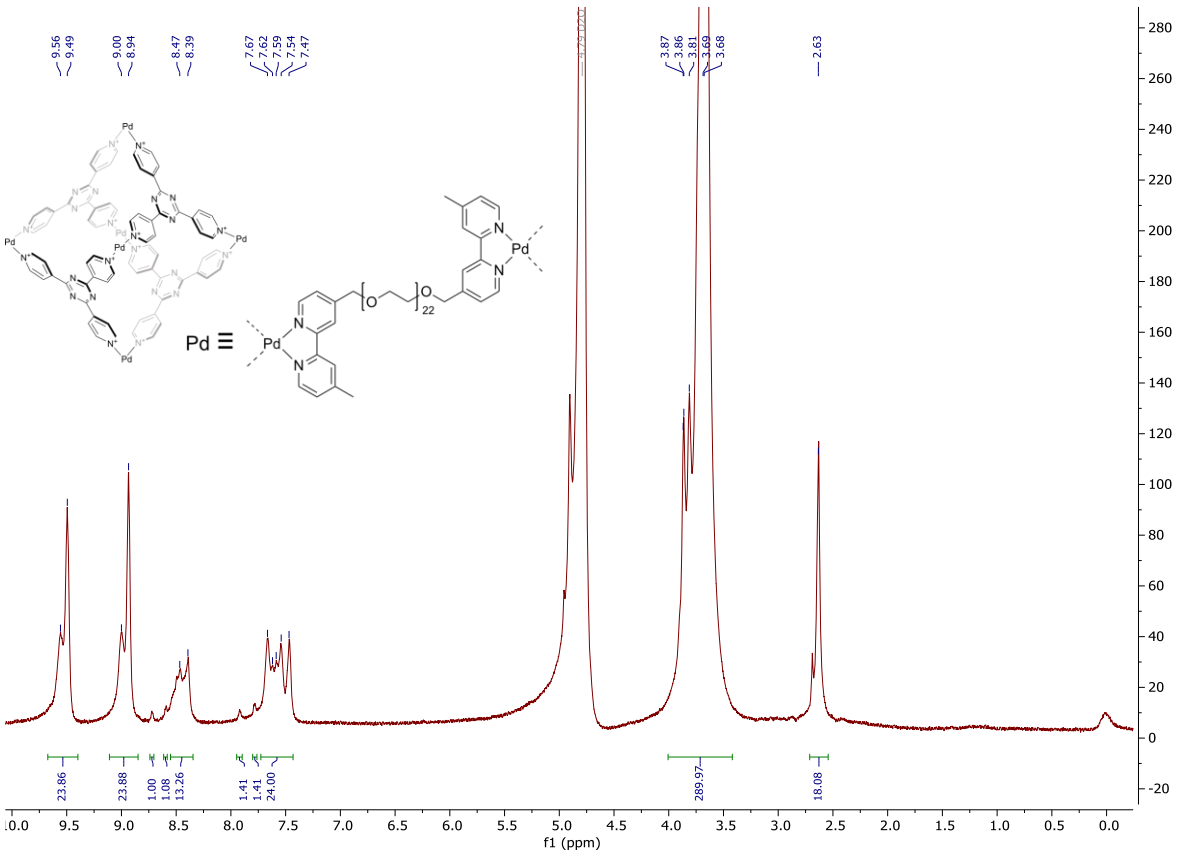

*Figure 279: ^{1}H NMR (600 MHz, D_2O) of **HG_1** after sonicating for 3 h (1 s on, 1 s off).*

Ibuprofen

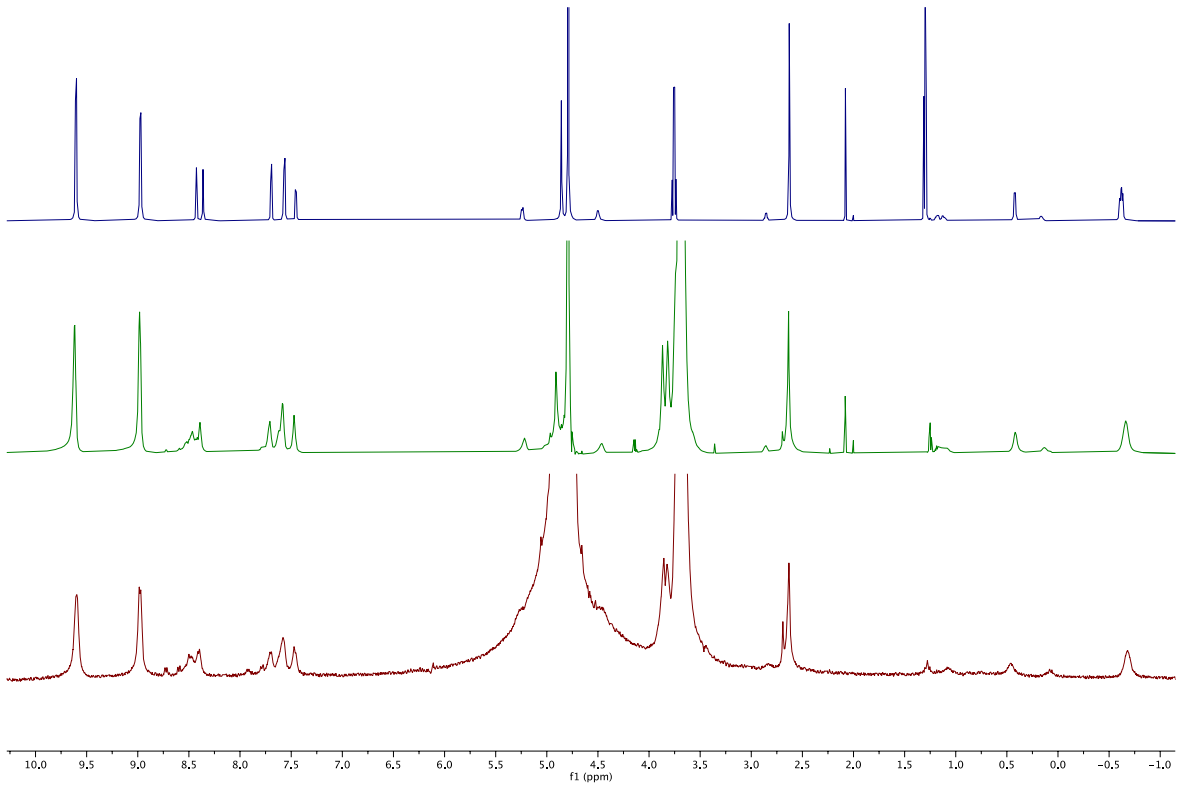

*Figure 280: ^{1}H NMR: Previously published **MOC$_1$•(ibuprofen)$_2$** (top), **HG$_1$•(ibuprofen)$_2$** before sonication (mid), **HG$_1$•(ibuprofen)$_2$** after sonication (bottom).*

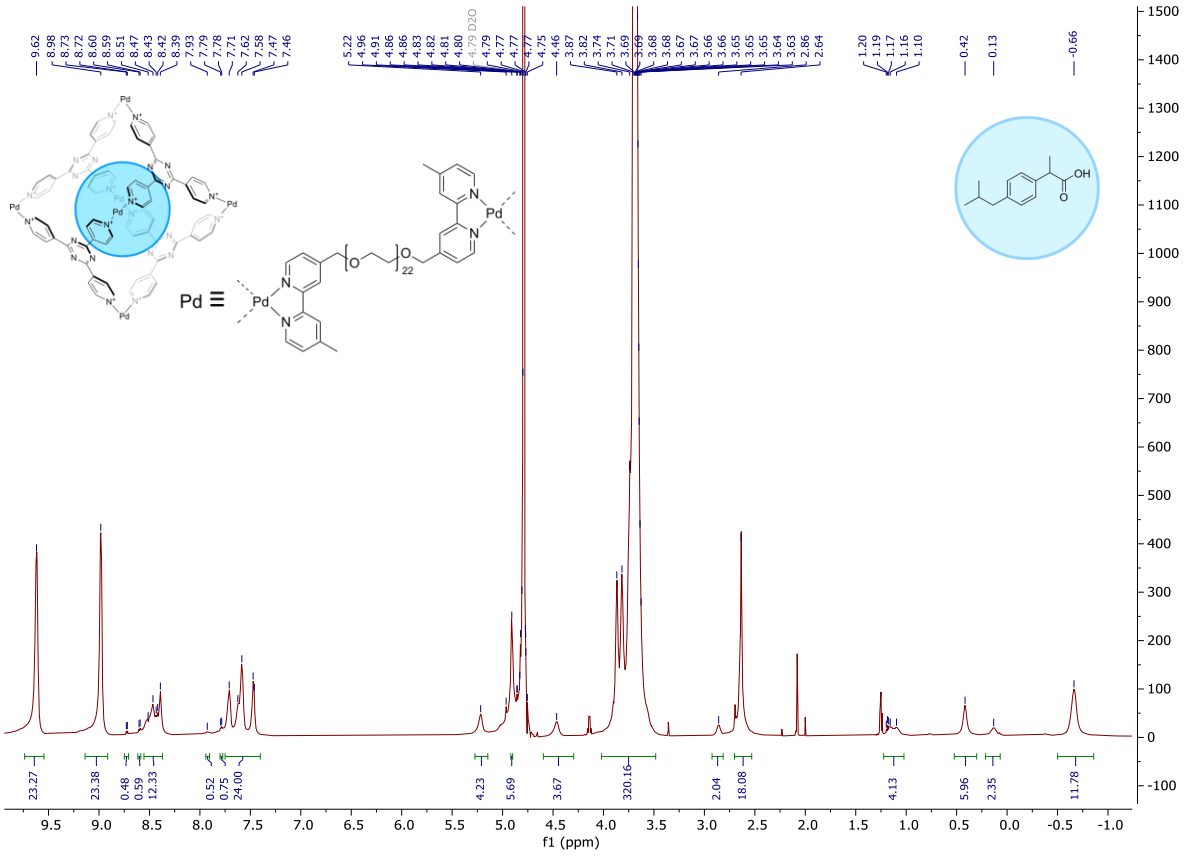

*Figure 281: ^{1}H NMR (600 MHz, D_2O) of **HG_1•(ibuprofen)$_2$** before sonication.*

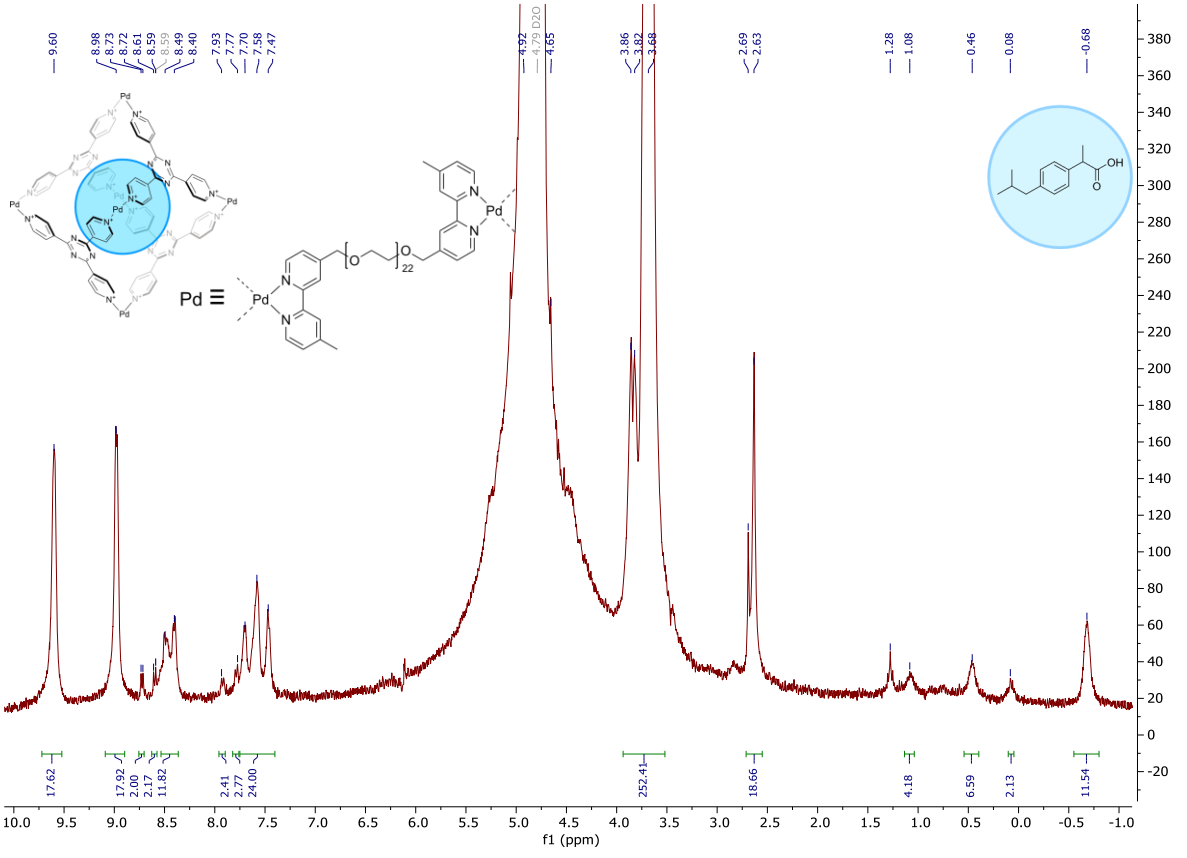

*Figure 282: ^{1}H NMR (600 MHz, D_2O) of **HG_1•(ibuprofen)$_2$** after sonicating 2 h (1 s on, 2 s off).*

HG_3

Empty

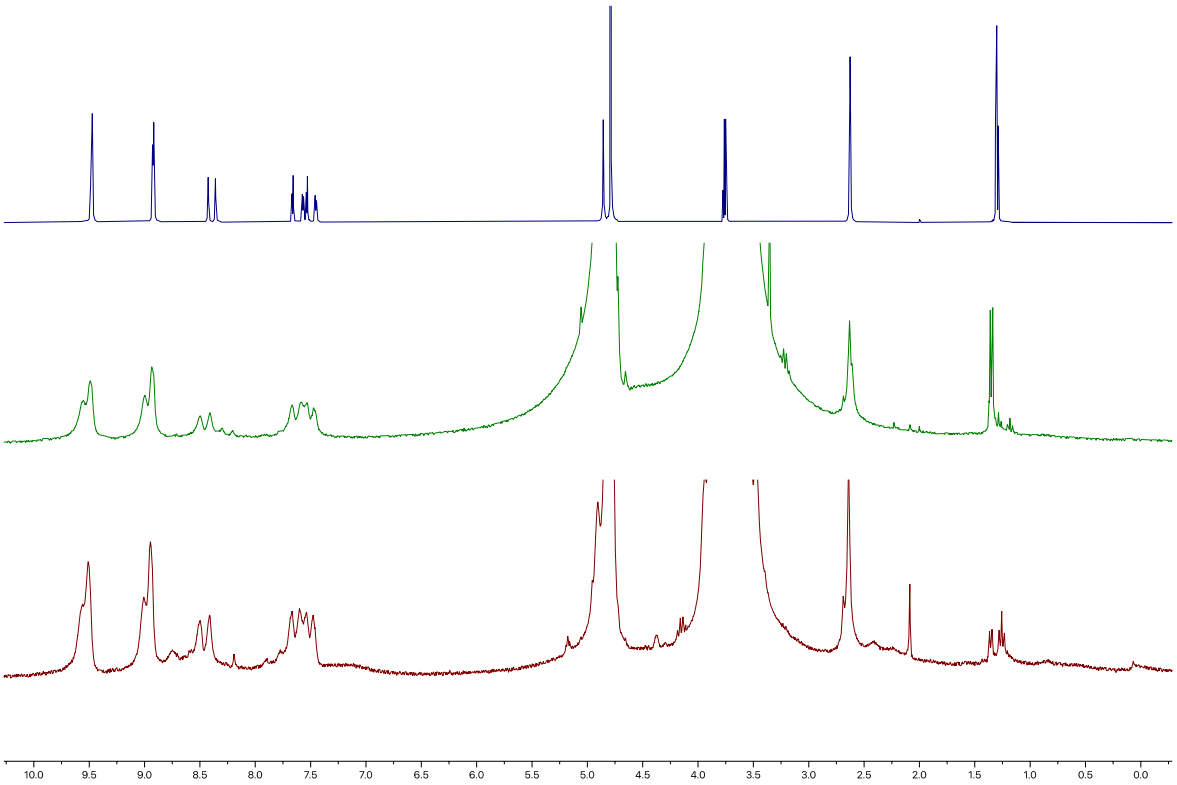

*Figure 283: ^{1}H NMR: Previously reported **MOC_1** (top), **HG_3** before sonication (mid), **HG_3** after sonication (bottom).*

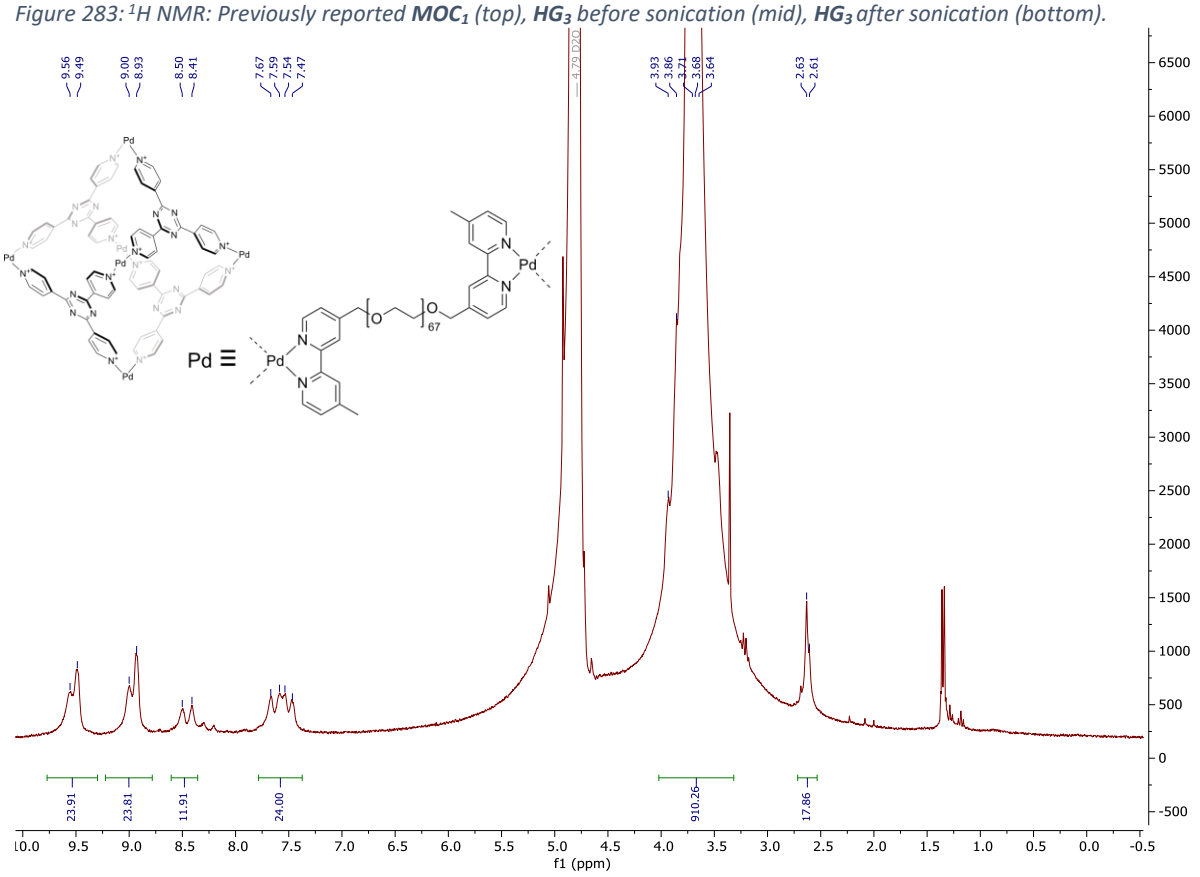

*Figure 284: ^{1}H NMR (300 MHz, D_2O) of **HG_3** before sonication.*

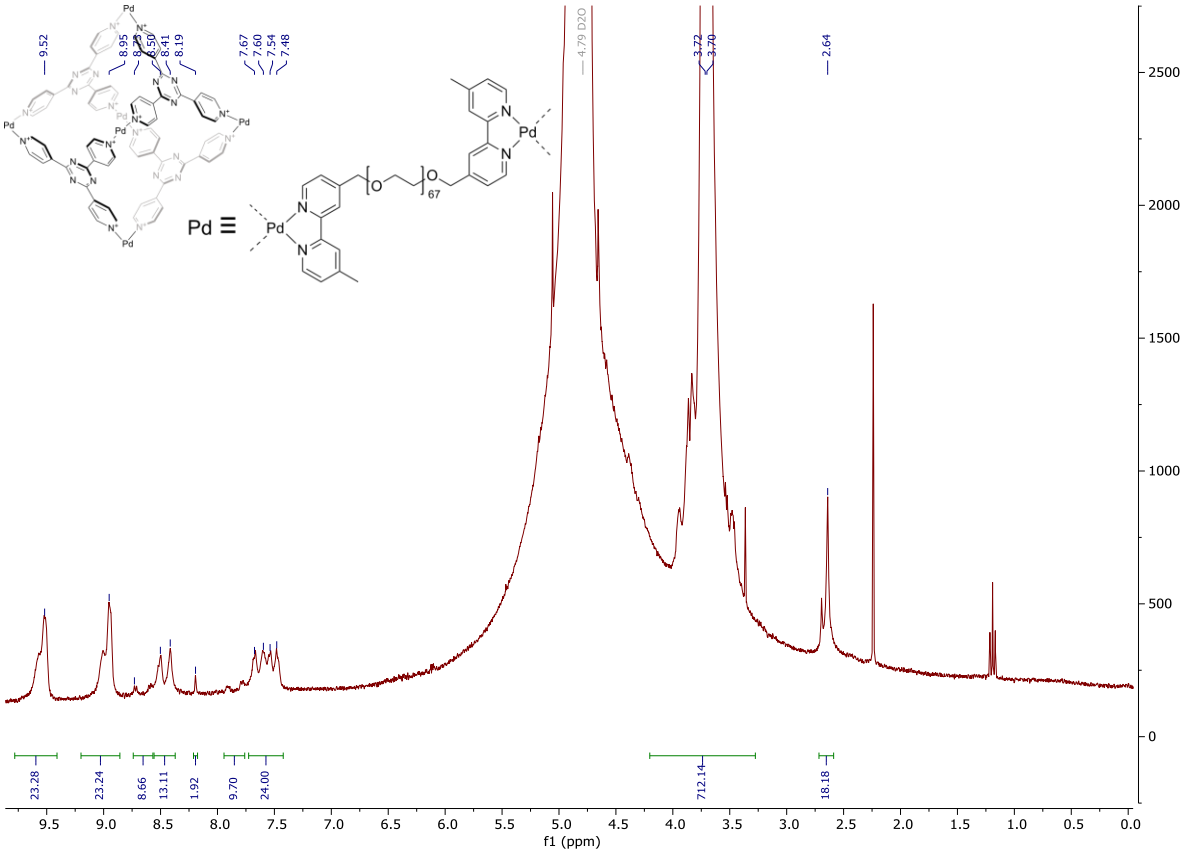

*Figure 285: ^{1}H NMR (300 MHz, D_2O) of **HG$_3$** after sonicating for 2 h (1 s on, 1 s off).*

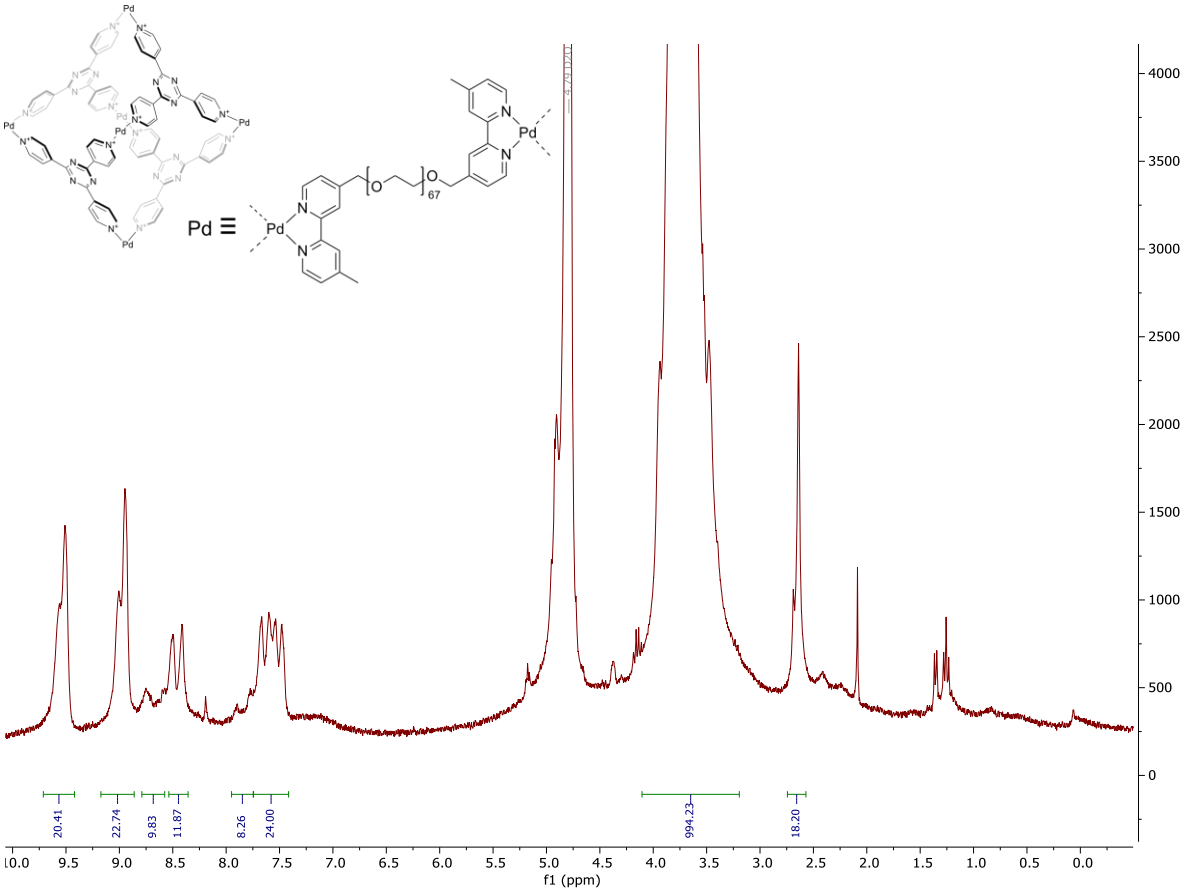

*Figure 286: ^{1}H NMR (300 MHz, D_2O) of **HG$_3$** after sonicating for 3 h (1 s on, 1 s off).*

Ibuprofen

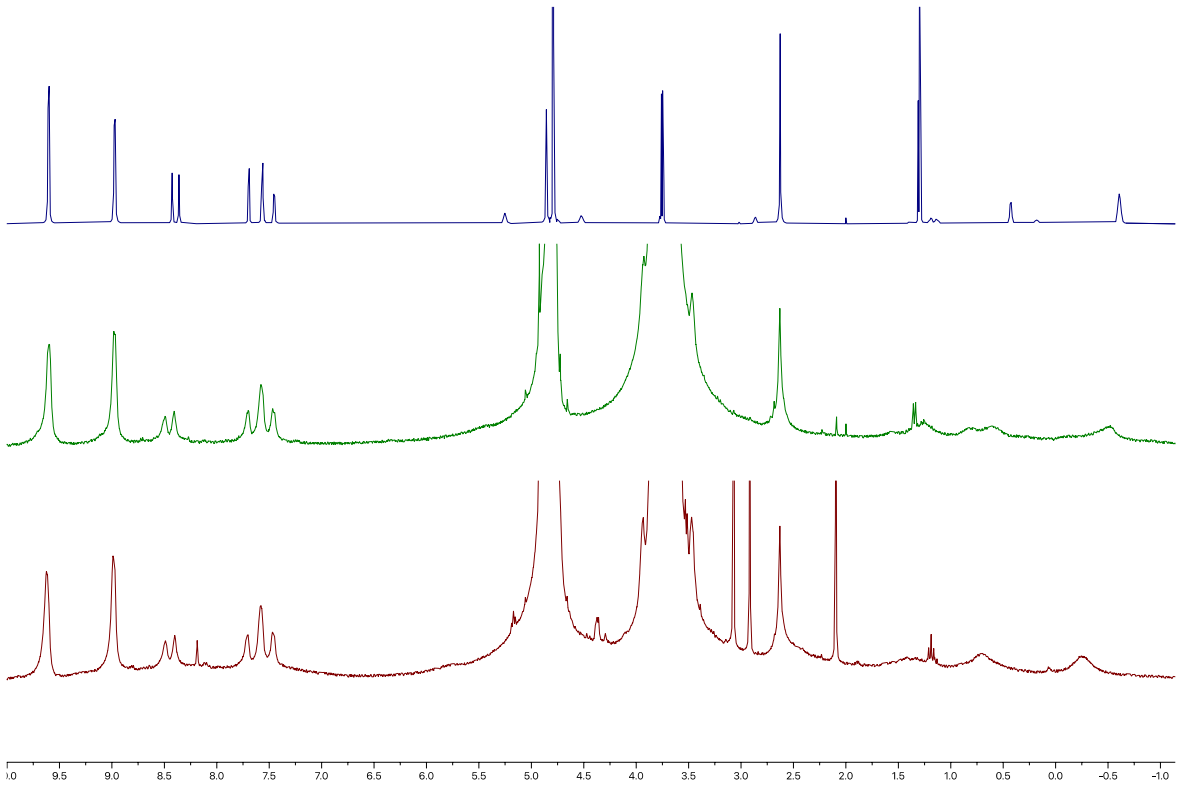

Figure 287: Previously reported ***MOC$_1$•(ibuprofen)$_2$*** *(top),* ***HG$_3$•(ibuprofen)$_2$*** *before sonication (mid),* ***HG$_3$•(ibuprofen)$_2$*** *after sonication (bottom).*

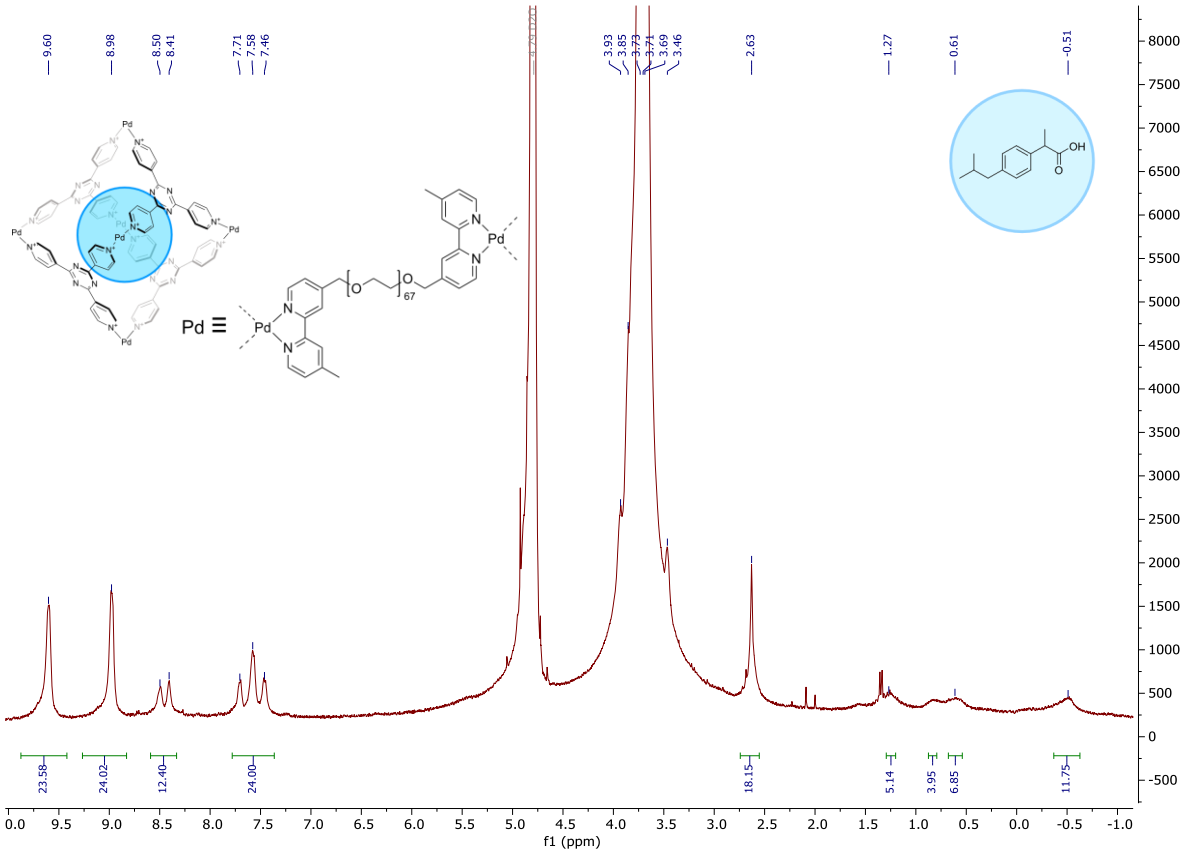

*Figure 288: ^{1}H NMR (300 MHz, D_2O) of **HG_3•(ibuprofen)$_2$** before sonication.*

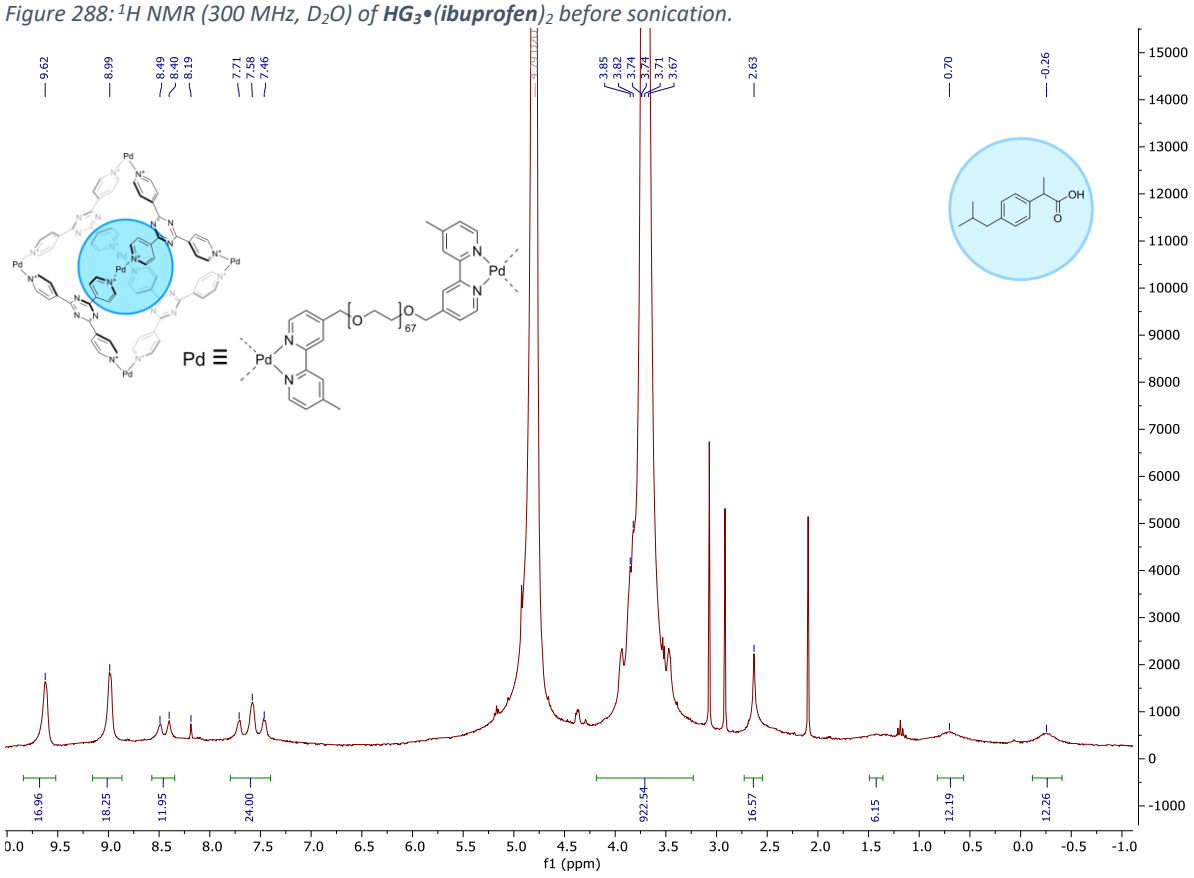

*Figure 289: ^{1}H NMR (300 MHz, D_2O) of **HG_3•(ibuprofen)$_2$** after sonicating for 3 h (1 s on, 1 s off).*

Progesterone

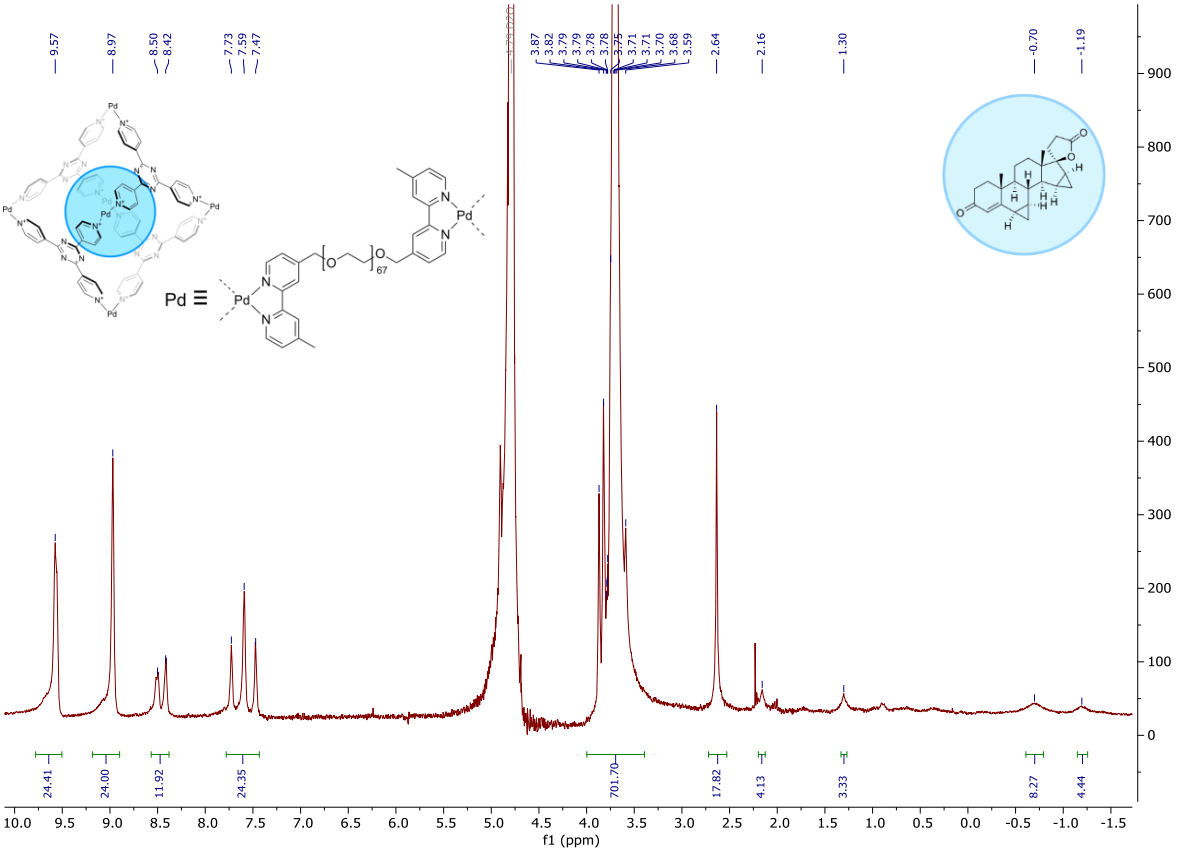

*Figure 290: ^{1}H NMR (600 MHz, D_2O) of **HG_3•(progesterone)**. Not all signals of progesterone could be assigned.*

Drospirenone

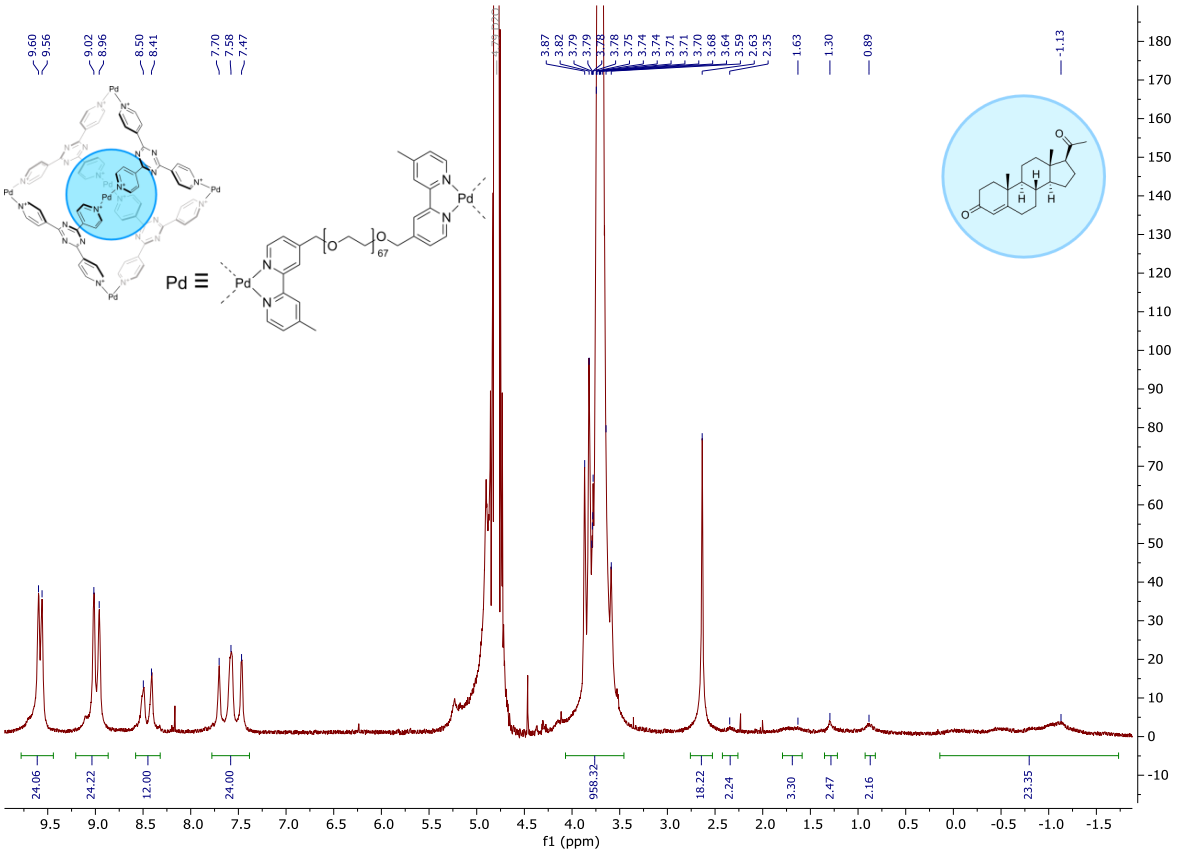

*Figure 291: ^{1}H NMR (600 MHz, D_2O) of **HG_3•(drospirenone)**. Not all signals of progesterone could be assigned.*

HG_6

Empty

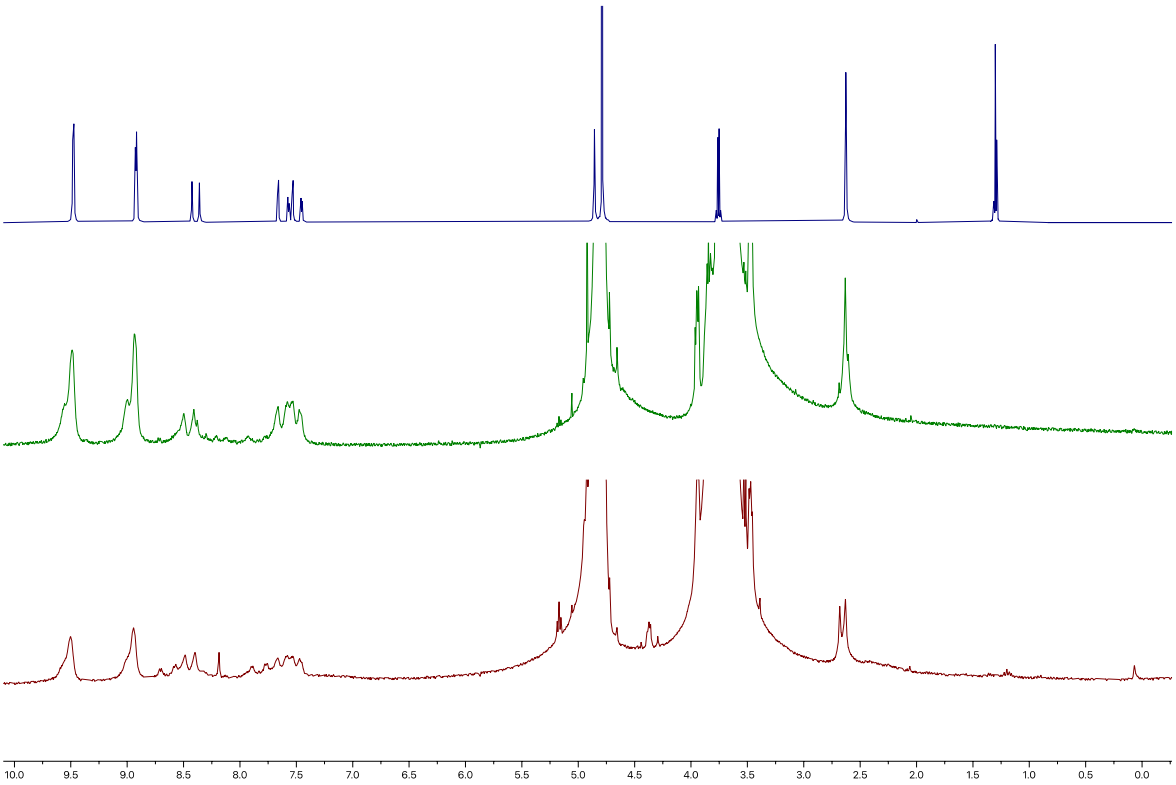

*Figure 292: ^{1}H NMR: Previously reported **MOC_1** (top), **HG_6** before sonication (mid), **HG_6** after sonication (bottom).*

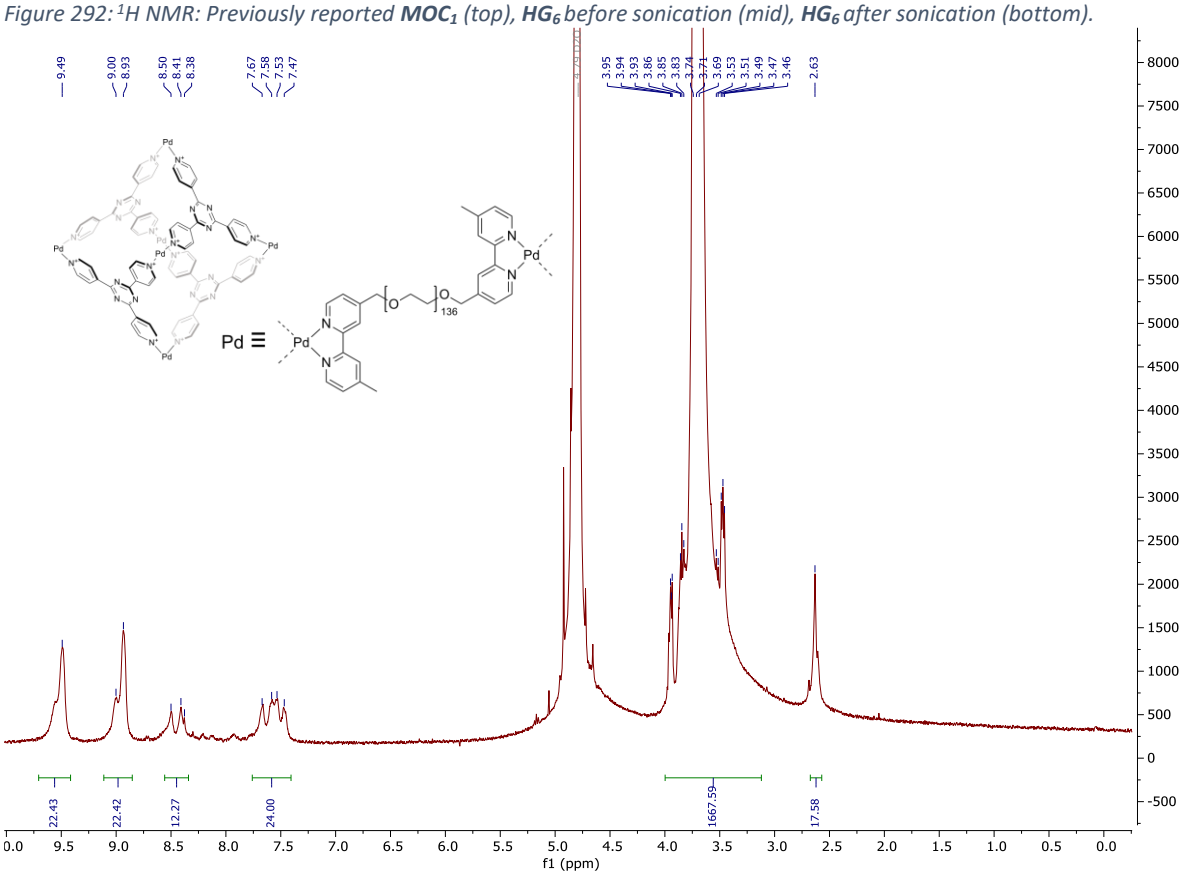

*Figure 293: ^{1}H NMR (300 MHz, D_2O) of **HG_6** before sonication.*

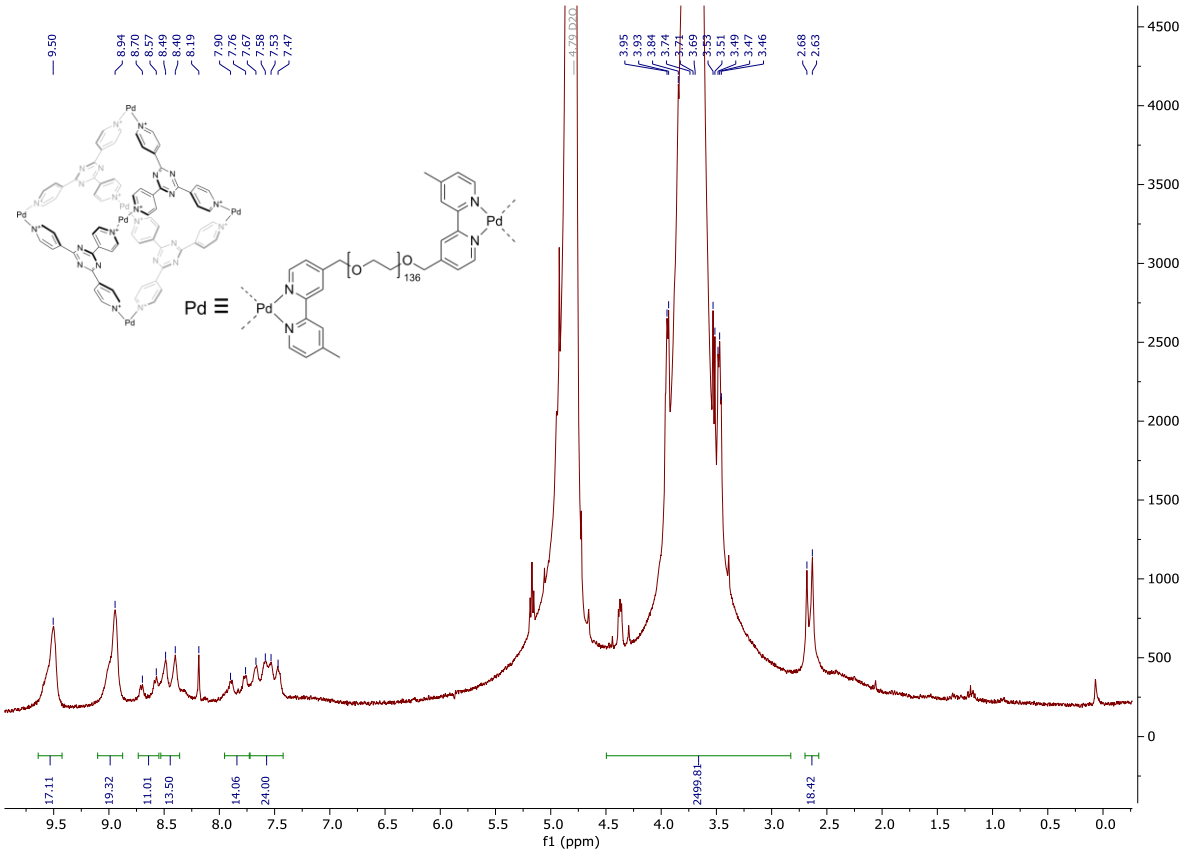

*Figure 294: ^{1}H NMR (300 MHz, D_2O) of **HG_6** after sonicating for 3 h (1 s on, 1 s off).*

Ibuprofen

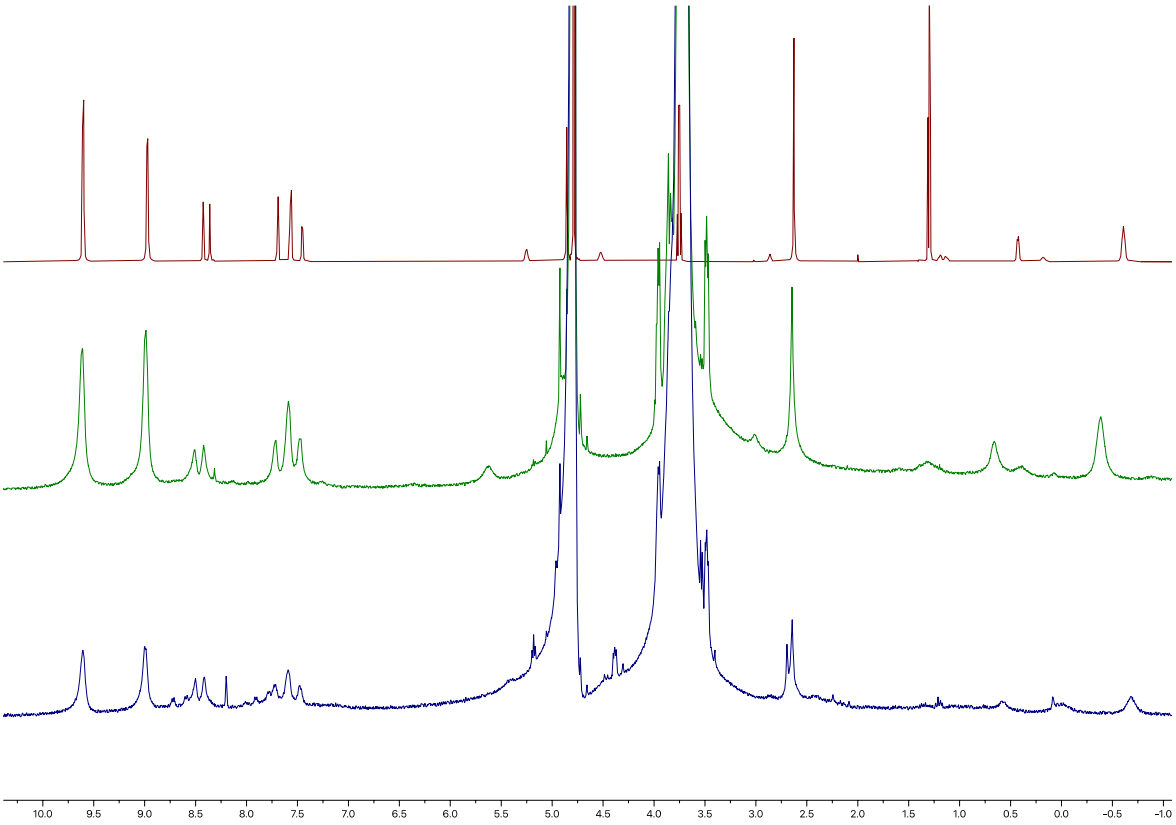

*Figure 295: ^{1}H NMR: Previously reported **MOC$_1$•(ibuprofen)$_2$** (top), **HG$_6$•(ibuprofen)$_2$** before sonication (mid), **HG$_6$•(ibuprofen)$_2$** after sonication (bottom).*

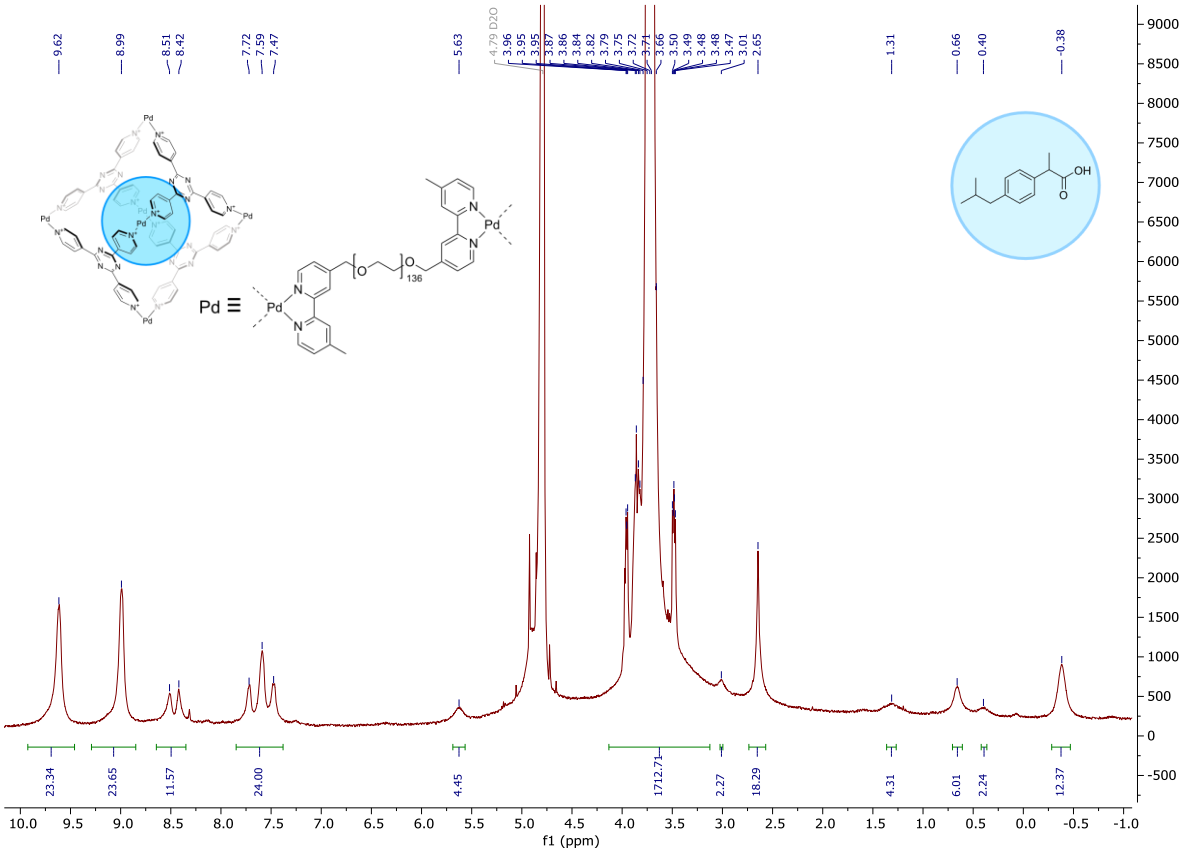

*Figure 296: ^{1}H NMR (300 MHz, D_2O) of **HG$_6$•(ibuprofen)$_2$** before sonication.*

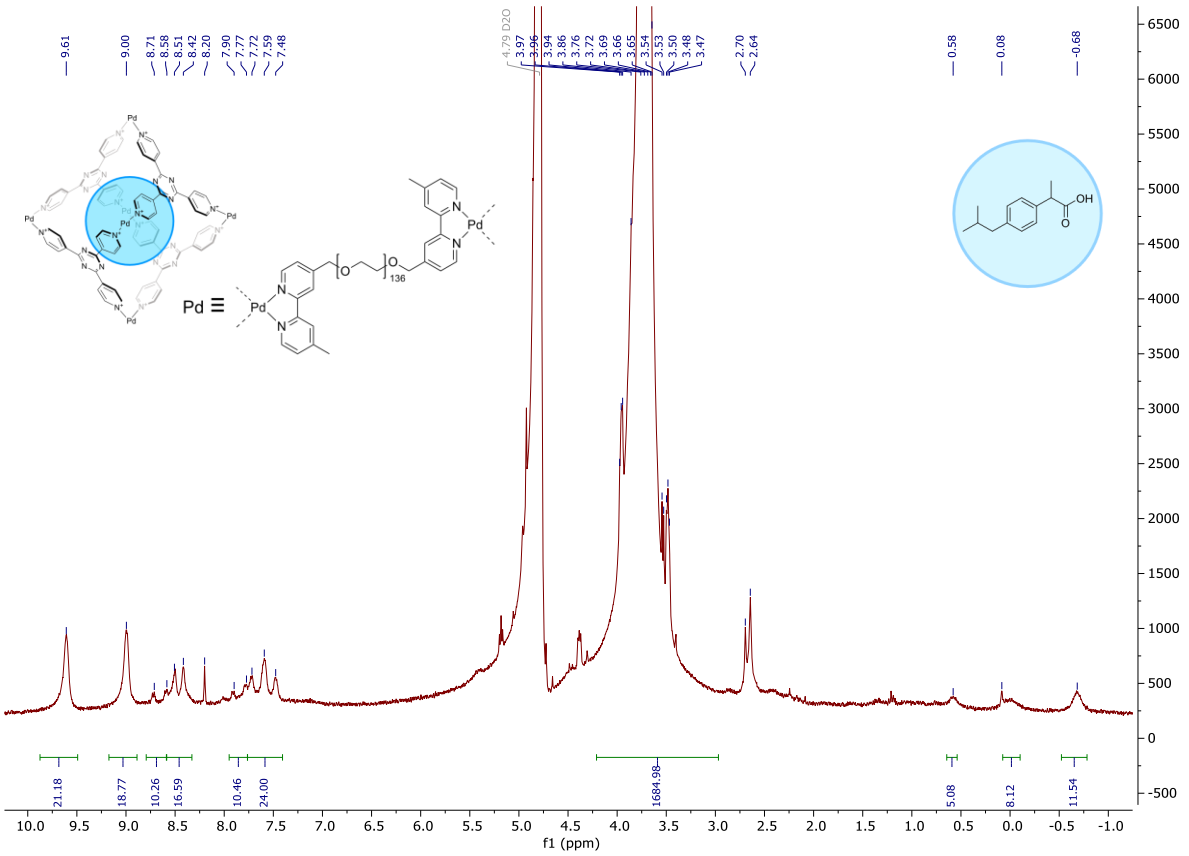

*Figure 297: ^{1}H NMR (300 MHz, D_2O) of **HG$_6$•(ibuprofen)$_2$** after sonicating for 3 h (1 s on, 1 s off).*

Empty with reference

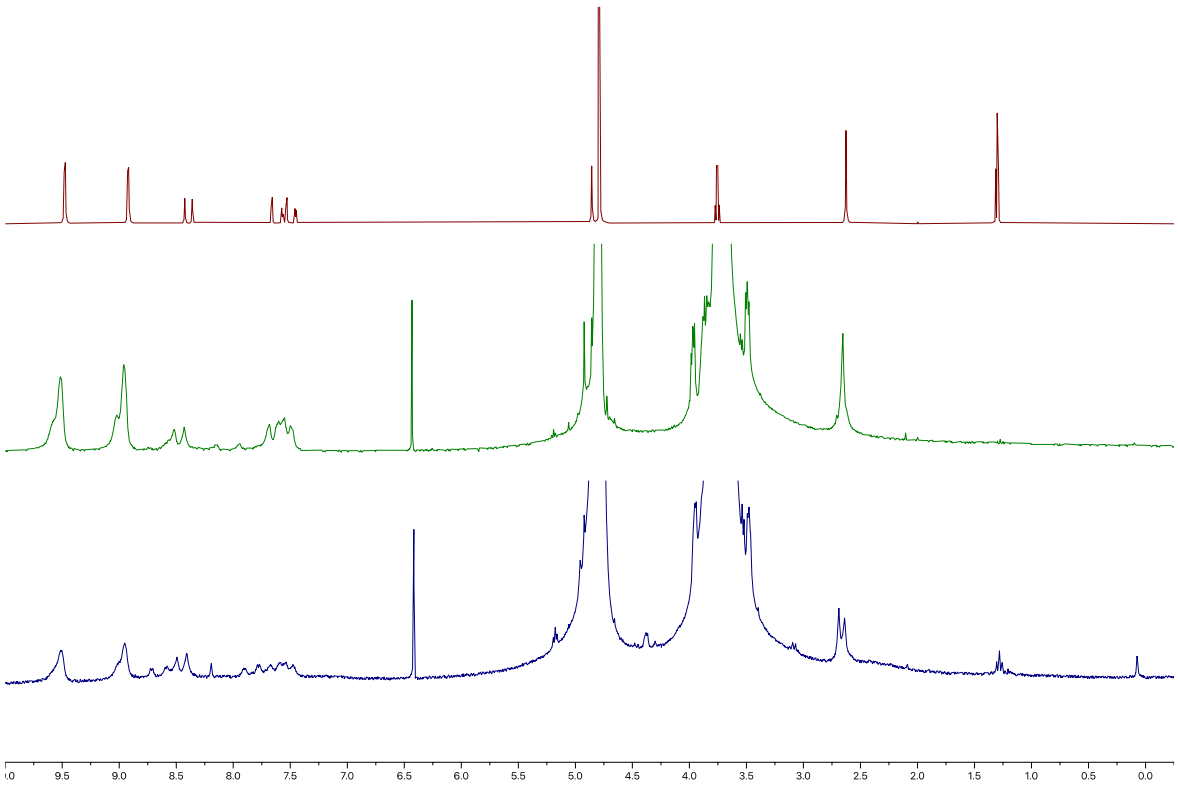

*Figure 298: ^{1}H NMR: Previously reported **MOC_1** (top), **HG_6** with maleic acid as external reference before sonication (mid), **HG_6** with maleic acid as external reference after sonication (bottom).*

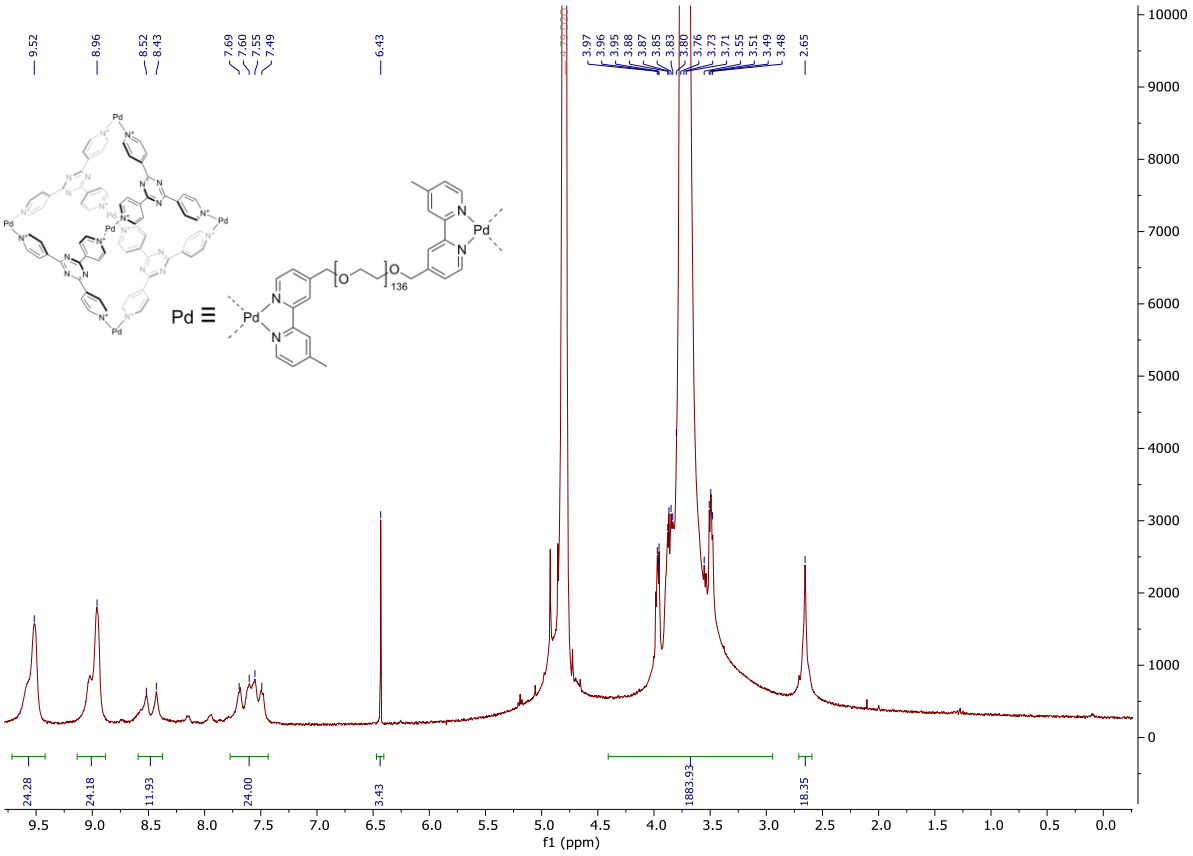

*Figure 299: ^{1}H NMR (300 MHz, D_2O) of **HG_6** with maleic acid as external reference before sonication. For this NMR 9.8 mg of the sample were dissolved in 0.7 ml D_2O.*

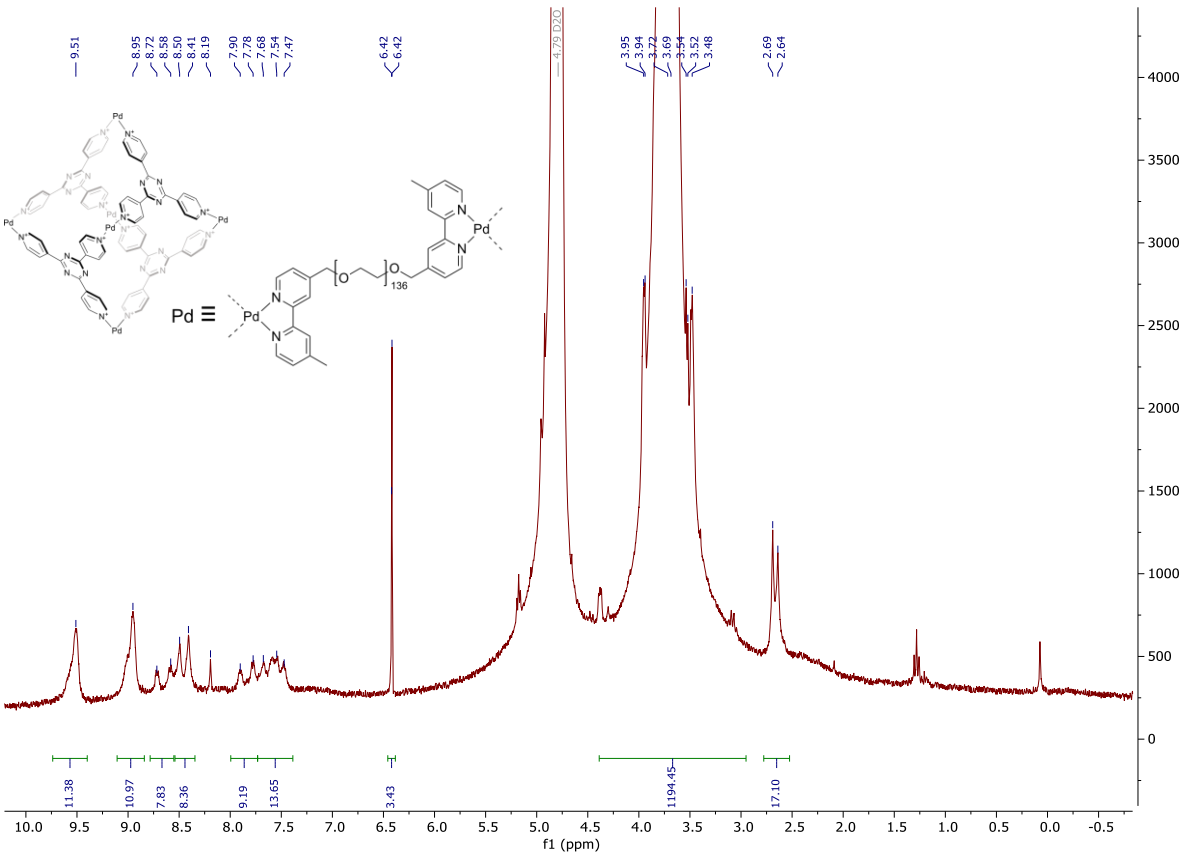

*Figure 300: ^{1}H NMR (300 MHz, D_2O) of **HG_6** with maleic acid as external reference after sonicating for 3 h (1 s on, 1 s off). For this NMR 9.8 mg of the sample were dissolved in 0.7 ml D_2O.*

Ibuprofen with reference

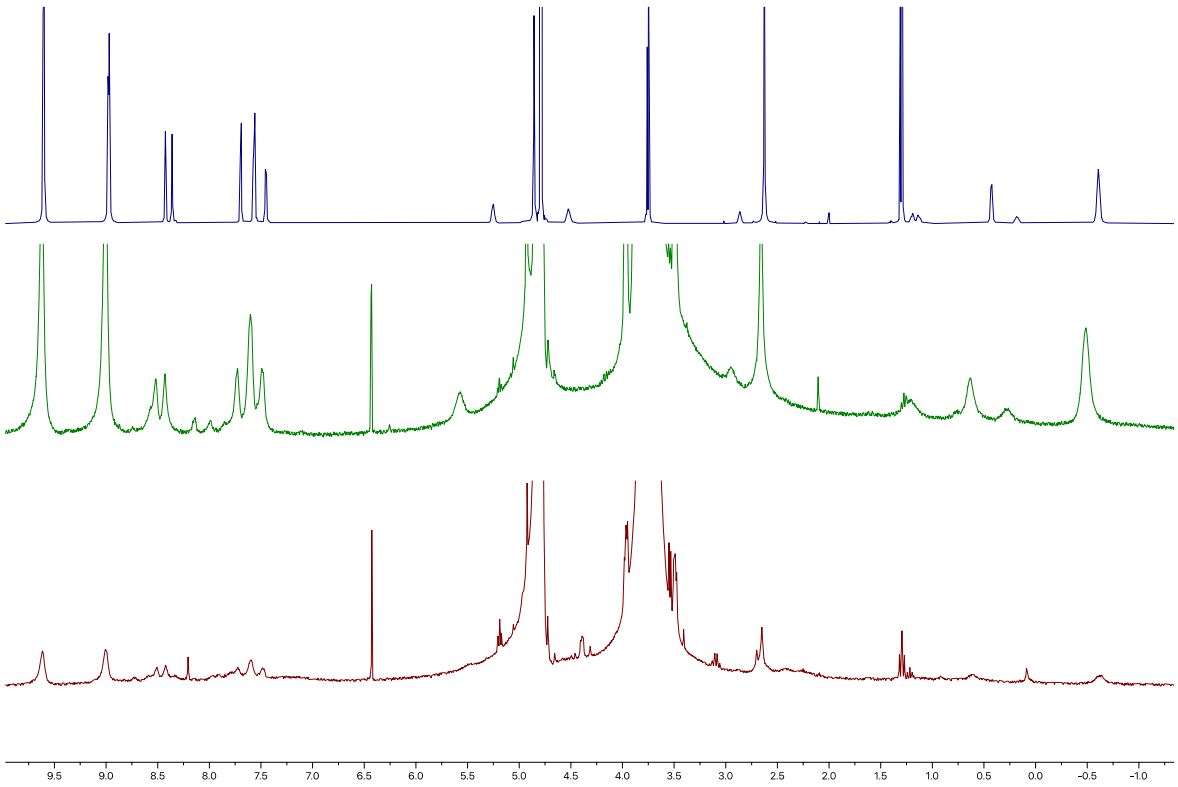

*Figure 301: ^{1}H NMR: Previously reported **MOC$_1$**•(ibuprofen)$_2$ (top), **HG$_6$**•(**ibuprofen**)$_2$ with maleic acid as external reference before sonication (mid), **HG$_6$**•(**ibuprofen**)$_2$ with maleic acid as external reference after sonication (bottom).*

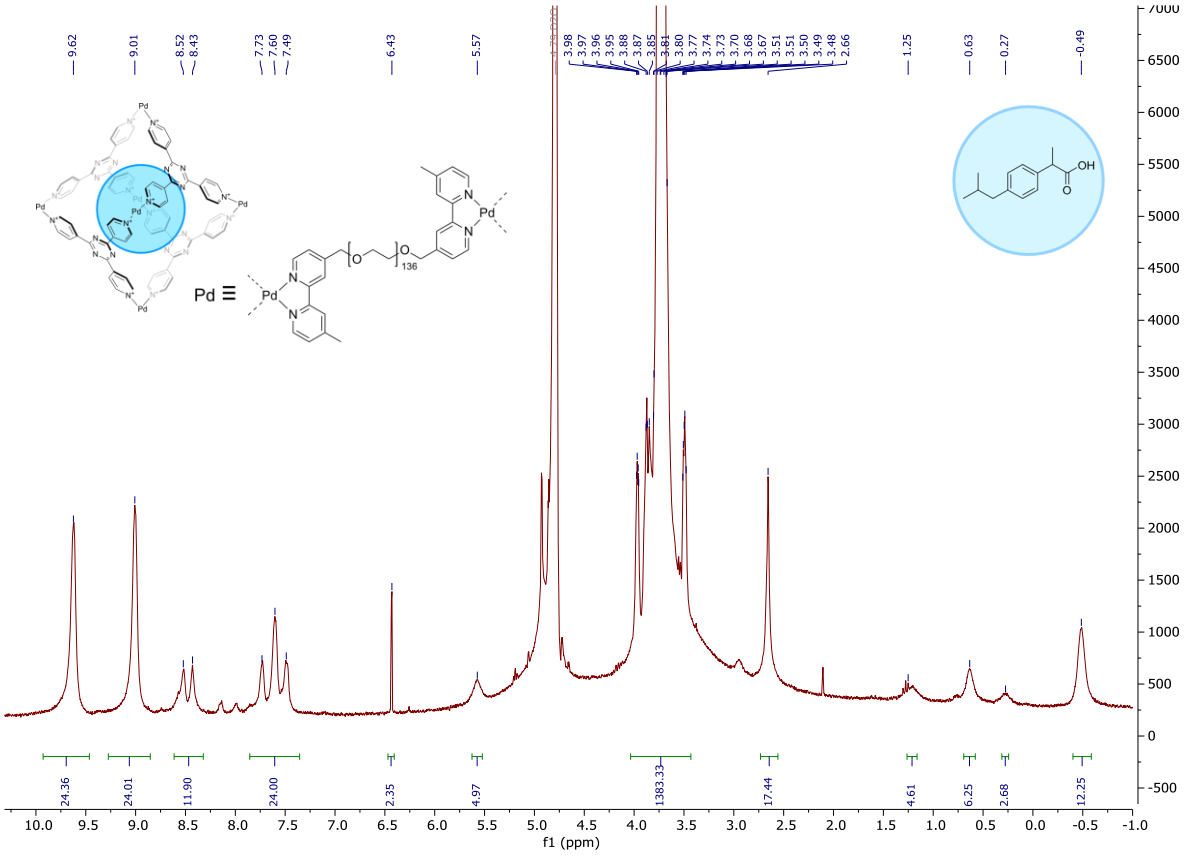

*Figure 302: ^{1}H NMR (300 MHz, D_2O) of **HG_6•(ibuprofen)$_2$** with maleic acid as external reference before sonication. For this NMR 10.9 mg of the sample were dissolved in 0.7 ml D_2O.*

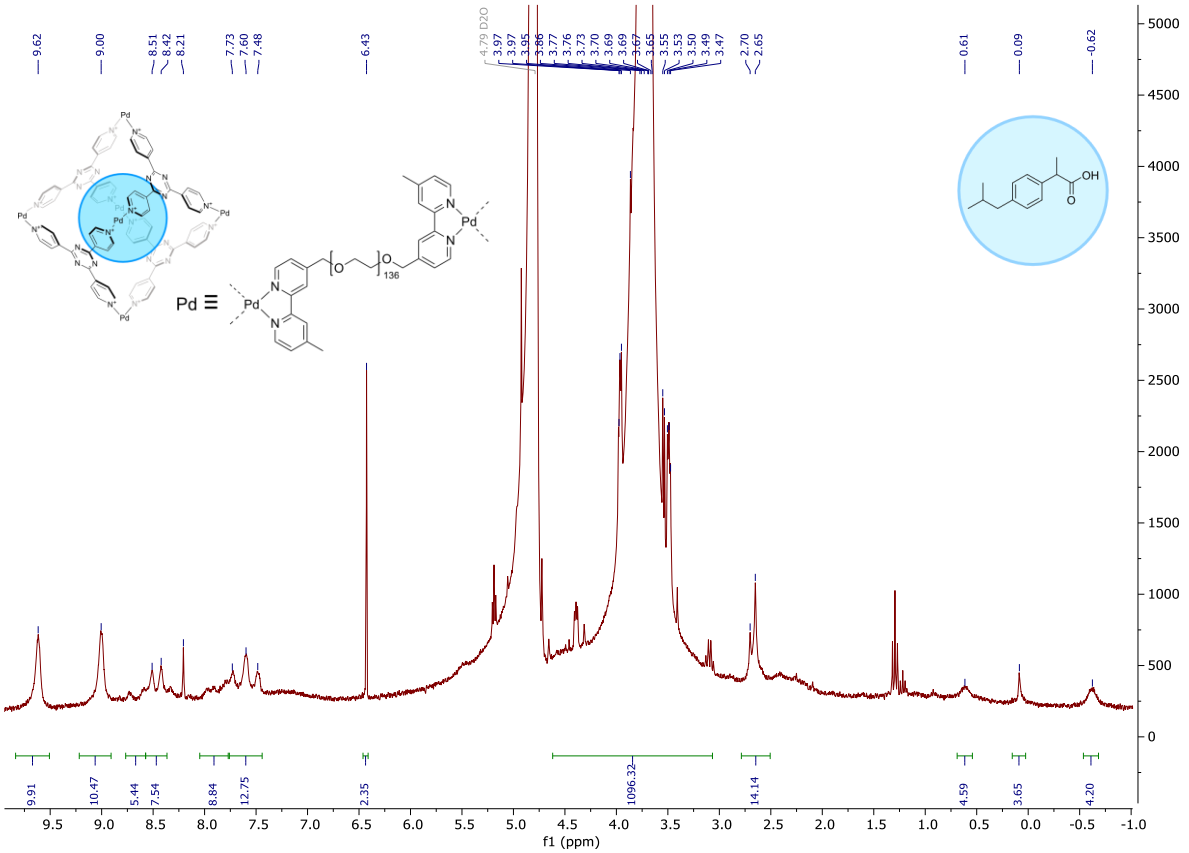

*Figure 303: ^{1}H NMR (300 MHz, D_2O) of **HG_6•(ibuprofen)$_2$** with maleic acid as external reference after sonicating for 3 h (1 s on, 1 s off). For this NMR 10.9 mg of the sample were dissolved in 0.7 ml D_2O.*

7 References

[1] COVID-19 Excess Mortality Collaborators, *Lancet*, 2022, *399*, 1513-1536.

[2] O. J. Watson, G. Barnsley, J. Toor, A. B. Hogan, P. Winskill, A. C. Ghani, *Lancet Infect. Dis.,* 2022, *9*, 1293-1302.

[3] J. R. Brown, J. L. Thornton, *Br. J. Ind. Med*., 1957, *14*, 68-70.

[4] Global Burden of Disease 2019 Cancer Collaboration, *JAMA Oncology*, 2022, *8*, 420-444.

[5] E. C. Hayden, *Nature*, 2009, *458*, 686-687.

[6] C. Pucci, C. Martinelli, G. Ciofani, *ecancer*, 2019, *13*, 961.

[7] GlobalSurg Collaborative and National Institute for Health Research Global Health Research Unit on Global Surgery, *Lancet*, 2021, *397*, 387-397.

[8] A. Roy, S.-D. Li, *Wiley Interdiscip. Rev. Nanomed. Nanobiotechnol.*, 2016, *8*, 891-908.

[9] D. T. Debela, S. G. Muzazu, K. D. Heraro, M. T. Ndalama, B. W. Mesele, D. C. Haile, S. K. Kitui, T. Manyazewal, *SAGE Open Med*., 2021, *9*, 20503121211034366.

[10] D. Peer, J. M. Karp, S. Hong et al., *Nat. Nanotechnol.*, 2007, *2*, 751.

[11] a) J. Li, D. Mooney, *Nat. Rev. Mater.*, *2016, 1*, 16071; b) T. R. Hoare, D. S. Kohane, *Polymer*, 2008, *49*, 1993e2007.

[12] J. K. Patra, G. Das, L. F. Fraceto, E. V. R. Campos, M. d. P. Rodriguez-Torres, L. S. Acosta-Torres, L. A. Diaz-Torres, R. Grillo, M. K. Swamy, S. Sharma, S. Habtemariam, H.-S. Shin, *J. Nanobiotechnol*., 2018, *16*, 71.

[13] X. Shi, K. Sun, J. R. Baker, *Phys. Chem. C*, 2008, *112*, 8251-8258.

[14] J. A. Foster, R. M. Parker, A. M. Belenguer, N. Kishi, S. Sutton, C. Abell, J. R. Nitschke*, J. Am. Chem. Soc.*, 2015, *137*, 9722-9729.

[15] N. Nasongkla, X. Shuai, H. Ai, B. D. Weinberg, J. Pink, D. A. Boothman, J. Gao, *Angew. Chem. Int. Ed*., 2004, *46*, 6323-6327.

[16] M. L. Jean, M.J. Fréchet, *Pharm. Sci. Technol. Today, 1999, 2*, 393-401.

[17] H. Lu, J. Wang, T. Wang, J. Zhong, Y. Bao, H. Hao, *J. Nanomater.*, 2016, 5762431.

[18] L. Qiao, H. Yang, S. Gao, L. Li, X. Fu, Q. Wei J., *Mater. Chem. B*, 2022, *10*, 1908-1922.

[19] J. H. Lee, Y. Yeo, *Chem. Eng. Sci.*, 2014, *24*, 75-84.

[20] a) L. Xu, L. Qiu, Y. Sheng, Y. Sun, L. Deng, X. Li, M. Bradley, R. Zhang, *J. Mater. Chem. B*, 2018, *6*, 510-517; b) S. M. Jansze, K. Severin, *J. Am. Chem. Soc.*, 2019, *141*, 815-819; c) S. M. Jansze, G. Cecot, K. Severin, *Chem. Sci.*, 2018, *9*, 4253-4257.

[21] G. Ma, W. Lin, Z. Yuan, J. Wu, H. Qian, L. Xua, S. Chen, *J. Mater. Chem. B*, 2017, *5*, 935-943.

[22] a) S. J. Wezenberg, Chem. Lett. 2020, 49, 609-615; b) L. Wang, Q. Lia, *Chem. Soc. Rev*., 2018, *47*, 1044-1097; c) A. J. McConnell, C. S. Wood, P. P. Neelakandan, J. R. Nitschke, *Chem. Rev*., 2015, *115*, 7729-7793.

[23] Z. A.-Ahmady, K. Kostarelos, *Chem. Rev*. 2016, *116*, 3883-3918.

[24] R. Küng, T. Pausch, D. Rasch, R. Göstl, B. M. Schmidt, *Angew. Chem. Int. Ed*., 2021, *60*, 13626-13630.

[25] a) S. H. Yun, S. J. J. Kwok, *Nat. Biomed*. *Eng*., 2017, *1*, 0008; b) W. A. Velema, W. Szymanski, B. L. Feringa, *J. Am. Chem. Soc.*, 2014, *136*, 2178-2191; c) K. Hüll, J. Morstein, D. Trauner, *Chem. Rev.*, 2018, *118*, 10710-10747.

[26] a) S. E. Ahmed, A. M. Martins, G. A. Husseini, *J. Drug. Target.*, 2015, *23*, 16-42; b) C. P. Phenix, M. Togtema, S. Pichardo, I. Zehbe, L. Curiel, *J. Pharm. Pharm. Sci.*, 2014, *17*, 136-153.

[27] S. Mitragotri, *Nat. Rev. Drug Discov.*, 2005, *4*, 255-260.

[28] Y. K. Kryschenko, S. R. Seidel, A. M. Arif, P. J. Stang, *J. Am. Chem. Soc.,* 2003, *125*, 5193-5198.

[29] P. J. Stang, *J. Am. Chem. Soc*. 2012, *134*, 11829-11830.

[30] R. Chakrabarty, P. S. Mukherjee, P. J. Stang, *Chem. Rev.*, 2011, *111*, 6810-6918.

[31] D. L. Caulder, K. N. Raymond, *Acc. Chem. Res.*, 1999, *32*, 975-982.

[32] B. J. Holliday, C. A. Mirkin, *Angew. Chem. Int. Ed.*, 2001, *40*, 2022-2043.

[33] M. Fujita, K. Umemoto, M. Yoshizawa, N. Fujita, T. Kusukawa, K. Biradha, *Chem. Commun.*, 2001, 509-518.

[34] P. J. Stang, D. H. Cao, *J. Am. Chem. Soc.*, 1994, *116*, 4981.

[35] a) M. Fujita, J. Yazaki, K. Ogura, *J. Am. Chem. Soc.*, 1990, *112*, 5645; b) M. Fujita, J. Yazaki, K. Ogura, *Chem. Lett.*, 1991, 1031.

[36] S. R. Seidel, P. J. Stang, *Acc. Chem. Res.*, 2002, *35*, 972-983.

[37] R. W. Saalfrank, A. Stark, K. Peters, H. G. von Schnering, *Angew. Chem. Int. Ed. Engl.*, 1988, *27*, 851-853.

[38] M. Fujita, D. Oguro, M. Miyazawa, H. Oka, K. Yamaguchi, K. Ogura, *Nature*, 1995, *378*, 469-471.

[39] F. Ibukuro, T. Kusukawa, M. Fujita, *J. Am. Chem. Soc.*, 1998, *120*, 8561-8562.

[40] K. Umemoto, K. Yamaguchi, M. Fujita, *J. Am. Chem. Soc.*, 2000, *122*, 7150-7151.

[41] N. Takeda, K. Umemoto, K. Yamaguchi, M. Fujita, *Nature*, 1999, *398*, 794-796.

[42] N. Fujita, K. Biradha, M. Fujita, S. Sakamoto, K. Yamaguchi, *Angew. Chem. Int. Ed.*, 2001, *40*, 1718.

[43] F. J. Rizzuto, J. P. Carpenter, J. R. Nitschke, *J. Am. Chem. Soc.*, 2019, *141*, 9087-9095.

[44] T. R. Cook, Y.-R. Zheng, P. J. Stang, *Chem. Rev.*, 2013, *113*, 734-777.

[45] O. Bistri O. Reinaud, *Org. Biomol. Chem.*, 2015, *13*, 2849-2865.

[46] M. Fujita, K. Ogura, *Bull. Chem. Soc. Jpn.*, 1996, *69*, 1471-1482.

[47] E. G. Percástegui, T. K. Ronson, J. R. Nitschke, *Chem. Rev.*, 2020, *120*, 13480-13544.

[48] Y. Fang, T. Murase, S. Sato, M. Fujita, *J. Am. Chem. Soc.*, 2013, *135*, 613-615.

[49] S.-Y. Yu, T. Kusukawa, K. Biradha, M. Fujita, *J. Am. Chem. Soc.*, 2000, *122*, 2665-2666.

[50] M. Fujita, M. Tominaga, A. Hori, B. Therrien, *Acc. Chem. Res.*, 2005, *38*, 369-378.

[51] A. I. Hanopolskyi, S. De, M. J. Białek, Y. Diskin-Posner, L. Avram, M. Feller, R. Klajn, *Beilstein J. Org. Chem.*, 2019, *15*, 2398-2407.

[52] A. Kumar, P. S. Mukherjee, *Chem. Eur. J.*, 2020, *26*, 4842-4849.

[53] a) P. Mal, D. Schultz, K. Beyeh, K. Rissanen, J. R. Nitschke, *Angew. Chem. Int. Ed.*, 2008, *47*, 8297-8301; b) D. Zhang, T. K. Ronson, J. R. Nitschke, *Acc. Chem. Res.*, 2018, *51*, 2423-2436.

[54] a) N. Kishi, Z. Li, K. Yoza, M. Akita, M. Yoshizawa, *J. Am. Chem. Soc.*, 2011, *133*, 11438-11441; b) M. Yamashina, Y. Sei, M. Akita, M. Yoshizawa, *Nat. Commun.*, 2014, *5*, 4662; c) K. Yazaki, M. Akita, S. Prusty, D. K. Chand, T. Kikuchi, H. Sato, M. Yoshizawa, *Nat. Commun.*, 2017, *8*, 1591.

[55] N. J. Oldenhuis, K. P Qin, S. Wang, H.-Z. Ye, E. A. Alt, A. P. Willard, T. V. Voorhis, S. L. Craig, Jeremiah A. Johnson, *Angew. Chem. Int. Ed.*, 2020, *59*, 2784-2792.

[56] D. Rasch, R. Göstl, *ACS Polym. Au*, 2021, *1*, 59-66.

[57] A. Charlet, V. Lutz-Bueno, R. Mezzenga, E. Amstad, *Nanoscale*, 2021, *13*, 4073.

[58] L. A. Estroff, A. D. Hamilton, *Chemical Reviews*, 2004, *104*, 3.

[59] a) M. Hamidi, A. Azadi, P. Rafiei, *Adv. Drug Deliv. Rev.*, 2008, 1638-1649; b) S. D. Palanivelu, N. A. Z. Armir, A. Zulkifli, A. H. A. Hair, K. M. Salleh, K. Lindsey, M. H. Che-Othman, S. Zakaria, *Polymers*, 2022, *14*, 2590; c) W. He, M. Reaume, M. Hennenfent, B. P. Lee, R. Rajachar, *Biomater. Sci.*, 2020, *8*, 3248.

[60] a) T. Aida, E. W. Meijer, S. I. Stupp, *Science*, 2012, *335*, 813; b) X. Yu, L. Chen, M. Zhang, T. Yi *Chem. Soc. Rev.*, 2014, *43*, 5346-5371; c) M. Burnworth, L Tang, J. R. Kumpfer, A. J. Duncan, F. L. Beyer, G. L. Fiore, S. J. Rowan, C. Weder, *Nature*, 2011, *472*, 334-337; d) B. Li, T. He, Y. Fan, X. Yuan, H. Qiu, S. Yin, *Chem. Commun.*, 2019, *55*, 8036-8059.

[61] N. Hosono, S. Kitagawa, *Acc. Chem. Res.*, 2018, *51*, 2437-2446.

[62] J. A. Foster, R. M. Parker, A. M. Belenguer, N. Kishi, S. Sutton, C. Abell, J. R. Nitschke, *J. Am. Chem. Soc.*, 2015, *137*, 9722-9729.

[63] A. V. Zhukhovitskiy, M. Zhong, E. G. Keeler, V. K. Michaelis, J. E. P. Sun, M. J. A. Hore, D. J. Pochan, R. G. Griffin, A. P. Willard, J A. Johnson, *Nat. Chem.*, 2016, *8*, 33-41.

[64] Y. Gu, E. A. Alt, H. Wang, X. Li, A. P. Willard, J. A. Johnson, *Nature*, 2018, *560*, 65-69.

[65] R.-J. Li, C. Pezzato, C. Berton, K. Severin, *Chem. Sci.*, 2021, *12*, 498.

[66] a) M. D. Pluth, K. N. Raymond, *Chem. Soc. Rev.*, 2007, *36*, 161-171; b) H.-J. Schneider, *Angew. Chem., Int. Ed.*, 2009, *48*, 3924-3977; c) P. Mal, B. Breiner, K. Rissanen, J. R. Nitschke, *Science*, 2009, *324*, 1697-1699.

[67] S. Mecozzi, J. Rebek, *Chem. Eur. J.*, 1998, *4*, 1016–1022.

[68] a) F. Biedermann, W. M. Nau, H.-J. Schneider, *Angew. Chem. Int. Ed.*, 2014, *53*, 11158-11171; b) M. Yoshizawa, T. Kusukawa, M. Kawano, T. Ohhara, I. Tanaka, K. Kurihara, N. Niimura, M. Fujita, *J. Am. Chem. Soc.*, 2005, *127*, 2798-2799.

[69] T. Kusukawa, M. Fujita, *J. Am. Chem. Soc.*, 2002, *124*, 13576-13582.

[70] P. Howlader, B. Mondal, P. C. Purba, E. Zangrando, P. S. Mukherjee, *J. Am. Chem. Soc.*, 2018, *140*, 7952-7960.

[71] A. Casini, B. Woods, M. Wenzel, *Inorg. Chem.*, 2017, *56*, 14715-14729.

[72] B. Therrien, G. Süss-Fink, P. Govindaswamy, A. K. Renfrew, P. J. Dyson, *Angew. Chem.*, 2008, *120*, 3833-3836.

[73] J. E. M. Lewis, E. L. Gavey, S. A. Cameron, J. D. Crowley, *Chem. Sci.*, 2012, *3*, 778-784.

[74] A. Schmidt, V. Molano, M. Hollering, A. Pöthig, A. Casini, F. E. Kühn, *Chem. Eur. J.*, 2016, *22*, 2253-2256.

[75] J. E. M. Lewis, A. B. S. Elliott, C. John McAdam, K. C. Gordon, J. D. Crowley, *Chem. Sci.*, 2014, *5*, 1833-1843.

[76] Y.-R. Zheng, K. Suntharalingam, T. C. Johnstone, S. J. Lippard, *Chem. Sci.*, 2015, *6*, 1189-1193.

[77] N. Deirram, C. H. Zhang, S. S. Kermaniyan, A. P. R. Johnston, G. K. Such, *Macromol. Rapid Commun*. 2019, *40*, 1800917.

[78] K. Hüll, J. Morstein, D. Trauner, *Chem. Rev.*, 2018, *118*, 10710-10747.

[79] S. H. Yun, S. J. J. Kwok, *Nat. Biomed.*, 2017, *1*, 0008.

[80] a) S. Huo, P. Zhao, Z. Shi, M. Zou, X. Yang, E. Warszawik, M. Loznik, R. Göstl, A. Herrmann, *Nat. Chem.*, 2021, *13*, 131-139. b) C. P. Phenix, M. Togtema, S. Pichardo, I. Zehbe, L. Curiel, *J. Pharm. Pharm. Sci.*, 2014, *17*, 136-153; c) F. Kiessling, S. Fokong, J. Bzyl, W. Lederle, M. Palmowski, T. Lammers, *Adv. Drug Deliv. Rev.*, 2014, *72*, 15–27.

[81] a) K. S. Suslick, G. J. Price, *Annu. ReV. Mater. Sci.* 1999, *29*, 295; b) J. M. J. Paulusse, R. P. Sijbesma, *Angew. Chem. Int. Ed.*, 2004, *43*, 4459; c) D. C. Church, G. I. Peterson, A. J. Boydston, A *CS Macro Lett.,* 2014, *3*, 648-651; d) Y. Sha, Y. Zhang, E. Xu, Z. Wang, T. Zhu, S. L. Craig, C. Tang, *ACS Macro Lett.*, 2018, *7*, 1174-1179; e) M. Stratigaki, R. Göstl, *ChemPlusChem*, 2020, *85*, 1095-1103.

[82] a) M. M. Caruso, D. A. Davis, Q. Shen, S. A. Odom, N. R. Sottos, S. R. White, J. S. Moore, *Chem. Rev.* 2009, *109*, 5755-5798. b) A. P. Esser-Kahn, S. A. Odom, N. R. Sottos,S. R. White, J. S. Moore *Macromolecules,* 2011, *44*, 5539-5553.

[83] M. Di Giannantonio, M. A. Ayer, E. Verde-Sesto, M. Lattuada, C. Weder, K. M. Fromm, *Angew. Chem. Int. Ed.*, 2018, *57*, 11445-11450; b) Y. Sha, Y. Zhang, E. Xu, C. Wayne McAlister, T. Zhu, S. L. Craig, C. Tang, *Chem. Sci.*, 2019, *10*, 4959.

[84] R. Küng, R. Göstl, B. M. Schmidt, *Chem. Eur. J.* 2022, *28*, e20210386.

[85] Y. Zhang, Z. Wang, T. B. Kouznetsova, Y. Sha, E. Xu, L. Shannahan, M. Fermen-Coker, Y. Lin, C. Tang, S. L. Craig, *Nat. Chem.*, 2020, *13*, 56-62.

[86] a) A. Piermattei, S. Karthikeyan, R. P. Sijbesma, *Nat. Chem.*, 2009, *1*, 133-137; b) R. T. M. Jakobs R. P. Sijbesma, *Organometallics*, 2012, *31*, 6, 2476-2481; c) R. T. M. Jakobs, S. Ma, R. P. Sijbesma, *ACS Macro Lett.*, 2013, *2*, 613-616.

[87] C. Nagamani, H. Liu, J. S. Moore, *J. Am. Chem. Soc*., 2016, *138*, 2540-2543.

[88] A. Levy, R. Feinstein, C. E. Diesendruck, *J. Am. Chem. Soc*., 2019, *141*, 7256-7260.

[89] a) M. H. Lee, J. L. Sessler, J. S. Kim, *Acc. Chem. Res*., 2015, *48*, 2935-2946; b) Z. Shi, Q. Song, R. Göstl, A. Herrmann, *J. Am. Chem. Soc*., 2020, *142*, 14725-14732; c) Z. Shi, Q. Song, R. Göstl, A. Herrmann, *Chem. Sci*., 2021, *12*, 1668-1674; d) Z. Shi, Q. Song, R. Göstl, A. Herrmann, *CCS Chem*., 2021, *3*, 2333-2344.

[90] Gun Kima, Qiong Wu, James L. Chu, Emily J. Smith, Michael L. Oelze, Jeffrey S. Moore, King C. Li, *PNAS*, 2022, *119*, e2109791119.

[91] M. W. Tibbitt, J. E. Dahlman, R. Langer, *J. Am. Chem. Soc*., 2016, *138*, 704-717.

[92] M. Huo, J. Yuan, L. Tao, Y. Wei, *Polym. Chem*., 2014, *5*, 1519-1528.

[93] F. Kiessling, S. Fokong, P. Koczera, W. Lederle, T. Lammers, *J. Nucl. Med*., 2012, *3*, 345-348.

[94] a) H. Takezawa, T. Murase, G. Resnati, P. Metrangolo, M. Fujita, *Angew. Chem. Int. Ed*., 2015, *54*, 8411-8414; b) H. Takezawa, S. Akiba, T. Murase, M. Fujita, *J. Am. Chem. Soc*., 2015, *137*, 7043-7046; c) H. Takezawa, K. Shitozawa, M. Fujita, *Nat. Chem.*, 2020, *12*, 574-578.

[95] L.-X. Cai, S.-C. Li, D.-N. Yan, L.-P. Zhou, F. Guo, Q.-F. Sun, *J. Am. Chem. Soc*., 2018, *140*, 4869-4876.

[96] Y. Fang, T. Murase, S. Sato, M. Fujita, *J. Am. Chem. Soc*., 2013, *135*, 613-615.

[97] K. L. Berkowski, S. L. Potisek, C. R. Hickenboth, J. S. Moore, *Macromolecules*, 2005, *38*, 8975-8978.

[98] A. T. Dickschat, F. Behrends, S. Surmiak, M. Weiß, H. Eckert, A. Studer, *Chem. Commun.*, 2013, *49*, 2195-2197.

[99] R. Fawzi Elsupikhe. M. B. Ahmad, K. Shameli, N. A. Ibrahim, N. Zainuddin, *TNANO*, 2016, *15*, 209-213.

[100] S. H. A. M. Leenders, R. Becker, T. Kumpulainen, B. de Bruin, T. Sawada, T. Kato, M. Fujita, J. N. H. Reek, *Chem. Eur. J*., 2016, *22*, 15468-15474.

[101] H. Takezawa M. Fujita, *Bull. Chem. Soc. Jpn*., 2021, *94*, 2351-2369.

[102] a) W. Ericson-Neilsen, A. D. Kaye, *Ochsner J*., 2014, *14*, 203-207; b) R. Bushra, N. Aslam, *Oman. Med. J.*, 2010, 25, 155-161.

[103] M. Salehnia, S. Zavareh, *Int. J. Fertil. Steril*., 2013, *7*, 74-81.

[104] J. J. Kim, E. C.-D. Semin. *Reprod. Med*., 2010, *28*, 81-90.

[105] S. Baik, F. F. Mehta, S.-H. Chung, *Am. J. Pathol*., 2019, *189,* 2459-2468.

[106] M.T. Taghizadeh, T. Asadpour, *Ultrason. Sonochem*., 2009, *16*, 280-286.

[107] S. P. Vijayalakshmi, G. Madras, *Polym*. *Degrad*. *Stab*. 2005, *90*, 116-122.

[108] a) T. Kusukawa, M. Fujita, *Angew. Chem. Int. Ed.*, 1998, *4,* 3142-3144; b) M. D. Plutha, K. N. Raymond, *Chem*. *Soc*. *Rev*., 2007, *36*, 161-171.

[109] PSS Polymer Standards Service GmbH, Full User's Guide PSS PROTEEMA GPC/SEC Columns.

[110] C.-C. Wang, Y.-H. Lai, Y.-M. Ou, H.-T. Chang, Y.-S Wang. *Phil. Trans. R. Soc.*, 2016, A374: 20150371.

[111] E. Schulz, M. Karas, F. Rosu, V. Gabelica, *J. Am. Soc. Mass. Spectrom*., 2006, *17*, 1005-1013.

[112] W. Li, H. Chung, C. Daeffler, J. A. Johnson, R. H. Grubbs, *Macromolecules*, 2012, *45*, 9595-9603.

[113] M. K. Beyer, *J. Chem. Phys*., 2000, *112*, 7307-7312.

[114] H. Chamkouri, M. Chamkouri, *Biomed Sci & Res*., 2021, *11*, 495-493.

[115] H. Yu, Q. Xiao, G. Qi, F. Chen, B. Tu, S. Zhang, Y. Li, Y. Chen, H. Yu, P. Duan, *Front. Bioeng. Biotechnol.*, 2022, 10:855013.

[116] M. Yamashina, S. Kusaba, M. Akita, T. Kikuchi, M. Yoshizawa, *Nat. Commun.*, 2018, *9*, 4227.

[117] E. M.Ahmed, *J. Adv. Res*., 2015, *6*, 105-121.

[118] B. Lee, Z. Niu, J. Wang, C. Slebodnick, S. L. Craig, *J. Am. Chem. Soc*., 2015, *137*, 10826-10832.

[119] M. F. Schulte, E. Izak-Nau, S. Braun, A. Pich, W. Richtering, R. Göstl, *Chem. Soc. Rev*., 2022, *51*, 2939-2956.

[120] a) M. B. Larsen, A. J. Boydston, *J. Am. Chem. Soc.*, 2013, *135*, 8189-8192; b*)* M. B. Larsen, A. J. Boydston, *J. Am. Chem. Soc.*, 2014, *136*, 1276-1279.

[121] J. T. Edward, *J. Chem. Educ.* 1970, *47*, 261-270.

[122] a) J. Kohlbrecher, A. Studer, *J. Appl. Cryst.*, 2017, *50*, 1395-1403; b) I. Bressler, J. Kohlbrecher, A. F. Thünemann, *J. Appl. Cryst.*, 2015, *48*, 1587-1598.

[123] P. G. Quintana, S. M. Romero, G. Vaamonde, A. Baldessari, *J. Mol. Catal. B Enzym*., 2013, *97*, 110-117.

[124] K. Hayamizu, O. Kamo, *Magn. Reson. Chem.*, 1990, *28*, 250-256.

[125] M.T. Ong, J. Leiding, H. Tao, A.M. Virshup, T.J. Martínez, *J. Am. Chem. Soc*., 2009, 6377-6379.

[126] P.J. Hay, W.R. Wadt, *J. Chem. Phys*., 1985, *82*, 299.

[127] S. Grimme, J. Antony, S. Ehrlich, H. Krieg, *J. Chem. Phys.,* 2010, *132*, 154104.

[128] S. Seritan, C. Bannwarth, B. S. Fales, E. G. Hohenstein, C. M. Isborn, S. I. L. Kokkila-Schumacher, X. Li., F. Liu, N. Luehr, J. W. Synder, C. Song, A. V. Titov, *WIREs Comput. Mol. Sci.*, 2020, *2*, e1494.

[129] I.S. Ufimtsev, T.J. Martínez, *J. Chem. Theory Comput*., 2008, *4*, 222-231.

[130] a) J. Kästner, J. M. Carr, T. W. Keal, W. Thiel, A. Wander, P. Sherwood, *J. Phys. Chem. A*., 2009, *113*, 11856; b) S. Metz, J. Kästner, A. A. Sokol, T. W. Keal, P. Sherwood, *WIREs Comput. Mol. Sci.* 2014, *4*, 101.

[131] TURBOMOLE V7.2 2017, a development of University of Karlsruhe and Forschungszentrum Karlsruhe GmbH, 1989-2007.

8 Selbstständigkeitserklärung

Ich versichere an Eides Statt, dass die Dissertation von mir selbständig und ohne unzulässige fremde Hilfe unter Beachtung der „Grundsätze zur Sicherung guter wissenschaftlicher Praxis an der Heinrich-Heine-Universität Düsseldorf“ erstellt worden ist.

Düsseldorf, den

Robin Küng